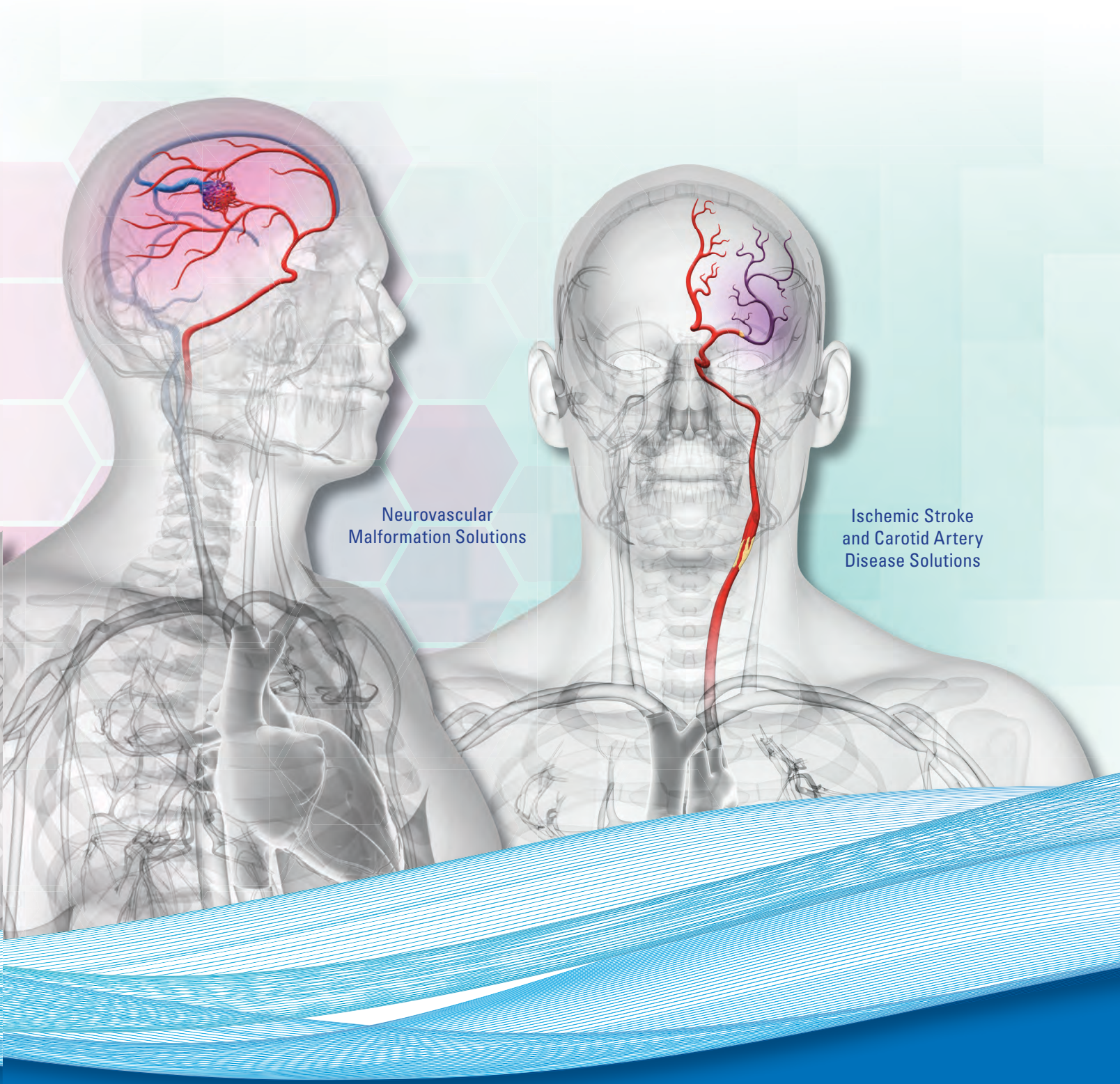


# Performance Based Solutions

**For more information or a product demonstration, contact your local MicroVention representative:**

MicroVention®
TERUMO

**MicroVention, Inc.**
**Worldwide Headquarters** PH +1.714.247.8000
1311 Valencia Avenue
Tustin, CA 92780 USA
MicroVention UK Limited PH +44 (0) 191 258 6777
MicroVention Europe, S.A.R.L. PH +33 (1) 39 21 77 46
MicroVention Deutschland GmbH PH +49 211 210 798-0

acandis®

ENGINEERING STROKE SOLUTIONS

# CREDO® Stent with NeuroSpeed® PTA Balloon Catheter

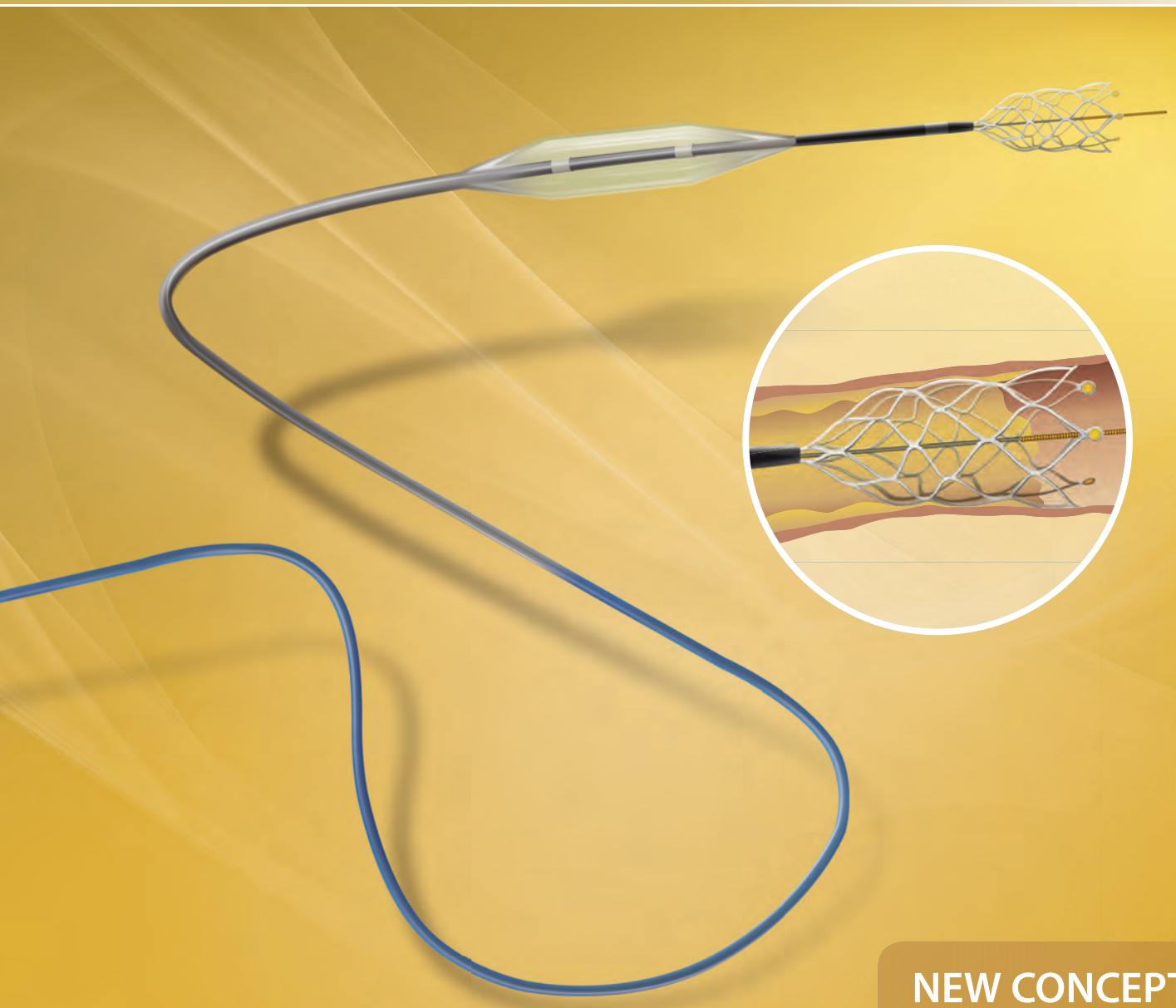

Not for sale within the territory of the United States

## NEW CONCEPT

- One access – two options
- Timesaving and effective

**CREDO® Stent** only available within **ASSISTENT – A**candi**S S**tenting of **I**ntracranial **STEN**osis-regis**T**ry

www.acandis.com

# BARRICADE™ COIL SYSTEM

## COILS THAT
# PERFORM

**Treatment and 10 Month Follow-up of Right ICA Terminus Aneurysm and Left Pcom Aneurysm**

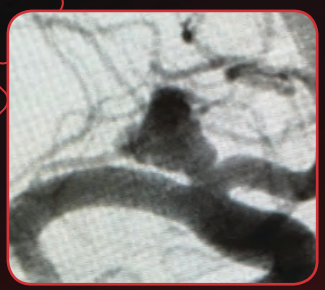

PRE-TREATMENT RIGHT ICA

POST-TREATMENT RIGHT ICA

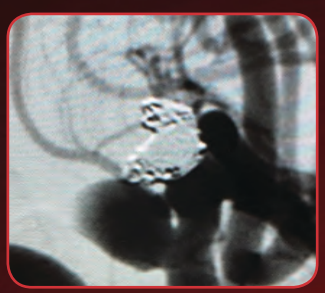

PRE-TREATMENT LEFT PCOM

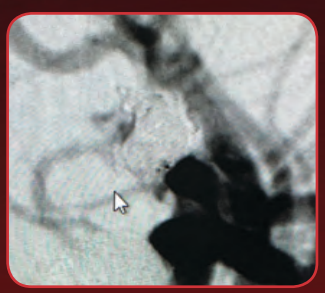

POST-TREATMENT LEFT PCOM

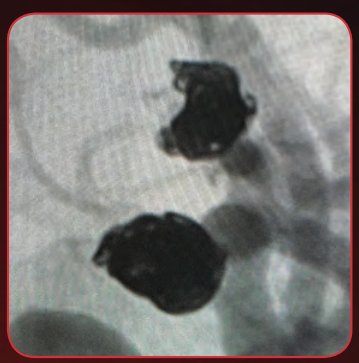

10 MONTH FOLLOW-UP

"The Barricade Coil System provided great versatility in treating these two aneurysms with diverse morphologies. I am impressed with the stable and complete occlusion of both aneurysms at follow-up."

*-Timothy Malisch, M.D.*

## COILS THAT
# SAVE $

**BARRICADE COILS SAVED $6,710***

*Images courtesy of Timothy Malisch, M.D.*

* Estimated savings in this case, data on file.

The Barricade Coil System is intended for the endovascular embolization of intracranial aneurysms and other neurovascular abnormalities such as arteriovenous malformations and arteriovenous fistulae. The System is also intended for vascular occlusion of blood vessels within the neurovascular system to permanently obstruct blood flow to an aneurysm or other vascular malformation and for arterial and venous embolizations in the peripheral vasculature. Refer to the instructions for use for complete product information.

18 TECHNOLOGY DRIVE #169, IRVINE CA 92618 | p: 949.788.1443 | f: 949.788.1444
**WWW.BLOCKADEMEDICAL.COM**

MKTG-060 Rev. A

BLOCKADE MEDICAL

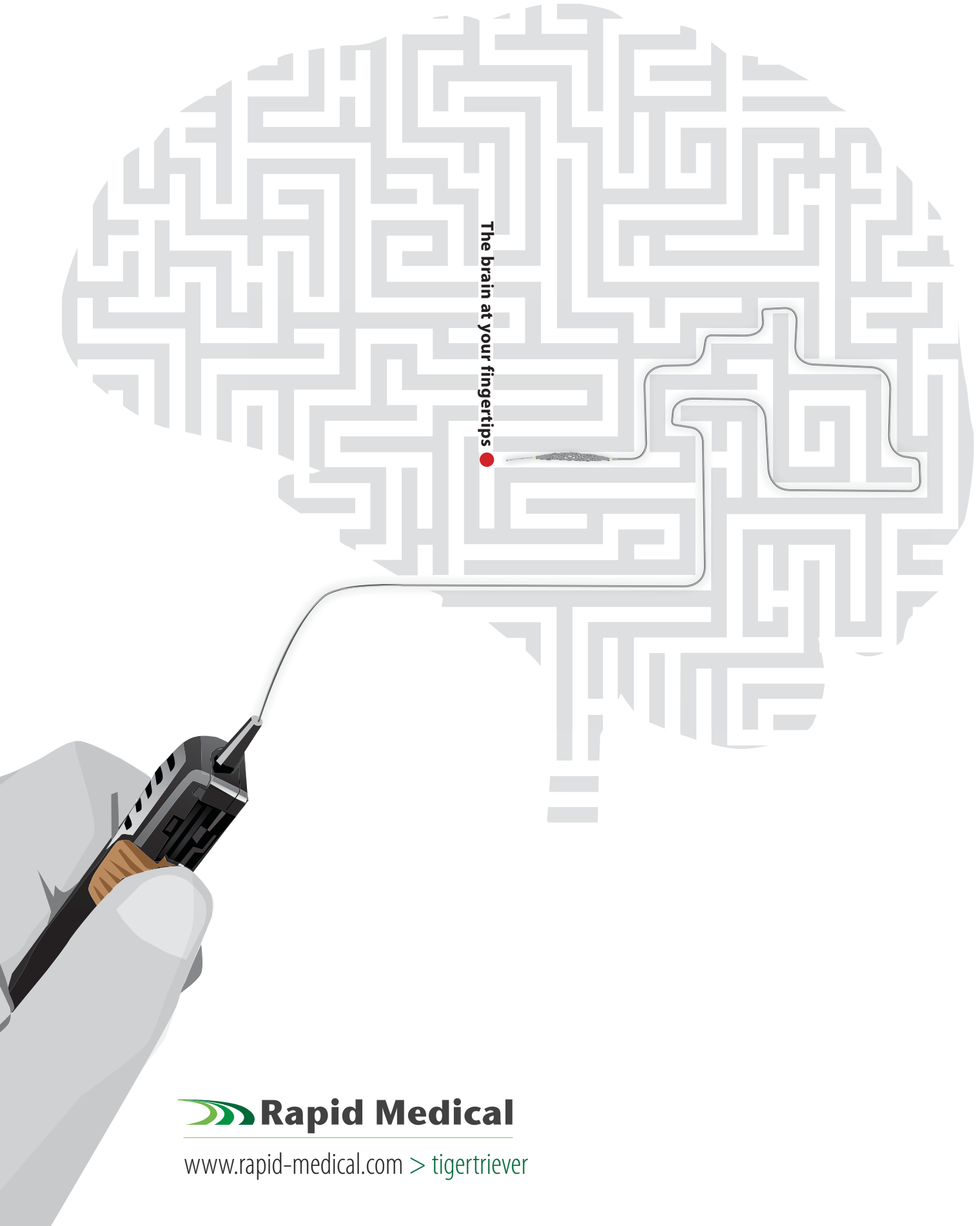


Rapid Medical

www.rapid-medical.com > tigertriever

stryker®
Neurovascular

Purposeful innovation in mind.

# Smooth and stable.

Target Detachable Coils deliver consistently smooth deployment and exceptional microcatheter stability. Designed to work seamlessly together for framing, filling and finishing. Target Coils deliver the high performance you demand.

For more information, please visit www.strykerneurovascular.com/Target or contact your local Stryker Neurovascular sales representative.

## Target®
DETACHABLE COILS

Copyright © 2016 Stryker
NV00018669.AA

AJNR

# CALL FOR AJNR EDITORIAL FELLOWSHIP CANDIDATES

**ASNR and AJNR are pleased once again to join efforts with other imaging-related journals that have training programs on editorial aspects of publishing for trainees or junior staff (3–5 years after training), including Radiology (Olmsted fellowship), AJR (Figley and Rogers fellowships), JACR (Bruce J. Hillman fellowship), and Radiologia.**

## 2017 Candidate Information and Requirements

## GOALS

- Increase interest in "editorial" and publication-related activities in younger individuals.
- Increase understanding and participation in the AJNR review process.
- Incorporate into AJNR's Editorial Board younger individuals who have previous experience in the review and publication process.
- Fill a specific need in neuroradiology not offered by other similar fellowships.
- Increase the relationship between "new" generation of neuroradiologists and more established individuals.
- Increase visibility of AJNR among younger neuroradiologists.

## ACTIVITIES OF THE FELLOWSHIP

- Serve as Editorial Fellow for one year. This individual will be listed on the masthead as such.
- Review at least one manuscript per month for 12 months. Evaluate all review articles submitted to AJNR.
- Learn how electronic manuscript review systems work.
- Be involved in the final decision of selected manuscripts together with the Editor-in-Chief.
- Participate in all monthly Senior Editor telephone conference calls.
- Participate in all meetings of the Editors and Publications Committee during the annual meetings of ASNR and RSNA as per candidate's availability. The Foundation of the ASNR will provide $2000 funding for this activity.
- Evaluate progress and adjust program to specific needs in annual meeting or telephone conference with the Editor-in-Chief.
- Embark on an editorial scientific or bibliometric project that will lead to the submission of an article to AJNR or another appropriate journal as determined by the Editor-in-Chief. This project will be presented by the Editorial Fellow at the ASNR annual meeting.
- Serve as liaison between AJNR and ASNR's Young Professionals Network and the 3 YPs appointed to AJNR as special consultants. Participate in meetings and telephone calls with this group. Design one electronic survey/year, polling the group regarding readership attitudes and wishes.
- Recruit trainees as reviewers as determined by the Editor-in-Chief.
- Participate in Web improvement projects.
- Serve as Guest Editor for an issue of AJNR's News Digest with a timely topic.

## QUALIFICATIONS

- Be a fellow in neuroradiology from North America, including Canada (this may be extended to include other countries).
- Be a junior faculty neuroradiology member (< 3 years) in either an academic or private environment.
- Be an "in-training" or member of ASNR in any other category.

## APPLICATION

- Include a short letter of intent with statement of goals and desired research project. CV must be included.
- Include a letter of recommendation from the Division Chief or fellowship program director. A statement of protected time to perform the functions outlined is desirable.
- Applications will be evaluated by AJNR's Senior Editors and the Chair of the Publications Committee prior to the ASNR meeting. The name of the selected individual will be announced at the meeting.
- Applications should be received by March 1, 2017 and sent to Ms. Karen Halm, AJNR Managing Editor, electronically at khalm@asnr.org.

Ultimate Tracking

# ONE **POWERFUL** SYSTEM

**Penumbra**

# SMART COIL®

Progressively **Soft**

Ingeniously **Practical**

Penumbra®

www.penumbrainc.com

Caution: Federal (USA) law restricts the device to sale by or on the order of a physician. Prior to use, please refer to the Instructions for Use for Penumbra System, Pump MAX and Penumbra SMART COIL System for complete product indications, contraindications, warnings, precautions, potential adverse events and detailed instructions for use. Product availability varies by country.

Copyright ©2016 Penumbra, Inc. All rights reserved. The Penumbra logo, Penumbra System, ACE, and Penumbra SMART COIL are registered trademarks or trademarks of Penumbra, Inc. in the USA and other countries.

11071, Rev. A 09/16 USA

Olea medical | Improved diagnosis for life™

# INTRODUCING THE FASTEST EVER **STROKE APPLICATIONS**

Olea Sphere

**ZERO CLICK**
**CALCULATION OF INFARCT, PENUMBRA & MISMATCH**

**AUTOMATED STROKE REPORT (MRI & CT) BY EMAIL**

**VENDOR-NEUTRAL & EASY INTEGRATION INTO IT SYSTEMS**

**FREE**
**ASK FOR A TRIAL**
**WWW.OLEA-MEDICAL.COM**

*" STROKE IS IN OUR **DNA** "*


Olea medical

**Olea Medical®**
93, avenue des Sorbiers - 13600 La Ciotat - FRANCE
TEL + 33 (0)4 42 71 24 20 - FAX +33 (0)4 42 71 24 27
contact@olea-medical.com

Olea medical USA

**Olea Medical® USA**
1955 Massachusetts Avenue Suite 12 & 14
Cambridge, MA 02140 - USA
TEL +1 (617) 354 0721 - FAX +1 (617) 812 0352
contact@olea-medical.com

# The Foundation of the ASNR Symposium 2017: *Discovery and Didactics* April 22-23, 2017

# ASNR 55th Annual Meeting: *Diagnosis and Delivery* April 24-27, 2017

Long Beach Convention & Entertainment Center
© Long Beach Convention & Visitors Bureau

**Jacqueline A. Bello, MD, FACR**
**ASNR 2017 Program Chair/President-Elect**

***Programming developed in cooperation with and appreciation of the…***

**American Society of Functional Neuroradiology (ASFNR)**
Kirk M. Welker, MD

**American Society of Head and Neck Radiology (ASHNR)**
Rebecca S. Cornelius, MD, FACR

**American Society of Pediatric Neuroradiology (ASPNR)**
Susan Palasis, MD

**American Society of Spine Radiology (ASSR)**
Joshua A. Hirsch, MD, FACR, FSIR

**Society of NeuroInterventional Surgery (SNIS)**
Blaise W. Baxter, MD

**American Society of Neuroradiology (ASNR) Health Policy Committee**
Robert M. Barr, MD, FACR

**Computer Sciences & Informatics (CSI) Committee**
John L. Go, MD, FACR

**Research Scientist Committee**
Dikoma C. Shungu, PhD and Timothy, P.L. Roberts, PhD

**The International Hydrocephalus Imaging Working Group (IHIWG)/CSF Flow Group**
William G. Bradley, Jr., MD, PhD, Harold L. Rekate, MD and Bryn A. Martin, PhD

**Abstract Deadline: Friday, December 9, 2016**
**Please visit 2017.asnr.org for more information**

**ASNR 55th Annual Meeting**
c/o American Society of Neuroradiology
800 Enterprise Drive, Suite 205 • Oak Brook, Illinois 60523-4216
Phone: 630-574-0220 • Fax: 630 574-0661 • 2017.asnr.org

2017 ASNR Long Beach, California
Discovery Didactics Diagnosis Delivery

ASFNR ASHNR ASPNR ASSR SNIS
THE FOUNDATION OF THE ASNR

**Come to the beach!** Please join us in Long Beach, California, April 22-27, 2017, for the 55th Annual Meeting of the ASNR. Known for its 5.5 miles of Pacific Ocean waterfront, this southern California beach resort boasts a blend of city sophistication and seaside serenity. ASNR is delighted to provide a **"4D"** focus for this meeting, as depicted by our meeting logo: ***Discovery and Didactics*** for The Foundation of the ASNR Symposium 2017: ***Diagnosis and Delivery*** for the ensuing Annual Meeting Program.

Centered on Discovery and Didactics, the symposium will feature sessions on "What's New?" in the role neuroimaging plays defining CNS disease mechanisms and how to best prepare for "What's Next?" for our subspecialty in terms of training, teaching, and leading the process of lifelong learning. The annual meeting programming will address best practices in Diagnosis and Delivery, as we strive to provide value, promote quality in better health and care and consider cost. Our discussions will consider how to navigate the changing landscape of healthcare reform and reimbursement as subspecialists in a field that is changing at an equally "fast forward" pace!

Hyatt Regency Long Beach
© Hyatt Regency Long Beach

Westin Long Beach
© The Westin Long Beach

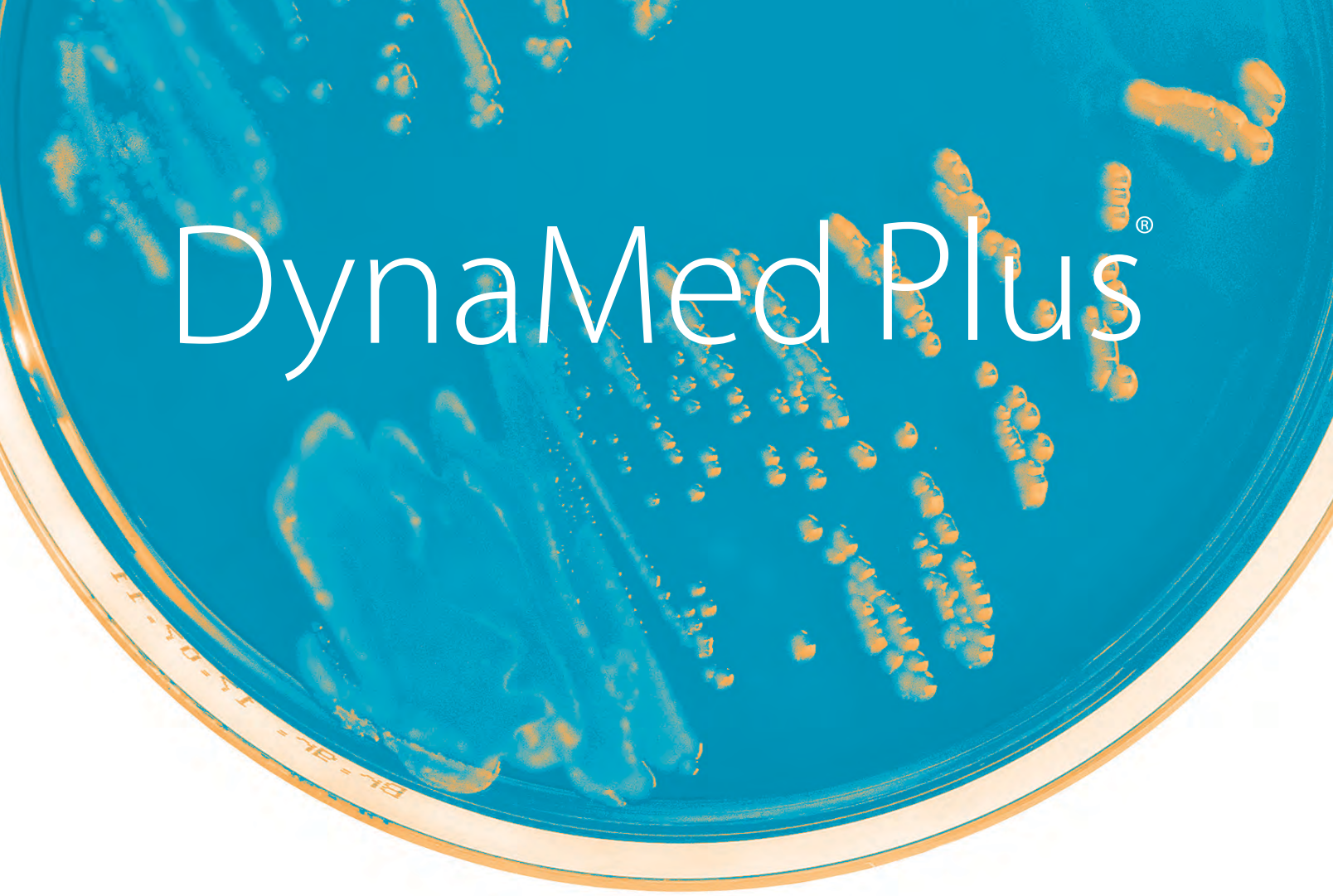


# The evidence is so clear.

*DynaMed Plus*® is a member benefit for AMA individual members and JAMA Network individual registered users

The American Medical Association and *DynaMed Plus* are joining forces. Now, AMA individual members and JAMA Network individual registered users get complimentary access to the most current clinical evidence available with *DynaMed Plus*, the next-generation clinical information resource.

Sign up today at
DynaMedPlusAMAOffer.com

AMA AMERICAN MEDICAL ASSOCIATION | JN The JAMA Network®

DynaMed Plus® EBSCO Health

## Trevo® XP ProVue Retrievers

**See package insert for complete indications, complications, warnings, and instructions for use.**

### INDICATIONS FOR USE

1. The Trevo Retriever is indicated for use to restore blood flow in the neurovasculature by removing thrombus for the treatment of acute ischemic stroke to reduce disability in patients with a persistent, proximal anterior circulation, large vessel occlusion, and smaller core infarcts who have first received intravenous tissue plasminogen activator (IV t-PA). Endovascular therapy with the device should start within 6 hours of symptom onset.
2. The Trevo Retriever is intended to restore blood flow in the neurovasculature by removing thrombus in patients experiencing ischemic stroke within 8 hours of symptom onset. Patients who are ineligible for intravenous tissue plasminogen activator (IV t-PA) or who fail IV t-PA therapy are candidates for treatment.

### COMPLICATIONS

Procedures requiring percutaneous catheter introduction should not be attempted by physicians unfamiliar with possible complications which may occur during or after the procedure. Possible complications include, but are not limited to, the following: air embolism; hematoma or hemorrhage at puncture site; infection; distal embolization; pain/headache; vessel spasm, thrombosis, dissection, or perforation; emboli; acute occlusion; ischemia; intracranial hemorrhage; false aneurysm formation; neurological deficits including stroke; and death.

### COMPATIBILITY

3x20mm retrievers are compatible with Trevo® Pro 14 Microcatheters (REF 90231) and Trevo® Pro 18 Microcatheters (REF 90238). 4x20mm retrievers are compatible with Trevo® Pro 18 Microcatheters (REF 90238). 4x30mm retrievers are compatible with Excelsior® XT-27® Microcatheters (150cm x 6cm straight REF 275081) and Trevo® Pro 18 Microcatheters (REF 90238). 6x25mm Retrievers are compatible with Excelsior® XT-27® Microcatheters (150cm x 6cm straight REF 275081). Compatibility of the Retriever with other microcatheters has not been established. Performance of the Retriever device may be impacted if a different microcatheter is used.

Balloon Guide Catheters (such as Merci® Balloon Guide Catheter and FlowGate® Balloon Guide Catheter) are recommended for use during thrombus removal procedures.

Retrievers are compatible with the Abbott Vascular DOC® Guide Wire Extension (REF 22260).

Retrievers are compatible with Boston Scientific RHV (Ref 421242).

### SPECIFIC WARNINGS FOR INDICATION 1

- The safety and effectiveness of the Trevo Retrievers in reducing disability has not been established in patients with large core infarcts (i.e., ASPECTS ≤ 7). There may be increased risks, such as intracerebral hemorrhage, in these patients.
- The safety and effectiveness of the Trevo Retrievers in reducing disability has not been established or evaluated in patients with occlusions in the posterior circulation (e.g., basilar or vertebral arteries) or for more distal occlusions in the anterior circulation.

### WARNINGS APPLIED TO BOTH INDICATIONS

- Administration of IV t-PA should be within the FDA-approved window (within 3 hours of stroke symptom onset).
- Contents supplied STERILE, using an ethylene oxide (EO) process. Nonpyrogenic.
- To reduce risk of vessel damage, adhere to the following recommendations:
  - Take care to appropriately size Retriever to vessel diameter at intended site of deployment.
  - Do not perform more than six (6) retrieval attempts in same vessel using Retriever devices.
  - Maintain Retriever position in vessel when removing or exchanging Microcatheter.
- To reduce risk of kinking/fracture, adhere to the following recommendations:
  - Immediately after unsheathing Retriever, position Microcatheter tip marker just proximal to shaped section. Maintain Microcatheter tip marker just proximal to shaped section of Retriever during manipulation and withdrawal.
  - Do not rotate or torque Retriever.
  - Use caution when passing Retriever through stented arteries.
- Do not resterilize and reuse. Structural integrity and/or function may be impaired by reuse or cleaning.
- The Retriever is a delicate instrument and should be handled carefully. Before use and when possible during procedure, inspect device carefully for damage. Do not use a device that shows signs of damage. Damage may prevent device from functioning and may cause complications.
- Do not advance or withdraw Retriever against resistance or significant vasospasm. Moving or torquing device against resistance or significant vasospasm may result in damage to vessel or device. Assess cause of resistance using fluoroscopy and if needed resheath the device to withdraw.
- If Retriever is difficult to withdraw from the vessel, do not torque Retriever. Advance Microcatheter distally, gently pull Retriever back into Microcatheter, and remove Retriever and Microcatheter as a unit. If undue resistance is met when withdrawing the Retriever into the Microcatheter, consider extending the Retriever using the Abbott Vascular DOC guidewire extension (REF 22260) so that the Microcatheter can be exchanged for a larger diameter catheter such as a DAC® catheter. Gently withdraw the Retriever into the larger diameter catheter.
- Administer anti-coagulation and anti-platelet medications per standard institutional guidelines.

### PRECAUTIONS

- Prescription only – device restricted to use by or on order of a physician.
- Store in cool, dry, dark place.
- Do not use open or damaged packages.
- Use by "Use By" date.
- Exposure to temperatures above 54°C (130°F) may damage device and accessories. Do not autoclave.
- Do not expose Retriever to solvents.
- Use Retriever in conjunction with fluoroscopic visualization and proper anti-coagulation agents.
- To prevent thrombus formation and contrast media crystal formation, maintain a constant infusion of appropriate flush solution between guide catheter and Microcatheter and between Microcatheter and Retriever or guidewire.
- Do not attach a torque device to the shaped proximal end of DOC® Compatible Retriever. Damage may occur, preventing ability to attach DOC® Guide Wire Extension.

**Concentric Medical**
301 East Evelyn Avenue
Mountain View, CA 94041

**Stryker Neurovascular**
47900 Bayside Parkway
Fremont, CA 94538

**strykerneurovascular.com**

Date of Release: SEP/2016

EX_EN_US

Copyright © 2016 Stryker
NV00018973.AB

## Target® Detachable Coil

**See package insert for complete indications, contraindications, warnings and instructions for use.**

### INTENDED USE / INDICATIONS FOR USE

Target Detachable Coils are intended to endovascularly obstruct or occlude blood flow in vascular abnormalities of the neurovascular and peripheral vessels.

Target Detachable Coils are indicated for endovascular embolization of:

- Intracranial aneurysms
- Other neurovascular abnormalities such as arteriovenous malformations and arteriovenous fistulae
- Arterial and venous embolizations in the peripheral vasculature

### CONTRAINDICATIONS

None known.

### POTENTIAL ADVERSE EVENTS

Potential complications include, but are not limited to: allergic reaction, aneurysm perforation and rupture, arrhythmia, death, edema, embolus, headache, hemorrhage, infection, ischemia, neurological/intracranial sequelae, post-embolization syndrome (fever, increased white blood cell count, discomfort), TIA/stroke, vasospasm, vessel occlusion or closure, vessel perforation, dissection, trauma or damage, vessel rupture, vessel thrombosis. Other procedural complications including but not limited to: anesthetic and contrast media risks, hypotension, hypertension, access site complications.

### WARNINGS

- Contents supplied STERILE using an ethylene oxide (EO) process. Do not use if sterile barrier is damaged. If damage is found, call your Stryker Neurovascular representative.
- For single use only. Do not reuse, reprocess or resterilize. Reuse, reprocessing or resterilization may compromise the structural integrity of the device and/or lead to device failure which, in turn, may result in patient injury, illness or death. Reuse, reprocessing or resterilization may also create a risk of contamination of the device and/or cause patient infection or cross-infection, including, but not limited to, the transmission of infectious disease(s) from one patient to another. Contamination of the device may lead to injury, illness or death of the patient.
- After use, dispose of product and packaging in accordance with hospital, administrative and/or local government policy.
- **This device should only be used by physicians who have received appropriate training in interventional neuroradiology or interventional radiology and preclinical training on the use of this device as established by Stryker Neurovascular.**
- Patients with hypersensitivity to 316LVM stainless steel may suffer an allergic reaction to this implant.
- MR temperature testing was not conducted in peripheral vasculature, arteriovenous malformations or fistulae models.
- The safety and performance characteristics of the Target Detachable Coil System (Target Detachable Coils, InZone Detachment Systems, delivery systems and accessories) have not been demonstrated with other manufacturer's devices (whether coils, coil delivery devices, coil detachment systems, catheters, guidewires, and/or other accessories). Due to the potential incompatibility of non Stryker Neurovascular devices with the Target Detachable Coil System, the use of other manufacturer's device(s) with the Target Detachable Coil System is not recommended.
- To reduce risk of coil migration, the diameter of the first and second coil should never be less than the width of the ostium.
- In order to achieve optimal performance of the Target Detachable Coil System and to reduce the risk of thromboembolic complications, it is critical that a continuous infusion of appropriate flush solution be maintained between a) the femoral sheath and guiding catheter, b) the 2-tip microcatheter and guiding catheters, and c) the 2-tip microcatheter and Stryker Neurovascular guidewire and delivery wire. Continuous flush also reduces the potential for thrombus formation on, and crystallization of infusate around, the detachment zone of the Target Detachable Coil.
- Do not use the product after the "Use By" date specified on the package.
- Reuse of the flush port/dispenser coil or use with any coil other than the original coil may result in contamination of, or damage to, the coil.
- Utilization of damaged coils may affect coil delivery to, and stability inside, the vessel or aneurysm, possibly resulting in coil migration and/or stretching.
- The fluoro-saver marker is designed for use with a Rotating Hemostatic Valve (RHV). If used without an RHV, the distal end of the coil may be beyond the alignment marker when the fluoro-saver marker reaches the microcatheter hub.
- If the fluoro-saver marker is not visible, do not advance the coil without fluoroscopy.
- Do not rotate delivery wire during or after delivery of the coil. Rotating the Target Detachable Coil delivery wire may result in a stretched coil or premature detachment of the coil from the delivery wire, which could result in coil migration.
- Verify there is no coil loop protrusion into the parent vessel after coil placement and prior to coil detachment. Coil loop protrusion after coil placement may result in thromboembolic events if the coil is detached.
- Verify there is no movement of the coil after coil placement and prior to coil detachment. Movement of the coil after coil placement may indicate that the coil could migrate once it is detached.
- Failure to properly close the RHV compression fitting over the delivery wire before attaching the InZone® Detachment System could result in coil movement, aneurysm rupture or vessel perforation.
- Verify repeatedly that the distal shaft of the catheter is not under stress before detaching the Target Detachable Coil. Axial compression or tension forces could be stored in the 2-tip microcatheter causing the tip to move during coil delivery. Microcatheter tip movement could cause the aneurysm or vessel to rupture.
- Advancing the delivery wire beyond the microcatheter tip once the coil has been detached involves risk of aneurysm or vessel perforation.
- The long term effect of this product on extravascular tissues has not been established so care should be taken to retain this device in the intravascular space.

Damaged delivery wires may cause detachment failures, vessel injury or unpredictable distal tip response during coil deployment. If a delivery wire is damaged at any point during the procedure, do not attempt to straighten or otherwise repair it. Do not proceed with deployment or detachment. Remove the entire coil and replace with undamaged product.

- After use, dispose of product and packaging in accordance with hospital, administrative and/or local government policy.

### CAUTIONS / PRECAUTIONS

- Federal Law (USA) restricts this device to sale by or on the order of a physician.
- Besides the number of InZone Detachment System units needed to complete the case, there must be an extra InZone Detachment System unit as back up.
- Removing the delivery wire without grasping the introducer sheath and delivery wire together may result in the detachable coil sliding out of the introducer sheath.
- Failure to remove the introducer sheath after inserting the delivery wire into the RHV of the microcatheter will interrupt normal infusion of flush solution and allow back flow of blood into the microcatheter.
- Some low level overhead light near or adjacent to the patient is required to visualize the fluoro-saver marker; monitor light alone will not allow sufficient visualization of the fluoro-saver marker.
- Advance and retract the Target Detachable Coil carefully and smoothly without excessive force. If unusual friction is noticed, slowly withdraw the Target Detachable Coil and examine for damage. If damage is present, remove and use a new Target Detachable Coil. If friction or resistance is still noted, carefully remove the Target Detachable Coil and microcatheter and examine the microcatheter for damage.
- If it is necessary to reposition the Target Detachable Coil, verify under fluoroscopy that the coil moves with a one-to-one motion. If the coil does not move with a one-to-one motion or movement is difficult, the coil may have stretched and could possibly migrate or break. Gently remove both the coil and microcatheter and replace with new devices.
- Increased detachment times may occur when:
  - Other embolic agents are present.
  - Delivery wire and microcatheter markers are not properly aligned.
  - Thrombus is present on the coil detachment zone.
- Do not use detachment systems other than the InZone Detachment System.
- Increased detachment times may occur when delivery wire and microcatheter markers are not properly aligned.
- Do not use detachment systems other than the InZone Detachment System.

**Stryker Neurovascular**
47900 Bayside Parkway
Fremont, CA 94538

**strykerneurovascular.com**

Date of Release: MAR/2016

EX_EN_US

Copyright © 2016 Stryker
NV00018669.AB

MicroVention®
TERUMO

*Leading the Way*
*in Neuroendovascular Therapy*

Aneurysm
Therapy Solutions

# A 360-Degree Approach to

**microvention.com**

MICROVENTION is a registered trademark of MicroVention, Inc. Refer to Instructions for Use for additional information.
© 2016 MicroVention, Inc. 08/16

stryker

# NEW

## Indication for Trevo® Retrievers

### A New Standard of Care in Stroke

1st

**FIRST**
mechanical thrombectomy device indicated to reduce disability in stroke.*

**FIRST**
new treatment indication for stroke in 20 years.

## Trevo XP
PROVUE RETRIEVER

Success accelerated.

*The Trevo Retriever is indicated for use to restore blood flow in the neurovasculature by removing thrombus for the treatment of acute ischemic stroke to reduce disability in patients with a persistent, proximal anterior circulation, large vessel occlusion, and smaller core infarcts who have first received intravenous tissue plasminogen activator (IV t-PA). Endovascular therapy with the device should start within 6 hours of symptom onset.

Copyright © 2016 Stryker
NV00018973.AB

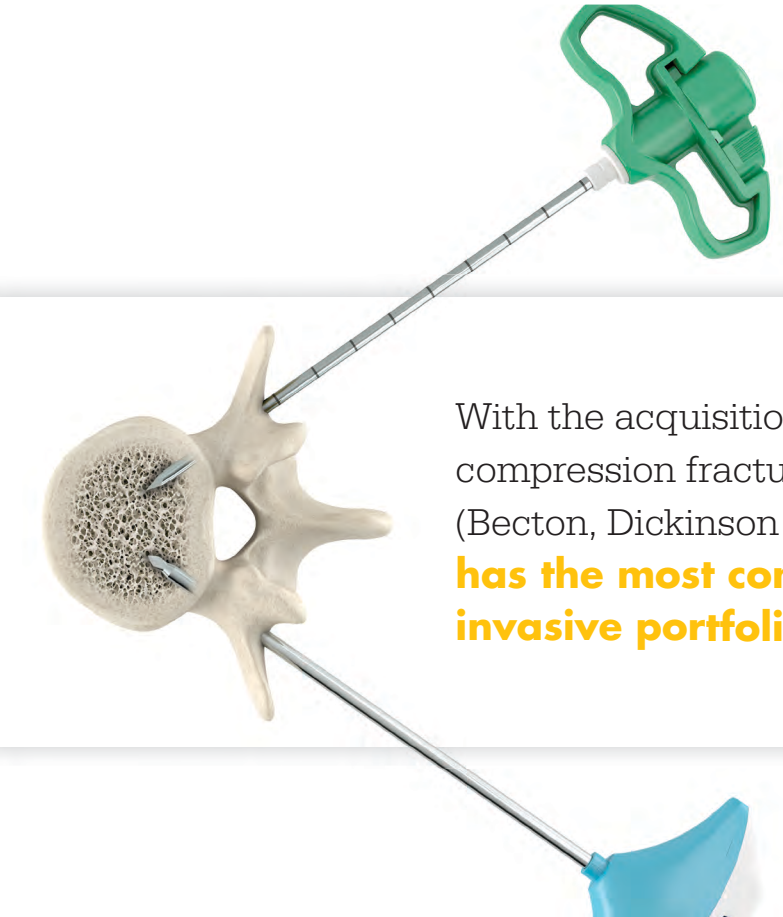

stryker

With the acquisition of the CareFusion vertebral compression fracture (VCF) portfolio from BD (Becton, Dickinson and Company), **Stryker has the most comprehensive and least invasive portfolio** of VCF treatment options

# Celebrating two years of **excellence**

An elegant, cost effective approach to large lesions. The **Venom Cannula and Electrode combination** celebrates **two years of excellence** in helping you achieve larger RF lesions[1] to treat your patients suffering from chronic pain.

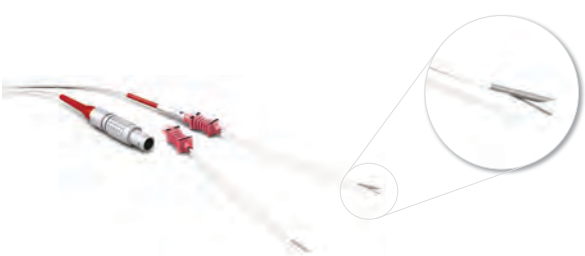

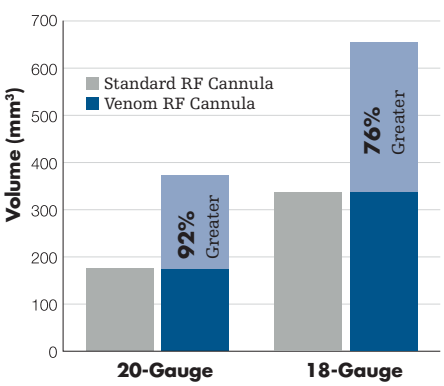


Stryker Corporation or its divisions or other corporate affiliated entities own, use or have applied for the following trademark: Venom. All other trademarks are trademarks of their respective owners or holders.

The information presented in this overview is intended to demonstrate the breadth of Stryker product offerings. Always refer to the package insert, product label and/or user instructions before using any Stryker product. Products may not be available in all markets. Product availability is subject to the regulatory or medical practices that govern individual markets. Please contact your Stryker representative if you have questions about the availability of Stryker products in your area.

1 Effect of the Stryker Venom Cannula and Venom Electrode combination on Lesion Size and Anesthesia Delivery During Radiofrequency Ablation Stryker Instruments, 4100 East Milham Avenue, Kalamazoo, Michigan 49001.

**strykerIVS.com**

1000-025-340 Rev C

# AJNR

## AMERICAN JOURNAL OF NEURORADIOLOGY

OCTOBER 2016
VOLUME 37
NUMBER 10
WWW.AJNR.ORG

THE JOURNAL OF DIAGNOSTIC AND INTERVENTIONAL NEURORADIOLOGY

Quantitative susceptibility mapping in MS
Ocular signs from dural fistula that do not involve cavernous sinus
*SMARCB1* (INI1)-deficient sinonasal carcinoma

Official Journal ASNR • ASFNR • ASHNR • ASPNR • ASSR

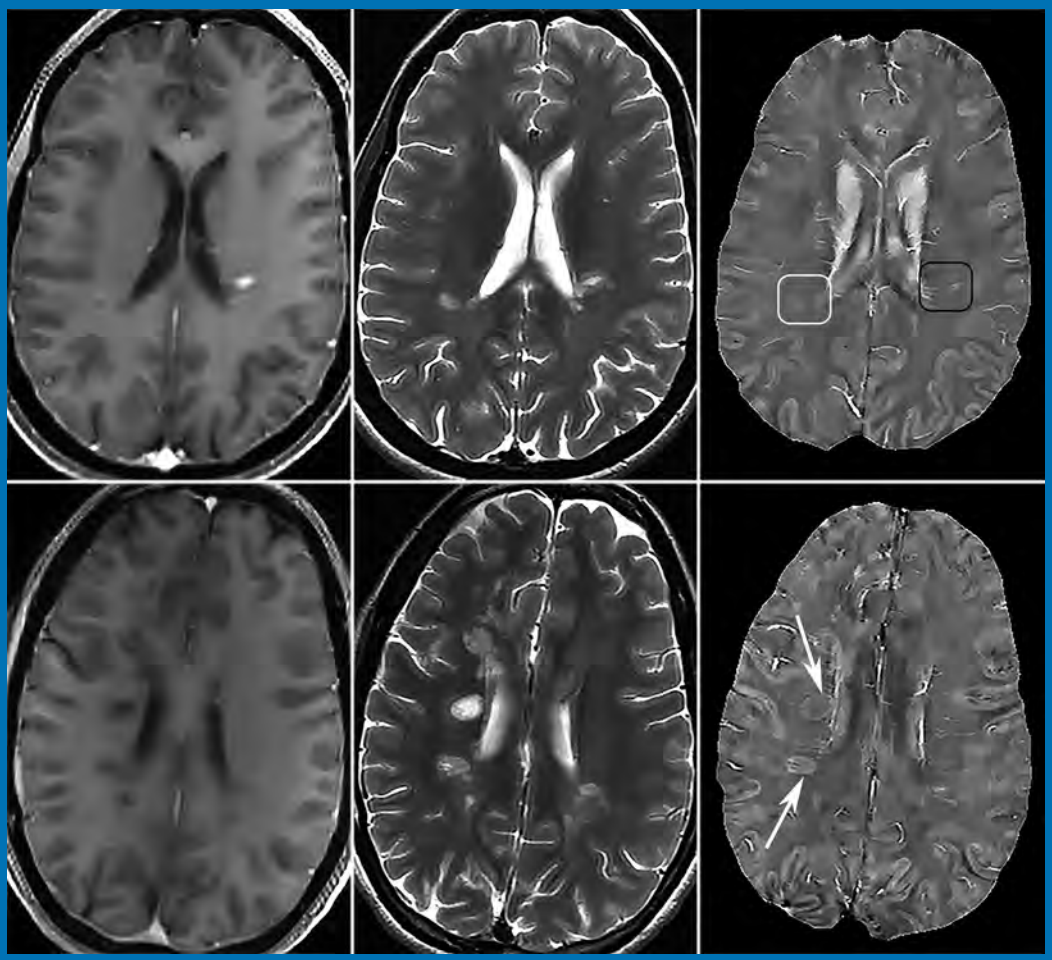

AJNR

AMERICAN JOURNAL OF NEURORADIOLOGY

OCTOBER 2016
VOLUME 37
NUMBER 10
WWW.AJNR.ORG

Publication Preview at www.ajnr.org features articles released in advance of print. Visit www.ajnrblog.org to comment on AJNR content and chat with colleagues and AJNR's News Digest at http://ajnrdigest.org to read the stories behind the latest research in neuroimaging.

1763 **PERSPECTIVES** *S. Mukherjee*

**EDITORIAL**

1764 **Neuroimaging Findings in Congenital Zika Syndrome** *A. Poretti, et al.*

**REVIEW ARTICLE**

1766 **Brain Perfusion Imaging in Neonates: An Overview** *M. Proisy, et al.* **PEDIATRICS**

**PATIENT SAFETY**

1774 **Cerebral CTA with Low Tube Voltage and Low Contrast Material Volume for Detection of Intracranial Aneurysms** *Q.Q. Ni, et al.* **ADULT BRAIN**

**GENERAL CONTENTS**

1781 **Effect of CTA Tube Current on Spot Sign Detection and Accuracy for Prediction of Intracerebral Hemorrhage Expansion** *A. Morotti, et al.* **ADULT BRAIN**

1787 **Discordant Observation of Brain Injury by MRI and Malignant Electroencephalography Patterns in Comatose Survivors of Cardiac Arrest following Therapeutic Hypothermia** *J.M. Mettenburg, et al.* **ADULT BRAIN**

1794 **Magnetic Susceptibility from Quantitative Susceptibility Mapping Can Differentiate New Enhancing from Nonenhancing Multiple Sclerosis Lesions without Gadolinium Injection** *Y. Zhang, et al.* **ADULT BRAIN**

1800 **Regional Frontal Perfusion Deficits in Relapsing-Remitting Multiple Sclerosis with Cognitive Decline** *R. Vitorino, et al.* **ADULT BRAIN**

1808 **In Vivo 7T MR Quantitative Susceptibility Mapping Reveals Opposite Susceptibility Contrast between Cortical and White Matter Lesions in Multiple Sclerosis** *W. Bian, et al.* **ADULT BRAIN**

1816 **Improved Automatic Detection of New T2 Lesions in Multiple Sclerosis Using Deformation Fields** *M. Cabezas, et al.* **ADULT BRAIN**

1824 **White Matter Hyperintensity Volume and Cerebral Perfusion in Older Individuals with Hypertension Using Arterial Spin-Labeling** *J.W. van Dalen, et al.* **ADULT BRAIN**

1831 **High-Convexity Tightness Predicts the Shunt Response in Idiopathic Normal Pressure Hydrocephalus** *W. Narita, et al.* **ADULT BRAIN**

**AJNR (Am J Neuroradiol** ISSN 0195–6108) is a journal published monthly, owned and published by the American Society of Neuroradiology (ASNR), 800 Enterprise Drive, Suite 205, Oak Brook, IL 60523. Annual dues for the ASNR include $170.00 for journal subscription. The journal is printed by Cadmus Journal Services, 5457 Twin Knolls Road, Suite 200, Columbia, MD 21045; Periodicals postage paid at Oak Brook, IL and additional mailing offices. Printed in the U.S.A. POSTMASTER: Please send address changes to American Journal of Neuroradiology, P.O. Box 3000, Denville, NJ 07834, U.S.A. Subscription rates: nonmember $390 ($460 foreign) print and online, $310 online only; institutions $450 ($520 foreign) print and basic online, $895 ($960 foreign) print and extended online, $370 online only (basic), extended online $805; single copies are $35 each ($40 foreign). Indexed by PubMed/Medline, BIOSIS Previews, Current Contents (Clinical Medicine and Life Sciences), EMBASE, Google Scholar, HighWire Press, Q-Sensei, RefSeek, Science Citation Index, and SCI Expanded. Copyright © American Society of Neuroradiology.

1838 **Dynamic Susceptibility Contrast-Enhanced MR Perfusion Imaging in Assessing Recurrent Glioblastoma Response to Superselective Intra-Arterial Bevacizumab Therapy** *R. Singh, et al.* — ADULT BRAIN

1844 **Differentiating Hemangioblastomas from Brain Metastases Using Diffusion-Weighted Imaging and Dynamic Susceptibility Contrast-Enhanced Perfusion-Weighted MR Imaging** *D. She, et al.* — ADULT BRAIN

1851 **Shear Stiffness of 4 Common Intracranial Tumors Measured Using MR Elastography: Comparison with Intraoperative Consistency Grading** *N. Sakai, et al.* — ADULT BRAIN

1860 **A Direct Aspiration, First Pass Technique (ADAPT) versus Stent Retrievers for Acute Stroke Therapy: An Observational Comparative Study** *B. Lapergue, et al.* — INTERVENTIONAL

1866 **Flow Diversion for Ophthalmic Artery Aneurysms** *A.M. Burrows, et al.* — INTERVENTIONAL

1870 **Ocular Signs Caused by Dural Arteriovenous Fistula without Involvement of the Cavernous Sinus: A Case Series with Review of the Literature** *T. Robert, et al.* — INTERVENTIONAL

1876 **Computational Modeling of Venous Sinus Stenosis in Idiopathic Intracranial Hypertension** *M.R. Levitt, et al.* — INTERVENTIONAL

1883 **Peritherapeutic Hemodynamic Changes of Carotid Stenting Evaluated with Quantitative DSA in Patients with Carotid Stenosis** *M.M.H. Teng, et al.* — INTERVENTIONAL, EXTRACRANIAL VASCULAR

1889 **Intervention versus Aggressive Medical Therapy for Cognition in Severe Asymptomatic Carotid Stenosis** *C.-J. Lin, et al.* — EXTRACRANIAL VASCULAR

1898 **Clinical Significance of the Champagne Bottle Neck Sign in the Extracranial Carotid Arteries of Patients with Moyamoya Disease** *C. Yasuda, et al.* — EXTRACRANIAL VASCULAR

1903 **Blood-Labyrinth Barrier Permeability in Menière Disease and Idiopathic Sudden Sensorineural Hearing Loss: Findings on Delayed Postcontrast 3D-FLAIR MRI** *M.N. Pakdaman, et al.* — HEAD & NECK

1909 **Evaluating Instantaneous Perfusion Responses of Parotid Glands to Gustatory Stimulation Using High-Temporal-Resolution Echo-Planar Diffusion-Weighted Imaging** *T.-W. Chiu, et al.* — HEAD & NECK

1916 **The CT Prevalence of Arrested Pneumatization of the Sphenoid Sinus in Patients with Sickle Cell Disease** *A.V. Prabhu, et al.* — HEAD & NECK

1920 **High-Resolution MRI Findings following Trigeminal Rhizotomy** *B.G. Northcutt, et al.* — HEAD & NECK

1925 **Imaging Appearance of *SMARCB1* (INI1)-Deficient Sinonasal Carcinoma: A Newly Described Sinonasal Malignancy** *D.R. Shatzkes, et al.* — HEAD & NECK

1930 **MRI Evaluation of Non-Necrotic T2-Hyperintense Foci in Pediatric Diffuse Intrinsic Pontine Glioma** *O. Clerk-Lamalice, et al.* — PEDIATRICS

1938 **Volumetric Description of Brain Atrophy in Neuronal Ceroid Lipofuscinosis 2: Supratentorial Gray Matter Shows Uniform Disease Progression** *U. Löbel, et al.* — PEDIATRICS

1944 **MR Imaging of the Cervical Spine in Nonaccidental Trauma: A Tertiary Institution Experience** *R. Jacob, et al.* — PEDIATRICS, SPINE

1951 **CT Fluoroscopy–Guided Blood Patching of Ventral CSF Leaks by Direct Needle Placement in the Ventral Epidural Space Using a Transforaminal Approach** *T.J. Amrhein, et al.* — SPINE

1957 **Automated Quantitation of Spinal CSF Volume and Measurement of Craniospinal CSF Redistribution following Lumbar Withdrawal in Idiopathic Intracranial Hypertension** *N. Alperin, et al.* — SPINE

## ONLINE FEATURES

### LETTERS


**E63** **Dual-Energy CT and Spot Sign** *M.I. Vargas, et al.*

**E64** ***Reply*** *A. Morotti, et al.*

**E65** **Comment on "SAPHO Syndrome: Imaging Findings of Vertebral Involvement"** *M. Colina*

**E67** ***Reply*** *A.M. McGauvran, et al.*

**E68** **Synthetic MR Imaging Sequence in Daily Clinical Practice** *M.I. Vargas, et al.*

**E70** ***Reply*** *T. Granberg*


### BOOK REVIEWS *R.M. Quencer, Section Editor*

Please visit www.ajnrblog.org to read and comment on Book Reviews.

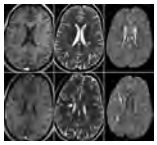

Comparison of new enhancing MS lesions (top row) and new nonenhancing MS lesions (bottom row) on T1-weighted enhanced (left), T2-weighted (middle), and quantitative susceptibility mapped images (right). New nonenhancing lesions show QSM hyperintensity with bright rims.

Indicates Editor's Choices selection

Indicates Fellows' Journal Club selection

Indicates open access to non-subscribers at www.ajnr.org

Indicates article with supplemental on-line table

Indicates article with supplemental on-line photo

Indicates article with supplemental on-line video

Evidence-Based Medicine Level 1

Evidence-Based Medicine Level 2

AJNR

# AMERICAN JOURNAL OF NEURORADIOLOGY

Publication Preview at www.ajnr.org features articles released in advance of print. Visit www.ajnrblog.org to comment on AJNR content and chat with colleagues and AJNR's News Digest at http://ajnrdigest.org to read the stories behind the latest research in neuroimaging.

OCTOBER 2016 • VOLUME 37 • NUMBER 10 • WWW.AJNR.ORG

**Official Journal:**
American Society of Neuroradiology
American Society of Functional Neuroradiology
American Society of Head and Neck Radiology
American Society of Pediatric Neuroradiology
American Society of Spine Radiology

**EDITOR-IN-CHIEF**

**Jeffrey S. Ross, MD**
*Professor of Radiology, Department of Radiology, Mayo Clinic College of Medicine, Phoenix, AZ*

**SENIOR EDITORS**

**Harry J. Cloft, MD, PhD**
Professor of Radiology and Neurosurgery, Department of Radiology, Mayo Clinic College of Medicine, Rochester, MN

**Thierry A.G.M. Huisman, MD**
Professor of Radiology, Pediatrics, Neurology, and Neurosurgery, Chairman, Department of Imaging and Imaging Science, Johns Hopkins Bayview, Director, Pediatric Radiology and Pediatric Neuroradiology, Johns Hopkins Hospital, Baltimore, MD

**C.D. Phillips, MD, FACR**
Professor of Radiology, Weill Cornell Medical College, Director of Head and Neck Imaging, New York-Presbyterian Hospital, New York, NY

**Pamela W. Schaefer, MD**
Clinical Director of MRI and Associate Director of Neuroradiology, Massachusetts General Hospital, Boston, Massachusetts, Associate Professor, Radiology, Harvard Medical School, Cambridge, MA

**Charles M. Strother, MD**
Professor of Radiology, Emeritus, University of Wisconsin, Madison, WI

**Jody Tanabe, MD**
Professor of Radiology and Psychiatry, Chief of Neuroradiology, University of Colorado, Denver, CO

**STATISTICAL SENIOR EDITOR**

**Bryan A. Comstock, MS**
Senior Biostatistician, Department of Biostatistics, University of Washington, Seattle, WA

**EDITORIAL BOARD**
Ashley H. Aiken, *Atlanta, GA*
Lea M. Alhilali, *Phoenix, AZ*
John D. Barr, *Dallas, TX*
Ari Blitz, *Baltimore, MD*
Barton F. Branstetter IV, *Pittsburgh, PA*
Jonathan L. Brisman, *Lake Success, NY*
Julie Bykowski, *San Diego, CA*
Keith Cauley, *Danville, PA*
Asim F. Choudhri, *Memphis, TN*
Alessandro Cianfoni, *Lugano, Switzerland*
J. Matthew Debnam, *Houston, TX*
Seena Dehkharghani, *New York, NY*
Colin Derdeyn, *Iowa City, IA*
Rahul S. Desikan, *San Francisco, CA*
Yonghong Ding, *Rochester, MN*
Clifford J. Eskey, *Hanover, NH*
Saeed Fakhran, *Phoenix, AZ*
Massimo Filippi, *Milan, Italy*
Allan J. Fox, *Toronto, Ontario, Canada*
Wende N. Gibbs, *Los Angeles, CA*
Christine M. Glastonbury, *San Francisco, CA*
John L. Go, *Los Angeles, CA*
Allison Grayev, *Madison, WI*
Brent Griffith, *Detroit, MI*
Wan-Yuo Guo, *Taipei, Taiwan*
Ajay Gupta, *New York, NY*
Rakesh K. Gupta, *Lucknow, India*
Lotfi Hacein-Bey, *Sacramento, CA*
Christopher P. Hess, *San Francisco, CA*
Andrei Holodny, *New York, NY*
Benjamin Huang, *Chapel Hill, NC*
George J. Hunter, *Boston, MA*
Mahesh V. Jayaraman, *Providence, RI*
Valerie Jewells, *Chapel Hill, NC*
Christof Karmonik, *Houston, TX*
Timothy J. Kaufmann, *Rochester, MN*
Hillary R. Kelly, *Boston, MA*
Toshibumi Kinoshita, *Akita, Japan*
Kennith F. Layton, *Dallas, TX*
Michael M. Lell, *Nürnberg, Germany*
Michael Lev, *Boston, MA*
Karl-Olof Lovblad, *Geneva, Switzerland*
Franklin A. Marden, *Chicago, IL*
M. Gisele Matheus, *Charleston, SC*
Joseph C. McGowan, *Merion Station, PA*
Stephan Meckel, *Freiburg, Germany*
Christopher J. Moran, *St. Louis, MO*
Takahisa Mori, *Kamakura City, Japan*
Suresh Mukherji, *Ann Arbor, MI*
Amanda Murphy, *Toronto, Ontario, Canada*
Alexander J. Nemeth, *Chicago, IL*
Sasan Partovi, *Cleveland, OH*
Laurent Pierot, *Reims, France*
Jay J. Pillai, *Baltimore, MD*
Whitney B. Pope, *Los Angeles, CA*
Andrea Poretti, *Baltimore, MD*
M. Judith Donovan Post, *Miami, FL*
Tina Young Poussaint, *Boston, MA*
Joana Ramalho, *Lisbon, Portugal*
Otto Rapalino, *Boston, MA*
Álex Rovira-Cañellas, *Barcelona, Spain*
Paul M. Ruggieri, *Cleveland, OH*
Zoran Rumboldt, *Rijeka, Croatia*
Amit M. Saindane, *Atlanta, GA*
Erin Simon Schwartz, *Philadelphia, PA*
Lubdha M. Shah, *Salt Lake City, UT*
Aseem Sharma, *St. Louis, MO*
J. Keith Smith, *Chapel Hill, NC*
Maria Vittoria Spampinato, *Charleston, SC*
Gordon K. Sze, *New Haven, CT*
Krishnamoorthy Thamburaj, *Hershey, PA*
Cheng Hong Toh, *Taipei, Taiwan*
Thomas A. Tomsick, *Cincinnati, OH*
Aquilla S. Turk, *Charleston, SC*
Willem Jan van Rooij, *Tilburg, Netherlands*
Arastoo Vossough, *Philadelphia, PA*
Elysa Widjaja, *Toronto, Ontario, Canada*
Max Wintermark, *Stanford, CA*
Ronald L. Wolf, *Philadelphia, PA*
Kei Yamada, *Kyoto, Japan*
Carlos Zamora, *Chapel Hill, NC*

**EDITORIAL FELLOW**
Daniel S. Chow, *San Francisco, CA*

**SPECIAL CONSULTANTS TO THE EDITOR**
**AJNR Blog Editor**
Neil Lall, *Denver, CO*
**Case of the Month Editor**
Nicholas Stence, *Aurora, CO*
**Case of the Week Editors**
Juan Pablo Cruz, *Santiago, Chile*
Sapna Rawal, *Toronto, Ontario, Canada*
**Classic Case Editor**
Sandy Cheng-Yu Chen, *Taipei, Taiwan*
**Facebook Editor**
Peter Yi Shen, *Sacramento, CA*
**Health Care and Socioeconomics Editor**
Pina C. Sanelli, *New York, NY*
**Physics Editor**
Greg Zaharchuk, *Stanford, CA*
**Podcast Editor**
Yvonne Lui, *New York, NY*
**Twitter Editor**
Ryan Fitzgerald, *Little Rock, AR*

**YOUNG PROFESSIONALS ADVISORY COMMITTEE**
Asim K. Bag, *Birmingham, AL*
Anna E. Nidecker, *Sacramento, CA*
Peter Yi Shen, *Sacramento, CA*

*Founding Editor*
Juan M. Taveras
*Editors Emeriti*
Mauricio Castillo, Robert I. Grossman, Michael S. Huckman, Robert M. Quencer

*Managing Editor*
Karen Halm
*Assistant Managing Editor*
Laura Wilhelm
*Executive Director, ASNR*
James B. Gantenberg
*Director of Communications, ASNR*
Angelo Artemakis

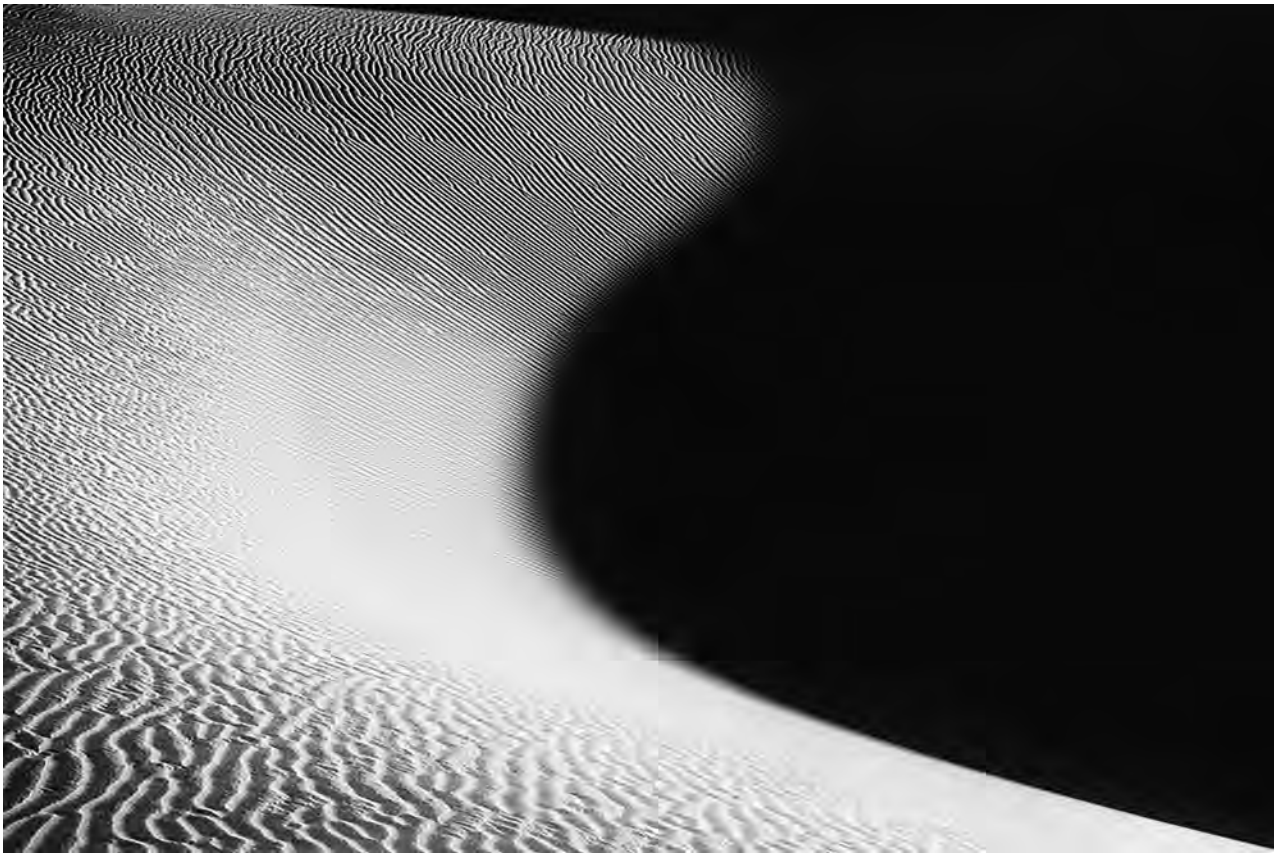

Title: Ying and Yang, Death Valley National Park, California. Death Valley is a place of incredible diversity in landscapes. The Mesquite Flat Sand Dunes represent an endless opportunity in capturing the ephemeral interplay of light and patterns.

*Sugoto Mukherjee, Associate Professor, Division of Neuroradiology, Department of Radiology and Medical Imaging, University of Virginia Health System, Charlottesville, Virginia*

# Neuroimaging Findings in Congenital Zika Syndrome

A. Poretti and T.A.G.M. Huisman

Since the early 2015 outbreak of the Zika virus, an arbovirus originally identified in Africa and Asia-Pacific and transmitted by *Aedes aegypti* mosquitoes, the virus has spread rapidly from Pernambuco State throughout Brazil and the Americas. In Brazil, more than 30,000 clinical cases have been reported so far.[1] While the total number of infected individuals is unknown, it is expected to reach more than 1 million in the next year.[2] In addition, the virus has been disseminated outside Brazil, and cases of Zika virus infection have been reported in 25 countries in the Americas, Africa, and Asia. The outbreak of Zika virus infection in Brazil was associated with an increase in congenital microcephaly by a factor of 20.[2] The suspected causal relationship between prenatal Zika virus infection and microcephaly has now been confirmed.[3] This confirmation was evidenced by several observations, including the following: 1) Zika virus infection during prenatal development at times that were consistent with the defects observed; 2) a specific, rare phenotype involving microcephaly and associated brain anomalies in fetuses or infants with presumed or confirmed congenital Zika virus infection, and 3) data that strongly support the biologic plausibility, including the identification of Zika virus in the brain tissue of affected fetuses and infants.[3-5] In addition, Zika virus infection has been associated with approximately 50 cases of Guillain-Barré syndrome,[2] suggesting that the disease is less benign than initially thought, making Zika a "public health emergency of international concern." In 2016, more than 700 scientific articles have been published on the Zika virus. Rarely before have scientists tackled a new research topic with such a sense of urgency. Finally, the major global impact of Zika virus has been shown by various discussions about the need to delay or relocate the 2016 Rio de Janeiro Olympic Games because of public health concerns over the risk of Zika virus infection for the Olympic community.

For neuroradiologists, a detailed knowledge of the potential neuroimaging findings in children with congenital Zika syndrome is needed to accurately make the diagnosis. Head CT studies have revealed intracranial calcifications in most patients with microcephaly.[6-8] Calcifications are typically located at the corticomedullary junction and involve mostly the frontal and parietal lobes. In about half of patients, calcifications may be seen in the basal ganglia and/or thalami, while calcifications within the periventricular white matter are less common. Calcifications within the cerebellum, brain stem, and spinal cord have been reported in only a few patients.[6,7] The calcifications are typically punctuate, but in some patients, they may be linear or bandlike (particularly at the corticomedullary junction) or coarse (especially within the basal ganglia and thalami). In addition, head CT studies showed cortical hypogyration in all patients.[6-8] Cortical hypogyration is typically severe (with only the Sylvian fissure obviously present) and can be better delineated with MR imaging. In children who underwent MR imaging, the main cortical abnormality included a simplified gyral pattern (normal cortical thickness) associated with areas of polymicrogyria or pachygyria (thick cortex) predominantly located in the frontal lobes.[6] In a few children, hemimegalencephaly and periventricular heterotopia have been reported.[6] Ventriculomegaly is an additional consistent finding seen on head CT and brain MR imaging studies.[6-8] Ventriculomegaly is usually moderate or severe, may involve the whole ventricular system or only the lateral ventricles with predominant enlargement of the trigones and posterior horns, and is most likely secondary to the thin cortical mantle and decreased white matter volume. An enlargement of the subarachnoid spaces is seen in most patients.[6,8] On head CT, diffusely abnormal hypodensity of the white matter is seen in most infants.[7] MR imaging studies revealed that the white matter hypodensity seen on CT represents, most likely, areas of dysmyelination or delayed myelination with secondary thinning of the corpus callosum.[6,8] Posterior fossa involvement may include global or unilateral cerebellar hypoplasia, brain stem hypoplasia, and mega-cisterna magna in some patients.[6-8] Finally, enlargement of the choroid plexus and intraventricular septations have also been reported in select patients.[8] Most of these findings (particularly intracranial calcifications and ventriculomegaly) may be detected prenatally by fetal sonography from 19 weeks of gestation.[4,9,10] Fetal MR imaging may provide additional information about cortical abnormalities and posterior fossa involvement.[10]

Abnormal cortical development and global cerebellar hypoplasia suggest an underlying disruptive pathomechanism caused by congenital Zika virus infection. Recently, experimental studies have shed more light on the neuropathogenesis of the congenital Zika virus syndrome and support a disruptive pathogenesis. In experimental models, Zika virus was shown to target human brain cells, reducing their viability and growth.[11-13] These results suggest that Zika virus abrogates neurogenesis during human brain development. In addition, Zika virus infection causes a downregulation of genes involved in cell cycle pathways, dysregulation of cell proliferation, and upregulation of genes involved in apoptotic pathways, resulting in cell death.[12]

In congenital Zika syndrome, the skull is also affected and has a pointed occiput with overriding bones mainly in the frontal and occipital regions.[8,14] The skull deformity seems to be secondary to the extensive brain abnormalities, but a primary involvement of the skull bones is not excluded. Ongoing studies should solve this hypothesis.

Many questions about Zika virus infection and congenital Zika syndrome need to be answered. For some of these open questions (eg, the most susceptible period of the fetus to the Zika virus infection, the risk and incidence of fetal microcephaly when the mother is infected with Zika virus, and the risk of developing motor and intellectual disabilities from brain abnormalities due to Zika virus infection), neuroimaging may be of great help in providing the answers and in better understanding the congenital Zika syndrome.

http://dx.doi.org/10.3174/ajnr.A4924

## REFERENCES


1. Faria NR, Azevedo Rdo S, Kraemer MU, et al. **Zika virus in the Americas: early epidemiological and genetic findings.** *Science* 2016; 352:345–49 CrossRef Medline
2. Araujo AQ, Silva MT, Araujo AP. **Zika virus-associated neurological disorders: a review.** *Brain* 2016 Jun 29. [Epub ahead of print] Medline
3. Rasmussen SA, Jamieson DJ, Honein MA, et al. **Zika virus and birth defects: reviewing the evidence for causality.** *N Engl J Med* 2016;374: 1981–87 CrossRef Medline
4. Mlakar J, Korva M, Tul N, et al. **Zika virus associated with microcephaly.** *N Engl J Med* 2016;374:951–58 CrossRef Medline
5. Calvet G, Aguiar RS, Melo AS, et al. **Detection and sequencing of Zika virus from amniotic fluid of fetuses with microcephaly in Brazil: a case study.** *Lancet Infect Dis* 2016;16:653–60 CrossRef Medline
6. de Fatima Vasco Aragao M, van der Linden V, Brainer-Lima AM, et al. **Clinical features and neuroimaging (CT and MRI) findings in presumed Zika virus related congenital infection and microcephaly: retrospective case series study.** *BMJ* 2016;353:i1901 CrossRef Medline
7. Hazin AN, Poretti A, Turchi Martelli CM, et al. **Computed tomographic findings in microcephaly associated with Zika virus.** *N Engl J Med* 2016;374:2193–95 CrossRef Medline
8. Cavalheiro S, Lopez A, Serra S, et al. **Microcephaly and Zika virus: neonatal neuroradiological aspects.** *Childs Nerv Syst* 2016;32: 1057–60 CrossRef Medline
9. Oliveira Melo AS, Malinger G, Ximenes R, et al. **Zika virus intrauterine infection causes fetal brain abnormality and microcephaly: tip of the iceberg?** *Ultrasound Obstet Gynecol* 2016;47:6–7 CrossRef Medline
10. Driggers RW, Ho CY, Korhonen EM, et al. **Zika virus infection with prolonged maternal viremia and fetal brain abnormalities.** *N Engl J Med* 2016;374:2142–51 CrossRef Medline
11. Garcez PP, Loiola EC, Madeiro da Costa R, et al. **Zika virus impairs growth in human neurospheres and brain organoids.** *Science* 2016; 352:816–18 CrossRef Medline
12. Tang H, Hammack C, Ogden SC, et al. **Zika virus infects human cortical neural progenitors and attenuates their growth.** *Cell Stem Cell* 2016;18:587–90 CrossRef Medline
13. Qian X, Nguyen HN, Song MM, et al. **Brain-region-specific organoids using mini-bioreactors for modeling ZIKV exposure.** *Cell* 2016;165:1238–54 CrossRef Medline
14. Dain Gandelman Horovitz D, da Silva Pone MV, Moura Pone S, et al. **Cranial bone collapse in microcephalic infants prenatally exposed to Zika virus infection.** *Neurology* 2016;87:118–19 CrossRef Medline

# Brain Perfusion Imaging in Neonates: An Overview

M. Proisy, S. Mitra, C. Uria-Avellana, M. Sokolska, N.J. Robertson, F. Le Jeune, and J.-C. Ferré


## ABSTRACT

**SUMMARY:** The development of cognitive function in children has been related to a regional metabolic increase and an increase in regional brain perfusion. Moreover, brain perfusion plays an important role in the pathogenesis of brain damage in high-risk neonates, both preterm and full-term asphyxiated infants. In this article, we will review and discuss several existing imaging techniques for assessing neonatal brain perfusion.


**ABBREVIATIONS:** ASL = arterial spin-labeling; HIE = hypoxic-ischemic encephalopathy; NIRS = near-infrared spectroscopy

Brain perfusion can be assessed by a number of imaging techniques that have been developed in recent decades. These include PET, SPECT, perfusion CT, diffuse optical spectroscopy, DSC–MR imaging, arterial spin-labeling (ASL), and sonography. The physiology of perfusion can be characterized by many parameters such as CBF (whole-brain or regional CBF to ≥1 anatomic region), CBV, and MTT. Some of these parameters may be obtained depending on the perfusion technique and type of tracer used.[1] The results of brain perfusion imaging techniques are usually expressed as CBF. Most of these techniques rely on the use of endogenous or exogenous tracers and involve different technical requirements and mathematic models.[2-4] Wintermark et al[5] published a literature review of brain perfusion imaging techniques in adults and addressed the feasibility of applying the techniques to children. However, in view of the features of neonatal physiology and pathology, the advantages and disadvantages may differ between adults and children. For example, bedside techniques are an advantage for high-risk neonates. Noninvasive and nonradiating methods that have been recently developed owing to advances in medical imaging techniques are highly suitable for neonates.[6,7] However, given the smaller head size and lower physiologic brain perfusion compared with older children and adults, noninvasive MR perfusion imaging is still challenging.

Neonatal encephalopathy secondary to hypoxic-ischemic injury around birth is an important problem worldwide. Diagnosis is based on clinical, electroencephalographic, and MR imaging findings. Hypoxic-ischemic encephalopathy (HIE) is a major cause of perinatal mortality and morbidity.[8] For a few years, induced hypothermia has been used as neuroprotective treatment for neonatal HIE, reducing the extent of neurologic damage and improving outcome.[9,10] However, a considerable number of infants still have an abnormal outcome. Several preclinical research studies are also being conducted on drugs that may act synergistically or additively with hypothermia.[11,12] Transfontanellar ultrasound and MR imaging provide invaluable information about neonates with HIE for determining positive findings and differential diagnoses, predicting neuromotor outcome, and helping to counsel parents about long-term outcome.[13] Moreover, MRI is an effective biomarker for treatment response.[14] In addition to conventional MR imaging scoring,[15] some quantitative biomarkers could provide more objective information, such as DWI with regional ADC measurements,[16] $^{1}$H-MR spectroscopy, and $^{31}$P-MR spectroscopy.[17]

Brain perfusion plays an important role in the pathogenesis of brain damage in high-risk neonates, both preterm and full-term asphyxiated neonates.[18,19] Hypoxic-ischemic injury leads to reduced blood flow to the brain followed by restoration of blood flow and the initiation of a cascade of pathways. The neurotoxic biochemical cascade of lesions after reperfusion, known as "reperfusion injury," is the primary target for neuroprotective inter-

From the Department of Radiology (M.P., J.-C.F.), Rennes University Hospital, France; Department of Neonatology (M.P., S.M., C.U.-A., N.J.R.), University College London Hospital, Institute for Women's Health, University College of London, London, UK; Inserm VisAGeS Unit U746 (M.P., J.-C.F.), Inria, Rennes 1 University, Rennes, France; Institute of Neurology (M.S.), University College of London, London, UK; and Department of Nuclear Medicine (F.L.J.), Centre Eugène Marquis, Rennes, France.

This work was performed with the support of the Société Française de Radiologie (2012 Research Grant).

Please address correspondence to Maïa Proisy, MD, Department of Radiology, Pediatric Imaging, Rennes University Hospital, 16 Boulevard de Bulgarie, BP 90347, 35203 Rennes Cedex 2, France; e-mail: maia.proisy@chu-rennes.fr

Indicates open access to non-subscribers at www.ajnr.org

Indicates article with supplemental on-line table.

http://dx.doi.org/10.3174/ajnr.A4778

ventions.[10,12] In preterm infants, white matter injury is a major cause of cerebral palsy, which is also assumed to be mainly due to a lack of blood flow and oxygen delivery.[20]

It is critical to understand the development of early changes in the injured neonatal brain. A better understanding of the pattern of perfusion and the relationship with other therapeutic and outcome biomarkers would serve as a decision aid to improve support for high-risk neonates.

In this article, we will review and discuss several existing imaging techniques for assessing neonatal brain perfusion (On-line Table).

### Practical Aspects of Data Acquisition in Neonates

There is no consensus regarding the practical aspects of data acquisition, and each institution may have its own practice. Often, infants younger than 3 months of age are imaged without sedation unless they are receiving sedative medication for clinical indications. We use the "feed and bundle" method to perform nonsedated neonatal MR imaging. Ventilated infants in the intensive care unit are usually sedated with morphine. Moreover, depending on the clinical condition, additional drugs may be given, antiepileptic drugs or vasopressors. In infants older than 3–5 months of age, sedation may be required. Sedation status remains an important consideration in pediatric imaging. Indeed, sedation may have an impact on cerebral perfusion. There are few data in the literature about how sedation or general anesthesia may alter perfusion.[21,22]

Without sedation, a rigid head stabilization (head lightly fixed) is required to perform most imaging (MR imaging, PET, SPECT, CTP). The longer the examination, the longer the immobilization is required. Near-infrared spectroscopy (NIRS) does not require rigid head stabilization because the optical fibers are embedded in a "cap" attached to the infant's head.

### Brain Perfusion Measurements by Using Nuclear Medicine Methods

Nuclear medicine methods were the first ones used to assess CBF in adults and neonates.[23,24] Correlation with structural information (CT or MR imaging) is highly desirable for accurate interpretation.

**Positron-Emission Tomography.** The PET technique measures radiopharmaceuticals labeled with positron emitters using a PET scanner. PET is used to assess regional CBF by using injected $H_2O$ or inhaled $CO_2$ labeled with the isotope oxygen 15 ($^{15}O$). PET with $^{15}O$ water provides an accurate and reproducible quantitative measurement of CBF and is considered the criterion standard method. However, $^{15}O$-PET uses ionizing radiation, and the technique is not widely available (there is a need for close proximity to a cyclotron) because the tracer has an extremely short half-life. Moreover, PET is not available at the bedside or for emergencies. Data processing to obtain maps is automatically generated by the workstation; then the results can be visually interpreted on a computer screen. The underlying mathematic model for data postprocessing is the Kety-Schmidt model.[5]

In 1983, Volpe et al[23] conducted the first study demonstrating the use of PET for determining regional CBF in neonates. Altman et al[25] measured mean CBF in 16 preterm infants (CBF = 4.9–23 mL/100 g/min) and 14 term infants (CBF = 9.0–73 mL/100 g/min). Volpe et al[18] studied regional CBF in 17 asphyxiated term infants during the acute stage of their illness and showed a symmetric decrease in CBF to the parasagittal regions, more marked posteriorly than anteriorly. Those findings explain the ischemic lesions related to impaired cerebral perfusion in the watershed regions.

PET by using $^{18}F$-fluorodeoxyglucose evaluates the regional cerebral metabolic rate (Fig 1). In neonates, the highest cerebral metabolic rates for glucose are located in the primary sensorimotor cortex, thalamus, brain stem, and cerebellar vermis. The cingulate cortex, basal ganglia, and hippocampal regions may also have a relatively high glucose metabolism compared with most of the cerebral cortex.[26] A recent study conducted on 60 infants, including 24 infants with HIE,[27] showed that cerebral glucose metabolism increased with gestational age and that the standardized uptake values were lower in infants with HIE than in healthy term infants, especially in the subcortical white matter, thalamus, and basal ganglia areas, and correlated with the degree of severity of HIE, except for the basal ganglia. Batista et al[28] suggested that there is a transient increase in glucose metabolism in the basal ganglia after perinatal hypoxia and that it may be associated with excess glutamatergic activity in the basal ganglia, leading to severe damage.

**Single-Photon Emission CT.** SPECT provides tomographic images of radiopharmaceutical distribution. It involves the inhalation or intravenous injection of xenon 133 ($^{133}Xe$), with technetium Tc99m hexamethylpropyleneamine oxime ($^{99m}$Tc-HMPAO) or iodine 123 *N*-isopropyl-p-iodoamphetamine ($^{123}$I-IMP). Due to neonatal brain physiology and biodistribution, HMPAO is a more reliable tracer of CBF distribution in neonates compared with adults.[29]

SPECT is a suitable bedside method that is cheaper and more widely available than PET imaging. HMPAO and IMP only show distribution and do not provide quantitative results, unlike xenon. The greatest disadvantage in using the SPECT technique in children is the ionizing radiation. The technique also yields poor resolution and requires a long examination time (20–25 minutes). Data processing to obtain maps takes about 5 minutes. The underlying mathematic model for data postprocessing is the Kety-Schmidt model for the $^{133}Xe$ and $^{123}$I-IMP or the microsphere principle for the Tc99m tracers. Because the uptake of $^{99m}$Tc-HMPAO is not linearly related to CBF, the maps obtained are not quantitative in the current standardized settings and require special correction. The relative CBF maps can be statistically evaluated compared with the healthy control to depict the regions with abnormal perfusion.[5]

Xenon clearance, by using inhaled xenon gas, is another technique that is closely related to SPECT and has been extensively used in adults and neonates.[30] Patient motion is a serious limitation of the technique, which, moreover, does not cover the whole brain. The mean CBF with the xenon technique has been estimated at around 50 mL/100 g/min in 7 healthy neonates[31] and 9.5–11.7 mL/100 g/min in 22 preterm infants during the first 3 days of life.[32] Changes in $^{123}$I-IMP uptake in neonates reflecting relative CBF during the first month of life have been shown to be related to myelination development.[33] In term neonates, up-

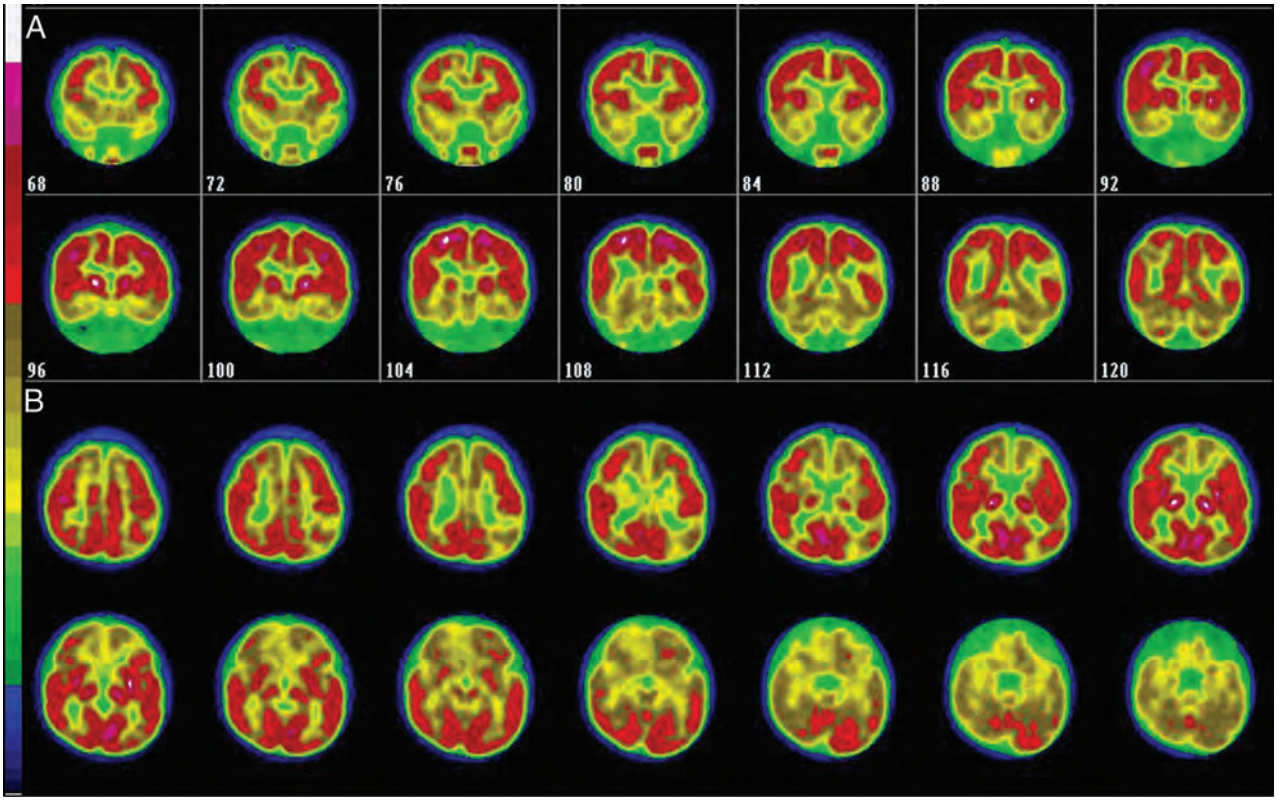


**FIG 1.** Coronal (*A*) and axial (*B*) cerebral $^{18}$F-FDG PET images of a 9-month-old infant with tuberous sclerosis show multiple hypometabolic areas in the frontal and temporal cortex. Courtesy of Prof. Eric Guedj, CHU Timone, Marseille, France.

take was predominantly located in the thalami, brain stem, and central cerebellum, with relatively less cortical activity, except in the perirolandic cortex. Moreover, Pryds and Greisen[32] showed that an intraindividual variation in CBF was positively related to changes in partial pressure of carbon dioxide in arterial blood and inversely related to changes in hemoglobin concentration.

### *Brain Perfusion Measurements by Using Perfusion CT*

Perfusion CT has been widely used in adults and can be performed easily and rapidly. This technique provides a reliable quantitative estimation of CBF, CBV, and MTT by using a first-pass tracer methodology after intravenous injection of a bolus of iodinated contrast material. It involves very rapid data acquisition that is feasible in emergency situations.[34,35] However, due to its invasive nature and radiation dose, very few studies have included neonates. Data processing requires perfusion CT software using either rate-of-upslope estimation of CBF or deconvolution analysis.[5] Images of CBF, CBV, and MTT maps are interpreted on a workstation with visual assessment and quantitative analysis with ROIs. Wintermark et al[36] assessed age-related variations in quantitative brain perfusion CT in children from 7 days to 18 years of age without brain abnormality, including 10 patients younger than 12 months of age. The rCBF findings were consistent with other techniques and showed age-specific variations with a peak at 2–4 years of age. The variation in CBF estimates was due to more pronounced age-related changes in MTT than in CBV.

### *Brain Perfusion Measurements by Using Near-Infrared Spectroscopy*

Near-infrared spectroscopy, described first by Jöbsis in 1977,[37] can be used as a continuous noninvasive real-time monitoring tool for assessment of cerebral oxygenation and hemodynamics. The principles of NIRS are based on the relative transparency of biologic tissues to light in the near-infrared spectrum (700–1000 nm) and different absorption of light by different chromophores in this spectrum (eg, hemoglobin and cytochrome C oxidase). NIRS measures the concentration changes of oxy- and deoxyhemoglobin, which can be used to derive changes in total hemoglobin (an indicator of cerebral blood volume) and hemoglobin difference (indicates cerebral oxygenation).[38] Using spatially resolved spectroscopy, NIRS measures regional oxygenation saturation and reflects the balance of tissue oxygen supply and demand. In comparison with other techniques, application of NIRS is relatively easier. Improved NIRS probes are now available in different sizes to cover premature infants to term neonates. Although NIRS monitors have been used in adult neurointensive care units and theaters for some time now, the introduction of these monitors into neonatal intensive care has been slow. In recent years, several NICUs have started using this as part of the routine decision-making process, particularly for the preterm population.

Edwards et al[39] first described the measurement of cerebral blood flow, and Meek et al[40] showed that low CBF on the first day of life is a risk factor for severe intraventricular hemorrhage. Diffuse correlation spectroscopy is a newer NIRS tech-

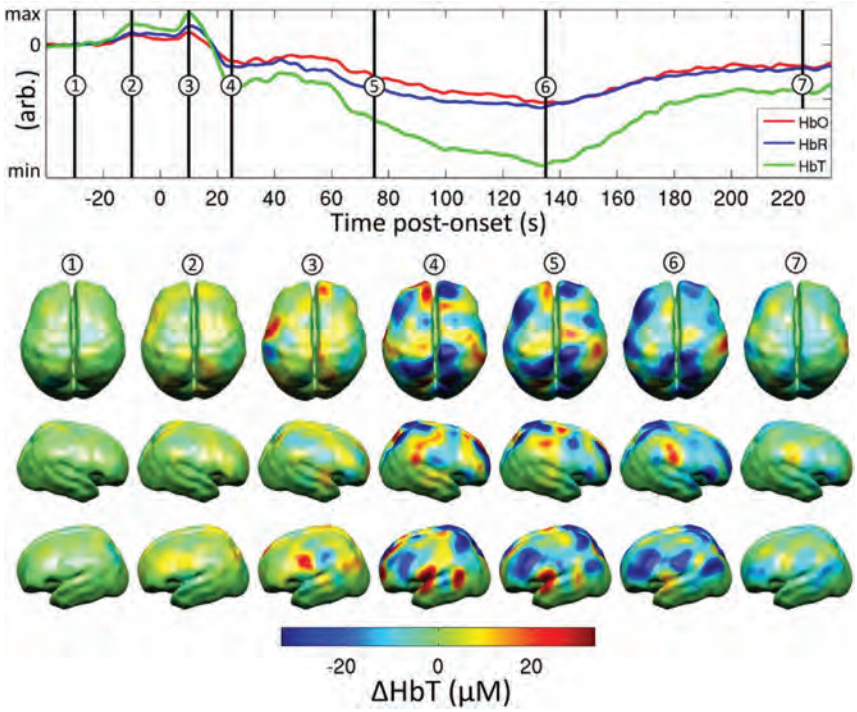


**FIG 2.** Reconstructed images showing the changes in cerebral blood volume (ΔHbT) in the dorsal and left and right lateral views during a seizure in a neonate with hypoxic-ischemic encephalopathy. The upper axes show the changes in hemoglobin concentration spatially averaged across the gray matter surface. Seven distinct time points are identified. All data are changes relative to a baseline, defined as the mean of the period between 60 and 30 seconds before the electrographic seizure onset. Reproduced from Singh et al.[48]

nique that offers a direct and continuous monitoring of microvascular cerebral blood flow.[41] Using hemoglobin difference as an indicator of CBF, Tsuji el al[42] described a high coherence between CBF and mean arterial blood pressure and a strong association of the loss of cerebral autoregulation with an increased incidence of severe germinal matrix–intraventricular hemorrhage or periventricular leukomalacia. The loss of autoregulation in the very preterm population was strongly related to mortality.[43]

Following perinatal hypoxia-ischemia in term infants, CBF and CBV were elevated and were associated with low oxygen extraction and the loss of reactivity to $CO_2$.[44] This loss of the autoregulatory mechanism with loss of cerebrovascular tone happens during the first 24 hours after the insult before secondary energy failure ensues. In a recent study, regional oxygenation saturation increased and fractional tissue oxygen extraction decreased after 24 hours in 18 neonates with poor outcome following HIE.[45] High tissue oxygenation values were noted on day 1 following perinatal hypoxia and were significantly higher in the group with abnormal 1-year outcome.[46] These findings were further supported by a combined NIRS-ASL study[47]: a strong correlation was noted between NIRS-measured regional cerebral oxygen saturation and CBF measured by ASL in infants with severe encephalopathy. Specific changes in cortical hemodynamics and oxygenation were described in previous NIRS studies during and after neonatal seizures (Fig 2).[48]

### *Brain Perfusion Measurements Using Sonography*

Kehrer et al[49,50] have shown the feasibility of measuring CBF volume with Doppler sonography of the extracranial cerebral arteries in infants. Another way to assess overall CBF is to measure the total blood flow to the brain (sum of blood flow in the internal carotid arteries and basilar artery) and to divide it by the brain volume. Doppler sonography is noninvasive, lacking radiation exposure, innocuous, and suitable for bedside follow-up and has good interobserver reproducibility.[51] However, the disadvantages include the absence of regional CBF measurements, the use of an estimated brain weight, the need for the patient to be motionless for about 20 minutes, and strict compliance with a standardized study protocol/meticulous examination to achieve accurate and reliable measurements.[50] In healthy term neonates, the velocities in the ICAs and basilar artery are between 15 and 35 cm/s.[52] As shown with other techniques, the values of CBF volume increased with postmenstrual age from 33 mL/min at 34 weeks to 85 mL/min at 42 weeks.[49] Approximate CBF (mL/100 g/min) was calculated by using an estimated brain weight (the equation was based on head circumference measurements). CBF also increases from 21 to 23 mL/100 g/min after birth to 46–53 mL/100 g/min at 6 months of age and remains stable from 6 to 30 months of age, reflecting rising metabolic demand.[53]

Microbubble ultrasound is a new and reliable cerebral perfusion imaging technique that provides a qualitative estimation of cerebral perfusion and has been described in healthy adults and patients with stroke.[54] Yet, to our knowledge, no study has been conducted on neonates, mainly because microbubble ultrasound is not licensed for use in children.

### *Brain Perfusion Measurements by Using MR Imaging*

Regarding practical aspects of MR imaging, one of the main advantages is that perfusion imaging is a part of the whole examination. The perfusion sequence could be added at the end of the morphologic MR imaging, which is usually clinically required.

Dynamic-Susceptibility Contrast MR Imaging. The dynamic-susceptibility contrast MR imaging technique measures the T2 or T2* decrease during the first pass of an exogenous endovascular susceptibility contrast agent. DSC–MR imaging is a nonradiating procedure, with high SNR and a higher spatial resolution than PET and SPECT, in addition to offering fast acquisition times. Regional hemodynamic changes can be assumed and different parameters such as CBV, TTP, and MTT can be estimated to calculate CBF. Parameters are calculated in a few minutes

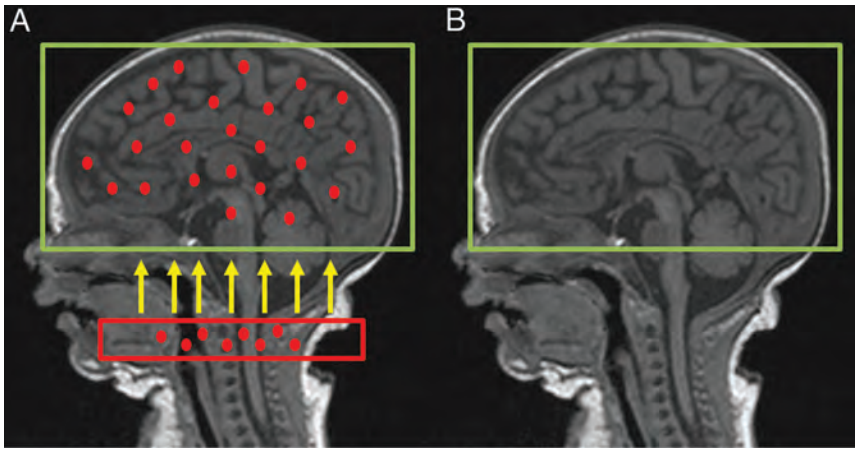


**FIG 3.** Schematic diagram of ASL shows the labeling plane (*red box*) in the neck and the imaging volume (*green box*). *A*, Acquisition of labeled image after a delay to allow the labeled blood to flow into the brain tissue. *B*, Acquisition of the control image.

by using commercially available software. However, the maps provide only relative measurements. Quantification of CBF by DSC is controversial, mainly due to the nonlinear relationship between signal intensity and gadolinium concentration.[55] Maps can be interpreted visually or semiquantitatively by calculating the ratio between the values in an ROI placed in the abnormal area and an ROI placed in the contralateral area considered a normal reference. Longitudinal studies involving repeated measurements during a single scanning session are not possible due to the lack of reliable absolute quantification. Despite the above-mentioned advantages, DSC–MR imaging can be difficult to perform in infants due to gadolinium administration. There have been fewer studies of DSC–MR imaging in children, and particularly neonates, than in adults.[56-59] Hand injections are preferred over power injections in infants, with less reproducibility. Wintermark et al[58] were the first to assess PWI in 5 term neonates with HIE on early (days 2–4) and late MR imaging (days 9–11). On the early MR imaging, a hyperperfusion pattern was detected in areas of hypoxic-ischemic brain damage, corresponding to the reperfusion phase. On the late scans, hyperperfusion persisted in the cortical gray matter.

**Phase-Contrast MR Imaging.** One other noninvasive, accurate, and reproducible MR imaging method has been reported in a small number of studies.[60,61] The blood flow in the internal carotid arteries and basilar artery at the base of the skull is measured by using phase-contrast MR imaging, and the brain volume is measured by using segmentation of anatomic MR images. Data processing consists of multiplying the mean velocity across an ROI (measured by the phase-contrast MR imaging sequence) by the vessel area. Flow to the brain is computed as the sum of flow in the 2 internal carotid arteries and the basilar artery. Brain volume is estimated by using segmentation software by using a dedicated neonatal brain segmentation algorithm. Mean CBF is computed by dividing the total flow to the brain by the brain volume.

In the study by Varela et al,[60] the results for 21 infants showed good agreement with literature data, with a rapid increase during the first year of life, from 25–60 mL/100 mL of tissue/min. The mean velocities (over the cardiac cycle, the area of each vessel and all 3 arteries) were <20 cm/s in term neonates and rose to 30 cm/s at 50 weeks. However, only mean overall CBF can be assessed with this method.

**Arterial Spin-Labeling.** Brain perfusion imaging by using arterial spin-labeling is a noninvasive technique that uses endogenous blood water as a freely diffusible tracer. Arterial blood protons are magnetically labeled with a radiofrequency inversion pulse applied below the imaging section in the neck vessels (Fig 1). Several labeling methods exist, including continuous ASL, pulsed ASL, and pseudocontinuous ASL.[62] In continuous ASL, a long flow-induced inversion pulse is applied. In pulsed ASL, a short inversion pulse is applied to a larger region of the neck. Pseudocontinuous ASL is a hybrid method that uses a train of short radiofrequency pulses to mimic the effects of continuous ASL (Fig 3). The best recommended ASL method is the pseudocontinuous ASL labeling method, mainly because of a higher SNR and less labeling artifacts.[63,64] However, there is a lack of data in the literature regarding the specific neonatal population, and more study is needed.

A labeled image is acquired after a sufficient time to allow the labeled spins to reach the imaging section, known as the postlabeling delay. A control image is acquired without labeling. Subtraction of the 2 images yields a perfusion-weighted image. Because the signal difference is only 0.5%–1.5% of the full signal, multiple repetitions are needed to improve the signal-to-noise ratio. Subsequently, to obtain a quantitative perfusion map, a quantitative model is required to calculate the relationship between the perfusion-weighted image and CBF.

Certain technical adjustments to the imaging parameters are required to account for the fundamental differences between the pediatric and adult populations.[65,66] It is challenging to perform ASL MR imaging in neonates due to the low baseline CBF compared with children and adults, coupled with the low SNR of the method. As an example, velocities are lower in neonates than in children, increasing with postmenstrual age,[67] and the optimum postlabeling delay for contrast-to-noise ratio has been correlated with the mean velocity in the carotid arteries.[68]

Moreover, in children and neonates, there is a physiologic improvement in the SNR compared with healthy adults due to a longer tissue T1, longer blood T1, and the higher blood-brain partition coefficient of water.[65] Blood T1 variations have a greater effect on perfusion than tissue T1 variations.[69] Varela et al[70] established a linear correlation between the inverse of blood T1 and hematocrit in 12 neonates. This may offer the possibility of blood T1 estimations from recent hematocrit measurements.

Measuring CBF in neonates by using ASL therefore requires several adaptations of acquisition and related parameters used for quantification. Another point is the lack of standardization of image-processing methods. In clinical practice, CBF maps are generally automatically generated by the manufac-

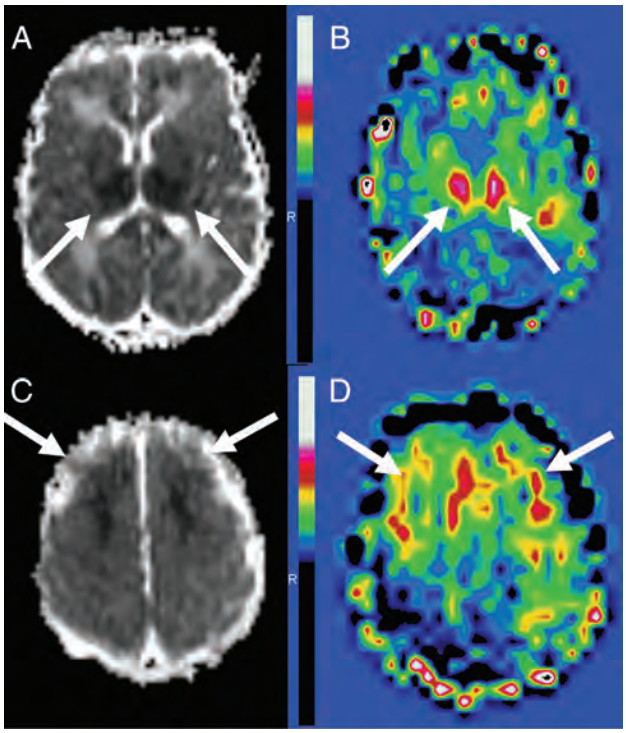


**FIG 4.** HIE ASL. Asphyxiated neonate treated with hypothermia showing ischemic injury on MR imaging obtained on day 3 of life. The ADC map shows restricted diffusion in the bilateral thalami and lentiform nuclei (*A*) and in the frontal watershed areas (*C*) (*arrows*). ASL perfusion map (*B* and *D*) reveals higher perfusion within the same areas (*arrows*).

turer workstation with assumed or measured quantification parameters.

A few studies have been conducted in neonates by using ASL. Miranda et al[71] were the first to show the feasibility of pulsed ASL at 1.5T in 29 unsedated healthy preterm infants at term-equivalent age and in term neonates. Other studies in healthy children show that ASL appears sensitive to regional and age-related differences in CBF in preterm, term neonates, and infants at 3 months[72] and from 3 to 5 months of age.[73] These results are consistent with previous studies demonstrating regional variation in brain maturation. Some studies have been conducted in asphyxiated neonates, showing early hyperperfusion in brain areas subsequently exhibiting injury,[74] and that regions with low ADC intensity are highly correlated with co-located regions of increased ASL CBF intensity (Fig 4).[75] Asphyxiated neonates treated with hypothermia developing brain injury usually displayed hypoperfusion on day of life 1 and hyperperfusion on day of life 2–3 in the study of Wintermark et al.[74] If performed during the second week of life, MR imaging reveals rather a hypoperfusion in the thalamus of infants with injury on MR imaging.[76] De Vis et al[77] showed a significant correlation between a higher perfusion in the basal ganglia and thalami, perfusion on day of life 2–7, and a worse neurodevelopmental outcome in neonates with HIE.

To summarize, ASL is a noninvasive method without venous cannulation or radiation that is repeatable within the same session and provides absolute quantification of CBF. Given the noninvasiveness of the technique, it is highly suitable for neonates.

## CONCLUSIONS

Brain perfusion may play a role in neonatal brain injury and therefore serves as a complementary biomarker to help determine neuroprotective therapeutic strategies. With the development of noninvasive methods, assessment of neonatal brain perfusion has become easier. ASL is a very promising tool for assessing neonatal brain perfusion: It is a totally noninvasive method easily available and providing quantitative regional CBF values. However, the method warrants technical adjustments to make it more widely available.

## ACKNOWLEDGMENTS

The authors thank Prof. Eric Guedj (CHU Timone, Marseille, France) for providing PET images and Ms Tracey Westcott for editorial assistance.

Disclosures: Maïa Proisy—*RELATED*: *Grant*: research grant 2012 Société Française de Radiologie (French Society of Radiology). Nicola J. Robertson—*UNRELATED*: *Grants/Grants Pending*: Chiesi Pharmaceutici S.p.A (research grant)*; *Royalties*: Chiesi, *Comments*: for licensing of intellectual property. *Money paid to the institution.

## REFERENCES

1. Leiva-Salinas C, Provenzale JM, Kudo K, et al. **The alphabet soup of perfusion CT and MR imaging: terminology revisited and clarified in five questions.** *Neuroradiology* 2012;54:907–18 CrossRef Medline
2. Kety SS, Schmidt CF. **The nitrous oxide method for the quantitative determination of cerebral blood flow in man: theory, procedure and normal values.** *J Clin Invest* 1948;27:476–83 CrossRef Medline
3. Meier P, Zierler KL. **On the theory of the indicator-dilution method for measurement of blood flow and volume.** *J Appl Physiol* 1954;6:731–44 Medline
4. Ostergaard L, Weisskoff RM, Chesler DA, et al. **High resolution measurement of cerebral blood flow using intravascular tracer bolus passages, Part I: mathematical approach and statistical analysis.** *Magn Reson Med* 1996;36:715–25 CrossRef Medline
5. Wintermark M, Sesay M, Barbier E, et al. **Comparative overview of brain perfusion imaging techniques.** *Stroke* 2005;36:e83–99 CrossRef Medline
6. Goff DA, Buckley EM, Durduran T, et al. **Noninvasive cerebral perfusion imaging in high-risk neonates.** *Semin Perinatol* 2010;34:46–56 CrossRef Medline
7. Wintermark P. **Injury and repair in perinatal brain injury: insights from non-invasive MR perfusion imaging.** *Semin Perinatol* 2015;39:124–29 CrossRef Medline
8. Volpe JJ. **Neonatal encephalopathy: an inadequate term for hypoxic-ischemic encephalopathy.** *Ann Neurol* 2012;72:156–66 CrossRef Medline
9. Gluckman PD, Wyatt JS, Azzopardi D, et al. **Selective head cooling with mild systemic hypothermia after neonatal encephalopathy: multicentre randomised trial.** *Lancet* 2005;365:663–70 CrossRef Medline
10. Shankaran S, Laptook AR, Ehrenkranz RA, et al; National Institute of Child Health and Human Development Neonatal Research Network. **Whole-body hypothermia for neonates with hypoxic-ischemic encephalopathy.** *N Engl J Med* 2005;353:1574–84 CrossRef Medline
11. Faulkner S, Bainbridge A, Kato T, et al. **Xenon augmented hypothermia reduces early lactate/N-acetylaspartate and cell death in perinatal asphyxia.** *Ann Neurol* 2011;70:133–50 CrossRef Medline
12. Kelen D, Robertson NJ. **Experimental treatments for hypoxic ischaemic encephalopathy.** *Early Hum Dev* 2010;86:369–77 CrossRef Medline

13. Rutherford M, Malamateniou C, McGuinness A, et al. **Magnetic resonance imaging in hypoxic-ischaemic encephalopathy.** *Early Hum Dev* 2010;86:351–60 CrossRef Medline
14. Rutherford M, Ramenghi LA, Edwards AD, et al. **Assessment of brain tissue injury after moderate hypothermia in neonates with hypoxic-ischaemic encephalopathy: a nested substudy of a randomised controlled trial.** *Lancet Neurol* 2010;9:39–45 CrossRef Medline
15. Barkovich AJ, Hajnal BL, Vigneron D, et al. **Prediction of neuromotor outcome in perinatal asphyxia: evaluation of MR scoring systems.** *AJNR Am J Neuroradiol* 1998;19:143–49 Medline
16. Alderliesten T, de Vries LS, Benders MJ, et al. **MR imaging and outcome of term neonates with perinatal asphyxia: value of diffusion-weighted MR imaging and $^{1}$H MR spectroscopy.** *Radiology* 2011;261:235–42 CrossRef Medline
17. Cheong JL, Cady EB, Penrice J, et al. **Proton MR spectroscopy in neonates with perinatal cerebral hypoxic-ischemic injury: metabolite peak-area ratios, relaxation times, and absolute concentrations.** *AJNR Am J Neuroradiol* 2006;27:1546–54 Medline
18. Volpe JJ, Herscovitch P, Perlman JM, et al. **Positron emission tomography in the asphyxiated term newborn: parasagittal impairment of cerebral blood flow.** *Ann Neurol* 1985;17:287–96 CrossRef Medline
19. Greisen G. **Autoregulation of cerebral blood flow in newborn babies.** *Early Hum Dev* 2005;81:423–28 CrossRef Medline
20. Back SA, Han BH, Luo NL, et al. **Selective vulnerability of late oligodendrocyte progenitors to hypoxia-ischemia.** *J Neurosci* 2002;22:455–63 Medline
21. Todd MM, Weeks J. **Comparative effects of propofol, pentobarbital, and isoflurane on cerebral blood flow and blood volume.** *J Neurosurg Anesthesiol* 1996;8:296–303 CrossRef Medline
22. Harreld JH, Helton KJ, Kaddoum RN, et al. **The effects of propofol on cerebral perfusion MRI in children.** *Neuroradiology* 2013;55:1049–56 CrossRef Medline
23. Volpe JJ, Herscovitch P, Perlman JM, et al. **Positron emission tomography in the newborn: extensive impairment of regional cerebral blood flow with intraventricular hemorrhage and hemorrhagic intracerebral involvement.** *Pediatrics* 1983;72:589–601 Medline
24. Fockele DS, Baumann RJ, Shih WJ, et al. **Tc-99m HMPAO SPECT of the brain in the neonate.** *Clin Nucl Med* 1990;15:175–77 CrossRef Medline
25. Altman DI, Powers WJ, Perlman JM, et al. **Cerebral blood flow requirement for brain viability in newborn infants is lower than in adults.** *Ann Neurol* 1988;24:218–26 CrossRef Medline
26. Chugani HT. **A critical period of brain development: studies of cerebral glucose utilization with PET.** *Prev Med* 1998;27:184–88 CrossRef Medline
27. Shi Y, Zhao JN, Liu L, et al. **Changes of positron emission tomography in newborn infants at different gestational ages, and neonatal hypoxic-ischemic encephalopathy.** *Pediatr Neurol* 2012;46:116–23 CrossRef Medline
28. Batista CE, Chugani HT, Juhász C, et al. **Transient hypermetabolism of the basal ganglia following perinatal hypoxia.** *Pediatr Neurol* 2007;36:330–33 CrossRef Medline
29. Børch K, Greisen G. **99mTc-HMPAO as a tracer of cerebral blood flow in newborn infants.** *J Cereb Blood Flow Metab* 1997;17:448–54 Medline
30. Greisen G. **Cerebral blood flow in preterm infants during the first week of life.** *Acta Paediatr Scand* 1986;75:43–51 CrossRef Medline
31. Chiron C, Raynaud C, Mazière B, et al. **Changes in regional cerebral blood flow during brain maturation in children and adolescents.** *J Nucl Med* 1992;33:696–703 Medline
32. Pryds O, Greisen G. **Effect of PaCO2 and haemoglobin concentration on day to day variation of CBF in preterm neonates.** *Acta Paediatr Scand Suppl* 1989;360:33–36 Medline
33. Tokumaru AM, Barkovich AJ, O'uchi T, et al. **The evolution of cerebral blood flow in the developing brain: evaluation with iodine-123 iodoamphetamine SPECT and correlation with MR imaging.** *AJNR Am J Neuroradiol* 1999;20:845–52 Medline
34. Eastwood JD, Lev MH, Provenzale JM. **Perfusion CT with iodinated contrast material.** *AJR Am J Roentgenol* 2003;180:3–12 CrossRef Medline
35. Wintermark M, Cotting J, Roulet E, et al. **Acute brain perfusion disorders in children assessed by quantitative perfusion computed tomography in the emergency setting.** *Pediatr Emerg Care* 2005;21:149–60 Medline
36. Wintermark M, Lepori D, Cotting J, et al. **Brain perfusion in children: evolution with age assessed by quantitative perfusion computed tomography.** *Pediatrics* 2004;113:1642–52 CrossRef Medline
37. Jöbsis FF. **Noninvasive, infrared monitoring of cerebral and myocardial oxygen sufficiency and circulatory parameters.** *Science* 1977;198:1264–67 CrossRef Medline
38. Wyatt JS, Cope M, Delpy DT, et al. **Quantification of cerebral oxygenation and haemodynamics in sick newborn infants by near infrared spectrophotometry.** *Lancet* 1986;2:1063–66 Medline
39. Edwards AD, Wyatt JS, Richardson C, et al. **Cotside measurement of cerebral blood flow in ill newborn infants by near infrared spectroscopy.** *Lancet* 1988;2:770–71 Medline
40. Meek JH, Tyszczuk L, Elwell CE, et al. **Low cerebral blood flow is a risk factor for severe intraventricular haemorrhage.** *Arch Dis Child Fetal Neonatal Ed* 1999;81:F15–18 CrossRef Medline
41. Roche-Labarbe N, Carp SA, Surova A, et al. **Noninvasive optical measures of CBV, StO(2), CBF index, and rCMRO(2) in human premature neonates' brains in the first six weeks of life.** *Hum Brain Mapp* 2010;31:341–52 CrossRef Medline
42. Tsuji M, Saul JP, du Plessis A, et al. **Cerebral intravascular oxygenation correlates with mean arterial pressure in critically ill premature infants.** *Pediatrics* 2000;106:625–32 CrossRef Medline
43. Wong FY, Leung TS, Austin T, et al. **Impaired autoregulation in preterm infants identified by using spatially resolved spectroscopy.** *Pediatrics* 2008;121:e604–11 CrossRef Medline
44. Meek JH, Elwell CE, McCormick DC, et al. **Abnormal cerebral haemodynamics in perinatally asphyxiated neonates related to outcome.** *Arch Dis Child Fetal Neonatal Ed* 1999;81:F110–15 CrossRef Medline
45. Toet MC, Lemmers PM, van Schelven LJ, et al. **Cerebral oxygenation and electrical activity after birth asphyxia: their relation to outcome.** *Pediatrics* 2006;117:333–39 CrossRef Medline
46. Zaramella P, Saraceni E, Freato F, et al. **Can tissue oxygenation index (TOI) and cotside neurophysiological variables predict outcome in depressed/asphyxiated newborn infants?** *Early Hum Dev* 2007;83:483–89 CrossRef Medline
47. Wintermark P, Hansen A, Warfield SK, et al. **Near-infrared spectroscopy versus magnetic resonance imaging to study brain perfusion in newborns with hypoxic-ischemic encephalopathy treated with hypothermia.** *Neuroimage* 2014;85:287–93 CrossRef Medline
48. Singh H, Cooper RJ, Wai Lee C, et al. **Mapping cortical haemodynamics during neonatal seizures using diffuse optical tomography: a case study.** *Neuroimage Clin* 2014;5:256–65 CrossRef Medline
49. Kehrer M, Krägeloh-Mann I, Goelz R, et al. **The development of cerebral perfusion in healthy preterm and term neonates.** *Neuropediatrics* 2003;34:281–86 CrossRef Medline
50. Kehrer M, Goelz R, Krägeloh-Mann I, et al. **Measurement of volume of cerebral blood flow in healthy preterm and term neonates with ultrasound.** *Lancet* 2002;360:1749–50 CrossRef Medline
51. Ehehalt S, Kehrer M, Goelz R, et al. **Cerebral blood flow volume measurements with ultrasound: interobserver reproducibility in preterm and term neonates.** *Ultrasound Med Biol* 2005;31:191–96 CrossRef Medline
52. Ilves P, Lintrop M, Talvik I, et al. **Developmental changes in cerebral and visceral blood flow velocity in healthy neonates and infants.** *J Ultrasound Med* 2008;27:199–207 Medline
53. Kehrer M, Schöning M. **A longitudinal study of cerebral blood flow**

**over the first 30 months.** *Pediatr Res* 2009;66:560–64 CrossRef Medline
54. Eyding J, Wilkening W, Postert T. **Brain perfusion and ultrasonic imaging techniques.** *Eur J Ultrasound* 2002;16:91–104 CrossRef Medline
55. Kiselev VG. **On the theoretical basis of perfusion measurements by dynamic susceptibility contrast MRI.** *Magn Reson Med* 2001;46:1113–22 CrossRef Medline
56. Huisman TA, Sorensen AG. **Perfusion-weighted magnetic resonance imaging of the brain: techniques and application in children.** *Eur Radiol* 2004;14:59–72 CrossRef Medline
57. Tanner SF, Cornette L, Ramenghi LA, et al. **Cerebral perfusion in infants and neonates: preliminary results obtained using dynamic susceptibility contrast enhanced magnetic resonance imaging.** *Arch Dis Child Fetal Neonatal Ed* 2003;88:F525–30 CrossRef Medline
58. Wintermark P, Moessinger AC, Gudinchet F, et al. **Perfusion-weighted magnetic resonance imaging patterns of hypoxic-ischemic encephalopathy in term neonates.** *J Magn Reson Imaging* 2008;28:1019–25 CrossRef Medline
59. Wintermark P, Moessinger AC, Gudinchet F, et al. **Temporal evolution of MR perfusion in neonatal hypoxic-ischemic encephalopathy.** *J Magn Reson Imaging* 2008;27:1229–34 CrossRef Medline
60. Varela M, Groves AM, Arichi T, et al. **Mean cerebral blood flow measurements using phase contrast MRI in the first year of life.** *NMR Biomed* 2012;25:1063–72 CrossRef Medline
61. Benders MJ, Hendrikse J, De Vries LS, et al. **Phase-contrast magnetic resonance angiography measurements of global cerebral blood flow in the neonate.** *Pediatr Res* 2011;69:544–47 CrossRef Medline
62. Ferré JC, Bannier E, Raoult H, et al. **Arterial spin labeling (ASL) perfusion: techniques and clinical use.** *Diagn Interv Imaging* 2013;94:1211–23 CrossRef Medline
63. Alsop DC, Detre JA, Golay X, et al. **Recommended implementation of arterial spin-labeled perfusion MRI for clinical applications: a consensus of the ISMRM perfusion study group and the European consortium for ASL in dementia.** *Magn Reson Med* 2015;73:102–16 CrossRef Medline
64. Boudes E, Gilbert G, Leppert IR, et al. **Measurement of brain perfusion in newborns: pulsed arterial spin labeling (PASL) versus pseudo-continuous arterial spin labeling (pCASL).** *Neuroimage Clin* 2014;6:126–33 CrossRef Medline
65. Wang J, Licht DJ, Jahng G-H, et al. **Pediatric perfusion imaging using pulsed arterial spin labeling.** *J Magn Reson Imaging* 2003;18:404–13 CrossRef Medline
66. Madan N, Grant PE. **MR perfusion imaging in pediatrics.** In: Barker PB, Golay X, Zaharchuk G, eds. *Clinical Perfusion MRI: Techniques and Applications.* Cambridge: Cambridge University Press; 2013:326–48
67. Kehrer M, Blumenstock G, Ehehalt S, et al. **Development of cerebral blood flow volume in preterm neonates during the first two weeks of life.** *Pediatr Res* 2005;58:927–30 CrossRef Medline
68. Ferré JC, Petr J, Barillot C, et al. **Optimal individual inversion time in brain arterial spin labeling perfusion magnetic resonance imaging: correlation with carotid hemodynamics measured with cine phase-contrast magnetic resonance imaging.** *J Comput Assist Tomogr* 2013;37:247–51 CrossRef Medline
69. Wu WC, St. Lawrence KS, Licht DJ, et al. **Quantification issues in arterial spin labeling perfusion magnetic resonance imaging.** *Top Magn Reson Imaging* 2010;21:65–73 CrossRef Medline
70. Varela M, Hajnal JV, Petersen ET, et al. **A method for rapid in vivo measurement of blood T1.** *NMR Biomed* 2011;24:80–88 CrossRef Medline
71. Miranda MJ, Olofsson K, Sidaros K. **Noninvasive measurements of regional cerebral perfusion in preterm and term neonates by magnetic resonance arterial spin labeling.** *Pediatr Res* 2006;60:359–63 CrossRef Medline
72. De Vis JB, Petersen ET, de Vries LS, et al. **Regional changes in brain perfusion during brain maturation measured non-invasively with arterial spin labeling MRI in neonates.** *Eur J Radiol* 2013;82:538–43 CrossRef Medline
73. Duncan AF, Caprihan A, Montague EQ, et al. **Regional cerebral blood flow in children from 3 to 5 months of age.** *AJNR Am J Neuroradiol* 2014;35:593–98 CrossRef Medline
74. Wintermark P, Hansen A, Gregas MC, et al. **Brain perfusion in asphyxiated newborns treated with therapeutic hypothermia.** *AJNR Am J Neuroradiol* 2011;32:2023–29 CrossRef Medline
75. Pienaar R, Paldino MJ, Madan N, et al. **A quantitative method for correlating observations of decreased apparent diffusion coefficient with elevated cerebral blood perfusion in newborns presenting cerebral ischemic insults.** *Neuroimage* 2012;63:1510–18 CrossRef Medline
76. Massaro AN, Bouyssi-Kobar M, Chang T, et al. **Brain perfusion in encephalopathic newborns after therapeutic hypothermia.** *AJNR Am J Neuroradiol* 2013;34:1649–55 CrossRef Medline
77. De Vis JB, Hendrikse J, Petersen ET, et al. **Arterial spin-labelling perfusion MRI and outcome in neonates with hypoxic-ischemic encephalopathy.** *Eur Radiol* 2015;25:113–21 CrossRef Medline

# Cerebral CTA with Low Tube Voltage and Low Contrast Material Volume for Detection of Intracranial Aneurysms

Q.Q. Ni, G.Z. Chen, U.J. Schoepf, M.A.J. Klitsie, C.N. De Cecco, C.S. Zhou, S. Luo, G.M. Lu, and L.J. Zhang

## ABSTRACT

**BACKGROUND AND PURPOSE:** Multidetector row CTA has become the primary imaging technique for detecting intracranial aneurysms. Technical progress enables the use of cerebral CTA with lower radiation doses and contrast media. We evaluated the diagnostic accuracy of 80-kV(peak) cerebral CTA with 30 mL of contrast agent for detecting intracranial aneurysms.

**MATERIALS AND METHODS:** Two hundred four patients were randomly divided into 2 groups. Patients in group A ($n = 102$) underwent 80-kVp CTA with 30 mL of contrast agent, while patients in group B ($n = 102$) underwent conventional CTA (120 kVp, 60 mL of contrast agent). All patients underwent DSA. Image quality, diagnostic accuracy, and radiation dose between the 2 groups were compared.

**RESULTS:** Diagnostic image quality was obtained in 100 and 99 patients in groups A and B, respectively ($P = .65$). With DSA as reference standard, diagnostic accuracy on a per-aneurysm basis was 89.9% for group A and 93.9% for group B. For evaluating smaller aneurysms (<3 mm), the diagnostic accuracy of groups A and B was 86.3% and 90.8%, respectively. There was no difference in diagnostic accuracy between each CTA group and DSA (all, $P > .05$) or between the 2 CTA groups (all, $P > .05$). The effective dose in group A was reduced by 72.7% compared with group B.

**CONCLUSIONS:** In detecting intracranial aneurysms with substantial radiation dose and contrast agent reduction, 80-kVp/30-mL contrast CTA provides the same diagnostic accuracy as conventional CTA.

**ABBREVIATIONS:** CNR = contrast-to-noise ratio; DLP = dose-length product; ED = effective dose; NPV = negative predictive value; PPV= positive predictive value

Approximately 85% of all subarachnoid hemorrhages result from ruptured intracranial aneurysms.[1] Such hemorrhages have high case fatality, particularly for relatively young patients, younger than 65 years of age.[2] Clinical urgency may sometimes be difficult to assess, given that some patients only present with headache and near-normal neurologic examination findings.[3] Thus early identification of underlying intracranial aneurysms seems to be especially important.

DSA is currently the criterion standard for the assessment of aneurysms but has some inherent drawbacks. This technology is invasive, time-consuming, and relatively expensive.[4] Furthermore, it uses a higher radiation dose and causes permanent neurologic complications in 0.12% of patients.[5] Multidetector row CT angiography has always been the primary imaging technique for the evaluation of intracranial aneurysms, especially for the critical patients presenting with subarachnoid hemorrhage, because of its wide availability, reduced imaging time, and high diagnostic accuracy.[4-7] Even for the patients with headache and near-normal neurologic examination findings, CTA may be important for screening. However, radiation exposure and contrast material–induced nephropathy are inherent drawbacks of CTA. Technical progress enables performing cerebral CTA with ever lower radiation doses and contrast media volumes while maintaining image quality.[8-12] However, previous studies did not fully assess the diagnostic accuracy of such gentler CTA protocols because few patients underwent DSA as a reference standard. For example, a study by Luo et al[8] included 120 patients who under-

Received December 11, 2015; accepted after revision March 6, 2016.

From the Department of Medical Imaging (Q.Q.N., G.Z.C., C.S.Z., S.L., G.M.L., L.J.Z.), Jinling Hospital, Medical School of Nanjing University, Nanjing, Jiangsu, China; and Department of Radiology and Radiological Science (U.J.S., M.A.J.K., C.N.D.C.), Medical University of South Carolina, Charleston, South Carolina.

U.J. Shoepf is a consultant for and/or receives research support from Bayer, Bracco, GE Healthcare, Medrad, and Siemens. The other authors have no conflicts of interest to declare.

This work was supported by the Program for New Century Excellent Talents in the University (NCET-12-0260).

Please address correspondence to Long Jiang Zhang, MD, Department of Medical Imaging, Jinling Hospital, Medical School of Nanjing University, Nanjing, Jiangsu, 210002, China; e-mail: kevinzhlj@163.com

Indicates open access to non-subscribers at www.ajnr.org

Indicates article with supplemental on-line tables.

http://dx.doi.org/10.3174/ajnr.A4803

went cerebral CTA with both low tube voltage and low contrast agent volume, but only 43 patients ($n < 15$ for the 2 low-dose groups) underwent DSA for comparison.

The purpose of our study was, therefore, to evaluate, in a large patient population, the diagnostic accuracy of 80-kV(peak) cerebral CTA with 30 mL of contrast agent for detecting intracranial aneurysms with DSA as the reference standard.

## MATERIALS AND METHODS

### Patients

This prospective study was approved by the Jinling Hospital institutional review board. Written informed consent was provided by all patients or their legal guardians. Two hundred four patients were included in our study between September 2013 and January 2015.

Inclusion criteria for this study were the following: 1) clinically suspected intracranial aneurysm, that is, patient presentation with subarachnoid hemorrhage or a suspicion of an intracranial aneurysm after medical examinations; 2) clinical referral for both cerebral CTA and DSA when patients were able to undergo the 2 examinations; and 3) cerebral CTA performed before DSA with no more than 3 days between procedures. Patients were excluded if they were younger than 18 years of age ($n = 1$), had a history of prior surgical clipping or endovascular coiling ($n = 2$), had a history of prior reaction to iodinated contrast media, or had known renal insufficiency (creatinine level, >120 mol/L) ($n = 0$).

Included patients who underwent CTA with different tube voltages and different volumes of iodinated contrast agent were randomly divided into 2 groups based on a computer-generated allocation sequence. The parity of each random number determined to which group the patients examined on the same day would be assigned (ie, odd numbers for group A and even numbers for group B), to avoid the change of contrast agent before each patient's examination. Group A consisted of 102 patients, including 50 men (mean age, 49 ± 12 years) and 52 women (mean age, 53 ± 13 years); group B consisted of 102 patients, including 47 men (mean age, 52 ± 14 years) and 55 women (mean age, 58 ± 13 years). There was no significant difference in sex between the 2 groups ($P > .05$). The mean age of patients in group A was 51 ± 14 years (range, 21–79 years), while patients in group B were somewhat older ($P = .024$), with a mean age of 55 ± 14 years (range, 22–81 years). The baseline characteristics of all patients are presented in On-line Table 1.

### Cerebral CT Angiography Acquisition

Cerebral CTA examinations were performed by using a dual-source CT system (Somatom Definition; Siemens, Erlangen, Germany). Routine automatic tube current modulation (CARE Dose4D; Siemens) was used at 230 mAs for each patient. The collimation was 64 × 0.6 mm, with a 0.33-second rotation time and a pitch of 1.5. Image reconstruction was performed with a 0.75-mm section thickness and 0.5-mm increment with a dedicated reconstruction algorithm (H30f).

In group A, patients received 30 mL of iodinated contrast medium (iopromide, Ultravist 300 mg I/mL; Bayer HealthCare, Berlin, Germany) and were imaged at 80 kVp (double low-dose protocol). In group B, the patients received 60 mL of the same contrast medium and were imaged at 120 kVp, which is the standard work-up CTA protocol in the clinic. The contrast agent was injected into the antecubital vein via an 18-ga catheter at the rate of 4.0 mL/s, followed by 30 mL of saline solution with the same flow rate.

Using a bolus-tracking technique, an ROI was placed in the right internal carotid artery. When the predefined threshold of 100 HU was reached, image acquisition started 2 seconds later. The acquisition lasted approximately 3–4 seconds.

### DSA Acquisition and Evaluation

DSA was performed with femoral catheterization with a biplane DSA unit with rotational capabilities (Axiom Artis dTA; Siemens). A single 3D-DSA acquisition was obtained before removing the catheter only in the target vessel with confirmed or suspected aneurysms, to reduce the radiation dose. Once the procedure was completed, the angiographic datasets were transferred to an adjacent 3D workstation (Siemens) for generation of 3D reformatted images. All angiographies were performed by a group of highly experienced (>10 years of experience) interventional neuroradiologists (not authors) who also performed evaluations of the presence, location, and size of intracranial aneurysms in the DSA images. If there was a strong suspicion of an aneurysm on CTA that was not found on DSA, repeat interpretation by at least 2 interventional neuroradiologists (not authors) was performed to arbitrate this discrepancy.

### Objective Image-Quality Evaluation

All CT images were transferred to a dedicated workstation (syngo MultiModality Workplace; Siemens). All CT measurements were independently performed by 2 radiologists (Q.Q.N. and S.L., with 1 and 5 years' experience in neuroradiology, respectively) twice with a 6-month interval between measurements. The CT attenuation values of vascular structures were measured by using a user-defined circular ROI with an area of 0.12–0.16 $cm^2$ in the bilateral ICAs and 0.04–0.06 $cm^2$ in the bilateral middle cerebral arteries on the transverse CT images. To mitigate partial volume effects and operator dependence of measurements, we prescribed 3 independent ROIs, respectively, on both sides of the cavernous segment of the ICA and the first segment of the MCA trunk. With Moyamoya disease and ICA or MCA occlusion, the CT attenuation values of vascular structures were not measured. The average attenuation values were used for statistical analysis.

Brain parenchyma was selected as the vascular background, and image noise was calculated as the SD of the attenuation values. The attenuation values of the brain parenchyma were measured by placing an ROI of 1 $cm^2$ in the white matter above the lateral ventricles. Signal-to-noise ratio and contrast-to-noise ratio (CNR) were calculated by using the following formulas[13,14]:

$$SNR_a = CTnumber_a/SD$$

$$CNR_a = (CTnumber_a - CTnumber_b)/SD,$$

where $CTnumber_a$ is the mean Hounsfield unit of the target artery, $CTnumber_b$ is the mean Hounsfield unit of brain parenchyma, and SD is the standard deviation of the attenuation value in the brain parenchyma.

### Subjective Image-Quality Evaluation

Subjective image-quality analysis of cerebral CTA was performed by using volume-rendering, multiplanar reconstructions, and maximum intensity projections. Two experienced neuroradiologists (L.J.Z. and G.Z.C., with 16 and 4 years' experience, respectively) blinded to the acquisition technique independently scored CTA images after a dedicated formal training in 20 patients who were not included in this study. After 6 months, repeated evaluations were performed to measure intrareader agreement. In the case of disagreement, a final consensus score was determined during joint interpretation.

Overall image quality was determined on the basis of the degree of image noise and vessel sharpness on a 4-point Likert Scale[15-18]: 1) poor, nondiagnostic, major degree of noise, blurry vessel outlines, rendering evaluation impossible; 2) moderate, substantial noise, suboptimal vessel sharpness; 3) good, moderate image noise and good vessel sharpness; and 4) excellent, minor-to-no noise, exquisite vessel delineation. Images with overall image quality scores of $\geq$3 were regarded as diagnostic.

### Intracranial Aneurysm Evaluation

Aneurysms were measured within the arteries of the anterior circulation (ie, anterior communicating, anterior cerebral, middle cerebral, internal carotid, and anterior choroidal arteries) and the arteries of the posterior circulation (vertebral and basilar, posterior communicating, posterior cerebral, anterior superior cerebellar, and posterior inferior cerebellar arteries).

The same 2 neuroradiologists performing the subjective image analysis independently evaluated the presence or absence of aneurysms on cerebral CTA. In case of disagreement, a third experienced neuroradiologist (C.S.Z. with 10 years' experience) arbitrated. For subarachnoid hemorrhage, other nonaneurysmal causes were also recorded.

### Radiation Dose Estimation

The volume CT dose index (milligray) and dose-length product (DLP, milligray $\times$ centimeter) were recorded from the dose report. The effective dose (ED, millisieverts) was calculated by using the formula ED = DLP $\times$ $\kappa$, by using a conversion factor ($\kappa$) for head CT imaging ($\kappa$ = 0.0021 mSv/mGy $\times$ cm).[19]

### Statistical Analysis

Statistical analyses were performed by using SPSS software (Version 21; IBM, Armonk, New York). Quantitative variables were expressed as mean $\pm$ SD, and categoric data were expressed as frequencies or percentages. Quantitative variables were tested for normal distribution by using the Kolmogorov-Smirnov test. The *t* test was used if the quantitative variables followed normal distribution, and if the quantitative variables did not follow normal distribution, the Mann-Whitney *U* test was used. A $\chi^2$ or Fisher exact test was used to analyze differences in categoric data for baseline characteristics and subjective image quality between groups A and B. $P < .05$ indicated a statistical difference. Intraclass correlation coefficient and $\kappa$ analysis were used to evaluate inter- and intrareader agreement for the measurement of subjective and objective image quality, respectively. An intraclass correlation coefficient or $\kappa$ value $< 0.20$ indicated poor agreement; 0.21–0.40, fair agreement; 0.41–0.60, moderate agreement; 0.61–0.80, good agreement; and 0.81–1.00, very good agreement.[15,20]

In this study, 3D-DSA was regarded as the reference standard for detection of intracranial aneurysms. Sensitivity, specificity, positive predictive value (PPV), negative predictive value (NPV), and accuracy were calculated on both a per-patient and per-aneurysm basis. The confidence intervals for per-aneurysm analysis were obtained by using bootstrapping. Two-sided 95% confidence intervals based on binomial probabilities were also provided. Comparisons between the 2 CTA groups and DSA were made by using the McNemar test. The $\chi^2$ or Fisher exact test was used to compare the sensitivity, specificity, PPV, NPV, and accuracy between the 2 different CTA groups. $P < .05$ was a statistically significant difference.

## RESULTS

### Image Quality

Mean attenuation, SNR, and CNR values for the ICA, MCA, and brain parenchyma for both groups are presented in On-line Table 2. The mean attenuation in the ICA and MCA of group A was higher than that of group B ($P < .01$). The mean $SNR_{ICA}$, $CNR_{ICA}$, $SNR_{MCA,}$ and $CNR_{MCA}$ of group A were lower than those of group B ($P < .01$). The mean image noise of group A was higher than that of group B ($P < .01$). Reliability analysis showed an excellent inter- and intraobserver agreement for measurements of objective image quality (all intraclass correlation coefficients, $> 0.80$).

Diagnostic-quality scores of $\geq$3 were given in 100 patients (98%) in group A and 99 patients (97%) in group B. There was no difference in diagnostic image quality in the 2 groups ($\chi^2 = 0.21$, $P = .65$), indicating that diagnostic image quality could be reliably obtained with either CTA protocol. The inter- and intrareader agreements for all subjective image-quality measurements were good with all $\kappa$ values $> 0.60$.

### Diagnostic Performance

Among 204 patients, 121 patients had 157 aneurysms based on 3D-DSA findings, while 83 patients had no aneurysms. Of 121 patients with aneurysms, 99 patients had a single aneurysm and 22 had multiple aneurysms. On-line Table 3 shows the aneurysm detection and other nonaneurysmal causes in each group.

Cerebral CTA correctly detected 143 aneurysms in 118 patients with 14 aneurysms missed and 6 false-positive aneurysm diagnoses against the 3D-DSA reference standard. CTA correctly demonstrated all nonaneurysmal causes in 12 patients. For group A, the sensitivity and specificity for detecting aneurysms on a per-patient basis were 96.8% and 97.5%, respectively, and 88.5% and 92.5%, respectively, on a per-aneurysm basis. For group B, sensitivity and specificity were 98.3% and 97.7% on a per-patient basis, respectively, and 94.3% and 93.3% on a per-aneurysm basis (Table 1 and Fig 1). There were no statistically significant differences in sensitivity, specificity, PPV, NPV, and diagnostic accuracy on a per-patient or per-aneurysm basis between the 2 cerebral CTA protocols and 3D-DSA (all $P > .05$). In addition, there was no difference in sensitivity, specificity, PPV, NPV, and diagnostic accuracy between the 2 cerebral CTA protocols (all, $P > .05$).

**Table 1: Aneurysm detection with cerebral CTA compared with a 3D-DSA reference standard[a]**

| Approach | Results (No.) | | | | Statistical Analysis (%) | | | | |
|---|---|---|---|---|---|---|---|---|---|
| | TP | TN | FP | FN | Sensitivity | Specificity | PPV | NPV | Accuracy |
| Per patient | | | | | | | | | |
| Group A | 60 | 39 | 1 | 2 | 96.8 (89.0–99.1) | 97.5 (87.1–99.6) | 98.4 (91.2–99.7) | 95.1 (83.9–98.7) | 97.0 (91.7–99.0) |
| Group B | 58 | 42 | 1 | 1 | 98.3 (91.0–99.7) | 97.7 (87.9–99.6) | 98.3 (91.0–99.7) | 97.7 (87.9–99.6) | 98.0 (93.1–99.5) |
| Per aneurysm | | | | | | | | | |
| Group A | 77 | 39 | 3 | 10 | 88.5 (81.6–95.4) | 92.9 (88.6–98.6) | 96.3 (91.3–100.0) | 79.6 (67.3–89.8) | 89.9 (84.5–94.6) |
| Group B | 66 | 42 | 3 | 4 | 94.3 (88.6–98.6) | 93.3 (84.4–100.0) | 95.7 (89.9–100.0) | 91.3 (82.6–97.8) | 93.9 (88.7–98.3) |

**Note:**—TP indicates true positive; TN, true negative; FP, false positive; FN, false negative.
[a] The data in parentheses are 95% confidence intervals.

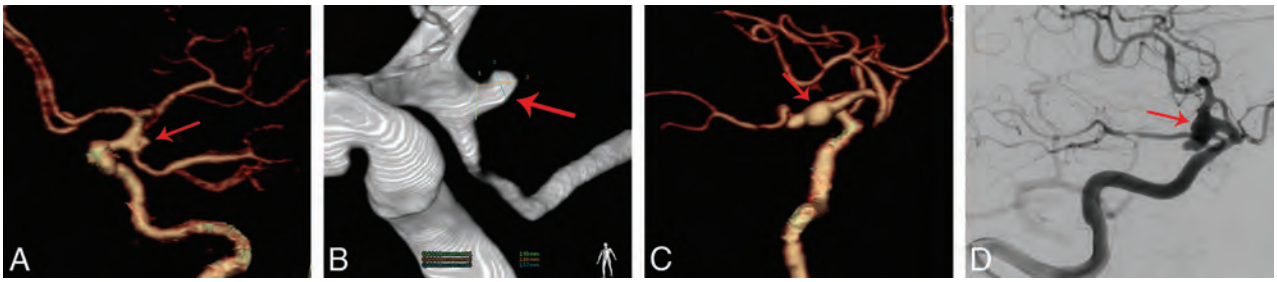


**FIG 1.** Comparison of the 2 CTA protocols for detecting an aneurysm in the posterior communicating artery. *A* and *B*, An 80-kVp cerebral CTA with 30 mL of contrast agent in a 49-year-old woman. A volume-rendered digital subtraction CTA image (*A*) shows an aneurysm in the left posterior communicating artery (*red arrow*), which is confirmed by 3D-DSA (*B*). *C* and *D*, A 120-kVp cerebral CTA with 60 mL of contrast agent in a 66-year-old woman. *C*, Volume-rendered digital subtraction CTA image (*C*) shows an aneurysm in the right posterior communicating artery (*red arrow*), which is confirmed by 2D-DSA (*D*).

**Table 2: Aneurysm detection with cerebral CTA according to aneurysm size[a]**

| Aneurysm Size | Results (No.) | | | | Statistical Analysis (%) | | | | |
|---|---|---|---|---|---|---|---|---|---|
| | TP | TN | FP | FN | Sensitivity | Specificity | PPV | NPV | Accuracy |
| <3 mm | | | | | | | | | |
| Group A | 24 | 39 | 2 | 8 | 75.0 (59.4–90.6) | 95.1 (87.8–100.0) | 92.3 (80.8–100.0) | 83.0 (72.3–93.6) | 86.3 (78.1–93.2) |
| Group B | 17 | 42 | 2 | 4 | 81.0 (61.9–95.2) | 95.5 (88.6–100.0) | 89.5 (73.7–100.0) | 91.3 (82.6–97.8) | 90.8 (83.1–96.9) |
| 3–8 mm | | | | | | | | | |
| Group A | 44 | 39 | 1 | 2 | 95.7 (89.1–100.0) | 97.5 (92.5–100.0) | 97.8 (93.3–100.0) | 95.1 (87.8–100.0) | 96.5 (93.0–100.0) |
| Group B | 38 | 42 | 1 | 0 | 100 (100.0–100.0) | 97.7 (93.0–100.0) | 97.4 (92.3–100.0) | 100 (100.0–100.0) | 98.8 (96.3–100.0) |
| >8 mm | | | | | | | | | |
| Group A | 9 | 39 | 0 | 0 | 100 (100.0–100.0) | 100 (100.0–100.0) | 100 (100.0–100.0) | 100 (100.0–100.0) | 100 (100.0–100.0) |
| Group B | 11 | 42 | 0 | 0 | 100 (100.0–100.0) | 100 (100.0–100.0) | 100 (100.0–100.0) | 100 (100.0–100.0) | 100 (100.0–100.0) |

**Note:**—TP indicates true positive; TN, true negative; FP, false positive; FN, false negative.
[a] The data in parentheses are 95% confidence intervals.

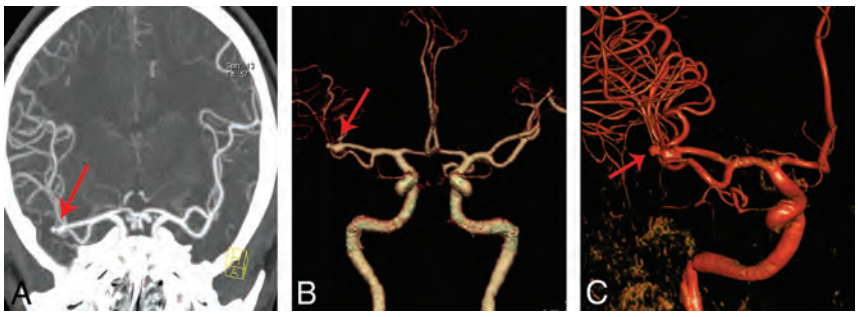


**FIG 2.** An 80-kVp cerebral CTA with 30 mL of contrast agent in a 45-year-old man. Maximum-intensity-projection image (*A*) and a volume-rendered digital subtraction CTA image (*B*) show an aneurysm in the right middle cerebral artery (*red arrow*), which is confirmed by 3D-DSA (*C*).

Of 157 total aneurysms, 53 were <3 mm, 84 were 3–8 mm, and 20 were >8 mm. Cerebral CTA had a sensitivity of 75.0%, 95.7%, and 100% in group A, and 81.0%, 100%, and 100% in group B for detecting aneurysms of <3 mm, 3–8 mm, and >8 mm, respectively. Diagnostic accuracy grouped by aneurysm size for group A was 86.4%, 96.5%, and 100%; for group B, it was 90.8%, 96.5%, and 100% (Table 2 and Fig 2). There was no difference in sensitivity, specificity, PPV, NPV, and diagnostic accuracy between the 2 cerebral CTA protocols for detecting aneurysms of different sizes, even for aneurysms of <3 mm (all, $P > .05$).

There were 88 aneurysms in the anterior circulation arteries and 69 in the posterior circulation arteries (Table 3). The detailed distribution of intracranial aneurysms detected by DSA and CTA is presented in On-line Table 4. Cerebral CTA had a sensitivity of 86.2% and 93.1% in group A and a sensitivity of 93.3% and 95.0% in group B for determining aneurysm locations in the anterior and posterior circulation, respectively. The diagnostic accuracies for detecting aneurysms in the anterior and posterior circulation were 90.8% and 94.3% in group A and 94.6% and 96.4% in group B. There was no difference in sensitivity,

**Table 3: Aneurysm detection with cerebral CTA according to aneurysm location[a]**

| Location | Results (No.) | | | | Statistical Analysis (%) | | | | |
|---|---|---|---|---|---|---|---|---|---|
| | TP | TN | FP | FN | Sensitivity | Specificity | PPV | NPV | Accuracy |
| Anterior circulation | | | | | | | | | |
| Group A | 50 | 39 | 1 | 8 | 86.2 (77.6–94.8) | 97.5 (92.5–100.0) | 98.0 (94.1–100.0) | 83.0 (70.2–93.6) | 90.8 (84.7–95.9) |
| Group B | 28 | 42 | 2 | 2 | 93.3 (83.3–100.0) | 95.5 (88.5–100.0) | 93.3 (83.3–100.0) | 95.5 (88.6–100.0) | 94.6 (89.2–98.6) |
| Posterior circulation | | | | | | | | | |
| Group A | 27 | 39 | 2 | 2 | 93.1 (82.8–100.0) | 95.1 (87.8–100.0) | 93.1 (82.8–100.0) | 95.1 (87.8–100.0) | 94.3 (88.6–98.6) |
| Group B | 38 | 42 | 1 | 2 | 95.0 (87.5–100.0) | 97.7 (93.0–100.0) | 97.4 (92.3–100.0) | 95.5 (88.6–100.0) | 96.4 (91.6–100.0) |

**Note:**—TP indicates true positive; TN, true negative; FP, false positive; FN, false negative.
[a] The data in parentheses are 95% confidence intervals.

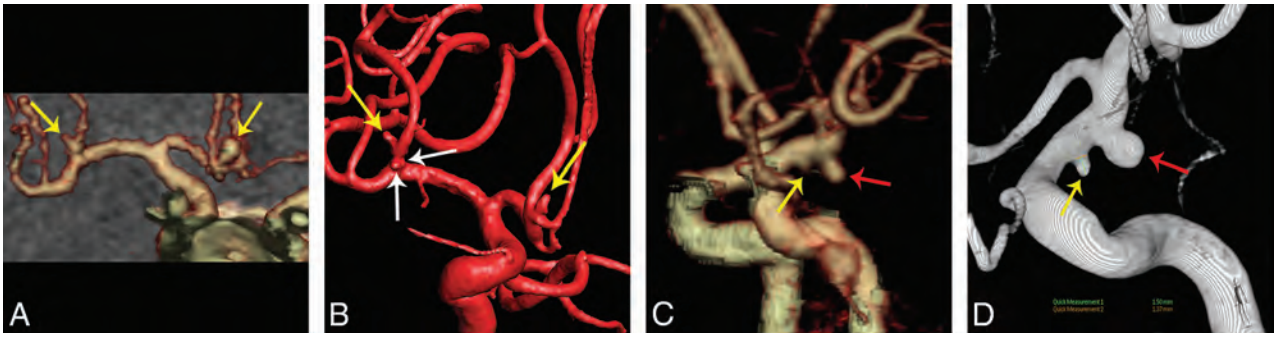


**FIG 3.** False-negative aneurysms in the 2 CTA protocols. *A* and *B*, An 80-kVp cerebral CTA with 30 mL of contrast agent in a 50-year-old man. A volume-rendered digital subtraction CTA image (*A*) shows 2 true-positive aneurysms in the anterior communicating artery and right middle cerebral artery, respectively (*yellow arrows*), while another 2 small aneurysms with diameters of 1.1 and 0.6 mm were found in the right middle cerebral artery (*white arrows*) on 3D-DSA (*B*), which were not found in the CTA image. *C* and *D*, A 120-kVp cerebral CTA with 60 mL of contrast agent in a 46-year-old man. The volume-rendered digital subtraction CTA image (*C*) shows a true-positive aneurysm in the left anterior choroidal artery (*red arrow*) and a false-negative aneurysm in the left posterior communicating artery (*yellow arrow*). The aneurysm in the left posterior communicating artery (*yellow arrow*) was found at repeat interpretation. 3D-DSA shows the 2 aneurysms (*D*).

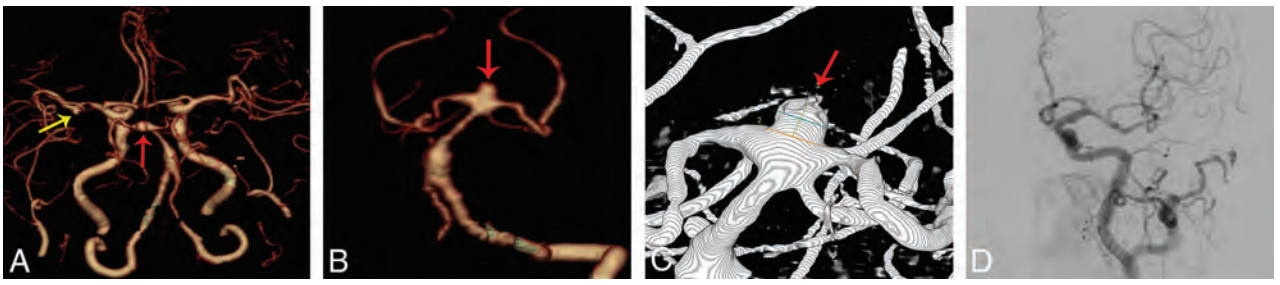


**FIG 4.** A 120-kVp cerebral CTA with 60 mL of contrast agent in a 70-year-old woman. *A* and *B*, Volume-rendered digital subtraction CTA images show a true-positive aneurysm in the top of basilar artery (*red arrow*), which was confirmed by 3D-DSA (*C*) and a false-positive aneurysm in the left middle cerebral artery (*yellow arrow*), which was not evident in 2D-DSA.

specificity, PPV, NPV, and diagnostic accuracy for detecting aneurysms in different locations between the 2 cerebral CTA protocols (all, $P > .05$).

From a total of 14 false-negative aneurysms (Fig 3), 12 aneurysms were <3 mm in diameter ($n = 8$ in group A, $n = 4$ in group B). The remaining 2 aneurysms with sizes of 5 and 7 mm were missed in group A. Of the 14 false-negative aneurysms, 10 aneurysms were located in anterior circulation arteries ($n = 8$ in group A, $n = 2$ in group B) and 4 aneurysms were located in posterior cerebral arteries ($n = 2$ in each group).

Of the 6 false-positive aneurysms (Fig 4), 4 aneurysms ($n = 2$ in each group) were <3 mm and 2 aneurysms ($n = 1$ for each group) were 3–8 mm. Three of the reported false-positive aneurysms ($n = 1$ for group A, $n = 2$ for group B) were located in the anterior circulation arteries, while the remaining 3 ($n = 2$ for group A, $n = 1$ for group B) were located in the posterior circulation arteries.

### *Radiation Dose*

The mean volume CT dose index, DLP, and ED of groups A and B are presented in On-line Table 5. The mean volume CT dose index, DLP, and ED of group A were 7.0 ± 0.4 mGy, 136.7 ± 8.8 mGy × cm, and 0.3 ± 0.0 mSv, respectively; for group B, these values were 25.9 ± 2.0 mGy, 507 ± 44.7 mGy × cm, and 1.1 ± 0.1 mSv, respectively. The volume CT dose index, DLP, and ED in group A were reduced by approximately 73.0%, 73.0%, and 72.7% compared with group B.

## DISCUSSION

Multidetector row CTA has been widely used to detect intracranial aneurysms due to its high diagnostic accuracy and image quality. However, radiation exposure and contrast material-induced nephropathy caused by CTA have received extensive atten-

tion. Currently, technical progress such as high-pitch technology, tube voltage, and tube current reduction enable performing cerebral CTA with ever lower radiation dose and contrast media volumes while maintaining image quality. This prospective study, conducted in a sizeable patient population with randomization, demonstrates that a low tube voltage, low contrast agent cerebral CTA protocol shows the same sensitivity and specificity as the standard protocol for detecting intracranial aneurysms compared with 3D-DSA as a reference standard. Cerebral CTA with 80 kVp/30 mL could reduce the effective radiation dose by approximately 73% and contrast agent volume by 50% without compromising diagnostic yield.

Our findings are in agreement with the results of previous investigations showing that lowering the tube voltage can reduce the effective dose without affecting diagnostic accuracy and image quality.[8,11,15] In 1 study, for example, no significant difference was found in the diagnostic accuracy between low-tube-voltage (80 kVp) and conventional-tube-voltage (120 kVp) CTA protocols in 48 patients.[11] In addition, low-tube voltage CTA also showed high sensitivity (75%) and specificity (100%) for detecting small aneurysms of <3 mm. In a recent study on 294 patients with spontaneous subarachnoid hemorrhage, 100-kVp cerebral CTA provided a high detection rate of 76.9% (10/13) for small aneurysms (< 3 mm), consistent with the results of our 120-kVp CTA protocol.[12] However, the effective dose of 100-kVp protocol was only reduced by 35.4% compared with our 120-kVp protocol. The application of dose-reduction strategies such as lower tube voltage or current has been reported to cause a trade-off in decreased image quality.[21,22] However, many technologic advances in CT techniques, such as iterative reconstruction, have been demonstrated to markedly improve the performance of low-dose CT acquisition.[23,24] Additionally, lowering tube voltage enhances the contrast attenuation in target vessels, thus maintaining a diagnostic CNR. As observed in our study, the mean image noise of the 80-kVp CTA protocol was statistically higher than that of the 120-kVp protocol; however, the image quality of the 80-kVp CTA protocol did not decrease despite the increase in noise.

Unlike the above-mentioned studies, our study used a double low-dose cerebral CTA (80-kVp tube voltage and 30-mL contrast agent) protocol in a relatively large group of patients, with a 73% reduction in the effective radiation dose. We found that the diagnostic accuracy of aneurysm detection of this double low-dose CTA protocol was identical to that of the conventional CTA protocol, even for small aneurysms (<3 mm). In addition, our study showed the high negative predictive value of the double low-dose CTA protocol for intracranial aneurysm detection based on a per-patient basis, which indicated that a negative finding of this double low-dose CTA protocol can reliably rule out intracranial aneurysms in the patients with subarachnoid hemorrhage. These observations suggest that an 80-kVp/30-mL cerebral CTA protocol may be suitable for intracranial aneurysm detection in clinical practice.

The double low-dose protocol showed a reduction in sensitivity for the detection of small aneurysms (<3 mm) in comparison with the standard protocol. Of all the 14 false-negative aneurysms, 12 were <3 mm. In our study, small aneurysms were not well-identified, mostly due to smaller size or infundibular dilation. There were still 7 undetected aneurysms, despite repetitive comparison between cerebral CTA and DSA. These aneurysms were either too small or were located overlying the bone structures, causing the missed diagnoses. Moreover, threshold selection will have an effect on the visualization of small aneurysms with the use of volume-rendering to reformat images. In addition, 10 of the 14 false-negative aneurysms were in 7 patients with multiple aneurysms, in which the chances of overlooking a small dilation are significantly higher. Additionally, satisfaction of searching intracranial aneurysms in patients with multiple aneurysms is also an important source of interpretation error.

Three of the false-positive findings were diagnosed by 3D-DSA as infundibular dilations at the origin of the posterior communicating artery. This finding reflects a well-known pitfall of cerebral CTA, namely the difficulty in distinguishing an infundibular dilation from a true aneurysm at this level unless the vessel emerging at the infundibular apex can be found.[25]

Our study has some limitations. First, the 2 CTA protocols in our study were not compared intraindividually; this omission may have introduced some bias. In this study, no statistical difference was found in the diagnostic image quality between the double low-dose CTA group and the conventional CTA group. Second, significantly higher image noise in the double low-dose CTA group was observed. This finding is explained by the application of standard filtered back-projection as a reconstruction technique instead of the more advanced iterative reconstruction, which was not available on the scanner used for this study. Iterative reconstruction is regarded as an effective technology for improving image quality by reducing image noise,[26-28] with a CNR reduction of up to 13%. Our CTA protocol also would likely benefit from the application of iterative reconstruction techniques and the predicted increase in overall image quality. Third, false-negatives with our double low-dose CTA protocol deserve special attention and careful interpretation because they are potentially lethal and subsequent DSA examination would result in additional contrast and radiation, especially for the CTA studies with false-negative findings; however, these results did not affect the diagnostic accuracy on a per-patient basis in our study. Of 10 missed aneurysms with the double low CTA protocol, 6 occurred in 3 patients with multiple ($n \geq 3$) aneurysms. Conventionally, DSA would be performed once there was a positive finding on CTA in patients with suspected aneurysms. Thus, although our protocol missed some small aneurysms in patients with multiple aneurysms, the false-negative results did not ultimately affect patient management compared with the traditional CTA protocol. Finally, the diagnostic accuracy of the double low-dose protocol for detecting small aneurysms of <5 mm needs to be further confirmed in even larger studies.

## CONCLUSIONS

An 80-kVp cerebral CTA with 30 mL of contrast agent has the same sensitivity and specificity for detecting intracranial aneurysms compared with a conventional cerebral CTA protocol. Furthermore, this protocol substantially reduces the radiation dose and contrast agent volume.

Disclosures: U. Joseph Schoepf—*UNRELATED*: *Consultancy*: Guerbet; *Grants/Grants Pending*: Astellas Pharma,* Bayer Schering Pharma,* Bracco,* GE Healthcare,* Medrad,* Siemens*; *Royalties*: Springer, Meetings-by-Mail. *Money paid to the institution.

## REFERENCES


1. van Gijn J, Kerr RS, Rinkel GJ. **Subarachnoid haemorrhage.** *Lancet* 2007;369:306–18 CrossRef Medline
2. Vlak MH, Algra A, Brandenburg R, et al. **Prevalence of unruptured intracranial aneurysms, with emphasis on sex, age, comorbidity, country, and time period: a systematic review and meta-analysis.** *Lancet Neurol* 2011;10:626–36 CrossRef Medline
3. Rabinstein AA, Lanzino G, Wijdicks EF. **Multidisciplinary management and emerging therapeutic strategies in aneurysmal subarachnoid haemorrhage.** *Lancet Neurol* 2010;9:504–19 CrossRef Medline
4. Lu L, Zhang LJ, Poon CS, et al. **Digital subtraction CT angiography for detection of intracranial aneurysms: comparison with three-dimensional digital subtraction angiography.** *Radiology* 2012;262:605–12 CrossRef Medline
5. Moran CJ. **Aneurysmal subarachnoid hemorrhage: DSA versus CT angiography—is the answer available?** *Radiology* 2011;258:15–17 CrossRef Medline
6. Chen W, Xing W, Peng Y, et al. **Cerebral aneurysms: accuracy of 320-detector row nonsubtracted and subtracted volumetric CT angiography for diagnosis.** *Radiology* 2013;269:841–49 CrossRef Medline
7. Westerlaan HE, van Dijk J, Jansen-van der Weide MC, et al. **Intracranial aneurysms in patients with subarachnoid hemorrhage: CT angiography as a primary examination tool for diagnosis—systematic review and meta-analysis.** *Radiology* 2011;258:134–45 CrossRef Medline
8. Luo S, Zhang LJ, Meinel FG, et al. **Low tube voltage and low contrast material volume cerebral CT angiography.** *Eur Radiol* 2014;24:1677–85 CrossRef Medline
9. Millon D, Derelle AL, Omoumi P, et al. **Nontraumatic subarachnoid hemorrhage management: evaluation with reduced iodine volume at CT angiography.** *Radiology* 2012;264:203–09 CrossRef Medline
10. Ramgren B, Björkman-Burtscher IM, Holtås S, et al. **CT angiography of intracranial arterial vessels: impact of tube voltage and contrast media concentration on image quality.** *Acta Radiol* 2012;53:929–34 CrossRef Medline
11. Sun G, Ding J, Lu Y, et al. **Comparison of standard-and low-tube voltage 320-detector row volume CT angiography in detection of intracranial aneurysms with digital subtraction angiography as gold standard.** *Acad Radiol* 2012;19:281–88 CrossRef Medline
12. Tang K, Li R, Lin J, et al. **The value of cerebral CT angiography with low tube voltage in detection of intracranial aneurysms.** *Biomed Res Int* 2015;2015:876796 CrossRef Medline
13. Cho ES, Chung TS, Oh DK, et al. **Cerebral computed tomography angiography using a low tube voltage (80 kVp) and a moderate concentration of iodine contrast material: a quantitative and qualitative comparison with conventional computed tomography angiography.** *Invest Radiol* 2012;47:142–47 CrossRef Medline
14. Furtado A, Adraktas D, Brasic N, et al. **The triple rule-out for acute ischemic stroke: imaging the brain, carotid arteries, aorta, and heart.** *AJNR Am J Neuroradiol* 2010;31:1290–96 CrossRef Medline
15. Chen GZ, Zhang LJ, Schoepf UJ, et al. **Radiation dose and image quality of 70 kVp cerebral CT angiography with optimized sinogram-affirmed iterative reconstruction: comparison with 120 kVp cerebral CT angiography.** *Eur Radiol* 2015;25:1453–63 CrossRef Medline
16. Söderman M, Holmin S, Andersson T, et al. **Image noise reduction algorithm for digital subtraction angiography: clinical results.** *Radiology* 2013;269:553–60 CrossRef Medline
17. Szucs-Farkas Z, Bensler S, Torrente JC, et al. **Nonlinear three-dimensional noise filter with low-dose CT angiography: effect on the detection of small high-contrast objects in a phantom model.** *Radiology* 2011;258:261–69 CrossRef Medline
18. Zhang WL, Li M, Zhang B, et al. **CT angiography of the head-and-neck vessels acquired with low tube voltage, low iodine, and iterative image reconstruction: clinical evaluation of radiation dose and image quality.** *PLoS One* 2013;8:e81486 CrossRef Medline
19. McCollough CH, Primak AN, Braun N, et al. **Strategies for reducing radiation dose in CT.** *Radiol Clin North Am* 2009;47:27–40 CrossRef Medline
20. Zhao H, Wang J, Liu X, et al. **Assessment of carotid artery atherosclerotic disease by using three-dimensional fast black-blood MR imaging: comparison with DSA.** *Radiology* 2015;274:508–16 CrossRef Medline
21. Smith AB, Dillon WP, Gould R, et al. **Radiation dose reduction strategies for neuroradiology CT protocols.** *AJNR Am J Neuroradiol* 2007;28:1628–32 CrossRef Medline
22. Graser A, Wintersperger BJ, Suess C, et al. **Dose reduction and image quality in MDCT colonography using tube current modulation.** *AJR Am J Roentgenol* 2006;187:695–701 CrossRef Medline
23. Hérin E, Gardavaud F, Chiaradia M, et al. **Use of Model-Based Iterative Reconstruction (MBIR) in reduced-dose CT for routine follow-up of patients with malignant lymphoma: dose savings, image quality and phantom study.** *Eur Radiol* 2015;25:2362–70 CrossRef Medline
24. Geyer LL, Schoepf UJ, Meinel FG, et al. **State of the art: iterative CT reconstruction techniques.** *Radiology* 2015;276:339–57 CrossRef Medline
25. Pereira BJA, Holanda VM, de Holanda CVM, et al. **Intracranial aneurysm arising from infundibular dilation.** *BMJ Case Rep* 2013;2013:pii: bcr2013200115 CrossRef Medline
26. Donmez H, Serifov E, Kahriman G, et al. **Comparison of 16-row multislice CT angiography with conventional angiography for detection and evaluation of intracranial aneurysms.** *Eur J Radiol* 2011;80:455–61 CrossRef Medline
27. Korn A, Bender B, Fenchel M, et al. **Sinogram affirmed iterative reconstruction in head CT: improvement of objective and subjective image quality with concomitant radiation dose reduction.** *Eur J Radiol* 2013;82:1431–35 CrossRef Medline
28. Moscariello A, Takx RA, Schoepf UJ, et al. **Coronary CT angiography: image quality, diagnostic accuracy, and potential for radiation dose reduction using a novel iterative image reconstruction technique—comparison with traditional filtered back projection.** *Eur Radiol* 2011;21:2130–38 CrossRef Medline

# Effect of CTA Tube Current on Spot Sign Detection and Accuracy for Prediction of Intracerebral Hemorrhage Expansion

A. Morotti, J.M. Romero, M.J. Jessel, H.B. Brouwers, R. Gupta, K. Schwab, A. Vashkevich, A. Ayres, C.D. Anderson, M.E. Gurol, A. Viswanathan, S.M. Greenberg, J. Rosand, and J.N. Goldstein

## ABSTRACT

**BACKGROUND AND PURPOSE:** Reduction of CT tube current is an effective strategy to minimize radiation load. However, tube current is also a major determinant of image quality. We investigated the impact of CTA tube current on spot sign detection and diagnostic performance for intracerebral hemorrhage expansion.

**MATERIALS AND METHODS:** We retrospectively analyzed a prospectively collected cohort of consecutive patients with primary intracerebral hemorrhage from January 2001 to April 2015 who underwent CTA. The study population was divided into 2 groups according to the median CTA tube current level: low current (<350 mA) and high current (≥350 mA). CTA first-pass readings for spot sign presence were independently analyzed by 2 readers. Baseline and follow-up hematoma volumes were assessed by semiautomated computer-assisted volumetric analysis. Sensitivity, specificity, positive and negative predictive values, and accuracy of spot sign in predicting hematoma expansion were calculated.

**RESULTS:** This study included 709 patients (288 and 421 in the low- and high-current groups, respectively). A higher proportion of low-current scans identified at least 1 spot sign (20.8% versus 14.7%, $P = .034$), but hematoma expansion frequency was similar in the 2 groups (18.4% versus 16.2%, $P = .434$). Sensitivity and positive and negative predictive values were not significantly different between the 2 groups. Conversely, high-current scans showed superior specificity (91% versus 84%, $P = .015$) and overall accuracy (84% versus 77%, $P = .038$).

**CONCLUSIONS:** CTA obtained at high levels of tube current showed better diagnostic accuracy for prediction of hematoma expansion by using spot sign. These findings may have implications for future studies using the CTA spot sign to predict hematoma expansion for clinical trials.

**ABBREVIATIONS:** HmA = high current; ICH = intracerebral hemorrhage; LmA = low current

The CTA spot sign is a validated predictor of expansion in intracerebral hemorrhage (ICH),[1,2] but the optimal acquisition protocol for spot sign identification is still unknown. There is great heterogeneity in CTA imaging parameters across centers, especially in CTA tube current, with reported milliampere (mA) values ranging from 140 to 770.[3-7] Furthermore, CT is a considerable source of radiation exposure,[8] and concerns remain regarding minimization of radiation delivery to patients who have experienced an acute stroke.[9] Tube current reduction is a common and effective strategy to minimize the global radiation exposure.[10] However, this parameter is also a major determinant of image noise, and excessive reduction of the tube current level might negatively affect image quality.[11] Defining the optimal CTA technical setting that predicts hematoma expansion might provide useful information for future clinical trials involving patients with ICH. Therefore, the main aim of our study was to investigate the influence of different CTA tube current levels on spot sign detection and accuracy in predicting ICH expansion.

## MATERIALS AND METHODS

### *Patient Selection*

Massachusetts General Hospital institutional review board approval was received for all aspects of our study, and all the procedures comply with the Health Insurance Portability and Accountability Act. Informed written or verbal consent was obtained from patients or family members or waived by the institutional review board. We performed a single-center, retrospective analysis of a

Received January 22, 2016; accepted after revision March 17.

From the Department of Clinical and Experimental Sciences (A.M.), Neurology Clinic, University of Brescia, Brescia, Italy; Neuroradiology Service, Department of Radiology (J.M.R., R.G.), J.P. Kistler Stroke Research Center (A.M., M.J.J., K.S., A. Vashkevich, A.A., C.D.A., M.E.G., A. Viswanathan, S.M.G., J.R., J.N.G.), Division of Neurocritical Care and Emergency Neurology (J.R., J.N.G.), and Department of Emergency Medicine (J.N.G.), Massachusetts General Hospital, Harvard Medical School, Boston, Massachusetts; and Department of Neurosurgery (H.B.B.), Brain Center Rudolf Magnus, University Medical Center, Utrecht, the Netherlands.

This study was supported by grants 5R01NS073344, K23AG02872605, K23 NS086873, and R01NS059727 from the National Institute of Neurological Disorders and Stroke, a component of the National Institutes of Health.

Please address correspondence to Andrea Morotti, MD, Massachusetts General Hospital, J.P. Kistler Stroke Research Center, 175 Cambridge St, Suite 300, Boston, MA 02114; e-mail: amorotti@mgh.harvard.edu, a.morotti@ymail.com

Indicates open access to non-subscribers at www.ajnr.org

http://dx.doi.org/10.3174/ajnr.A4810

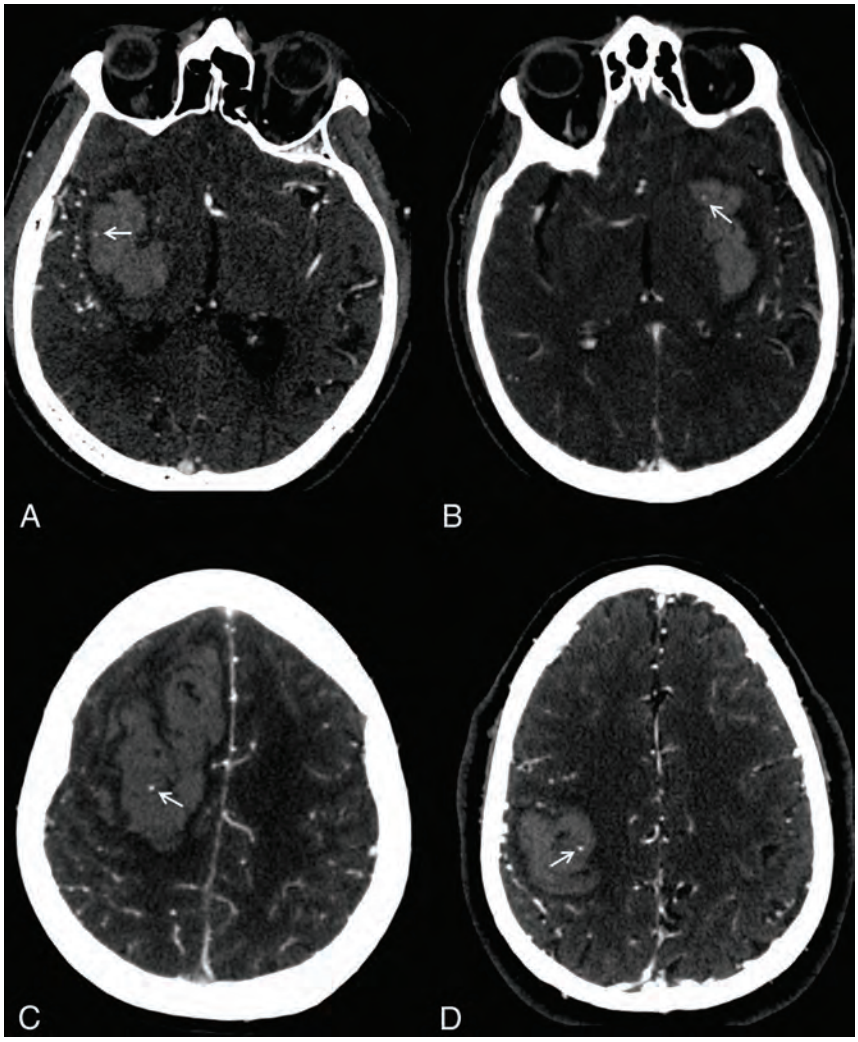


**FIG 1.** Appearance of the spot sign (*arrows*) on CTA images obtained at low tube current (*A*, 170 mA; *B*, 235 mA) versus high tube current (*C*, 350 mA; *D*, 350 mA). All images were acquired on the same scanner at 120 kVp.

previously described prospectively collected cohort of consecutive patients with primary ICH.[12,13]

Patients were included if they presented from January 2001 to April 2015 with primary ICH and underwent CTA within 48 hours from symptom onset and follow-up NCCT. Patient exclusion criteria were 1) the presence of a vascular lesion or neoplastic lesion determined or suspected to be the cause of the ICH, 2) surgical evacuation of the hematoma, 3) traumatic intracranial bleeding, 4) absence of axial thin-section CTA images (section thickness, 0.625–1.25 mm), and 5) unknown CTA acquisition protocol.

Both CTA tube current and voltage are important determinants of image quality.[11] However, although there is great variability in the reported current values for CTA acquisition, this is not the case for voltage.[3-7] Indeed, in our cohort and in most of the previous spot sign studies, most CTA images for spot sign detection were acquired at a tube voltage level equal or above 120 kVp (peak).[3-7] For this reason, we decided to focus our analysis on the effects of tube current on diagnostic performance. Therefore, patients with CTAs obtained at low tube voltage level ($<$ 120 kVp) were excluded from the final analysis.

### *Clinical Variables*

Clinical information was collected from patients, families, or the medical record and included age, sex, history of hypertension, and treatment with antithrombotic medications, including antiplatelet drugs or anticoagulant therapy. Time from symptom onset to baseline NCCT and CTA was also collected.

### *Image Acquisition*

Axial NCCT examinations were obtained with 5-mm section thickness reconstruction. CTA was performed as part of standard clinical care by scanning from the skull base to the vertex by using an axial technique, 0.5 section pitch, 1.25-mm collimation, and 120–140 kVp. Previous publications of an overlapping cohort described that CTA scans at our institution were typically acquired at either 235 or 350 mA.[14,15] On detailed review, we found that a wide milliampere range (80–630) was used in clinical practice. Intravenous iodinated contrast material (65–85 mL) was administered by power injector with an infusion rate of 4–5 mL/s with SmartPrep (GE Healthcare, Milwaukee, Wisconsin), a semiautomatic contrast bolus triggering technique. The contrast materials used were Isovue 370 and Isovue 300 (Bracco, Princeton, New Jersey). Volume CT dose index ranged from 34.7–89.4 mGy (mean, 60.9; SD, 16.6) and dose-length product ranged from 628.7–3763.4 mGy $\times$ cm (mean, 1923.6; SD, 957.5).

### *Image Analysis*

The patients included in the study were divided into 2 groups: low-current ($<$350 mA [LmA]) and high-current ($\geq$350 mA [HmA]) scans. This cutoff was determined according to the median mA value. Illustrative spot sign–positive CTA images acquired at LmA versus HmA are shown in Fig 1.

Baseline NCCT scans were reviewed to determine the ICH location (deep, lobar, or infratentorial) and presence of associated intraventricular hemorrhage. Baseline and follow-up ICH volumes were calculated with semiautomated computer-assisted volumetric analysis (Analyze 11.0 software; AnalyzeDirect, Overland Park, Kansas), and hematoma expansion was defined a priori as a total volume increase greater than 6 mL or a relative volume increase greater than 30% from the baseline volume as previously described.[5,16] For spot sign identification, first-pass CTA images were independently reviewed by 2 experienced readers (A.M., M.J.J.) blinded to CTA acquisition protocol, clinical information, and results of the follow-up NCCT. Any disagreement in reader interpretation was adjudicated by consensus agreement under the

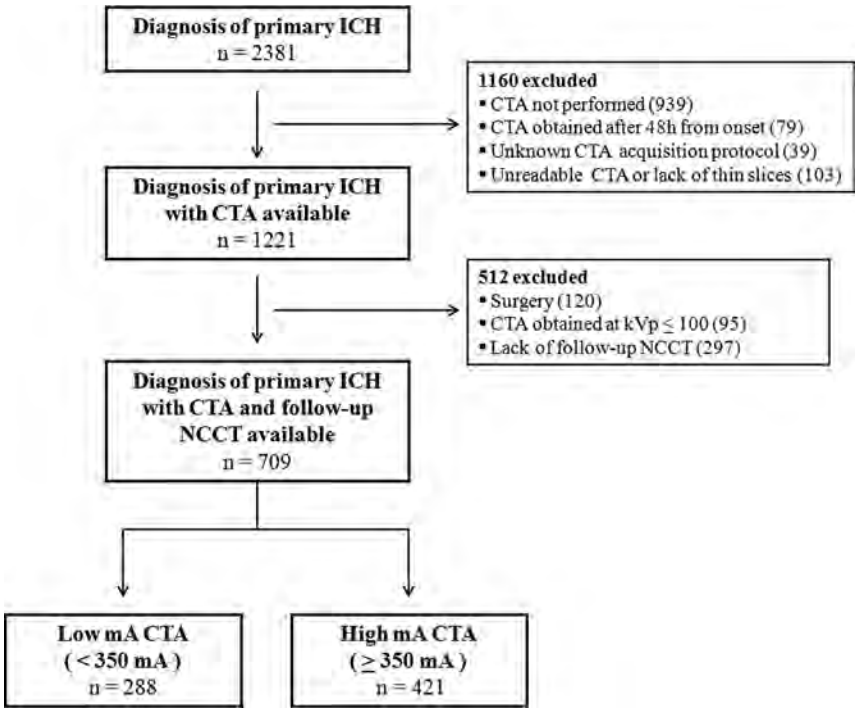


**FIG 2.** Cohort selection flowchart.

**Table 1: Baseline study cohort characteristics**

| Parameters | |
|---|---|
| No. of patients | 709 |
| Age (median) (IQR) (y) | 74 (62–82) |
| Sex, male (*n*) (%) | 396 (55.9) |
| History of hypertension (*n*) (%) | 553 (78.0) |
| Antiplatelet treatment (*n*) (%) | 314 (44.3) |
| Anticoagulant treatment (*n*) (%) | 132 (18.6) |
| ICH location (*n*) (%) | |
| Lobar | 346 (48.8) |
| Deep | 299 (42.2) |
| Infratentorial | 64 (9.0) |
| IVH presence (*n*) (%) | 312 (44.0) |
| Baseline ICH volume (median) (IQR) (mL) | 17 (6–39) |
| Baseline IVH volume (median) (IQR) (mL) | 0 (0–4) |
| Time from symptom onset to CTA (median) (IQR) (h) | 5 (3–10) |
| CTA spot sign presence (*n*) (%) | 122 (17.2) |
| ICH expansion (*n*) (%) | 121 (17.1) |

**Note:**—IQR indicates interquartile range; IVH, intraventricular hemorrhage.

supervision of an expert neuroradiologist (J.M.R.). Axial CTA source images were reviewed in "spot windows" (width 200, level 110) as previously described by using the following radiologic criteria for spot sign identification: 1) ≥ 1 focus of contrast pooling within the ICH, 2) an attenuation ≥ 120 HU, 3) discontinuous from normal or abnormal vasculature adjacent to the hematoma, and 4) of any size and morphology.[16]

### *Statistical Analysis*

All statistical analyses were performed with SPSS Version 21 (IBM, Armonk, New York). Discrete variables are summarized as count (%). Normally distributed continuous variables are summarized as mean (SD) and continuous variables with nonnormal distribution are expressed as median (interquartile range). Differences in the 2 study groups were examined with the $\chi^2$ test for comparison between categoric variables, *t* test for continuous variables with normal distribution, and Mann-Whitney *U* test for continuous variables with nonnormal distribution. Interrater and intrarater reliability for the identification of any spot sign were determined by using the Cohen $\kappa$ statistic. Subsequently, we calculated and compared sensitivity, specificity, positive predictive value, negative predictive value, and accuracy for hematoma expansion. All 95% CIs were obtained by exact binomial methods. Comparison of the sensitivity, specificity, positive predictive value, negative predictive value, and accuracy percentages between LmA and HmA was performed by using the $\chi^2$ test. A $P$ value $< .05$ was considered statistically significant.

## RESULTS

A total of 2381 consecutive patients with primary ICH were screened. After application of the eligibility and exclusion criteria, 709 patients were available for the analyses (Fig 2). There were 288 patients included in the LmA group and 421 included in the HmA group. The baseline characteristics of the study population are listed in Table 1. Hematoma expansion occurred in 121 (17.1%) patients, and at least 1 spot sign was detected in 122 (17.2%) scans. Interrater and intrarater reliability measures for spot sign detection were excellent ($\kappa$ = 0.85 and $\kappa > 0.90$, respectively). Median time from symptom onset to CTA was 5 hours (interquartile range 3–10 hours). Table 2 illustrates the comparison between LmA and HmA demographic, clinical, and imaging characteristics. We observed a higher number of spot sign positive scans in the LmA group compared with the HmA group (60/288 [20.8%] versus 62/421 [14.7%], $P = .034$), whereas no differences were noted in the frequency of hematoma expansion (53/288 [18.4%] versus 68/421 [16.2%], $P = .434$).

The diagnostic performance of spot sign in predicting ICH expansion stratified by tube current levels is shown in Table 3. The LmA setting was associated with a higher frequency of false-positive cases (36/288 [12.5%] versus 31/421 [7.4%], $P = .022$) and the false-negative proportion was similar between the 2 groups (29/288 [10.1%] versus 37/421 [8.9%], $P = .564$). At HmA level, spot sign showed significantly superior specificity than at LmA level (91% versus 84%, $P = .015$). The overall accuracy was superior in HmA scans (84% versus 77%, $P = .038$).

Because there are multiple definitions of ICH expansion, we repeated the analyses using another commonly used definition: absolute growth > 12.5 mL or relative growth > 33%.[17] We confirmed the superior specificity (91% versus 83%, $P = .004$) and

**Table 2: Patient characteristics stratified by tube current**

| Characteristic | LmA | HmA | *P* Value |
|---|---|---|---|
| No. of patients | 288 | 421 | |
| Age, median (IQR) (y) | 74 (62–82) | 73 (62–82) | .904 |
| Sex, male (*n*) (%) | 163 (56.6) | 233 (55.3) | .741 |
| History of hypertension (*n*) (%) | 219 (76.0) | 334 (79.3) | .299 |
| Antiplatelet treatment (*n*) (%) | 123 (42.7) | 191 (45.4) | .484 |
| Anticoagulant treatment (*n*) (%) | 49 (17.0) | 83 (19.7) | .364 |
| Admission INR (median) (IQR) | 1.03 (1.00–1.20) | 1.10 (1.00–1.20) | .331 |
| ICH location | | | .227 |
| Lobar | 130 (45.1) | 216 (51.3) | |
| Deep | 128 (44.4) | 171 (40.6) | |
| Infratentorial | 30 (10.4) | 34 (8.1) | |
| IVH presence (*n*) (%) | 138 (47.9) | 174 (41.3) | .083 |
| Baseline ICH volume (median) (IQR) (mL) | 18 (6–46) | 15 (6–36) | .018 |
| Baseline IVH volume (median) (IQR) (mL) | 0 (0–7) | 0 (0–3) | .074 |
| Time from symptom onset to CTA (median) (IQR) (h) | 5 (3–10) | 5 (3–10) | .342 |
| CTA spot sign presence (*n*) (%) | 60 (20.8) | 62 (14.7) | .034 |
| ICH expansion (*n*) (%) | 53 (18.4) | 68 (16.2) | .434 |
| $CTDI_{vol}$ (mean ± SD) (mGy) | 43.3 ± 8.9 | 71.4 ± 9.8 | <.001 |
| DLP (mean ± SD) (mGy × cm) | 1258.3 ± 618.3 | 2342.1 ± 864.7 | <.001 |

**Note:**—$CTDI_{vol}$ indicates volume CT dose index; DLP, dose-length product; INR, international normalized ratio; IQR, interquartile range; IVH, intraventricular hemorrhage.

**Table 3: Spot sign prediction of hematoma expansion[a]**

| Variable | LmA | HmA | *P* Value |
|---|---|---|---|
| No. of patients | 288 | 421 | |
| Sensitivity (95% CI) | 0.45 (0.32–0.59) | 0.45 (0.34–0.58) | .973 |
| Specificity (95% CI) | 0.84 (0.79–0.89) | 0.91 (0.88–0.94) | .015 |
| Positive predictive value (95% CI) | 0.40 (0.28–0.53) | 0.50 (0.37–0.63) | .267 |
| Negative predictive value (95% CI) | 0.87 (0.82–0.91) | 0.90 (0.86–0.93) | .367 |
| Accuracy | 0.77 | 0.84 | .038 |

[a] Significant expansion was defined as >30 % or >6 mL increase from baseline hematoma volume.

accuracy (84% versus 76%, $P = .008$) of HmA scans with no significant differences in sensitivity, positive predictive value, and negative predictive value (all $P$ values $> .1$).

## DISCUSSION

This study investigated the relationship between CTA tube current, spot sign detection, and diagnostic accuracy for predicting ICH expansion. We found that the tube current level had a relevant influence on spot sign detection and diagnostic accuracy of CTA spot sign. In particular, CTA acquired with high tube current levels (≥350 mA) showed higher specificity.

Our results are consistent with previous findings on the relationship between CT tube current, radiation delivery, and image quality. CTA is a commonly available tool for the emergency work-up of patients with ICH, but additional radiation exposure is one of the main drawbacks of this technique.[18] CT tube current is directly associated with radiation exposure in a linear, dose-dependent relationship,[11,19] and as expected, we observed a significantly higher radiation dose in the HmA group. Decreasing CT tube current results in increased image noise and inferior quality of CTA images.[19,20]

In our study, the presence of at least 1 spot sign was significantly more frequent in the LmA group. Baseline hematoma volume is a strong predictor of spot sign presence[21] and hematoma expansion.[13] Therefore, this finding may simply reflect that patients in the LmA group had higher baseline ICH volumes. Another possible explanation is the well-known inverse relationship between image noise and CT tube current.[10,11,22] Severe background noise in the LmA group might have led to detection of false spot signs because of increased graininess of the scan. Indeed, despite the higher rate of spot sign detection, the LmA setting was not associated with a significant gain in sensitivity comparing the 2 current settings. Conversely, the specificity and overall diagnostic accuracy were significantly better in the HmA group. The observed difference between the diagnostic performances of the 2 current settings may be driven by the higher frequency of false-positive cases in the LmA group. In other words, the fact that sensitivity was not affected suggests that if contrast extravasates into the hematoma, it can be successfully detected even with LmA imaging. However, HmA may optimize the ability to distinguish such contrast from natural heterogeneity of the hematoma and avoid the detection of false spot signs. It may be that dual-energy CT can help address this issue by distinguishing contrast from blood in a more robust way.[23,24]

Several CTA acquisition parameters can be varied to reduce the radiation dose without compromising the image quality.[25] Our results suggest that if the goal of CTA is to detect spot signs, such dose reduction comes at a cost.

CTA is widely used in the work-up of ICH,[26] and the CTA spot sign is a promising marker for early identification of patients with ICH who have the greatest opportunity to benefit from anti-expansion therapies.[27,28] Therefore, patients with a false-positive spot sign may be exposed to potentially harmful anti-expansion hemostatic treatments despite having a low probability of hematoma expansion.

The only multicenter study focused on spot sign as a predictor of hematoma expansion[1] had inferior diagnostic accuracy compared with single-center studies.[5,16,17] Heterogeneity in the CTA acquisition protocols and image quality across various institutions might have accounted for these differences. The results of our study and the above-mentioned issues suggest the need to develop a standardized CTA acquisition protocol to optimize spot sign detection in patients with ICH.

Some limitations of the present study should be mentioned. First, this was a nonrandomized, single-center, prospective observational study with retrospective analysis of the data. In addition, the number of patients in the LmA group was relatively small. Therefore, it is best interpreted as hypothesis generating, and the findings need to be confirmed by future stud-

ies. Second, the most relevant change in our institution's CTA protocol was the introduction of 90-second-delayed CTA images. Such images are known to capture additional spot signs,[29] and it may be that the influence of current on spot sign detection is different when such images are taken into account. Third, image noise and quality were not objectively measured, so we can only speculate that image graininess and increased background noise are the mechanisms responsible for lower accuracy observed in the LmA group. Fourth, CTA tube current is not the only determinant of image quality, and other factors not considered in this study, such as different scanner models and contrast types, also may influence diagnostic accuracy. Finally, our study was designed to explore the possibility that excessive lowering of tube current reduces the diagnostic accuracy of spot sign rather than to define the optimal balance between radiation exposure, image quality, and clinical outcome. Therefore, we are not able to evaluate the clinical impact of improving CTA specificity and accuracy.

## CONCLUSIONS

CTA acquisition protocol influences spot sign detection and accuracy in predicting hematoma expansion. If confirmed, our findings may have important implications for future studies using the CTA spot sign to predict hematoma expansion. Further investigations are needed to establish the optimal balance between radiation delivery, image quality, and diagnostic performance.

Disclosures: Andrea Morotti—*RELATED*: *Grant*: National Institute of Neurological Disorders and Stroke (5R01NS073344).* Anastasia Vashkevich—*RELATED*: *Grant*: National Institutes of Health.* Christopher Anderson—*RELATED*: *Grant*: National Institute of Neurological Disorders and Stroke (K23 NS086873)*; *UNRELATED*: *Grants/Grants Pending*: National Institute of Neurological Disorders and Stroke (K23 NS086873).* Anand Viswanathan—*RELATED*: *Grant*: National Institutes of Health (R01AG047975-02, K23 AG028726-05)*; *UNRELATED*: *Consultancy*: Roche Pharmaceuticals (served on Data Safety Monitoring Board as a consultant). Jonathan Rosand—*RELATED*: *Grant*: National Institutes of Health*; *UNRELATED*: *Grants/Grants Pending*: National Institutes of Health.* Joshua Goldstein—*RELATED*: *Grant*: National Institute of Neurological Disorders and Stroke*; *Support for Travel to Meetings for the Study or Other Purposes*: National Institute of Neurological Disorders and Stroke*; *UNRELATED*: *Consultancy*: CSL Behring, Boehringer Ingelheim; *Grants/Grants Pending*: National Institute of Neurological Disorders and Stroke.* *Money paid to the institution.

## REFERENCES

1. Demchuk AM, Dowlatshahi D, Rodriguez-Luna D, et al. **Prediction of haematoma growth and outcome in patients with intracerebral haemorrhage using the CT-angiography spot sign (PREDICT): a prospective observational study.** *Lancet Neurol* 2012;11:307–14 CrossRef Medline
2. Brouwers HB, Goldstein JN, Romero JM, et al. **Clinical applications of the computed tomography angiography spot sign in acute intracerebral hemorrhage: a review.** *Stroke* 2012;43:3427–32 CrossRef Medline
3. Havsteen I, Ovesen C, Christensen AF, et al. **Showing no spot sign is a strong predictor of independent living after intracerebral haemorrhage.** *Cerebrovasc Dis* 2014;37:164–70 CrossRef Medline
4. Huynh TJ, Demchuk AM, Dowlatshahi D, et al. **Spot sign number is the most important spot sign characteristic for predicting hematoma expansion using first-pass computed tomography angiography: analysis from the PREDICT study.** *Stroke* 2013;44:972–77 CrossRef Medline
5. Wada R, Aviv RI, Fox AJ, et al. **CT angiography "spot sign" predicts hematoma expansion in acute intracerebral hemorrhage.** *Stroke* 2007;38:1257–62 CrossRef Medline
6. Romero JM, Brouwers HB, Lu J, et al. **Prospective validation of the computed tomographic angiography spot sign score for intracerebral hemorrhage.** *Stroke* 2013;44:3097–102 CrossRef Medline
7. Goldstein JN, Fazen LE, Snider R, et al. **Contrast extravasation on CT angiography predicts hematoma expansion in intracerebral hemorrhage.** *Neurology* 2007;68:889–94 CrossRef Medline
8. Brenner DJ, Hall EJ. **Computed tomography–an increasing source of radiation exposure.** *N Engl J Med* 2007;357:2277–84 CrossRef Medline
9. Mnyusiwalla A, Aviv RI, Symons SP. **Radiation dose from multidetector row CT imaging for acute stroke.** *Neuroradiology* 2009;51:635–40 CrossRef Medline
10. Cohnen M, Fischer H, Hamacher J, et al. **CT of the head by use of reduced current and kilovoltage: relationship between image quality and dose reduction.** *AJNR Am J Neuroradiol* 2000;21:1654–60 Medline
11. Smith AB, Dillon WP, Gould R, et al. **Radiation dose-reduction strategies for neuroradiology CT protocols.** *AJNR Am J Neuroradiol* 2007;28:1628–32 CrossRef Medline
12. Biffi A, Cortellini L, Nearnberg CM, et al. **Body mass index and etiology of intracerebral hemorrhage.** *Stroke* 2011;42:2526–30 CrossRef Medline
13. Brouwers HB, Chang Y, Falcone GJ, et al. **Predicting hematoma expansion after primary intracerebral hemorrhage.** *JAMA Neurol* 2014;71:158–64 CrossRef Medline
14. Delgado Almandoz JE, Yoo AJ, Stone MJ, et al. **The spot sign score in primary intracerebral hemorrhage identifies patients at highest risk of in-hospital mortality and poor outcome among survivors.** *Stroke* 2010;41:54–60 CrossRef Medline
15. Delgado Almandoz JE, Kelly HR, Schaefer PW, et al. **CT angiography spot sign predicts in-hospital mortality in patients with secondary intracerebral hemorrhage.** *J Neurointerv Surg* 2012;4:442–47 CrossRef Medline
16. Delgado Almandoz JE, Yoo AJ, Stone MJ, et al. **Systematic characterization of the computed tomography angiography spot sign in primary intracerebral hemorrhage identifies patients at highest risk for hematoma expansion: the spot sign score.** *Stroke* 2009;40:2994–3000 CrossRef Medline
17. Li N, Wang Y, Wang W, et al. **Contrast extravasation on computed tomography angiography predicts clinical outcome in primary intracerebral hemorrhage: a prospective study of 139 cases.** *Stroke* 2011;42:3441–46 CrossRef Medline
18. Macellari F, Paciaroni M, Agnelli G, et al. **Neuroimaging in intracerebral hemorrhage.** *Stroke* 2014;45:903–08 CrossRef Medline
19. Kumamaru KK, Hoppel BE, Mather RT, et al. **CT angiography: current technology and clinical use.** *Radiol Clin North Am* 2010;48:213–35 CrossRef Medline
20. Waaijer A, Prokop M, Velthuis BK, et al. **Circle of Willis at CT angiography: dose reduction and image quality–reducing tube voltage and increasing tube current settings.** *Radiology* 2007;242:832–39 CrossRef Medline
21. Radmanesh F, Falcone GJ, Anderson CD, et al. **Risk factors for computed tomography angiography spot sign in deep and lobar intracerebral hemorrhage are shared.** *Stroke* 2014;45:1833–35 CrossRef Medline
22. Solomon JB, Li X, Samei E. **Relating noise to image quality indicators in CT examinations with tube current modulation.** *AJR Am J Roentgenol* 2013;200:592–600 CrossRef Medline
23. Gupta R, Phan CM, Leidecker C, et al. **Evaluation of dual-energy CT for differentiating intracerebral hemorrhage from iodinated contrast material staining.** *Radiology* 2010;257:205–11 CrossRef Medline

24. Won SY, Schlunk F, Dinkel J, et al. **Imaging of contrast medium extravasation in anticoagulation-associated intracerebral hemorrhage with dual-energy computed tomography.** *Stroke* 2013;44:2883–90 CrossRef Medline
25. Raman SP, Mahesh M, Blasko RV, et al. **CT scan parameters and radiation dose: practical advice for radiologists.** *J Am Coll Radiol* 2013;10:840–46 CrossRef Medline
26. Khosravani H, Mayer SA, Demchuk A, et al. **Emergency noninvasive angiography for acute intracerebral hemorrhage.** *AJNR Am J Neuroradiol* 2013;34:1481–87 CrossRef
27. Goldstein J, Brouwers H, Romero J, et al. **SCORE-IT: the Spot Sign score in restricting ICH growth—an Atach-II ancillary study.** *J Vasc Interv Neurol* 2012;5:20–25
28. Meretoja A, Churilov L, Campbell BC, et al. **The spot sign and tranexamic acid on preventing ICH growth–AUStralasia Trial (STOP-AUST): protocol of a phase II randomized, placebo-controlled, double-blind, multicenter trial.** *Int J Stroke* 2014;9:519–24 CrossRef Medline
29. Ciura VA., Brouwers HB, Pizzolato R, et al. **Spot sign on 90-second delayed computed tomography angiography improves sensitivity for hematoma expansion and mortality: prospective study.** *Stroke* 2014;45:3293–97 CrossRef Medline

# Discordant Observation of Brain Injury by MRI and Malignant Electroencephalography Patterns in Comatose Survivors of Cardiac Arrest following Therapeutic Hypothermia

J.M. Mettenburg, V. Agarwal, M. Baldwin, and J.C. Rittenberger

## ABSTRACT

**BACKGROUND AND PURPOSE:** Malignant electroencephalography patterns are considered predictive of poor outcome in comatose survivors of cardiac arrest. We hypothesized that malignant patterns on electroencephalography are associated with evidence of more severe brain injury on MR imaging.

**MATERIALS AND METHODS:** Retrospective review of clinical, imaging, and electroencephalography data of 33 adult comatose survivors of cardiac arrest following therapeutic hypothermia was performed. Outcomes measured included discharge destination and survival. Imaging studies were visually scored for severity of brain injury. Mean whole-brain apparent diffusion coefficient and percentage of severely injured brain (ADC $< 700 \times 10^{-6}$ mm$^2$/s) were calculated. Continuous electroencephalographic interpretation was characterized as malignant or nonmalignant. Nonparametric tests were performed to assess the relationship of patient outcome, MR imaging, and electroencephalography patterns.

**RESULTS:** Subjects with anatomic evidence of diffuse brain injury were less likely to have malignant electroencephalography patterns. Subjects with malignant electroencephalography patterns, invariably associated with bad outcomes, were observed to have whole-brain apparent diffusion coefficient measures similar to those in subjects with nonmalignant electroencephalography patterns and good outcome and different from those in subjects with nonmalignant electroencephalography patterns and bad outcomes. Regional hippocampal or basal ganglia injury was associated with a bad outcome regardless of electroencephalography findings.

**CONCLUSIONS:** We found discordant evidence of brain injury by MR imaging and electroencephalography, refuting our initial hypothesis. Malignant electroencephalography patterns were generally more frequent in subjects with less severe brain injury by MR imaging. These findings suggest a complementary role of MR imaging and electroencephalography and support the aggressive treatment of malignant electroencephalography patterns in this population.

**ABBREVIATIONS:** EEG = electroencephalography; GPD = generalized periodic discharges; wbADC = whole-brain apparent diffusion coefficient

Prognostication of survival and functional outcome in comatose survivors of cardiac arrest is challenging. A multimodal approach to prognostication, including continuous electroencephalography (EEG) patterns, clinical assessment of initial illness severity, MR imaging, spontaneous and evoked potentials, and serum biomarkers, has been recommended.[1-5] The role of MR imaging is not standardized despite relatively good sensitivity and specificity documented in studies performed before routine therapeutic hypothermia.[6,7] However, brain imaging and malignant EEG patterns following therapeutic hypothermia have not been comprehensively described, to our knowledge. We hypothesize that malignant EEG patterns are associated with greater extent of brain injury evident on MR imaging, which would explain the typically poor outcomes within this subset of patients. Understanding the relationship between these modalities may establish an evidenced-based role for MR imaging in prognostication following cardiac arrest.

## MATERIALS AND METHODS

This study was approved by the University of Pittsburgh institutional review board. Informed consent was not required by the

Received September 2, 2015; accepted after revision April 16, 2016.

From the Departments of Radiology (J.M.M., V.A.), Neurology (M.B.), and Emergency Medicine (J.C.R.), University of Pittsburgh, Pittsburgh, Pennsylvania.

This work was supported by the National Institutes of Health through grant No. UL1-TR-000005.

Please address correspondence to Joseph M. Mettenburg, MD, PhD, UPMC, Presbyterian Shadyside, Department of Radiology, 200 Lothrop St, PUH 2nd Floor, Suite 200 East Wing, Pittsburgh, PA 15213; e-mail: mettenburgjm@upmc.edu

Indicates open access to non-subscribers at www.ajnr.org
Indicates article with supplemental on-line table.

http://dx.doi.org/10.3174/ajnr.A4839

institutional review board for this retrospective study because these data are included as part of an ongoing quality-assurance initiative.

### Study Population

All subjects were comatose adults 24–80 years of age admitted at a single tertiary care center following resuscitation from an in- or out-of-hospital cardiac arrest between April 14, 2010, and October 29, 2011. All subjects underwent a standardized care plan including therapeutic hypothermia for 24 hours with a target temperature of 33°C.[8] This plan includes aggressive coronary revascularization for patients with coronary ischemia, given its association with improved outcomes.[9] MRI and EEG were ordered at the discretion of the attending physician, and only individuals with both continuous EEG and MR imaging were included. Continuous EEG monitoring was performed for at least 48 hours and was initiated within a median time of 9 hours.[10] EEG recordings were continued beyond 48 hours in those with malignant EEG patterns.

### Demographics, Details of Cardiac Arrest, and Outcome

A review of the clinical record was performed to obtain the following: age, sex, initial cardiac rhythm, survival, disposition at the time of hospital discharge, EEG pattern, time from arrest to MR imaging, Glasgow Coma Scale at the time of MR imaging, and length of stay in the hospital. Demographics were compared between groupings on the basis of clinical outcome and EEG patterns by using nonparametric Kruskal-Wallis and Fisher exact tests. Outcome was based on survival and disposition at the time of hospital discharge.[11] A good outcome was defined as survival with discharge home or acute inpatient rehabilitation. Other dispositions, including death, persistent vegetative state, and nursing home admission, were considered bad outcomes (Online Table 1).

### EEG Interpretation

EEG interpretations were characterized as previously defined.[2,10] EEG data and reports were analyzed and classified by using 3 EEG categories, depending on the presence of malignant EEG patterns, pure suppression burst, or nonmalignant EEG patterns. We characterized the following EEG patterns as malignant: seizures, generalized periodic discharges (GPD), status epilepticus, and myoclonic status epilepticus. The EEG classification definitions are based on the American Clinical Neurophysiological Society Standardized Critical Care EEG Terminology to define equivocal patterns seen in patients with encephalopathy and for management of status epilepticus.[12-15] All EEGs were independently reviewed by a board-certified neurophysiologist with specialization in EEG and with expertise in postarrest EEG interpretation (M.B.).[16] The electrophysiologist reviewing these studies may have provided the initial clinical interpretation; however, determination of malignant patterns was performed at a time remote from the initial clinical presentation and was blinded to the patient's outcome and initial presentation.

### MR Imaging and Analysis

All included subjects underwent clinical MR imaging of the brain during their hospitalization, with typical imaging parameters (Optima 450w 1.5T; GE Healthcare, Milwaukee, Wisconsin; DWI acquisition parameters: b-value = 1000, 3 directions, TR = 8000 ms, TE = minimum, FOV = 26, 5/1 section/gap with a 128 × 128 matrix size, asset-enabled for artifacts reduction; T2-FLAIR acquisition parameters: TE = 120–160 ms, TR = 8000–10,000 ms, TI ~ 2250 ms, FOV = 22, 5/1 section/gap with a 256 × 192 matrix size, NEX = 1). The extent of supratentorial gyral restricted diffusion was visually scored[17-19] as subtotal or diffuse (examples in Fig 1). The subtotal manifestations included a normal appearance or restricted diffusion evident in focal areas, more posterior involvement, or basal ganglia only. Involvement of the hippocampus and basal ganglia (unilateral or bilateral) was recorded independently. Diffuse gyral edema as evidenced by expansile gyral T2 signal abnormality and sulcal effacement, independent of DWI findings, was recorded as present or absent. All images were visually inspected by 3 Certificate of Added Qualification–certified neuroradiologists (J.M.M., V.A., H. Kale) who were blinded to clinical data and whole-brain ADC measures; disagreement was mediated by 2/3 consensus.

### Whole-Brain ADC Measurements

ADC maps were retrospectively segmented by using a mask derived from the FSL Brain Extraction Tool (http://fsl.fmrib.ox.ac.uk/fsl/fslwiki/BET) by using the B0 image of the DWI and thresholding to include only voxels with ADC $< 1000 \times 10^{-6}$ mm$^2$/s, to exclude CSF-containing spaces. All extracted and thresholded ADC maps were visually inspected for artifacts or errors of processing. Whole-brain mean ADC (wbADC) values were generated by using fslstats (http://fsl.fmrib.ox.ac.uk/fsl/fslwiki/Fslutils). In addition, the percentage of whole-brain voxels with ADC values $<700 \times 10^{-6}$ mm$^2$/s was determined by dividing the number of voxels in the brain below $700 \times 10^{-6}$ mm$^2$/s by the total number of voxels contained in the extracted and thresholded ADC maps.[6]

### Statistical Analysis

Subjects were divided according to patterns of brain injury observed by MR imaging: diffuse cortical restricted diffusion compared with those with no, focal, or posterior patterns of restricted diffusion; the presence or absence of hippocampal injury on DWI/ADC; and the presence or absence of gyral edema. Fisher exact test analyses of the association of EEG patterns with imaging findings were performed.

Values of wbADC were compared among the following subjects: 1) those with a malignant EEG pattern, 2) those without a malignant EEG pattern who had a good outcome, and 3) subjects without a malignant EEG pattern who had a bad outcome. There were no subjects with a malignant EEG pattern and a good outcome. Median values and interquartile ratings of wbADC were determined; nonparametric Kruskal-Wallis testing was performed to evaluate the distribution of observed values across groups, including age, time from arrest to MR imaging, and whole brain ADC measures. The Pearson correlation coefficient was calculated to determine the relationship of mean whole-brain ADC and time from arrest to MR imaging.

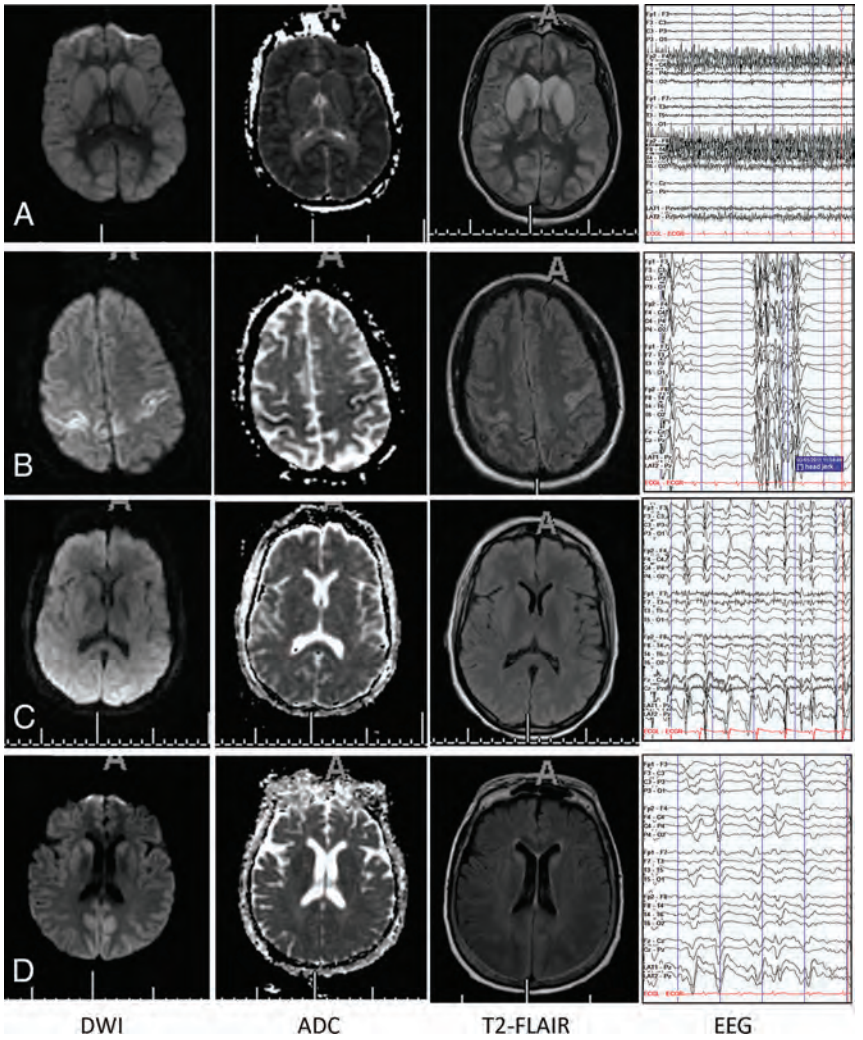


**FIG 1.** Selected examples of patterns of DWI, ADC, and T2-FLAIR abnormalities in subjects without *(A)* and with *(B–D)* malignant EEG patterns (longitudinal bipolar montage [low-frequency filter, 1 Hz; high-frequency filter, 70 Hz; 60-Hz notch on; sensitivity, 7 uV/mm]). All of these subjects had bad outcomes (death, coma, or persistent vegetative state at discharge). *A*, Diffuse gyral edema and restricted diffusion, wbADC = 666 × $10^{-6}$ $mm^2$/s. EEG (nonmalignant) pattern of diffuse background slowing. *B*, Focal diffusion abnormality involves the sensorimotor cortices, wbADC = 835 × $10^{-6}$ $mm^2$/s. EEG demonstrates a (malignant) suppression burst pattern. Bursts are associated with clinical jerks. *C*, Essentially normal MR imaging appearance of the brain, wbADC = 782 × $10^{-6}$ $mm^2$/s. EEG demonstrates a (malignant) pattern of generalized periodic discharges. *D*, Posterior (parietal) diffusion abnormality with little gyral edema, wbADC = 824 × $10^{-6}$ $mm^2$/s. EEG (malignant) pattern of GPDs.

## RESULTS

No subjects were excluded after visual inspection of masked and thresholded ADC maps for artifacts or obvious errors. Basic demographics comparing the groupings on the basis of a malignant pattern of EEG and outcome are presented in Table 1. Length of stay did not differ among the 3 groups. The Glasgow Coma Scale score on the day of MR imaging did not differ between those with malignant or nonmaliganant EEGs who experienced poor neurologic outcomes.

### *EEG Pattern and Outcome*

Among the 9 patients with malignant EEG patterns, all (100%) had bad outcomes. Among the 24 patients with nonmalignant EEG patterns, 12 had bad outcomes ($P = .012$, Fisher exact test). Of note, all except 1 of the patients with a malignant pattern demonstrated GPDs alone (see examples, Fig 1*C*, -*D*). The remaining patients' continuous EEGs demonstrated epileptiform discharges and myoclonic status epilepticus in addition to GPDs (Fig 1*B*).

### *Patterns of Brain Injury Associated with Groupings Based on EEG Pattern and Outcome*

Table 2 demonstrates associations of patterns of brain injury evident on MR imaging with groupings based on EEG patterns and outcome. There was no significant difference in the presence or absence of diffuse gyral edema among the groups; however, there were significant differences based on the pattern of restricted diffusion and evidence of either basal ganglia or hippocampal involvement.

### *Whole-Brain ADC Measures*

There were no subjects with a good outcome and malignant EEG patterns. The distribution of the number of days from arrest to MR imaging was not significantly different among groups on the basis of outcome and EEG findings. There was no significant correlation of mean wbADC values with the time from arrest to MR imaging (Pearson $r$ = 0.22).

Nonparametric testing of the distribution of mean wbADC and percentage of brain voxels with ADC values $<700 \times 10^{-6}$ $mm^2$/s between groups based on outcome and EEG patterns resulted in $P$ values of .151 and .082, respectively (Fig 2). There was a large variance evident in the population with nonmalignant EEG and bad outcome.

## DISCUSSION

This study demonstrates a discordant pattern of brain injury demonstrated on MR imaging, continuous EEG patterns, and outcome in comatose survivors of cardiac arrest. While this and other studies have demonstrated that a malignant EEG pattern is associated with poor outcome, it was assumed that the underlying brain injury evident by MR imaging was also severe and extensive.[10,20,21] Our study suggests otherwise. Although associated with poor outcomes, patients with malignant EEG patterns were observed to have less extensive evidence of structural brain injury by MR imaging, despite similar Glasgow Coma Scale scores at the time of MR imaging.

Under the current clinical protocol, continuous EEG is obtained during the first 48 hours, including a period of therapeutic

**Table 1: Demographics of groups based on EEG pattern and outcome[a]**

| | Malignant EEG ($n$ = 0) | Malignant EEG ($n$ = 9) | Nonmalignant EEG ($n$ = 12) | Nonmalignant EEG ($n$ = 12) | $P$ Value |
|---|---|---|---|---|---|
| Outcome | Good | Bad | Good | Bad | |
| Age (median) (IQR) | NA | 50 (42.5–59.5) | 53.5 (43.5–63.0) | 58.5 (43–66.0) | .252 |
| Female (No.) (%) | NA | 8 (89) | 4 (33) | 6 (50) | .051 |
| Arrest to MRI (median days) (IQR) | NA | 3 (2.5–5.0) | 5 (4.3–10.3) | 4 (3–4) | .065 |
| Length of stay (median days) (IQR) | NA | 9 (5–18) | 23 (13–27) | 13.5 (6–24.5) | .077 |
| GCS at time of MRI (median score) (IQR) | | 4 (3–6) | 10[b] (8.5–14) | 6 (3.5–8) | .0014 |
| Rhythm of arrest (No.) | | | | | |
| Asystole | NA | 2 | 3 | 3 | .71 |
| PEA | NA | 2 | 1 | 4 | |
| VF/VT | NA | 4 | 6 | 5 | |
| Unknown | NA | 1 | 2 | 0 | |
| Location of arrest (No.) | | | | | |
| In hospital | NA | 2 | 1 | 3 | .53 |
| Out of hospital | NA | 7 | 11 | 9 | |

**Note:**—IQR indicates interquartile range; PEA, pulseless electrical activity; VF/VT, ventricular fibrillation/ventricular tachycardia; NA, not applicable; GCS, Glasgow Coma Scale.
[a] There were no individuals with malignant EEG and good outcome in this cohort. There were no significant differences by groupings using Kruskal-Wallis and Fisher exact tests for nonparametric analysis of continuous and categoric variables, respectively; sex and days from arrest to MRI were nearly significant with $P = .051$ and .065, respectively.
[b] $P < .01$ for comparison with the bad outcome groups; nonsignificant difference between the bad outcome groups.

**Table 2: Patterns of brain injury evident on MRI with groupings based on EEG and outcome with the Fisher exact test**

| | Malignant EEG ($n$ = 0) | Malignant EEG ($n$ = 9) | Nonmalignant EEG ($n$ = 12) | Nonmalignant EEG ($n$ = 12) | $P$ Value |
|---|---|---|---|---|---|
| Outcome | Good | Bad | Good | Bad | |
| No. with diffuse pattern of restricted diffusion (%) | NA | 0 (0) | 1 (8.3) | 5 (41.7) | .05 |
| No. with diffuse pattern of gyral edema (%) | NA | 3 (33) | 1 (17) | 6 (50) | .25 |
| No. with restricted diffusion in basal ganglia (any) (%) | NA | 4 (44) | 1 (17) | 10 (83) | .005 |
| No. with restricted diffusion in the hippocampi (%) | NA | 1 (11) | 0 (0) | 5 (50) | .009 |

**Note:**—NA indicates not applicable.

hypothermia. Our findings suggest that a malignant EEG pattern may not reflect diffuse cortical injury. Patients with malignant EEG patterns do not reliably demonstrate MR imaging evidence of anatomic injury. Therefore, mechanisms other than cortical injury may influence the development of malignant EEG patterns. Aggressive pre-emptive treatment to prevent the development or persistence of malignant EEG patterns may also prevent additional brain injury and improve patient outcomes.[22]

Dysregulation of electrophysiology networks, leading to periodic-type malignant patterns, may contribute to a comatose state in the absence of anatomic injury evident by MR imaging. The underlying mechanism generating these patterns is not well-understood but is supported by the observation that most patients with epilepsy do not have lesions. Furthermore, injured subcortical and brain stem generators of electrophysiologic activity may contribute to malignant patterns when disproportionately affected, compared with cortical structures. Cobb and Hill[23] first proposed a theory of "cortical isolation," suggesting that severing connectivity between the cortex and subcortical structures resulted in periodic patterns. These cortical-subcortical networks have been characterized in preclinical models of seizures,[24-26] and others have reported periodic EEG patterns generated by injury to cortical-subcortical white matter in the absence of cortical injury.[27,28] Gloor et al[29] reviewed postmortem examinations of patients with periodic lateralized epileptiform discharges and saw gray matter lesions only, and metabolic or electrophysiologic etiologies were also implicated in GPDs.[30,31] These findings suggest a role for the coordination of cortical and subcortical/brain stem structures in maintaining healthy network electrophysiology.

This discordant findings of malignant pattern/poor outcome and relatively benign MR imaging appearance may explain, in part, why the prognostic value of MR imaging and ADC mapping has been limited by a poor predictive performance, given a large number of false-negatives (ie, individuals with relatively normal-appearing findings on MRI yet with poor outcome).[6,7,32] Although some of these patients die from causes unrelated to ongoing CNS pathology, diffuse cortical brain injury may be incompatible with the generation of malignant EEG patterns, whereas focal insults and/or relative preservation of regions of uninjured brain may predispose to the development of malignant EEG patterns, in particular GPDs. Unfortunately, it is unclear to what extent therapeutic hypothermia may alter brain MR imaging findings after cardiac arrest. Given the results of the targeted temperature management trial,[33] future work may address this question.

Although nonparametric testing of whole-brain measures of ADC did not reach a significance of $P < .5$ (Fig 2), there was a clear disproportionate trend evident in the population with malignant EEG patterns and bad outcome that was discordant from the population with bad outcome and no evidence of malignant EEG patterns, best demonstrated by evaluation of the extent of ADC values $<700 \times 10^{-6}$ mm$^2$/s. Future neuroprognostication tools will need to characterize patients on the basis of clinical, electrophysiologic, and neuroanatomic testing to determine optimal therapy and predict outcomes.

Once thought to be a rare pattern, GPD has increasingly been observed in patients in the intensive care unit due to more aggres-

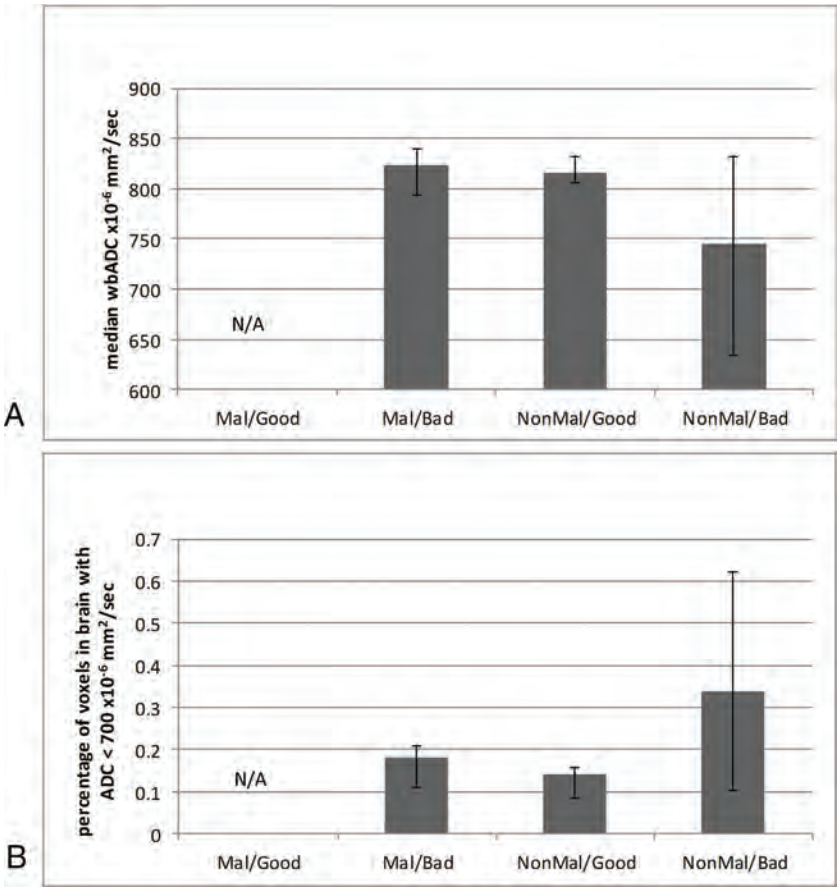


**FIG 2.** Whole-brain median ADC values compared among groups based on a pattern of EEG and outcome (median ± interquartile ratio). *A*, Whole-brain ADC $\times 10^{-6}$ mm$^2$/s. *B*, Percentage of brain voxels with ADC $< 700 \times 10^{-6}$ mm$^2$/s. There were no subjects with a malignant pattern and good outcome. Mal indicates malignant EEG; NonMal, nonmalignant EEG.

sive continuous EEG monitoring. However, there is still no consensus on the pathophysiologic generators of GPD, seen in diverse settings: infectious processes (Creutzfeldt-Jakob disease, subacute sclerosing panencephalitis), drug overdoses (lithium, ketamine, phencyclidine, baclofen), anoxia (cardiac arrest), status epilepticus, and metabolic states (hepatic and uremic encephalopathy).[30,31] GPD is associated with poor outcome following cardiac arrest, except when observed in isolation.[34] In our study, GPD was common and associated with less extensive evidence of brain injury by MR imaging. A prior study reported that 21.4% of patients with GPD patterns had normal imaging findings.[30] Hippocampal DWI signal abnormality was more commonly associated with bad outcome[35] but was also significantly more frequent in those without malignant EEG patterns.

Injury to the basal ganglia and hippocampus as evidenced by restricted diffusion had a greater likelihood of a bad outcome, though these findings were not uniformly associated with the presence of a malignant EEG pattern. Regional variations in brain injury have been shown in cardiac arrest preceded by respiratory arrest,[36] and hippocampal injury is associated with poor outcome.[35] Initial arrest may result in a watershed-type injury to both hippocampi.[37] Impaired bilateral limbic network function may preclude meaningful recovery despite intact cortical networks and motor function. Such findings may reflect a different mechanism of injury or may be related to extracranial multiorgan dysfunction. Within this retrospective cohort, there was aggressive treatment of epileptiform activity with antiepileptic drugs, which may alter the nature of ictal discharges. However, 8 of the 9 subjects with a malignant pattern demonstrated this pattern on day 1, before initiation of antiepileptiform drugs. No EEG was obtained after day 3, indicating that all malignant patterns were successfully suppressed by this time. However, some individuals may have delayed development of malignant EEG patterns not captured in this retrospective study but perhaps contributing to subsequent imaging findings. Most important, these findings suggest that anatomic lesions may not be good predictors of pathologic electrophysiology.

One hypothesis is that abnormal interactions between the "deranged cortex" and deeper "triggering" structures in the setting of increased local cortical irritability likely contribute to periodic patterns.[29,38] These abnormal interactions may or may not be associated with lesions evident on MR imaging. Herpes encephalitis and posterior reversible encephalopathy syndrome are processes in which malignant EEG patterns can be seen with normal MR imaging findings and are potentially reversible. Quantitative analysis of continuous EEGs may help clarify underlying neuropathophysiology in cardiac arrest and subsequent resuscitation. Complex patterns involving subcortical networks have been described by Moretti et al[39] in memory impairment and dementias. This type of quantitative analysis may provide a fundamentally different observation than the current qualitative assessment presented here.

The primary limitations of this study include a small sample size and the retrospective nature of the study. There is a selection bias against the most severely ill patients, who were perhaps never imaged. Furthermore, the MR imaging and EEG interpretations were available to the treating physicians and likely influenced decisions to withdraw support, potentially resulting in a self-fulfilling prophecy. However, length of stay did not differ among the groups, suggesting that there was no systematic bias based on early withdrawal of care, and the mean length of stay for all groups substantially exceeded published clinical guidelines.[40,41] Prospective studies including MR imaging and EEG are indicated to mitigate this potential bias. Whole-brain measures of ADC do not evaluate regional brain injury. Future studies should evaluate long-term outcomes at least 3 months postdischarge; the recovery phase is dynamic and may require up to 1 year.[42]

Early malignant EEG patterns identified within a subset of comatose patients after cardiac arrest treated with therapeutic hy-

pothermia are not associated with more extensive evidence of brain injury on MR imaging. The prevalent recording of global periodic discharges in this cohort suggests a possible metabolic or reversible etiology for the periodic pattern, or intact cortex salvageable if further injury is prevented. Regional injury to hippocampal or basal ganglia structures may predict poor outcome irrespective of EEG findings, potentially reflecting different mechanisms of arrest. These findings demonstrate the importance of considering both EEG and MR imaging data for comatose survivors of cardiac arrest and support aggressive treatment of malignant patterns.

## CONCLUSIONS

Patients with malignant EEG patterns were observed to have less MR imaging evidence of brain injury yet remained associated with poor outcome in this retrospective study. GPD, a pattern that was previously considered rare, was the most common malignant pattern observed. This electrophysiologic pattern may be more common in the posttherapeutic hypothermia era and may represent a reversible injury. These findings demonstrate the importance of integrating both EEG and MR imaging data when evaluating comatose survivors of cardiac arrest. Aggressive pre-emptive treatment to prevent the development, persistence, or progression of malignant EEG patterns may prevent additional brain injury and improve patient outcomes.

## ACKNOWLEDGMENTS

We are appreciative of the excellent clinical care and data collection by the Post Cardiac Arrest Service at the University of Pittsburgh Medical Center. Special thanks are extended to Dr Hrishikesh Kale for his contribution to the imaging analysis.

Disclosures: Jon M. Rittenberger—*UNRELATED*: *Grants/Grants Pending*: National Institutes of Health funding, American Heart Association Grant-in-Aid, and Laerdal Foundation for Acute Medicine, *Comments*: grant support for other projects germane to anoxic brain injury.

## REFERENCES

1. Bouwes A, Binnekade JM, Verbaan BW, et al. **Predictive value of neurological examination for early cortical responses to somatosensory evoked potentials in patients with postanoxic coma.** *J Neurol* 2012;259;537–41 CrossRef Medline
2. Coppler PJ, Elmer J, Calderon L, et al; Post Cardiac Arrest Service. **Validation of the Pittsburgh Cardiac Arrest Category illness severity score.** *Resuscitation* 2015;89:86–92 CrossRef Medline
3. Levy DE, Caronna JJ, Singer BH, et al. **Predicting outcome from hypoxic-ischemic coma.** *JAMA* 1985;253:1420–26 Medline
4. Taccone F, Cronberg T, Friberg H, et al. **How to assess prognosis after cardiac arrest and therapeutic hypothermia.** *Crit Care* 2014;18:202 CrossRef Medline
5. Young GB. **Clinical practice: neurologic prognosis after cardiac arrest.** *N Engl J Med* 2009;361:605–11 CrossRef Medline
6. Wijman CA, Mlynash M, Caulfield AF, et al. **Prognostic value of brain diffusion-weighted imaging after cardiac arrest.** *Ann Neurol* 2009;65:394–402 CrossRef Medline
7. Choi SP, Park KN, Park HK, et al. **Diffusion-weighted magnetic resonance imaging for predicting the clinical outcome of comatose survivors after cardiac arrest: a cohort study.** *Crit Care* 2010;14:R17 CrossRef Medline
8. Rittenberger JC, Guyette FX, Tisherman SA, et al. **Outcomes of a hospital-wide plan to improve care of comatose survivors of cardiac arrest.** *Resuscitation* 2008;79:198–204 CrossRef Medline
9. Reynolds JC, Callaway CW, El Khoudary SR, et al. **Coronary angiography predicts improved outcome following cardiac arrest: propensity-adjusted analysis.** *J Intensive Care Med* 2009;24:179–86 CrossRef Medline
10. Rittenberger JC, Popescu A, Brenner RP, et al. **Frequency and timing of nonconvulsive status epilepticus in comatose post-cardiac arrest subjects treated with hypothermia.** *Neurocrit Care* 2012;16:114–22 CrossRef Medline
11. Rittenberger JC, Tisherman SA, Holm MB, et al. **An early, novel illness severity score to predict outcome after cardiac arrest.** *Resuscitation* 2011;82:1399–404 CrossRef Medline
12. Chong DJ, Hirsch LJ. **Which EEG patterns warrant treatment in the critically ill? Reviewing the evidence for treatment of periodic epileptiform discharges and related patterns.** *J Clin Neurophysiol* 2005;22:79–91 CrossRef Medline
13. Hirsch LJ, LaRoche SM, Gaspard N, et al. **American Clinical Neurophysiology Society's Standardized Critical Care EEG Terminology: 2012 version.** *J Clin Neurophysiol* 2013;30:1–27 CrossRef Medline
14. Westhall E, Rosén I, Rossetti AO, et al. **Interrater variability of EEG interpretation in comatose cardiac arrest patients.** *Clin Neurophysiol* 2015;126:2397–404 CrossRef Medline
15. Brophy GM, Bell R, Claassen J, et al; Neurocritical Care Society Status Epilepticus Guideline Writing Committee. **Guidelines for the evaluation and management of status epilepticus.** *Neurocrit Care* 2012;17:3–23 CrossRef Medline
16. Amorim E, Rittenberger JC, Baldwin ME, et al; Post Cardiac Arrest Service. **Malignant EEG patterns in cardiac arrest patients treated with targeted temperature management who survive to hospital discharge.** *Resuscitation* 2015;90:127–32 CrossRef Medline
17. Arbelaez A, Castillo M, Mukherji SK. **Diffusion-weighted MR imaging of global cerebral anoxia.** *AJNR Am J Neuroradiol* 1999;20:999–1007 Medline
18. Wijdicks EF, Campeau NG, Miller GM. **MR imaging in comatose survivors of cardiac resuscitation.** *AJNR Am J Neuroradiol* 2001;22:1561–65 Medline
19. Singhal AB, Topcuoglu MA, Koroshetz WJ. **Diffusion MRI in three types of anoxic encephalopathy.** *J Neurol Sci* 2002;196:37–40 Medline
20. Knight WA, Hart KW, Adeoye OM, et al. **The incidence of seizures in patients undergoing therapeutic hypothermia after resuscitation from cardiac arrest.** *Epilepsy Res* 2013;106:396–402 CrossRef Medline
21. Sadaka F, Doerr D, Hindia J, et al. **Continuous electroencephalogram in comatose postcardiac arrest syndrome patients treated with therapeutic hypothermia: outcome prediction study.** *J Intensive Care Med* 2015;30:292–96 CrossRef Medline
22. Brain Resuscitation Clinical Trial I Study Group. **Randomized clinical study of thiopental loading in comatose survivors of cardiac arrest.** *N Engl J Med* 1986;314:397–403 CrossRef Medline
23. Cobb W, Hill D. **Electroencephalogram in subacute progressive encephalitis.** *Brain* 1950;73:392–404 CrossRef Medline
24. Avoli M, Kostopoulos G. **Participation of corticothalamic cells in penicillin-induced generalized spike and wave discharges.** *Brain Res* 1982;247:159–63 CrossRef Medline
25. Gioanni Y, Gioanni H, Mitrovic N. **Seizures can be triggered by stimulating non-cortical structures in the quaking mutant mouse.** *Epilepsy Res* 1991;9:19–31 Medline
26. Gloor P. **Generalized epilepsy with bilateral synchronous spike and wave discharge: new findings concerning its physiological mechanisms.** *Electroencephalogr Clin Neurophysiol Suppl* 1978;(34):245–49 Medline
27. Vercueil L, Hirsch E. **Seizures and the basal ganglia: a review of the clinical data.** *Epileptic Disord* 2002;4(suppl 3):S47–54 Medline
28. Badawy RA, Lai A, Vogrin SJ, et al. **Subcortical epilepsy?** *Neurology* 2013;80:1901–07 Medline
29. Gloor P, Kalabay O, Giard N. **The electroencephalogram in diffuse encephalopathies: electroencephalographic correlates of grey and white matter lesions.** *Brain* 1968;91:779–802 CrossRef

30. Yemisci M, Gurer G, Saygi S, et al. **Generalised periodic epileptiform discharges: clinical features, neuroradiological evaluation and prognosis in 37 adult patients.** *Seizure* 2003;12:465–72 CrossRef Medline
31. Janati A, Chesser MZ, Husain MM. **Periodic lateralized epileptiform discharges (PLEDs): a possible role for metabolic factors in pathogenesis.** *Clin Electroencephalogr* 1986;17:36–43 Medline
32. Greer D, Scripko P, Bartscher J, et al. **Clinical MRI interpretation for outcome prediction in cardiac arrest.** *Neurocrit Care* 2012;17:240–44 CrossRef Medline
33. Nielsen N, Wetterslev J, Cronberg T, et al; TTM Trial Investigators. **Targeted temperature management at 33°C versus 36°C after cardiac arrest.** *N Engl J Med* 2013;369:2197–206 CrossRef Medline
34. Foreman B, Claassen J, Abou Khaled K, et al. **Generalized periodic discharges in the critically ill: a case-control study of 200 patients.** *Neurology* 2012;79:1951–60 CrossRef Medline
35. Greer DM, Scripko PD, Wu O, et al. **Hippocampal magnetic resonance imaging abnormalities in cardiac arrest are associated with poor outcome.** *J Stroke Cerebrovasc Dis* 2013;22:899–905 CrossRef Medline
36. Drabek T, Foley LM, Janata A, et al. **Global and regional differences in cerebral blood flow after asphyxial versus ventricular fibrillation cardiac arrest in rats using ASL-MRI.** *Resuscitation* 2014;85:964–71 CrossRef Medline
37. Walha K, Ricolfi F, Béjot Y, et al. **Hippocampus: a "forgotten" border zone of brain ischemia.** *J Neuroimaging* 2013;23:98–101 CrossRef Medline
38. Brenner RP, Schaul N. **Periodic EEG patterns: classification, clinical correlation, and pathophysiology.** *J Clin Neurophysiol* 1990;7:249–67 CrossRef Medline
39. Moretti DV, Paternicò D, Binetti G, et al. **Analysis of grey matter in thalamus and basal ganglia based on EEG $\alpha 3/\alpha 2$ frequency ratio reveals specific changes in subjects with mild cognitive impairment.** *ASN Neuro* 2012;4:e00103 CrossRef Medline
40. Callaway CW, Donnino MW, Fink EL, et al. **Part 8: Post-Cardiac Arrest Care—2015 American Heart Association Guidelines Update for Cardiopulmonary Resuscitation and Emergency Cardiovascular Care.** *Circulation* 2015;132:S465–82 CrossRef Medline
41. Peberdy MA, Callaway CW, Neumar RW, et al; American Heart Association. **Part 9: Post-Cardiac Arrest Care—2010 American Heart Association Guidelines for Cardiopulmonary Resuscitation and Emergency Cardiovascular Care.** *Circulation* 2010;122:S768–86 CrossRef Medline
42. Raina KD, Rittenberger JC, Holm MB, et al. **Functional outcomes: one year after a cardiac arrest.** *Biomed Res Int* 2015;2015:283608 CrossRef Medline

# Magnetic Susceptibility from Quantitative Susceptibility Mapping Can Differentiate New Enhancing from Nonenhancing Multiple Sclerosis Lesions without Gadolinium Injection

Y. Zhang, S.A. Gauthier, A. Gupta, L. Tu, J. Comunale, G.C.-Y. Chiang, W. Chen, C.A. Salustri, W. Zhu, and Y. Wang

## ABSTRACT

**BACKGROUND AND PURPOSE:** Magnetic susceptibility values of multiple sclerosis lesions increase as they change from gadolinium-enhancing to nonenhancing. Can susceptibility values measured on quantitative susceptibility mapping without gadolinium injection be used to identify the status of lesion enhancement in surveillance MR imaging used to monitor patients with MS?

**MATERIALS AND METHODS:** In patients who had prior MR imaging and quantitative susceptibility mapping in a current MR imaging, new T2-weighted lesions were evaluated for enhancement on conventional T1-weighted imaging with gadolinium, and their susceptibility values were measured on quantitative susceptibility mapping. Receiver operating characteristic analysis was used to assess the diagnostic accuracy of using quantitative susceptibility mapping in distinguishing new gadolinium-enhancing from new nonenhancing lesions. A generalized estimating equation was used to assess differences in susceptibility values among lesion types.

**RESULTS:** In 54 patients, we identified 86 of 133 new lesions that were gadolinium-enhancing and had relative susceptibility values significantly lower than those of nonenhancing lesions ($\beta = -17.2$; 95% CI, −20.2 to −14.2; $P < .0001$). Using susceptibility values to discriminate enhancing from nonenhancing lesions, we performed receiver operating characteristic analysis and found that the area under the curve was 0.95 (95% CI, 0.92–0.99). Sensitivity was measured at 88.4%, and specificity, at 91.5%, with a cutoff value of 11.2 parts per billion for quantitative susceptibility mapping–measured susceptibility.

**CONCLUSIONS:** During routine MR imaging monitoring to detect new MS lesion activity, quantitative susceptibility mapping can be used without gadolinium injection for accurate identification of the BBB leakage status in new T2WI lesions.

**ABBREVIATIONS:** Gd = gadolinium; GRE = gradient echo; ppb = parts per billion; QSM = quantitative susceptibility mapping

Multiple sclerosis is an inflammatory disease of the central nervous system, characterized by focal T-cell and macrophage infiltrates associated with demyelination.[1,2] Because stages of relapse and remission alternate during disease progression,[3] identification and characterization of active lesions are critical for correct diagnosis and therapy.[4] In clinical practice, current active lesion assessment is based on gadolinium (Gd) enhancement on T1-weighted (T1WI+Gd) MR imaging. However, because Gd enhancement reflects leakage of the blood-brain barrier, it is only an indirect measure of inflammation that is preceded and outlasted by infiltration of immune cells.[5] The activation of resident innate immune cells may not be captured on T1WI+Gd.[6] In ad-

Received December 27, 2015; accepted after revision April 15, 2016.

From the Department of Radiology (Y.Z., W.C., W.Z.), Tongji Hospital, Tongji Medical College, Huazhong University of Science and Technology, Wuhan, China; Department of Radiology (Y.Z., C.A.S., Y.W.), Weill Cornell Medical College, New York, New York; Departments of Neurology (S.A.G.) and Radiology (A.G., J.C., G.C.-Y.C.), Weill Cornell Medical College, New York-Presbyterian Hospital, New York, New York; School of Applied and Engineering Physics (L.T.) and Department of Biomedical Engineering (Y.W.), Cornell University, Ithaca, New York; and Institute of Cognitive Sciences and Technologies (C.A.S.), Fatebenefratelli Hospital, Rome, Italy.

Authors contributed to this work in the following manner: Ms Yan Zhang, acquisition of data, analysis and interpretation of data, drafting the manuscript; Dr Susan Gauthier, conception and design, acquisition of data, clinical study, revision of the manuscript; Drs Ajay Gupta, Weiwei Chen, Joseph Comunale, and Gloria Chia-Yi Chiang, acquisition of data, interpretation of image data, revision of the manuscript; Mr Lijie Tu, acquisition of data, analysis of data, revision of the manuscript; Dr Carlo Salustri, conception and design, analysis and interpretation of data, revision of the manuscript; Dr Wenzhen Zhu, conception and design, revision of the manuscript, study supervision; and Dr Yi Wang, study concept and design, critical revision of the manuscript for important intellectual content, study supervision.

All authors had the final approval of the version to be published and agreement to be accountable for all aspects of the work in ensuring that questions related to the accuracy or integrity of any part of the work are appropriately investigated and resolved.

This work was supported by the US Department of Health and Human Services, National Institutes of Health–National Institute of Neurological Disorders and Stroke, grant number R01 NS090464; US Department of Health and Human Services, National Institutes of Health–National Institute of Biomedical Imaging and Bioengineering, grant number R01 EB013443; and the National Natural Science Foundation of China, grant number 81401390.

Please address correspondence to Yi Wang, PhD, Department of Radiology, Weill Cornell Medical College, 515 East 71th St, S-104, New York, NY 10021; e-mail: yiwang@med.cornell.edu

Indicates open access to non-subscribers at www.ajnr.org

http://dx.doi.org/10.3174/ajnr.A4856

dition, concerns over repeat Gd exposure have recently been raised in light of new data showing long-term Gd retention in the brains of patients who have undergone multiple Gd injections,[7,8] including patients with MS in whom Gd retention seems to be associated with degradation into secondary progression.[9] There has been interest in identifying Gd-enhancing MS lesions without the use of a contrast agent to reduce scan time, cost, and Gd contraindications.[10-13]

It is known that microglia and macrophages in an alternative activation (M2 types) remove myelin debris from MS lesions where they enter peripheral circulation[14-17]; the classic proinflammatory activation (M1 type) tends to accumulate iron.[18] Both myelin debris removal from and iron accumulation in active MS lesions increase lesion magnetic susceptibility. Analyses of tissue susceptibility changes in sensitive tissues by using gradient-echo (GRE) MR imaging have demonstrated that during lesion development, the magnetic susceptibility of an MS lesion as measured on quantitative susceptibility mapping (QSM) increases rapidly as the lesion changes from gadolinium-enhancing to nonenhancing.[19-21] This finding suggests that during MS lesion development, changes in the Gd-enhancing pattern on T1WI can be indicated by a susceptibility change measured on QSM. Accordingly, this study was designed to assess whether QSM is a viable technique to identify new enhancing MS lesions without Gd injection.

## MATERIALS AND METHODS

The Weill Cornell Medical College institutional review board approved this retrospective study and waived the requirement for informed consent.

### Patient Population

We examined MR images of patients with MS from August 2011 to January 2015 with at least 2 successive MR imaging sessions that included T2-weighted, Gd-enhanced T1-weighted, and GRE imaging. QSM was constructed in an automated manner from GRE data by deconvolving phase with the dipole kernel that connects tissue susceptibility with the magnetic field estimated from the MR imaging phase.[19,22,23] We compared the lesions on 2 successive MRIs and identified patients with at least 1 new T2WI lesion (ie, a lesion that was not present in prior brain MR imaging in a follow-up MR imaging that was <1 year from the baseline MR imaging). All the new lesions were then grouped into enhancing and nonenhancing on T1WI+Gd images.

### MR Imaging Examination Protocol

All examinations were performed on a 3T MR imaging scanner (Signa HDxt; GE Healthcare, Milwaukee, Wisconsin) with an 8-channel head coil. The sequences for each patient were the following: T2WI fast spin-echo, pre- and postgadolinium 3D inversion recovery–prepared T1WI fast spoiled gradient-echo, and 3D T2*WI spoiled multiecho GRE. Imaging parameters for the multiecho GRE sequence were as follows: TR, 57 ms; number of echoes, 11; first TE, 4.3 ms; TE spacing, 4.8 ms; flip angle, 20°; bandwidth, 244 kHz; FOV, 24 cm; matrix, 416 × 320; section thickness, 2 mm. The GRE sequence was performed before Gd injection. The total imaging time was 16 minutes 30 seconds.

QSM was constructed from GRE data by using the morphology-enabled dipole inversion.[24] The images obtained by the other modalities were registered to QSM by using the FMRIB Linear Image Registration Tool (FLIRT; http://www.fmrib.ox.ac.uk).[25]

### Data Analysis

After localizing all new T2WI lesions by comparing them with their previous MRIs, 3 neuroradiologists (J.C., A.G., and G.C.-Y.C, with 18, 9, and 8 years of experience, respectively) used the T1WI+Gd images to classify those lesions as enhancing or nonenhancing. They also classified all lesions on QSM as hyperintense and isointense relative to the adjacent white matter. All differences in lesion classification were resolved by the majority.

One neuroradiologist (Y.Z., with 4 years of experience) drew the areas of each localized lesion on the T2WI while blinded to the Gd-enhancement classification. White matter regions without abnormal signal on T1WI and T2WI were identified as normal-appearing white matter. For a zero reference, an ROI was chosen on the normal-appearing white matter at the contralateral mirror site of an identified lesion with a similar shape and size on T2WI. Then, the ROIs of lesions and normal-appearing white matter references were overlaid on the QSM images by using a semiautomatic software to assess the values of lesion susceptibility. Veins or artifacts inside the ROIs were excluded by inspection.

### Statistical Analysis

Using relative susceptibilities as a means for distinguishing enhancing from nonenhancing lesions, we assessed the receiver operating characteristic to determine sensitivity, specificity, and the optimal cutoff susceptibility value (in parts per billion [ppb]). Bootstrapped estimates of the area under the curve and 95% confidence intervals were produced to evaluate variance. The jackknife cross-validation technique was used to evaluate predictive performance of the model. A generalized estimating equation was used to predict QSM values from 3 lesion types: nodular, shell, and nonenhancing. This model assumes a Gaussian distribution and an exchangeable correlation structure to account for the multiple lesions per patient. The generalized estimating equation analysis was also used to predict QSM values from enhancing and nonenhancing lesions, accounting for repeat measurements per patient. All statistical analyses were performed by using SPSS for Windows (Version 16.0; IBM, Armonk, New York). $P < .05$ was considered statistically significant. The accuracy for identifying patients with enhancing lesions was also calculated.

## RESULTS

From the eligible 482 patients with MS, we identified 55 patients with at least 1 new T2WI lesion; there were 133 new T2WI lesions. (One patient was excluded because of motion artifacts on GRE images.) The mean age of the 54 remaining patients (11 men and 43 women) was 34.7 years ± 8.1 (range, 20–52 years). The disease duration for these patients ranged from 0 to 18 years (mean, 5.71 ± 4.51 years) and the Expanded Disability Status Scale scores ranged from 0 to 6. The Table shows the demographics of these patients.

On T1WI+Gd, 86 (64.7%) of the 133 lesions from 33 patients were identified as enhancing, and 47 (35.3%), as nonenhancing

from 25 patients (4 patients had both enhancing and nonenhancing lesions), with complete agreement among the 3 readers. For enhancing lesions, 69 (80.2%) of 86 were found to be isointense on QSM, and 17 (19.8%), slightly hyperintense in contrast to adjacent white matter. According to their enhancement on T1WI+Gd, the enhancing lesions were divided into 69 nodular and 17 shell. Thirteen of the 17 hyperintense enhancing lesions were shell-enhancing. All 47 nonenhancing lesions were hyperintense on QSM, but 4 (8.5%) of them were only slightly hyperintense. Sample images are illustrated in Fig 1.

The mean susceptibility of the lesions relative to normal-appearing white matter was 20.26 ± 7.55 ppb for nonenhancing lesions and 2.49 ± 6.39 ppb for enhancing lesions (both nodular and shell), and their distributions are illustrated by histograms in Fig 2. In the generalized estimating equation analysis of lesion susceptibility values among the 3 lesion types, both nodular-enhancing ($\beta = -19.6$; 95% CI, −23.5 to −15.8; $P < .0001$) and shell-enhancing lesions ($\beta = -13.5$; 95% CI, −19.0 to −8.0; $P < .0001$) had significantly lower susceptibility values compared with nonenhancing lesions. In the generalized estimating equation analysis of susceptibility values between enhancing and nonenhancing lesions, enhancing lesions had significantly lower susceptibility values compared nonenhancing lesions ($\beta = -17.2$; 95% CI, −20.2 to −11.2; $P < .0001$). The exchangeable correlation coefficient was 0.12 for the lesion-susceptibility model.

**Patient demographics**

| | Patients with Enhancing Lesions | Patients with Nonenhancing Lesions | *P* Value |
|---|---|---|---|
| No. of patients | 33 | 25 | |
| Sex (F/M) | 28:5 | 18:7 | |
| Age (yr) (mean) | 36.24 ± 8.37 | 32.40 ± 6.43 | .07 |
| Disease duration (yr) (mean) | 5.85 ± 4.49 | 5.32 ± 4.05 | .65 |
| EDSS (mean) | 1.70 ± 1.57 | 1.50 ± 1.69 | .66 |

**Note:**—EDSS indicates Expanded Disability Status Scale.

The receiver operating characteristic curve constructed from the mean relative susceptibility values of lesions is shown in Fig 3. The cross-validated area under the curve was 0.9530 (95% CI, 0.9201–0.9859) and the bootstrapped area under the curve was 0.9594 (95% CI, 0.9305–0.9884) for identifying enhancing lesions from QSM-measured susceptibility values. A relative susceptibility cutoff of 11.2 ppb to distinguish enhancing from nonenhancing lesions had a sensitivity and specificity of 88.4% and 91.5%, respectively.

## DISCUSSION

Our data suggest that QSM and T2WI together allow accurate identification of enhancing lesions in patients with MS without Gd injection within new lesions on serial MR imaging. This may be a potential clinical application of the reported observation that the magnetic susceptibility of an MS lesion increases rapidly as it changes from Gd-enhancing to nonenhancing.[19,21] Our study suggests that in serial MR imaging during regular monitoring of patients with MS, QSM may a substitute for Gd enhancement in assessing inflammatory activity.

Enhancement on T1WI+Gd is the current standard method to assess ongoing CNS inflammation for monitoring optimizing inflammation-suppressing treatment. Following the initial inflammatory reaction, the BBB opens and immune cells infiltrate the brain for about 3 weeks; therefore, T1WI+Gd may only offer a small window into lesion pathology.[26] During this period, the microglia and macrophages take up and degrade myelin fragments; this process is reflected in the initial lack of change in the susceptibilities of active lesions on QSM. However, after the BBB seals, immune cells remain active in the brain tissue.[17] For example, microglia and macrophages remove diamagnetic myelin fragments, and at the same time or afterward, microglia and macrophage cells with paramagnetic iron gather both at the periphery and within a lesion to further promote inflammation.[16] Thus, both myelin debris removal and iron ac-

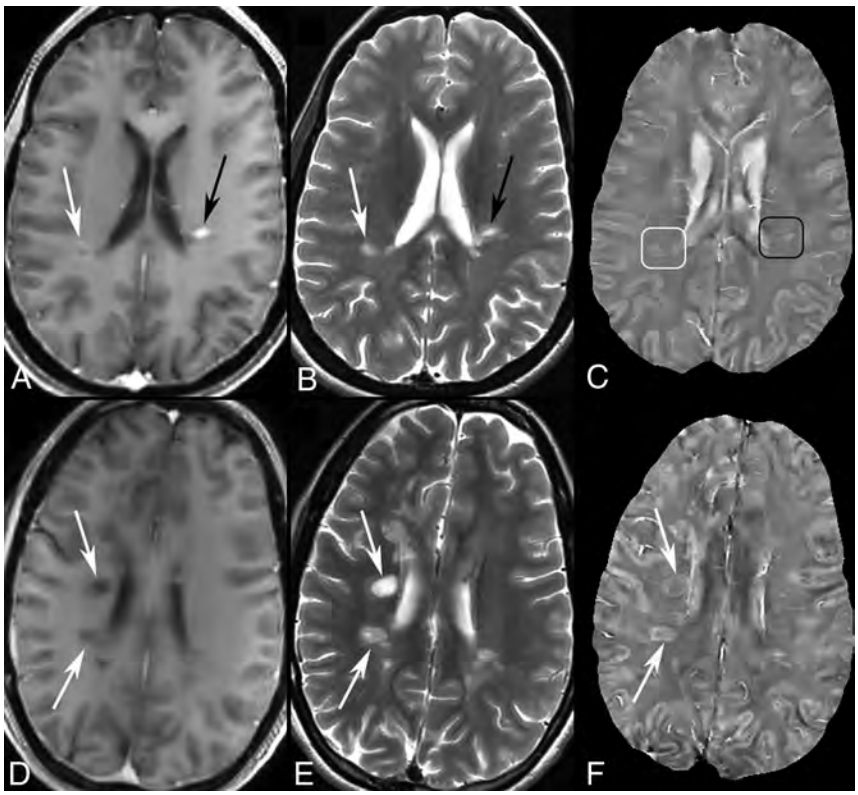


**FIG 1.** MR images of enhancing and nonenhancing new MS lesions. T1WI+Gd (*A*), T2WI (*B*), and QSM (*C*) in a 44-year-old woman with relapsing-remitting MS. Two enhancing lesions (*A* and *B*, *arrows*) are found in T1WI+Gd. One is shell-enhancing (*A*, *white arrow*) and another is nodular-enhancing (*A*, *black arrow*). The shell-enhancing lesion appears slightly QSM-hyperintense (*C*, *white box*) and the nodular one appears QSM isointense (*C*, *black box*). T1WI+Gd (*D*), T2WI (*E*), and QSM (*F*) in a 35-year-old woman with relapsing-remitting MS. Two new nonenhancing lesions (*D* and *E*, *arrows*) are found in T1WI+Gd and T2WI compared with MR imaging 6 months prior. The 2 lesions both appear QSM-hyperintense with bright rims (*F*, *arrows*).

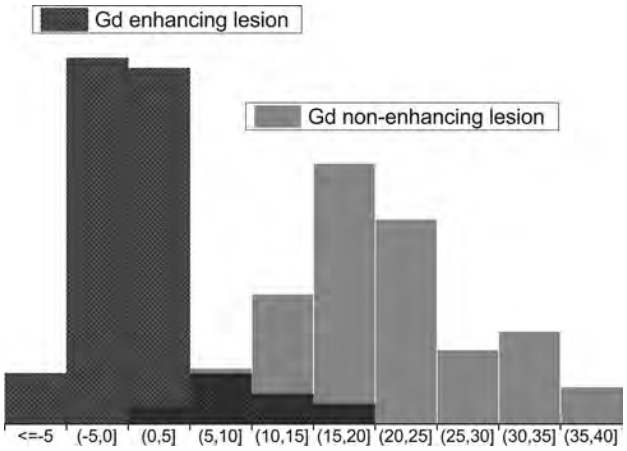


**FIG 2.** Susceptibility value histogram of enhancing and nonenhancing new lesions. The x-axis is the susceptibility value in parts per billion.

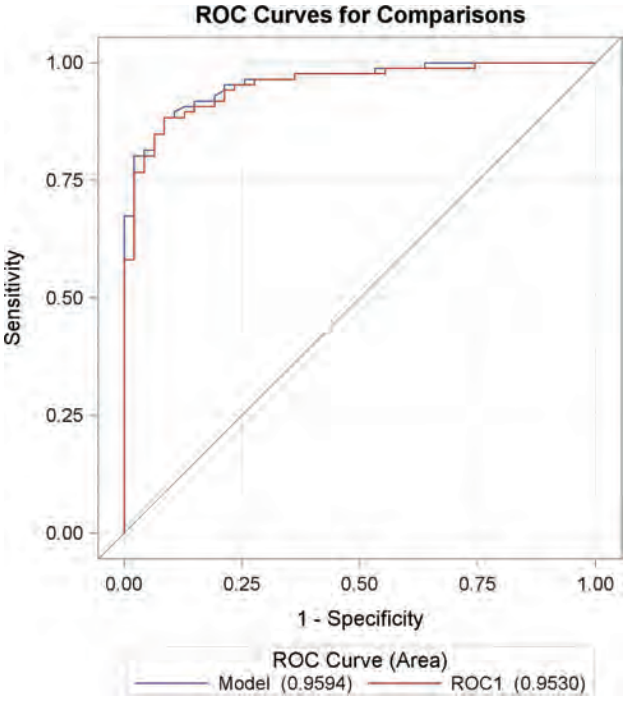


**FIG 3.** Receiver operator characteristic curves for susceptibility relative to normal-appearing white matter to predict lesion-enhancing status. The area under the curve is 0.9594 from bootstrapped model and 0.9530 from the jackknife cross-validated ROC1.

cumulation likely contribute to the increase in lesion susceptibility observed on QSM. MS lesions are hyperintense for a few years, typically with bright rims on QSM[19]; these bright rims can be interpreted as iron.[27] Therefore, including QSM rather than Gd enhancement alone, in an MR imaging protocol for patients with MS may provide more detailed insight into early lesion dynamics in MS.

There has been interest in reducing scan time and cost when identifying the BBB leakage without Gd injection.[10-13] Getting rid of the Gd injection may be necessary for patients with known contraindications to Gd, including those patients who are allergic to Gd or pregnant. Furthermore, the long-term safety of repeat Gd injections has undergone scrutiny by the FDA because of recent reports showing Gd accumulation in the brains of patients with normal kidney function[7,8] (http://www.fda.gov/Safety/MedWatch/SafetyInformation/SafetyAlertsforHumanMedicalProducts/ucm456012.htm). The mechanism of Gd retention is not yet fully understood but may involve the Gd ion disassociating with the chelator in the contrast agent and binding to metal transporter and storage proteins in brain tissue. Of particular concern is that Gd accumulation in MS brains seems to be associated with degradation into secondary progression.[9] Therefore, alternative imaging strategies that accurately characterize MS disease activity without Gd should be actively investigated, established, and disseminated to the MS community. Previous effort in identifying Gd-enhancing lesions has not been satisfactory, yielding a diagnostic accuracy of an area under the curve of 0.83 in receiver operating characteristic analysis by using semiquantitative and quantitative T1WI and T2WI[10,12] and an accuracy of 72.1% by using diffusion-weighted imaging.[13] Fundamentally, relaxation time and the diffusion coefficient are proportional to the correlation time, which reflects cellular content in a voxel and cannot differentiate Gd-enhancing and nonenhancing lesions. QSM used in this work reflects myelin debris removal and iron accumulation in MS lesions and improves the diagnostic accuracy to an area under the curve of 0.96, which may be accurate enough to serve as an alternative method for monitoring new inflammatory activity in patients with MS without Gd injection.

QSM used in this study is processed from complex data (both real and imaginary or both magnitude and phase) acquired in gradient-echo MR imaging.[23] Because of its sensitivity to magnetic susceptibility, GRE has been used in previous studies to observe MS lesions.[19,20,28-36] There are many ways to process or present GRE data; however, some of them are not direct measurements of tissue susceptibility. The commonly used magnitude hypointensity (T2*-weighted) and phase contrast at a given voxel depend on not only the tissue susceptibility in that voxel but also that of the nearby voxels in a convoluted manner, as well as imaging parameters, including field strength, TE, and object orientation. These blooming artifacts are problematic for depicting MS lesions[27] but are addressed in QSM by deconvolving GRE phase data with the dipole kernel that connects tissue susceptibility with the magnetic field estimated from the GRE phase.[22,23]

In this study, we tried to connect QSM, a potential new biomarker for assessing inflammation in MS, with Gd enhancement, which has been established in the clinical literature as a surrogate indicator for inflammation.[4] It seems that there is enough temporal correlation between the 2 aspects of inflammation activity—BBB leakage and myelin debris removal/iron accumulation. This correlation may explain the very encouraging diagnostic sensitivity and specificity observed in this study when using only QSM to identify enhancing lesions in serial MR imaging examinations of new MS lesions. The evolution of an individual lesion in an MS brain may be regarded as independent from other lesions in the same MS brain,[26] which may explain the observed similar areas under the curve for both jackknifing and bootstrapping receiver operating characteristic analysis.

This study has several limitations: 1) It was limited to assessing new enhancing lesions without Gd by using QSM in serial MR imaging. MS lesions older than 5 years may be chronically silent and QSM-isointense,[19] confounding the interpretation of acute

lesions that are also QSM isointense on the first or a single MR imaging. This outcome would limit the role of QSM to monitoring new lesions in serial or longitudinal MR imaging. This serious limitation requires us to continue seeking other non-contrast agent MR imaging features that differentiate old chronic lesions from new enhancing ones. Alternatively, because T1WI+Gd reflects the BBB leakage and QSM reflects myelin debris removal and iron accumulation, it may be useful to integrate T1WI+Gd and QSM information to form a comprehensive score to characterize acute MS lesion activity. 2) The sensitivity was not perfect because some new enhancing lesions demonstrated moderate hyperintensity on QSM, most of which (82.3%,14/17) were shell-enhancing on T1WI+Gd instead of the common nodular-enhancing type. Shell-enhancing lesions may be considered in the late stage of enhancing lesions,[26,37,38] when myelin debris with negative susceptibility is being removed from the lesion and enters the peripheral circulation.[16,17] 3) While QSM data are acquired by using the widely available 3D gradient-echo sequence and are processed in an automated manner, MS lesion susceptibility value measurement required manually drawing an ROI, which is laborious and may be alleviated by automated or semi-automated MS lesion ROI drawing tools. 4) This study is limited in sample size. Future studies should include applying the susceptibility cutoff value identified here to a larger cohort of patients with MS for evaluating the diagnostic accuracy in identifying new enhancing lesions.

## CONCLUSIONS

QSM can be used in routine serial MR imaging monitoring of patients with MS to accurately identify the BBB leakage of new T2WI lesions without the use of a gadolinium contrast agent.

Disclosures: Susan A. Gauthier—*UNRELATED*: *Consultancy*: Biogen, Genentech, Genzyme; *Grants/Grants Pending*: Biogen,* Genzyme,* Mallincrodt,* Novartis,* EMD Serono.* Ajay Gupta—*UNRELATED*: *Grants/Grants Pending*: Foundation of the American Society of Neuroradiology Scholar Award,* AUR-Radiology Research Academic Fellowship award.* Weiwei Chen—*RELATED*: *Grant*: This study is partly supported by the National Natural Science Foundation of China (grant number 81401390).* Yi Wang—*RELATED*: *Grant*: National Institutes of Health (R01EB013443, R01NS090464)*; *UNRELATED*: *Patents (planned, pending or issued)*: Cornell University,* *Comments*: I am one of the inventors on the QSM patent. No money has been paid yet; *Stock/Stock Options*: Medimagemetric, *Comments*: partner ownership of Medimagemetric LLC, which is interested in QSM commercialization. No money paid. *Money paid to the institution.

## REFERENCES

1. Trapp BD, Peterson J, Ransohoff RM, et al. **Axonal transection in the lesions of multiple sclerosis.** *N Engl J Med* 1998;338:278–85 CrossRef Medline
2. McFarland HF, Martin R. **Multiple sclerosis: a complicated picture of autoimmunity.** *Nat Immunol* 2007;8:913–19 CrossRef Medline
3. Lublin FD, Reingold SC. **Defining the clinical course of multiple sclerosis: results of an international survey: National Multiple Sclerosis Society (USA) Advisory Committee on Clinical Trials of New Agents in Multiple Sclerosis.** *Neurology* 1996;46:907–11 CrossRef Medline
4. Polman CH, Reingold SC, Banwell B, et al. **Diagnostic criteria for multiple sclerosis: 2010 revisions to the McDonald criteria.** *Ann Neurol* 2011;69:292–302 CrossRef Medline
5. Vellinga MM, Oude Engberink RD, Seewann A, et al. **Pluriformity of inflammation in multiple sclerosis shown by ultra-small iron oxide particle enhancement.** *Brain* 2008;131:800–07 CrossRef Medline
6. Ladewig G, Jestaedt L, Misselwitz B, et al. **Spatial diversity of blood-brain barrier alteration and macrophage invasion in experimental autoimmune encephalomyelitis: a comparative MRI study.** *Exp Neurol* 2009;220:207–11 CrossRef Medline
7. Kanda T, Osawa M, Oba H, et al. **High signal intensity in dentate nucleus on unenhanced T1-weighted MR images: association with linear versus macrocyclic gadolinium chelate administration.** *Radiology* 2015;275:803–09 CrossRef Medline
8. Radbruch A, Weberling LD, Kieslich PJ, et al. **Gadolinium retention in the dentate nucleus and globus pallidus is dependent on the class of contrast agent.** *Radiology* 2015;275:783–91 CrossRef Medline
9. Roccatagliata L, Vuolo L, Bonzano L, et al. **Multiple sclerosis: hyperintense dentate nucleus on unenhanced T1-weighted MR images is associated with the secondary progressive subtype.** *Radiology* 2009;251:503–10 CrossRef Medline
10. Shinohara RT, Goldsmith J, Mateen FJ, et al. **Predicting breakdown of the blood-brain barrier in multiple sclerosis without contrast agents.** *AJNR Am J Neuroradiol* 2012;33:1586–90 CrossRef Medline
11. Treabă CA, Bălaşa R, Podeanu DM, et al. **Cerebral lesions of multiple sclerosis: is gadolinium always irreplaceable in assessing lesion activity?** *Diagn Interv Radiol* 2014;20:178–84 CrossRef Medline
12. Blystad I, Håkansson I, Tisell A, et al. **Quantitative MRI for analysis of active multiple sclerosis lesions without gadolinium-based contrast agent.** *AJNR Am J Neuroradiol* 2016;37:94–100 CrossRef Medline
13. Lo CP, Kao HW, Chen SY, et al. **Comparison of diffusion-weighted imaging and contrast-enhanced T1-weighted imaging on a single baseline MRI for demonstrating dissemination in time in multiple sclerosis.** *BMC Neurol* 2014;14:100 CrossRef Medline
14. Lee SC, Moore GR, Golenwsky G, et al. **Multiple sclerosis: a role for astroglia in active demyelination suggested by class II MHC expression and ultrastructural study.** *J Neuropathol Exp Neurol* 1990;49:122–36 CrossRef Medline
15. Brück W, Porada P, Poser S, et al. **Monocyte/macrophage differentiation in early multiple sclerosis lesions.** *Ann Neurol* 1995;38:788–96 CrossRef Medline
16. Mehta V, Pei W, Yang G, et al. **Iron is a sensitive biomarker for inflammation in multiple sclerosis lesions.** *PLoS One* 2013;8:e57573 CrossRef Medline
17. Kutzelnigg A, Lassmann H. **Pathology of multiple sclerosis and related inflammatory demyelinating diseases.** *Handb Clin Neurol* 2014;122:15–58 CrossRef Medline
18. Cairo G, Recalcati S, Mantovani A, et al. **Iron trafficking and metabolism in macrophages: contribution to the polarized phenotype.** *Trends Immunol* 2011;32:241–47 CrossRef Medline
19. Chen W, Gauthier SA, Gupta A, et al. **Quantitative susceptibility mapping of multiple sclerosis lesions at various ages.** *Radiology* 2014;271:183–92 CrossRef Medline
20. Wiggermann V, Hernández Torres E, Vavasour IM, et al. **Magnetic resonance frequency shifts during acute MS lesion formation.** *Neurology* 2013;81:211–18 CrossRef Medline
21. Zhang Y, Gauthier SA, Gupta A, et al. **Longitudinal change in magnetic susceptibility of new enhanced multiple sclerosis (MS) lesions measured on serial quantitative susceptibility mapping (QSM).** *J Magn Reson Imaging* 2016 Jan 22. [Epub ahead of print] CrossRef Medline
22. de Rochefort L, Liu T, Kressler B, et al. **Quantitative susceptibility map reconstruction from MR phase data using Bayesian regularization: validation and application to brain imaging.** *Magn Reson Med* 2010;63:194–206 CrossRef Medline
23. Wang Y, Liu T. **Quantitative susceptibility mapping (QSM): decoding MRI data for a tissue magnetic biomarker.** *Magn Reson Med* 2015;73:82–101 CrossRef Medline
24. Liu J, Liu T, de Rochefort L, et al. **Morphology enabled dipole inversion for quantitative susceptibility mapping using structural consistency between the magnitude image and the susceptibility map.** *Neuroimage* 2012;59:2560–68 CrossRef Medline
25. Jenkinson M, Bannister P, Brady M, et al. **Improved optimization for**

**the robust and accurate linear registration and motion correction of brain images.** *Neuroimage* 2002;17:825–41 CrossRef Medline
26. Gaitán MI, Shea CD, Evangelou IE, et al. **Evolution of the blood-brain barrier in newly forming multiple sclerosis lesions.** *Ann Neurol* 2011;70:22–29 CrossRef Medline
27. Wisnieff C, Ramanan S, Olesik J, et al. **Quantitative susceptibility mapping (QSM) of white matter multiple sclerosis lesions: interpreting positive susceptibility and the presence of iron.** *Magn Reson Med* 2015;74:564–70 CrossRef Medline
28. Haacke EM, Makki M, Ge Y, et al. **Characterizing iron deposition in multiple sclerosis lesions using susceptibility weighted imaging.** *J Magn Reson Imaging* 2009;29:537–44 CrossRef Medline
29. Khalil M, Enzinger C, Langkammer C, et al. **Quantitative assessment of brain iron by R(2)* relaxometry in patients with clinically isolated syndrome and relapsing-remitting multiple sclerosis.** *Mult Scler* 2009;15:1048–54 CrossRef Medline
30. Ropele S, de Graaf W, Khalil M, et al. **MRI assessment of iron deposition in multiple sclerosis.** *J Magn Reson Imaging* 2011;34:13–21 CrossRef Medline
31. Khalil M, Langkammer C, Ropele S, et al. **Determinants of brain iron in multiple sclerosis: a quantitative 3T MRI study.** *Neurology* 2011;77:1691–97 CrossRef Medline
32. Hagemeier J, Heininen-Brown M, Poloni GU, et al. **Iron deposition in multiple sclerosis lesions measured by susceptibility-weighted imaging filtered phase: a case control study.** *J Magn Reson Imaging* 2012;36:73–83 CrossRef Medline
33. Paling D, Tozer D, Wheeler-Kingshott C, et al. **Reduced R2′ in multiple sclerosis normal appearing white matter and lesions may reflect decreased myelin and iron content.** *J Neurol Neurosurg Psychiatry* 2012;83:785–92 CrossRef Medline
34. Bagnato F, Hametner S, Welch EB. **Visualizing iron in multiple sclerosis.** *Magn Reson Imaging* 2013;31:376–84 CrossRef Medline
35. Bian W, Harter K, Hammond-Rosenbluth KE, et al. **A serial in vivo 7T magnetic resonance phase imaging study of white matter lesions in multiple sclerosis.** *Mult Scler* 2013;19:69–75 CrossRef Medline
36. Absinta M, Sati P, Gaitan MI, et al. **Seven-Tesla phase imaging of acute multiple sclerosis lesions: a new window into the inflammatory process.** *Ann Neurol* 2013;74:669–78 CrossRef Medline
37. Cotton F, Weiner HL, Jolesz FA, et al. **MRI contrast uptake in new lesions in relapsing-remitting MS followed at weekly intervals.** *Neurology* 2003;60:640–46 CrossRef Medline
38. Guttmann CR, Ahn SS, Hsu L, et al. **The evolution of multiple sclerosis lesions on serial MR.** *AJNR Am J Neuroradiol* 1995;16:1481–91 Medline

# Regional Frontal Perfusion Deficits in Relapsing-Remitting Multiple Sclerosis with Cognitive Decline

R. Vitorino, S.-P. Hojjat, C.G. Cantrell, A. Feinstein, L. Zhang, L. Lee, P. O'Connor, T.J. Carroll, and R.I. Aviv

## ABSTRACT

**BACKGROUND AND PURPOSE:** Cortical dysfunction, quantifiable by cerebral perfusion techniques, is prevalent in patients with MS, contributing to cognitive impairment. We sought to localize perfusion distribution differences in patients with relapsing-remitting MS with and without cognitive impairment and healthy controls.

**MATERIALS AND METHODS:** Thirty-nine patients with relapsing-remitting MS (20 cognitively impaired, 19 nonimpaired) and 19 age- and sex-matched healthy controls underwent a neurocognitive battery and MR imaging. Voxel-based analysis compared regional deep and cortical GM perfusion and volume among the cohorts.

**RESULTS:** After we adjusted for localized volumetric differences in the right frontal, temporal, and occipital lobes, progressive CBF and CBV deficits were present in the left middle frontal cortex for all cohorts and in the left superior frontal gyrus for patients with cognitive impairment compared with patients without impairment and controls. Compared with healthy controls, reduced CBF was present in the limbic regions of patients with cognitive impairment, and reduced CBV was present in the right middle frontal gyrus in patients with cognitive impairment and in the temporal gyrus of relapsing-remitting MS patients without cognitive impairment.

**CONCLUSIONS:** Consistent regional frontal cortical perfusion deficits are present in patients with relapsing-remitting MS, with more widespread hypoperfusion in those with cognitive impairment, independent of structural differences, indicating that cortical perfusion may be a useful biomarker of cortical dysfunction and cognitive impairment in MS.

**ABBREVIATIONS:** BA = Brodmann area; DARTEL = Diffeomorphic Anatomical Registration Through Exponentiated Lie Algebra; HC = healthy controls; MNI = Montreal Neurological Institute; qCBF = quantitative cerebral blood flow; qCBV = quantitative cerebral blood volume; RRMS = relapsing-remitting multiple sclerosis; VBM = voxel-based morphometry

MS is traditionally considered a demyelinating-inflammatory WM disorder; however, GM involvement is recognized in 50%–93% of patients,[1,2] contributing to cognitive impairment, which is present in 40%–68% of cases.[3,4] Patients with MS may display deficits in several cognitive domains, including working memory, learning and memory retrieval, executive function, and especially information-processing speed.[2,5]

Multiple studies have quantified the relative contributions of WM T2 hyperintense lesions and, to a lesser extent, GM cortical lesions to cognition in MS. The relationship between WM T2 hyperintense lesion burden and cognitive impairment is modest,[6] and GM and WM damage may occur interdependently,[1] with cortical abnormalities reported in the absence of WM disease.[7] Both atrophy and cortical lesion load are important predictors of cognitive deficits in patients with MS[5]; nevertheless, cortical lesion burden is increasingly reported as a stronger and independent predictor of cognitive performance in comparison with cortical volume.[8]

Current clinical imaging techniques used for cortical lesion detection, such as double inversion recovery, detect few lesions (around 18%) compared with histopathologic studies.[9] Several studies have proposed new strategies to detect cortical abnormalities, including cortical lesion volume or more subtle ultrastructural (magnetization transfer ratio[10,11] and DTI[12,13]) or perfusion

Received January 6, 2016; accepted after revision March 17.

From the Departments of Psychiatry (A.F.), Neurology (L.L.), and Medical Imaging (R.V., S.-P.H., L.Z., R.I.A.), Sunnybrook Health Sciences Centre, Toronto, Ontario, Canada; Departments of Medicine (L.L., P.O.), Psychiatry (A.F.), and Medical Imaging (S.-P.H., R.I.A.), University of Toronto, Toronto, Ontario, Canada; and Departments of Biomedical Engineering (C.G.C., T.J.C) and Radiology (T.J.C.), Northwestern University, Chicago, Illinois.

Dr. Aviv was supported by Canadian Institutes of Health Research operating grant (130366). Drs. Aviv and Hojjat are supported by a Biogen Fellowship Funding Award. Charles Cantrell is supported by the American Heart Association (14PRE20380310). Dr. Carroll is supported by the US National Institutes of Health (1R21EB017928-01A1).

Please address correspondence to Rita Vitorino, BSc, Sunnybrook Health Sciences Centre, 2075 Bayview Ave, Room AB204, Toronto, Ontario, Canada M4N 3M5; e-mail: rita.vitorino@sunnybrook.ca

Indicates open access to non-subscribers at www.ajnr.org

http://dx.doi.org/10.3174/ajnr.A4824

abnormalities, in the clinical setting. GM is inherently sensitive to perfusion changes caused by both physiologic and pathologic alterations, due to its high vascularity and metabolic activity. Cortical perfusion can be evaluated with multiple imaging techniques, including fMRI, arterial spin-labeling, and gadolinium-based MR imaging techniques, such as DSC, which is the most widely performed clinical perfusion technique. By using pre- and postgadolinium scans to calibrate DSC, the bookend technique offers accurate cerebral perfusion quantification with high PET correlation and interobserver reliability.[14,15]

Previous perfusion studies have shown that regardless of MS clinical subtype, cerebral hypoperfusion is an early and integral occurrence,[16,17] including in early relapsing-remitting MS (RRMS), in which reduction may be seen in the absence of structural differences compared with healthy controls (HC).[18] Studies explicitly exploring cognitive impairment in both RRMS and secondary-progressive MS describe significant and focal frontal cortical correlations between CBV and CBF reductions and cognitive deficits.[16,19-21]

In the present study, we sought to localize CBF and CBV in HC and RRMS patients with and without cognitive impairment to determine whether a similar pattern of involvement is present compared with that previously reported for secondary-progressive multiple sclerosis. We hypothesized that patients with RRMS with cognitive impairment similarly exhibit localized frontal cerebral CBF and CBV reduction in functionally consistent brain regions, compared with patients without impairment and HC. We further evaluated the consistency of the localized findings before and after accounting for any structural group differences.

## MATERIALS AND METHODS

### Patient Cohort

Thirty-nine patients with RRMS (modified McDonald criteria, 2010[22]) were prospectively recruited during a 1-year period from 2 tertiary referral MS clinics at Sunnybrook and St. Michael's hospitals. Initially, 20 patients with cognitive impairment were recruited followed by the remaining patients without impairment and 19 HC (with no previous history of neurologic disorders) who were selected to reflect the overall distribution of sex and age of the impaired cohort. Charts of potential patients were reviewed by a senior neurologist (20 years' experience) before recruitment. Exclusion criteria included relapse or corticosteroid use within the past 3 months; history of drug/alcohol abuse; premorbid (pre-MS) psychiatric history; head injury, including loss of consciousness; concurrent morbidity; and MR imaging/gadolinium contraindications. All study participants were purposely recruited for this study. At the time of consent, the small potential risks associated with gadolinium injection were discussed, referencing American College of Radiology and FDA communications. Consent was obtained following confirmation of MR imaging (and gadolinium) eligibility on the basis of a standardized MR imaging contraindication questionnaire and glomerular filtration rate determination. The study was approved by the research ethics board of both Sunnybrook Health Sciences Centre and St. Michael's Hospital, and informed consent was obtained from all participants.

### Neurocognitive Testing

All patients underwent clinical assessments within 1 week of image acquisition, documenting demographic data and medical history, including relapse history. Disability was assessed by using the Expanded Disability Status Scale.[23] All participants were tested by using the Minimal Assessment of Cognitive Function in Multiple Sclerosis battery covering 5 cognitive domains: working memory and processing speed (Paced Auditory Serial Addition Test; Symbol Digit Modalities Test); learning and memory (Brief Visual Memory Test-Revised; California Verbal Learning Test-II); executive function (Delis-Kaplan Executive Function System); verbal fluency (Controlled Word Association Test); and visuospatial perception (Judgment of Line Orientations).[24] Raw scores of each individual test were converted to *z* scores by using widely available normative data, which correct for age and sex. Norms for 3 of the key components of the neurocognitive battery (Paced Auditory Serial Addition Test; Symbol Digit Modalities Test; Controlled Word Association Test) also correct for education. Patients scoring 1.5 SDs below normative data on ≥2 cognitive tests were considered cognitively impaired.[25] The Hospital Anxiety and Depression Scale was also administered.

### MR Imaging Acquisition

All scans were acquired on a 3T MR imaging system (Achieva; Philips Healthcare, Best, the Netherlands) with an 8-channel phased array head coil receiver. Conventional MR imaging sequences were acquired for structural and lesion characterization, including axial volumetric TSE T1 (TR/TE/flip angle = 9.5/2.3 ms/12°; FOV = 24 cm; acquisition matrix = 256 × 219; section thickness = 1.2 mm); axial proton-density/T2 (TR/TE/flip angle = 2500/10.7 ms/90°; FOV = 23 cm; acquisition matrix = 256 × 263; section thickness = 3 mm); axial phase-sensitive inversion recovery (TR/TE = 3374/15 ms; FOV = 23 cm; acquisition matrix = 400 × 255; section thickness = 3 mm); and axial field-echo echo-planar DSC (TR/TE/flip angle = 1633/30 ms/60°; FOV = 22 cm; acquisition matrix = 96 × 93; section thickness = 4 mm; no gap; signal bandwidth = 1260 Hz/pixel; sections = 24). A segmented inversion recovery Look-Locker EPI sequence was performed immediately before and after the axial DSC sequence (TR/TE/flip angle = 29/14 ms/20°; TI = 15.8 ms; FOV = 22 cm; acquisition matrix = 128 × 126; 15 lines in *k*-space per acquisition; section thickness = 4 mm; 60 time points). Ten milliliters of 1 mmol/mL concentration of gadobutrol (Gadovist; Bayer Schering Pharma, Berlin, Germany) was administered by power injector at a rate of 5 mL/s, followed by a 25-mL bolus of saline at 5 mL/s. Sixty images were acquired at 1.6-second intervals with the injection occurring at the fifth volume. A 3-second delay was placed after the last imaging time point to facilitate longitudinal magnetization recovery.

### Image Processing

Perfusion Maps. Quantitative CBF (qCBF) and CBV (qCBV) maps were generated from the DSC and Look-Locker echo-planar images (T1-weighted pre- and postgadolinium reference scans) by using the bookend technique.[15] Briefly, these Look-Locker EPI scans allow DSC calibration, independent of an arterial input function, by quantifying WM T1 signal changes relative to the

blood pool to calculate the steady-state CBV in WM by using a water-correction factor to correct for intra- to extravascular water exchange. Deconvolution of tissue-concentration–time curves by the arterial input function by using singular value decomposition yields the relative CBF, while relative CBV is determined by calculating the ratio of the area under the tissue-concentration–time curve and the arterial input function. Final perfusion quantification of qCBV and qCBF is then performed as previously described.[26]

**Lesion Load.** Structural T1- and proton-density/T2-weighted images were coregistered by using linear registration (SPM8 software; http://www.fil.ion.ucl.ac.uk/spm/). Lesions were manually traced with Analyze 8.0 software (AnalyzeDirect, Overland Park, Kansas) by an experienced clinician (10 years' experience) by using phase-sensitive inversion recovery for cortical lesion tracing and proton-density/T2 and T1 scans for WM T2 hyperintense lesions and T1 black hole tracing, respectively.

**Voxel-Based Morphometry Analysis.** Voxel-based morphometry (VBM) analysis was performed in SPM8 by using Diffeomorphic Anatomical Registration Through Exponentiated Lie Algebra (DARTEL) and the unified segmentation model for structural and perfusion images, respectively.[27,28]

**Structural VBM.** T1 structural images were segmented by using both a unified segmentation model and DARTEL functions in SPM8 and then checked for accuracy. A group-specific template was created by using the DARTEL space segmentations. Each participant's native space segmentations were registered to this template with a nonlinear transformation; then they were affine-transformed into Montreal Neurological Institute (MNI, McGill University) space before being smoothed with an 8-mm full width at half maximum isotropic Gaussian kernel. The segmentations were aligned to MNI152 space via the DARTEL template by using the same transformations in a single step.

**Perfusion VBM.** A mean DSC series was constructed for each patient by averaging the 60 EPI DSC acquisitions and then normalizing them to MNI152 space by using SPM8. A group-specific perfusion template was then created in MNI space. The DSC sequence was linearly registered to the group template by using the FMRIB Linear Image Registration Tool (FLIRT; http://www.fmrib.ox.ac.uk) followed by nonlinear intensity modulation and multiresolution nonlinear registration with 4 subsampling levels (FMRIB Nonlinear Registration Tool, FNIRT; http://fsl.fmrib.ox.ac.uk/fsl/fslwiki/FNIRT).[29] These sequences were smoothed at each respective resolution level during the registration by using full width at half maximum Gaussian kernels of 6, 4, 2, and 2 mm. This transformation matrix was then applied to the intrinsically coregistered bookend perfusion maps of qCBF and qCBV.

### *Statistical Analysis*

**Clinical and Demographic Measures.** Demographic, neurologic, and neuropsychological data were summarized in HC and patients with RRMS with and without cognitive impairment by using means and SDs for continuous variables and counts for categoric variables. Statistical Analysis Software (SAS, Version 9.4; SAS Institute, Cary, North Carolina) was used to compare each clinical, demographic, and volumetric measure among the 3 groups; general linear regression or logistic regression analysis was applied for continuous or categoric variables. Any variables demonstrating significant group differences ($P < .017$, $P < .05$ corrected for multiple comparisons among the 3 cohorts) were included as covariates for the respective mass univariate analysis.

**VBM Analysis.** Perfusion maps and structural images were compared by using the mass univariate technique used by SPM. On the basis of previous research,[16,19] we hypothesized cortical perfusion changes in the frontal cortex. With this a priori hypothesis, VBM analysis was restricted to GM and clusters with ≥20 contiguous voxels, with a voxelwise $P$ value threshold of $P < .001$ considered significant. VBM analysis was repeated for perfusion measures with structural findings as covariates. Brain regions identified by SPM as statistically significant were identified by using xjView software 8.12 (http://www.alivelearn.net/xjview).

## RESULTS

### *Demographic, Clinical, and Volumetric Data*

Demographic, clinical, and volumetric data are summarized in Table 1. Similar group characteristics were present with the exception of lower education in patients with RRMS with cognitive impairment compared with HC ($P = .004$). RRMS patients with and without cognitive impairment scored higher on the anxiety measure than HC ($P = .0004$ and $P = .012$, respectively), and patients with cognitive impairment also showed higher depression scores compared with those with RRMS without impairment and HC ($P < .0001$, $P = .0001$). Furthermore, patients with cognitive impairment were more functionally disabled compared with those without impairment ($P = .014$) as measured by the Expanded Disability Status Scale. With respect to structural/volumetric differences, patients with RRMS with cognitive impairment had a reduction in WM ($P = .008$) and thalamic volume ($P = .014$).

### *Neurocognitive Performance*

There was no difference in cognitive performance between HC and those with nonimpaired RRMS. Patients with RRMS with cognitive impairment performed significantly worse on all cognitive tests compared with both HC and those without impairment (Table 1), except for the Delis-Kaplan Executive Function System and the Judgment of Line Orientations test.

### *VBM Data (Perfusion and Structural)*

Mass univariate SPM analysis detected significantly reduced qCBF and qCBV in the left middle frontal gyrus (encompassing Brodmann areas [BAs] 10, 11, 46) for all group comparisons ($P_{\text{uncorrected}} < .001$). Patients with cognitive impairment showed qCBF and qCBV reduction compared with those with RRMS without impairment and HC in the bilateral superior frontal gyrus (BAs 6, 8, 10), left fusiform gyrus (BA 20), and right limbic lobe, including the cingulate gyrus (BA 24).

Compared with unimpaired RRMS, those with RRMS and cognitive impairment showed lower qCBF in the left thalamus (including the medial dorsal nuclei) and lower qCBV in the right anterior cingulate (BA 25), left posterior cingulate (BA 31), right inferior parietal lobule (BA 40), right lingual gyrus, and left cau-

**Table 1: Demographic, neurologic, and neuropsychological data of healthy controls and patients with RRMS[a]**

| | Healthy Controls ($n$ = 19) | Cognitively Nonimpaired RRMS ($n$ = 19) | Cognitively Impaired RRMS ($n$ = 20) |
|---|---|---|---|
| Demographic and clinical data | | | |
| Age (yr) | 49.0 ± 7.1 | 46.4 ± 7.2 | 48.1 ± 4.7 |
| Sex (F/M) | 14:5 | 15:4 | 12:8 |
| Education (yr) | 16.9 ± 2.9[b] | 16.1 ± 1.3 | 14.6 ± 1.9[b] |
| Disease duration (yr) | NA | 11.8 ± 5.4 | 11.6 ± 4.9 |
| EDSS | NA | 1.8 ± 0.7[c] | 2.6 ± 0.7[c] |
| HADS-Anxiety | 4.4 ± 4.3[b,d] | 6.37 ± 3.1[d] | 8.5 ± 3.7[b] |
| HADS-Depression | 2.3 ± 2.3[b] | 3.5 ± 3.2[c] | 7.6 ± 2.9[b,c] |
| Treatment | NA | | |
| $\beta$-interferon | | 4 (21%) | 3 (15%) |
| Other immune suppressors | | 11 (58%) | 12 (60%) |
| None | | 4 (21%) | 5 (25%) |
| Presence of enhancing lesions | NA | 1 (5%) | 5 (25%) |
| Volumetric data ($cm^3$) | | | |
| GM | 653.37 ± 81.51 | 618.83 ± 53.94 | 605.09 ± 60.90 |
| WM | 458.22 ± 65.02[b] | 421.84 ± 39.29 | 414.53 ± 71.56[b] |
| BG | 19.41 ± 2.75 | 18.68 ± 2.52 | 18.04 ± 2.93 |
| Th | 9.83 ± 1.92[b] | 9.14 ± 1.98 | 7.91 ± 1.88[b] |
| CL | 0.00 ± 0.00[b] | 0.12 ± 0.11 | 0.22 ± 0.36[b] |
| T2H | 0.00 ± 0.00[b] | 9.37 ± 10.02 | 13.47 ± 13.30[b] |
| T1bh | 0.00 ± 0.00[b] | 3.21 ± 2.98 | 5.85 ± 6.77[b] |
| CSF | 320.89 ± 210.43[b] | 353.22 ± 131.71 | 400.29 ± 173.78[b] |
| Neurocognitive tests ($z$ score) | | | |
| COWAT-FAS | −0.67 ± 0.83 | −0.26 ± 1.06[c] | −1.16 ± 0.89[c] |
| COWAT-Animals | −0.13 ± 1.14 | −0.41 ± 0.95[c] | −0.59 ± 1.18[c] |
| BVMT-IR | −0.37 ± 1.15[b] | −0.07 ± 1.04[c] | −1.68 ± 1.34[b,c] |
| BVMT-DR | −0.40 ± 1.14[b] | −0.42 ± 0.77[c] | −1.62 ± 1.48[b,c] |
| PASAT-3 | −0.39 ± 0.94[b] | −0.05 ± 0.61[c] | −1.71 ± 0.82[b,c] |
| PASAT-2 | −0.21 ± 0.89[b] | −0.26 ± 0.66[c] | −1.80 ± 0.57[b,c] |
| JLO | −0.98 ± 0.20 | −0.83 ± 0.56 | −0.40 ± 0.67 |
| SDMT | −0.14 ± 0.92[b] | −0.02 ± 0.75[c] | −1.80 ± 1.17[b,c] |
| CVLT II-IR | −0.25 ± 1.05[b] | −0.23 ± 1.04[c] | −1.94 ± 1.36[b,c] |
| CVLT II-DR | −0.11 ± 0.66[b] | −0.21 ± 0.92[c] | −2.20 ± 1.61[b,c] |
| DKEFS-ST | −0.51 ± 0.73 | −0.26 ± 0.61 | −0.20 ± 1.25 |

**Note:**—NA indicates not applicable; EDSS, Expanded Disability Status Score; HADS, Hospital Anxiety and Depression Scale; COWAT, Controlled Oral Word Association Test; BVMT, Brief Visuospatial Test- Revised; PASAT, Paced Auditory Serial Addition Test; JLO, Judgment of Line Orientation Test; SDMT, Symbol Digit Modalities Test; CVLT II, California Verbal Learning Test-II; IR, immediate recall; DR, delayed recall; DKEFS-ST, Delis-Kaplan Executive Function System Sorting Test; BG, basal ganglia; Th, thalamus; CL, cortical lesions; T2H, T2 hyperintensities; T1bh, T1 black holes.

[a] Significance at $P < .017$, corrected for multiple comparisons; all values are means unless specified.

[b] Healthy controls vs patients with RRMS with cognitive impairment.

[c] Patients with RRMS without impairment vs those with cognitive impairment.

[d] Healthy controls vs patients with RRMS without impairment.

date. Furthermore, those with RRMS and cognitive impairment showed qCBF reductions compared with HC in the right middle frontal gyrus (BA 6, 10) and qCBV deficits in the right precentral (BA 4) and right parahippocampal gyri (BA 28).

Regional volume of the right superior frontal gyrus (BA 6, 10) was decreased in those with cognitively impaired RRMS compared with those without it, and those without impairment compared with healthy controls. Additionally, patients with RRMS and cognitive impairment showed focal atrophy in the right precentral (BA 6) and transtemporal gyri (BA 42) compared with patients with nonimpaired RRMS and in the right inferior occipital gyrus (BA 18) compared with HC.

VBM analysis conducted with regional volumes of focal atrophy included as covariates found that cortical hypoperfusion (qCBF and qCBV) was maintained in the left middle frontal gyrus (BAs 10, 11, 46) for all group comparisons and in the left superior frontal gyrus (BAs 6, 10) for patients with RRMS and cognitive impairment compared with both patients without impairment and HC (Figure and Table 2). Patients with cognitive impairment continued showing qCBV deficits in the right lingual gyrus (with additional qCBF reduction in the left BA 18), right inferior parietal lobule (BA 40), and left fusiform gyrus (BA 20) and qCBF reductions in the caudate head and thalamic medial dorsal nuclei in comparison with those with RRMS without impairment, and decreased qCBF in the right middle frontal gyrus (BA 6) and decreased qCBV in the left parahippocampal gyrus (BA 28) in comparison with HC. Reduced qCBV in cognitively impaired compared with nonimpaired patients with RRMS was present in the left inferior frontal gyrus (BA 46) and diminished qCBF, in the right caudate body. Compared with HC, patients without impairment showed reduced qCBF in the superior temporal lobe (BA 38).

## DISCUSSION

Consistent perfusion deficits in the frontal cortex are present in patients with RRMS independent of global or regional atrophy. Significantly different and progressive qCBF and qCBV reduction among all groups was demonstrated in the middle frontal cortex and the left superior frontal gyrus in the impaired RRMS compared with the other 2 cohorts, after considering confounding variables of disability, anxiety, depression, and education. Patients with RRMS and HC were further distinguished by qCBV reductions in the right limbic and qCBF reductions in the right frontal (for impaired) and right temporal region (for nonimpaired). Finally, qCBV deficits were found in cognitively impaired compared with nonimpaired patients with RRMS in the left frontal (inferior frontal gyrus), right parietal (inferior parietal lobule), left temporal (fusiform gyrus), and bilateral occipital (lingual gyrus) lobes, and qCBF deficits, in deep GM structures, including the bilateral caudate and the left thalamus (medial dorsal nuclei).

Distribution of qCBF and qCBV reductions in the superior frontal, middle frontal, and parahippocampal gyri is similar to that reported in a recent pseudocontinuous arterial spin-labeling study comparing HC and patients with very early RRMS.[18] That study also showed additional qCBF reduction in multiple other areas not demonstrated in the present study; however, the discrepancies could be explained by different MR imaging techniques (pseudocontinuous arterial spin-labeling versus bookend perfusion) and patient populations. Unlike findings in our RRMS

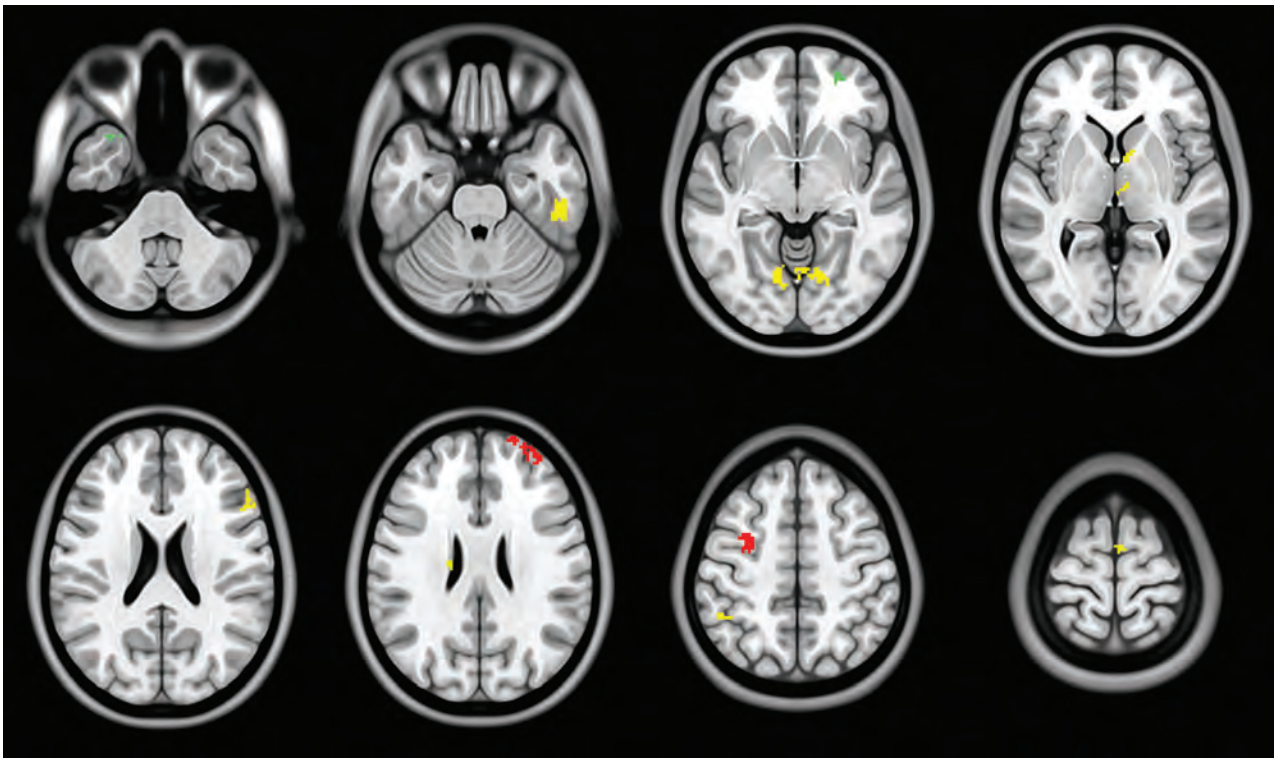

**FIGURE.** Areas of significantly ($P_{uncorrected} < .001$) reduced cortical perfusion in RRMS subgroups and healthy controls, with volumes for atrophied regions added as covariates. Green indicates healthy controls versus nonimpaired RRMS; red, healthy controls versus cognitively impaired RRMS; and yellow, nonimpaired RRMS versus cognitively impaired RRMS.

**Table 2: Areas of significantly ($P_{uncorrected} < .001$) reduced cortical perfusion in RRMS subgroups and healthy controls, with volumes for atrophied regions added as covariates**

| | | | | MNI Coordinates | | | *t* Values | | |
|---|---|---|---|---|---|---|---|---|---|
| qCBF | qCBV | Anatomic Regions | Cluster Size | x | y | z | HC vs CI | HC vs NI | NI vs CI |
| √ | √ | Left superior frontal gyrus (BAs 6, 10)[a] | 78 | −32 | 50 | 28 | 3.52 | | 3.62 |
| √ | | Right middle frontal gyrus (BA 6)[a] | 26 | 34 | 0 | 64 | 3.31 | | |
| √ | √ | Left middle frontal gyrus (BAs 10, 11, 46)[a] | 100 | −22 | 56 | 26 | 4.79 | 4.56 | 3.21 |
| | √ | Left inferior frontal gyrus (BA 46) | 21 | −48 | 30 | 20 | | | 3.29 |
| | √ | Right parahippocampal gyrus (BA 28)[a] | 27 | 24 | −22 | −12 | 4.15 | | |
| √ | √ | Right lingual gyrus[a] | 101 | 12 | −72 | −2 | | | 5.11 |
| √ | | Left lingual gyrus (BA 18) | 72 | −6 | −68 | 2 | | | 3.99 |
| | √ | Right inferior parietal lobule (BA 40)[a] | 22 | 48 | −40 | 56 | | | 3.98 |
| √ | | Right superior temporal gyrus (BA 38) | 38 | 28 | 10 | −46 | | 3.64 | |
| | √ | Left temporal fusiform gyrus (BA 20)[a] | 134 | −44 | −22 | −30 | | | 3.74 |
| √ | | Left caudate head[a] | 36 | −10 | 6 | 4 | | | 3.64 |
| √ | | Right caudate body | 24 | 18 | −20 | 26 | | | 3.68 |
| √ | | Left thalamic medial dorsal nuclei[a] | 31 | −6 | −18 | 6 | | | 3.63 |

**Note:**—CI indicates patients with RRMS with cognitive impairment; NI, patients with RRMS without impairment; √, anatomic region was present in VBM analysis for this map.
[a] Anatomic regions remained significant from previous VBM analysis without atrophy areas added as covariates.

patients without impairment, who are cognitively indistinguishable from healthy controls, Debernard et al[18] reported a borderline significant Brief Visuospatial Test reduction and demonstrated a lower white matter volume in their early RRMS cohort, suggesting a greater level of disease burden in the patient sample (supported by a higher upper Expanded Disability Status Scale score of 4.5 compared with 3.5 in our sample). In contrast to that study, we demonstrated regional cortical GM volume reduction within the right frontal, temporal, and occipital lobes consistent with that observed by Riccitelli et al.[30] Reduced superior frontal gyrus, thalamic, and caudate nuclei perfusion was similarly reported in a secondary-progressive multiple sclerosis with cognitive impairment patient cohort, suggesting that the frontal reduction may be a marker of impairment in patients with both RRMS and secondary-progressive multiple sclerosis, even after controlling for structural differences.[19]

The frontal areas, BAs 6, 10, and 46, affected in our patients with RRMS, are responsible for memory processing, particularly working memory, memory encoding, and retrieval.[31,32] Several studies relate BA 10 with prospective memory and "intentional forgetting," suggesting involvement of BA 10 in controlling and manipulating memory.[32,33] BA 46 activation is associated with

working memory processes and memory manipulation.[31,33] It has been assumed that working memory is involved in a diversity of cognitive processes, including planning,[34] reasoning,[35] and problem-solving.[36] On the other hand, involvement of BA 6 in memory and attention may be due to the activation of an extended brain network in which the middle frontal gyrus has a fundamental task in memory strategy organization and memory control.[37] Hypoperfusion (qCBF and qCBV) in the left middle frontal and right superior temporal gyri with preservation of perfusion within the remaining medial prefrontal cortex in patients with RRMS who are nonimpaired compared with those who are cognitively impaired likely reflects increased cortical plasticity, because the medial prefrontal cortex has been previously shown to adaptively compensate for functional impairment in patients with MS.[38] Patients with RRMS and secondary-progressive multiple sclerosis performing a processing speed and attention task (Counting Stroop Task) were found to have activation predominantly in the left medial frontal region (left middle frontal gyrus/superior frontal sulcus and bilateral superior frontal gyri, corresponding to BAs 8, 9, 10), while HC had greater right frontal activation (inferior frontal gyrus, BA 45; and right basal ganglia).[38]

Last, BAs 28 and 38 are also implicated in memory, particularly nonverbal memory (right parahippocampal gyrus)[39] and multimodal memory retrieval (superior temporal gyrus).[40] Supporting the validity of the structural and progressive perfusion differences in patients with RRMS with cognitive impairment described above, significant impairment in working memory (Paced Auditory Serial Addition Test and Symbol Digit Modalities Test), visual and verbal learning, and memory retrieval (Brief Visual Memory Test-Revised and California Verbal Learning Test-II) was present compared with patients who were nonimpaired and HC.

Our VBM analysis by necessity controlled for a number of important potential confounding covariates; for example, the effect of depression was accounted for by the inclusion of Hosptial Anxiety and Depression Scale. Differing educational levels among cohorts was accounted for by the "normalization" of raw neurocognitive battery scores against representative population datasets. Cortical lesions and, to a lesser extent, T2 hyperintense lesion burden are both implicated in cognitive impairment of patients with MS. Comparisons between patient groups and HC included lesion volumes as covariates in our VBM analysis. However, no significant difference in lesion burden was present between MS groups, precluding a quid pro quo comparison.

Cerebral blood volume (amount of blood in 100 g of brain tissue) and blood flow (amount of blood flowing through 100 g of brain tissue per minute) abnormalities are found in a number of neurologic conditions such as stroke, characterized by ischemia. The physiopathology leading to cerebral hypoperfusion is unknown and may be multifactorial. While evidence does not support a primary neuronal loss mechanism given multiple findings of reduced cortical perfusion in the absence of GM volume loss,[16,18,19] mitochondrial disturbances and vascular abnormalities have been implicated in cerebral hypoperfusion in MS. Mitochondrial dysfunction can contribute to cerebral hypoperfusion in the form of a diminished mitochondrial capacity resulting from reductions in gene products specific for the mitochondrial electron transport chain[41] or due to intra-axonal mitochondrial pathology triggered by macrophage-derived reactive oxygen and nitrogen species, which may precede axonal damage.[42] Cerebral hypoperfusion can also be secondary to vascular abnormalities. Increased levels of endothelin-1, a potent vasoconstrictive peptide, are found in patients with MS, suggesting that cerebral blood flow reductions are mediated by elevated levels of this peptide.[43] Astrocytes of patients with MS are deficient in the $\beta$2-adrenergic receptor, resulting in cellular metabolic dysfunction affecting potassium uptake after synaptic activity and its subsequent release to the perivascular space, thus reducing arteriolar vasodilation.[44]

Venous changes are also well-described in MS; and given that venous capacitance accounts for approximately 70% of CBV, pathologies that decrease venous capacitance should greatly impact qCBV. For example, Ge et al[45] demonstrated reduced visibility of periventricular venous vasculature in patients with MS by using susceptibility-weighted imaging. The authors suggested that this reduction could be attributable to decreased vein number or size secondary to venous occlusion and perivenular inflammation. Such pathology could also be driven by obliterative vasculitis, which preferentially disrupts venous changes.[46,47] Additionally, intrastriatal injections of proinflammatory cytokine tumor necrosis factor-$\alpha$, found elevated in MS brains,[48] in rat models resulted in significant reductions of cerebral blood flow.[49] Cerebral hypoperfusion is characterized by both blood flow and volume changes, and these perfusion metrics may be differentially affected by the physiopathologic methods proposed. Additional studies should be conducted to explore the differences in cerebral blood flow and volume and their relation to physiopathology.

Limitations include the need for contrast agent injection required for DSC perfusion, precluding its use in patients with contraindications such as renal impairment. DSC is a relatively low-resolution technique in comparison with structural imaging but comparable with other functional techniques such as diffusion tensor and arterial spin-labeling techniques, which were previously applied to MS. DSC enables whole-brain scanning in approximately 2 minutes, therefore, minimally prolonging scanning time with higher signal-to-noise than arterial spin-labeling. Because the classes of disease-modifying drugs were evenly represented in both cognitively impaired and nonimpaired groups, we did not adjust for this factor. However, given that the effects of such treatments on cortical perfusion abnormalities are unclear, it would be prudent to adjust for disease-modifying drugs in future studies if difference occurs. Similarly, fatigue, experienced by 78%–90% of patients with MS,[50] may be associated with impaired cognitive function and should be accounted for in future studies.[51] Despite the relatively small sample size, consistent frontal perfusion deficits were demonstrated in our RRMS sample. According to our a priori hypothesis, this comparison was uncorrected but included several confounders. These results should be validated in a larger patient cohort. Longitudinal studies would also be helpful in determining whether perfusion measurements are sensitive to disease progression.

## CONCLUSIONS

Consistent regional frontal cortical perfusion deficits are found in patients with RRMS, with more widespread hypoperfusion in

cognitively impaired RRMS, independent of structural differences. Our findings suggest a potential role for cortical perfusion as a useful biomarker of cortical dysfunction and cognitive impairment in MS.

Disclosures: Charles G. Cantrell—*RELATED*: *Grant*: American Heart Association (14PRE20380810).* Liesly Lee—*UNRELATED*: *Consultancy*: Biogen Canada, Novartis Canada, Genyzme Canada, Teva Neurosciences, Serono Canada, *Comments*: advisory board member; *Payment for Manuscript Preparation*: Biogen Canada, *Comments*: publication of review article; *Travel/Accommodations/Meeting Expenses Unrelated to Activities Listed*: Biogen Canada, Novartis Canada, *Comments*: travel to conferences and advisory boards; *OTHER*: Biogen Canada,* Novartis Canada,* Teva Neurosciences,* *Comments*: clinical trial funding. Timothy J. Carroll—*RELATED*: *Grant*: National Institutes of Health,* *Comments*: I hold a National Institutes of Health research grant related to cerebral perfusion; *UNRELATED*: *Grants/Grants Pending*: National Institutes of Health,* American Hospital Association,* *Comments*: In addition to the National Institutes of Health and American Hospital Association grants that support this work, I have research grants that are independent of the work presented in this article. Richard I. Aviv—*RELATED*: *Grant*: Canadian Institutes of Health Research,* Biogen.* *Money paid to the institution.

## REFERENCES

1. Calabrese M, De Stefano N, Atzori M, et al. **Detection of cortical inflammatory lesions by double inversion recovery magnetic resonance imaging in patients with multiple sclerosis.** *Arch Neurol* 2007; 64:1416–22 CrossRef Medline
2. Calabrese M, Rocca MA, Atzori M, et al. **A 3-year magnetic resonance imaging study of cortical lesions in relapse-onset multiple sclerosis.** *Ann Neurol* 2010;67:376–83 CrossRef Medline
3. Deloire MS, Salort E, Bonnet M, et al. **Cognitive impairment as marker of diffuse brain abnormalities in early relapsing remitting multiple sclerosis.** *J Neurol Neurosurg Psychiatry* 2005;76:519–26 CrossRef Medline
4. Heaton RK, Nelson LM, Thompson DS, et al. **Neuropsychological findings in relapsing-remitting and chronic-progressive multiple sclerosis.** *J Consult Clin Psychol* 1985;53:103–10 CrossRef Medline
5. Calabrese M, Agosta F, Rinaldi F, et al. **Cortical lesions and atrophy associated with cognitive impairment in relapsing-remitting multiple sclerosis.** *Arch Neurol* 2009;66:1144–50 Medline
6. Rao SM, Leo GJ, Bernardin L, et al. **Cognitive dysfunction in multiple sclerosis, I: frequency, patterns, and prediction.** *Neurology* 1991; 41:685–91 CrossRef Medline
7. Calabrese M, Gallo P. **Magnetic resonance evidence of cortical onset of multiple sclerosis.** *Mult Scler* 2009;15:933–41 CrossRef Medline
8. Calabrese M, Poretto V, Favaretto A, et al. **Cortical lesion load associates with progression of disability in multiple sclerosis.** *Brain* 2012;135(pt 10):2952–61 CrossRef Medline
9. Seewann A, Enzinger C, Filippi M, et al. **MRI characteristics of atypical idiopathic inflammatory demyelinating lesions of the brain: a review of reported findings.** *J Neurol* 2008;255:1–10 Medline
10. Tardif CL, Bedell BJ, Eskildsen SF, et al. **Quantitative magnetic resonance imaging of cortical multiple sclerosis pathology.** *Mult Scler Int* 2012;2012:742018 CrossRef Medline
11. Chen JT, Easley K, Schneider C, et al. **Clinically feasible MTR is sensitive to cortical demyelination in MS.** *Neurology* 2013;80:246–52 CrossRef Medline
12. Poonawalla AH, Hasan KM, Gupta RK, et al. **Diffusion-tensor MR imaging of cortical lesions in multiple sclerosis: initial findings.** *Radiology* 2008;246:880–86 CrossRef Medline
13. Calabrese M, Rinaldi F, Seppi D, et al. **Cortical diffusion-tensor imaging abnormalities in multiple sclerosis: a 3-year longitudinal study.** *Radiology* 2011;261:891–98 CrossRef Medline
14. Shin W, Horowitz S, Ragin A, et al. **Quantitative cerebral perfusion using dynamic susceptibility contrast MRI: evaluation of reproducibility and age- and gender-dependence with fully automatic image postprocessing algorithm.** *Magn Reson Med* 2007;58:1232–41 CrossRef Medline
15. Vakil P, Lee JJ, Mouannes-Srour JJ, et al. **Cerebrovascular occlusive disease: quantitative cerebral blood flow using dynamic susceptibility contrast MR imaging correlates with quantitative H2[15O] PET.** *Radiology* 2013;266:879–86 CrossRef Medline
16. Aviv RI, Francis PL, Tenenbein R, et al. **Decreased frontal lobe gray matter perfusion in cognitively impaired patients with secondary-progressive multiple sclerosis detected by the bookend technique.** *AJNR Am J Neuroradiol* 2012;33:1779–85 CrossRef Medline
17. Rashid W, Parkes LM, Ingle GT, et al. **Abnormalities of cerebral perfusion in multiple sclerosis.** *J Neurol Neurosurg Psychiatry* 2004; 75:1288–93 CrossRef Medline
18. Debernard L, Melzer TR, Van Stockum S, et al. **Reduced grey matter perfusion without volume loss in early relapsing-remitting multiple sclerosis.** *J Neurol Neurosurg Psychiatry* 2014;85:544–51 CrossRef Medline
19. Francis PL, Jakubovic R, O'Connor P, et al. **Robust perfusion deficits in cognitively impaired patients with secondary-progressive multiple sclerosis.** *AJNR Am J Neuroradiol* 2013;34:62–67 CrossRef Medline
20. Hojjat SP CC, Vitorino R, Feinstein A, et al. **Regional reduction in cortical blood flow among cognitively impaired adults with relapsing-remitting multiple sclerosis patients.** *Mult Scler* 2016 Jan 11. [Epub ahead of print] Medline
21. Hojjat SP CC, Carroll TJ, Vitorino R, et al. **Perfusion reduction in the absence of structural differences in cognitively impaired versus unimpaired RRMS patients.** *Mult Sclel* 2016 Feb 4. [Epub ahead of print] Medline
22. Polman CH, Reingold SC, Banwell B, et al. **Diagnostic criteria for multiple sclerosis: 2010 revisions to the McDonald criteria.** *Ann Neurol* 2011;69:292–302 CrossRef Medline
23. Kurtzke JF. **Rating neurologic impairment in multiple sclerosis: an expanded disability status scale (EDSS).** *Neurology* 1983;33:1444–52 CrossRef Medline
24. Benedict RH, Fischer JS, Archibald CJ, et al. **Minimal neuropsychological assessment of MS patients: a consensus approach.** *Clin Neuropsychol* 2002;16:381–97 CrossRef Medline
25. Benedict RH, Bruce JM, Dwyer MG, et al. **Neocortical atrophy, third ventricular width, and cognitive dysfunction in multiple sclerosis.** *Arch Neurol* 2006;63:1301–06 CrossRef Medline
26. Shah MK, Shin W, Parikh VS, et al. **Quantitative cerebral MR perfusion imaging: preliminary results in stroke.** *J Magn Reson Imaging* 2010;32:796–802 CrossRef Medline
27. Ashburner J, Friston KJ. **Unified segmentation.** *Neuroimage* 2005;26: 839–51 CrossRef Medline
28. Ashburner J. **A fast diffeomorphic image registration algorithm.** *Neuroimage* 2007;38:95–113 CrossRef Medline
29. Jenkinson M, Beckmann CF, Behrens TE, et al. **FSL.** *Neuroimage* 2012;62:782–90 CrossRef Medline
30. Riccitelli G, Rocca MA, Pagani E, et al. **Mapping regional grey and white matter atrophy in relapsing-remitting multiple sclerosis.** *Mult Scler* 2012;18:1027–37 CrossRef Medline
31. Ranganath C, Johnson MK, D'Esposito M. **Prefrontal activity associated with working memory and episodic long-term memory.** *Neuropsychologia* 2003;41:378–89 CrossRef Medline
32. Leung HC, Gore JC, Goldman-Rakic PS. **Sustained mnemonic response in the human middle frontal gyrus during on-line storage of spatial memoranda.** *J Cogn Neurosci* 2002;14:659–71 CrossRef Medline
33. Zhang JX, Leung HC, Johnson MK. **Frontal activations associated with accessing and evaluating information in working memory: an fMRI study.** *Neuroimage* 2003;20:1531–39 CrossRef Medline
34. Law AS, Trawley SL, Brown LA, et al. **The impact of working memory load on task execution and online plan adjustment during multitasking in a virtual environment.** *Q J Exp Psychol (Hove)* 2013;66: 1241–58 CrossRef Medline
35. Suss HM, Oberauer K, Wittmann WW, et al. **Working-memory capacity explains reasoning ability—and a little bit more.** *Intelligence* 2002;30:161–288 CrossRef

36. Wiley J, Jarosz AF. **Working memory capacity, attentional focus, and problem solving.** *Curr Dir Psychol Sci* 2012;21:258–62 CrossRef
37. Haxby JV, Petit L, Ungerleider LG, et al. **Distinguishing the functional roles of multiple regions in distributed neural systems for visual working memory.** *Neuroimage* 2000;11(5 pt 1):380–91 CrossRef Medline
38. Parry AM, Scott RB, Palace J, et al. **Potentially adaptive functional changes in cognitive processing for patients with multiple sclerosis and their acute modulation by rivastigmine.** *Brain* 2003;126(pt 12): 2750–60 CrossRef Medline
39. Köhler S, Black SE, Sinden M, et al. **Memory impairments associated with hippocampal versus parahippocampal-gyrus atrophy: an MR volumetry study in Alzheimer's disease.** *Neuropsychologia* 1998;36: 901–14 CrossRef Medline
40. Takashima A, Nieuwenhuis IL, Rijpkema M, et al. **Memory trace stabilization leads to large-scale changes in the retrieval network: a functional MRI study on associative memory.** *Learn Mem* 2007;14: 472–79 CrossRef Medline
41. Dutta R, McDonough J, Yin X, et al. **Mitochondrial dysfunction as a cause of axonal degeneration in multiple sclerosis patients.** *Ann Neurol* 2006;59:478–89 CrossRef Medline
42. Nikić I, Merkler D, Sorbara C, et al. **A reversible form of axon damage in experimental autoimmune encephalomyelitis and multiple sclerosis.** *Nat Med* 2011;17:495–99 CrossRef Medline
43. D'Haeseleer M, Hostenbach S, Peeters I, et al. **Cerebral hypoperfusion: a new pathophysiologic concept in multiple sclerosis?** *J Cereb Blood Flow Metab* 2015;35:1406–10 CrossRef Medline
44. De Keyser J, Steen C, Mostert JP, et al. **Hypoperfusion of the cerebral white matter in multiple sclerosis: possible mechanisms and pathophysiological significance.** *J Cereb Blood Flow Metab* 2008;28: 1645–51 CrossRef Medline
45. Ge Y, Zohrabian VM, Osa EO, et al. **Diminished visibility of cerebral venous vasculature in multiple sclerosis by susceptibility-weighted imaging at 3.0 Tesla.** *J Magn Reson Imaging* 2009;29:1190–94 CrossRef Medline
46. Tanaka R, Iwasaki Y, Koprowski H. **Ultrastructural studies of perivascular cuffing cells in multiple sclerosis brain.** *Am J Pathol* 1975;81:467–78 Medline
47. Adams CW, Poston RN, Buk SJ, et al. **Inflammatory vasculitis in multiple sclerosis.** *J Neurol Sci* 1985;69:269–83 CrossRef Medline
48. Woodroofe MN, Cuzner ML. **Cytokine mRNA expression in inflammatory multiple sclerosis lesions: detection by non-radioactive in situ hybridization.** *Cytokin* 1993;5:583–88 Medline
49. Sibson NR, Blamire AM, Perry VH, et al. **TNF-alpha reduces cerebral blood volume and disrupts tissue homeostasis via an endothelin- and TNFR2-dependent pathway.** *Brain* 2002;125(pt 11):2446–59 CrossRef Medline
50. Fisk JD, Pontefract A, Ritvo PG, et al. **The impact of fatigue on patients with multiple sclerosis.** *Can J Neurol Sci* 1994;21:9–14 CrossRef Medline
51. Krupp LB, Elkins LE. **Fatigue and declines in cognitive functioning in multiple sclerosis.** *Neurology* 2000;55:934–39 CrossRef Medline

# In Vivo 7T MR Quantitative Susceptibility Mapping Reveals Opposite Susceptibility Contrast between Cortical and White Matter Lesions in Multiple Sclerosis

W. Bian, E. Tranvinh, T. Tourdias, M. Han, T. Liu, Y. Wang, B. Rutt, and M.M. Zeineh

## ABSTRACT

**BACKGROUND AND PURPOSE:** Magnetic susceptibility measured with quantitative susceptibility mapping has been proposed as a biomarker for demyelination and inflammation in patients with MS, but investigations have mostly been on white matter lesions. A detailed characterization of cortical lesions has not been performed. The purpose of this study was to evaluate magnetic susceptibility in both cortical and WM lesions in MS by using quantitative susceptibility mapping.

**MATERIALS AND METHODS:** Fourteen patients with MS were scanned on a 7T MR imaging scanner with T1-, T2-, and T2*-weighted sequences. The T2*-weighted sequence was used to perform quantitative susceptibility mapping and generate tissue susceptibility maps. The susceptibility contrast of a lesion was quantified as the relative susceptibility between the lesion and its adjacent normal-appearing parenchyma. The susceptibility difference between cortical and WM lesions was assessed by using a *t* test.

**RESULTS:** The mean relative susceptibility was significantly negative for cortical lesions ($P < 10^{-7}$) but positive for WM lesions ($P < 10^{-22}$). A similar pattern was also observed in the cortical ($P = .054$) and WM portions ($P = .043$) of mixed lesions.

**CONCLUSIONS:** The negative susceptibility in cortical lesions suggests that iron loss dominates the susceptibility contrast in cortical lesions. The opposite susceptibility contrast between cortical and WM lesions may reflect both their structural (degree of myelination) and pathologic (degree of inflammation) differences, in which the latter may lead to a faster release of iron in cortical lesions.

**ABBREVIATIONS:** MPFLAIR = magnetization-prepared fluid-attenuated inversion recovery; QSM = quantitative susceptibility mapping

Multiple sclerosis is a debilitating chronic inflammatory disorder of the central nervous system. MS pathogenesis is not fully understood and is thought to involve the whole brain. While previous MS imaging studies have been largely focused on white matter, recent investigations have focused on the importance of cortical gray matter damage,[1] because cortical lesions may be more relevant to physical and cognitive disability in patients than WM lesions.[2] This difference raises questions about the various underlying pathologic aspects of cortical and WM lesions. Histochemical staining has shown that cortical lesions have a lower degree of inflammation[3] and blood-brain barrier damage than WM lesions,[4] implying that the cortical lesion may be partly independent of inflammation.[5] Because it is useful to evaluate cortical and WM lesions in vivo across the whole brain, MR imaging is an important tool that complements histochemical staining.

While traditional water content– and proton mobility–based MR imaging modalities show similar abnormalities for both cortical and WM lesions, advanced high-field-strength MR imaging with susceptibility-weighted contrasts such as R2*/T2* mapping and quantitative susceptibility mapping (QSM) may have the potential to discriminate features of cortical and WM lesions. In active and chronic WM lesions, 7T MR imaging studies have shown that regions with decreased R2* and increased magnetic susceptibility correspond to histologically verified regions with demyelination- and/or inflammation-associated iron accumulation.[6-9] More recently, R2*/T2* mapping at 7T has shown de-

Received December 21, 2015; accepted after revision April 4, 2016.

From the Departments of Radiology (W.B., E.T., B.R., M.M.Z.) and Neurology (M.H.), Stanford University School of Medicine, Palo Alto, California; Service de NeuroImagerie Diagnostique et Thérapeutique (T.T.), Centre Hospitalier Universitaire de Bordeaux, Bordeaux Cedex, France; Institut National de la Santé et de la Recherche Médicale U 862 (T.T.), Université de Bordeaux, Bordeaux Cedex, France; and Department of Radiology (T.L., Y.W.), Weill Medical College of Cornell University, New York, New York.

This work was supported by GE Healthcare (B.R. and M.M.Z.); National Institutes of Health grants P41EB015891 (B.R. and M.M.Z), S10RR026351 (B.R. and M.M.Z), and RO1NS090464 (Y.W.); and grants from Association pour l'aide à la Recherche contre la Sclérose en Plaques and Translational Advanced Imaging Laboratory (T.T).

Please address correspondence to M.M. Zeineh, MD, PhD, Department of Radiology, Stanford University School of Medicine, Lucas Center for Imaging, Room P271, 1201 Welch Rd, Stanford, CA 94305-5488; e-mail: mzeineh@stanford.edu

Indicates open access to non-subscribers at www.ajnr.org

http://dx.doi.org/10.3174/ajnr.A4830

**Table 1: Patient demographic/clinical data and lesion counts[a]**

| | Sex | Age (yr) | Disease Duration (yr) | Treatment Type | Minimum WM Lesion Age (mo) | Cortical Lesion | WM Lesion | Mixed Lesion |
|---|---|---|---|---|---|---|---|---|
| Patient | | | | | | | | |
| 1 | F | 37 | 11 | Copaxone[b] | 12 | 2 | 6 | 1 |
| 2 | M | 42 | 12 | Copaxone | 10 | 1 | 11 | 0 |
| 3 | F | 42 | 3 | Copaxone | 8 | 0 | 2 | 0 |
| 4 | F | 30 | 3 | Tysabri[c] | 9 | 5 | 23 | 1 |
| 5 | F | 49 | 2 | Rebif[d] | 18 | 7 | 13 | 1 |
| 6 | M | 32 | 6 | Copaxone | 10 | 3 | 30 | 4 |
| 7 | M | 42 | 1 | Copaxone | 7 | 1 | 5 | 0 |
| 8 | F | 33 | 1 | Copaxone | 10 | 0 | 4 | 0 |
| 9 | F | 44 | 15 | No Treatment | 6 | 0 | 4 | 1 |
| 10 | F | 31 | 1 | No Treatment | 3 | 0 | 12 | 0 |
| 11 | F | 41 | 16 | Tysabri | 4 | 2 | 15 | 1 |
| 12 | F | 58 | 25 | Copaxone | 6 | 6 | 7 | 0 |
| 13 | M | 37 | 8 | Copaxone | 13 | 0 | 15 | 0 |
| 14 | M | 48 | 6 | Copaxone | 5 | 0 | 0 | 0 |
| Mean | | 40.4 ± 7.9 | 7.9 ± 7.2 | | 8.6 ± 4.0 | 1.9 ± 2.3 | 10.5 ± 8.4 | 0.64 ± 1.1 |
| Total | | | | | | 27 | 147 | 9 |

[a] Patients 9 and 10 were not on any disease-modifying treatment at the time of their 7T scans. Patient 9 was on Tysabri, but it was stopped 6 months prior to her 7T scan. All patients had relapsing-remitting MS except patient 11, who was in a transitional stage between relapsing-remitting MS and secondary-progressive MS but was still being treated for relapsing-remitting MS. Patient 14 had lesions that all regressed before the 7T scan.
[b] Glatiramer acetate injection.
[c] Natalizumab.
[d] Interferon $\beta$-1a.

**Table 2: Parameters for MR imaging sequences[a]**

| Parameters | T2* SPGR | T1 WM-Nulled MPRAGE | T1 CSF-Nulled MPRAGE | T2 MPFLAIR |
|---|---|---|---|---|
| Acquisition | 2D axial | 3D coronal | 3D coronal | 3D coronal |
| TR | 1200 ms | 8.3 ms | 3.9 ms | 8000 ms |
| TE | 17.7 ms | 3.7 ms | 8.5 ms | 109.8 ms |
| TI | NA | 680 ms | 1200 ms | 2135 ms |
| Flip angle | 60° | 4° | 6° | 90° |
| Bandwidth | 19.2 kHz | 15.6 kHz | 19.2 kHz | 62.5 kHz |
| FOV | 180 | 180 | 180 | 180 |
| Matrix | 384 × 384 | 180 × 180 | 224 × 224 | 224 × 224 |
| No. of sections | 90 | 256 | 256 | 256 |
| Resolution | 0.47 × 0.47 × 1 $mm^3$ | 1 × 1 × 1 $mm^3$ | 0.8 × 0.8 × 0.8 $mm^3$ | 0.8 × 0.8 × 0.8 $mm^3$ |
| Acceleration factor | ASSET 2 | ARC 1.5 × 1.5 | ASSET 2.5 | ARC 2 × 2 |
| Acquisition time (min:s) | 6:39 | 5:54 | 6:20 | 5:48 |

**Note:**—ASSET indicates array spatial sensitivity encoding technique; SPGR, spoiled gradient-recalled; ARC, Autocalibrating Reconstruction for Cartesian; NA, not applicable.
[a] Two patients had a slightly different resolution for T2* SPGR. One (patient 4 in Table 1) had a resolution of 0.47 × 0.47 × 1.2 $mm^3$ and the other (patient 11 in Table 1) had a resolution of 0.47 × 0.47 × 1.1 $mm^3$.

creased R2*/increased T2* in cortical lesions, indicating loss of both iron and myelin.[10-13]

However, simultaneous assessment of the susceptibility contrast in both cortical and WM lesions has not been performed, in particular by using in vivo QSM, which can measure tissue magnetic susceptibility with high reproducibility, even in the cortex.[14] Compared with other susceptibility-based imaging techniques such as phase imaging, susceptibility-weighted imaging, and R2*/T2* mapping, the deconvolution inherent in QSM removes the interfering effects of the susceptibility sources external to a voxel and makes the susceptibility sources within the voxel quantifiable.[15,16] In addition, the high SNR and resolution at a high field strength of 7T increase the in vivo quantification quality of QSM to benefit the characterization of small cortical lesions.

The purpose of this study was to use QSM at 7T to measure and compare in vivo susceptibility contrast in both cortical and WM lesions and identify differences that may reflect the known pathologic difference between the 2 subtypes of lesions.

## MATERIALS AND METHODS

### Patients

We recruited 15 patients with MS from February 2013 to August 2013 at the Stanford University MS clinic. Informed consent was obtained from each patient, and the study was approved by our institutional review board. An MS neurologist (M.H., with 10 years' experience) evaluated patients on the basis of their clinical presentations, investigative work-ups, and the McDonald criteria.[17] While quantitative clinical metrics of disability were not available for our subjects, patient medications taken at the time of the study are shown in Table 1. One patient was excluded from analysis because of a data-acquisition error prohibiting QSM reconstruction.

### MR Imaging

All MR images were performed on a 7T scanner (Discovery MR950; GE Healthcare, Milwaukee, Wisconsin) with a 32-channel phased array receive coil (Nova Medical, Wilmington, Massachusetts). The imaging protocol (Table 2) covering the supraten-

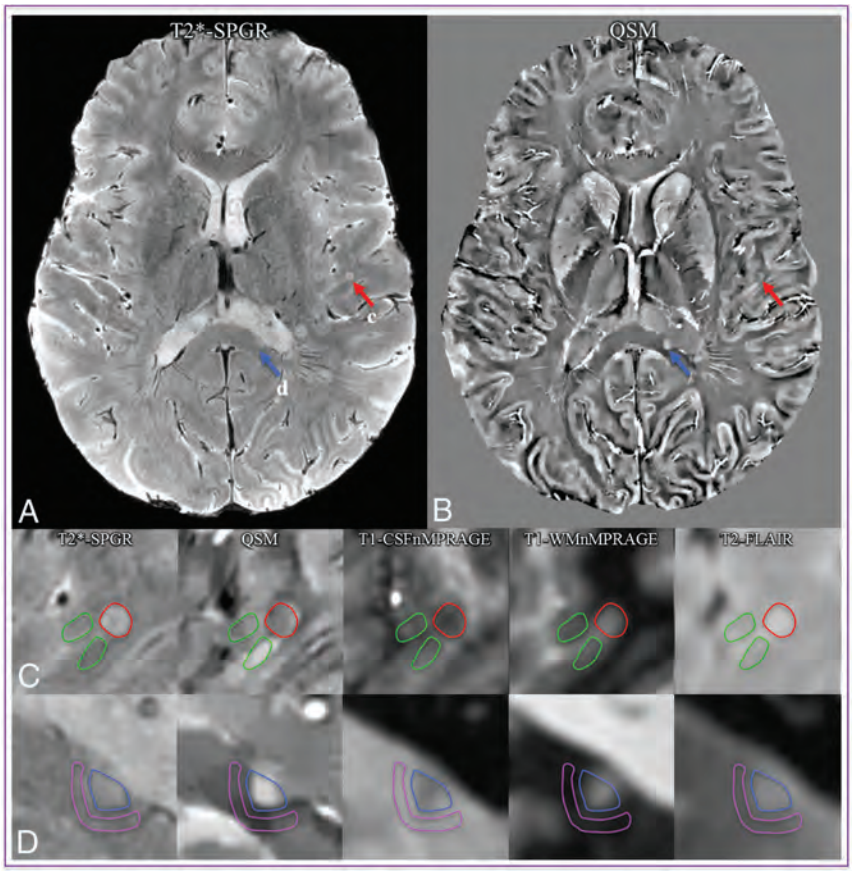


**FIG 1.** ROI definition. A whole section of magnitude (*A*) and QSM images (*B*) show 1 cortical lesion (*red arrows*) and 1 WM lesion (*blue arrows*). *C*, The ROIs of the cortical lesion and its adjacent normal-appearing cortical gray matter counterpart are delineated in *red and green lines*, respectively. *D*, The ROIs of the WM lesion and its adjacent normal-appearing white matter counterpart are delineated in *blue and pink lines*, respectively. ROIs were first defined on T2*-spoiled gradient-recalled images and then transferred to the other coregistered images. The gap between the lesion ROIs and the adjacent normal-appearing parenchyma reduces the partial volume effect in the segmentation. CSFnMPRAGE indicates CSF-nulled MPRAGE; WMnMPRAGE, WM-nulled MPRAGE.

torial brain included the following: 1) a T2*-weighted multisection 2D fast spoiled gradient-recalled sequence, 2) a coronal T1-weighted 3D WM-nulled MPRAGE sequence,[18] 3) a coronal T1-weighted 3D CSF-nulled MPRAGE sequence, and 4) a coronal 3D T2-weighted magnetization-prepared fluid-attenuated inversion recovery (MPFLAIR) sequence.[19] The T1- and T2-weighted images were acquired to aid in lesion identification and segmentation. The T2*-spoiled gradient-recalled images were first reconstructed into both magnitude and phase images, and then QSM images were computed by using the morphology-enabled dipole inversion method,[20] which performs Laplacian phase unwrapping first, followed by phase deconvolution by using $L_1$-norm minimization. To reduce the artifacts at the edge of brain while preserving as much as possible of the cortex, we eroded the unwrapped phase by 2.5 mm (~5 pixels) before the deconvolution. For each patient, the T1-WM-nulled MPRAGE, T1-CSF-nulled MPRAGE, and T2-MPFLAIR images were rigidly coregistered to the T2*-magnitude images by using the FMRIB Linear Image Registration Tool (FLIRT; http://www.fmrib.ox.ac.uk/) in FSL [21] with a mutual information cost function.

### *Lesion Identification and Segmentation*

All images were examined by raters and determined to be of adequate quality for MS lesion detection and characterization. MS lesions were defined as having abnormal signal on all traditional imaging sequences (hypointense on T1-CSF-nulled MPRAGE and hyperintense on T2*-spoiled gradient-recalled, T1-WM-nulled MPRAGE, and T2-MPFLAIR) by the most votes from 3 experienced MS imaging investigators who reviewed images independently and were blinded to QSM images (E.T., neuroradiologist with 6 years' experience; W.B., neuroimaging scientist with 6 years' experience; M.M.Z., neuroradiologist, with 11 years' experience). Only lesions of ≥2 mm were identified. All available 3T clinical scans before the current 7T scan were evaluated to identify whether any WM lesions were new or enhancing. The gray-white matter boundary on the T1-CSF-nulled MPRAGE images was used to distinguish WM, cortical, or mixed cortical-WM lesions: All WM lesions were completely within the WM, all cortical lesions were primarily (>75%) within the cortex, and all mixed lesions were 25%–75% within both the WM and cortex.

On T2*-spoiled gradient-recalled images, ROIs covering all hyperintense voxels were manually drawn jointly by W.B. and E.T. on multiple continuous image sections. WM and cortical lesion ROIs were drawn only within the WM and cortex, respectively, and each mixed lesion had 2 adjacent ROIs defined separately in its cortical and WM portions. Reference ROIs were drawn on adjacent normal-appearing WM for WM lesions or adjacent normal-appearing GM for cortical lesions. These normal-appearing ROIs were delineated from a single central section that contained the lesion (Fig 1). A donut-shaped region of adjacent homogeneous WM was used for normal-appearing WM; a homogeneous region of adjacent cortex continuous with both sides of the lesion was used for the normal-appearing GM. For a mixed lesion, 2 adjacent normal-appearing ROIs were defined separately for their corresponding normal-appearing cortical and WM portions. The adjacent normal-appearing ROI was within a 10-pixel vicinity of the lesion. A small gap was left between the lesion ROI and its adjacent normal-appearing ROI to reduce potential partial volume artifacts. After all ROIs had been segmented, the ROIs of lesions were overlaid on QSM images for a final quality control evaluation. Any blood vessels in the ROIs were removed, and any cortical or mixed lesions that were eroded or contaminated with artifacts due to QSM postprocessing were excluded from analysis.

The susceptibility contrast of a lesion was quantified as the relative susceptibility between the lesion and its normal-appearing parenchyma, which was calculated by subtracting the mean susceptibility in the normal-appearing ROI from that in the lesion ROI.

### Statistics

The relative susceptibility values for the set of cortical lesions, cortical portions of mixed lesions, WM lesions, and the WM portions of mixed lesions were each compared with zero by using the 1-sample *t* test. The relative susceptibility values in all cortical and WM lesions in the same subject were also averaged respectively; then, the above *t* test were repeated. The statistical significance threshold was set as $P < .05$, with multiple comparisons corrected by the Bonferroni method.

## RESULTS

Of the 14 patients (40.4 ± 7.9 years of age, 7.9 ± 7.2 years of disease duration; see more detail in Table 1), 13 patients had relapsing-remitting MS, while 1 patient had relapsing-remitting MS but was transitioning to secondary-progressive MS. Twelve patients were undergoing disease-modifying therapy. A total of 183 lesions were identified (after removing 1 cortical lesion that contained notable artifacts on the QSM image): 27 (14.8%) cortical, 147 (80.3%) WM, and 9 (4.9%) mixed. Eight of the 14 patients had cortical lesions (Table 1). Prior clinical 3T MR images indicated that all WM lesions were older than 3 months, and 8 of them (all from patient 4) were once contrast-enhancing >9 months before the 7T scan (Table 1), suggesting (but not proving) that none of the WM lesions in our sample were acute. Cortical lesions could not be reliably identified on prior 3T clinical images, and their ages were not determined. All patients were clinically stable between the time of the prior scan and the 7T scan.

The mean relative susceptibility values for 147 WM and 27 cortical lesions were 0.014 ± 0.014 ppm and −0.018 ± 0.013 ppm, respectively. The relative susceptibility value was positive for 132 of the 147 (89.8%) WM lesions, but negative for 25 of the 27 (92.6%) cortical lesions (Figs 2*A* and 3). Of 2 cortical lesions whose susceptibility was positive, one had a susceptibility of 0.008 ppm (with a dark center and an asymmetric bright rim, Fig 4) and the other had a susceptibility that was almost zero (0.0004 ppm). The mean relative susceptibility value was significantly higher than zero for WM lesions ($P < 10^{-22}$) but significantly lower than zero for cortical lesions ($P < 10^{-7}$) (Table 3).

After we averaged the susceptibility across lesions within each patient, all 13 patients had positive average relative susceptibility values for WM lesions (0.014 ± 0.010 ppm), and 7 of the 8 patients with cortical lesions had a negative average relative susceptibility value for cortical lesions (−0.015 ± 0.009 ppm) (Fig 2*B*). The patient with a positive average relative cortical susceptibility value for cortical lesions had only 1 cortical lesion (Fig 4). This patient-averaged relative susceptibility value was again significantly higher than zero ($P < .0004$) for WM lesions but significantly lower than zero ($P < .004$) for cortical lesions (Table 3).

The relative susceptibility values for WM and cortical portions in 9 mixed lesions were 0.014 ± 0.018 ppm and −0.009 ± 0.012 ppm, respectively. All 9 mixed lesions had higher relative susceptibility values in their WM portions compared with their cortical counterparts. Seven of the 9 (77.8%) lesions had positive relative susceptibility values in their WM portions ($P = .043$), and the same percentage of lesions had negative relative susceptibility values in their cortical portions ($P = .054$) (Figs 2*A* and 5 and Table 3).

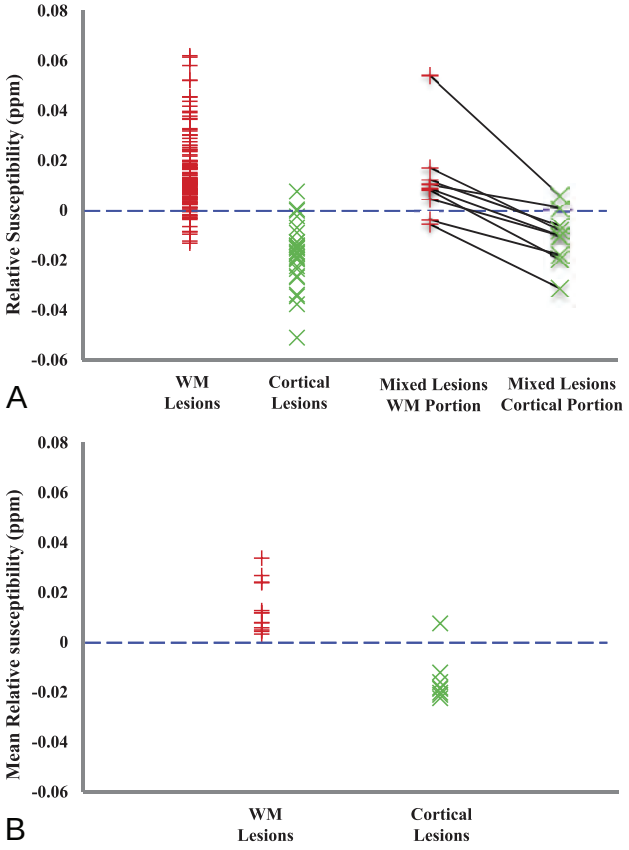


**FIG 2.** Relative susceptibility in MS lesions. *A*, The relative susceptibility in each individual lesion. Each *black line* on the right connects a pair of WM and cortical portions in a mixed lesion. *B*, The mean relative susceptibility after averaging the relative susceptibility across all lesions per type for each patient (13 patients had WM lesions, and 8 patients had cortical lesions).

## DISCUSSION

Our data demonstrate that the magnetic susceptibility values relative to normal-appearing adjacent parenchyma are negative for cortical lesions but positive for WM lesions, and a similar pattern was also found in the cortical and WM portions of mixed lesions, consistent with a recent postmortem study.[22] The divergent contrast between cortical and WM lesions on QSM images cannot be revealed by using traditional MR imaging contrasts, including T2, T1, and T2*.

### Positive Relative Susceptibility of WM Lesions

Our observation of positive relative susceptibility for WM lesions is in line with data from previous studies, in which most WM lesions appeared QSM hyperintense/isointense relative to normal-appearing WM.[9,23] Demyelination (loss of diamagnetic myelin) has been identified as a contributor to the increased susceptibility.[6-8] Accumulation of highly paramagnetic iron is also often found in microglia/macrophages near

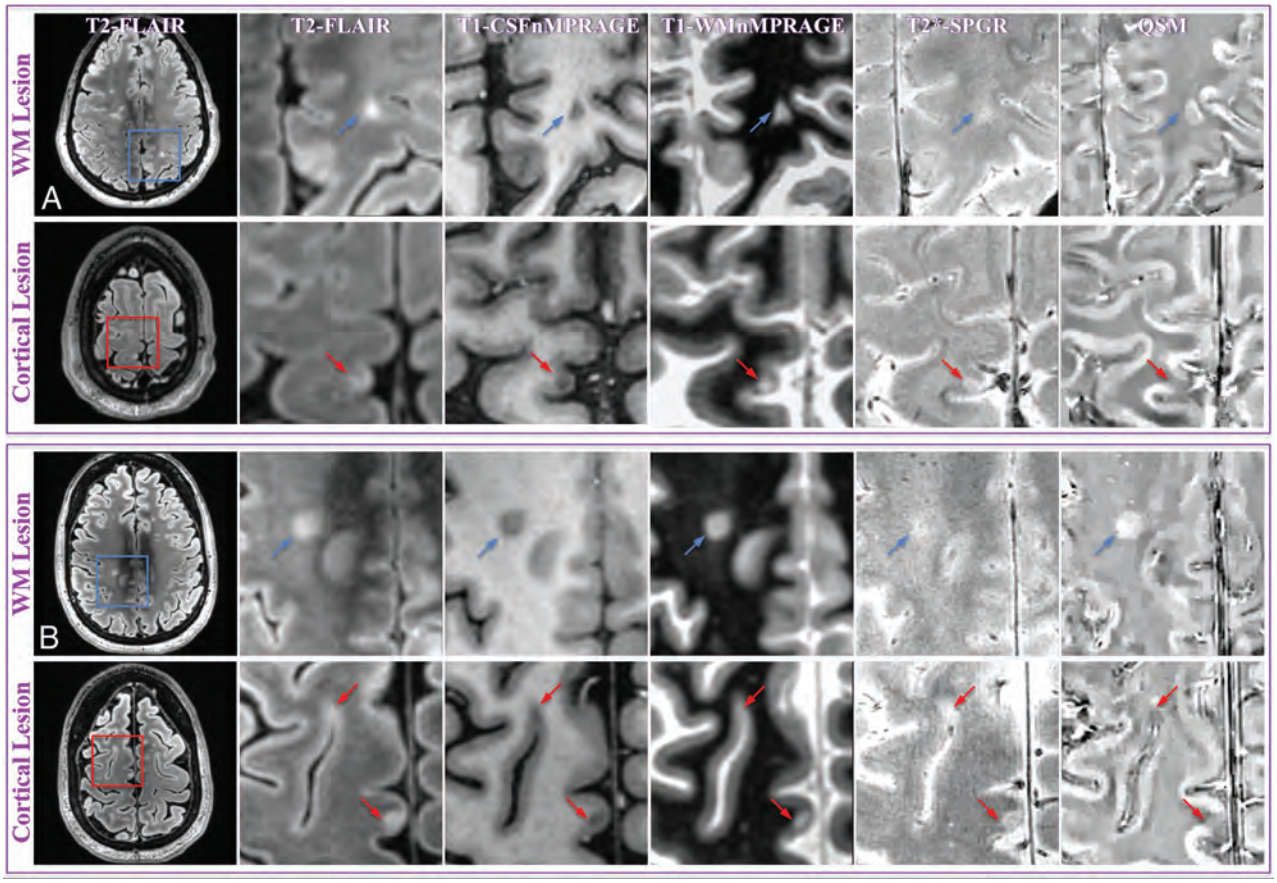


**FIG 3.** MR images of representative WM and cortical lesions from patients 4 (*A*) and 5 (*B*). A whole section of the T2-MPFLAIR image is displayed on the left column with a zoomed-in region (*blue/red square*) for all image contrasts. Two WM lesions (*blue arrows*) and 3 cortical lesions (*red arrows*) are shown. WM and cortical lesions are hyper- and hypointense relative to their adjacent parenchyma on QSM images, respectively, while both types of lesions show an identical contrast on all other images. CSFnMPRAGE indicates CSF-nulled MPRAGE; WMnMPRAGE, WM-nulled MPRAGE.

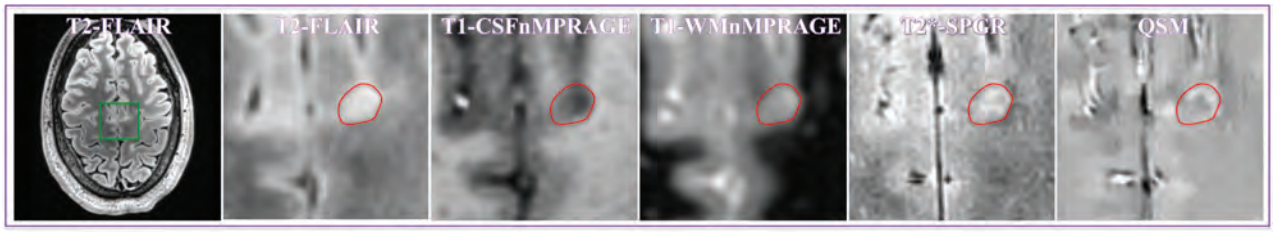


**FIG 4.** MR images of the only cortical lesion from patient 2. The lesion had a positive relative susceptibility and demonstrated a hyperintense core surrounded by an asymmetric hyperintense rim, suggesting that the lesion may have iron at its edge. Please see the Fig 3 legend for image descriptions.

**Table 3: Mean lesion susceptibility relative to normal-appearing parenchyma[a]**

| | | | Mixed Lesions | |
|---|---|---|---|---|
| | WM Lesions | Cortical Lesions | WM Portion | Cortical Portion |
| Relative susceptibility (ppm) (per lesion type) | 0.014 ± 0.014 | −0.018 ± 0.013 | 0.014 ± 0.018 | −0.009 ± 0.012 |
| *t* test | $P < 10^{-22}$ | $P < 10^{-7}$ | $P < .043$ | $P < .054$ |
| Relative susceptibility (ppm) (per lesion type per subject) | 0.014 ± 0.010 | −0.015 ± 0.009 | – | – |
| *t* test | $P < .0004$ | $P < .004$ | – | – |

[a] The null hypothesis of the *t* test is that the mean of relative susceptibility = 0. The significance level is .0083 after correcting multiple comparisons of 6 using the Bonferroni method.

the rim of acute and chronic active MS lesions,[6,7,24,25] which can also contribute to an increased susceptibility. However, iron in most MS lesions will regress as disease duration increases, and in some inactive lesions, iron content could even be lower than that in normal-appearing WM.[25] This may explain the presence of a few WM lesions with negative relative susceptibility. Nevertheless, because the susceptibility in most WM lesions was still positive relative to normal-

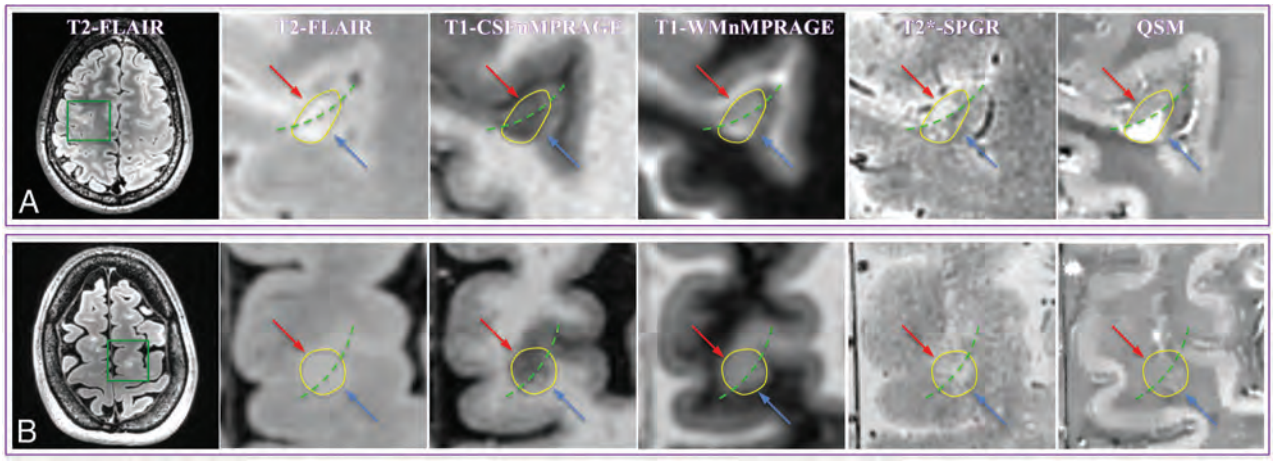


**FIG 5.** MR images of representative mixed lesions (*yellow circles*) from patients 1 (*A*) and 6 (*B*). The *green dashed line* divides a mixed lesion into its cortical (*red arrow*) and WM (*blue arrow*) components. *A*, The lesion has a QSM hypointense cortical portion and a hyperintense WM portion relative to adjacent normal-appearing GM and normal-appearing WM, respectively. *B*, The cortical component is hypointense compared with normal-appearing GM, while the white matter component is centrally isointense but peripherally slightly hyperintense compared with normal-appearing WM. Please see the Fig 3 legend for image descriptions.

appearing WM in our current study and previous studies,[9,23] it is likely that the effect of iron loss often does not completely offset that of demyelination.

### *Negative Relative Susceptibility of Cortical Lesions*

In contrast to the positive relative susceptibility of WM lesions, the negative relative susceptibility of cortical lesions is counterintuitive, though supported by a recent postmortem study.[22] Potential factors for susceptibility decrease are an iron decrease and/or a myelin increase. In theory, after initial demyelination, remyelination is possible in MS, but the regenerated myelin sheath is typically thinner than normal myelin[26]; this finding is consistent with overall reduced myelin relative to normal-appearing gray matter in histologic studies.[10,27] Accompanying demyelination, loss of iron in cortical lesions has also been observed.[10] The 2 contributions both lead to a decreased R2* (or increased T2*), as has been consistently reported in recent MR imaging studies.[10-13] However, unlike their similar effects on R2*/T2*, demyelination increases whereas the loss of iron decreases susceptibility. Therefore, in this particular case, QSM resolves a limitation of R2*/T2* mapping because it allows us to further conclude that in cortical lesions, iron loss dominates the susceptibility contrast over demyelination.

### *Interpretation of the Different Susceptibility Contrast*

The different susceptibility contrast between cortical and WM lesions may be partly because the degree of myelination in the cortex is much less than that in WM, while the difference in their iron concentration is small.[28] When both demyelination and iron loss are present, less iron loss is required to overwhelm demyelination in cortical lesions compared with WM. Indeed, in the cortex, iron has already been demonstrated to be the dominant source of MR susceptibility contrast and is well-correlated to both susceptibility and R2*/T2*.[29,30] Alternatively, this finding suggests that whenever there is increased iron in cortical lesions, a positive susceptibility value should be expected. The observation of iron accumulation in active cortical lesions has been reported in a previous study,[27] and the positive susceptibility for cortical lesions did occur in our study. However, these positive susceptibility lesions were only 7.4% of all our cortical lesions. Although one may argue that this could be because most of our cortical lesions were in their chronic stage, in chronic WM lesions, an increased iron level can be maintained for several years.[9,31] Moreover, recent results from R2*/T2* mapping consistently showed reduced R2* (or increased T2*) in cortical lesions,[10-13] and this could be even independent of disease stage.[11,12] Thus, the underlying structural difference between the white matter and cortex alone may not explain all of the susceptibility difference, and pathologic changes that evolve differentially with time may also play a role.

Pathologically, an intact BBB and low degree of inflammation in cortical lesions suggest that there are fewer macrophages/microglia (either infiltrated or locally activated) than in WM lesions, especially at the active and chronic active phases.[6,25] These cells phagocytize iron released from damaged oligodendrocytes and retain the iron in chronic WM lesions until the macrophages and microglia degenerate.[25] Therefore, the paucity of these iron holders in cortical lesions may reduce the time interval for an increased iron level in these lesions. Thus, we speculate that compared with WM lesions, the time window for the initial phase of iron accumulation is narrower in cortical lesions due to their faster iron release secondary to the lack of inflammatory cells. This narrow time window could make it difficult for susceptibility-contrast MR imaging to depict the stage of iron accumulation in cortical lesions. Because free iron can cause oxidative neurodegeneration,[25] the faster release of iron in cortical lesions may partly explain why cortical lesion load is more strongly correlated to the degree of neurodegeneration in MS.[2] Nevertheless, this speculation warrants further investigation with longitudinal and contrast-enhanced studies.

Several limitations in our study should be addressed. First, due to the still low in vivo sensitivity of MR imaging to cortical lesions,[10] our sampling of cortical lesions was likely incomplete and

could be biased. The number of cortical lesions that can be analyzed can be further reduced after QSM reconstruction. Second, although we examined the lesion age by looking at the most recent clinically available contrast-enhanced 3T MR imaging, this can be imprecise for white matter and offers no information for cortical lesions. Given the lack of prior 7T imaging and/or concurrent gadolinium contrast administration, the acute nature of each individual lesion was not definitively ascertainable. Third, the relevance of the presumed iron loss in cortical lesions to clinical disability was not quantified. Last, QSM alone cannot distinguish the contribution of demyelination from that of an iron increase, which would often be seen at the acute phase of both cortical and WM lesions because QSM exhibits a positive sign in both cases, while R2* will decrease for demyelination and increase for iron deposition. To completely distinguish the susceptibility contributions from myelin and iron, our future studies will combine information from both QSM and R2* mapping.

## CONCLUSIONS

QSM reveals an average negative magnetic susceptibility in cortical lesions and an average positive magnetic susceptibility in WM lesions, relative to their adjacent normal-appearing parenchyma. The negative susceptibility in cortical lesions suggests that iron loss dominates their susceptibility contrast. The different susceptibility contrast between cortical and WM lesions may reflect both their structural (degree of myelination) and pathologic (degree of inflammation) differences, in which the latter may lead to a faster release of iron in cortical lesions.


## ACKNOWLEDGMENTS

The authors thank Dr Maged Goubran for his insightful discussion and suggestions in the preparation of the manuscript. We also extend our gratitude to the editor and 2 anonymous reviewers for their constructive comments, which greatly helped us improve the final version of the manuscript.

Disclosures: Thomas Tourdias—*RELATED*: *Grant*: Association pour la Recherche sur la Sclérose En Plaques, Labex Translational Research and Advanced Imaging Laboratory. May Han—*UNRELATED*: *Consultancy*: Pfizer. Yi Wang—*RELATED*: *Grant*: National Institutes of Health (R01NS090464)*; *UNRELATED*: *Patents (planned, pending or issued)*: Cornell University,* *Comments*: one of the inventors on the QSM patent; *OTHER RELATIONSHIPS*: in discussion with Cornell regarding QSM technology–based startup. Brian Rutt—*RELATED*: *Grant*: GE Healthcare.* Michael M. Zeineh—*UNRELATED*: *Grants/Grants Pending*: Doris Duke Charitable Foundation,* Dana Foundation,* Radiological Society of North America,* *Other*: GE Healthcare, *Comments*: some research support.* *Money paid to the institution.


## REFERENCES


1. Calabrese M, Filippi M, Gallo P. **Cortical lesions in multiple sclerosis.** *Nat Rev Neurol* 2010;6:438–44 CrossRef Medline
2. Harrison DM, Roy S, Oh J, et al. **Association of cortical lesion burden on 7-T magnetic resonance imaging with cognition and disability in multiple sclerosis.** *JAMA Neurol* 2015;72:1004–12 CrossRef Medline
3. Peterson JW, Bo L, Mörk S, et al. **Transected neurites, apoptotic neurons, and reduced inflammation in cortical multiple sclerosis lesions.** *Ann Neurol* 2001;50:389–400 CrossRef Medline
4. van Horssen J, Brink BP, de Vries HE, et al. **The blood-brain barrier in cortical multiple sclerosis lesions.** *J Neuropathol Exp Neurol* 2007;66:321–28 CrossRef Medline
5. Louapre C, Lubetzki C. **Neurodegeneration in multiple sclerosis is a process separate from inflammation: yes.** *Mult Scler* 2015;21:1626–28 CrossRef Medline
6. Bagnato F, Hametner S, Yao B, et al. **Tracking iron in multiple sclerosis: a combined imaging and histopathological study at 7 Tesla.** *Brain* 2011;134:3602–15 CrossRef Medline
7. Yao B, Bagnato F, Matsuura E, et al. **Chronic multiple sclerosis lesions: characterization with high-field-strength MR imaging.** *Radiology* 2012;262:206–15 CrossRef Medline
8. Wisnieff C, Ramanan S, Olesik J, et al. **Quantitative susceptibility mapping (QSM) of white matter multiple sclerosis lesions: interpreting positive susceptibility and the presence of iron.** *Magn Reson Med* 2015;74:564–70 CrossRef Medline
9. Chen W, Gauthier SA, Gupta A, et al. **Quantitative susceptibility mapping of multiple sclerosis lesions at various ages.** *Radiology* 2014;271:183–92 CrossRef Medline
10. Yao B, Hametner S, van Gelderen P, et al. **7 Tesla magnetic resonance imaging to detect cortical pathology in multiple sclerosis.** *PLoS One* 2014;9:e108863 CrossRef Medline
11. Mainero C, Louapre C, Govindarajan ST, et al. **A gradient in cortical pathology in multiple sclerosis by in vivo quantitative 7 T imaging.** *Brain* 2015;138:932–45 CrossRef Medline
12. Louapre C, Govindarajan ST, Gianni C, et al. **Beyond focal cortical lesions in MS: an in vivo quantitative and spatial imaging study at 7T.** *Neurology* 2015;85:1702–09 CrossRef Medline
13. Jonkman LE, Fleysher L, Steenwijk MD, et al. **Ultra-high field MTR and qR2* differentiates subpial cortical lesions from normal-appearing gray matter in multiple sclerosis.** *Mult Scler* 2015 Dec 16. [Epub ahead of print] Medline
14. Deh K, Nguyen TD, Eskreis-Winkler S, et al. **Reproducibility of quantitative susceptibility mapping in the brain at two field strengths from two vendors.** *J Magn Reson Imaging* 2015;42:1592–600 CrossRef Medline
15. Wang Y, Liu T. **Quantitative susceptibility mapping (QSM): decoding MRI data for a tissue magnetic biomarker.** *Magn Reson Med* 2015;73:82–101 CrossRef Medline
16. Liu C, Li W, Tong KA, et al. **Susceptibility-weighted imaging and quantitative susceptibility mapping in the brain.** *J Magn Reson Imaging* 2015;42:23–41 CrossRef Medline
17. McDonald WI, Compston A, Edan G, et al. **Recommended diagnostic criteria for multiple sclerosis: guidelines from the International Panel on the Diagnosis of Multiple Sclerosis.** *Ann Neurol* 2001;50:121–27 CrossRef Medline
18. Saranathan M, Tourdias T, Bayram E, et al. **Optimization of white-matter-nulled magnetization prepared rapid gradient echo (MP-RAGE) imaging.** *Magn Reson Med* 2015;73:1786–94 CrossRef Medline
19. Saranathan M, Tourdias T, Kerr AB, et al. **Optimization of magnetization-prepared 3-dimensional fluid attenuated inversion recovery imaging for lesion detection at 7 T.** *Invest Radiol* 2014;49:290–98 CrossRef Medline
20. Liu J, Liu T, de Rochefort L, et al. **Morphology enabled dipole inversion for quantitative susceptibility mapping using structural consistency between the magnitude image and the susceptibility map.** *Neuroimage* 2012;59:2560–68 CrossRef Medline
21. Smith SM, Jenkinson M, Woolrich MW, et al. **Advances in functional and structural MR image analysis and implementation as FSL.** *Neuroimage* 2004;23(suppl 1):S208–19 CrossRef Medline
22. Wisnieff C, Ryan R, Pitt D, et al. **Investigation of susceptibility contrast in grey and white matter multiple sclerosis lesions.** In: *Proceedings of the Annual Scientific Meeting of the International Society for Magnetic Resonance in Medicine,* Milan, Italy. May 10–16, 2014
23. Li X, Harrison DM, Liu H, et al. **Magnetic susceptibility contrast variations in multiple sclerosis lesions.** *J Magn Reson Imaging* 2016;43:463–73 CrossRef Medline
24. Mehta V, Pei W, Yang G, et al. **Iron is a sensitive biomarker for**

**inflammation in multiple sclerosis lesions.** *PLoS One* 2013;8:e57573 CrossRef Medline
25. Hametner S, Wimmer I, Haider L, et al. **Iron and neurodegeneration in the multiple sclerosis brain.** *Ann Neurol* 2013;74:848–61 CrossRef Medline
26. Chari DM. **Remyelination in multiple sclerosis.** *Int Rev Neurobiol* 2007;79:589–620 CrossRef Medline
27. Pitt D, Boster A, Pei W, et al. **Imaging cortical lesions in multiple sclerosis with ultra-high-field magnetic resonance imaging.** *Arch Neurol* 2010;67:812–18 CrossRef Medline
28. Haacke EM, Cheng NY, House MJ, et al. **Imaging iron stores in the brain using magnetic resonance imaging.** *Magn Reson Imaging* 2005; 23:1–25 CrossRef Medline
29. Fukunaga M, Li TQ, van Gelderen P, et al. **Layer-specific variation of iron content in cerebral cortex as a source of MRI contrast.** *Proc Natl Acad Sci U S A* 2010;107:3834–39 CrossRef Medline
30. Langkammer C, Krebs N, Goessler W, et al. **Susceptibility induced gray-white matter MRI contrast in the human brain.** *Neuroimage* 2012;59:1413–19 CrossRef Medline
31. Bian W, Harter K, Hammond-Rosenbluth KE, et al. **A serial in vivo 7T magnetic resonance phase imaging study of white matter lesions in multiple sclerosis.** *Mult Scler* 2013;19:69–75 CrossRef Medline

# Improved Automatic Detection of New T2 Lesions in Multiple Sclerosis Using Deformation Fields

M. Cabezas, J.F. Corral, A. Oliver, Y. Díez, M. Tintoré, C. Auger, X. Montalban, X. Lladó, D. Pareto, and À. Rovira

## ABSTRACT

**BACKGROUND AND PURPOSE:** Detection of disease activity, defined as new/enlarging T2 lesions on brain MR imaging, has been proposed as a biomarker in MS. However, detection of new/enlarging T2 lesions can be hindered by several factors that can be overcome with image subtraction. The purpose of this study was to improve automated detection of new T2 lesions and reduce user interaction to eliminate inter- and intraobserver variability.

**MATERIALS AND METHODS:** Multiparametric brain MR imaging was performed at 2 time points in 36 patients with new T2 lesions. Images were registered by using an affine transformation and the Demons algorithm to obtain a deformation field. After affine registration, images were subtracted and a threshold was applied to obtain a lesion mask, which was then refined by using the deformation field, intensity, and local information. This pipeline was compared with only applying a threshold, and with a state-of-the-art approach relying only on image intensities. To assess improvements, we compared the results of the different pipelines with the expert visual detection.

**RESULTS:** The multichannel pipeline based on the deformation field obtained a detection Dice similarity coefficient close to 0.70, with a false-positive detection of 17.8% and a true-positive detection of 70.9%. A statistically significant correlation ($r = 0.81$, $P$ value = 2.2688e-09) was found between visual detection and automated detection by using our approach.

**CONCLUSIONS:** The deformation field–based approach proposed in this study for detecting new/enlarging T2 lesions resulted in significantly fewer false-positives while maintaining most true-positives and showed a good correlation with visual detection annotations. This approach could reduce user interaction and inter- and intraobserver variability.

**ABBREVIATIONS:** BL = baseline; CIS = clinically isolated syndrome; DSC = Dice similarity coefficient; DF = deformation fields; FP = false-positive; FPf = false-positive fraction; FU = follow-up; PD = proton density; TP = true-positive; TPf = true-positive fraction

MR imaging has become a core paraclinical tool for diagnosing and predicting long-term disability and treatment response in patients with multiple sclerosis. Of particular note, several criteria and strategies have been proposed for prompt identification of suboptimal response in individual patients based on a combination of clinical and MR imaging measures assessed during the first 6–12 months after treatment initiation.[1-6] These criteria are related to detection of disease activity on follow-up brain MR imaging studies compared with baseline scans, defined as either gadolinium-enhancing lesions or new/enlarging T2 lesions. However, detection of active T2 lesions in patients with MS can be hindered by several factors, such as a high burden of inactive T2 lesions, the presence of small and confluent lesions, inadequate repositioning, and high interobserver variability.[7] Image subtraction after image registration can overcome these issues by visually cancelling stable disease (lesions that stay the same over time) and providing good visualization and quantification of active T2 lesions (either positively or negatively).[8,9]

Techniques for automatic detection of active T2 lesions can be classified into 2 categories: intensity-based and deformation-based approaches.[10] In the former, successive scans are analyzed by point-to-point (voxel-to-voxel) comparison, whereas in the

Received October 13, 2015; accepted after revision March 21, 2016.

From the Section of Neuroradiology, Department of Radiology (M.C., J.F.C., C.A., D.P., À.R.), and Centre d'Esclerosi Múltiple de Catalunya, Department of Neurology/Neuroimmunology (M.T., X.M.), Vall d'Hebron University Hospital, Vall d'Hebron Research Institute, Autonomous University of Barcelona, Barcelona, Spain; and Visió per Computador i Robòtica group (M.C., A.O., Y.D., X.L.), University of Girona, Girona, Spain.

Mariano Cabezas held a European Research Committee for Treatment and Research in Multiple Sclerosis/Magnetic Resonance Imaging in MS 2014 fellowship grant. This work has been partially supported by "La Fundació la Marató de TV3", Retos de Investigación grant TIN2014–55710-R, and an MPC UdG 2016/022 grant.

Paper previously presented in part at: Annual Meeting of the American Society of Neuroradiology and Foundation of the ASNR Symposium, April 25–30, 2015; Chicago, Illinois.

Please address correspondence to Mariano Cabezas, PhD, Computer Vision and Robotics Group, Department of Computer Architecture and Technology, Polytechnic School - P-IV Building, University of Girona, 17071 Girona, Spain; e-mail: mariano.cabezas@vhir.org, mcabezas@eia.udg.edu

http://dx.doi.org/10.3174/ajnr.A4829

latter, deformation fields obtained by nonrigid registration of the 2 scans are analyzed.

Most of the proposed techniques to detect changes on follow-up images use an image-subtraction process that identifies new T2 lesions[11-13] and include statistical models of intensity changes between scans or other, more complex, supervised strategies. Although segmentation of subtraction images enables quantification of new, enlarging, and resolving MS lesions, automated image analysis that differentiates a true lesion change and noise or artifacts would save considerable time and effort.

Nonrigid registration techniques usually provide a discrete vector field that defines deformations occurring between 2 different images. This vector field can be used to detect evolving processes, including new T2 lesions. Several approaches that use deformation fields (DF) to detect positive changes occurring in longitudinal MR studies have been reported.[14,15] These approaches focus on detecting and explaining processes undergoing change (ie, lesions shrinking or growing), but not on detecting new lesions, a measure that is now under consideration as a biomarker for monitoring and predicting treatment response.[16]

The purpose of this study was to improve automated detection of new T2 lesions on successive brain MR images, by using a novel approach that combines subtraction and DF analysis. This new pipeline will be compared with other approaches, in which a threshold is applied or a postprocessing step is incorporated on the basis of intensity rules.

## MATERIALS AND METHODS

### Patients

We prospectively analyzed previously acquired data from a cohort of 36 patients with clinically isolated syndrome (CIS) or early relapsing MS (13 women and 23 men; 35.4 ± 7.1 years of age) who underwent brain MR imaging in our center for diagnosis or for monitoring disease evolution or treatment response. All patients with CIS and early relapsing MS demonstrated new T2 lesions on the follow-up scans and were diagnosed according to recent definitions and criteria.[17,18] Two brain MR imaging acquisitions were obtained in each patient, the first within the first 3 months after the onset of symptoms (baseline [BL]) and the second at 12 months' follow-up after onset (FU). The Vall d'Hebron hospital's ethics committee approved the study, and written informed consent was signed by the participating patients.

### MR Image Acquisition

All patients underwent brain MR imaging at BL and FU on the same 3T magnet (Tim Trio; Siemens, Erlangen, Germany) with a 12-channel phased array head coil. The MR imaging protocol included the following sequences: 1) transverse proton density (PD)- and T2-weighted fast spin-echo (TR= 3080 ms/TE = 21–91 ms, voxel size = 0.78 × 0.78 × 3.0 $mm^3$), 2) transverse fast T2-FLAIR (TR = 9000 ms, TE = 87 ms, TI= 2500 ms, flip angle = 120°, voxel size = 0.49 × 0.49 × 3.0 $mm^3$), and 3) sagittal T1-weighted 3D magnetization-prepared rapid acquisition of gradient echo (TR = 2300 ms, TE = 2.98 ms, TI = 900 ms, voxel size = 1.0 × 1.0 × 1.2 $mm^3$).

### Expert Analysis

All new and enlarging T2 lesions visually detected on the FU scan were annotated on T2-FLAIR images by using the semiautomated tool included in Jim 5.0 (http://www.xinapse.com/home.php). This task was performed by a trained technician who first detected changes visually by using the BL and FU scan and then delineated them semiautomatically by using a subtraction image and both scans. This task was later confirmed by an expert neuroradiologist. The results of this analysis served as the reference standard for comparisons in the study.

### Preprocessing

On both BL and FU PD-weighted images, a brain mask was identified and delineated by using the FSL Brain Extraction Tool (bet2 command) (http://fsl.fmrib.ox.ac.uk/fsl/fslwiki/BET) with the robust center estimation, neck clean-up, and default threshold parameters. The mask was then applied to the other coregistered images (T2-, T2-FLAIR-, and T1-weighted), and the N4 algorithm from the ITK library (http://www.itk.org/)[19] was used to correct for bias with the standard parameters for a maximum of 400 iterations. The last preprocessing step was to normalize BL and FU intensity values by using a histogram-matching approach.

### Registration and Subtraction

In each patient, T1- and T2-FLAIR-weighted images from the same study were coregistered to the PD-weighted image by using a 3D affine transformation similar to that in previous works.[20] The Mattes Mutual Information cost function was minimized by Regular Step Gradient Descent Optimization (https://itk.org/Doxygen320/html/classitk_1_1RegularStepGradientDescentOptimizer.html), and B-spline interpolation was applied. This framework was implemented by using ITK.

The same 3D affine-registration framework was also used before subtraction to warp the BL images to the FU space because patients with CIS and early relapsing MS present with small (or no) overall anatomic changes.[21] The registration was conducted between both PD-weighted images. After the transformation had been obtained, we applied it to the other images by using B-spline interpolation to subtract the BL PD-, T2-, and T2-FLAIR-weighted images from their corresponding FU images. In the case of BL T2-FLAIR-weighted images, the 2 affine transformations were combined to avoid interpolating more than once.

Affine registration methods are robust to the presence of lesions, and when new lesions appear, deformable models usually show distortions to compensate for the anomalous regions. On the basis of the characteristics of these approaches, we were able to analyze the DF obtained after applying these nonrigid techniques to the registered images. In this study, we applied the multiresolution Demons registration approach[22] from ITK initialized with the previous affine transformation. Concretely, we used the DemonsRegistrationFilter (SD = 1) (http://www.itk.org/Doxygen320/html/classitk_1_1DemonsRegistrationFilter.html) with MultiResolutionPDEDeformableRegistration (http://www.itk.org/Doxygen320/html/classitk_1_1MultiResolutionPDEDeformableRegistration.html) (iterations = 50, levels = 2). This algorithm can produce large localized deformations and has been widely used in brain MR imaging.

### Threshold

New and enlarging T2 lesions appear hyperintense in the subtraction image. However, certain regions outside the white matter may also appear hyperintense due to artifacts, noise, inhomogeneity, registration errors, or small anatomic differences. Because our goal was to detect new and enlarging T2 WM lesions, we restricted our search to areas within the WM. To define this region, we applied an automated tissue-segmentation algorithm[23] to the BL and FU scans. This nonparametric algorithm uses an atlas registered to the T1-weighted image in conjunction with the T1-, T2-, and PD-weighted images. This segmentation was applied before the registration step between the 2 image sets. After registration, a final WM mask was obtained as the union of the 2 WM segmentations in the FU space. After defining WM, we smoothed the subtracted images by using the ITK 3D Gaussian filter (DiscreteGaussianImageFilter; http://www.itk.org/Doxygen/html/classitk_1_1DiscreteGaussianImageFilter.html) with a 0.5 SD to reduce the impact of spurious hyperintense regions.[20] An automated threshold was then computed for each subtraction image (PD, T2, and T2-FLAIR) and applied separately to obtain 3 initial lesion masks. The thresholds were computed as the mean of the subtraction image within the WM plus 5 SDs to guarantee that only hyperintense regions were detected and to maintain a large number of true-positives (TPs), as proposed previously.[20] Lesions of <3 voxels were excluded to reduce the effects of noise.

### Lesion Mask Combination

To differentiate between errors and true lesions in each mask, we used the intersection of the 3 masks (PD, T2, and T2-FLAIR). Because differences in the initial masks might still result in false-positive (FP) detections of 1 or 2 voxels, we also applied the lesion size restriction to the combined mask to reduce this effect.

Afterward, the 2 different postprocessing approaches were used independently in order to compare them.

### Postprocessing Based on Intensity

While the aforementioned restrictions usually exclude a large number of FPs, they do not completely eliminate this problem. As has been reported,[20] some FPs can arise from low intensities in the BL images, caused, for example, by skull-stripping errors. To reduce the effect of these factors and to include local information, we applied a set of suggested intensity-based rules to the BL and FU images[20]:

- Global rule: To avoid regions with a low intensity, candidate lesions with a mean value under $\mu_{basal} - 2\sigma_{basal}$ are discarded, where $\mu_{basal}$ and $\sigma_{basal}$ are the mean and SD of the basal intensities inside the WM ROI.
- Basal neighborhood ratio: New lesions should appear as WM in the basal image. To ensure that, we compute a ratio between the neighboring pixels of the candidate lesions ($\mu_{lesion}/\mu_{neighbors}$). If this ratio is <0.9, we discard the candidate lesion. That usually means that there is a dark spot that might appear as a hyperintensity in the subtraction image.
- Follow-up neighborhood ratio: Similarly, new lesions should actually be lesions in the follow-up image. To ensure that, we compute the same ratio. If this ratio is <1, the candidate lesion has a lower intensity profile than its neighboring area, so we discard it.

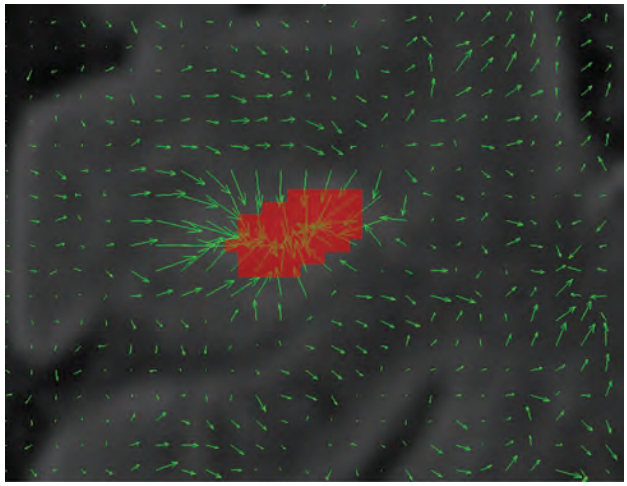

**FIG 1.** Example of the deformation field inside a new lesion. All *arrows* point to the lesion center.

### Postprocessing Based on Deformation Fields

The Demons algorithm provides DF representing a transformation from the target image (FU scan) to the source image (BL scan). To compensate for hyperintense lesions, the DF go from outside the lesion to its center (shrinking it), as is illustrated in Figs 1 and 2. Vectors within and in the vicinity of the lesion have a higher modulus than those in other regions of the image. Moreover, no sinking patterns with independent behavior between neighboring vectors are observed far from lesions.

To be able to model and automatically detect this behavior, we defined 3 regional metrics computed from the DF inside each candidate lesion:

- Divergence[15]: This vector operator is defined as the volume density of the outward flux of a vector field from an infinitesimal volume around a given point. Given a continuously differentiable vector field $\vec{F}$, the divergence at a given point is equal to the scalar-valued function:

$$div\vec{F} = \frac{\partial F_x}{\partial_x} + \frac{\partial F_y}{\partial_y} + \frac{\partial F_z}{\partial_z}.$$

In our case,

$$divDF = G(x)_x + G(y)_y + G(z)_z,$$

where $G(i)_j$ is the $j$ component of the gradient in the $i$ component of the vector field volume.

For new T2 lesions, deformations have an inward flux that is represented by a negative value (*div DF* of <0). Therefore, we excluded lesions that had a positive mean value.

- Jacobian[14]: We used the Jacobian operator to analyze the DF at each candidate lesion. Values of <1 represent a shrinking process. Regions with a higher value were excluded.
- Concentricity: Due to the inward flux of the vector field within lesions, all vectors point to the center of mass of the lesion. We defined a new operator on the basis of that notion. For each lesion voxel, we computed the vector between the voxel and the center of mass of the lesion. We then com-

puted the scalar product between the DF vector and this concentric vector. Concentric vector fields should have an absolute mean value close to 1; therefore, we excluded all candidate lesions with an absolute value lower than 0.75. This value indicates that the deformation vector and the concentric vector have a maximum angle of 15°.

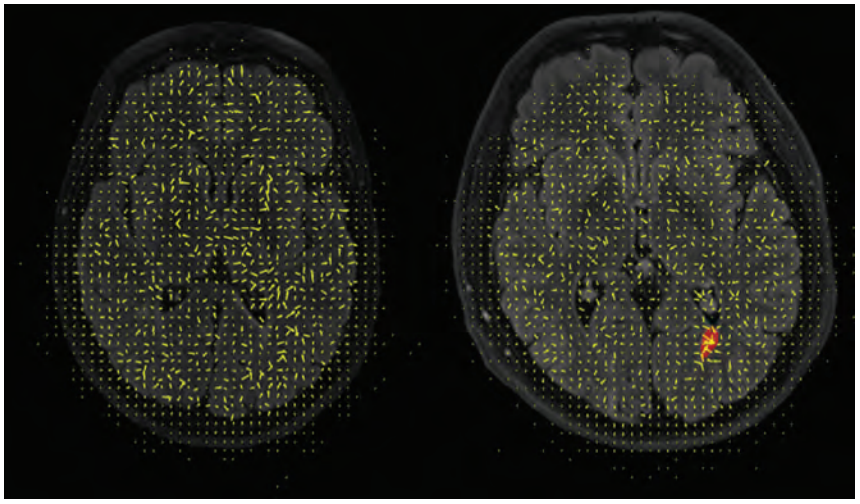

**FIG 2.** Example of the deformation field for 2 sections. The first image does not contain lesions and presents large deformations with no clear sinking patterns, while in the second image with a lesion, all the *arrows* inside the lesion point to the center.

### *Evaluation and Statistical Analysis*

To validate use of the DF and the benefits they provide when automatically detecting new T2 lesions, we compared the proposed pipeline to a state-of-the-art approach[20] with detection-based measures. In this approach, a lesion is considered TP if it overlaps a ground truth lesion, FP is a detected lesion with no overlap, and FN is a lesion that has not been detected.

The TP fraction (TPf) and FP fraction (FPf) are the ratio measures of TP versus ground truth lesions and FP versus all lesions found, respectively. Therefore, perfect detection would be 100% TPf and 0% FPf. To complement and summarize these measures, we also computed the Dice similarity coefficient (DSC):

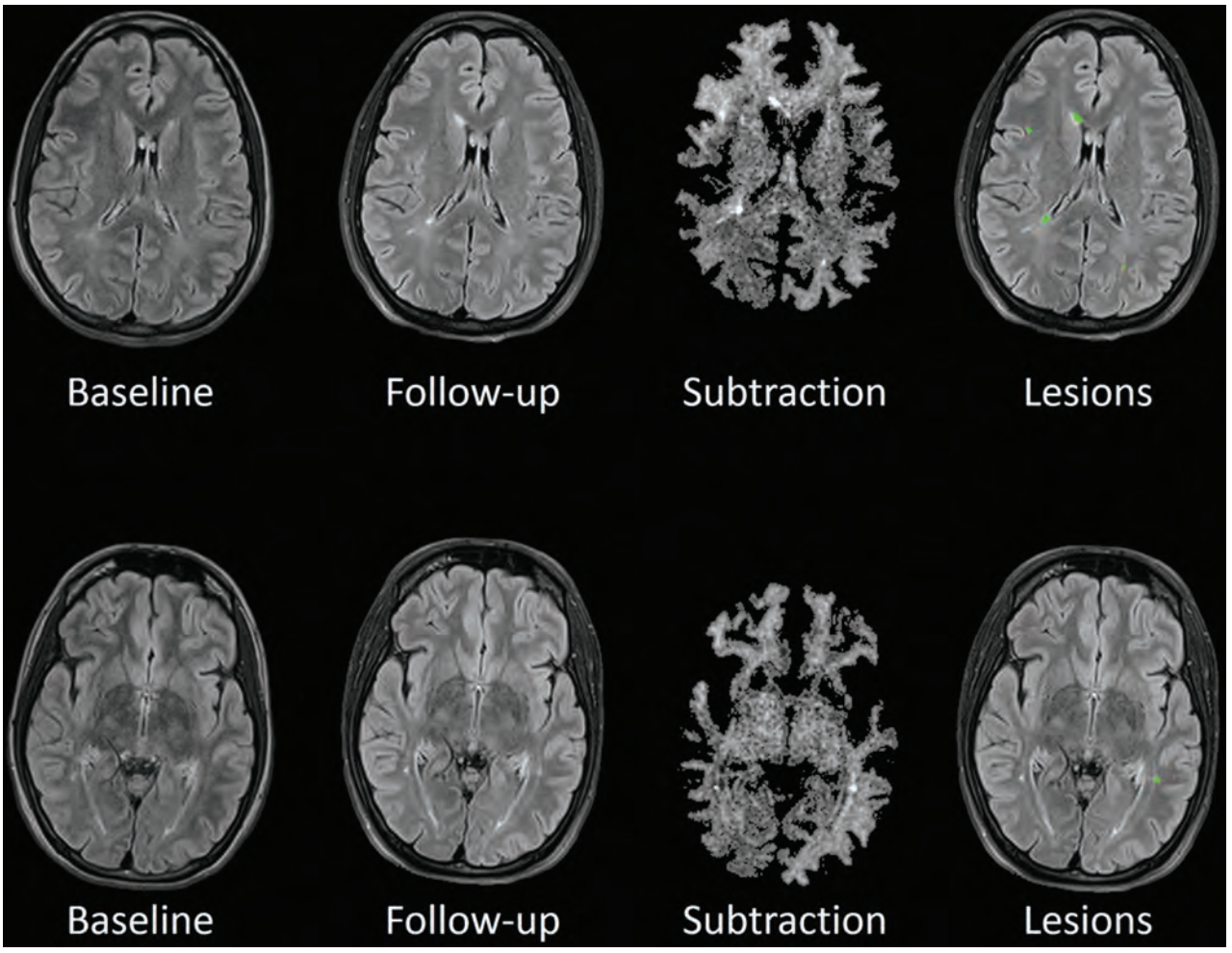


**FIG 3.** New lesion detection. For each row, the first image is the baseline image, the second is the follow-up image, the third is the subtraction, and the fourth is the lesion analysis over the follow-up image (green = true-positive). The patient has a large number of TPs (100%), with a small number of FPs (0%).

**Table 1: Lesion detections obtained for our data base using various approaches**

| Image | Method | ASD | TPf | FPf | DSC (Lesions) | DSC (Volume) |
|---|---|---|---|---|---|---|
| PD | Threshold | 25.80 | 92.28 | 93.18 | 0.11 | 0.31 |
| | Intensity rules[20] | 21.90 | 80.61 | 83.01 | 0.24 | 0.35 |
| | DF | 19.91 | 73.18 | 77.02 | 0.30 | 0.37 |
| T2 | Threshold | 25.22 | 93.89 | 95.88 | 0.07 | 0.25 |
| | Intensity rules[20] | 22.22 | 64.09 | 86.35 | 0.17 | 0.25 |
| | DF | 17.76 | 81.79 | 80.84 | 0.26 | 0.34 |
| T2-FLAIR | Threshold | 27.22 | 90.24 | 92.79 | 0.10 | 0.26 |
| | Intensity rules[20] | 21.17 | 78.34 | 80.77 | 0.25 | 0.31 |
| | DF | 21.14 | 81.22 | 77.11 | 0.30 | 0.33 |
| Combination | Threshold | 13.07 | 91.05 | 85.61 | 0.22 | 0.45 |
| | Intensity rules[20] | 30.80 | 51.62 | 35.87 | 0.46 | 0.37 |
| | Proposal | 7.89 | 70.93 | 17.80 | 0.68 | 0.52 |

**Note:**—ASD indicates average surface distance.

**Table 2: Permutation test ranking of DSC values for the approaches applied on each image separately[a]**

| | Method | Mean *P* Value |
|---|---|---|
| Rank 1 ($<1\ \sigma$) | T2-FLAIR-DF | .75 |
| | PD-DF | .56 |
| | T2-DF | .53 |
| Rank 2 ($<2\ \sigma$) | T2-FLAIR[20] | .22 |
| | PD[20] | .16 |
| Rank 3 ($<3\ \sigma$) | T2[20] | −.22 |
| | PD-threshold | −.56 |
| | T2-FLAIR-threshold | −.67 |
| | T2-threshold | −.78 |

[a] Methods were ranked relative to the mean and SD of the method with the highest DSC value. Methods in the same rank have similar results, whereas methods in different ranks show significant differences.

$$DSC = \frac{2 \times TP}{2 \times TP + FP + FN}.$$

Furthermore, we also performed an evaluation of the actual overlap between lesions by using the volumetric DSC.

Finally, we also included the average surface distance measure from the MICCAI MS Lesion Segmentation Challenge 2008 (http://www.ia.unc.edu/MSseg/).[24] The border voxels of segmentation and reference are determined. For each voxel along one border, the closest voxel along the other border is determined (by using unsigned Euclidean distance in real-world distances). All these distances are stored, and their average is computed. This value is zero for a perfect segmentation.

A statistical analysis was performed to evaluate the significance of the results obtained. To determine the performance of each key step in our pipeline, we conducted 3 sets of experiments, each focusing on a different aspect. The naïve approach consisted of applying the threshold defined in the "Materials and Methods" section to each subtraction image. We also applied different postprocessing approaches to the initial masks separately, and finally, we compared the results of the threshold mask combination to our proposal and a state-of-the-art approach.

First, we performed a Lilliefors test on the measures evaluated and their differences. Due to the number of pipelines evaluated and the statistically proved non-normal distribution of the measures, pair-wise *t* tests were inappropriate. Hence, permutation tests[20,25] were used to determine significant differences among applying a threshold, using intensity and neighborhood rules, and using DF. Permutation tests yield the mean ($\mu$) and SD ($\sigma$) of the fraction of times that the difference in a given measure for a given method is smaller than the remaining methods, with a *P* value ≤ .05. The methods were then ranked by the mean and SD of the method with the highest measured value. Methods in the same rank had similar results, whereas methods in different ranks showed significant differences.

We also performed a Wilcoxon rank sum test among the DSC, TPf, and FPf results for each independent image after the threshold was applied. Finally, the Pearson correlation was used to analyze the manual annotations and the automatic detections obtained with our approach.

## RESULTS

The mean results for new T2 lesion detection and segmentation by using each of the approaches are summarized in Table 1. The DSC results with our approach were 0.68 in terms of detection (regions) and 0.52 in terms of segmentation (volume). Moreover, we obtained the lowest average surface difference (7.89 mm) in contrast to the joint threshold (13.07 mm) and with intensity rules (30.80 mm). While the volumetric agreement was lower, it was high enough to validate our detection definition of 1 voxel overlap.

### *Impact of Postprocessing per Image*

Our first set of experiments consisted of applying a threshold to PD-weighted, T2-weighted, and T2-FLAIR-weighted images separately. We compared this naïve approach with a state-of-the-art approach[26] based on intensity and spatial rules and the DF rules presented here on each image.

According to Table 1, application of a threshold alone missed some ground truth lesions and resulted in a large number of FPs. Lowering the threshold to include all ground truth detections would be counterproductive because of the number of FPs. In terms of sensitivity alone, both PD-weighted and FLAIR subtractions yielded similar results.

Rankings obtained by statistical permutation testing for the DSC are summarized in Table 2. Negative values indicate lower performance than the method with the highest DSC value. Rank 1 only included approaches that relied on the DF after applying a threshold, whereas rank 2 included approaches that used intensity and neighborhood rules for the PD and T2-FLAIR subtractions. Rank 3 included all methods based on thresholds with a negative *P* value. Because ranking between the approaches differed, we can conclude that there was a significant difference between using DF and intensity/neighboring rules.

Paired rank sum testing between strategies revealed no significant difference in DSC or TPf among the 3 image subtractions, thus indicating that all 3 images provided similar sensitivity for lesion detection. However, we obtained significant differences for FPf, suggesting that FP detection differed among the images. This difference supports our idea of combining the masks obtained for each subtraction.

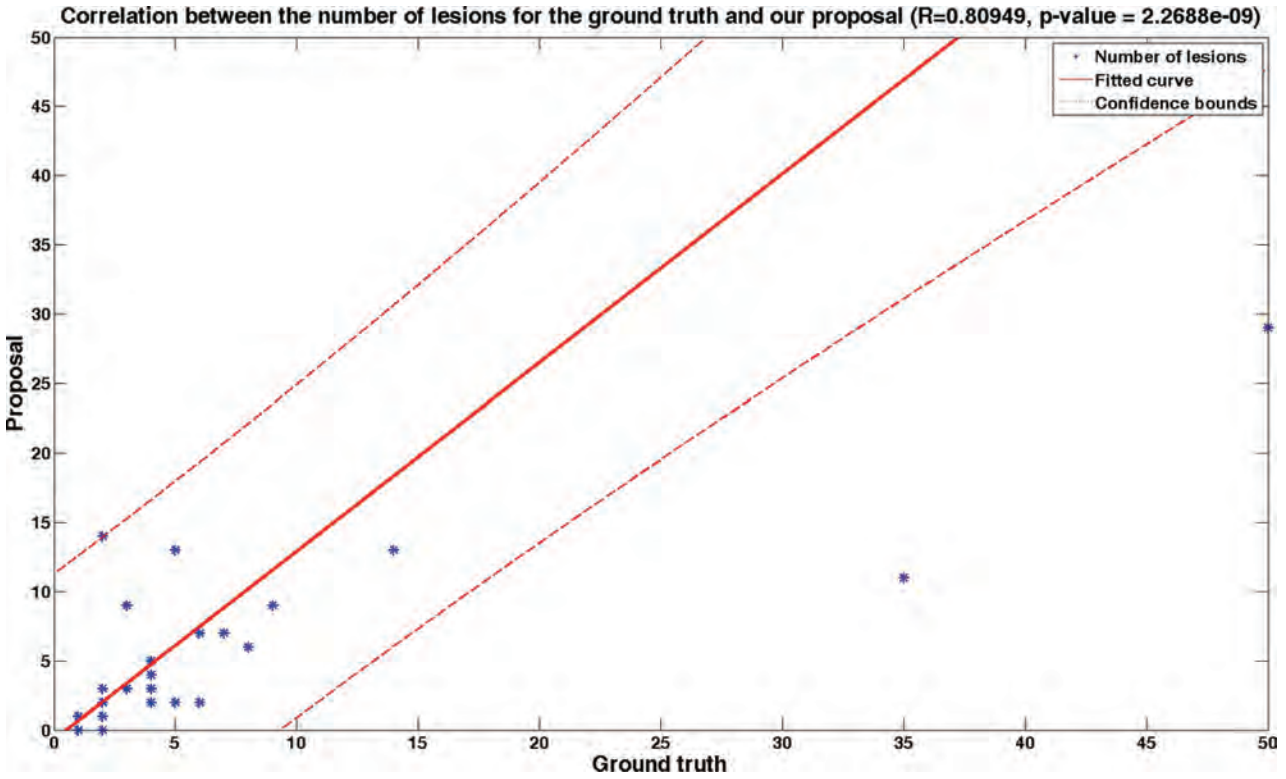


**FIG 4.** Correlation between the number of ground truth lesions and the number of automatically detected ones (Pearson coefficient = 0.81, $P$ = 2.2688e-09).

### *Impact of the Lesion Mask Combination*

When the initial masks for each image were analyzed independently, almost all new T2-WM lesions were detected. However, FP detections were visually different among the images in most cases and, therefore, highly related to the image being visualized.

To validate the assumption that combining the masks significantly improves the results, we performed a second set of experiments and comparisons by using rank sum testing between the lesion mask after applying a threshold to each image independently and the intersection of all 3 masks. Significant differences were found for FPf and DSC ($P < .05$) but not for TPf. Again, this finding suggests that combining all masks reduces the number of FPs without significantly affecting TP detections.

### *Pipeline Comparison*

We also performed an analysis of the last group in Table 1 (mask combination in the 3 different strategies). In this case, we obtained significant differences ($P < .05$) for all 3 measures (DSC, TPf, and FPf) between the intersection mask and the 2 approaches based on postprocessing. This result indicates that the DSC improvement was due to the considerable decrease in FPs detrimental to the number of TPs. This is the usual trade-off encountered when dealing with postprocessing techniques, in which some TPs are excluded (eg, due to image artifacts) to reduce the number of FPs. We also found significant differences ($P < .05$) in all 3 measures between the 2 automatic approaches (our proposal and that of Ganiler et al[20]), reinforcing the notion that our DF strategy yields better performance. Qualitative examples of the results obtained with our proposal are shown in Fig 3.

**Table 3: Analysis of the TPf before and after postprocessing with deformation fields for different sizes[a]**

| Image | Method | 3–10 | 11–50 | 50+ |
|---|---|---|---|---|
| Combination | Combination (threshold) | 71.43 | 72.38 | 95.16 |
| | Proposal | 42.86 | 48.57 | 77.42 |

[a] Lesions between 3 and 10 voxels are considered small; lesions between 11 and 50 voxels, medium; and lesions with >50 voxels, large.

A significant correlation ($r = 0.81$, $P$ = 2.2688e-09) was found between annotations based on visual detection and our automated approach for detecting new T2 lesions (Fig 4). We then analyzed the effect of the 3 DF-based measures and found that they all had a similar impact in most cases; however, some FPs were only detected by one of them, with no apparent pattern.

### *Lesion Analysis per Volume*

Finally, we analyzed lesion detection by groups of similar size. Table 3 summarizes the results before and after postprocessing by using the deformation field obtained. As expected, lesions with a small size (between 3 and 10 voxels) have a low detection rate (42.86%). Due to their small size, the deformation field cannot fully capture them and they are discarded during the postprocessing step. As the volume increases, the deformation field presents a clearer pattern that we can detect with the rules presented in this article. Even though for lesions of a medium size (between 11 and 50 voxels) the TPf is still lower than 50% (48.57%), this value increases for large lesions of >50 voxels (77.42%). Moreover, the TPf decreases from 69.23% before postprocessing to 23.08% with lesions of <7 voxels.

## DISCUSSION

New/enlarging T2 lesion count is a common measure used to monitor and predict treatment response in patients with MS.[1-6] Trained radiologists perform this task by visual analysis of 2 successive MR images, a time-consuming task associated with high interobserver variability.[7] The pipeline proposed in this study may be of value for assisting or even replacing visual analysis for detecting active MS lesions on T2-weighted images.

The method is completely autonomous and automated and does not require user input or a training set. Furthermore, the process is computationally fast because it mainly relies on subtraction and registration. With an optimized Demons algorithm, it takes only minutes to segment all new T2 lesions in a single patient, with a low number of FP detections.

We obtained significant results with a data base of 36 patients, and we also tested our algorithm without any modification with a small clinical trial dataset. This dataset had a reduced number of images ($n = 10$) that were provided by 3 different centers. Even though promising results were obtained with this initial test (DSC for lesions = 0.79, DSC for volume = 0.60, TPf = 74.15, FPf = 9.61), an exhaustive analysis with a larger number of patients should be performed to prove that the method performs similarly with different acquisition setups.

However, currently, it is not possible to detect new black holes (even though a postprocessing step could be included to differentiate between new lesions and new black holes by using the T1-weighted images).

Current studies are working on the definition and implementation of a new "no evidence of disease activity" treatment.[6,27] This decision model relies on, among others, the detection of new/enlarging T2 lesions as a biomarker and requires a high specificity and sensitivity because the number of FPs could suggest an undesirable change in treatment. Therefore, reducing the number of FPs when using automatic tools is a key factor. However, current subtraction techniques usually rely on intensity information, which can misguide detection due to local inhomogeneities or small changes. While these FPs can be reduced by using spatial information, a registration technique that overfits a free-form deformation incorporates this local information and provides better insight into changes occurring due to development of a new lesion or one that changes in size.

Automated algorithms usually obtain better scores when lesion count or lesion volume is high, but they often have shortcomings when the lesion volume or volume change is small.[11-13,20] We also compared ours to a current state-of-the-art technique that has been validated with 1.5T imaging. 3T imaging provides better resolution and a higher signal-to-noise ratio, from which registration techniques can benefit. Therefore, to demonstrate that DF provide a better means to differentiate subtraction artifacts and true disease activity (in terms of lesions), we used 3T imaging, in which DF provide a better understanding of evolving processes.

## CONCLUSIONS

We have presented a new automated pipeline to detect new brain T2 lesions and positive changes in disease activity in patients with clinically isolated syndrome or early relapsing multiple sclerosis. This technique relies on DF information and provides more reliable measurement of changes occurring between 2 successive MR images than other currently available approaches. Significant differences in accurate lesion detection were found between this technique and other current approaches, and a strong correlation and higher overlap were seen between our approach and visual lesion detection. These findings indicate that the proposed technique may be of value for application in clinical studies investigating disease activity, monitoring, and treatment effects, providing a decrease in user interaction and likely a reduction in inter- and intraobserver variability.

Disclosures: Mariano Cabezas—*RELATED*: *Grant*: Magnetic Resonance Imaging in MS (MAGNIMS), *Comments*: MAGNIMS/European Research Committee for Treatment and Research in Multiple Sclerosis (ECTRIMS) Fellowship 2014. Further information can be found at http://www.ectrims.eu/wp-content/uploads/2013/04/ECTRIMS-MAGNIMS-MRI-fellowship-awardees_for-website_2015.pdf. Mar Tintoré—*UNRELATED*: *Board Membership*: Genzyme, Roche, Biogen, Novartis, Teva, Merck, Sanofi, Almirall, Bayer; *Consultancy:* Biogen; *Grants/Grants Pending*: Genzyme,* Roche,* Biogen,* Novartis,* Teva,* Merck,* Sanofi,* Almirall,* Bayer*; *Payment for Lectures (including service on Speakers Bureaus)*: Genzyme, Roche, Biogen, Novartis, Teva, Merck, Sanofi, Almirall, Bayer; *Payment for Manuscript Preparation*: Biogen; *Payment for Development of Educational Presentations*: Biogen. Cristina Auger—*UNRELATED*: *Payment for Lectures (including service on Speakers Bureaus)*: Novartis, Stendhal America, Biogen. Xavier Montalban—*UNRELATED*: *Consultancy*: Actelion, Almirall, Bayer, Biogen, Genzyme, Merck, Novartis, Octapharma, Receptos, Roche, Sanofi-Genzyme.* Deborah Pareto—*UNRELATED*: *Payment for Lectures (including service on Speakers Bureaus)*: Novartis, Genzyme. Àlex Rovira—*UNRELATED*: *Consultancy*: Biogen Idec, Genzyme, Novartis, Olea Medical; *Payment for Lectures (including service on Speakers Bureaus)*: Biogen Idec, Stendhal America, Genzyme, Novartis, Olea Medical; *Payment for Development of Educational Presentations*: Novartis, Stendhal America, Genzyme, Biogen. *Money paid to the institution.

## REFERENCES

1. Río J, Castilló J, Rovira A, et al. **Measures in the first year of therapy predict the response to interferon beta in MS.** *Mult Scler* 2009;15:848–53 CrossRef Medline
2. Sormani MP, De Stefano N. **Defining and scoring response to IFN-β in multiple sclerosis.** *Nat Rev Neurol* 2013;9:504–12 CrossRef Medline
3. Sormani MP, Río J, Tintorè M, et al. **Scoring treatment response in patients with relapsing multiple sclerosis.** *Mult Scler* 2013;19:605–12 CrossRef Medline
4. Prosperini L, Mancinelli CR, De Giglio L, et al. **Interferon beta failure predicted by EMA criteria or isolated MRI activity in multiple sclerosis.** *Mult Scler* 2014;20:566–76 CrossRef Medline
5. Freedman MS, Selchen D, Arnold DL, et al; Canadian Multiple Sclerosis Working Group. **Treatment optimization in MS: Canadian MS Working Group updated recommendations.** *Can J Neurol Sci* 2013;40:307–23 CrossRef Medline
6. Stangel M, Penner IK, Kallmann BA, et al. **Towards the implementation of 'no evidence of disease activity' in multiple sclerosis treatment: the multiple sclerosis decision model.** *Ther Adv Neurol Disord* 2015;8:3–13 CrossRef Medline
7. Altay EE, Fisher E, Jones SE, et al. **Reliability of classifying multiple sclerosis disease activity using magnetic resonance imaging in a multiple sclerosis clinic.** *JAMA Neurol* 2013;70:338–44 CrossRef Medline
8. Moraal B, Wattjes MP, Geurts JJ, et al. **Improved detection of active multiple sclerosis lesions: 3D subtraction imaging.** *Radiology* 2010;255:154–63 CrossRef Medline
9. Moraal B, van den Elskamp IJ, Knol DL, et al. **Long-interval T2-weighted subtraction magnetic resonance imaging: a powerful new outcome measure in multiple sclerosis trials.** *Ann Neurol* 2010;67:667–75 CrossRef Medline
10. Lladó X, Ganiler O, Oliver A, et al. **Automated detection of multiple**

**sclerosis lesions in serial brain MRI.** *Neuroradiology* 2012;54:787–807 CrossRef Medline
11. Battaglini M, Rossi F, Grove RA, et al. **Automated identification of brain new lesions in multiple sclerosis using subtraction images.** *J Magn Reson Imaging* 2014;39:1543–49 Medline
12. Elliott C, Arnold DL, Collins DL, et al. **Temporally consistent probabilistic detection of new multiple sclerosis lesions in brain MRI.** *IEEE Trans Med Imaging* 2013;32:1490–503 CrossRef Medline
13. Sweeney EM, Shinohara RT, Shea CD, et al. **Automatic lesion incidence estimation and detection in multiple sclerosis using multisequence longitudinal MRI.** *AJNR Am J Neuroradiol* 2013;34:68–73 CrossRef Medline
14. Rey D, Subsol G, Delingette H, et al. **Automatic detection and segmentation of evolving processes in 3D medical images: application to multiple sclerosis.** *Med Image Anal* 2002;6:163–79 CrossRef Medline
15. Thirion JP, Calmon G. **Deformation analysis to detect and quantify active lesions in three-dimensional medical image sequences.** *IEEE Trans Med Imaging* 1999;18:429–41 CrossRef Medline
16. Vrenken H, Jenkinson M, Horsfield MA, et al; MAGNIMS Study Group. **Recommendations to improve imaging and analysis of brain lesion load and atrophy in longitudinal studies of multiple sclerosis.** *J Neurol* 2013;260:2458–71 CrossRef Medline
17. Lublin FD, Reingold SC, Cohen JA, et al. **Defining the clinical course of multiple sclerosis: the 2013 revisions.** *Neurology* 2014;83:278–86 CrossRef Medline
18. Polman CH, Reingold SC, Banwell B, et al. **Diagnostic criteria for multiple sclerosis: 2010 revisions to the McDonald criteria.** *Ann Neurol* 2011;69:292–302 CrossRef Medline
19. Tustison NJ, Avants BB, Cook PA, et al. **N4ITK: improved N3 bias correction.** *IEEE Trans Med Imaging* 2010;29:1310–20 CrossRef Medline
20. Ganiler O, Oliver A, Diez Y, et al. **A subtraction pipeline for automatic detection of new appearing multiple sclerosis lesions in longitudinal studies.** *Neuroradiology* 2014;56:363–74 CrossRef Medline
21. Diez Y, Oliver A, Cabezas M, et al. **Intensity based methods for brain MRI longitudinal registration: a study in multiple sclerosis patients.** *Neuroinformatics* 2014;12:365–79 CrossRef Medline
22. Thirion JP. **Image matching as a diffusion process: an analogy with Maxwell's demons.** *Med Image Anal* 1998;2:243–60 CrossRef Medline
23. Cabezas M, Oliver A, Roura E, et al. **Automatic multiple sclerosis lesion detection in brain MRI by FLAIR thresholding.** *Comput Methods Programs Biomed* 2014;115:147–61 CrossRef Medline
24. Styner M, Lee J, Chin B, et al. **3D segmentation in the clinic: a grand challenge II: MS lesion segmentation.** *MIDAS J* 2008;1–6
25. Menke J, Martinez TR. **Using permutations instead of Student's t distribution for p-values in paired-difference algorithm comparisons**. In: *Proceedings of the 2004 IEEE International Joint Conference of Neural Networks,* Budapest, Hungary. July 25–29, 2004
26. Dancey C, Reidy J. *Statistics without Maths for Psychology: Using SPSS for Windows.* New York: Prentice Hall; 2004
27. Tintore M, Rovira À, Río J, et al**. Defining high, medium and low impact prognostic factors for developing multiple sclerosis.** *Brain* 2015;138(pt 7):1863–74 CrossRef Medline

# White Matter Hyperintensity Volume and Cerebral Perfusion in Older Individuals with Hypertension Using Arterial Spin-Labeling

J.W. van Dalen, H.J.M.M. Mutsaerts, A.J. Nederveen, H. Vrenken, M.D. Steenwijk, M.W.A. Caan, C.B.L.M. Majoie, W.A. van Gool, and E. Richard

## ABSTRACT

**BACKGROUND AND PURPOSE:** White matter hyperintensities of presumed vascular origin in elderly patients with hypertension may be part of a general cerebral perfusion deficit, involving not only the white matter hyperintensities but also the surrounding normal-appearing white matter and gray matter. We aimed to study the relation between white matter hyperintensity volume and CBF and assess whether white matter hyperintensities are related to a general perfusion deficit.

**MATERIALS AND METHODS:** In 185 participants of the Prevention of Dementia by Intensive Vascular Care trial between 72 and 80 years of age with systolic hypertension, white matter hyperintensity volume and CBF were derived from 3D FLAIR and arterial spin-labeling MR imaging, respectively. We compared white matter hyperintensity CBF, normal-appearing white matter CBF, and GM CBF across quartiles of white matter hyperintensity volume and assessed the continuous relation between these CBF estimates and white matter hyperintensity volume by using linear regression.

**RESULTS:** Mean white matter hyperintensity CBF was markedly lower in higher quartiles of white matter hyperintensity volume, and white matter hyperintensity volume and white matter hyperintensity CBF were negatively related (standardized $\beta = -0.248$, $P = .001$) in linear regression. We found no difference in normal-appearing white matter or GM CBF across quartiles of white matter hyperintensity volume or any relation between white matter hyperintensity volume and normal-appearing white matter CBF (standardized $\beta = -0.065$, $P = .643$) or GM CBF (standardized $\beta = -0.035$, $P = .382$) in linear regression.

**CONCLUSIONS:** Higher white matter hyperintensity volume in elderly individuals with hypertension was associated with lower perfusion within white matter hyperintensities, but not with lower perfusion in the surrounding normal-appearing white matter or GM. These findings suggest that white matter hyperintensities in elderly individuals with hypertension relate to local microvascular alterations rather than a general cerebral perfusion deficit.

**ABBREVIATIONS:** ATT = arterial transit time; $\beta$ = standardized $\beta$; NAWM = normal-appearing white matter; preDIVA = Prevention of Dementia by Intensive Vascular Care trial; preDIVA-M = MRI substudy of the preDIVA trial; WMH = white matter hyperintensity

White matter hyperintensities (WMHs) of presumed vascular origin are a common finding on brain MR imaging in elderly individuals. WMH prevalence estimates in asymptomatic older individuals range from 45% to >90%, depending on age and severity.[1] Clinically, WMHs are associated with cognitive decline, neuropsychiatric symptoms, loss of functional independence, and increased mortality.[2,3] Advanced age and hypertension are the strongest risk factors for WMHs, especially for the confluent subtype.[1-4]

The pathophysiology of WMHs has not yet been fully elucidated. They often appear together with other signs of cerebral small-vessel disease, an umbrella term for neuroradiologic anomalies often found in asymptomatic elderly individuals.[4,5] Histologically, confluent WMHs appear as a continuum of increasing

Received January 11, 2016; accepted after revision March 31.

From the Departments of Neurology (J.W.v.D., W.A.v.G., E.R.) and Radiology (H.J.M.M.M., A.J.N., M.W.A.C., C.B.L.M.M.), Academic Medical Center, University of Amsterdam, Amsterdam, the Netherlands; Departments of Radiology and Nuclear Medicine (H.V., M.D.S.) and Physics and Medical Technology (H.V.), Neuroscience Campus Amsterdam, VU University Medical Center Amsterdam, Amsterdam, the Netherlands; and Department of Neurology (E.R.), Radboud University Medical Center, Nijmegen, the Netherlands.

None of the authors have any conflicts of interest.

This study was funded by the Dutch Ministry of Health, grant No. 50-50110-98-020; the Innovatiefonds Zorverzekeraars, grant No. 05-234; ZonMW grant No. 620000015; and the Internationale Stichting Alzheimer Onderzoek, grant No. 10157.

None of the funding sources had any involvement in the design of the study or in the collection, analysis, and interpretation of the data.

Please address correspondence to Jan Willem van Dalen, MSc, Room H2-235, Department of Neurology, Academic Medical Center, Meibergdreef 9, 1105 AZ, Amsterdam, the Netherlands; e-mail: j.vandalen@amc.nl

Indicates open access to non-subscribers at www.ajnr.org
Indicates article with supplemental on-line tables.
Indicates article with supplemental on-line photos.

http://dx.doi.org/10.3174/ajnr.A4828

tissue damage resembling chronic low-grade ischemia.[1,5] Therefore, WMHs may be the result of chronic low-grade white matter hypoperfusion.[1,5,6] In agreement, CBF within WMHs is lower compared with normal-appearing WM (NAWM).[7-14]

Whether WMHs are associated with a lower cerebral perfusion in general, also involving the surrounding NAWM and gray matter, is unclear. Some findings suggest that WMHs may relate to lower whole-brain or GM perfusion,[7,11,15,16] and WMHs have been associated with reduced blood flow velocity in the large intracranial arteries, outside the WM.[17-19] On a broader level, the association between WMHs and chronic cardiac disease also hints at a relation with general perfusion.[20] WMHs primarily originate in physiologically poorly perfused areas (ie, the periventricular and deep WM), explaining how even a slight cerebral perfusion deficit could provoke low-grade ischemia in those regions associated with WMHs.[21,22] Low perfusion in NAWM has also been associated with subsequent WMH development.[23] While these findings seem to suggest that WMHs are related to a perfusion deficit extending beyond the WMHs, current evidence remains circumstantial.

In this study, we address the hypothesis that WMHs are associated with lower cerebral perfusion, not only within the WMHs but also in the surrounding NAWM and GM. If so, this could be a first step in determining why WMHs form in elderly individuals and toward preventive treatment. Because age and hypertension are the strongest risk factors for asymptomatic WMHs, we tested this hypothesis in a large cohort of community-dwelling elderly with hypertension, by using noninvasive arterial spin-labeling MR imaging. Arterial spin-labeling was chosen because this method of perfusion measurement allows noninvasive (ie, without contrast) MR imaging measurement of CBF within a scanning time of as little as 4 minutes, facilitating large-scale CBF measurement in research settings and eventually enabling clinical application.

## MATERIALS AND METHODS

### Participants

This study was approved by the Academic Medical Centre institutional review board in accordance with the Declaration of Helsinki and the ethical standards of the institution. All participants provided written informed consent before MR imaging. Participants were recruited from the Prevention of Dementia by Intensive Vascular Care trial (preDIVA). This is an ongoing randomized controlled trial in community-dwelling elderly individuals without dementia to study the efficacy of a nurse-led intervention aimed at vascular risk factor modification to prevent dementia.[24] A random subset of participants with systolic hypertension (>140 mm Hg) at baseline without dementia and any other severe medical conditions likely to impede 4-year follow-up (eg, terminal illness, late-stage heart failure, and chronic obstructive pulmonary disease) were invited to participate in the preDIVA-MR imaging (preDIVA-M) substudy. In total, 195 participated in preDIVA-M, equally distributed across intervention ($n = 96$) and control ($n = 99$) groups of the preDIVA trial. Because the preDIVA trial intervention, consisting of rigorous implementation of normal cardiovascular health guidelines, is unlikely to affect the relation between WMHs and CBF, for the current analyses, the group was considered as a single cohort irrespective of treatment allocation. MR imaging was performed after the second preDIVA clinical assessment took place, between 2 and 4 years after the preDIVA baseline assessment. Clinical data used in this study were derived from this second assessment. The median time between clinical assessment and MR imaging was 238 days (interquartile range, 147–429 days). Collected data included the presence of vascular risk factors (systolic and diastolic blood pressure, smoking status [current, former, never], and body mass index). Medical history was obtained through self-reporting, cross-referenced with the general practitioner's medical records, and included diabetes mellitus, stroke, TIA, and cardiovascular disease, comprising angina pectoris, myocardial infarction, and peripheral arterial disease.

### MR Imaging Acquisition

All imaging was performed on a 3T Intera scanner (Philips Healthcare, Best, the Netherlands) with a sensitivity encoding 8-channel head coil. Foam padding was used to restrict head motion. An isotropic 1-mm$^3$ 3D T1-weighted sequence (TR, 6.6 ms; TE, 3.1 ms; flip angle, 9°; FOV, 270 × 270 mm$^2$; 170 sagittal sections; 1.2-mm section thickness; 1.1 × 1.1 mm$^2$ in-plane resolution) and an isotropic 1-mm$^3$ 3D FLAIR sequence (TR/TE, 4800/355 ms; TI, 1650 ms; FOV, 250 × 250 mm$^2$; 160 sagittal sections; 1.12-mm thickness, interpolated to 0.56-mm thick [overcontiguous] sections during reconstruction; 1.1 × 1.1 mm$^2$ in-plane resolution) were performed. Consecutively, 2 gradient-echo single-shot echo-planar imaging pseudocontinuous arterial spin-labeling sequences (matrix, 64 × 64; TR/TE, 4000/17 ms; flip angle, 90°; FOV, 240 × 240 mm; 17 axial sections; no gap; 7-mm section thickness; sensitivity encoding, 2.5; postlabel delay, 1525–2120 ms; labeling duration, 1650 ms) were obtained: one with flow-crushing diffusion gradients in 3 directions (CBF crushed, b-value = 0.6 s/mm$^2$, velocity-encoding 50 mm/s) and one without (CBF noncrushed, b-value = 0 s/mm$^2$). Twenty dynamics were acquired for each scan, resulting in a total scan duration of 2 × 160 = 320 seconds. Background suppression was implemented with 2 inversion pulses, respectively, 1710 and 2860 ms after a prelabeling saturation pulse. The labeling plane was positioned parallel to the imaging volume, 9 cm inferior to the center of the imaging volume.[25]

### Image Processing

An overview of image processing is provided in On-line Fig 1. WMH segmentation was performed by using a k-Nearest-Neighbors algorithm with tissue-type priors, described and validated previously.[26] In total, 194 scans were automatically segmented.

MR imaging data were further processed by using the Statistical Parametric Mapping 8 toolbox (SPM8; http://www.fil.ion.ucl.ac.uk/spm/software/) and custom scripts in Matlab 7.12.0 (MathWorks, Natick, Massachusetts). Arterial spin-labeling data processing and quantification were performed by H.J.M.M.M. (postdoctoral researcher, 6 years of experience) and are described in more detail elsewhere.[27] In short, T1-weighted images were segmented into GM and WM probability maps. After motion correction, 2 × 20 pairs of arterial spin-labeled and control images were pair-wise subtracted and subsequently averaged to gen-

erate perfusion-weighted maps, which were converted to milliliter/100 g/min by using a single compartment model.[28,29] No distinction was made between the quantification of GM and WM voxels. After quantification, the CBF crushed maps were rigid-body registered to the CBF noncrushed maps. For the main analyses, CBF was derived from the crushed CBF maps.

### MR Imaging Outcome Measures

WMH volume was calculated from the automatic segmentation maps and was logarithmically transformed to approach a normal distribution. This logarithmically transformed WMH volume was used for all statistical analyses.

Median CBF estimates were taken for the segmented GM, WM, WMHs, and NAWM, operationalized as the WM outside the WMHs. Although extreme values, or outliers, of CBF measurements would be less representative of the study population, they could have a disproportionally large influence on linear regression results. To avoid the strong influence of outliers on the main analyses, we excluded participants with median GM, WM, NAWM, and WMH CBF values differing ≥3 SDs from the group mean.

Atrophy and arterial transit times were considered as MR imaging–derived parameters, potentially confounding the correlation between WMH and CBF. As a proxy for atrophy, which is a longitudinal measure and thus could not be measured, the brain parenchymal fraction was calculated as the ratio (GM + WM volume)/(intracranial volume). Arterial transit time (ATT), which represents the mean arterial transit time from the labeling plane at the level of the cervical arteries to the GM tissue arterioles (On-line Fig 2), was calculated from crushed and noncrushed CBF values by using the flow encoding arterial spin tagging equation,[28] as published previously.[27]

Computations were performed by using Matlab 7.12.0; SPM8 8; the Oxford Centre for Functional MR Imaging of the Brain Software Library, Version 5.0[30] (FSL; http://www.fmrib.ox.ac.uk/fsl); and SPSS statistics, Versions 20 and 21 (IBM, Armonk, New York) by H.J.M.M.M. (postdoctoral researcher, 6 years of experience) and J.W.v.D. (researcher, 4 years of experience) with the support of M.W.A.C. (postdoctoral researcher, 10 years of experience).

### Statistical Analysis

Significance for *P* values was set at <.05. Two-tailed paired sample *t* tests were used to compare GM CBF with WM CBF and NAWM CBF with WMH CBF. Differences in mean CBF between quartiles of WMH volume were compared by using 1-way analysis of variance followed by Tukey post hoc testing to identify which quartiles differed significantly from each other.

The relation between WMH volume and CBF in the WMHs, NAWM, and GM was assessed in separate linear regression analyses. In model 1, these analyses were adjusted for total brain volume. In model 2, analyses were additionally adjusted for potential confounders. To identify which confounders to include in model 2, we performed separate linear regression analyses for age, sex, brain parenchymal fraction, ATT, smoking status (current, former, never), history of stroke (including transient ischemic attack), history of other cardiovascular diseases (peripheral arterial disease, angina pectoris, myocardial infarction), diabetes mellitus, body mass index, antihypertensive drug use, systolic blood pressure, and diastolic blood pressure, because these could all potentially affect both CBF and WMH volumes.[1,4,5,31,32] Any of these variables individually associated with WMH volume adjusted for total brain volume with a *P* value ≤ .1 were included as potential confounders in model 2.

Finally, 3 post hoc sensitivity analyses were performed. First, because previous findings suggested that CBF in WMHs, NAWM, and GM may only decrease from a certain minimum threshold of WMH volume,[33] the above-mentioned analyses were repeated with exclusion of the participants in the lowest quartile of WMH volume. Second, to assess the influence of excluding participants with CBF values differing ≥3 SDs from the mean from the main analyses, we repeated the main analyses without excluding these participants. Third, because different mechanisms for WMH formations may occur in participants with and without cerebrovascular disease, we performed a sensitivity analysis in which we excluded participants with a history of cerebrovascular disease or lacunar infarcts on MR imaging. For the sensitivity analyses, the outcomes of the adjusted model (model 2) are shown in the "Results" section.

**Table 1: General characteristics[a]**

| Characteristics (*n* = 181) | |
|---|---|
| Age (yr) | 77 (2) |
| Female | 96 (53%) |
| MMSE | 29 (28–30) |
| BMI (kg/m$^2$) | 26 (24–28) |
| History of stroke or TIA | 19 (11%) |
| History of cardiovascular disease | 41 (23%) |
| Diabetes mellitus | 20 (11%) |
| Smoking status | |
| Never | 82 (45%) |
| Former | 88 (49%) |
| Current | 11 (6%) |
| Antihypertensive drug use | 108 (60%) |
| World Health Organization hypertension grade: | |
| Normotension | 47 (26%) |
| Grade I hypertension | 73 (41%) |
| Grade II hypertension | 38 (21%) |
| Grade III hypertension | 20 (11%) |
| Systolic blood pressure (mm Hg) | 148 (138–165) |
| Diastolic blood pressure (mm Hg) | 81 (74–90) |
| Brain parenchymal fraction | 0.61 (0.025) |
| WMH volume (mL) | 6.5 (3.6–11.2) |

**Note:**—MMSE indicates Mini-Mental State Examination; BMI, body mass index.
[a] Reported are means and SDs, numbers and valid percentages, or medians with interquartile range. Cardiovascular disease comprises peripheral arterial disease, angina pectoris, and myocardial infarction. Brain parenchymal fraction = (total cerebral volume)/total intracranial volume.

## RESULTS

### Descriptives

The mean age of the population was 77 ± 2 years, and 53% were women. At the most recent clinical assessment before scanning, 26% of participants' hypertension was under control; 41% had grade I hypertension according to World Health Organization standards; 21%, grade II hypertension; and 11%, grade III hypertension. Other participant characteristics are listed in Table 1. Data of 10 participants were discarded because of processing er-

rors in CBF ($n = 9$) or WMH ($n = 1$) assessment. Another 4 participants were excluded from the main analyses due to CBF estimates differing >3 SDs from the mean. Excluded participants ($n = 14$) did not significantly differ from the included participants ($n = 181$) regarding demographics and structural MR imaging parameters (On-line Table 1). The median WMH volume was 6.5 mL (interquartile range, 3.6–11.2 mL; range, 0.2–52.1 mL). The mean population CBF in the GM, WM, NAWM, and WMHs is depicted in Fig 1. The mean GM CBF was significantly higher than the WM CBF (43.8 ± 14.2 versus 21.9 ± 7.5 mL/100 g/min, $P < .001$), and the mean NAWM CBF was significantly higher than the mean WMH CBF (22.5 ± 7.7 versus 10.6 ± 6.3 mL/100 g/min, $P < .001$).

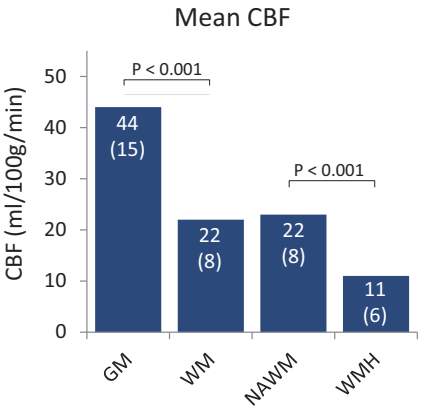


**FIG 1.** Regional cerebral blood flow. Cerebral blood in the gray matter, white matter, normal-appearing white matter unaffected by WMHs (NAWM), and white matter hyperintensities. Shown are means (SDs) and *P* values of paired sample *t* tests.

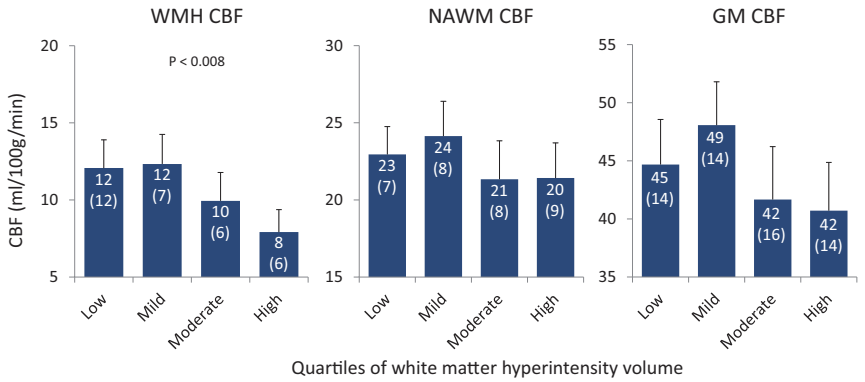


**FIG 2.** Cerebral blood flow per quartiles of WMH load. Cerebral blood flow in the gray matter, normal-appearing white matter unaffected by WMHs, and white matter hyperintensities in subgroups based on quartiles of WMH volume. Shown are means (SDs) and significant *P* values of 1-way analysis of variance.

**Table 2: Association between cerebral perfusion and white matter hyperintensity volume[a]**

| | Model 1 | | | Model 2 | | |
|---|---|---|---|---|---|---|
| Predictor | β | *P* Value | $R^2$ | β | *P* Value | $R^2$ |
| CBF in WMH | −.248 | .001 | 0.06 | −.201 | .029 | 0.06 |
| CBF in NAWM | −.035 | .643 | 0.00 | .175 | .098 | 0.05 |
| CBF in GM | −.065 | .382 | 0.00 | .175 | .133 | 0.05 |

[a] $R^2$ is the adjusted $R^2$ representing the proportion of variation in white matter hyperintensity volume explained by all variables in the model, corrected for the number of variables—model 1: adjusted for total brain volume; model 2: adjusted for total brain volume, age, antihypertensive use, brain parenchymal fraction, and transit time.

### *Analyses per Quartile of WMH Volume*

Mean WMH, NAWM, and GM CBF values per quartile of WMH volume are depicted in Fig 2 and On-line Table 2. WMH load in the lowest quartile ($n = 45$, 24%) was ≤3.58 mL (low WMHs); in the second quartile ($n = 48$, 26%), 3.59–6.40 mL (mild WMHs); in the third quartile ($n = 48$, 26%), 6.41–11.18 mL (moderate WMHs); and in the highest quartile ($n = 44$, 24%), ≥11.18 mL (high WMHs). WMH and CBF maps per quartile of WMH volume are illustrated in On-line Fig 3. From the lower 2 quartiles upward, the mean WMH CBF declined with increasing WMH volume (Fig 2 and On-line Table 2). The mean NAWM and GM CBF did not show any clear relation with WMH volume (Fig 2 and On-line Table 2). One-way analysis of variance showed a significant difference between quartiles of WMH volume in WMH CBF ($P = .002$) but not in NAWM CBF ($P = .244$) or GM CBF ($P = .059$). Tukey post hoc testing revealed that WMH CBF in the quartile with the highest WMH load was significantly lower compared with the quartiles with the lowest (mean difference, 4.2 mL/100 g/min; $P = .007$) and the second lowest (mean difference, 4.41 mL/100 g/min; $P = .007$) WMH load.

### *Linear Regression*

Results of the linear regression analyses are listed in Table 2. Adjusted for total brain volume (model 1), a higher WMH volume was associated with a lower CBF in WMHs (standardized beta [β] = −0.25, $P = .001$). No association was found between WMH volume and CBF in NAWM (β = −0.04, $P = .643$) or GM (β = −0.07, $P = .382$).

Results of linear regression of potential confounders with WMH volume are listed in On-line Table 3. Age (β = 0.13, $P = .09$), brain parenchymal fraction (β = −0.13, $P = .10$), GM ATT (β = 0.15, $P = .046$), and antihypertensive use (β = 0.14, $P = .07$) were associated with WMH volume with a *P* value ≤ .1 and therefore were included as covariates in model 2. There was no association between WMH and female sex (β = 0.07, $P = .47$), systolic blood pressure (β = −0.04, $P = .63$), diastolic blood pressure (β = 0.01, $P = .88$), smoking status (current versus never, β = −0.06, $P = .45$; former versus never, β = −0.08, $P = .29$), history of stroke (β = 0.10, $P = .23$), history of other cardiovascular diseases (β = −0.06, $P = .41$), diabetes mellitus (β = 0.01, $P = .89$), or body mass index (β = −0.10, $P = .19$).

Adjusted for total brain volume, age, brain parenchymal fraction, and ATT (model 2), WMH volume remained significantly inversely associated with WMH CBF (β = −0.20, $P = .029$). The relation between WMH volume and GM or NAWM CBF was not significant (Table 2 and Fig 3). There were no statistical interactions between CBF and any of the covariates adjusted for in

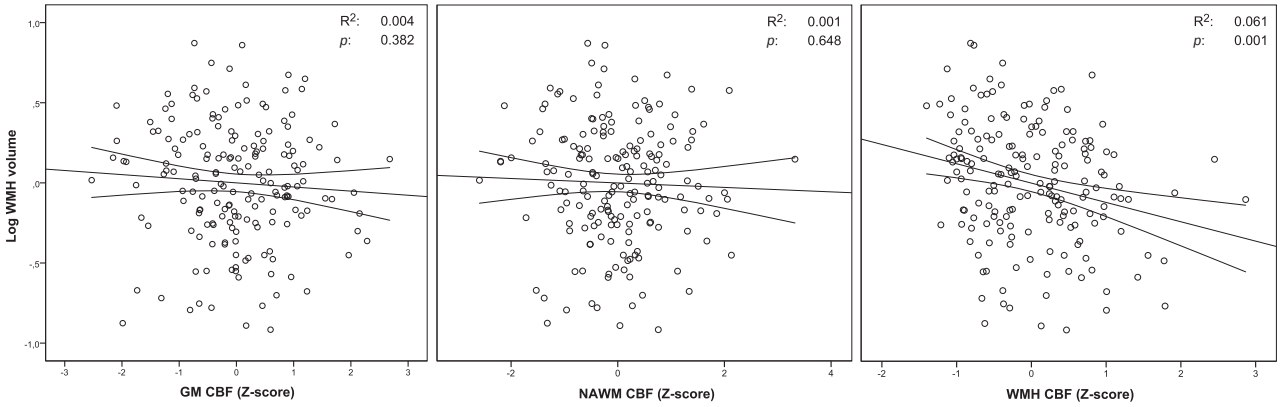


**FIG 3.** Scatterplots of relations between CBF and WMH volume, adjusted for total brain volume. Lines denote the regression line with 95% CI. Log WMH volume is logarithmically transformed.

model 2, indicating that the statistical relation between CBF and WMH volume was independent of any of these covariates. The sensitivity analysis without participants in the lowest quartile of WMH volume ($n = 132$) yielded similar results for the relation between WMH volume and WMH CBF ($\beta = -0.25$, $P = .02$), NAWM CBF ($\beta = 0.05$, $P = .69$), and GM CBF ($\beta = -0.02$, $P = .74$). The sensitivity analysis, which included participants whose mean CBF values deviated >3 SDs from the mean, gave somewhat inflated results for the relation between WMH volume and WMH CBF ($\beta = -0.34$, $P < .001$), but similar results for NAWM CBF ($\beta = 0.18$, $P = .09$) and GM CBF ($\beta = 0.18$, $P = .11$). The sensitivity analysis in participants without a history of stroke or lacunar infarcts on the MR imaging ($n = 150$) attenuated results for the relation between WMH volume and WMH CBF ($\beta = -0.178$, $P = .09$) but yielded similar results for NAWM CBF ($\beta = 0.20$, $P = .10$) and GM CBF ($\beta = 0.18$, $P = .16$).

## DISCUSSION

In a cohort of community-dwelling elderly individuals with hypertension, we found that CBF within WMHs is lower than CBF in NAWM and that WMH CBF decreases with increasing WMH volume. Contrary to our hypothesis, we did not find any indications that CBF in the NAWM or GM is also lower in patients with WMHs. These results suggest that WMHs in elderly individuals with hypertension are not related to a general decrease of cerebral perfusion. Higher GM ATT was also associated with higher WMH volume.

Because the surrounding NAWM does not seem to be affected, hypoperfusion within WMHs may be a direct consequence of local extensive tissue damage and obliteration of capillaries.[5,6] Recent findings link WMHs to an accumulation of tiny infarctions,[34] which could cause such tissue damage. However, WMHs primarily develop in regions with low perfusion, suggesting that low perfusion is involved in WMH conception.[21,22] Conceivably, tiny infarctions interact with low-grade hypoperfusion, for example, originating when perfusion in a small area drops below a certain threshold. Such low-grade hypoperfusion could be too small to measure with current techniques and only becomes apparent after WMHs develop due to tissue damage.[5,6,35] Microvascular alterations associated with aging and exacerbated by hypertension (luminal narrowing, vessel wall stiffening) may impede sufficient perfusion, especially distally in the WM where perfusion pressure is the lowest (On-line Fig 2).[5,6] A similar mechanism could operate in diseases associated with cerebral perfusion deficits in which hypertension exacerbates WMH development, for example, heart failure and Alzheimer disease.[14,20,36]

GM perfusion does seem altered in patients with WMHs, in the sense that higher GM ATT was associated with higher WMH volume. Interpretation of this finding is not straightforward. ATT depends on the length of the blood flow trajectory from the cervical arteries to the cerebral capillaries and on the blood flow velocity along this trajectory.[32] WMHs have been associated with reduced blood flow velocity in the large intracranial arteries, of which longer ATT could be a proxy.[17-19] This velocity reduction could be caused by increased resistance due to large-vessel atherosclerosis or small-vessel arteriolosclerosis, which are both associated with WMHs.[6,37,38] The association between antihypertensive medication use and a higher WMH volume may be due to antihypertensive use being associated with more chronic and severe hypertension. Hypothetically antihypertensive drugs may lead to hypoperfusion, aggravating WMHs, but recent study findings make that possibility unlikely.[39,40] Although our study was conducted in an elderly population with hypertension in the Netherlands, approximately 70% in this age range have hypertension,[41] suggesting that our findings may apply to a large part of the general population. Findings of similar studies were in small or selected populations,[7,10,11,15] and may be less readily translatable to the general elderly community.

Our finding that CBF values within WMHs are lower in participants with higher WMH volume is in line with previous findings.[13] This lower CBF within WMH may be caused by the increase in tissue damage and disturbance of the microvascular blood supply to the center of WMHs as they increase in size.[13] The absence of a relation between WMH volume and NAWM or GM CBF is somewhat surprising because results of other studies have hinted at such a relation.[7,11,15] Our findings may be because CBF in GM and NAWM only diminishes with increasing WMH volume from a certain threshold of WMH volume.[33] However, our sensitivity analysis in which this possibility was evaluated did not alter our findings. Another reason may lie in the differences between study populations. Studies linking WMHs to lower overall cerebral or GM perfusion were

performed in mixed populations, including patients with mild cognitive impairment and Alzheimer disease.[7,11,15] Mild cognitive impairment and Alzheimer disease are themselves associated with alterations in CBF.[37] These perfusion alterations may be linked to WMH formation in these conditions by diminishing the blood supply to WM already susceptible to developing WMHs.[14] Recent reports that a negative correlation between GM CBF and WMHs does exist in patients with Alzheimer disease but not in patients in a memory clinic without mild cognitive impairment or dementia support this explanation.[15]

This study has some limitations. The variance in CBF explained in our regression models was small, and the cross-sectional nature of our analysis prohibits inferences about any temporal or causal relation between CBF and WMHs. In addition, WMHs are associated with slight perfusion deficits in the NAWM and GM. The physiologic variability of CBF may be too great to reveal such small differences among participants. ATT may be less physiologically variable and thereby a more sensitive marker of these slight differences.[27] Furthermore, because in arterial spin-labeling, longer ATT may cause lower CBF estimates, especially distally, the association between ATT and WMH volume may have affected our WMH CBF estimates.[32] However, adjustment for ATT alone did not much affect the association between WMH CBF and WMH volume.

Another limitation is that it is uncertain whether the signal-to-noise ratio of WM perfusion by using arterial spin-labeling is sufficient to accurately estimate WM CBF within our short scanning time.[42,43] However, although current arterial spin-labeling techniques may be unable to measure WM CBF with high accuracy on a voxel-level, on an ROI level, as used in this study, it has been shown that WM CBF can be measured within a scanning time of as little as 5 minutes.[44-46] Our measurements were precise enough to measure significant differences in CBF between the NAWM and WMH and between the whole WM and the NAWM only. Moreover, the reliability of our findings is supported by the ratios between the GM, WM, NAWM, and WMH CBF, which are similar to those reported in studies in which exogenous contrast agents were used.[9,13,14] Finally, as a more general limitation, WMH volume may be linked to impaired autoregulation.[47,48] Because in MR imaging, CBF is measured with the patient in the supine position, in patients with impaired cerebral autoregulation, regional CBF differences that occur while the patient is upright may be obscured.

Future studies using arterial spin-labeling to compare WMHs, NAWM, and GM CBF may benefit from new developments that increase signal-to-noise ratios and spatial resolution. In addition, they may be conducted in a more general population of elderly individuals with hypertension. Our population was a somewhat healthy selection because hypertension was under control in 26% and those with relatively severe medical conditions were excluded. In addition, it may be valuable to compare CBF estimates in patients with hypertension and WMHs with elderly individuals with asymptomatic WMHs without hypertension to discern potentially different etiologies and to chart the longitudinal relation between apparent perfusion deficits and WMH development.

## CONCLUSIONS

Higher WMH volume in elderly patients with hypertension was associated with lower perfusion within WMHs, but not with lower perfusion in the surrounding NAWM or GM. These results suggest that WMH formation in these patients is associated with hypoperfusion locally in the WMHs, rejecting our hypothesis that WMHs in this population are the result of a general perfusion deficit. Our findings may contribute to the understanding of the pathophysiology of WMHs in advanced age and hypertension, potentially helping to develop better targeted prevention and treatment strategies for WMHs and their clinical correlates.


## ACKNOWLEDGMENTS

We are much indebted to C.E. Miedema and I.M. Steinman for planning and logistics and Dr F.E. de Leeuw for his critical review of the manuscript.

Disclosures: Hugo Vrenken—*UNRELATED: Grants/Grants Pending*: Novartis,* Teva,* Merck Serono,* *Comments*: research grants in multiple sclerosis brain imaging; *Patents (planned, pending or issued)*: VU University Medical Center,* *Comments*: planned patent on brain atrophy measurement. Charles Majoie—*UNRELATED: Payment for Lectures (including service on Speakers Bureaus)*: Stryker.* *Money paid to the institution.


## REFERENCES


1. Schmidt R, Schmidt H, Haybaeck J, et al. **Heterogeneity in age-related white matter changes.** *Acta Neuropathol* 2011;122:171–85 CrossRef Medline
2. Debette S, Markus HS. **The clinical importance of white matter hyperintensities on brain magnetic resonance imaging: systematic review and meta-analysis.** *BMJ* 2010;341:c3666 CrossRef Medline
3. Schmahmann JD, Smith EE, Eichler FS, et al. **Cerebral white matter: neuroanatomy, clinical neurology, and neurobehavioral correlates.** *Ann N Y Acad Sci* 2008;1142:266–309 CrossRef Medline
4. Moran C, Phan TG, Srikanth VK. **Cerebral small vessel disease: a review of clinical, radiological, and histopathological phenotypes.** *Int J Stroke* 2012;7:36–46 CrossRef Medline
5. Pantoni L. **Cerebral small vessel disease: from pathogenesis and clinical characteristics to therapeutic challenges.** *Lancet Neurol* 2010;9:689–701 CrossRef Medline
6. Brown WR, Thore CR. **Review: cerebral microvascular pathology in ageing and neurodegeneration.** *Neuropathol Appl Neurobiol* 2011; 37:56–74 CrossRef Medline
7. Bastos-Leite AJ, Kuijer JP, Rombouts SA, et al. **Cerebral blood flow by using pulsed arterial spin-labeling in elderly subjects with white matter hyperintensities.** *AJNR Am J Neuroradiol* 2008;29:1296–301 CrossRef Medline
8. Markus HS. **Reduced cerebral blood flow in white matter in ischaemic leukoaraiosis demonstrated using quantitative exogenous contrast based perfusion MRI.** *J Neurol Neurosurg Psychiatry* 2000; 69:48–53 CrossRef Medline
9. O'Sullivan M, Lythgoe DJ, Pereira AC, et al. **Patterns of cerebral blood flow reduction in patients with ischemic leukoaraiosis.** *Neurology* 2002;59:321–26 CrossRef Medline
10. Brickman AM, Zahra A, Muraskin J, et al. **Reduction in cerebral blood flow in areas appearing as white matter hyperintensities on magnetic resonance imaging.** *Psychiatry Res* 2009;172:117–20 CrossRef Medline
11. Zhang Q, Stafford RB, Wang Z, et al. **Microvascular perfusion based on arterial spin labeled perfusion MRI as a measure of vascular risk in Alzheimer's disease.** *J Alzheimers Dis* 2012;32:677–87 CrossRef Medline
12. Marstrand JR, Garde E, Rostrup E, et al. **Cerebral perfusion and cerebrovascular reactivity are reduced in white matter hyperintensities.** *Stroke* 2002;33:972–76 CrossRef Medline

13. Sachdev P, Wen W, Shnier R, et al. **Cerebral blood volume in T2-weighted white matter hyperintensities using exogenous contrast based perfusion MRI.** *J Neuropsychiatry Clin Neurosci* 2004;16:83–92 Medline
14. Makedonov I, Black SE, MacIntosh BJ. **Cerebral small vessel disease in aging and Alzheimer's disease: a comparative study using MRI and SPECT.** *Eur J Neurol* 2013;20:243–50 CrossRef Medline
15. Benedictus MR, Binnewijzend MA, Kuijer JP, et al. **Brain volume and white matter hyperintensities as determinants of cerebral blood flow in Alzheimer's disease.** *Neurobiol Aging* 2014;35:2665–70 CrossRef Medline
16. Crane DE, Black SE, Ganda A, et al. **Gray matter blood flow and volume are reduced in association with white matter hyperintensity lesion burden: a cross-sectional MRI study.** *Front Aging Neurosci* 2015;7:131 CrossRef Medline
17. Tzourio C, Lévy C, Dufouil C, et al. **Low cerebral blood flow velocity and risk of white matter hyperintensities.** *Ann Neurol* 2001;49:411–14 CrossRef Medline
18. Novak V, Last D, Alsop DC, et al. **Cerebral blood flow velocity and periventricular white matter hyperintensities in type 2 diabetes.** *Diabetes Care* 2006;29:1529–34 CrossRef Medline
19. Heliopoulos I, Artemis D, Vadikolias K, et al. **Association of ultrasonographic parameters with subclinical white-matter hyperintensities in hypertensive patients.** *Cardiovasc Psychiatry Neurol* 2012;2012:1–8 CrossRef Medline
20. Alosco ML, Brickman AM, Spitznagel MB, et al. **Independent and interactive effects of blood pressure and cardiac function on brain volume and white matter hyperintensities in heart failure.** *J Am Soc Hypertens* 2013;7:336–43 CrossRef Medline
21. Holland CM, Smith EE, Csapo I, et al. **Spatial distribution of white-matter hyperintensities in Alzheimer disease, cerebral amyloid angiopathy, and healthy aging.** *Stroke* 2008;39:1127–33 CrossRef Medline
22. Ten Dam VH, van den Heuvel DM, de Craen AJ, et al. **Decline in total cerebral blood flow is linked with increase in periventricular but not deep white matter hyperintensities.** *Radiology* 2007;243:198–203 CrossRef Medline
23. Promjunyakul N, Lahna D, Kaye JA, et al. **Characterizing the white matter hyperintensity penumbra with cerebral blood flow measures.** *Neuroimage Clin* 2015;8:224–29 CrossRef Medline
24. Richard E, Van den Heuvel E, Moll van Charante EP, et al. **Prevention of dementia by intensive vascular care (PreDIVA): a cluster-randomized trial in progress.** *Alzheimer Dis Assoc Disord* 2009;23:198–204 CrossRef Medline
25. Alsop DC, Dai W, Grossman M, et al. **Arterial spin labeling blood flow MRI: its role in the early characterization of Alzheimer's disease.** *J Alzheimers Dis* 2010;20:871–80 CrossRef Medline
26. Steenwijk MD, Pouwels PJ, Daams M, et al. **Accurate white matter lesion segmentation by k nearest neighbor classification with tissue type priors (kNN-TTPs).** *Neuroimage Clin* 2013;3:462–69 CrossRef Medline
27. Mutsaerts HJ, van Dalen JW, Heijtel DF, et al. **Cerebral perfusion measurements in elderly with hypertension using arterial spin labeling.** *PLoS One* 2015;10:e0133717 CrossRef Medline
28. Wang J, Alsop DC, Song HK, et al. **Arterial transit time imaging with flow encoding arterial spin tagging (FEAST).** *Magn Reson Med* 2003;50:599–607 CrossRef Medline
29. Buxton RB, Frank LR, Wong EC, et al. **A general kinetic model for quantitative perfusion imaging with arterial spin labeling.** *Magn Reson Med* 1998;40:383–96 CrossRef Medline
30. Jenkinson M, Beckmann CF, Behrens TE, et al. **FSL.** *Neuroimage* 2012;62:782–90 CrossRef Medline
31. Gouw AA, Seewann A, van der Flier WM, et al. **Heterogeneity of small vessel disease: a systematic review of MRI and histopathology correlations.** *J Neurol Neurosurg Psychiatry* 2011;82:126–35 CrossRef Medline
32. Yang Y, Engelien W, Xu S, et al. **Transit time, trailing time, and cerebral blood flow during brain activation: measurement using multislice, pulsed spin-labeling perfusion imaging.** *Magn Reson Med* 2000;44:680–85 Medline
33. Wen W, Sachdev P, Shnier R, et al. **Effect of white matter hyperintensities on cortical cerebral blood volume using perfusion MRI.** *Neuroimage* 2004;21:1350–56 CrossRef Medline
34. Conklin J, Silver FL, Mikulis DJ, et al. **Are acute infarcts the cause of leukoaraiosis? Brain mapping for 16 consecutive weeks.** *Ann Neurol* 2014;76:899–904 CrossRef Medline
35. Qureshi AI, Caplan LR. **Intracranial atherosclerosis.** *Lancet* 2014;383:984–98 CrossRef Medline
36. Benedictus MR, Goos JD, Binnewijzend MA, et al. **Specific risk factors for microbleeds and white matter hyperintensities in Alzheimer's disease.** *Neurobiol Aging* 2013;34:2488–94 CrossRef Medline
37. de la Torre JC. **Cerebral hemodynamics and vascular risk factors: setting the stage for Alzheimer's disease.** *J Alzheimers Dis* 2012;32:553–67 CrossRef Medline
38. Macintosh BJ, Marquardt L, Schulz UG, et al. **Hemodynamic alterations in vertebrobasilar large artery disease assessed by arterial spin-labeling MR imaging.** *AJNR Am J Neuroradiol* 2012;33:1939–44 CrossRef Medline
39. Tryambake D, He J, Firbank MJ, et al. **Intensive blood pressure lowering increases cerebral blood flow in older subjects with hypertension.** *Hypertension* 2013;61:1309–15 CrossRef Medline
40. Muller M, van der Graaf Y, Visseren FL, et al. **Blood pressure, cerebral blood flow, and brain volumes: the SMART-MR study.** *J Hypertens* 2010;28:1498–505 CrossRef Medline
41. The Netherlands National Institute for Health and the Environment (RIVM) blood pressure statistics (Dutch). https://www.volksgezondheidenzorg.info/onderwerp/bloeddruk/cijfers-context/huidige-situatie#!node-verhoogde-bloeddruk-naar-leeftijd. Accessed November 26, 2015
42. van Gelderen P, de Zwart JA, Duyn JH. **Pittfalls of MRI measurement of white matter perfusion based on arterial spin labeling.** *Magn Reson Med* 2008;59:788–95 CrossRef Medline
43. Petersen ET, Zimine I, Ho YC, et al. **Non-invasive measurement of perfusion: a critical review of arterial spin labelling techniques.** *Br J Radiol* 2006;79:688–701 CrossRef Medline
44. Mutsaerts HJ, Richard E, Heijtel DF, et al. **Gray matter contamination in arterial spin labeling white matter perfusion measurements in patients with dementia.** *Neuroimage Clin* 2014;4:139–44 CrossRef Medline
45. Wu WC, Lin SC, Wang DJ, et al. **Measurement of cerebral white matter perfusion using pseudocontinuous arterial spin labeling 3T magnetic resonance imaging: an experimental and theoretical investigation of feasibility.** *PLoS One* 2013;8:e82679 CrossRef Medline
46. van Osch MJ, Teeuwisse WM, van Walderveen MA, et al. **Can arterial spin labeling detect white matter perfusion signal?** *Magn Reson Med* 2009;62:165–73 CrossRef Medline
47. Brickman AM, Guzman VA, Gonzalez-Castellon M, et al. **Cerebral autoregulation, beta amyloid, and white matter hyperintensities are interrelated.** *Neurosci Lett* 2015;592:54–58 CrossRef Medline
48. Birns J, Jarosz J, Markus HS, et al. **Cerebrovascular reactivity and dynamic autoregulation in ischaemic subcortical white matter disease.** *J Neurol Neurosurg Psychiatry* 2009;80:1093–98 CrossRef Medline

# High-Convexity Tightness Predicts the Shunt Response in Idiopathic Normal Pressure Hydrocephalus

W. Narita, Y. Nishio, T. Baba, O. Iizuka, T. Ishihara, M. Matsuda, M. Iwasaki, T. Tominaga, and E. Mori

## ABSTRACT

**BACKGROUND AND PURPOSE:** Although neuroimaging plays an important role in the diagnosis of idiopathic normal pressure hydrocephalus, its predictive value for response to shunt surgery has not been established. The purpose of the current study was to identify neuroimaging markers that predict the shunt response of idiopathic normal pressure hydrocephalus.

**MATERIALS AND METHODS:** Sixty patients with idiopathic normal pressure hydrocephalus underwent presurgical brain MR imaging and clinical evaluation before and 1 year after shunt surgery. The assessed MR imaging features included the Evans index, high-convexity tightness, Sylvian fissure dilation, callosal angle, focal enlargement of the cortical sulci, bumps in the lateral ventricular roof, and deep white matter and periventricular hyperintensities. The idiopathic normal pressure hydrocephalus grading scale total score was used as a primary clinical outcome measure. We used measures for individual symptoms (ie, the idiopathic normal pressure hydrocephalus grading scale subdomain scores, such as gait, cognitive, and urinary scores), the Timed Up and Go test, and the Mini-Mental State Examination as secondary clinical outcome measures. The relationships between presurgical neuroimaging features and postoperative clinical changes were investigated by using simple linear regression analysis. To identify the set of presurgical MR imaging features that best predict surgical outcomes, we performed multiple linear regression analysis by using a bidirectional stepwise method.

**RESULTS:** Simple linear regression analyses demonstrated that presurgical high-convexity tightness, callosal angle, and Sylvian fissure dilation were significantly associated with the 1-year changes in the clinical symptoms. A multiple linear regression analysis demonstrated that presurgical high-convexity tightness alone predicted the improvement of the clinical symptoms 1 year after surgery.

**CONCLUSIONS:** High-convexity tightness is a neuroimaging feature predictive of shunt response in idiopathic normal pressure hydrocephalus.

**ABBREVIATIONS:** DESH = disproportionately enlarged subarachnoid space hydrocephalus; DWMH = deep white matter hyperintensity; iNPH = idiopathic normal pressure hydrocephalus; iNPHGS = idiopathic normal pressure hydrocephalus grading scale; MMSE = Mini-Mental State Examination; PVH = periventricular hyperintensity; TUG = Timed Up and Go test

Idiopathic normal pressure hydrocephalus (iNPH) has been increasingly recognized as a common cause of gait disturbance and cognitive impairment in elderly individuals. The prevalence of iNPH is estimated to be 1.1%–2.1%,[1,2] which is greater than that of Parkinson disease (approximately 1% in those older than 60 years of age).[3] Differentiating iNPH from neurodegenerative diseases is critical because effective surgical treatment is available for iNPH. Neuroimaging plays an important role in the differential diagnosis of iNPH. Specifically, disproportionately enlarged subarachnoid space hydrocephalus (DESH) on MR imaging or CT is now accepted as a useful diagnostic marker.[4,5]

Shunt surgery is the criterion standard treatment for iNPH.

Received February 10, 2016; accepted after revision April 18.

From the Departments of Behavioral Neurology and Cognitive Neuroscience (W.N., Y.N., T.B., O.I., T.I., M.M., E.M.) and Neurosurgery (M.I., T.T.), Tohoku University School of Medicine, Sendai, Japan.

Drs Narita and Nishio had full access to all the data in the study and take responsibility for the integrity of the data and the accuracy of the data analysis. Contributions were the following: study concept and design, Narita, Nishio; acquisition, analysis, or interpretation of data, all authors; drafting of the manuscript, Narita, Nishio; critical revision of the manuscript for important intellectual content, all authors; statistical analysis, Narita, Nishio; obtained funding, Mori; administrative, technical, or material support: Baba, Ishihara, Iizuka, Matsuda, Iwasaki, Tominaga, Mori; study supervision. Tominaga, Mori.

This study was supported by a Health and Labor Sciences Research Grant for Research on Intractable Diseases, Ministry of Health, Labor and Welfare.

Please address correspondence to Wataru Narita, MD, Department of Behavioral Neurology and Cognitive Neuroscience, Tohoku University School of Medicine, 2–1, Seiryo-machi, Aoba-ku, Sendai 980-8575, Japan; e-mail: naritaw@med.tohoku.ac.jp, or Yoshiyuki Nishio, MD, PhD, Department of Behavioral Neurology and Cognitive Neuroscience, Tohoku University School of Medicine, 2–1, Seiryo-machi, Aoba-ku, Sendai 980-8575 Sendai, Japan; e-mail: nishiou@med.tohoku.ac.jp

Indicates open access to non-subscribers at www.ajnr.org

Indicates article with supplemental on-line table.

http://dx.doi.org/10.3174/ajnr.A4838

Although symptomatic improvement following shunt surgery is observed in up to 70% of patients, the effectiveness varies from patient to patient.[6,7] Although predictive markers for surgical outcomes are necessary for decision-making regarding the surgical indications, this need is currently unmet. For example, the sensitivity and specificity of the CSF tap tests, which have been widely used to predict shunt response in clinical practice,[1,8] remain at 42%–93% and 20%–100%, respectively.[9-12] A previous study demonstrated that elevated overnight intracranial pressure pulse amplitude and CSF pulse amplitude during lumbar infusion predicted better shunt response.[13] However, these procedures are invasive and not widely available. To explore an easily available marker predictive of shunt response, the current study investigated presurgical neuroimaging features associated with better surgical outcome in iNPH.

## MATERIALS AND METHODS

This study was conducted in accordance with the Declaration of Helsinki, and the protocol was approved by the ethics committee of the Tohoku University Hospital. Written informed consent was obtained from all participants.

### *Diagnosis of iNPH*

Although several diagnostic criteria for iNPH have been proposed, there is still lack of consensus on how to diagnose iNPH preoperatively.[8,14] It is indispensable to determine the presence or absence of comorbid neurologic diseases, such as Alzheimer disease, Parkinson disease, and cerebrovascular diseases and their contributions to clinical symptoms, to select appropriate candidates for shunt surgery. The presence of DESH alone is not informative enough to know whether hydrocephalus is the primary pathology associated with clinical symptoms because >60% of those who have DESH on MR imaging do not have any of the triad of symptoms.[15] Thus, we made the diagnosis of iNPH on the basis of comprehensive symptomatic and neuroimaging investigations. Our diagnostic procedures were as follows:

1) All patients who were referred to the Department of Behavioral Neurology and Cognitive Neuroscience of Tohoku University Hospital due to progressive cognitive impairment and/or gait disturbance underwent neurologic and neuropsychological examinations, routine laboratory testing, brain MR imaging, and/or CT. When patients exhibited ≥1 of the triad of symptoms and neuroimaging features of DESH, they were diagnosed as having probable iNPH[1,14] and were invited for inpatient evaluation.

2) The patients who were admitted to the Department of Behavioral Neurology and Cognitive Neuroscience were given comprehensive neurologic and neuropsychological assessments by behavioral neurologists and speech-language pathologists, and they underwent 3D volumetric MR imaging or CT, single-photon emission CT, and a CSF tap test.

3) If patients exhibited clinical and/or neuroimaging features pathognomonic of neurologic disease other than iNPH (eg, severe and dissociated amnesia suggestive of Alzheimer disease and severe sympathetic denervation on iodine 123 metaiodobenzylguanidine myocardial scintigraphy indicative of Parkinson disease or dementia with Lewy bodies), they were excluded as candidates for surgical intervention.

**Table 1: Presurgical clinical characteristics of patients ($n = 60$)[a]**

| Characteristics | |
|---|---|
| Age (yr) | 76.4 (3.8) |
| Sex, male | 34 (57%) |
| Education (yr) | 10.2 (3.0) |
| Duration of symptoms (yr) | 3.3 (1.6) |
| LP shunt | 23 (38%) |
| Medical history | |
| Hypertension | 36 (60%) |
| Diabetes | 18 (30%) |
| Lipid disorder | 18 (30%) |
| Current smoker | 6 (10%) |
| Prevalence of symptoms[b] | |
| Triad (all 3 symptoms) | 27 (45%) |
| Gait and cognitive | 21 (35%) |
| Gait and urinary | 3 (5%) |
| Cognitive and urinary | 1 (2%) |
| Gait only | 5 (8%) |
| Cognitive only | 2 (3%) |
| Urinary only | 0 |

**Note:**—LP indicates lumboperitoneal.

[a] Age, education, and the duration of symptoms are indicated as the means (SDs). The other variables are indicated as the number of patients (%).

[b] Each symptom was regarded as positive when the corresponding score of the iNPH grading scale was ≥2.

4) Given the insufficient sensitivity of the CSF tap test, we recommended shunt surgery to patients with clinical and neuroimaging features suggestive of iNPH without comorbid neurologic diseases regardless of the response to the tap test.

5) Patients with previous histories of subarachnoid hemorrhage, meningitis, or head injury and those with neuroimaging evidence of aqueductal stenosis or a Blake pouch cyst were diagnosed as having secondary normal pressure hydrocephalus and were not included in the study.

### *Selection of Surgical Methods*

In the earlier part of this study, ventriculoperitoneal shunt was preferentially performed in our institution. In the last half of the study, we performed lumboperitoneal shunt unless contraindications were present or patients requested ventriculoperitoneal shunt. The contraindications for lumboperitoneal shunt included severe spinal canal stenosis or lumbar spine deformity, which was diagnosed on the basis of neurologic examination, spinal MR imaging, and observations on lumbar puncture.

### *Subjects*

We identified 103 consecutive patients with iNPH who were admitted to the Department of Behavioral Neurology and Cognitive Neuroscience and underwent shunt surgery between December 19, 2005, and May 13, 2013. Of these 103 consecutive patients, we retrospectively selected 60 patients who underwent presurgical MR imaging evaluation and completed 1-year postsurgical follow-up. The demographic and clinical profiles of the patients are summarized in Table 1. Forty-three patients were excluded from the study for the following reasons: Two patients died, 4 developed shunt system problems, 2 developed pneumonia, 1 developed a femoral fracture, 1 developed a cerebral infarction, 16 moved to hospitals that were nearer to their homes, 13 did not return for follow-up visits for other reasons, and 4 were excluded

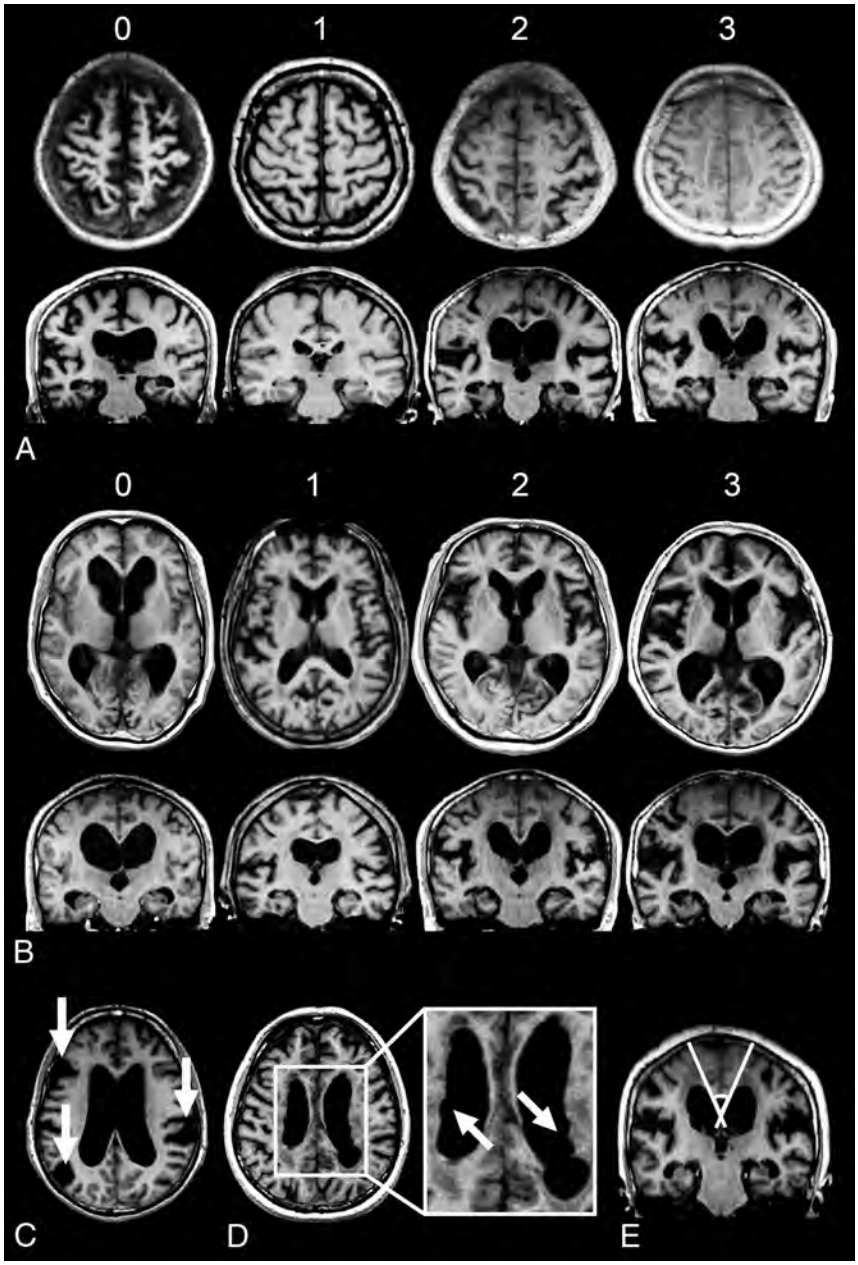


**FIG 1.** Visual rating scales for neuroimaging features in iNPH. *A*, High-convexity tightness: 0, dilated; 1, normal; 2, mildly tight; 3, severely tight. *B*, Sylvian fissure dilation: 0, narrowed; 1, normal; 2, mildly dilated; 3, severely dilated. *C*, Focal dilation of the sulci (indicated by the *arrows*). *D*, Bumps in the lateral ventricular roof (indicated by the *arrows*). *E*, Callosal angle.

due to incomplete clinical or imaging data. The demographic and clinical characteristics of the excluded patients are shown in the On-line Table.

All the clinical and neuroimaging data described below were gathered in a prospective manner.

### Clinical Assessments

All subjects in this study were evaluated before and 1 year after shunt surgery. The total score of the idiopathic normal pressure hydrocephalus grading scale (iNPHGS),[16] which represents the global severity of clinical symptoms, was used as a primary outcome measure. We included the following measures for individual symptoms of the classic triad as secondary outcome measures:

1) Gait was assessed with the iNPHGS gait score and the Timed Up and Go test (TUG).[17]

2) Cognitive function was assessed with the iNPHGS cognitive score and the Mini-Mental State Examination (MMSE).[18]

3) Urinary function was assessed with the iNPHGS urinary score.

### Neuroimaging

Neuroimaging analyses were conducted on axial and coronal reconstructed images of 3D volumetric MR imaging. In 44 patients, transverse fluid-attenuated inversion recovery images were used for the evaluation of ischemic changes of the brain.

### MR Imaging Acquisition and Preprocessing

3D T1-weighted (transverse 3D-spoiled gradient-recalled: TR, 20 ms; TE, 4.1 ms; thickness, 1.5 mm; FOV, 25 × 25 cm; and matrix, 256 × 256) and FLAIR (TR, 11,002 ms; TE, 120 ms; thickness, 6.0 mm; gap, 1.0 mm; FOV, 21 × 21 cm; and matrix, 256 × 256) images were obtained with a Signa 1.5T MR imaging unit (GE Healthcare, Milwaukee, Wisconsin) before shunt surgery. The 3D T1-weighted images were resliced into sections that were parallel (transverse) and perpendicular (coronal) to the anteroposterior commissural plane and were spaced at 6-mm intervals in each direction.

### MR Imaging Measures

To explore the presurgical MR imaging features that predicted the response to shunt surgery, we used the following measures (Fig 1):

1) The Evans index was calculated as the ratio of the maximum diameter of the frontal horns of the lateral ventricles to the maximum inner diameter of the skull on transverse sections.[19]

2) The callosal angle, the angle between the left and right corpus callosum, was measured on a coronal plane at the posterior commissure.[20]

3) We evaluated the tightness of the high-convexity subarachnoid space on the 4 uppermost contiguous transverse sections and the 3 contiguous coronal sections on and anterior to the posterior commissure. The severity of the high-convexity tightness was visually rated as follows: 0, dilated; 1, normal; 2, mildly tight (tightness was observed over less than three-quarters of the high-

**Table 2: Changes in the clinical symptoms at 1 year[a]**

| | Presurgical Score | | Postsurgical Score | | Difference | | Postsurgical Changes (No.) (%) | | |
|---|---|---|---|---|---|---|---|---|---|
| | No. | Median (IQR) | No. | Median (IQR) | Median (IQR) | *P* Value[b] | Improved | Stable | Deteriorated |
| iNPHGS total [12] | 60 | 6.0 (5.0–8.0) | 60 | 5.0 (3.0–6.0) | 1.0 (0.5–3.0) | <.001 | 45 (75) | 10 (17) | 5 (8) |
| iNPHGS gait [4] | 60 | 2.0 (2.0–3.0) | 60 | 2.0 (1.0–3.0) | 1.0 (0.5–1.0) | <.001 | 32 (53) | 24 (40) | 4 (7) |
| iNPHGS cognitive [4] | 60 | 2.0 (2.0–3.0) | 60 | 2.0 (1.3–3.0) | 0 (0–1.0) | .001 | 20 (33) | 36 (60) | 4 (7) |
| iNPHGS urinary [4] | 60 | 2.5 (1.0–3.0) | 60 | 1.0 (0–1.0) | 0 (0–1.0) | <.001 | 29 (48) | 24 (40) | 7 (12) |
| TUG | 55 | 15.1 (11.0–20.6) | 53 | 11.5 (9.2–14.5) | 2.5 (0.8–4.2) | <.001 | 35 (66) | 13 (25) | 5 (9) |
| MMSE [30] | 60 | 22.0 (20.0–24.8) | 59 | 23.0 (21.0–27.0) | 1 (−1–3.0) | .014 | 19 (32) | 32 (54) | 8 (14) |

**Note:**—IQR indicates interquartile range.
[a] Clinical improvement and deterioration were defined as ≥1-point improvement or deterioration on the iNPHGS, ≥10% reduction or increase in TUG time, and ≥3 points gained or lost on the MMSE. The numbers in square brackets refer to the maximum scores for the tests.
[b] Wilcoxon signed rank test for pre- and postsurgery comparisons.

convexity space); and 3, severely tight (tightness was observed over three-quarters or more of the high-convexity space).

4) The width of the Sylvian fissure was assessed on transverse sections. We used the following visual rating scale: 0, narrowed; 1, normal; 2, mildly dilated; and 3, severely dilated on the axial images.

5) The presence (rated as 1) and absence (rated as 0) of focal enlargement of the cortical sulci were visually evaluated on transverse sections.

6) Bumps in the lateral ventricular roof, which are often observed in patients with iNPH,[21] were visually assessed on transverse sections above the top of the thalamus and rated as present (1) or absent (0).

7) Deep white matter hyperintensities (DWMHs) and periventricular hyperintensities (PVHs) were assessed according to Fazekas et al.[22]

Visual ratings 3–7 were independently evaluated by 2 raters (W.N. and Y.N.) who were blinded to the clinical profiles and surgical outcomes of the patients. The interrater reliability was calculated by using linearly weighted $\kappa$ coefficients. The mean scores of the 2 raters were used for the subsequent analyses.

### *Statistical Analysis*

The Wilcoxon signed rank test was used to analyze 1-year changes in clinical scores. Simple linear regression analysis was performed to investigate relationships between presurgical neuroimaging features and 1-year changes in the clinical scores (ie, iNPHGS, TUG, and MMSE). Given the exploratory nature of the analysis, no multiple comparison corrections were used.

To identify the set of presurgical MR imaging features that best predicts surgical outcomes, we performed multiple linear regression analysis by using a bidirectional (forward/backward) stepwise method. The outcome variables were 1-year changes of iNPHGS total score (primary outcome measure) and subdomain (gait, cognition, and urinary function) scores (secondary outcome measures). The explanatory variables were the Evans index, high-convexity tightness, Sylvian fissure dilation, and callosal angle on MR imaging. Sex and age were included as nuisance variables. The cutoff *P* value for inclusion was set at <.05 and for exclusion, <.10. Statistical analysis was performed by using SPSS version 22.0 (IBM, Armonk, New York).

## RESULTS

### *Changes in Clinical Symptoms 1 Year after Shunt Surgery*

The results of the clinical assessments before and 1 year after shunt surgery are shown in Table 2. Overall, all clinical measures were significantly improved (Wilcoxon signed rank test, $P < .05$). Seventy-five percent of the patients were improved on the iNPHGS total score; 53%, on the gait score; 33%, on the cognitive score; and 48%, on the urinary score. Improvement of ≥3 points on the MMSE was noted in 32% of patients.

**Table 3: Presurgical neuroimaging features**

| | Score[a] (Median [IQR]) | Reliability ($\kappa_w$) |
|---|---|---|
| High-convexity tightness | 2.5 (2.0–3.0) | 0.68 |
| Sylvian fissure dilation | 3.0 (2.5–3.0) | 0.50 |
| Focal enlargement of cortical sulci | 0.5 (0–1.0) | 0.27 |
| Bumps in the lateral ventricular roof | 1.0 (0.1–1.0) | 0.66 |
| DWMHs[b] | 2.0 (2.0–3.0) | 0.71 |
| PVHs[b] | 2.5 (2.0–3.0) | 0.64 |
| Evans index | 0.32 (0.31–0.36 | – |
| Callosal angle | 79.7 (65.5–100.1) | – |

**Note:**—IQR indicates interquartile range; $\kappa_w$, linear weighted $\kappa$ coefficient.
[a] The visual rating scores indicate the mean scores of the 2 raters.
[b] The DWMHs and PVHs were obtained from 44 patients.

### *Presurgical Neuroimaging Characteristics*

The presurgical MR imaging findings are summarized in Table 3. The linearly weighted $\kappa$ coefficients for the visual rating scale were 0.27–0.71. All of the ratings, with the exception of the focal enlargement of the cortical sulci, exhibited moderate-to-substantial agreement.

High-convexity tightness (rated as ≥2) and Sylvian fissure dilation (rated as ≥2) were observed in 92% and 100% of patients, respectively. Focal enlargement of the cortical sulci and bumps in the lateral ventricular roof were present in 32% and 60% of the patients, respectively. Severe DWMHs and PVHs (rated as 3) were noted in 36% and 39% of the patients, respectively. The Evans indices were >0.3 in 82% of the patients. The callosal angles were <90° in 63% of patients.

### *Presurgical Neuroimaging Findings that Predict the Shunt Response*

The results of the simple and multiple linear regression analyses are shown in Tables 4 and 5. Simple linear regression analysis demonstrated that presurgical high-convexity tightness was significantly associated with the 1-year changes in the iNPHGS total score (regression coefficient [B] = 1.23, coefficient of determination [$R^2$] = 0.13, $P = .004$), the 1-year changes in the iNPHGS gait score (B = 0.59, $R^2 = 0.16$, $P = .002$), and the 1-year changes in the MMSE (B = 2.56, $R^2 = 0.17$, $P = .001$). There were significant associations between the presurgical callosal angle and the 1-year

changes in the MMSE (B = −0.04, $R^2$ = 0.08, $P$ = .035) and between presurgical Sylvian fissure dilation and the 1-year changes in the iNPHGS gait (B = 0.59, $R^2$ = 0.08, $P$ = .029).

A multiple linear regression analysis demonstrated that presurgical high-convexity tightness alone predicted the 1-year changes in the iNPHGS total score (B = 0.99, $R^2$ = 0.24, $P$ = .017) and the gait score (B = 0.52, $R^2$ = 0.21, $P$ = .006).

## DISCUSSION

The primary focus of neuroimaging studies of hydrocephalus has been the differentiation of hydrocephalus from other neurologic diseases. Although ventriculomegaly is a primary morphologic feature of hydrocephalus, it is also observed in brain atrophy. Earlier studies claimed that the absence of Sylvian fissure dilation is a neuroimaging feature that differentiates hydrocephalus from brain atrophy.[23,24] However, later studies suggested that Sylvian fissure dilation is present in most patients with iNPH. Thus, high-convexity tightness was subsequently proposed as an alternative feature for differentiating iNPH from brain atrophy.[25] The combination of high-convexity tightness, Sylvian fissure dilation, and ventriculomegaly has been termed "disproportionately enlarged subarachnoid space hydrocephalus," and it has been increasingly recognized as a neuroimaging hallmark of iNPH.[26] The value of DESH in differentiating iNPH from other neurologic diseases has been confirmed by several studies.[27-30]

Several diagnostic criteria for iNPH have recently been proposed.[1,8] One recent study reported that the effectiveness of shunt surgery for patients who were diagnosed according to one of these guidelines remained at 62.7% in terms of the mRS.[31] The incorporation of neuroimaging features that are predictive of surgical outcomes into the diagnostic criteria would thus improve the efficacy of shunt surgery. However, this issue has been systematically investigated in only a few studies. The current study demonstrates that high-convexity tightness, which is a component of DESH, is the most predictive neuroimaging feature. Additionally, Sylvian fissure dilation and a small callosal angle were associated with better shunt responses.

The shunt response in patients with iNPH is governed by 2 factors: namely, reversibility and comorbidity. Previous studies have demonstrated that symptomatic improvements following shunt surgery are associated with less severe symptoms and shorter disease duration, which suggest that reversibility declines as the disease progresses. The relationship between shunt response and brain tissue resilience is also supported by a previous neuroimaging study in which volume decreases of the lateral ventricle were found to be significantly correlated with symptomatic improvement.[32] In agreement with these findings, recent studies have suggested that delayed shunt surgery is associated with poorer symptomatic improvement.[31,33,34]

In addition to reversibility, other neurologic comorbid diseases have a significant influence on shunt response. A recent positron-emission tomography study demonstrated that patients with significant cortical amyloid deposits exhibit less cognitive improvement following shunt surgery.[35] High-convexity tightness or DESH is probably more strongly related to comorbidity than to reversibility. Elderly individuals who exhibit DESH on MR imaging can be asymptomatic for 5 or more years,[36] which suggests that DESH is not well-correlated with pathophysiologic severity and reversibility. On the other hand, DESH or high-convexity tightness may be associated with the purity of iNPH pathology. Patients who exhibited weak typicality of DESH or mild high-convexity tightness may have comorbid pathologies with higher probabilities compared with those with typical DESH or severe high-convexity tightness. The results of our study may reflect this "typicality" effect.

Virhammar et al[21] recently investigated the neuroimaging features predictive of shunt responses in 108 patients with iNPH. These authors demonstrated that DESH and a small callosal angle, not high-convexity tightness or Sylvian fissure dilation, were associated with better shunt responses. Although the study of Virhammar et al and our own agree about the importance of DESH, the studies also differ in some ways. Several factors may be associated with these discrepancies. First, the studies differed in their neuroimaging inclusion criteria. Virhammar et al used only ventriculomegaly for study inclusion, whereas the current study used high-convexity tightness, Sylvian fissure dilation, and ventriculomegaly. Because the pathophysiology of iNPH is presumably heterogeneous, these differences in the inclusion criteria may have led to a substantial bias. Second, the differences in the statistical procedures used in these studies should be noted. Univariate logistic regression with a dichotomous outcome measure (ie, the presence or absence of shunt response) was used in the study by Virhammar et al, whereas our study used multiple linear regression with ordinary outcome measures. Whether patients whose symptoms remain unchanged before

**Table 4: Results of simple linear regression analysis for presurgical neuroimaging features associated with surgical outcome: 1-year changes**

| Neuroimaging Findings | iNPHGS | | | | TUG | MMSE |
|---|---|---|---|---|---|---|
| | Total | Gait | Cognitive | Urinary | | |
| Evans Index | 7.34 | 1.00 | 0.97 | 5.37 | 60.96 | 9.22 |
| Callosal angle | −0.02 | −0.01 | −0.01 | −0.01 | −0.12 | −0.04[a] |
| High-convexity tightness | 1.23[b] | 0.59[b] | 0.22 | 0.42 | −3.17 | 2.56[b] |
| Sylvian fissure dilation | 1.03 | 0.59[a] | −0.09 | 0.53 | −2.65 | 1.00 |
| Focal enlargement of cortical sulci | 0.71 | 0.19 | 0.00 | 0.53 | −2.25 | 1.19 |
| Bumps in the lateral ventricle | 0.47 | 0.31 | 0.11 | 0.05 | 2.20 | 1.20 |
| DWMHs | −0.20 | −0.07 | 0.01 | −0.14 | 0.53 | 0.10 |
| PVHs | −0.33 | −0.05 | −0.10 | −0.19 | 3.19 | −0.25 |

[a] $P < .05$.
[b] $P < .01$.

**Table 5: Results of stepwise multiple linear regression analysis**

| 1-Year Changes | Neuroimaging Findings | B | SE B | 95% CI B | $\beta$ | $R^2$ | $P$ Value |
|---|---|---|---|---|---|---|---|
| iNPHGS total | High-convexity tightness | 0.99 | 0.40 | 0.18–1.80 | 0.29 | 0.24 | .017 |
| iNPHGS gait | High-convexity tightness | 0.52 | 0.18 | 0.16–0.88 | 0.35 | 0.21 | .006 |

**Note:**—B indicates regression coefficient; $\beta$, standardized regression coefficient; $R^2$, coefficient of determination; SE B, standard error of the regression coefficient.

and after surgery are assigned to the "responsive" or "unresponsive" group may have a significant impact on results. We argue that the lack of symptomatic deterioration for ≥1-year observation probably should be interpreted as "responsive" because previous studies have demonstrated that conditions of patients with iNPH who did not receive surgical intervention deteriorated within a year.[37,38]

The current study has several limitations. First, patients with large cerebrovascular lesions and those strongly suspected of having neurodegenerative diseases were excluded from this study. Thus, the applicability of our findings to patients with other comorbid neurologic diseases is unknown. Second, the visual rating scale for the morphologic features of iNPH used in the current study has not been validated. Although we chose a visual inspection method because of its clinical utility, our rating system may be suboptimal. The validity of our findings should be examined in comparison with those based on other neuroimaging methods, such as MR imaging volumetry. Finally, this study was conducted in a single center and used a single MR imaging scanner. Future multicenter studies are needed to further verify the neuroimaging features that predict surgical outcome in iNPH.

## CONCLUSIONS

We investigated the predictive values of neuroimaging features frequently observed in iNPH, including the Evans index, high-convexity tightness, Sylvian fissure dilation, callosal angle, focal enlargement of the cortical sulci, bumps in the lateral ventricular roof, and deep white matter and periventricular hyperintensities, for response to shunt surgery. Among them, high-convexity tightness was the best predictor of shunt response in iNPH.

Disclosures: Yoshiyuki Nishio—*UNRELATED*: *Grants/Grants Pending*: Ministry of Education, Culture, Sports, Science and Technology Japan,* *Comments*: research grant for a study on cognitive problems in patients with epilepsy; *Payment for Development of Educational Presentations*: Eisai, *Comments*: educational lectures on dementia with Lewy bodies and other dementias. Toru Baba—*UNRELATED*: *Payment for Lectures (including service on Speakers Bureaus)*: Boehringer Ingelheim, Novartis Pharmaceuticals, Eisai, Daiichi Sankyo, Kyowa Hakko Kirin, Dainippon Sumitomo Pharma. Etsuro Mori—*RELATED*: *Grant*: Ministry of Health, Labour and Welfare, Japan, *Comments*: Health and Labor Sciences Research Grants for Research on Intractable Diseases; *UNRELATED*: *Payment for Lectures (including service on Speakers Bureaus)*: Johnson & Johnson, Medtronic, Toshiba, Nihon Medi-Physics, *Comments*: Honoraria. *Money paid to the institution.

## REFERENCES

1. Mori E, Ishikawa M, Kato T, et al. **Guidelines for management of idiopathic normal pressure hydrocephalus: second edition.** *Neurol Med Chir (Tokyo)* 2012;52:775–809 CrossRef Medline
2. Jaraj D, Rabiei K, Marlow T, et al. **Prevalence of idiopathic normal-pressure hydrocephalus.** *Neurology* 2014;82:1449–54 CrossRef Medline
3. de Lau LM, Breteler MM. **Epidemiology of Parkinson's disease.** *Lancet Neurol* 2006;5:525–35 CrossRef Medline
4. Malm J, Graff-Radford NR, Ishikawa M, et al. **Influence of comorbidities in idiopathic normal pressure hydrocephalus: research and clinical care—a report of the ISHCSF task force on comorbidities in INPH.** *Fluids Barriers CNS* 2013;10:22 CrossRef Medline
5. Williams MA, Relkin NR. **Diagnosis and management of idiopathic normal-pressure hydrocephalus.** *Neurol Clin Pract* 2013;3:375–85 CrossRef Medline
6. Hebb AO, Cusimano MD. **Idiopathic normal pressure hydrocephalus: a systematic review of diagnosis and outcome.** *Neurosurgery* 2001;49:1166–84; discussion 1184–86 CrossRef Medline
7. Klinge P, Hellström P, Tans J, et al; European iNPH Multicentre Study Group. **One-year outcome in the European multicentre study on iNPH.** *Acta Neurol Scand* 2012;126:145–53 CrossRef Medline
8. Relkin N, Marmarou A, Klinge P, et al. **Diagnosing idiopathic normal-pressure hydrocephalus.** *Neurosurgery* 2005;57:S4–16; discussion ii–v Medline
9. Kahlon B, Sundbärg G, Rehncrona S. **Comparison between the lumbar infusion and CSF tap tests to predict outcome after shunt surgery in suspected normal pressure hydrocephalus.** *J Neurol Neurosurg Psychiatry* 2002;73:721–26 CrossRef Medline
10. Sand T, Bovim G, Grimse R, et al. **Idiopathic normal pressure hydrocephalus: the CSF tap-test may predict the clinical response to shunting.** *Acta Neurol Scand* 1994;89:311–16 Medline
11. Walchenbach R, Geiger E, Thomeer RT, et al. **The value of temporary external lumbar CSF drainage in predicting the outcome of shunting on normal pressure hydrocephalus.** *J Neurol Neurosurg Psychiatry* 2002;72:503–06 Medline
12. Ishikawa M, Hashimoto M, Mori E, et al. **The value of the cerebrospinal fluid tap test for predicting shunt effectiveness in idiopathic normal pressure hydrocephalus.** *Fluids Barriers CNS* 2012;9:1 CrossRef Medline
13. Eide PK, Brean A. **Cerebrospinal fluid pulse pressure amplitude during lumbar infusion in idiopathic normal pressure hydrocephalus can predict response to shunting.** *Cerebrospinal Fluid Res* 2010;7:5 CrossRef Medline
14. Ishikawa M, Hashimoto M, Kuwana N, et al. **Guidelines for management of idiopathic normal pressure hydrocephalus.** *Neurol Med Chir (Tokyo)* 2008;48(suppl):S1–23 CrossRef Medline
15. Iseki C, Kawanami T, Nagasawa H, et al. **Asymptomatic ventriculomegaly with features of idiopathic normal pressure hydrocephalus on MRI (AVIM) in the elderly: a prospective study in a Japanese population.** *J Neurol Sci* 2009;277:54–57 CrossRef Medline
16. Kubo Y, Kazui H, Yoshida T, et al. **Validation of grading scale for evaluating symptoms of idiopathic normal-pressure hydrocephalus.** *Dement Geriatr Cogn Disord* 2008;25:37–45 CrossRef Medline
17. Podsiadlo D, Richardson S. **The timed "Up & Go": a test of basic functional mobility for frail elderly persons.** *J Am Geriatr Soc* 1991;39:142–48 CrossRef Medline
18. Mori E, Mitani Y, Yamadori A. **Usefulness of Japanese version of the Mini-Mental State Examination in neurological patients** [in Japanese]. *Jpn J Neuropsychol* 1985;1:82–90
19. Evans WA. **An encephalographic ratio for estimating ventricular enlargement and cerebral atrophy.** *Arch NeurPsych* 1942;47:931–37 CrossRef
20. Ishii K, Kanda T, Harada A, et al. **Clinical impact of the callosal angle in the diagnosis of idiopathic normal pressure hydrocephalus.** *Eur Radiol* 2008;18:2678–83 CrossRef Medline
21. Virhammar J, Laurell K, Cesarini KG, et al. **Preoperative prognostic value of MRI findings in 108 patients with idiopathic normal pressure hydrocephalus.** *AJNR Am J Neuroradiol* 2014;35:2311–18 CrossRef Medline
22. Fazekas F, Chawluk JB, Alavi A, et al. **MR signal abnormalities at 1.5 T in Alzheimer's dementia and normal aging.** *AJR Am J Roentgenol* 1987;149:351–56 CrossRef Medline
23. Gunasekera L, Richardson AE. **Computerized axial tomography in idiopathic hydrocephalus.** *Brain* 1977;100:749–54 CrossRef Medline
24. Benzel EC, Pelletier AL, Levy PG. **Communicating hydrocephalus in adults: prediction of outcome after ventricular shunting procedures.** *Neurosurgery* 1990;26:655–60 CrossRef Medline
25. Kitagaki H, Mori E, Ishii K, et al. **CSF spaces in idiopathic normal pressure hydrocephalus: morphology and volumetry.** *AJNR Am J Neuroradiol* 1998;19:1277–84 Medline
26. Hashimoto M, Ishikawa M, Mori E, et al; Study of INPH on neurological improvement (SINPHONI). **Diagnosis of idiopathic normal pressure hydrocephalus is supported by MRI-based scheme: a prospective cohort study.** *Cerebrospinal Fluid Res* 2010;7:18 CrossRef Medline
27. Yamashita F, Sasaki M, Takahashi S, et al. **Detection of changes in**

**cerebrospinal fluid space in idiopathic normal pressure hydrocephalus using voxel-based morphometry.** *Neuroradiology* 2010;52:381–86 CrossRef Medline

28. Yamashita F, Sasaki M, Saito M, et al. **Voxel-based morphometry of disproportionate cerebrospinal fluid space distribution for the differential diagnosis of idiopathic normal pressure hydrocephalus.** *J Neuroimaging* 2014;24:359–65 CrossRef Medline
29. Ishii K, Soma T, Shimada K, et al. **Automatic volumetry of the cerebrospinal fluid space in idiopathic normal pressure hydrocephalus.** *Dement Geriatr Cogn Dis Extra* 2013;3:489–96 CrossRef Medline
30. Kojoukhova M, Koivisto AM, Korhonen R, et al. **Feasibility of radiological markers in idiopathic normal pressure hydrocephalus.** *Acta Neurochir (Wien)* 2015;157:1709–18; discussion 1719 CrossRef Medline
31. Kazui H, Miyajima M, Mori E, et al; SINPHONI-2 Investigators. **Lumboperitoneal shunt surgery for idiopathic normal pressure hydrocephalus (SINPHONI-2): an open-label randomised trial.** *Lancet Neurol* 2015;14:585–94 CrossRef Medline
32. Hiraoka K, Yamasaki H, Takagi M, et al. **Changes in the volumes of the brain and cerebrospinal fluid spaces after shunt surgery in idiopathic normal-pressure hydrocephalus.** *J Neurol Sci* 2010;296:7–12 CrossRef Medline
33. Caruso R, Cervoni L, Vitale AM, et al. **Idiopathic normal-pressure hydrocephalus in adults: result of shunting correlated with clinical findings in 18 patients and review of the literature.** *Neurosurg Rev* 1997;20:104–07 CrossRef Medline
34. Andrén K, Wikkelso C, Tisell M, et al. **Natural course of idiopathic normal pressure hydrocephalus.** *J Neurol Neurosurg Psychiatry* 2014;85:806–10 CrossRef Medline
35. Hiraoka K, Narita W, Kikuchi H, et al. **Amyloid deposits and response to shunt surgery in idiopathic normal-pressure hydrocephalus.** *J Neurol Sci* 2015;356:124–28 CrossRef Medline
36. Iseki C, Takahashi Y, Wada M, et al. **Incidence of idiopathic normal pressure hydrocephalus (iNPH): a 10-year follow-up study of a rural community in Japan.** *J Neurol Sci* 2014;339:108–12 CrossRef Medline
37. Razay G, Vreugdenhil A, Liddell J. **A prospective study of ventriculoperitoneal shunting for idiopathic normal pressure hydrocephalus.** *J Clin Neurosci* 2009;16:1180–83 CrossRef Medline
38. Scollato A, Tenenbaum R, Bahl G, et al. **Changes in aqueductal CSF stroke volume and progression of symptoms in patients with unshunted idiopathic normal pressure hydrocephalus.** *AJNR Am J Neuroradiol* 2008;29:192–97 CrossRef Medline

# Dynamic Susceptibility Contrast-Enhanced MR Perfusion Imaging in Assessing Recurrent Glioblastoma Response to Superselective Intra-Arterial Bevacizumab Therapy

R. Singh, K. Kesavabhotla, S.A. Kishore, Z. Zhou, A.J. Tsiouris, C.G. Filippi, J.A. Boockvar, and I. Kovanlikaya

## ABSTRACT

**BACKGROUND AND PURPOSE:** Recurrent glioblastoma currently has no established standard of care. We evaluated the response of recurrent glioblastoma to superselective intra-arterial cerebral infusion of bevacizumab by using dynamic susceptibility contrast-enhanced MR perfusion imaging. We hypothesized that treatment response would be associated with decreased relative CBV and relative CBF.

**MATERIALS AND METHODS:** Patients were accrued for this study from larger ongoing serial Phase I/II trials. Twenty-five patients (14 men, 11 women; median age, 55 years) were analyzed. Four distinct ROIs were chosen: 1) normal-appearing white matter on the contralateral side, 2) the location of the highest T1 enhancement in the lesion (maximum enhancing), 3) the location of highest relative CBV in the lesion (maximum relative CBV), and 4) nonenhancing T2 hyperintense signal abnormality surrounding the tumor (nonenhancing T2 hyperintensity).

**RESULTS:** There was a statistically significant median percentage change of −32.34% ($P = .001$) in relative CBV in areas of maximum relative CBV following intra-arterial bevacizumab therapy. There was also a statistically significant median percentage decrease in relative CBF of −30.67 ($P = .001$) and −27.25 ($P = .037$) in areas of maximum relative CBV and maximum tumor enhancement, respectively. Last, a trend toward statistical significance for increasing relative CBV in nonenhancing T2 hyperintense areas (median percent change, 30.04; $P = .069$) was noted.

**CONCLUSIONS:** Dynamic susceptibility contrast-enhanced MR perfusion imaging demonstrated a significant decrease in tumor perfusion metrics within recurrent glioblastomas in response to superselective intra-arterial cerebral infusion of bevacizumab; however, these changes did not correlate with time to progression or overall survival.

**ABBREVIATIONS:** BV = bevacizumab; DSC-MRP = dynamic susceptibility contrast-enhanced MR perfusion; GBM = glioblastoma; max = maximum; NAWM = normal-appearing white matter; OS = overall survival; RANO = Response Assessment in Neuro-Oncology; rCBF = relative cerebral blood flow; rCBV = relative cerebral blood volume; SIACI = superselective intra-arterial cerebral infusion; TTP = time to progression

Glioblastoma (GBM) is the most common and lethal primary malignancy of the central nervous system. Despite a 3-pronged intervention consisting of surgical resection followed by radiation with both concurrent and adjuvant temozolomide chemotherapy, the 5-year overall survival rate of patients remains approximately 10%.[1]

While there is no established standard of care for recurrent GBM, bevacizumab (BV, Avastin) has emerged as a potential treatment option for recurrent GBM. BV is a humanized monoclonal antibody that exerts antineoplastic effects by inhibiting the angiogenic effects of vascular endothelial growth factor-A.[2,3] Our group has used superselective intra-arterial cerebral infusion (SIACI) following blood-brain barrier disruption to improve BV delivery.[4] Recently published studies from our group have shown promising results on the safety and efficacy of using SIACI delivery for BV.[5,6]

Although treatment with BV produces a dramatic decrease in MR imaging contrast enhancement, the degree to which these findings reflect actual antitumor effects remains unclear.[7] BV re-

Received November 9, 2015; accepted after revision March 30, 2016.

From the Departments of Neurological Surgery (R.S., Z.Z.) and Radiology (S.A.K., A.J.T., I.K.), Weill Cornell Medical College, New York, New York; Department of Neurological Surgery (K.K.), Northwestern University Feinberg School of Medicine, Chicago, Illinois; and Departments of Radiology (C.G.F.) and Neurological Surgery (J.A.B.), Lenox Hill Hospital, Hofstra–North Shore-LIJ School of Medicine, New York, New York.

This work was partly supported by the Carolyn L. Kuckein Student Research Fellowship (R.S.), the Radiological Society of North America Research Medical Student Grant (K.K.), and National Cancer Institute grant No. CA130985 (J.A.B.).

Please address correspondence to Ilhami Kovanlikaya, MD, 515 71 E St Room S-119, New York, NY 10021; e-mail: ilk2002@med.cornell.edu

Indicates open access to non-subscribers at www.ajnr.org

Indicates article with supplemental on-line tables.

http://dx.doi.org/10.3174/ajnr.A4823

duces vessel permeability, which may contribute to changes in enhancement features and potentially confound the relationship between enhancement and tumor response. Hence, the ability of conventional MR imaging to determine tumor response, progression, and posttreatment effects is not well-established.[8] Our group previously reported that $^{1}$H-MR spectroscopy may be a viable method to determine GBM response following SIACI BV, to overcome the limitations of conventional MR imaging.[7]

Here we evaluate the potential for using dynamic susceptibility contrast-enhanced MR perfusion (DSC-MRP) to determine GBM response to SIACI BV. Previous studies have highlighted the utility of using DSC-MRP in assessing tumor response, treatment effectiveness, and clinical outcomes in patients with GBM.[9,10] Specifically, decreases in tumor relative CBV (rCBV) and tumor relative CBF (rCBF) are associated with favorable clinical outcome, suggesting that changes in rCBV and rCBF could serve as biomarkers for treatment response.[9,10] We hypothesized that treatment response to SIACI BV is associated with decreased rCBV and rCBF, which will correlate with improved survival outcomes.

## MATERIALS AND METHODS

### Subjects

Patients were accrued for this study from larger ongoing serial Phase I/II trials of SIACI BV and were retrospectively analyzed with approval from the institutional review board of Weill Cornell Medical College. Inclusion criteria for the Phase I/II SIACI BV trials were recurrent World Health Organization grade IV glioma refractory to previous combined radiation treatment and chemotherapy with temozolomide, a Karnofsky Performance Scale score of >60, and <12 doses of prior intravenous BV treatment. Poorly circumscribed enhancing tumors, multifocal tumors, or leptomeningeal spread of tumors were not exclusion criteria. Recurrent GBM was diagnosed by using follow-up MR imaging, Response Assessment in Neuro-Oncology (RANO) criteria for progression,[11] and clinical evaluation. Patients with the following were diagnosed with recurrent disease: 1) an increase in a contrast-enhancing lesion; 2) an increase in a nonenhancing T2/FLAIR lesion in 1 or 2 follow-up scans, which showed mass effect, infiltration of the cortical ribbon, or lesion location outside the radiation field; 3) any new lesions; or 4) clinical deterioration diagnosed with recurrent disease. Follow-up MR imaging was compared with MR imaging obtained within 48 hours after the operation to appropriately differentiate tumor recurrence from postoperative changes.

Inclusion criteria for the current study were patients from the above Phase I/II trials who underwent brain DSC-MRP imaging within 1–10 days before and 3–5 weeks after SIACI BV. Twenty-five patients (14 men, 11 women; median age, 55 years; range, 29–81 years) met the inclusion criteria (On-line Table 1). Seven of the 25 patients (28%) received intravenous BV before SIACI BV for a mean of 4.7 cycles (range, 0.5–9 cycles). All except 2 patients received steroids. Time to progression (TTP) and overall survival (OS) were calculated by using the date of the operation for primary GBM to the date of radiologic progression of disease after SIACI BV and date of death. The date of radiologic progression was determined by using strict RANO criteria by a board-certified diagnostic radiologist with a Certificate of Added Qualification in neuroradiology (A.J.T., 11 years of experience) and a trained senior neuroradiologist (I.K., 20 years of subspecialty experience).[11]

### Treatment Protocol

We have previously described the technical specifications of SIACI and BV treatment.[4-6,12] Briefly, 25% mannitol (1.4 mol/L) was infused at 10 mL/120 seconds to facilitate transient BBB disruption followed by SIACI BV. Subsequently, the appropriate dose of BV was infused during 15 minutes. However, because the Phase I trial aimed to determine the maximum tolerated dose of SIACI BV with analysis of 10 escalating doses (2, 4, 6, 8, 10, 11, 12, 13, 14, and 15 mg/kg), the administered dose varied among patients selected for this study. The mean SIACI BV dose received was 12.4 mg/kg (range, 4–15 mg/kg), with 15 patients (60%) receiving the maximum dose of 15 mg/kg. After a mean of 27 ± 5 days of observation, all included patients underwent postinfusion imaging. No additional therapy was initiated before the post-SIACI BV MR imaging–DSC-MRP was completed. Fourteen of 25 patients (56%) underwent various subsequent treatments after SIACI BV that included intra-arterial cetuximab, temozolomide, and/or intravenous BV. We included all imaging studies up to 6 months and then at 1 year posttreatment if available.

### Brain MR Imaging and DSC-MR Imaging Data Collection and Processing

All neuroimaging examinations were conducted on a 3T HDxt 15x MR imaging scanner (GE Healthcare, Milwaukee, Wisconsin). Conventional MR imaging with a dedicated standardized SIACI BV imaging protocol (previously described) was performed.[7] DSC-MR imaging data were acquired by using single-echo gradient recalled-echo echo-planar imaging, with a flip angle of 60°; TR/TE of 2000/20 ms; FOV of 240 mm; 129 × 96; section thickness/gap of 5 mm/0; NEX of 1; number of shots of 1. The first 0.1 mmol/kg of gadolinium administration was used as a preload for the subsequent DSC study to correct the T1-weighted effects of vascular leakage on rCBV. Next, 0.10 mmol/kg of gadolinium at 3–5 mL/s was administered at least 5 minutes after the preload injection.[13,14] The negative enhancement integration and linear fitting correction method was used for postprocessing to calculate corrected rCBV and rCBF.[13] Functional rCBV and rCBF maps were obtained and analyzed by using Olea Sphere Version 2.3 SP2 (Olea Medical, La Ciotat, France).

### Selection of ROIs and Evaluation of Data

Up to 4 distinct ROIs ranging in size from 10 to 12 voxels were chosen from the coregistered precontrast T1-weighted, postcontrast T1-weighted, and T2-FLAIR images and rCBV maps (Fig 1): 1) normal-appearing white matter (NAWM) on the contralateral side (Fig 1*A*), which was used to normalize rCBV and rCBF maps on a voxelwise basis [Normalized rCBV = rCBV (Lesion) / rCBV (NAWM)]; 2) the location of highest T1 enhancement in the lesion (maximum [max] enhancing) (Fig 1*B*); 3) the location of the highest rCBV in the lesion (max rCBV) (Fig 1*C*); and 4) nonenhancing T2 hyperintense signal abnormality surrounding the tumor (nonenhancing T2 hyper-

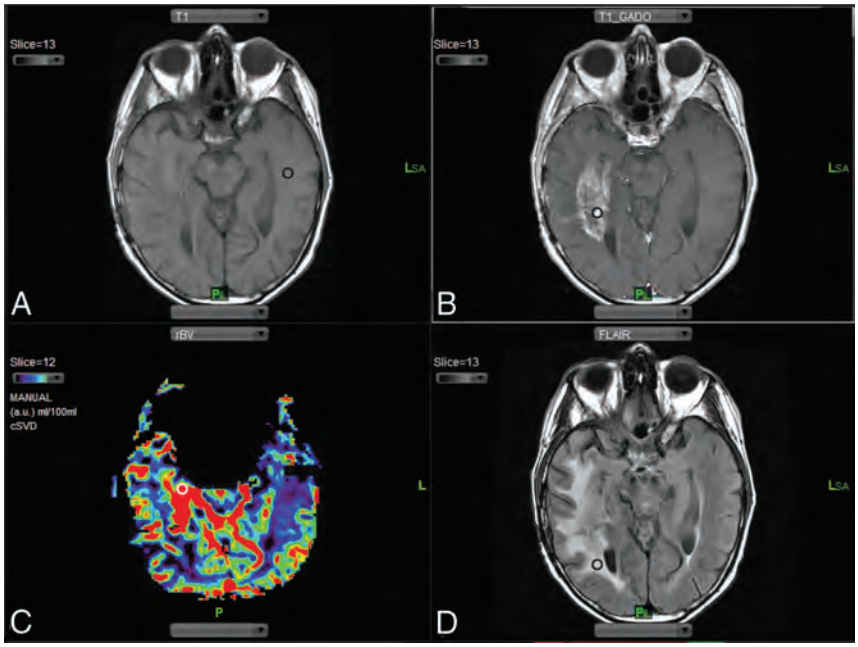


**FIG 1.** ROI selection. *A*, Precontrast T1-weighted images are used to select the ROI in the normal-appearing white matter on the side contralateral to the lesion (*black circle*). *B*, Postcontrast T1-weighted images are compared with the precontrast T1-weighted images to select the ROI representing the area of max contrast enhancement (*black circle*). *C*, Region of max rCBV is selected by using rCBV maps (*white circle*). *D*, T2-FLAIR images are used to select areas representing the nonenhancing T2 hyperintense signal abnormality surrounding the tumor (*black circle*).

intensity) (Fig 1*D*). The same size and anatomically matching ROIs were manually constructed by using contrast-enhanced T1-weighted and T2-weighted images as a reference from the pre- and posttreatment MR imaging scans. Only 1 investigator (S.A.K.) placed ROIs, and all ROI placements were overseen by 2 senior investigators (A.J.T. and I.K.).

### Statistical Analysis

Differences in rCBV and rCBF from pre- to post-SIACI BV (defined as median percentage change: [(Posttreatment − Pretreatment)/Pretreatment × 100%]) were determined by using the Wilcoxon signed rank test. The Spearman correlation was used to assess the correlation between changes in rCBV and rCBF in the various ROIs and TTP and OS. Differences of rCBV and rCBF changes in ROIs were tested by using ANOVA within subjects.

## RESULTS

DSC-MRP showed that SIACI BV produced changes in rCBV and rCBF (Fig 2 and On-line Table 2). Median percentage change values are reported, which were not significantly different from the mean percentage change values (On-line Table 3).

### Cerebral Blood Volume

When one compared pre- and post-SIACI BV, there was a statistically significant median percentage change of −32.34 (range, −79.18–38.90; $P = .001$) in rCBV in areas of max rCBV. There was a trend toward statistical significance in areas of max tumor enhancement (median percentage change, −27.29; range, −66.30–117.64; $P = .074$) and in nonenhancing T2 hyperintense areas (median percentage change, 30.04; range, −83.26–255.42%; $P = .069$). The change in rCBV was not found to be statistically significant in contralateral NAWM (median percentage change, −4.255; range, −82.35–143.75; $P = .568$). The median percentage change in rCBV in the nonenhancing T2 hyperintense region showed a trend toward statistically significant correlation with the presence of previous cycles of BV ($P = .062$). Median TTP and OS were 571 and 683 days, respectively. None of the rCBV changes correlated with prolonged TTP or OS. Last, the rCBV changes were significantly different among the 4 ROIs ($P = .0003$).

### Cerebral Blood Flow

There was a statistically significant median percentage change of −30.67 (range, −76.40–44.18; $P = .001$) and −27.25 (range, −65.99–55.60%; $P = .037$) in rCBF in areas of max rCBV and max tumor enhancement, respectively, from pre- to post-SIACI BV. The change in rCBF was not found to be statistically significant in contralateral NAWM (median percentage change, 0.363; range, −68.77–68.95; $P = .696$) and in the nonenhancing T2 hyperintense areas (median percentage change, 20.99; range, −63.85–208.97; $P = .216$). None of the rCBF changes correlated with prolonged TTP or OS. Last, the rCBF changes were significantly different among the 4 ROIs ($P = .021$).

## DISCUSSION

Conventional MR imaging is currently unable to provide consistent and accurate assessment of pathology-specific tumor progression and therapeutic response, which limit its diagnostic and prognostic utility.[8] This limitation has led to the development of advanced quantitative imaging techniques that provide critical information on the molecular, physiologic, and metabolic processes and properties of tumors.[15] Previously, we showed that MR spectroscopic imaging, specifically choline/*N*-acetylaspartate ratios, provided a useful tool to assess treatment response following SIACI BV.[7] In the current study, we used DSC-MRP to assess GBM perfusion changes associated with SIACI BV to determine whether DSC-MRP provided useful biomarkers to determine treatment response. We also wanted to explore whether biomarkers obtained from DSC-MR imaging could reveal aspects of the complex mechanism underlying the tumoricidal effects of BV.

Antiangiogenic agents such as BV produce a marked decrease in contrast enhancement, termed "pseudoresponse," and a notable decrease in the nonenhancing T2 hyperintense areas. Standardized criteria for assessing brain tumor treatment response, including the Macdonald and the RANO criteria, fall short of definitively distinguishing tumor progression, pseudoresponse, and pseudoprogression.[16] The inability of the Macdonald and RANO criteria to differentiate tumor progression, pseudore-

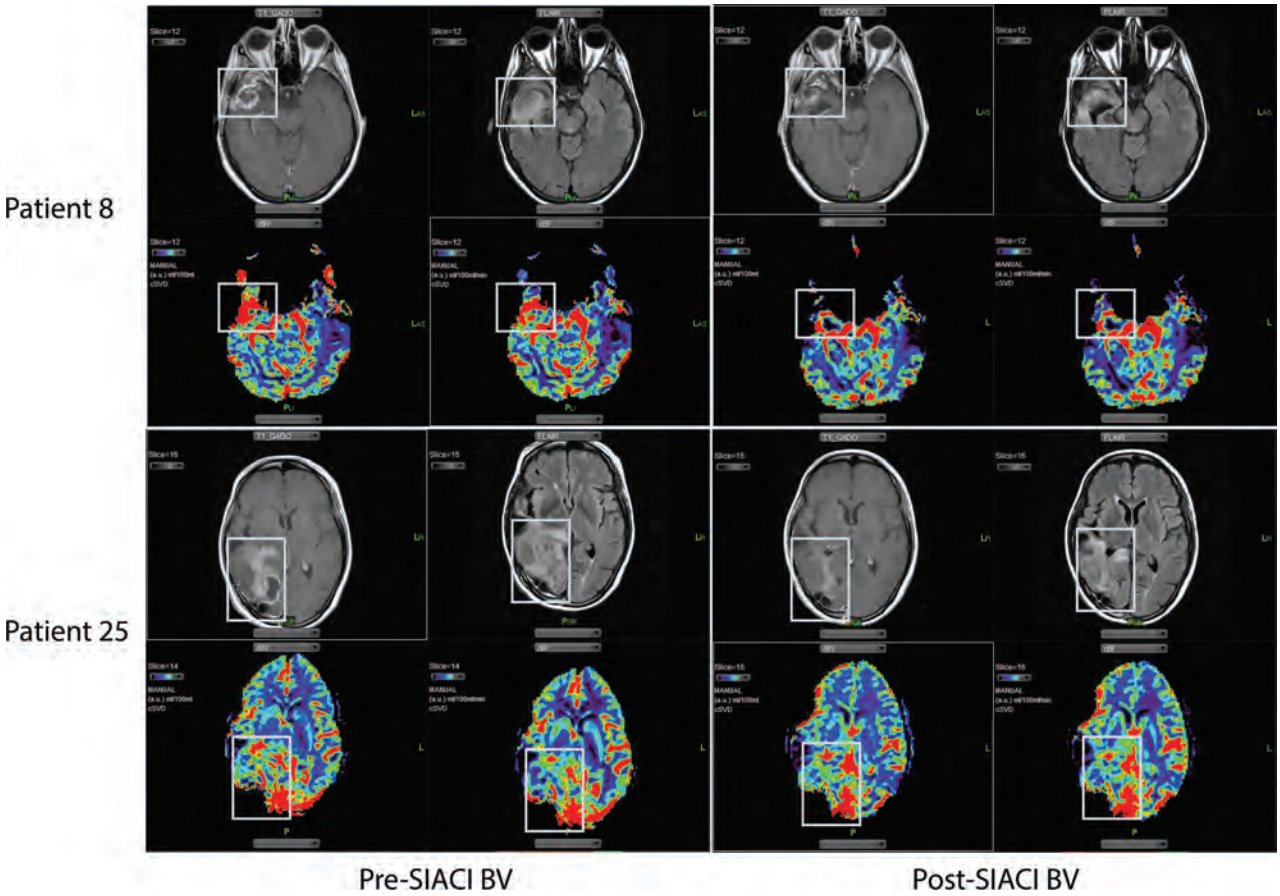


**FIG 2.** MR imaging changes from SIACI BV treatment. Imaging from 2 patients (study patients 8 and 25) demonstrates a decrease in contrast enhancement, T2 signal abnormalities, rCBV, and rCBF following SIACI BV.

sponse, and pseudoprogression is noteworthy and could lead to conflicting and confusing outcome evaluations in BV treatment. Recognition of pseudoresponse and pseudoprogression in antiangiogenic therapy is critical to appropriately determine whether the decrease in contrast enhancement reflects a true decrease in tumor burden or is simply due to normalization of BBB and tumor vasculature.

It remains unclear whether BV acts by pruning tumor vessels and killing a fraction of tumor cells; by normalizing existing tumor vasculature and the tumor microenvironment, thus increasing the delivery of chemotherapy; or by reducing the number of blood-circulating endothelial and progenitor cells, thus inhibiting neovascularization.[17-19] MR diffusion-weighted, perfusion-weighted, and spectroscopy imaging may provide quantitative data on the molecular and metabolic processes that underlie tumorigenesis and tumor response. MR spectroscopic imaging can be used to study neurochemical changes that may help explain the tumoricidal effects of BV.[7] DSC-MRP offers another appealing parametric imaging technique to potentially elucidate the mechanism of action of BV.

DSC-MRP tracks the first pass of a bolus of gadolinium-based contrast agent through brain tissue by a series of rapid T2- or T2*-weighted MR images. The susceptibility effect of the paramagnetic contrast agent leads to transient decreases in T2 and T2* relaxation times, resulting in signal loss in the signal intensity–time curve. The signal information can then be converted into a contrast medium concentration–time curve and used to generate parametric maps of rCBV, rCBF, and K2 (leakage coefficient).[20,21] DSC-MRP is particularly sensitive to changes in tumor vasculature, which is noteworthy given that BV affects blood vessels. DSC-MRP, therefore, may be useful in both assessing tumor response to BV and better understanding the tumoricidal effects of BV.

In the present study, DSC-MRP was used to assess tumor response in 25 patients with recurrent GBM treated with SIACI BV. rCBV and rCBF were reliable biomarkers for assessing tumor response to SIACI BV. The change in rCBV from pre- to post-SIACI BV was statistically significant in the ROIs in max rCBV. The change in rCBV also showed a trend toward statistical significance in ROIs in max tumor enhancement, which was associated with an observable decrease in the contrast enhancement of the lesion. No statistically significant changes or trends were found in the contralateral NAWM. The change in rCBF was statistically significant in ROIs in max rCBV and max tumor enhancement, and not statistically significant in ROIs in contralateral NAWM. Collectively, these data show that the SIACI BV acted locally at the site of tumor, with minimal effect in the contralateral NAWM. A recent study reported that perfusion decreased in ipsilateral and contralateral normal-appearing brain after BV treatment.[22] This study, however, obtained absolute CBV, and the route of BV administration was different from that in our study, which may explain the different findings.

In our patients, SIACI BV produced a marked decrease in rCBV and rCBF in the max rCBV and max tumor-enhancing regions on DSC-MRP imaging. Most interesting, we also observed a trend toward statistical significance in rCBV increase in the nonenhancing T2 hyperintense areas surrounding the lesion. This may suggest that while the contrast-enhancing region within the tumor may reflect the treatment response to SIACI BV, it may not adequately reflect tumor burden, treatment effect, or tumor progression during or after SIACI BV treatment. It is unclear whether the increase in rCBV in the nonenhancing T2 hyperintense region reflects an increase in tumor volume or perhaps an increase in tumor invasiveness. Because several preclinical and clinical studies have reported that antiangiogenic therapy increases tumor invasiveness,[23-25] the increased rCBV in the nonenhancing T2 hyperintense region approximately 1 month after SIACI BV in our study may be reflective of this phenomenon. However, increased T2 hyperintensity occurs more commonly after long-term IV BV exposure and histologically represents a low-grade infiltrative phenotype. In our study, there was no statistically significant difference in TTP and OS among patients who received intravenous BV before SIACI BV compared with those who did not. Combined radiologic and pathologic correlative studies are needed to better understand the imaging biomarkers of tumor invasiveness, especially as they pertain to antiangiogenic therapy.

Post-SIACI BV changes in MRP biomarkers did not correlate with prolonged TTP and OS. It is difficult to conclusively state whether this was due to lack of treatment effect or other confounding variables. The sample size was small and clinical heterogeneity in patients selected for inclusion in the Phase I/II SIACI BV trials should be considered. Notably, more than a quarter of our patients were exposed to BV before enrolling in SIACI BV clinical trials, and not every patient received the maximum dose of SIACI BV. Furthermore, more than half of our patients received subsequent treatment after SIACI BV, making it difficult to accurately assess the true implications of this potential treatment. Given the design, the study had limitations inherent in all retrospective reviews: Namely, our results demonstrate correlation and not causation. The subjectivity in selecting matching ROIs on pre- and posttreatment scans may have introduced sampling error. To minimize this, only one investigator (K.K.) placed ROIs, and all ROI placements were overseen by 2 senior investigators (A.J.T. and I.K.). Another limitation was that histologic specimens were not available to confirm the diagnosis of recurrent disease. While it is ideal to obtain histologic specimens of recurrent disease, it is not realistic to expect patients to agree to an additional surgical procedure for open biopsy. Furthermore, even if a biopsy is obtained, correlation with posttreatment MRP changes may not be feasible because the exact site of biopsy is often not known or identifiable after biopsy, making it difficult to correlate MRP changes with histopathologic examination. Future studies by using SIACI BV should attempt to obtain biopsy specimens of recurrent disease by using specified coordinates and match these coordinates voxel-by-voxel to post–SIACI BV treatment MRP scans.

## CONCLUSIONS

This study suggests that GBM response to SIACI BV can be assessed by comparing pre- and posttreatment rCBV and rCBF changes in regions of the tumor with max rCBV and max enhancement. However, there was no correlation between these significant MRP biomarker changes, TTP, and OS.

Disclosures: Christopher G. Filippi—*UNRELATED*: *Consultancy*: Syntactx, Guerbet, *Comments*: review of brain MR images for a clinical research trial; attended Advisory Board Meeting for Guerbet in Boston as a consultant; *Grants/Grants Pending*: Katz Institute for Women's Health (KIWH),* Coulter,* *Comments*: KIWH grant, coinvestigator, funded from September 2015 to October 2016 for grant determining optimum imaging strategy for women with acute stroke; and Coulter grant, Principal Investigator, on the development of a novel semiautomated computer software algorithm for core infarct detection. *Money paid to the institution.

## REFERENCES

1. Stupp R, Hegi ME, Mason WP, et al; European Organisation for Research and Treatment of Cancer Brain Tumour and Radiation Oncology Groups, National Cancer Institute of Canada Clinical Trials Group. **Effects of radiotherapy with concomitant and adjuvant temozolomide versus radiotherapy alone on survival in glioblastoma in a randomised phase III study: 5-year analysis of the EORTC-NCIC trial.** *Lancet Oncol* 2009;10:459–66 CrossRef Medline
2. Chinot OL. **Bevacizumab-based therapy in relapsed glioblastoma: rationale and clinical experience to date.** *Expert Rev Anticancer Ther* 2012;12:1413–27 CrossRef Medline
3. Mukherji SK. **Bevacizumab (Avastin).** *AJNR Am J Neuroradiol* 2010; 31:235–36 CrossRef Medline
4. Riina HA, Fraser JF, Fralin S, et al. **Superselective intraarterial cerebral infusion of bevacizumab: a revival of interventional neuro-oncology for malignant glioma.** *J Exp Ther Oncol* 2009;8:145–50 Medline
5. Boockvar JA, Tsiouris AJ, Hofstetter CP, et al. **Safety and maximum tolerated dose of superselective intraarterial cerebral infusion of bevacizumab after osmotic blood-brain barrier disruption for recurrent malignant glioma: clinical article.** *J Neurosurg* 2011;114: 624–32 CrossRef Medline
6. Burkhardt JK, Riina H, Shin BJ, et al. **Intra-arterial delivery of bevacizumab after blood-brain barrier disruption for the treatment of recurrent glioblastoma: progression-free survival and overall survival.** *World Neurosurg* 2012;77:130–34 CrossRef Medline
7. Jeon JY, Kovanlikaya I, Boockvar JA, et al. **Metabolic response of glioblastoma to superselective intra-arterial cerebral infusion of bevacizumab: a proton MR spectroscopic imaging study.** *AJNR Am J Neuroradiol* 2012;33:2095–102 CrossRef Medline
8. Upadhyay N, Waldman AD. **Conventional MRI evaluation of gliomas.** *Br J Radiol* 2011;84(Spec No 2):S107–11 CrossRef Medline
9. Kickingereder P, Wiestler B, Burth S, et al. **Relative cerebral blood volume is a potential predictive imaging biomarker of bevacizumab efficacy in recurrent glioblastoma.** *Neuro Oncol* 2015;17: 1139–47 CrossRef Medline
10. Schmainda KM, Zhang Z, Prah M, et al. **Dynamic susceptibility contrast MRI measures of relative cerebral blood volume as a prognostic marker for overall survival in recurrent glioblastoma: results from the ACRIN 6677/RTOG 0625 multicenter trial.** *Neuro Oncol* 2015;17:1148–56 CrossRef Medline
11. Wen PY, Macdonald DR, Reardon DA, et al. **Updated response assessment criteria for high-grade gliomas: response assessment in neuro-oncology working group.** *J Clin Oncol* 2010;28:1963–72 CrossRef Medline
12. Shin BJ, Burkhardt JK, Riina HA, et al. **Superselective intra-arterial cerebral infusion of novel agents after blood-brain disruption for the treatment of recurrent glioblastoma multiforme: a technical case series.** *Neurosurg Clin N Am* 2012;23:323–29, ix–x CrossRef Medline
13. Boxerman JL, Schmainda KM, Weisskoff RM. **Relative cerebral blood volume maps corrected for contrast agent extravasation sig-**

**nificantly correlate with glioma tumor grade, whereas uncorrected maps do not.** *AJNR Am J Neuroradiol* 2006;27:859–67 Medline
14. Paulson ES, Schmainda KM. **Comparison of dynamic susceptibility-weighted contrast-enhanced MR methods: recommendations for measuring relative cerebral blood volume in brain tumors.** *Radiology* 2008;249:601–13 CrossRef Medline
15. Kalpathy-Cramer J, Gerstner ER, Emblem KE, et al. **Advanced magnetic resonance imaging of the physical processes in human glioblastoma.** *Cancer Res* 2014;74:4622–37 CrossRef Medline
16. Huang RY, Neagu MR, Reardon DA, et al. **Pitfalls in the neuroimaging of glioblastoma in the era of antiangiogenic and immuno/targeted therapy: detecting illusive disease, defining response.** *Front Neurol* 2015;6:33 CrossRef Medline
17. Falk AT, Barrière J, François E, et al. **Bevacizumab: a dose review.** *Crit Rev Oncol Hematol* 2015;94:311–22 CrossRef Medline
18. Jain RK, Duda DG, Clark JW, et al. **Lessons from phase III clinical trials on anti-VEGF therapy for cancer.** *Nat Clin Pract Oncol* 2006;3:24–40 CrossRef Medline
19. Okonogi N, Shirai K, Oike T, et al. **Topics in chemotherapy, molecular-targeted therapy, and immunotherapy for newly-diagnosed glioblastoma multiforme.** *Anticancer Res* 2015;35:1229–35 Medline
20. Essig M, Shiroishi MS, Nguyen TB, et al. **Perfusion MRI: the five most frequently asked technical questions.** *AJR Am J Roentgenol* 2013;200:24–34 CrossRef Medline
21. Jahng GH, Li KL, Ostergaard L, et al. **Perfusion magnetic resonance imaging: a comprehensive update on principles and techniques.** *Korean J Radiol* 2014;15:554–77 CrossRef Medline
22. Stadlbauer A, Pichler P, Karl M, et al. **Quantification of serial changes in cerebral blood volume and metabolism in patients with recurrent glioblastoma undergoing antiangiogenic therapy.** *Eur J Radiol* 2015;84:1128–36 CrossRef Medline
23. de Groot JF, Fuller G, Kumar AJ, et al. **Tumor invasion after treatment of glioblastoma with bevacizumab: radiographic and pathologic correlation in humans and mice.** *Neuro Oncol* 2010;12:233–42 CrossRef Medline
24. Iwamoto FM, Abrey LE, Beal K, et al. **Patterns of relapse and prognosis after bevacizumab failure in recurrent glioblastoma.** *Neurology* 2009;73:1200–06 CrossRef Medline
25. Keunen O, Johansson M, Oudin A, et al. **Anti-VEGF treatment reduces blood supply and increases tumor cell invasion in glioblastoma.** *Proc Natl Acad Sci U S A* 2011;108:3749–54 CrossRef Medline

# Differentiating Hemangioblastomas from Brain Metastases Using Diffusion-Weighted Imaging and Dynamic Susceptibility Contrast-Enhanced Perfusion-Weighted MR Imaging

D. She, X. Yang, Z. Xing, and D. Cao

## ABSTRACT

**BACKGROUND AND PURPOSE:** On DWI and DSC-PWI, hemangioblastomas and brain metastases may exhibit different signal intensities depending on their cellularity and angiogenesis. The purpose of this study was to evaluate whether a hemangioblastoma can be differentiated from a single brain metastasis with DWI and DSC-PWI.

**MATERIALS AND METHODS:** We retrospectively reviewed DWI, DSC-PWI, and conventional MR imaging of 21 patients with hemangioblastomas and 30 patients with a single brain metastasis. Variables of minimum ADC and relative ADC were acquired by DWI and the parameter of relative maximum CBV, by DSC-PWI. Minimum ADC, relative ADC, and relative maximum CBV values were compared between hemangioblastomas and brain metastases by using the nonparametric Mann-Whitney test. The sensitivity, specificity, positive and negative predictive values, accuracy, and the area under the receiver operating characteristic curve were determined.

**RESULTS:** Both the minimum ADC values and relative ADC ratios were significantly higher in hemangioblastomas compared with brain metastases ($P < .001$ for both minimum ADC values and relative ADC ratios). The same was true for the relative maximum CBV ratio ($P < .002$). The threshold value of ≥6.59 for relative maximum CBV provided sensitivity, specificity, and accuracy of 95.24%, 53.33%, and 70.59%, respectively, for differentiating hemangioblastomas from brain metastases. Compared with relative maximum CBV, relative ADC had high sensitivity (95.24%), specificity (96.67%), and accuracy (96.08%) using the threshold value of ≥1.54. The optimal threshold value for minimum ADC was $\geq 1.1 \times 10^{-3}$ mm$^2$/s.

**CONCLUSIONS:** DWI and DSC-PWI are helpful in the characterization and differentiation of hemangioblastomas from brain metastases. DWI appears to be the most efficient MR imaging technique for providing a distinct differentiation of the 2 tumor types.

**ABBREVIATIONS:** $ADC_{min}$ = minimum ADC; rADC = relative ADC; rCBV = relative CBV; rCBVmax = relative maximum CBV; ROC = receiver operating characteristic; AUC = area under the curve

Hemangioblastomas are benign World Health Organization grade I tumors of vascular origin, which account for 7% of posterior fossa tumors in adults.[1,2] Brain metastases are the most common type of brain malignant neoplasms, and posterior fossa metastases represent about 8.7%–10.9% of all brain metastases.[3-5] Preoperative differentiation of hemangioblastomas and brain metastases is of high clinical relevance because surgical planning, therapeutic decisions, and prognosis vary substantially for each tumor type. In patients with hemangioblastomas, complete surgical resection is the treatment of choice,[6] whereas patients with brain metastases usually undergo surgery, stereotactic surgery, whole-brain radiation therapy, chemotherapy, or combined therapy.[7] Furthermore, hemangioblastomas are potentially curable and are often associated with a longer survival.[8] However, brain metastases are associated with notable mortality and morbidity.[5] In addition, the surgical resection of hemangioblastomas can be complicated by profuse intraoperative bleeding. Sometimes preoperative embolization of the feeding arteries may reduce the tumor blood supply, which can lessen intraoperative hemorrhage.[9] In many cases, the 2 entities can be differentiated by using clinical history and conventional MR imaging. However, in some instances, particularly when the clinical findings are noncontributory and hemangioblastomas appear as solid contrast-enhancing masses with peritumoral edema, conventional MR imaging cannot be used to distinguish the 2 tumor types.

Because the clinical management and prognosis of these 2 types of tumor are vastly different, it is important to distinguish them with certainty. Advanced MR imaging approaches includ-

Received December 13, 2015; accepted after revision March 18, 2016.

From the Department of Radiology, First Affiliated Hospital of Fujian Medical University, Fuzhou, P.R. China.

Please address correspondence to Dairong Cao, MD, Department of Radiology, First Affiliated Hospital of Fujian Medical University, 20 Cha-Zhong Rd, Fuzhou, Fujian 350005, P.R. China; e-mail: dairongcao@163.com

http://dx.doi.org/10.3174/ajnr.A4809

ing DWI and DSC-PWI might complement physiologic information in addition to that obtained with conventional MR imaging. DWI could assess the Brownian movement of water in the microscopic tissue environment and reflect cellularity of the tissue by ADC values, which may aid conventional MR imaging in the characterization of brain tumors and other intracranial diseases.[10-12] DSC-PWI that provides noninvasive morphologic and functional information of the tumor microvasculature can be useful in the preoperative diagnosis and grading of brain tumors. MR imaging parameters of relative cerebral blood volume (rCBV) have become some of the most robust hemodynamic variables used in the characterization of the brain tumors.[13-15] Hemangioblastomas may present with histopathologic structures vastly different from those found in brain metastases. Thus, the application of DWI and DSC-PWI may better evaluate and discriminate the cytostructural and hemodynamic differences between hemangioblastomas and brain metastases.

Only a few small studies have evaluated the advanced MR imaging features of a hemangioblastoma,[12,16,17] particularly when assessing their differentiation from a single brain metastasis.[18] The purpose of this study was to evaluate whether a hemangioblastoma can be differentiated from a single brain metastasis with DWI and DSC-PWI.

## MATERIALS AND METHODS

### Patients

The institutional review board of our hospital approved this retrospective study, and the requirement for patient informed consent was waived due to its retrospective nature. Potentially eligible patients with histologically confirmed hemangioblastomas and brain metastases from January 2010 through September 2015 were identified. For the selection of appropriate patients, those with multiple brain lesions, hemorrhagic lesions, and previously treated or nonenhancing tumor were excluded. Pretreament MR images of consecutive patients were reviewed retrospectively, and DWI and DSC-PWI were requested in addition to conventional MR imaging.

### MR Imaging Techniques

MR imaging examinations were performed in the routine clinical work-up on a 3T MR imaging system (Magnetom Verio Tim; Siemens, Erlangen, Germany) by using an 8-channel head matrix coil. The conventional MR imaging protocols consisted of the following sequences: axial T2-weighted turbo spin-echo imaging (TR/TE, 4000 /96 ms), axial T1-weighted spin-echo imaging (TR/TE, 250 /2.48 ms), axial fluid-attenuated inversion recovery (TR, 9000 ms; TE, 94 ms; TI, 2500 ms), and contrast-enhanced gradient-echo T1-weighted imaging (TR/TE, 250 ms/2.48 ms) in 3 orthogonal planes, which was acquired following the acquisition of the DSC-PWI sequences. FOV at 220 × 220 mm, section thickness of 5 mm, and intersection gap of 1 were uniform in all sequences. Before the injection of contrast material, DWI was performed in the axial plane with a spin-echo echo-planar sequence. The imaging parameters used were as follows: TR/TE, 8200/102 ms; NEX, 2.0; FOV, 220 × 220; section thickness, 5 mm; intersection gap, 1 mm. The b-values were 0 and 1000 s/mm$^2$ with diffusion gradients encoded in the 3 orthogonal directions to generate 3 sets of diffusion-weighted images (x-, y-, and z-directions). Processing of the ADC map was generated automatically on the MR imaging scanner.

The DSC-PWI was obtained with a gradient-recalled T2*-weighted echo-planar imaging sequence. The imaging parameters used were as follows: TR/TE, 1000–1250/54 ms; flip angle, 35°; FOV, 220 × 220; NEX, 1.0; section thickness, 5 mm; intersection gap, 1 mm. During the first 3 phases, images were scanned before injecting the contrast material to establish a precontrast baseline. When the scan was to the fourth phase of DSC-PWI, 0.1 mmol/kg body weight of gadopentetate dimeglumine was injected intravenously with an MR imaging–compatible power injector at a flow rate of 5 mL/s through an intravenous catheter placed in the right or left antecubital vein, followed by 20 mL of continuous saline flush. The series of 20 sections, 60 phases, and 1200 images was obtained in 1 minute 36 seconds.

### Data Processing

All imaging assessments were performed on an off-line Siemens syngo MR B19 work station (NUMARIS/4) with standard software. For evaluation of conventional MR images, a neuroradiologist who was blinded to the tumor histology retrospectively reviewed the images and evaluated each lesion on the basis of location, tumor characteristics (solid-cystic or solid), presence or absence of signal void on T2-weighted imaging, and contrast enhancement pattern (homogeneous or heterogeneous). For evaluation of DWI data, qualitative assessment of the signal intensity in the enhancing solid portion of the tumors on contrast-enhanced T1-weighted images was performed. The signal intensity of the tumor was classified as hypointense, isointense, or hyperintense compared with normal white matter. The ADC values were measured by manually placing ROIs inside the tumor regions on the ADC maps. At least 5 small round ROIs (30–40 mm$^2$) were placed inside the tumors on the ADC maps, and the minimum ADC values ($ADC_{min}$) were taken into consideration. The ROI placements were made from the enhancing solid portion of the lesion, avoiding hemorrhagic, necrotic, cystic, or apparent blood vessel regions that might influence the ADC values. For each patient, the enhancing solid portion of the tumor was identified on contrast-enhanced axial T1-weighted images and matching ADC maps. The same method was applied to a corresponding area in the contralateral unaffected white matter judged as normal on both T2- and contrast-enhanced T1-weighted images. The relative ADC (rADC) ratios of the tumors were calculated as the ratios of the minimum ADC of the tumors divided by the mean ADC of the contralateral unaffected white matter. $ADC_{min}$ values were expressed as $\times 10^{-3}$ mm$^2$/s.

For evaluation of DSC-PWI data, whole-brain CBV maps were generated by using a single-compartment model and an automated arterial input function. Measurements of rCBV values were performed with the same ROIs as those used for ADC measurements, and the maximum rCBV ($rCBV_{max}$) values were taken into consideration. To minimize variances in the rCBV values in an individual patient, we calculated the rCBV ratios of the tumors as the ratios of the rCBV values from ROIs of the tumors divided by the mean rCBV value of the contralateral unaffected white matter. The ROIs for the ADC and rCBV measurements were not

identical and were not from the same solid contrast-enhancing region of the tumor in each single patient. The signal intensity on DWI, $ADC_{min}$, rADC, and $rCBV_{max}$ parameters was acquired by another neuroradiologist who was experienced with diffusion and perfusion data acquisition and blinded to the tumor histology. This method for the measurements of maximal abnormality has been shown to provide the highest interobserver and intraobserver reproducibility.[19]

### *Data Analysis*

All hemangioblastoma and brain metastasis parameters are presented as means ± SDs. Comparisons of $ADC_{min}$ ($\times 10^{-3}$ $mm^2/s$), rADC, and $rCBV_{max}$ values between patients with hemangioblastomas and those with brain metastases were made with nonparametric Mann-Whitney statistical tests. Comparisons of the signal intensity on DWI between patients with hemangioblastomas and those with brain metastases were made with $\chi^2$ tests. The receiver operating characteristic (ROC) analysis curves were obtained to decide the diagnostic accuracy and optimum cutoff value of $ADC_{min}$, rADC, and $rCBV_{max}$ for differentiating hemangioblastomas from brain metastases. The sensitivity, specificity, positive predictive value, negative predictive value, accuracy, and area under the curve (AUC) based on optimum thresholds for $ADC_{min}$ and $rCBV_{max}$ were calculated to differentiate hemangioblastomas from brain metastases. The cutoff values chosen were those that provided optimal sensitivity and specificity jointly. In addition, comparison of AUCs for different quantitative variables was made with a *Z*-test. Statistical analysis was performed in Excel 2007 (Microsoft, Redmond, Washington) and the Statistical Package for the Social Sciences (Version 17.0; IBM, Armonk, New York). *P* values $< .05$ were statistically significant.

**Table 1: The main clinical features of hemangioblastomas and brain metastases**

| | Hemangioblastomas | Brain Metastases |
|---|---|---|
| No. of patients (male/female) | 10:11 | 19:11 |
| Mean age (yr) | 41.1 ± 15.8 | 57.5 ± 12.0 |
| Localization | | |
| Cerebellar hemisphere | 19 | 5 |
| Frontal lobe | 1 | 12 |
| Choroid fissure | 1 | |
| Parietal lobe | | 8 |
| Occipital lobe | | 1 |
| Temporal lobe | | 4 |
| Origin of brain metastases | | |
| Lung carcinoma | | 19 |
| Breast carcinoma | | 2 |
| Gastric carcinoma | | 2 |
| Esophagus carcinoma | | 1 |
| Liver carcinoma | | 2 |
| Melanoma | | 1 |
| Colon carcinoma | | 1 |
| Carcinoma of unknown origin | | 2 |

## RESULTS

Fifty-one histologically proved cases, including 21 cases with hemangioblastomas and 30 cases with brain metastases, were enrolled in this study. The main clinical features of the hemangioblastomas and brain metastases are summarized in Table 1. The characteristics of hemangioblastomas and brain metastases on conventional MR imaging are shown in Table 2.

The $ADC_{min}$ values, rADC ratios, and $rCBV_{max}$ calculated for hemangioblastomas and brain metastases are given in Table 3. On DWI, the signal intensity in the solid portions of hemangioblastomas were hypointense ($n = 3$), isointense ($n = 13$), and hyperintense ($n = 5$) relative to normal-appearing white matter. Conversely, the signal intensity of brain metastases was hypointense ($n = 1$), isointense ($n = 3$), and hyperintense ($n = 26$). The signal intensity in the solid contrast-enhancing portions of hemangioblastomas was significantly lower than that of brain metastases ($P < .001$). Both the $ADC_{min}$ values and rADC ratios were significantly higher in hemangioblastomas compared with brain metastases (Table 3 and Figs 1*B* and 2*B*).

The $rCBV_{max}$ values in patients with hemangioblastomas were significantly higher than those in patients with brain metastases (Table 3 and Figs 1*C* and 2*C*). Twenty of 21 (95.23%) hemangioblastomas showed markedly elevated perfusion (rCBVmax > 6.0), while 16/30 (53.33%) brain metastases showed significantly elevated perfusion.

The results of the ROC curve analysis are shown in Table 4 and Fig 3, which summarize the sensitivity, specificity, positive predictive values, negative predictive values, accuracy, and AUC for the different quantitative parameters for differentiating hemangioblastomas from brain metastases. From the ROC analysis, the highest AUC was obtained for rADC compared with rCBVmax (0.971 versus 0.756, $Z = 3.075$, $P = .002$) in the differentiation of hemangioblastomas and brain metastases, which corresponded to histopathologic findings in 95.24% (20 of 21) of patients with hemangioblastomas and 96.67% (29 of 31) of those with brain metastases. With a threshold value of ≥1.54 for rADC values, the accuracy in the diagnosis of hemangioblastomas was 96.08%.

## DISCUSSION

In our study, we used 2 diagnostic parameters derived from DWI and DSC-PWI to differentiate hemangioblastomas and brain metastases, which are sometimes not distinguishable with conventional MR imaging. Our study showed that patients with heman-

**Table 3: Comparison of the hemangioblastomas and brain metastases with regard to the variables of interest (mean ± SD)**

| | Hemangioblastomas | Brain Metastases | *P* Value |
|---|---|---|---|
| $ADC_{min}$ | $1.5 \pm 0.52 \times 10^{-3}$ $mm^2/s$ | $0.79 \pm 0.21 \times 10^{-3}$ $mm^2/s$ | <.001 |
| rADC | 2.3 ± 0.76 | 1.12 ± 0.32 | <.001 |
| $rCBV_{max}$ | 8.5 ± 2.45 | 6.4 ± 2.0 | .002 |

**Table 2: Characteristics of hemangioblastomas and brain metastases on conventional MR imaging**

| | | | | Contrast-Enhancement Pattern | |
|---|---|---|---|---|---|
| Tumor | Solid-Cystic | Solid | Presence/Absence of SV | Homogeneous | Heterogeneous |
| Hemangioblastomas | 12/21 (57.1%) | 9/21 (42.9%) | 12/9 | 15/21 (71.5%) | 6/21 (28.5%) |
| Brain metastases | 6/30 (20%) | 24/30 (80%) | 6/24 | 5/30 (16.7%) | 25/30 (83.3%) |

**Note:**—SV indicates signal void.

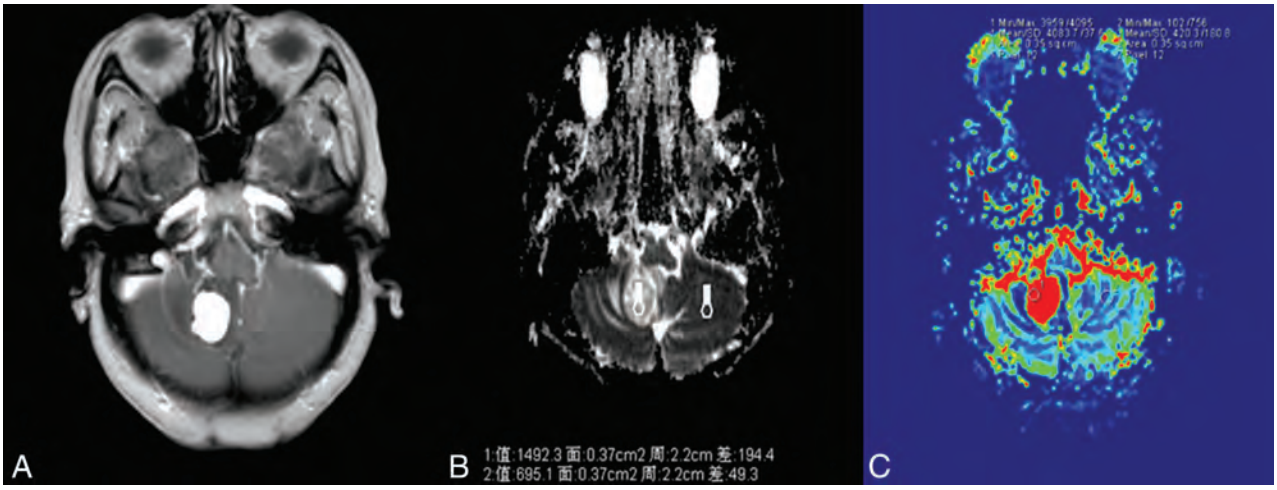


**FIG 1.** A 54-year-old woman with hemangioblastoma. *A*, Contrast-enhanced axial T1-weighted image demonstrates an obvious contrast-enhancing lesion on the right cerebellar hemisphere. *B*, A corresponding ADC map shows the tumor with an increased ADC value ($ADC_{min}$ = 1492.3 × $10^{-3}$ $mm^2/s$, rADC = 2.15). *C*, Correlative color CBV image shows significant elevated perfusion with the calculated $rCBV_{max}$ of 9.72.

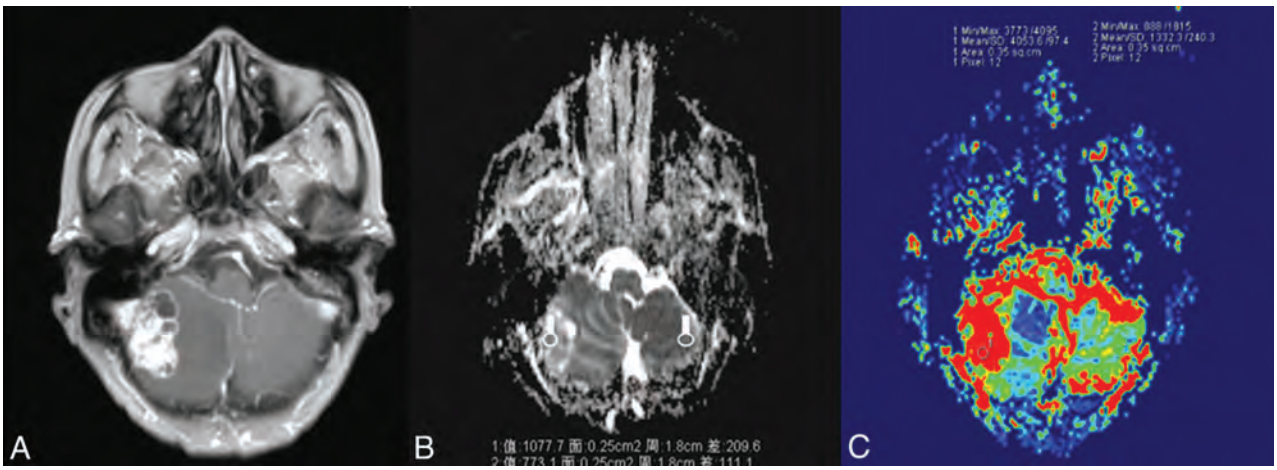


**FIG 2.** A 70-year-old man with a single brain metastasis. *A*, Contrast-enhanced axial T1-weighted image demonstrates a contrast-enhancing lesion on the right cerebellar hemisphere. *B*, A corresponding ADC map shows the tumor to have a slightly increased ADC value ($ADC_{min}$ = 1077.7 × $10^{-3}$ $mm^2/s$, rADC = 1.39). *C*, A correlative color CBV image shows moderately elevated perfusion with the calculated $rCBV_{max}$ of 3.04.

**Table 4: Measures of sensitivity, specificity, PPV, NPV, accuracy, and AUC of $ADC_{min}$ values, rADC ratios, and $rCBV_{max}$ ratios for differentiation of hemangioblastomas and brain metastases**

| | TV | Sensitivity | Specificity | PPV | NPV | Accuracy | AUC |
|---|---|---|---|---|---|---|---|
| $ADC_{min}$ | 1.10 | 90.48% | 96.67% | 95.0% | 93.5% | 94.12% | 0.968 |
| rADC | 1.54 | 95.24% | 96.67% | 95.2% | 96.7% | 96.08% | 0.971 |
| $rCBV_{max}$ | 6.59 | 95.24% | 53.33% | 58.8% | 94.1% | 70.59% | 0.756 |

**Note:**—PPV indicates positive predictive value; NPV, negative predictive value; TV, threshold value; AUC, area under the curve.

gioblastomas demonstrated significantly higher $ADC_{min}$ and $rCBV_{max}$ values than those with brain metastases.

Hemangioblastomas typically present in the cerebellar hemisphere and in the third-through-fifth decades of life. Hemangioblastomas have been traditionally described as a marked enhancing mural nodule with a large surrounding cyst. Large draining and feeding vessels within the periphery and solid nodule are commonly seen in hemangioblastomas. Therefore, when MR imaging shows a typically cystic mass with a solid enhancing mural nodule and internal/periphery vessels located in the cerebellum in a younger adult, the most probable diagnosis is hemangioblastoma. These MR imaging features were found in 57.1% of the hemangioblastomas and in only 20% of brain metastases in our study. Whereas when a solitary necrotic tumor with heterogeneous enhancement is found in older adults on the MR images, the most probable diagnosis is brain metastasis. However, when an intense enhancing solid tumor without internal/periphery dilated vessels is demonstrated, as in 42.9% of the hemangioblastomas, there is less certainty as to whether the tumor is a hemangioblastoma or a single brain metastasis. Furthermore, the diagnosis was also confusing when a hemangioblastoma occurred in a 70-year-old patient in our series, whose age favors a diagnosis of brain metastases.

DWI has been widely used to evaluate brain tumors, ischemic stroke, abscesses, and other intracranial diseases and has become an indispensable part of brain MR imaging protocols. ADC values represent the mobility of free water molecules within tissue and appear to be correlated with the tumor cellularity, which might be

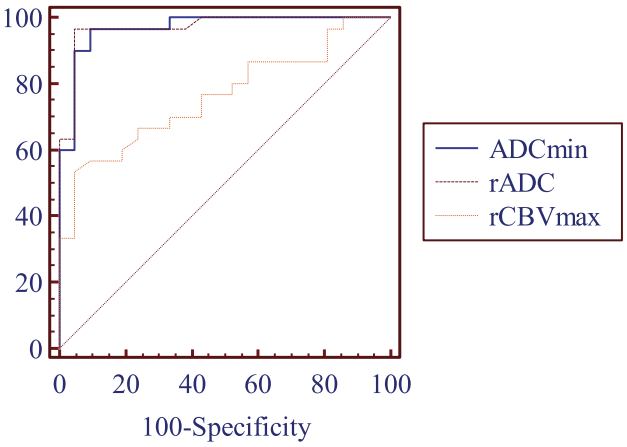


**FIG 3.** Comparison of ROC curves of $ADC_{min}$, rADC, and $rCBV_{max}$ in the contrast-enhancing lesions for differentiating hemangioblastomas from brain metastases.

a useful adjunct in the preoperative management of patients with common brain tumors, including cerebellar tumors. There are few studies in the literature regarding the DWI findings of hemangioblastomas. In a small group study of 22 cerebellar tumors, Quadery and Okamoto[12] reported that the ADC values were increased ($\geq 1.27 \pm 0.14 \times 10^{-3}$ $mm^2/s$) in 10 hemangioblastomas, while other tumors, including 3 metastatic tumors, had lower or similar ADC values compared with those of cerebellar parenchyma (without statistical analysis).[20] In this study, we found that the signal intensity in the solid contrast-enhancing portions of hemangioblastomas tended to be hypointense or isointense relative to normal-appearing white matter on DWI. In addition, they had significantly lower signal intensity than brain metastases. Furthermore, the ADC values of solid contrast-enhancing areas in this study were higher than those of normal brain parenchyma in all hemangioblastomas, consistent with previous findings.[12] To the best of our knowledge, the application of ADC values obtained from DWI in distinguishing hemangioblastomas from brain metastases has not been studied previously. This study also revealed that the rate of water diffusion of hemangioblastomas, as reflected by ADC values, was significantly higher than that of brain metastases ($P < .001$). Several studies have reported that calculated ADC values were inversely related to tumor cellular attenuation and tumor nucleus/cytoplasm ratios in terms of water diffusivity within intracranial tumors.[21,22]

Densely packed tumor cells can inhibit effective movement of free water molecules and can, therefore, restrict diffusion. Low diffusion could translate into high signal intensity on DWI, with low values on ADC maps. Histopathologically, hemangioblastomas are World Health Organization grade I tumors characterized by stromal cells with plump foamy cytoplasm and an abundant capillary network.[20] Lower signal intensity on DWI combined with higher ADC values in hemangioblastomas may reflect the lower cellular attenuation and nucleus/cytoplasm ratios compared with metastatic tumors. Furthermore, high vascular spaces in hemangioblastomas may also result from low signal on DWI with increased ADC values.[12] In a study of 26 metastatic brain lesions, Hayashida et al[23] found that the signal intensity of well-differentiated adenocarcinomas on DWI tended to be significantly lower than that of poorly differentiated adenocarcinomas and lesions other than adenocarcinomas. They reported that the ADC values of the solid portions of brain metastases were correlated with tumor cellularity and that the signal intensity on DWI may predict the histology of brain metastases.[23] Therefore, our findings suggest that preoperative determination of the ADC values of the cerebellar tumors in adults may aid in the differential diagnosis of hemangioblastomas and brain metastases.

rCBV measurement derived from DSC-PWI is a useful parameter to evaluate tumor angiogenesis and to differentiate various types of the brain tumors because it adds functional information not available with conventional MR imaging.[13-15] In vivo measurement of rCBV has been shown to correlate with tumor vascularity and serve as an indicator of tumor grade.[14,24] In addition, rCBV has also been demonstrated to strongly correlate with vascular endothelial growth factor expression in nonenhancing gliomas.[25] A maximum rCBV value of $9.4 \pm 2.37$ or $7.7 \pm 1.0$ for hemangioblastomas has been identified in 2 different studies.[16,26] Hakyemez et al[18] showed that the rCBV ratios of 6 hemangioblastomas were significantly higher than those of 25 brain metastases ($11.4 \pm 4.40$ versus $5.3 \pm 3.22$, $P < .05$). In our group of hemangioblastomas, the $rCBV_{max}$ value calculated from the solid contrast-enhancing portion was $8.5 \pm 2.45$, significantly higher than that of brain metastases ($6.4 \pm 2.0$). The $rCBV_{max}$ value for hemangioblastomas or metastases is in good agreement with values reported previously.[16,18,26]

Hemangioblastomas have abundant tumor vessels within tumors due to overexpression of vascular endothelial growth factor,[20,27] which causes significantly increased rCBV. However, the histopathologic features of brain metastatic tumor vessels have not been established because of a variety of macroscopic and microscopic features connected to the histopathologic characteristics of the primary tumor. Tsougos et al[28] demonstrated that the rCBV value of metastases was $10.80 \pm 5.13$ in a study consisting of 6 lung and 8 breast primary tumors. Gaudino et al[29] showed that the rCBV value in lesions was higher ($3.30 \pm 1.59$) than that of white matter in a series of 59 solitary brain metastases. Our study showed that the rCBV value of brain metastases was $5.3 \pm 3.22$, which is not consistent with that in previous studies, probably due to the heterogeneity of brain metastases of different primary tumors. Thus, brain metastases originating from melanoma or breast carcinoma, which are highly vascular, may present with higher rCBV than those from lung cancer, known to be less vascular.

In this study, the rCBV values in lesions were found to be markedly high (>7.5) in 2 breast carcinomas and 1 melanoma. More defined rCBV values in brain metastases are worth further investigation with larger sample size. Regardless, our results suggest that high $rCBV_{max}$ appears to be indicative of hemangioblastomas, whereas a low $rCBV_{max}$ is suggestive of brain metastases. One could assume that when an intense-enhancing solid tumor in the posterior fossa presents with a marked increase of rCBV, the most probable diagnosis is hemangioblastoma. In this case, preoperative embolization should be considered to control inaccessible arterial supply and reduce the tumor vascularity, which could aid in the resection of the hemangioblastoma. This approach is often used in spinal hemangioblastoma to reduce the

operative complication rates and intraoperative bleeding.[9,30,31] Therefore, DSC-PWI may be helpful for both accurate preoperative diagnosis of hemangioblastomas and postembolization follow-up.

All 3 MR imaging parameters were significant for contrast-enhancing tumoral regions to differentiate hemangioblastomas from brain metastases. However, from the ROC analysis, the sensitivity, specificity, and accuracy levels were significantly higher for diffusion parameters (accuracy for rADC, 96.08%) than for perfusion parameters (accuracy for $rCBV_{max}$, 70.59%). In addition, there was moderate overlap of the $rCBV_{max}$ parameter for differentiating hemangioblastomas and brain metastases, with a specificity of only 53.33%. Thus, this study indicated that rADC is a robust parameter with high sensitivity (95.24%) and specificity (96.67%), which may be helpful in differentiating hemangioblastomas from brain metastases. As a part of a multiparametric MR imaging protocol, MR spectroscopy may allow further characterization of intracranial tumor by providing metabolic information about the tumor tissue.[32,33] It has been widely reported that Cho levels correlate with the degree of malignancy in brain tumor and are linearly correlated with cell density.[33] To our knowledge, no study has evaluated the ability of MR spectroscopy in the differentiation of hemangioblastomas from brain metastases.

There are some limitations to our study. The most significant one was its retrospective nature, which may have led to bias in case selection. Another potential limitation was that the number of the metastatic tumors originating from primary sites other than lung were few. Further prospective studies with a larger number of metastatic tumors are required. Third, we could not exclude the presence of tiny intratumoral hemorrhage within lesions that may result in susceptibility blooming, and in turn interfere with DWI and PWI evaluation, though there was no obvious evidence of hemorrhage on conventional MR imaging and DWI. It is also recognized that the lack of a susceptibility sequence in the MR imaging protocol was also a limitation because that would have been helpful in excluding hemorrhagic metastasis.

## CONCLUSIONS

This study demonstrates that DWI and DSC-PWI MR imaging measurements in the contrast-enhancing tumoral region allow differentiation of hemangioblastomas from brain metastases. On DWI, higher rADC and $ADC_{min}$ values in hemangioblastomas than in the brain metastases were the most consistent finding in our study. Therefore, DWI appears to be an efficient MR imaging technique for the possible differentiation of hemangioblastomas from brain metastases.

## REFERENCES


1. Louis DN, Ohgaki H, Wiestler OD, et al. **The 2007 WHO classification of tumours of the central nervous system.** *Acta Neuropathol* 2007;114:97–109 CrossRef Medline
2. Young S, Richardson AE. **Solid haemangioblastomas of the posterior fossa: radiological features and results of surgery.** *J Neurol Neurosurg Psychiatry* 1987;50:155–58 CrossRef Medline
3. Yoshida S, Takahashi H. **Cerebellar metastases in patients with cancer.** *Surg Neurol* 2009;71:184–87; discussion 187 CrossRef Medline
4. Kanner AA, Suh JH, Siomin VE, et al. **Posterior fossa metastases: aggressive treatment improves survival.** *Stereotact Funct Neurosurg* 2003;81:18–23 CrossRef Medline
5. Alexandru D, Bota DA, Linskey ME. **Epidemiology of central nervous system metastases.** *Prog Neurol Surg* 2012;25:13–29 CrossRef Medline
6. Bründl E, Schödel P, Ullrich OW, et al. **Surgical resection of sporadic and hereditary hemangioblastoma: our 10-year experience and a literature review.** *Surg Neurol Int* 2014;5:138 CrossRef Medline
7. Tabei Y, Miyamoto S, Suzuki I. **Multidisciplinary approach to management of patients with brain metastases** [in Japanese]. *Gan To Kagaku Ryoho* 2013;40:1288–94 Medline
8. Le Reste PJ, Henaux PL, Morandi X, et al. **Sporadic intracranial haemangioblastomas: surgical outcome in a single institution series.** *Acta Neurochir (Wien)* 2013;155:1003–09; discussion 1009 CrossRef Medline
9. Sakamoto N, Ishikawa E, Nakai Y, et al. **Preoperative endovascular embolization for hemangioblastoma in the posterior fossa.** *Neurol Med Chir (Tokyo)* 2012;52:878–84 CrossRef Medline
10. Schaefer PW, Grant PE, Gonzalez RG. **Diffusion-weighted MR imaging of the brain.** *Radiology* 2000;217:331–45 CrossRef Medline
11. Kang Y, Choi SH, Kim YJ, et al. **Gliomas: histogram analysis of apparent diffusion coefficient maps with standard- or high-b-value diffusion-weighted MR imaging–correlation with tumor grade.** *Radiology* 2011;261:882–90 CrossRef Medline
12. Quadery FA, Okamoto K. **Diffusion-weighted MRI of haemangioblastomas and other cerebellar tumours.** *Neuroradiology* 2003;45:212–19 Medline
13. Kickingereder P, Wiestler B, Sahm F, et al. **Primary central nervous system lymphoma and atypical glioblastoma: multiparametric differentiation by using diffusion-, perfusion-, and susceptibility-weighted MR imaging.** *Radiology* 2014;272:843–50 CrossRef Medline
14. Guzmán-De-Villoria JA, Mateos-Pérez JM, Fernández-García P, et al. **Added value of advanced over conventional magnetic resonance imaging in grading gliomas and other primary brain tumors.** *Cancer Imaging* 2014;14:35 CrossRef Medline
15. Ho CY, Cardinal JS, Kamer AP, et al. **Relative cerebral blood volume from dynamic susceptibility contrast perfusion in the grading of pediatric primary brain tumors.** *Neuroradiology* 2015;57:299–306 CrossRef Medline
16. Kumar VA, Knopp EA, Zagzag D. **Magnetic resonance dynamic susceptibility-weighted contrast-enhanced perfusion imaging in the diagnosis of posterior fossa hemangioblastomas and pilocytic astrocytomas: initial results.** *J Comput Assist Tomogr* 2010;34:825–29 CrossRef Medline
17. She DJ, Xing Z, Zeng Z, et al. **Differentiation of hemangioblastomas from pilocytic astrocytomas using 3-T magnetic resonance perfusion-weighted imaging and MR spectroscopy.** *Neuroradiology* 2015;57:275–81 CrossRef Medline
18. Hakyemez B, Erdogan C, Bolca N, et al. **Evaluation of different cerebral mass lesions by perfusion-weighted MR imaging.** *J Magn Reson Imaging* 2006;24:817–24 CrossRef Medline
19. Wetzel SG, Cha S, Johnson G, et al. **Relative cerebral blood volume measurements in intracranial mass lesions: interobserver and intraobserver reproducibility study.** *Radiology* 2002;224:797–803 CrossRef Medline
20. Cuccurullo L, Prudente ME, Maffia S, et al. **An ultrastructural study of the histogenesis of haemangioblastoma.** *Pathologica* 2009;101:1–5 Medline
21. Guo AC, Cummings TJ, Dash RC, et al. **Lymphomas and high-grade astrocytomas: comparison of water diffusibility and histologic characteristics.** *Radiology* 2002;224:177–83 CrossRef Medline
22. Barajas RF Jr, Rubenstein JL, Chang JS, et al. **Diffusion-weighted MR imaging derived apparent diffusion coefficient is predictive of clinical outcome in primary central nervous system lymphoma.** *AJNR Am J Neuroradiol* 2010;31:60–66 CrossRef Medline
23. Hayashida Y, Hirai T, Morishita S, et al. **Diffusion-weighted imaging of metastatic brain tumors: comparison with histologic type and tumor cellularity.** *AJNR Am J Neuroradiol* 2006;27:1419–25 Medline
24. Jain R, Gutierrez J, Narang J, et al. **In vivo correlation of tumor blood volume and permeability with histologic and molecular angiogenic**

**markers in gliomas.** *AJNR Am J Neuroradiol* 2011;32:388–94 CrossRef Medline
25. Maia AC Jr, Malheiros SM, da Rocha AJ, et al. **MR cerebral blood volume maps correlated with vascular endothelial growth factor expression and tumor grade in nonenhancing gliomas.** *AJNR Am J Neuroradiol* 2005;26:777–83 Medline
26. Bing F, Kremer S, Lamalle L, et al. **Value of perfusion MRI in the study of pilocytic astrocytoma and hemangioblastoma: preliminary findings** [in French]. *J Neuroradiol* 2009;36:82–87 CrossRef Medline
27. Hussein MR. **Central nervous system capillary haemangioblastoma: the pathologist's viewpoint.** *Int J Exp Pathol* 2007;88:311–24 CrossRef Medline
28. Tsougos I, Svolos P, Kousi E, et al. **Differentiation of glioblastoma multiforme from metastatic brain tumor using proton magnetic resonance spectroscopy, diffusion and perfusion metrics at 3 T.** *Cancer Imaging* 2012;12:423–36 CrossRef Medline
29. Gaudino S, Di Lella GM, Russo R, et al. **Magnetic resonance imaging of solitary brain metastases: main findings of nonmorphological sequences.** *Radiol Med* 2012;117:1225–41 CrossRef Medline
30. Biondi A, Ricciardi GK, Faillot T, et al. **Hemangioblastomas of the lower spinal region: report of four cases with preoperative embolization and review of the literature.** *AJNR Am J Neuroradiol* 2005;26:936–45 Medline
31. Chu BC, Terae S, Hida K, et al. **MR findings in spinal hemangioblastoma: correlation with symptoms and with angiographic and surgical findings.** *AJNR Am J Neuroradiol* 2001;22:206–17 Medline
32. Horská A, Barker PB. **Imaging of brain tumors: MR spectroscopy and metabolic imaging.** *Neuroimaging Clin N Am* 2010;20:293–310 CrossRef Medline
33. Brandão LA, Castillo M. **Adult brain tumors: clinical applications of magnetic resonance spectroscopy.** *Neuroimaging Clin N Am* 2013;23:527–55 CrossRef Medline

# Shear Stiffness of 4 Common Intracranial Tumors Measured Using MR Elastography: Comparison with Intraoperative Consistency Grading

N. Sakai, Y. Takehara, S. Yamashita, N. Ohishi, H. Kawaji, T. Sameshima, S. Baba, H. Sakahara, and H. Namba

## ABSTRACT

**BACKGROUND AND PURPOSE:** The stiffness of intracranial tumors affects the outcome of tumor removal. We evaluated the stiffness of 4 common intracranial tumors by using MR elastography and tested whether MR elastography had the potential to discriminate firm tumors preoperatively.

**MATERIALS AND METHODS:** Thirty-four patients with meningiomas, pituitary adenomas, vestibular schwannomas, and gliomas scheduled for resection were recruited for MR elastography. On the elastogram, the mean and the maximum shear stiffnesses were measured by placing an ROI on the tumor. Blinded to the MR elastography findings, surgeons conducted qualitative intraoperative assessment of tumor consistency by using a 5-point scale. Histopathologic diagnosis was confirmed by using the resected specimens. The mean and maximum shear stiffnesses were compared with histopathologic subtypes, and the intraoperative tumor consistency was graded by the surgeons.

**RESULTS:** The mean and maximum shear stiffnesses were the following: 1.9 ± 0.8 kPa and 3.4 ± 1.5 kPa for meningiomas, 1.2 ± 0.3 kPa and 1.8 ± 0.5 kPa for pituitary adenomas, 2.0 ± 0.4 kPa and 2.7 ± 0.8 kPa for vestibular schwannomas, and 1.5 ± 0.2 kPa and 2.7 ± 0.8 kPa for gliomas. The mean and maximum shear stiffnesses for meningiomas were higher than those of pituitary adenomas ($P < .05$). The mean and maximum shear stiffnesses were significantly correlated with the surgeon's qualitative assessment of tumor consistency ($P < .05$). The maximum shear stiffness for 5 firm tumors was higher than that of nonfirm tumors ($P < .05$).

**CONCLUSIONS:** MR elastography could evaluate intracranial tumors on the basis of their physical property of shear stiffness. MR elastography may be useful in discriminating firm tumors preoperatively.

**ABBREVIATIONS:** MRE = MR elastography; MEG = motion-encoding gradient; $_{max}$SS = maximum shear stiffness; $_{mean}$SS = mean shear stiffness

Many histopathologic processes in tumors, for example cell proliferation, angiogenesis, fibrosis, calcification, necrosis, and cyst formation, cause marked changes in the viscoelastic properties of tissue. Therefore, physicians have used palpation of the body to detect tumors in daily clinical settings. Regarding intracranial tumors, however, there is no clinical precedent for tumor stiffness. Only neurosurgeons have had the privilege of palpating intracranial tumors at the time of tumor resection. The degree of tumor stiffness or consistency is critical information for precise neurosurgical resection of intracranial tumors such as meningiomas, pituitary adenomas, and vestibular schwannomas, especially those surrounded by important neurovascular structures. Differences in histopathologic characteristics, namely meningothelial-versus-fibrous meningiomas, fibrous-versus-nonfibrous pituitary adenomas, Antoni A- versus Antoni B-dominant schwannomas, and high- versus-low-grade gliomas, might be correlated to the viscoelastic properties of intracranial tumors. Although conventional MR imaging and some other MR imaging sequences have been reported capable of predicting intracranial tumor consistency or fibrosis, they have not been used to directly assess the viscoelastic properties of tumors.[1-3]

MR elastography (MRE) is an emerging technology enabling the noninvasive assessment of the viscoelastic properties of tissues in vivo.[4,5] MRE uses continuous shear waves generated by an extracorporeal mechanical wave driver, imaging the propagating shear waves with a phase-contrast MR

Received August 6, 2015; accepted after revision April 11, 2016.

From the Departments of Neurosurgery (N.S., H.K., T.S., H.N.), Radiology (Y.T., N.O.), Diagnostic Radiology and Nuclear Medicine (S.Y., H.S.), and Diagnostic Pathology (S.B.), Hamamatsu University Hospital, Hamamatsu, Japan.

Naoto Sakai and Yasuo Takehara contributed equally to this study.

Please address correspondence to Naoto Sakai, MD, PhD, Department of Neurosurgery, Hamamatsu University School of Medicine, 1-20-1, Handayama, Higashi-ku, Hamamatsu 431-3192, Japan; e-mail: nsakaineurosurg@gmail.com

Indicates open access to non-subscribers at www.ajnr.org

http://dx.doi.org/10.3174/ajnr.A4832

image, and processing the wave images with an inversion algorithm to obtain a quantitative cross-sectional image of the shear stiffness map known as an elastogram.[6] Since its first description by Muthupillai et al in 1995,[4] many clinical applications have been studied, especially for assessing liver disease. Multiple studies have demonstrated a strong correlation between MRE-measured hepatic stiffness and the stage of fibrosis at histology. MRE can serve as a more accurate alternative to invasive biopsy, which has been the criterion standard for the diagnosis and staging of liver fibrosis.[7] Although MRE is not common in a neurologic setting, a series of attempts have been made to measure the stiffness of the brain affected by Alzheimer disease,[8,9] multiple sclerosis,[10] and normal-pressure hydrocephalus.[11,12] As for intracranial tumors, only a few studies involving meningiomas and glioblastomas have been published.[13,14] In these studies, a correlation between histopathologic characteristics and MRE has not been described in detail. The purposes of the present study were the following: 1) to evaluate tumor stiffness by using MRE in relation to the histopathology, and 2) to test whether MRE has the potential to discriminate firm tumor preoperatively.

## MATERIALS AND METHODS

### Ethics

Written informed consent was obtained from all patients in our institutional review board–approved study.

### Patients

Between September 2014 and June 2015, MR imaging examinations, including MRE, were performed on 34 consecutive patients (11 men and 23 women; mean age, 54 years; range, 31–77 years) scheduled for resection with previously identified meningiomas, pituitary adenomas, vestibular schwannomas, and gliomas by using conventional MR imaging with contrast. All patients underwent microscopic surgery performed by experienced neurosurgeons at our university hospital. Blinded to the MRE results, surgeons graded tumor stiffness at the time of resection. The dominant tissue consistency was graded by using a 5-point scale previously reported by Murphy et al[13] as follows: 1, soft; 2, mostly soft; 3, intermediate; 4, mostly firm (at least 75%–80% of the tumor was firm and required ultrasonic aspiration at a high setting); and 5, firm (most of the tumor required ultrasonic aspiration at a maximum setting). We used an ultrasonic aspirator (Sonopet Ultrasonic Aspirator; Stryker, Kalamazoo, Michigan) when we could not resect tumors by using an air suction tube. In this study, tumors on the scale of 4 and 5 were defined as "firm," and tumors on the scale of 1–3 were defined as "nonfirm" by surgeons. All surgical procedures were recorded by using a digital video recorder (DATA Gen Pro; Seventh Dimension Design, Hyogo, Japan) and were reviewed for this assessment.

### MR Elastography

MRE was performed by using a 3T clinical unit (Discovery MR750W; GE Healthcare, Milwaukee, Wisconsin) with a 12-channel phased array Neurovascular Array Coil (Medrad, Indianola, Pennsylvania). A passive pneumatic driver with a diameter of 19 cm was positioned underneath the occipital portion of the head. Shear waves were introduced in the brain by using the MR Touch system (GE Healthcare) (Fig 1). The imaging parameters for spin-echo echo-planar imaging–based MRE were as follows: TR, 1000 ms; TE, 86.4 ms; FOV, 24 cm; bandwidth, ± 250 kHz; 64 × 64 matrix (256 × 256 reconstruction matrix with zero-filled interpolation); and section

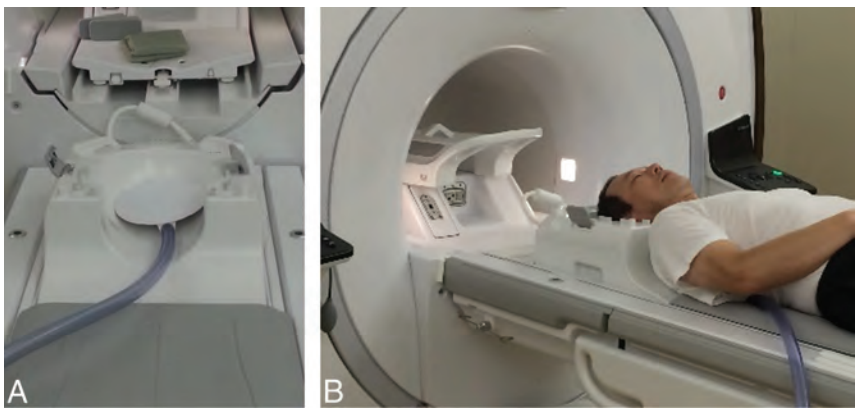


**FIG 1.** A passive pneumatic driver (MR Touch; GE Healthcare) was placed in a 12-channel phased array Neurovascular Array Coil (*A*). Shear waves were introduced in the brain by using this system (*B*).

**Table 1: Summary of patient histopathologic characteristics: meningiomas (13 cases)**

| Age (yr)/Sex | Location | Size (mm) | Mean Shear Stiffness (kPa) | Maximum Shear Stiffness (kPa) | Intraoperative Tumor Consistency; Scale 1~5 | Histopathologic Subtypes |
|---|---|---|---|---|---|---|
| 44/F | Parasagittal | 46 | 2.1 | 4.7 | 3 (not firm) | Meningothelial meningioma |
| 57/M | Tuberculum sellar | 53 | 1.6 | 3.0 | 3 (not firm) | Meningothelial meningioma |
| 68/M | Parasagittal | 94 | 1.6 | 3.3 | 3 (not firm) | Anaplastic meningioma |
| 67/F | Convexity | 66 | 1.4 | 4.1 | 4 (firm) | Atypical meningioma |
| 50/F | Parasagittal | 23 | 2.2 | 3.8 | 5 (firm) | Transitional meningioma |
| 40/F | Cavernous sinus | 35 | 2.6 | 4.7 | 3 (not firm) | Meningothelial meningioma |
| 52/F | Convexity | 52 | 1.7 | 2.5 | 3 (not firm) | Atypical meningioma |
| 58/F | Petroclival | 20 | 1.2 | 1.6 | 3 (not firm) | Meningothelial meningioma |
| 51/F | Sphenoid ridge | 28 | 1.8 | 2.4 | 3 (not firm) | Meningothelial meningioma |
| 66/F | CP angle | 51 | 4.4 | 7.2 | 4 (firm) | Fibrous meningioma |
| 38/F | Tuberculum sellar | 14 | 1.7 | 2.3 | 2 (not firm) | Meningothelial meningioma |
| 38/F | Petroclival | 23 | 1.2 | 1.8 | 2 (not firm) | Angiomatous meningioma |
| 77/M | Convexity | 25 | 1.7 | 2.6 | 2 (not firm) | Meningothelial meningioma |

**Note:**—CP indicates cerebellopontine.

thickness, 5 mm. These acquisitions were performed with a single-shot, 1-signal average, 8 MRE time points, 10–13 sections, MRE motion-encoding in the through-plane direction; and no flow compensation or spatial presaturation. Parallel imaging (array spatial sensitivity encoding technique) was used with a reduction factor of 2. To optimize the motion-encoding gradient (MEG) frequency and the external driver frequency, we tested various MEG frequencies from 40- to 120-Hz and from 40- to 120-Hz driver frequencies at every 20 Hz, otherwise under the same imaging conditions, on a healthy volunteer before commencement of this study. The images generated by using MRE included wave images, depicting the tissue motion, and stiffness images (elastograms).

The criteria for optimization were the presence of noninterfering parallel waves in the wave images, homogeneity of the stiffness distributions for the white matter of the cerebral and the cerebellar hemispheres, and the image signal-to-noise ratio. The previously reported stiffness values for normal white and gray matter were also compared with the measured values from the stiffness map. The red and blue stripes on the wave images show the mechanical waves propagating within the brain. The deepness of the colors reflects the wave amplitude, and their width indicates the wavelength. A longer wavelength reflects faster wave propagation in the media, which indicates higher elasticity of the tissue. The wave information is processed to produce 2D color-coded elastograms and 2D quantitative gray-scale elastograms. ROIs can be drawn on the gray-scale elastograms to measure the elasticity (typically reported in kilopascals). A cross-hatching pattern superimposed on the elastograms indicates less reliable areas for measurement of the elasticity based on the wave amplitude, the pattern of the waves in the wave images, and the signal-to-noise ratio of the magnitude images.

In this study, elastograms were qualitatively assessed for the degree of image quality, such as the extent of signal loss, and quantitatively for the areas without cross-hatches. After determining the optimal motion-encoding gradient frequency, we also examined the external driver amplitudes, namely 50% versus 70%. As a result, an MEG of 60 Hz, an external driver frequency of 40 Hz, and an amplitude of 50% were determined to be optimal in this settings. The choice of motion and MEG frequencies was determined subjectively during this optimization process. The acquisition time for MRE was 50 seconds at most.

### *Conventional MR Imaging*

Conventional MR imaging with contrast media and arterial spin-labeled perfusion imaging were also performed in the current study to correctly demarcate the tumor area, which became the reference when ROI placement on the elastogram was performed. The imaging parameters have been described previously.[14-18]

### *Stiffness Measurement on MR Elastogram*

The signal intensity reflects the stiffness on each elastogram. For the measurement of tumor stiffness, the largest possible ROI was placed on the tumors by avoiding the interference fringes on the wave image and cross-hatches on the stiffness map. The mean shear stiffness ($_{mean}$SS) and the maximum shear stiffness ($_{max}$SS) were measured in kilopascals. Because the anatomic boundary of the tumor was difficult to discern on the stiffness map alone, T2-weighted axial images, fat saturated T1-weighted images obtained pre- and postcontrast administration, and the axial diffusion-weighted image of the corresponding sections with the stiffness map of the corresponding section were also simultaneously displayed. ROIs ranging from 79 to 1874 pixels were drawn freehand on the workstation display. If the tumor was partially covered by cross-hatches, lesion stiffness in the area without cross-hatches was measured. The measurements were repeated twice for each region, and the values were averaged.

**Table 2: Pituitary adenomas (11 cases)**

| Age (yr)/Sex | Endocrinologic Subtypes | Size (mm) | Mean Shear Stiffness (kPa) | Maximum Shear Stiffness (kPa) | Intraoperative Tumor Consistency; Scale 1~5 |
|---|---|---|---|---|---|
| 71/F | Nonfunctioning | 22 | 1.4 | 2.0 | 1 (not firm) |
| 40/F | GH producing | 27 | 1.0 | 1.7 | 1 (not firm) |
| 47/F | Nonfunctioning | 40 | 1.1 | 1.7 | 1 (not firm) |
| 38/M | Nonfunctioning | 34 | 1.4 | 2.0 | 1 (not firm) |
| 31/F | GH producing | 17 | 1.3 | 1.8 | 1 (not firm) |
| 41/F | FSH producing | 17 | 0.9 | 1.1 | 1 (not firm) |
| 57/F | Nonfunctioning | 58 | 1.6 | 2.5 | 2 (not firm) |
| 45/M | Nonfunctioning | 24 | 0.6 | 0.8 | 1 (not firm) |
| 71/M | Nonfunctioning | 39 | 1.0 | 1.6 | 3 (not firm) |
| 63/F | Nonfunctioning | 22 | 1.6 | 2.1 | 4 (firm) |
| 38/F | Nonfunctioning | 27 | 1.6 | 2.0 | 3 (not firm) |

**Note:**—GH indicates growth hormone; FSH, follicle-stimulating hormone.

**Table 3: Vestibular schwannomas (6 cases)**

| Age (yr)/Sex | Size (mm) | Mean Shear Stiffness (kPa) | Maximum Shear Stiffness (kPa) | Intraoperative Tumor Consistency; Scale 1~5 |
|---|---|---|---|---|
| 57/F | 28 | 1.7 | 2.5 | 2 (not firm) |
| 50/F | 33 | 2.5 | 3.3 | 3 (not firm) |
| 46/F | 16 | 1.6 | 2.0 | 3 (not firm) |
| 77/F | 24 | 2.2 | 3.2 | 3 (not firm) |
| 50/M | 21 | 1.5 | 1.7 | 2 (not firm) |
| 43/M | 34 | 2.2 | 3.7 | 4 (firm) |

**Table 4: Gliomas (4 cases)**

| Age (yr)/Sex | Location | Size (mm) | Mean Shear Stiffness (kPa) | Maximum Shear Stiffness (kPa) | Intraoperative Tumor Consistency; Scale 1~5 | Histopathologic Subtypes |
|---|---|---|---|---|---|---|
| 75/M | Frontal lobe | 32 | 1.2 | 2.4 | 1 (not firm) | Anaplastic astrocytoma |
| 77/M | Cerebellum | 22 | 1.7 | 2.3 | 1 (not firm) | Glioblastoma |
| 36/M | Frontal lobe | 65 | 1.4 | 3.8 | 2 (not firm) | Glioblastoma |
| 61/F | Insula | 55 | 1.5 | 2.2 | 3 (not firm) | Glioblastoma |

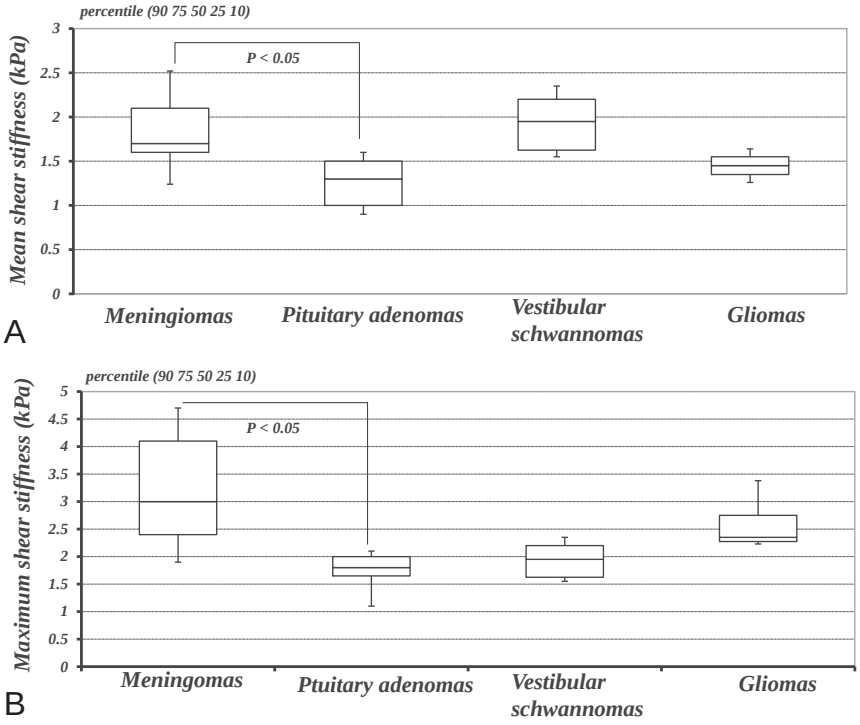


**FIG 2.** Comparison of the $_{mean}$SS and $_{max}$SS determined by using MRE among histopathologically variable intracranial tumors: 13 cases of meningiomas ($_{mean}$SS = 1.9 ± 0.8 kPa, $_{max}$SS = 3.4 ± 1.5 kPa), 11 cases of pituitary adenomas ($_{mean}$SS = 1.2 ± 0.3 kPa, $_{max}$SS = 1.8 ± 0.5 kPa), 6 cases of vestibular schwannomas ($_{mean}$SS = 2.0 ± 0.4 kPa, $_{max}$SS = 2.7 ± 0.8 kPa), and 4 cases of gliomas ($_{mean}$SS = 1.5 ± 0.2 kPa, $_{max}$SS = 2.7 ± 0.8 kPa). The $_{mean}$SS and $_{max}$SS of meningiomas were higher than those of the pituitary adenomas ($P < .05$). Box-and-whisker plots show the $_{mean}$SS (*A*) and $_{max}$SS (*B*). The lower and upper hinges of the boxes denote the 25th and 75th percentiles, respectively. The median (50th percentile) of each distribution is indicated by the line. The whiskers on each side denote the 10th and 90th percentiles.

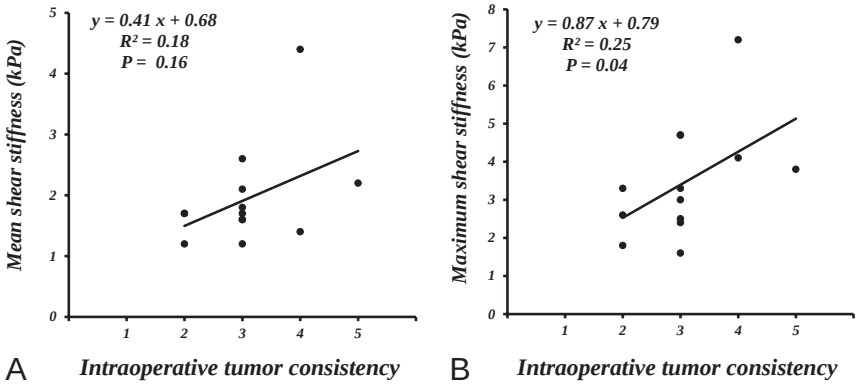


**FIG 3.** Scatterplot of the $_{mean}$SS and $_{max}$SS (kPa) determined by using MRE and a 5-point scale of intraoperative qualitative assessment of tumor consistency in 13 patients with meningiomas. Although the $_{mean}$SS did not significantly correlate with the grading (*A*), significant correlations between the $_{max}$SS and the grading were obtained (*B*) ($P < .05$) (Spearman rank order test).

### *Histopathologic Evaluation*

Sections were stained with hematoxylin-eosin for routine histopathology. Immunohistochemical stains were also used for the following: epithelial membrane antigen and vimentin for meningiomas; adenocorticotrophic hormone, prolactin, growth hormone, luteinizing hormone, follicle-stimulating hormone, thyroid-stimulating hormone, and cytokeratin CAM5.2 for pituitary adenomas; S-100 for vestibular schwannomas; and glial fibrillary acidic protein, oligodendrocyte transcription factor (Olig2), anti-*O6-methylguanine methyltransferase*, isocitrate dehydrogenase 1, and p53 for gliomas. Additionally, Ki-67 was examined for all samples. On the basis of the results, an experienced pathologist (S.B.) determined the histopathologic diagnosis.

### *Statistical Analysis*

The $_{mean}$SS and $_{max}$SS were compared among meningiomas, pituitary adenomas, vestibular schwannomas, and gliomas by using the Kruskal-Wallis H test following the Mann-Whitney *U* test with Bonferroni correction. The correlations between the $_{mean}$SS and $_{max}$SS and a 5-point scale of intraoperative tumor consistency were examined by using the Spearman rank order test. The $_{mean}$SS and $_{max}$SS were compared between the intraoperative firm tumors (intraoperative consistency scale, 4 and 5) and those that were nonfirm (intraoperative consistency scale, 1~3) by using the Mann-Whitney *U* test. Probability values of $<.05$ were considered significant. For the statistical analysis, the freely available software EZR (Saitama Medical Center, Jichi Medical University; http://www.jichi.ac.jp/saitama-sct/SaitamaHP.files/statmed.html) was used.

## RESULTS

The patient characteristics, tumor location, size, mean and maximum tumor shear stiffness assessed by using MRE, and the intraoperative tumor consistency in 34 patients are summarized by histopathologic subtypes in Tables 1–4.

The mean $_{mean}$SS and $_{max}$SS were as follows: 1.9 ± 0.8 kPa and 3.4 ± 1.5 kPa, respectively, for 13 patients with meningiomas; 1.2 ± 0.3 kPa and 1.8 ± 0.5 kPa, respectively, for 11 patients with pituitary adenomas; 2.0 ± 0.4 kPa and 2.7 ± 0.8 kPa, respectively, for 6 patients with vestibular schwannomas; and 1.5 ± 0.2 kPa and 2.7 ± 0.8 kPa, respectively, for 4 patients with gliomas. The $_{mean}$SS and $_{max}$SS of meningiomas were higher than those of pituitary adenomas ($P < .05$) (the Kruskal-Wallis H test following the Mann-Whitney *U* test with Bonferroni correction) (Fig 2). Although the $_{mean}$SS of meningiomas did not significantly correlate with the intraoperative grading (Fig 2*A*), significant correlations between the $_{max}$SS and the surgeon's qualitative assessment of tumor consistency were obtained ($P < .05$) (Spearman rank order test) (Fig 3). Regarding all intracranial tumors, both the $_{mean}$SS and $_{max}$SS

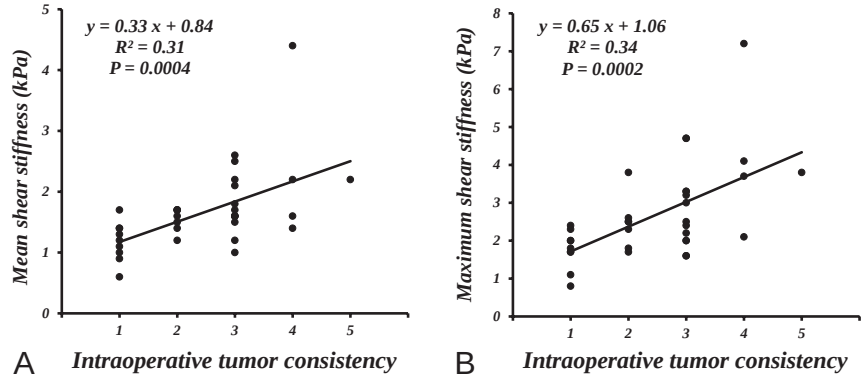


**FIG 4.** Scatterplot of the $_{mean}$SS and $_{max}$SS (kPa) determined by using MRE and a 5-point scale of intraoperative qualitative assessment of tumor consistency in 34 patients with 4 common intracranial tumors. Both the $_{mean}$SS and $_{max}$SS were significantly correlated with the surgeon's grading ($P < .05$) (Spearman rank order test).

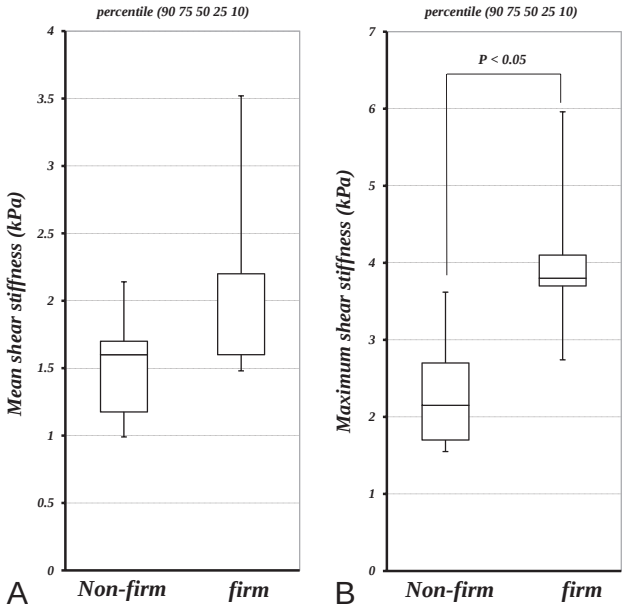


**FIG 5.** Comparison of the $_{mean}$SS and $_{max}$SS was determined by using MRE among tumors with an intraoperative consistency scale of 1–3 that were nonfirm and those with a scale of 4 and 5 that were firm; there were 29 cases that were nonfirm ($_{mean}$SS = 1.6 ± 2.6 kPa; $_{max}$SS = 2.4 ± 1.2 kPa) and 5 cases that were firm ($_{mean}$SS = 3.0 ± 2.6 kPa; $_{max}$SS = 4.2 ± 1.9 kPa). The $_{max}$SS values in firm tumors were higher than those in nonfirm tumors ($P < .05$; Mann-Whitney *U* test). Box-and-whisker plots show the $_{mean}$SS (*A*) and $_{max}$SS (*B*). The lower and upper hinges of the boxes denote the 25th and 75th percentiles, respectively. The median (50th percentile) of each distribution is indicated by the line. Whiskers on each side denote the 10th and 90th percentiles.

significantly correlated with the surgeon's grading ($P < .05$) (Spearman rank order test) (Fig 4). In this study, 29 cases were nonfirm (intraoperative consistency scale, 1~3), whereas 5 tumors were firm (intraoperative consistency scale, 4 and 5), requiring ultrasonic aspiration at high settings. The $_{mean}$SS and $_{max}$SS of tumors that were not firm were 1.6 ± 2.6 kPa and 2.4 ± 1.2 kPa, respectively. The $_{mean}$SS and $_{max}$SS of tumors that were firm were 3.0 ± 2.6 kPa and 4.2 ± 1.9 kPa, respectively. Although the $_{mean}$SS for the firm tumors was not significantly higher than that of tumors that were not firm, the $_{max}$SS for the firm tumors was significantly higher than that of tumors that were not firm ($P < .05$, the Mann-Whitney *U* test) (Fig 5).

Representative cases of a meningioma (case 44/female, right parasagittal meningothelial meningioma), a pituitary adenoma (case 41/female, follicle-stimulating hormone–producing adenoma), a vestibular schwannoma (case 51/male, left cerebellopontine angle), and a glioma (case 61/female, right insular glioblastoma) involving contrast-enhanced T1-weighted and T2-weighted MRI, wave MRE images, elastograms, and hematoxylin-eosin–stained sections (original magnification, ×100) are shown in Fig 6. Representative cases of firm tumors (case 51/male, left cerebellopontine angle fibrous meningioma; case 63/female, recurrent fibrous nonfunctioning pituitary adenoma) involving contrast-enhanced T1-weighted and T2-weighted MRI, wave MRE images, elastograms, and hematoxylin-eosin–stained sections (original magnification, ×100) are shown in Fig 7.

## DISCUSSION

In this study, we measured the shear stiffness of 4 major intracranial tumors, namely meningiomas, pituitary adenomas, vestibular schwannomas, and gliomas by using MRE. Murphy et al[13] reported the stiffness of meningiomas. Regarding pituitary adenomas and vestibular schwannomas, this is the first study to describe the direct measurement of shear stiffness by using MRE, to our knowledge. In relation to gliomas, Streitberger et al[14] reported that the mean shear stiffness of glioblastomas in 22 patients was 1.32 ± 0.26 kPa; although the number of our glioma cases was small, the mean value of the shear stiffness was similar to their results. A significant difference was observed between the shear stiffness of meningiomas and that of pituitary adenomas. The result was compatible with our intraoperative impression of the consistency of these tumors during excision.

We have evaluated the dominant tissue consistency at tumor resection by using a 5-point scale as previously reported by Murphy et al.[13] They found that the relative shear stiffness assessed by using MRE in meningiomas (13 cases) was significantly correlated with the 5-point scale. Although we could not reveal a significant correlation between the $_{mean}$SS and the grading, we have demonstrated the significant correlation between the $_{max}$SS and our stiffness grading. We presume that this was partially the result of the surgeon's judgment of tumor stiffness, in which the scoring tended to be dependent on the hardest portions. It is also presumed that the statistical significance was affected by our coarse spatial resolution, which averaged the stiffness of the tissue. Therefore, the maximum average stiffness result became significant, but the average stiffness was not the result of further averaging.

We also demonstrated significant correlation for both the

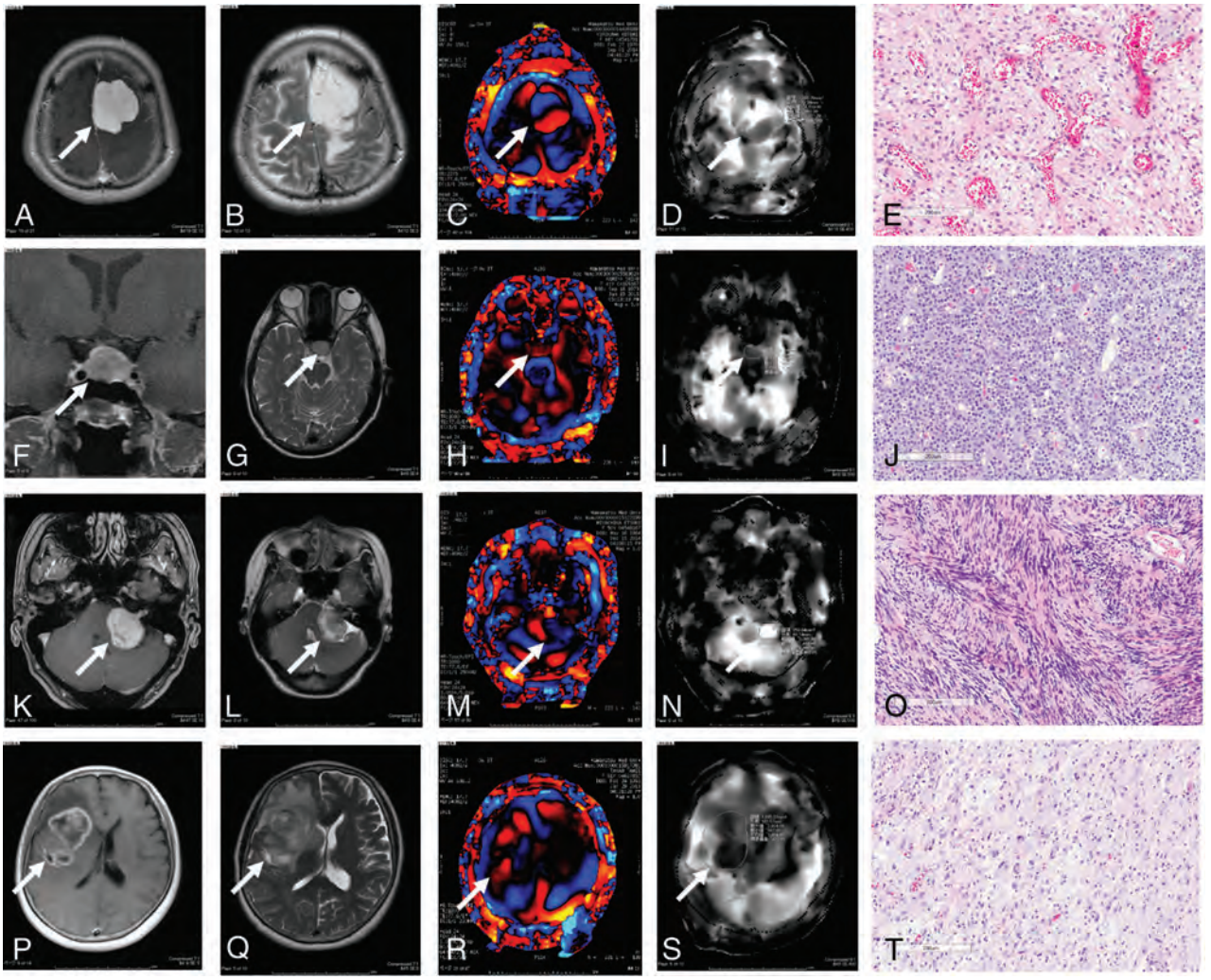


**FIG 6.** Upper: Left parasagittal meningioma in a 44-year-old woman. *A*, Axial postcontrast T1-weighted MR imaging shows a strongly enhanced tumor (*arrow*). *B*, Axial T2-weighted MR imaging shows a hyperintense tumor (*arrow*). *C*, Wave MRE image (*arrow*). *D*, Elastogram shows tumor shear stiffness (*arrow*) ($_{mean}$SS = 2.1 kPa; $_{max}$SS = 4.7 kPa). The intraoperative tumor consistency was intermediate (scale 3). *E*, Histopathologic examination of the resected tumor indicates meningothelial meningioma (hematoxylin-eosin stain; scale bar, 200 $\mu$m). Upper middle: follicle-stimulating hormone–producing adenoma in a 41-year-old woman. *F*, Axial postcontrast T1-weighted MR imaging shows a weakly enhanced tumor (*arrow*). G, Axial T2-weighted MR imaging shows an isointense tumor (*arrow*). *H*, Wave MRE image (*arrow*). *I*, Elastogram shows tumor shear stiffness (*arrow*) ($_{mean}$SS = 0.9 kPa; $_{max}$SS = 1.1 kPa). The intraoperative tumor consistency was soft (scale 1). *J*, Histopathologic examination of the resected tumor indicates diffuse adenoma (hematoxylin-eosin stain; scale bar, 200 $\mu$m). Lower middle: Left vestibular schwannoma in a 50-year-old woman. *K*, Axial postcontrast T1-weighted MR imaging shows a strongly enhanced tumor (*arrow*). *L*, Axial T2-weighted MR imaging shows a mixed intensity tumor (*arrow*). *M*, Wave MRE image (*arrow*). *N*, Elastogram shows tumor shear stiffness (*arrow*) ($_{mean}$SS = 2.5 kPa; $_{max}$SS = 3.3 kPa). The intraoperative tumor consistency was moderate (scale 3). *O*, Histopathologic examination of the resected tumor indicates a schwannoma with a dominant Antoni A-type region (hematoxylin-eosin stain; scale bar, 200 $\mu$m). *Lower*: Right insular glioma in a 55-year-old woman. *P*, Axial postcontrast T1WI MR imaging shows a ring-enhanced tumor (*arrow*). *Q*, Axial T2-weighted MR imaging shows a mixed intensity tumor (*arrow*). *R*, Wave MRE image (*arrow*). *S*, Elastogram shows tumor shear stiffness (*arrow*) ($_{mean}$SS = 1.5 kPa; $_{max}$SS = 2.2 kPa). The intraoperative tumor consistency was moderate (scale 3). *T*, Histopathologic examination of the resected tumor indicates glioblastoma (hematoxylin-eosin stain; scale bar, 200 $\mu$m).

$_{mean}$SS and $_{max}$SS with the stiffness grading of all of the intracranial tumors.

In addition, we found a significant difference in the maximum shear stiffness between tumors that were firm (intraoperative tumor consistency scale 4 and 5) and tumors that were nonfirm (intraoperative tumor consistency scale, 1~3). The results suggest that MRE may be able to find firm tumors that may require special care in surgical planning or tumor removal.

In the current study, we demonstrated MRE and histopathologic findings representative of intraoperative firm tumors. In fibrous meningiomas (Fig 7, upper), the shear stiffness correlated with firm consistency intraoperatively. Meningothelial, fibrous, and transitional meningiomas are the most common histopathologic subtypes of meningiomas.[19] Using MRE, we might differentiate relatively firm meningiomas such as fibrous and transitional meningiomas from relatively soft meningiomas such as meningothelial meningiomas. Most pituitary adenomas are soft and can be easily resected, preserving the tumor capsule by using suction and curettes with transsphenoidal surgery. However, as shown in Fig 7, lower part, some tumors are firm and fibrous and consequently difficult to resect. In transsphenoidal surgery for such firm pituitary adenomas, excessive maneuvers increase morbidity and mortality related to visual disturbance, panhypophysis, and intra- and extracapsular hemorrhage. Although previous studies have

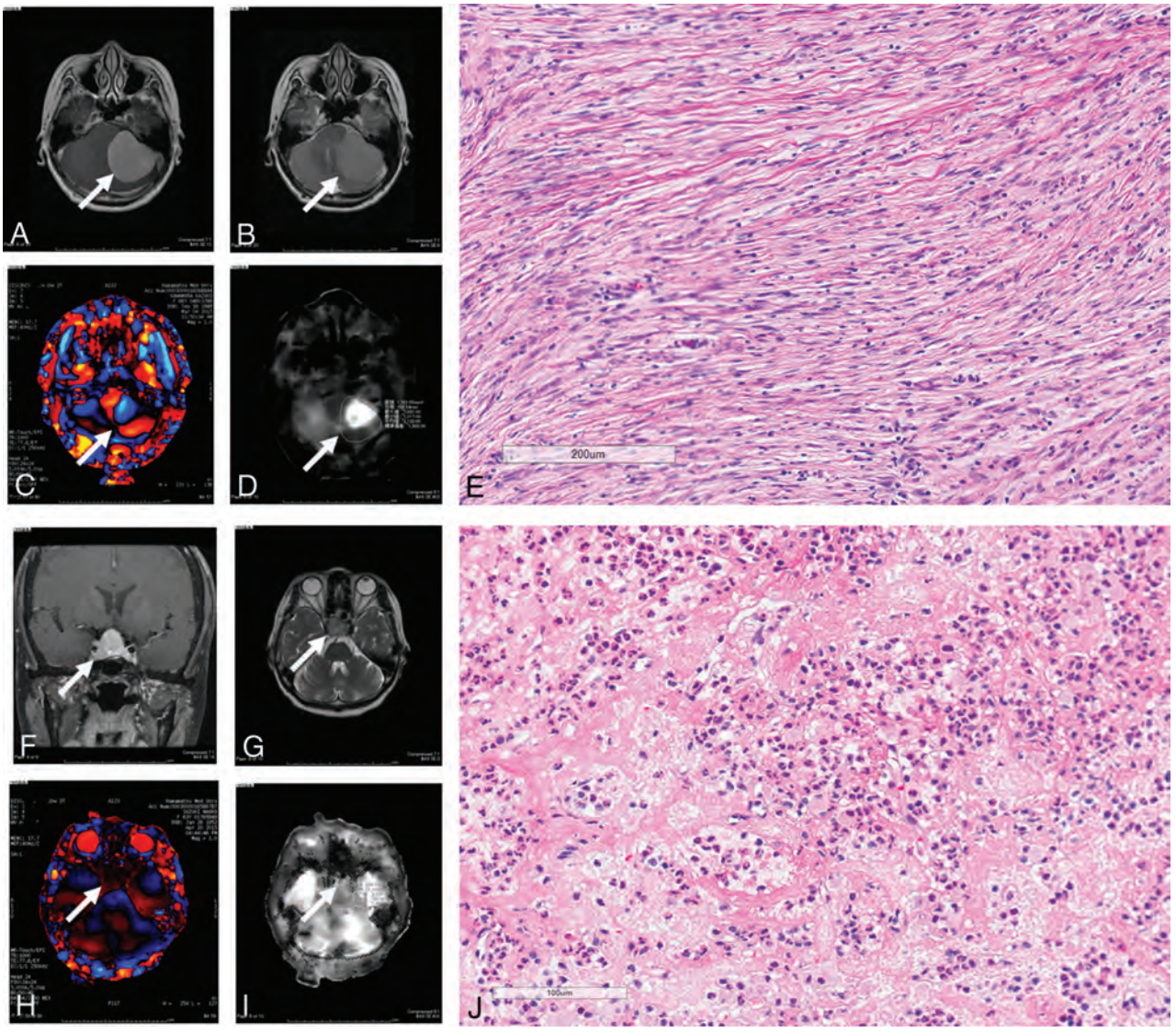


**FIG 7.** Intraoperative tumors with a firm consistency. Upper: Left cerebellopontine angle meningioma in a 51-year-old man. *A*, Axial postcontrast T1-weighted MR imaging shows a strongly enhanced tumor (*arrow*). *B*, Axial T2-weighted MR imaging shows an isointense tumor (*arrow*). *C*, Wave MRE image (*arrow*). *D*, Elastogram shows tumor shear stiffness (*arrow*) ($_{mean}$SS = 4.4 kPa; $_{max}$SS = 7.2 kPa). The intraoperative tumor consistency was mostly firm, requiring ultrasonic aspiration at a high setting (scale 4). *E*, Histopathologic examination of the resected tumor indicates fibrous meningioma (hematoxylin-eosin stain; scale bar, 200 $\mu$m). Lower: Nonfunctioning recurrent pituitary adenoma in a 63-year-old woman. *F*, Axial postcontrast T1-weighted MR imaging shows a strongly enhanced tumor (*arrow*). *G*, Axial T2-weighted MR imaging shows an isointense tumor (*arrow*). *H*, Wave MRE image (*arrow*). *I*, Elastogram shows tumor shear stiffness (*arrow*) ($_{mean}$SS = 1.6 kPa; $_{max}$SS = 2.1 kPa). The intraoperative tumor consistency was mostly firm, requiring ultrasonic aspiration at a high setting (scale 4). *J*, Histopathologic examination of the resected tumor indicates diffuse adenoma with fibrosis (hematoxylin-eosin stain; scale bar, 200 $\mu$m).

attempted to predict the consistency of pituitary adenomas with conventional MR imaging,[1] diffusion-weighted MR imaging,[2] and contrast-enhanced 3D FIESTA,[3] these methods did not directly measure the shear stiffness of pituitary adenomas. To the best of our knowledge, our study is the first to demonstrate the shear stiffness of pituitary adenomas by using MRE.

The consistency of pituitary adenomas depends on the level of fibrosis that correlates with collagenous contents.[20] MRE might be reflecting the collagenous content of pituitary adenomas. As for vestibular schwannomas, differences in the percentage of the Antoni A component (areas of compact, elongated cells with occasional nuclear palisading) and the Antoni B component (less cellular, with loosely textured cells with indistinct processes and variable lipidization) might determine the shear stiffness. Although the preoperative consistency of vestibular schwannoma has not been studied, the difficulties associated with the recently recommended subcapsular tumor dissection for the preservation of facial and cochlear nerve functions in vestibular schwannomas[21] are related to tumor consistency. Therefore, as in transsphenoidal surgery for pituitary adenomas, preoperative assessment of vestibular schwannoma consistency would be recognized as being more important. MRE will be one of the choices in predicting the consistency of vestibular schwannomas preoperatively.

Although most brain MRE studies have been performed by using custom-built transducers in various laboratories worldwide, they have not been approved for their reliability and safety. In our study, we adapted a passive pneumatic driver (MR Touch)

originally designed for abdominal MRE for introducing shear waves into the brain. Indeed, this was the only commercially available system that could be used for patients in Japan during this study. A higher motion frequency may be useful for superficial tumors, and a lower motion frequency may be useful for deep tumors. In the preliminary study with volunteers, we used the same MEG (60 Hz) and external driver frequency (60 Hz) reported by Murphy et al.[13] However, we found that an external driver frequency of 60 Hz was not adequate for our system because the shear waves did not reach the center of the brain. This might be caused by the loose contact between the head and the external driver in our system. With reference to the cross-hatching area, we found that an MEG of 60 Hz, an external driver frequency of 40 Hz, and an amplitude of 50% were optimal in this system. The precise reason why a MEG frequency that is not equal to the external driver frequency works better is unclear; however, this technique has been widely used in the MRE literature as a means to reduce TE[22] or to create broadband sensitivity for multifrequency MRE.[23-26]

Although the spatial resolution in our system was very low because of the low external driver frequency and limited matrix size, the shear stiffness of healthy regions of the brain such as the cerebellum was consistent among patients. Therefore, we used absolute values for both for the mean and maximum shear stiffness (kilopascal) in this study. We speculated that the region with the maximum shear stiffness indicated the region with firm consistency in tumors. However, we observed a case of glioma in which the region with maximum shear stiffness was the center of the cyst in the tumor. Our review of the published literature revealed that the stiffness of the glioma cyst has not been previously reported. The reason for the center of the cyst showing maximum shear stiffness was unclear. Although it is more likely artifacts than anything related to the intracystic pressure, it may be partially explained as follows: Because fluid is a less viscoelastic material, the shear stiffness of the cyst is increased when the intracyst fluid is tensely filled with fluid. Actually, in neurosurgical practice, the tense cyst in tumors is firmer than the surrounding normal brain tissue until it is opened; additionally, when obstructive hydrocephalus is present, the brain surface is firm until ventricular drainage is performed.

The current study had several limitations. First, the spatial resolution of the voxels (3.75 mm in-plane and 5 mm through-plane) used in our study was so coarse that the stiffness presented might include not only tumor tissue but also other surrounding tissue, including brain tissue, bone, and CSF. In a recent study by Murphy et al,[23] the use of 2-mm, or at most 3-mm, voxels, with the exclusion of the edge pixels from the analysis in ROIs, was recommended because of errors associated with estimating spatial derivatives in the inversion algorithm and also for the minimization of partial-volume effects.

A higher spatial resolution would allow shear stiffness measurements in smaller tumors and provide more accurate regional shear stiffness measurements in large tumors with heterogeneous consistency. To overcome the low spatial resolution of MRE at the single harmonic driver frequency that we used, Sack et al[27] at Charité established a multifrequency MRE to generate high-resolution elastograms.[10,11,14,24]

The recent development of a 3D multislab, multishot acquisition for whole-brain MRE could achieve high signal-to-noise efficacy.[25-29] 3D analysis could improve the results if the wave propagation is complicated, especially if there is through-plane oblique wave propagation that a 2D analysis would not visualize correctly.

Second, the scaling of tumor consistency in our study involved a qualitative assessment by surgeons at the time of resection; a quantitative assessment of tumor consistency would be preferable. Third, because of the small sample size, we could not examine the histopathologic components corresponding to tumor consistency in detail. The correlation between shear stiffness measured by using MRE and meningioma subtypes, collagenous contents in pituitary adenomas, and heterogeneity of the Antoni pattern in vestibular schwannomas should be investigated in the future.

## CONCLUSIONS

The shear stiffness measured by MRE could be used to evaluate histopathologic subtypes of intracranial tumors. MRE may be useful in the preoperative discrimination of firm tumors.


## ACKNOWLEDGMENTS

The authors thank Masanori Kawate and Kenichi Terashima for their technical assistance.

Disclosures: Naoto Sakai—*RELATED*: *Grant*: JSPS KAKENHI (grant No. 15K10359).


## REFERENCES


1. Iuchi T, Saeki N, Tanaka M, et al. **MRI prediction of fibrous pituitary adenomas.** *Acta Neurochir (Wien)* 1998;140:779–86 CrossRef Medline
2. Pierallini A, Caramia F, Falcone C, et al. **Pituitary macroadenomas: preoperative evaluation of consistency with diffusion-weighted MR imaging—initial experience.** *Radiology* 2006;239:223–31 CrossRef Medline
3. Yamamoto J, Kakeda S, Shimajiri S, et al. **Tumor consistency of pituitary macroadenomas: predictive analysis on the basis of imaging features with contrast-enhanced 3D FIESTA at 3T.** *AJNR Am J Neuroradiol* 2014;35:297–303 CrossRef Medline
4. Muthupillai R, Lomas DJ, Rossman PJ, et al. **Magnetic resonance elastography by direct visualization of propagating acoustic strain waves.** *Science* 1995;269:1854–57 CrossRef Medline
5. Muthupillai R, Ehman RL. **Magnetic resonance elastography.** *Nat Med* 1996;2:601–03 CrossRef Medline
6. Kruse SA, Rose GH, Glaser KJ, et al. **Magnetic resonance elastography of the brain.** *Neuroimage* 2008;39:231–37 CrossRef Medline
7. Venkatesh SK, Yin M, Ehman RL. **Magnetic resonance elastography of liver: technique, analysis, and clinical applications.** *J Magn Reson Imaging* 2013;37:544–55 CrossRef Medline
8. Murphy MC, Huston J 3rd, Jack CR Jr, et al. **Decreased brain stiffness in Alzheimer's disease determined by magnetic resonance elastography.** *J Magn Reson Imaging* 2011;34:494–98 CrossRef Medline
9. Murphy MC, Curran GL, Glaser KJ, et al. **Magnetic resonance elastography of the brain in a mouse model of Alzheimer's disease: initial results.** *Magn Reson Imaging* 2012;30:535–39 CrossRef Medline
10. Streitberger KJ, Sack I, Krefting D, et al. **Brain viscoelasticity alteration in chronic-progressive multiple sclerosis.** *PLoS One* 2012;7:e29888 CrossRef Medline
11. Streitberger KJ, Wiener E, Hoffmann J, et al. **In vivo viscoelastic**

**properties of the brain in normal pressure hydrocephalus.** *NMR Biomed* 2011;24:385–92 CrossRef Medline
12. Freimann FB, Streitberger KJ, Klatt D, et al. **Alteration of brain viscoelasticity after shunt treatment in normal pressure hydrocephalus.** *Neuroradiology* 2012;54:189–96 CrossRef Medline
13. Murphy MC, Huston J 3rd, Glaser KJ, et al. **Preoperative assessment of meningioma stiffness using magnetic resonance elastography.** *J Neurosurg* 2013;118:643–48 CrossRef Medline
14. Streitberger KJ, Reiss-Zimmermann M, Freimann FB, et al. **High-resolution mechanical imaging of glioblastoma by multifrequency magnetic resonance elastography.** *PLoS One* 2014;9:e110588 CrossRef Medline
15. Kawaji H, Koizumi S, Sakai N, et al. **Evaluation of tumor blood flow after feeder embolization in meningiomas by arterial spin-labeling perfusion magnetic resonance imaging.** *J Neuroradiol* 2013;40:303–06 CrossRef Medline
16. Sakai N, Koizumi S, Yamashita S, et al. **Arterial spin-labeled perfusion imaging reflects vascular density in nonfunctioning pituitary macroadenomas.** *AJNR Am J Neuroradiol* 2013;34:2139–43 CrossRef Medline
17. Sakai N, Yamashita S, Takehara Y, et al. **Evaluation of the antiangiogenic effects of octreotide on growth hormone-producing pituitary adenoma using arterial spin-labeling perfusion imaging.** *Magn Reson Med Sci* 2015;14:73–76 CrossRef Medline
18. Koizumi S, Sakai N, Kawaji H, et al. **Pseudo-continuous arterial spin labeling reflects vascular density and differentiates angiomatous meningiomas from non-angiomatous meningiomas.** *Neurooncol* 2015;121:549–56 CrossRef Medline
19. Louis DN, Ohgaki H, Wiestler OD, et al. **The 2007 WHO classification of tumours of the central nervous system.** *Acta Neuropathol* 2007;114:97–109 CrossRef Medline
20. Naganuma H, Satoh E, Nukui H. **Technical considerations of transsphenoidal removal of fibrous pituitary adenomas and evaluation of collagen content and subtype in the adenomas.** *Neurol Med Chir (Tokyo)* 2002;42:202–12 CrossRef Medline
21. Sasaki T, Shono T, Hashiguchi K, et al. **Histological considerations of the cleavage plane for preservation of facial and cochlear nerve functions in vestibular schwannoma surgery.** *J Neurosurg* 2009;110:648–55 CrossRef Medline
22. Shinagawa Y, Mitsufuji T, Morimoto S, et al. **Optimization of scanning parameters for MR elastography at 3.0 T clinical unit: volunteer study.** *Japan J Radiol* 2014;32:441–46 CrossRef Medline
23. Murphy MC, Huston J 3rd, Jack CR Jr, et al. **Measuring the characteristic topography of brain stiffness with magnetic resonance elastography.** *PLoS One* 2013;8:e81668 CrossRef Medline
24. Dittmann F, Hirsch S, Tzschätzsch H, et al. **In vivo wideband multifrequency MR elastography of the human brain and liver.** *Magn Reson Med* 2015 Oct 20. [Epub ahead of print] CrossRef Medline
25. Garteiser P, Sahebjavaher RS, Ter Beek LC, et al. **Rapid acquisition of multifrequency, multislice and multidirectional MR elastography data with a fractionally encoded gradient echo sequence.** *NMR Biomed* 2013;26:1326–35 CrossRef Medline
26. Rump J, Klatt D, Braun J, et al. **Fractional encoding of harmonic motions in MR elastography.** *Magn Reson Med* 2007;57:388–95 CrossRef Medline
27. Sack I, Beierbach B, Hamhaber U, et al. **Non-invasive measurement of brain viscoelasticity using magnetic resonance elastography.** *NMR Biomed* 2008;21:265–71 CrossRef Medline
28. Yin Z, Kearney SP, Magin RL, et al. **Concurrent 3D acquisition of diffusion tensor imaging and magnetic resonance elastography displacement data (DTI-MRE): theory and in vivo application.** *Magn Reson Med* 2016 Jan 20. [Epub ahead of print] CrossRef Medline
29. Johnson CL, Holtrop JL, McGarry MD, et al. **3D multislab, multishot acquisition for fast, whole-brain MR elastography with high signal-to-noise efficiency.** *Magn Reson Med* 2014;71:477–85 CrossRef Medline

# A Direct Aspiration, First Pass Technique (ADAPT) versus Stent Retrievers for Acute Stroke Therapy: An Observational Comparative Study

B. Lapergue, R. Blanc, P. Guedin, J.-P. Decroix, J. Labreuche, C. Preda, B. Bartolini, O. Coskun, H. Redjem, M. Mazighi, F. Bourdain, G. Rodesch, and M. Piotin

## ABSTRACT

**BACKGROUND AND PURPOSE:** Mechanical thrombectomy with stent retrievers is now the standard therapy for selected patients with ischemic stroke. The technique of A Direct Aspiration, First Pass Technique for the Endovascular Treatment of Stroke (ADAPT) appears promising with a high rate of recanalization. We compared ADAPT versus stent retrievers (the Solitaire device) for efficacy and safety as a front-line endovascular procedure.

**MATERIALS AND METHODS:** We analyzed 243 consecutive patients with large intracranial artery occlusions of the anterior circulation, treated within 6 hours with mechanical thrombectomy by either ADAPT or the Solitaire stent. Th primary outcome was complete recanalization (modified TICI ≥ 2b); secondary outcomes included complication rates and procedural and clinical outcomes.

**RESULTS:** From November 2012 to June 2014, 119 patients were treated with stent retriever (Solitaire FR) and 124 by using the ADAPT with Penumbra reperfusion catheters. The median baseline NIHSS score was the same for both groups (Solitaire, 17 [interquartile range, 11–21] versus ADAPT, 17 [interquartile range, 12–21]). Time from groin puncture to recanalization (Solitaire, 50 minutes [range, 25–80 minutes] versus ADAPT, 45 minutes [range, 27–70 minutes], $P = .42$) did not differ significantly. However, compared with the Solitaire group, patients treated with ADAPT achieved higher final recanalization rates (82.3% versus 68.9%; adjusted relative risk, 1.18; 95% CI, 1.02–1.37; $P = .022$), though differences in clinical outcomes between the cohorts were not significant. Use of an adjunctive device was more frequent in the ADAPT group (45.2% versus 13.5%, $P < .0001$). The rate of embolization in new territories or symptomatic hemorrhage did not differ significantly between the 2 groups.

**CONCLUSIONS:** Front-line ADAPT achieved higher recanalization rates than the Solitaire device. Further randomized controlled trials are warranted to define the best strategy for mechanical thrombectomy.

**ABBREVIATIONS:** ADAPT = A Direct Aspiration, First Pass Technique for the Endovascular Treatment of Stroke; MT = mechanical thrombectomy; mTICI = modified TICI

Mechanical thrombectomy (MT) has now been validated through several large randomized controlled trials in the treatment of acute ischemic stroke due to large-vessel occlusion.[1-5] These studies demonstrated a major decrease in disability. Successful revascularization has been shown to increase the likelihood of a good clinical outcome.[6] However, these randomized controlled trials, by using the latest generation of stent retriever devices available at the time, reported successful revascularization rates ranging between 58% and 72% in the 2 largest studies.[1,3] Although the randomized controlled trials proved that MT was beneficial, more than one-third of the procedures resulted in failure to recanalize.[7,8] Improvement in the rate of successful recanalization is thus a critical issue. The stent retriever procedure starts with the common transfemoral access, followed by the introduction of the stent retrievers via a microcatheter through a balloon-guide catheter. The balloon-guide catheter is inflated to create

Received February 2, 2016; accepted after revision April 18.

From the Division of Neurology (B.L., J.-P.D., F.B.), Stroke Center, Foch Hospital, University Versailles Saint-Quentin en Yvelines, Suresnes, France; Department of Diagnostic and Interventional Neuroradiology (P.G., O.C., G.R.), Foch Hospital, Suresnes, France; Department of Diagnostic and Interventional Neuroradiology (R.B., B.B., H.R., M.P.), Rothschild Foundation, Paris, France; Department of Biostatistics (J.L.), Univiversity of Lille, Centre Hospitalier Universitaire Lille, Santé Publique: Epidémiologie et Qualité des Soins, Lille, France; Laboratoire de Mathématiques Paul Painlevé (C.P.), Unité Mixte de Recherche CNRS 8524, Lille, France; and Department of Neurology and Stroke Center (M.M.), Lariboisière Hospital, Paris, France.

The authors contributed to the article in the following manner: F.B., B.L., R.B, M.P., M.M., J.L. participated in the conception and design of the study; B.L, R.B., F.B., M.P., J.L., M.M., C.P. analyzed and interpreted the data; B.L., F.B., J.-P.D., R.B., P.G., B.B., O.C., H.R., F.B., G.R., M.P. were responsible for the provision of study materials or patients; F.B., B.L., J.-P.D., R.B., M.P. were responsible for collection, assembly, and possession of the raw data; C.P. and J.L. were responsible for statistical expertise; and B.L., R.B., M.P., M.M., F.B. were responsible for drafting the article.

Please address correspondence to Bertrand Lapergue, MD, PhD, Division of Neurology, Stroke Center, Foch Hospital, University Versailles Saint-Quentin en Yvelines, Suresnes, France; e-mail: b.lapergue@hopital-foch.org

Indicates article with supplemental on-line appendix and table.
Indicates article with supplemental on-line photo.

http://dx.doi.org/10.3174/ajnr.A4840

flow arrest while retrieving the stent retrievers. Another approach is A Direct Aspiration, First Pass Technique for the Endovascular Treatment of Stroke (ADAPT),[9] which involves using front-line aspiration alone to remove the thrombus through a highly trackable, atraumatic, large-bore aspiration catheter. Its success is based on using the largest catheter permitted by the vessel, ensuring greater aspiration power for thrombus extraction. In case of failure with the front-line ADAPT approach, the large-bore aspiration catheter can be used as a conduit for introducing a stent retriever or another adjunctive device; the system is thus versatile.

We aimed to compare the recanalization efficiency, clinical outcome, and complication rate of ADAPT and stent retrievers, 2 strategies of mechanical thrombectomy.

## MATERIALS AND METHODS

A prospective clinical registry was used to consecutively identify and analyze patients with acute ischemic stroke treated at 2 comprehensive stroke centers between November 2012 and June 2014 (EFFECTS Registry, Endovascular Treatment at Foch Hospital-Rothschild Foundation in Ischemic Stroke). All patients were assessed for the presence of large intracranial artery occlusions of the anterior circulation and received front-line MT by using either the Solitaire (Covidien, Irvine, California) device or ADAPT by using the 5MAX or 5MAX ACE Reperfusion Catheter (Penumbra, Alameda, California) (On-line Appendix). Most patients underwent brain MR imaging in the acute phase. In cases of MR imaging contraindications, brain CT and CT angiography were performed.

### *Standard Protocol Approvals*

Locally ethics committees and French Data Protection Agency approved the use of patient data for this retrospective analysis.

### *Inclusion and Exclusion Criteria*

The following criteria were required for inclusion in this study:

- Proximal middle cerebral artery occlusion or intracranial internal carotid artery occlusion, without associated cervical internal carotid artery occlusion/critical stenosis, was present. Patients referred for acute ischemic stroke with cervical internal carotid occlusion/critical stenosis and basilar occlusion were excluded from this study to decrease bias due to the heterogeneity of patients and endovascular approaches.

- Patients were eligible if they were treatable by MT within 6 hours of stroke onset, with bridging therapy (previous IV rtPA) or standalone thrombectomy. The interventional neuroradiologist could, in the case of recanalization failure (modified TICI [mTICI] $<$ 2b) with the ADAPT or the Solitaire system, use another thrombectomy device of the operator's choice (rescue therapy).

### *Data Collection and Definitions*

Information on patient characteristics, medical history, laboratory and imaging findings, vital signs before treatment, severity of ischemic stroke, and clinical outcome was collected prospectively by using the same structured questionnaire. The severity of the ischemic stroke was assessed by using the NIHSS score at admission and 24 hours later. We defined early neurologic improvement as an NIHSS score of 0–1 at 24 hours or a decrease of at least 4 points in the NIHSS score. Good functional outcome was defined as a 90-day mRS score of $\leq$2. Excellent outcome was defined as a 90-day mRS score of $\leq$1. All patients underwent a CT or MR imaging 24 hours after treatment to assess hemorrhagic complications. Symptomatic intracranial hemorrhage was defined according to the ECASS-II (European Co-operative Acute Stroke Study-II) definition: any intracerebral hemorrhage with an increase of at least 4 NIHSS points within 24 hours, or resulting in death. Symptomatic intracranial hemorrhage was assessed in a blinded manner by noninvolved senior neuroradiologists (R.B., H.R.) and vascular neurologists (B.L., J.-P.D.). The blinded assessment of symptomatic intracranial hemorrhage was specifically performed for this study to assess both aspects of mechanical thrombectomy (successful recanalization rate and hemorrhage complications). During the MT procedure, the presence of embolization in a new territory (defined as an angiographic occlusion in a previously unaffected vascular territory observed on the angiogram after clot removal), the time from symptom onset to groin puncture and from groin puncture to maximal mTICI, and the mTICI score were also monitored. The modified Rankin Scale score at 90 days was assessed by trained research nurses unaware of the study group assignments, during face-to-face interviews or via telephone conversations.

### *Endovascular Procedure*

**ADAPT Group.** Patients received aspiration thrombectomy by ADAPT by using the 5MAX ACE (Penumbra) as front-line therapy. The detailed technical procedure has been published previously.[9] In brief, access was achieved through the femoral artery in compliance with the standard of care. Large-bore catheters were placed distally into the internal carotid artery to provide access for the 5MAX ACE aspiration catheter. Adhering to the instructions for use, the 5MAX ACE catheter was advanced to the level of the occlusion over a microcatheter and a microguidewire. Continuous aspiration was then performed by using the Penumbra aspiration pump for at least 90 seconds in all cases. After engagement of the thrombus with the aspiration catheter, the catheter was allowed to aspirate for at least 30 seconds before its withdrawal with the engaged thrombus. Angiography was performed following recovery to evaluate the flow rate. The preceding steps were repeated until successful revascularization to mTICI 2b–3 was achieved, while adhering to the admissible treatment window ($<$6 hours from stroke onset).The interventional neuroradiologist could, in the case of recanalization failure (mTICI $<$ 2b) with ADAPT, use another thrombectomy device of the operator's choice (rescue therapy).

**Solitaire Group.** All MT procedures were performed by using the Solitaire FR (Covidien) via the femoral artery approach. Following the instructions for use of the Solitaire FR, a balloon catheter was positioned within the internal carotid artery to allow flow arrest during thrombus retrieval. The Solitaire FR device was delivered through a microcatheter and deployed inside the thrombus. A control angiogram was performed to determine the immediate reperfusion status, and the device was left deployed for a minimum of 3 minutes. Before retrieval of the stent retriever, the

**Table 1: Baseline characteristics in patients with acute ischemic stroke treated by ADAPT or a conventional stent retriever front-line approach[a]**

| | Solitaire Group ($n$ = 119) | ADAPT Group ($n$ = 124) | $P$ Value |
|---|---|---|---|
| Age (yr) (mean) | 65.5 ± 14.7 | 64.3 ± 15.7 | .52 |
| Men | 55 (46.2) | 61 (49.1) | .64 |
| Medical history | | | |
| Hypertension | 56 (47.5) | 72 (59.0) | .073 |
| Diabetes | 7 (5.9) | 21 (17.2) | .007 |
| Hypercholesterolemia | 31 (26.3) | 32 (26.2) | .99 |
| Current smoking | 20 (18.4) | 27 (22.1) | .48 |
| Antithrombotic therapy | 43 (36.1) | 44 (35.8) | .95 |
| NIHSS score (mean) | 15.9 ± 6.1 | 15.9 ± 6.5 | .99 |
| ASPECTS value at admission (median) (IQR) | 8 (7–10) | 9 (8–10) | .64 |
| Occlusion site | | | |
| ICA (isolated or tandem with MCA) | 32 (26.9) | 38 (30.7) | .52 |
| Isolated MCA | 87 (73.1) | 86 (69.3) | |
| Previous use of IV thrombolysis | 54 (45.4) | 82 (66.1) | .001 |
| Onset-to-groin puncture time (min) (median) (IQR) | 235 (181–300) | 247 (206–308) | .18 |

**Note:**—IQR indicates interquartile range.
[a] Values are expressed as number (percentages) unless otherwise indicated.

microcatheter was advanced to cover the proximal marker of the device. Then, the balloon-guide catheter was inflated to induce proximal internal carotid occlusion and flow arrest during withdrawal of the stent retriever. Subsequently, the Solitaire device and microcatheter were slowly recovered as a single unit under constant aspiration with a 60-mL syringe through the balloon-guide catheter. A control angiogram was performed to confirm revascularization and reperfusion.[10,11] This sequence was repeated until TICI 2b or 3 flow (defined as successful revascularization) was established with a maximal delay of 6 hours from symptom onset to maximal TICI. The interventional neuroradiologist could, in the case of recanalization failure (mTICI < 2b) with the Solitaire device, use another thrombectomy device of the operator's choice (rescue therapy).

### *Primary and Secondary Outcomes*

The primary outcome was the rate of successful recanalization defined angiographically as mTICI2b–3 on the angiogram at the end of procedure (ie, ADAPT or Solitaire front-line approach and rescue therapy if needed). Secondary outcomes included safety issues, procedural times of the 2 recanalization thrombectomy strategies, and clinical outcome (early neurologic improvement, 90-day excellent and favorable outcomes, and 90-day all-cause mortality).

### *Statistical Analysis*

Data are presented as means (SD) or medians (interquartile range) for continuous variables and percentages (count) for categoric variables. Normality of distributions was assessed by using histograms and the Shapiro-Wilk test. Bivariate comparisons were performed between the ADAPT and Solitaire groups by using $\chi^2$ tests for categoric variables (the Fisher exact test was used when the expected cell frequency was <5) and Student $t$ tests for continuous variables (the Mann-Whitney $U$ test was used for non-Gaussian distributions). Differences in primary and secondary outcomes between the study groups were expressed as relative risks with 95% confidence intervals. We assessed the heterogeneity in outcome effect across centers by using the Breslow-Day test. Comparisons in primary and secondary outcomes were further adjusted for baseline differences (at $P < .20$ in bivariate analyses) by using a Poisson regression model with robust error variance.[12] Statistical testing was performed at the 2-tailed $\alpha$ level of .05 except for tests of heterogeneity in which an $\alpha$ level of .10 was chosen. Data were analyzed by using SAS software, Version 9.3 (SAS Institute, Cary, North Carolina).

## RESULTS

Two hundred forty-three consecutive patients with ischemic stroke secondary to occlusions of the ICA or MCA were admitted and treated by mechanical thrombectomy at 2 comprehensive stroke centers. Among them, 119 patients were treated by a conventional front-line stent retriever approach, and 124 patients, by ADAPT. Patient characteristics are shown in Table 1, according to the MT approach. Patients treated by the ADAPT approach had more frequent hypertension and diabetes and more often received IV thrombolysis before MT. No significant between-group differences were found with regard to acute stroke severity (assessed by the NIHSS at presentation), arterial occlusion site, or stroke onset-to-groin puncture time.

### *Successful Recanalization and MT Approaches*

Overall, 184 patients (75.7%) achieved a successful revascularization within a median duration of 45 minutes (interquartile range, 26–73) from groin puncture. In univariate analysis, successful revascularization at final angiography was significantly more often achieved in patients treated with ADAPT (82.3%) as opposed to the front-line stent retriever approach (68.9%) ($P = .015$) (Table 2). We found no significant heterogeneity in between-group differences across centers ($P = .62$, On-line Figure). After adjustment for baseline differences, the ADAPT approach remained associated with a significant relative increase of 18% (95%, CI, 2%–37%) in successful revascularization. Notably, a higher rate of use of additional devices occurred in the ADAPT group, 45.2% ($n = 56$), versus 13.5% ($n = 16$) in the Solitaire group, ($P < .0001$, On-line Table). The success rate (TICI 2b–3) of the 56 patients treated by ADAPT first-line and rescue therapy was 39/56 (69.6%). However, we found no significant difference in time between groin puncture and recanalization according to the MT procedure (Figure).

### *Clinical Outcomes and MT Approaches*

We found no difference in clinical efficacy outcomes between the 2 MT approaches in univariate or multivariate analyses (Table 2). Overall, good functional outcomes defined by an mRS of 0–2 at 90 days occurred in 54.8% ($n = 63$) in the stent retriever group

**Table 2: Outcomes in ADAPT or Solitaire group**

| Outcomes[a] | Solitaire Group (*n* = 119) | ADAPT Group (*n*= 124) | Relative Risk | *P* Value | Relative Risk[b] | *P* Value[b] |
|---|---|---|---|---|---|---|
| Successful revascularization at final angiogram | 82 (68.9) | 102 (82.3) | 1.19 (1.03–1.38) | .015 | 1.18 (1.02–1.37) | .022 |
| Early neurologic improvement | 61 (55.5) | 56 (57.1) | 1.03 (0.81–1.31) | .81 | 1.00 (0.78–1.28) | .99 |
| 90-day excellent outcome | 44 (38.3) | 45 (39.1) | 1.02 (0.73–1.42) | .89 | 1.10 (0.78–1.56) | .58 |
| 90-day favorable outcome | 63 (54.8) | 61 (53.0) | 0.97 (0.76–1.23) | .79 | 1.05 (0.82–1.35) | .70 |
| 90-day mortality | 20 (17.4) | 26 (22.6) | 1.30 (0.77–2.19) | .32 | 1.14 (0.64–2.01) | .65 |
| ENT | 8 (6.8) | 7 (5.7) | – | .70 | – | – |
| sICH | 7 (5.9) | 3 (2.4) | – | .21 | – | – |

**Note:**—ENT indicates embolization in a new territory rate; sICH, symptomatic intracranial hemorrhage.

[a] Early neurologic improvement is defined as an NIHSS score 0–1 at 24 hours or a decrease of ≥4 points in NIHSS scores at 24 hours. Excellent outcome is defined as an mRS score of ≤1; favorable outcome, an mRS score of ≤2; and successful recanalization, an mTICI score of 2b–3 at final angiography.

[b] Adjusted for between-group differences in hypertension, diabetes, prior IV thrombolysis, and onset-to-groin puncture time (calculated with a robust Poisson regression model).

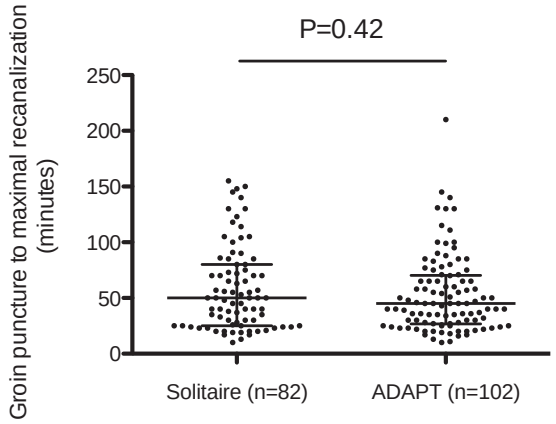


**FIGURE.** Time from groin puncture to maximal revascularization after a front-line Solitaire stent retriever approach compared with ADAPT. *P* value for the comparison in time from groin puncture to maximal recanalization is reported (Mann-Whitney *U* test). Bars indicate the medians with interquartile range values, which were 50 minutes (range, 25–80 minutes) in the Solitaire group and 45 minutes (27–70 minutes) in the ADAPT group.

and 53.0% ($n = 61$) in the ADAPT group. A total of 46 deaths and 10 symptomatic intracerebral hemorrhages occurred, with no evidence of a difference between the 2 MT approaches (Table 2). Embolization to a new territory caused by MT occurred in 5.7% ($n = 7$) in the ADAPT group and 6.8% ($n = 8$) in the Solitaire group ($P = .70$).

## DISCUSSION

Mechanical thrombectomy by using the latest generation devices has revolutionized the treatment of acute ischemic stroke, in part because the final rate of complete revascularization is higher than recorded rates by using intra-arterial fibrinolysis or the Merci thrombectomy device (Concentric Medical, Mountain View, California).[13,14] Nevertheless, the rate of revascularization failure remains high, with an occurrence of up to 40% in large-vessel occlusive strokes.[7,15,16] Successful reperfusion has been correlated with favorable outcomes.[3,6,15,17-22] To the authors' knowledge, no studies comparing ADAPT with stent retrievers have been previously published. Assessment of new revascularization strategies is needed to understand how to optimize thrombectomy procedures.

We found that front-line MT by the ADAPT approach achieved a higher rate of complete revascularization at final angiography than a front-line stent retriever–based strategy (82.3% versus 68.9%, adjusted $P = .022$). The use of adjunctive devices was higher in the ADAPT group than in the Solitaire group (ADAPT, 38.7%, versus Solitaire, 13.3%). Most interesting, this higher rate of adjunctive device use in the ADAPT group did not impact the groin puncture-to-recanalization time ($P = .42$, Fig 1). The benefit of the front-line ADAPT strategy is thus mainly derived from a higher percentage of rescue therapy. One explanation may be related to the ease of setting up a stent retriever through the large-bore aspiration catheter (Solumbra technique). Starting with a 5MAX ACE, required for the ADAPT technique, thus provides a versatile platform that can readily incorporate devices with different mechanisms of action.

Although the rate of revascularization in the ADAPT cohort was higher, the clinical outcomes did not differ from those in the Solitaire group. This outcome should be interpreted with caution given the comparative observational design of the study.

Periprocedural embolization to a new territory is a concern when performing a mechanical thrombectomy procedure. No differences in rates of embolization in a new territory between ADAPT (5.7%) and stent retriever (6.8%) front-line strategies were observed. However, our sample size was limited; experimental work suggests that a combined strategy with aspiration with adjunct stent retrievers may decrease the rate of embolization in a new territory.[23]

Symptomatic hemorrhagic complications, defined in this study as an ECASS-evident intracranial hemorrhage with an increase of ≥4 on the NIHSS scale at 24 hours from baseline, were lower after the ADAPT approach. Study results yielded symptomatic intracranial hemorrhage rates (2.4% for ADAPT versus 5.9% for Solitaire) similar to those of recent randomized controlled trials studying stroke.[1-5] Retrospective studies have reported a high rate of revascularization (TICI 2b/3 > 90%) with the ADAPT approach, with low complication rates such as 2% embolization in a new territory and no incidence of symptomatic intracranial hemorrhage.[24,25]

The imbalance of prior rtPA use, which was higher in the ADAPT group (66.1% versus 45.4% in the Solitaire group), may have impacted the rate of successful recanalization. However, the adjusted analysis for all confounding factors, including rtPA use, confirms the higher rate of recanalization in the ADAPT group. The direct effect of rtPA use with adjunctive MT remains controversial.[26]

The present findings are derived from observational analyses, which are subject to well-known limitations. The first is the potential for confounding by measured or unmeasured variables, which cannot be ruled out, even after adjustment for baseline between-group differences. The second concerns the potential evaluation bias in clinical outcomes in the absence of blinded evaluation. In addition, no formal study sample size was calculated, and we could not exclude some differences being overlooked due to the lack of adequate statistical power. In a posterior power calculation (not taking into account the adjustment), we calculated the smallest significant between-group difference (expressed as effect size by using relative risk) that our study sample size allowed us to detect with a power of 80%. Assuming an incidence of good outcome of 10% and 50% in the reference group (Solitaire), we could respectively detect a relative risk of 2.34 and 1.35 (or 0.43 and 0.74 for a detrimental effect).

We suggest that future studies follow a randomized controlled trial with core imaging performed by an independent neurointerventionalist to further support those findings.

We are currently starting the Interest of Direct Aspiration First Pass Technique (ADAPT) for Thrombectomy Revascularisation of Large Vessel Occlusion in Acute Ischaemic Stroke trial, a randomized, controlled, multicentric, blinded-end-point study (ClinicalTrials.gov, NCT02523261).

## CONCLUSIONS

Front-line ADAPT as an MT strategy achieved higher recanalization rates compared with the Solitaire device, though ADAPT requires higher rates of rescue therapy. Further randomized controlled trials are warranted to define the best strategy for mechanical thrombectomy.


## ACKNOWLEDGMENTS

We thank Mary Osborne-Pellegrin for help in editing the final draft of the manuscript.

Disclosures: Bertrand Lapergue—*RELATED*: *Grant*: An institutional grant has been provided by Penumbra for ASTER TRIAL (ADAPT versus stent retriever in acute ischemic stroke); *Support for Travel to meetings for the study or other purposes*: travel support by Medtronic; *Payment for lectures (including service of Speakers Bureaus)*: speaker's honoraria from Penumbra. Bruno Bartolini—*UNRELATED*: *Consultancy*: Stryker Neurovascular. Mikael Mazighi—*UNRELATED*: *Consultancy*: Servier, *Comments*: honoraria for teaching engagements as a consultant; *Payment for Lectures (including service on Speakers Bureaus)*: Covidien; *Travel/Accommodations/Meeting Expenses Unrelated to Activities Listed*: Bayer A.G., Boehringer Ingelheim, Covidien. Michel Piotin—*UNRELATED*: *Consultancy*: Medtronic,* Stryker,* MicroVention,* Penumbra*; *Payment for Lectures (including service on Speakers Bureaus)*: Medtronic,* Penumbra*; *Grants/grants pending*: institutional grants from Stryker, Medtronic, MicroVention, Balt; *OTHER*: institutional grant from Medtronic for training and proctoring physicians using Pipeline. Raphael Blanc—*UNRELATED*: *Grants/grants pending*: institutional grants from Stryker, Medtronic, MicroVention, Balt; *OTHER*: institutional grant from Medtronic for training and proctoring physicians using Pipeline. *Money paid to the institution.


## REFERENCES


1. Berkhemer OA, Fransen PSS, Beumer D, et al. **A randomized trial of intraarterial treatment for acute ischemic stroke.** *N Engl J Med* 2015;372:11–20 CrossRef Medline
2. Jovin TG, Chamorro A, Cobo E, et al; REVASCAT Trial Investigators. **Thrombectomy within 8 hours after symptom onset in ischemic stroke.** *N Engl J Med* 2015;372:2296–306 CrossRef Medline
3. Goyal M, Demchuk AM, Menon BK, et al; ESCAPE Trial Investigators. **Randomized assessment of rapid endovascular treatment of ischemic stroke.** *N Engl J Med* 2015;372:1019–30 CrossRef Medline
4. Campbell BC, Mitchell PJ, Kleinig TJ, et al; EXTEND-IA Investigators. **Endovascular therapy for ischemic stroke with perfusion-imaging selection.** *N Engl J Med* 2015;372:1009–18 CrossRef Medline
5. Saver JL, Goyal M, Bonafe A, et al.; SWIFT PRIME Investigators. **Stent-retriever thrombectomy after intravenous t-PA vs. t-PA alone in stroke.** *N Engl J Med* 2015;372:2285–95 CrossRef Medline
6. Khatri P, Yeatts SD, Mazighi M, et al; IMS III Trialists. **Time to angiographic reperfusion and clinical outcome after acute ischaemic stroke: an analysis of data from the Interventional Management of Stroke (IMS III) phase 3 trial.** *Lancet Neurol* 2014;13:567–74 CrossRef Medline
7. Smith WS, Sung G, Saver J, et al. **Mechanical thrombectomy for acute ischemic stroke: final results of the Multi MERCI trial.** *Stroke* 2008;39:1205–12 CrossRef Medline
8. Kidwell CS, Jahan R. **Endovascular treatment of acute ischemic stroke.** *Neurol Clin* 2015;33:401–20 CrossRef Medline
9. Turk AS, Spiotta A, Frei D, et al. **Initial clinical experience with the ADAPT technique: a direct aspiration first pass technique for stroke thrombectomy.** *J Neurointerv Surg* 2014;6:231–37 CrossRef Medline
10. Yoo AJ, Simonsen CZ, Prabhakaran S, et al; Cerebral Angiographic Revascularization Grading Collaborators. **Refining angiographic biomarkers of revascularization: improving outcome prediction after intra-arterial therapy.** *Stroke* 2013;44:2509–12 CrossRef Medline
11. Zaidat OO, Yoo AJ, Khatri P, et al; Angiographic Revascularization Grading (CARG) Collaborators, STIR Revascularization working group, STIR Thrombolysis in Cerebral Infarction (TICI) Task Force. **Recommendations on angiographic revascularization grading standards for acute ischemic stroke: a consensus statement.** *Stroke* 2013;44:2650–63 CrossRef Medline
12. Zou G. **A modified Poisson regression approach to prospective studies with binary data.** *Am J Epidemiol* 2004;159:702–06 CrossRef Medline
13. Song D, Kim BM, Kim DJ, et al. **Comparison of stent retriever and intra-arterial fibrinolysis in patients with acute ischaemic stroke.** *Eur J Neurol* 2014;21:779–84 CrossRef Medline
14. Broussalis E, Trinka E, Hitzl W, et al. **Comparison of stent-retriever devices versus the Merci retriever for endovascular treatment of acute stroke.** *AJNR Am J Neuroradiol* 2013;34:366–72 CrossRef Medline
15. Rha JH, Saver JL. **The impact of recanalization on ischemic stroke outcome: a meta-analysis.** *Stroke* 2007;38:967–73 CrossRef Medline
16. Smith WS, Sung G, Starkman S, et al; MERCI Trial Investigators. **Safety and efficacy of mechanical embolectomy in acute ischemic stroke: results of the MERCI Trial.** *Stroke* 2005;36:1432–38 CrossRef Medline
17. Campbell BC, Donnan GA, Lees KR, et al. **Endovascular stent thrombectomy: the new standard of care for large vessel ischaemic stroke.** *Lancet Neurol* 2015;14:846–54 CrossRef Medline
18. Khatri P, Hacke W, Fiehler J, et al; VISTA-Endovascular Collaboration. **State of acute endovascular therapy: report from the 12th thrombolysis, thrombectomy, and acute stroke therapy conference.** *Stroke* 2015;46:1727–34 CrossRef Medline
19. Saver JL, Jahan R, Levy EI, et al; SWIFT Trialists. **Solitaire flow restoration device versus the Merci retriever in patients with acute ischaemic stroke (SWIFT): a randomised, parallel-group, non-inferiority trial.** *Lancet* 2012;380:1241–49 CrossRef Medline
20. Nogueira RG, Lutsep HL, Gupta R, et al; TREVO 2 Trialists. **Trevo versus Merci retrievers for thrombectomy revascularisation of large vessel occlusions in acute ischaemic stroke (TREVO 2): a randomised trial.** *Lancet* 2012;380:1231–40 CrossRef Medline
21. Tomsick T, Broderick J, Carrozella J, et al; Interventional Management of Stroke II Investigators. **Revascularization results in the In-**

**terventional Management of Stroke II Trial.** *AJNR Am J Neuroradiol* 2008;29:582–87 CrossRef Medline
22. Sarraj A, Gupta R. **Endovascular treatment for ischemic strokes with large vessel occlusion: proven therapy and bright future.** *Stroke* 2015;46:1431–32 CrossRef Medline
23. Chueh JY, Puri AS, Wakhloo AK, et al. **Risk of distal embolization with stent retriever thrombectomy and ADAPT.** *J Neurointerv Surg* 2016;8:197–202 CrossRef Medline
24. Turk AS, Frei D, Fiorella D, et al. **ADAPT FAST study: a direct aspiration first pass technique for acute stroke thrombectomy.** *J Neurointerv Surg* 2014;6:260–64 CrossRef Medline
25. KowollA, WeberA, Mpotsaris A, et al. **Direct aspiration first pass technique for the treatment of acute ischemic stroke: initial experience at a European stroke center.** *J Neurointerv Surg* 2016;8:230–34 CrossRef Medline
26. Guedin P, Larcher A, Decroix JP, et al. **Prior IV thrombolysis facilitates mechanical thrombectomy in acute ischemic stroke.** *J Stroke Cerebrovasc Dis* 2015;24:952–57 CrossRef Medline

# Flow Diversion for Ophthalmic Artery Aneurysms

A.M. Burrows, W. Brinjikji, R.C. Puffer, H. Cloft, D.F. Kallmes, and G. Lanzino

## ABSTRACT

**SUMMARY:** Endovascular treatments of ophthalmic segment aneurysms are commonly used but visual outcomes remain a concern. We performed a retrospective review of patients with carotid-ophthalmic aneurysms treated with flow diversion from June 2009 to June 2015. The following outcomes were studied through chart review: visual outcomes, complications, postoperative stroke and intraparenchymal hemorrhage, and clinical outcomes. Angiographic outcomes were studied with angiography and MRA at 6 months, 1 year, and 3 years. We evaluated 50 carotid-ophthalmic aneurysms in 48 patients, among whom 44 patients with 46 aneurysms underwent treatment. The mean clinical follow-up was 29 ± 22 months (range, 0–65 months). There were no permanent adverse visual outcomes. There was 1 death because of late intraparenchymal hemorrhage (2.2%). Six-month angiography showed complete occlusion in 24 of 37 patients (64.9%), and 3-year angiography results showed occlusion in 24 of 25 patients (96%). In conclusion, flow diversion is a safe and effective treatment for carotid-ophthalmic aneurysms in carefully selected patients. The risk of adverse visual outcomes is low, and most aneurysms progress to complete occlusion.

**ABBREVIATION:** PED = Pipeline Embolization Device

Flow-diverting stents work by directing blood flow away from the aneurysm into the parent vessel, leading to stasis of blood flow within the aneurysm, thrombosis, and, ultimately, complete exclusion of the aneurysm from circulation via endothelial proliferation along the struts of the device.[1-3] Initial preclinical studies suggested that branch vessels covered by the device remain patent because the flow gradient at the branch vessel takeoff inhibits endothelial proliferation.[2-5] In practice, flow diverters have been shown to lead to aneurysm occlusion rates ranging from 69%–94% at 6 months, increasing to 86.8%–95% at 1 year.[6-10] These initial series also reported a wide range of postprocedure morbidity and mortality up to 19%.[6-10] Recently, several series have been published on the specific treatment of paraclinoid aneurysms with the Pipeline Embolization Device (PED; Covidien, Irvine, California) and Surpass Device (Stryker Neurovascular, Kalamazoo, Michigan), reporting complete or near-complete occlusion rates of 75%–92.1% at final angiographic follow-up with very low rates of postprocedure morbidity.[11-14] Many of these series were relatively small, with short angiographic follow-up, and included vastly diverse aneurysms with a common denominator of involvement of the paraclinoid ICA. In this study, we reported on a large series of patients with carotid-ophthalmic artery aneurysms, focusing on periprocedural complications as well as mid- and long-term angiographic and clinical outcomes, including visual outcomes.

## MATERIALS AND METHODS

### Patient Population

Consecutive prospectively collected data on 175 patients evaluated for treatment with PED or, more recently, with Surpass flow diversion were retrospectively analyzed. Patients with carotid-ophthalmic artery aneurysms were identified and analyzed. Carotid-ophthalmic aneurysms were defined as those aneurysms arising from the proximal supraclinoid ICA at the takeoff of the ophthalmic artery with a superior orientation of the aneurysm sac. Information prospectively collected as part of an internal quality assurance project included patient demographics; aneurysm location, classification, and size; symptomatic or asymptomatic status; type and number of devices used; adjunctive coiling; periprocedural technical and clinical complications; length of hospital stay; and angiographic and clinical follow-up.

### Procedure Details

Patients undergoing placement of the PED were premedicated with aspirin and clopidogrel for a minimum of 5 days, and the device was placed while the patient was under full anticoagulation

Received November 25, 2015; accepted after revision March 23, 2016.

From the Departments of Neurologic Surgery (A.M.B., R.C.P., G.L.) and Radiology (W.B., H.C., D.F.K., G.L.), Mayo Clinic, Rochester, Minnesota.

Please address correspondence to Waleed Brinjikji, MD, Mayo Clinic, Department of Radiology, 200 First St SW, Rochester, MN 55905; e-mail: brinjikji.waleed@mayo.edu; @wbrinjikji

http://dx.doi.org/10.3174/ajnr.A4835

(activated clotting time of 250–300 seconds). After the procedure, patients were maintained on dual antiplatelet therapy for 3 months. After 3 months, clopidogrel was discontinued and aspirin was continued indefinitely. The antiplatelet regimen was the same in all patients. No patient underwent testing for clopidogrel response except for the lone patient treated with the Surpass device who underwent the genetic test for *CYP219* as part of the prospective study under which they were treated. All of the procedures were performed with the patient under general endotracheal anesthesia. A bi- or triaxial access technique was used to obtain distal access past the segment of the vessel with the targeted aneurysm. PEDs were sized to match the maximum diameter of the target vessel. At the discretion of the operators, 1 or multiple devices were used to maximize the chance of complete aneurysm occlusion and/or to ensure adequate coverage of the aneurysm neck and of a segment of parent artery proximal and distal to it (usually at least 5 mm). DSA was performed at 2 frames per second before and after placement of the flow diverter. The lone patient treated with the Surpass device was treated in accordance with the Surpass Study Group protocol,[11] which was functionally similar to the operative technique for placement of the PED.

### Study Outcomes

Studied outcomes included new visual symptoms (including vision loss and cranial nerve palsy), angiographic occlusion, patency of the ophthalmic artery at previous angiographic follow-up, perioperative complications, delayed rupture, postoperative stroke and intraparenchymal hemorrhage, and long-term clinical outcomes. All angiographic outcomes were assessed by 1 of 3 senior neurointerventionalists/endovascular neurosurgeons.

### Statistical Analysis

No comparative statistical analysis was performed. Continuous variables are reported as mean and standard deviation. Categoric variables are reported as *n* (%). All analyses were performed by using JMP 10.0 (SAS Institute, Cary, North Carolina).

## RESULTS

We evaluated 50 aneurysms in 48 patients. Flow diversion was attempted but not deployed in 4 patients (8%) because of vessel tortuosity in 3 and aneurysm perforation in 1. In total, 46 carotid-ophthalmic aneurysms were treated in 44 patients, of whom 2 were treated for mirror aneurysms. The mean patient age was 52 ± 14 years, and 41 aneurysms (93%) were found in women. Recurrence after previous non–stent-assisted coiling in patients with prior SAH was the presenting symptom in 4 of 46 aneurysms (8.7%). Of all 46 aneurysms, 10 (21.7%) were symptomatic unruptured aneurysms (including 5 causing vision loss or diplopia) and 32 (69.6%) were asymptomatic unruptured aneurysms.

Of the 46 aneurysms, 24 (52%) were 10 mm or smaller (range, 3.5–10 mm), 21 (45.7%) were large (10–25 mm), and 1 (2.3%) was giant (25 mm). Twelve (26.1%) of the aneurysms had been previously coiled and were treated with the PED for aneurysm recurrence or as a planned staged procedure. One aneurysm was treated with the Surpass device and 45 were treated with PED. Most aneurysms (32 [69.6%]) were treated with 1 device, 9 (19.6%) were treated with 2 devices, and 5 (10.8%) were treated with 3 devices.

The mean clinical follow-up was 29 ± 22 months (range, 0–65) and no patient was lost to clinical follow-up. At 12 days, 1 patient with a 21-mm aneurysm died of a delayed distal intraparenchymal hemorrhage not related to aneurysm rupture (procedure related mortality, 2.2%), and 3 patients died of newly diagnosed (after the treatment) metastatic cancer at a mean of 40.7 months (range, 31–53 months). There were no delayed aneurysm ruptures. At 3 months, 1 patient experienced transient peripheral vision loss, possibly related to ipsilateral embolism from the device based upon MRI, which showed several small foci of restricted diffusion. She did not experience permanent vision loss. At 3 and 6 months after PED placement, 2 patients experienced possible amaurosis fugax that resolved after reestablishing dual antiplatelet therapy. The ophthalmic artery remained patent in all these patients. No other ophthalmologic complications were noted, and aside from the patient who suffered distal intraparenchymal hemorrhage, no other patient suffered a permanent neurologic deterioration because of the immediate or delayed effect of the procedure.

Among the 46 aneurysms, 37 (80.4%) had 6-month angiographic follow-up, which showed complete occlusion in 24 (64.9%) and persistent filling in 13 (35.1%) based on strict angiographic criteria. Exclusion from 6-month angiography was found for the following reasons: death (1 patient), and refusal (2 patients). Six patients have not had angiographic follow-up due to the fact that they were less than 6 months out from the procedure at the time of this study. At 1 year, 29 of these 37 aneurysms (78.4%) were completely occluded and 8 (21.6%) showed persistent filling. At 3-year follow-up, 24 of 25 aneurysms (96%) were occluded (Figure). No aneurysms shown to be occluded were found to have recanalized on later angiography. Among patients with angiographic follow-up, the ophthalmic artery was patent in 29 (78.4%). Among the 8 patients in whom ophthalmic artery occlusion was noted, all had reconstitution of the ophthalmic artery through collaterals. In 7 patients, this occurred through external carotid artery collaterals, and in 1 patient, it occurred through the inferolateral trunk.

## DISCUSSION

Our study of 44 patients with 46 ophthalmic segment aneurysms treated with flow diversion demonstrated high rates of angiographic occlusion with low rates of clinical adverse events, which included worsening of visual function. Rates of complete occlusion at 6 months, 1 year, and 3 years were 65%, 78%, and 96%, respectively. Only 1 patient experienced procedure-related morbidity or mortality, and no patients had permanent loss of visual function after treatment of ophthalmic segment aneurysms. Of 37 aneurysms that had 6-month angiography, there were 8 cases of ophthalmic artery occlusion after treatment, which were all asymptomatic. These findings are important because they suggest that flow diversion of ophthalmic segment aneurysms is safe and effective. In our opinion, flow diversion is now the treatment of choice for these aneurysms.

Several recent studies have reported series of patients with carotid-ophthalmic aneurysms treated by flow diversion. In a

**FIGURE.** This 42-year-old woman underwent treatment with 3 PEDs for symptomatic left cavernous and ophthalmic segment aneurysms (shown in 3D rotation angiography, *A*). Immediate postdeployment early arterial lateral angiography shows both aneurysms filling (*B*), while late arterial phase shows contrast stasis in both aneurysms (*C*). After 6 months (*D*), 1 year (*E*), and 3 years (*F*), a lateral early arterial phase angiogram shows persistent ophthalmic aneurysm filling (*black arrows*), persistent ophthalmic artery filling, and a partially obliterated cavernous aneurysm with persistent filling through the posterior portion of the aneurysm. Because the aneurysm was nearly completely occluded at 3 years, a 5-year follow-up MRA was recommended for further follow-up.

subgroup analysis of the Pipeline for Uncoilable or Failed Aneurysms (PUFS) trial, Salhein et al[15] examined the neuro-ophthalmologic outcomes of 98 patients with ICA aneurysms who had neuro-ophthalmologic follow-up. Of the 30 paraophthalmic segment aneurysms treated in this study, 8 presented with visual field or cranial nerve deficits, and 7 patients reported improvement in symptoms with treatment. There were no cases of worsening of visual field or cranial nerve deficits among paraophthalmic aneurysms in this study. Similar results have been reported in other large series of paraophthalmic aneurysms receiving flow-diverter treatment.[11,13] Likewise, in our series of 44 patients with 46 aneurysms, no patients experienced visual worsening after flow-diverter treatment. A recent international retrospective review of aneurysms treated with flow diversion revealed that complications were more likely in aneurysms larger than 10 mm and among those in the posterior circulation.[16] The lone death in our series occurred in a patient with a 21-mm aneurysm.

In general, complete or near-complete occlusion rates after flow-diverter treatment are on the order of 90% and rates of neurologic complications are low. In our series of 46 ophthalmic segment aneurysms, we saw a progressive increase in the rate of complete occlusion over time, starting with an occlusion rate of 64.9% at 6 months that increased to 96% at 3 years. There was only 1 death related to the procedure.[6]

Similar to prior studies, we found very few instances of ophthalmic artery occlusion after placement of a flow diverter across the ophthalmic artery ostium. In a series of 95 patients in which the ophthalmic artery was covered by at least 1 flow diverter, Chalouhi et al[17] found that the ophthalmic artery remained patent in nearly 95% of patients. Puffer et al[18] found that the ophthalmic artery was patent in over 80% of patients after placement of a PED across its ostium. In our study, the ophthalmic artery was occluded in 21.6% of patients, and in no patient did this result in any new visual symptoms. Ophthalmic artery occlusion after placement of flow diverters across the origin of the artery is more likely to occur if patients have robust collaterals. In patients with inadequate collaterals, the ophthalmic artery stays open akin to important perforating vessels covered by these devices. In such cases, the pressure gradient across the artery (present because of the lack of important collaterals) maintains the patency of the vessel. Because occlusion of the ophthalmic artery occurs almost exclusively in patients with adequate collaterals, patients do not experience symptoms related to occlusion.

Other treatment options for ophthalmic segment aneurysms include microsurgical clipping and coiling with or without stent assistance. Complex ophthalmic segment aneurysms can be treated microsurgically with acceptable rates of complete occlusion (53%), but the complexity of the surgical procedure may put

the patient at risk of worsened visual symptoms postoperatively (with up to 21% of patients with preoperative visual symptoms having postoperative worsening in some series).[19] Conventional endovascular coiling for ophthalmic segment aneurysms carries low risk based on published series (1.4% morbidity, 0% mortality), but 12% of patients treated via conventional endovascular coiling required retreatment.[20,21]

### Limitations

Our study is limited by the retrospective nature of the review, despite the prospectively maintained data base. The data base used for this study included patients treated with flow diversion over several years, and procedural techniques as well as aneurysm morphology deemed amenable to flow diversion have likely changed over that time. It is unclear what effect these changes would have on the analysis, but this still should be noted. Visual field testing was not performed in all patients, and thus, true deficits may be underrepresented. Finally, the 1 patient treated with the Surpass device precludes flow-diverter comparison. Despite these limitations, our series provides a contemporary snapshot of results for a specific subset of aneurysms (true carotid-ophthalmic aneurysms) in an institution where flow diversion has been considered the treatment of choice since its inception.

## CONCLUSIONS

Endovascular flow diversion is a viable treatment option for ophthalmic segment aneurysms, resulting in a high rate of complete or near-complete occlusion and a low rate of complications (specifically, no permanent visual field deficits). Further studies examining neuro-opthalmalolgic outcomes after flow-diverter treatment of paraophthalmic aneurysms would be helpful to confirm these findings.

Disclosures: David F. Kallmes—*UNRELATED*: *Board Membership*: GE Healthcare (Cost effectiveness board)*; *Consultancy*: Medtronic,* *Comments*: Planning and implementing clinical trials; *Grants/Grants Pending*: Microvention,* Medtronic,* Codman,* Surmodics,* Sequent,* Neurosigma,* *Comments*: Preclinical research and clinical trials; *Travel/Accommodations/Meeting Expenses Unrelated to Activities Listed*: Medtronic,* *Comments*: Presentation at FDA panel meeting. Giuseppe Lanzino—*UNRELATED*: *Consultancy*: Covidien/Medtronic.* *Money paid to the institution.

## REFERENCES

1. D'Urso PI, Lanzino G, Cloft HJ, et al. **Flow diversion for intracranial aneurysms: a review.** *Stroke* 2011;42:2363–68 CrossRef Medline
2. Fang S, Lanzino G. **Paraclinoid aneurysms: is there a new endovascular standard?** *Neurol Res* 2014;36:314–22 CrossRef Medline
3. Wakhloo AK, Tio FO, Lieber BB, et al. **Self-expanding nitinol stents in canine vertebral arteries: hemodynamics and tissue response.** *AJNR Am J Neuroradiol* 1995;16:1043–51 Medline
4. Kallmes DF, Ding YH, Dai D, et al. **A new endoluminal, flow-disrupting device for treatment of saccular aneurysms.** *Stroke* 2007;38:2346–52 CrossRef Medline
5. Trager AL, Sadasivan C, Seong J, et al. **Correlation between angiographic and particle image velocimetry quantifications of flow diverters in an in vitro model of elastase-induced rabbit aneurysms.** *J Biomech Eng* 2009;131:034506 CrossRef Medline
6. Becske T, Kallmes DF, Saatci I, et al. **Pipeline for uncoilable or failed aneurysms: results from a multicenter clinical trial.** *Radiology* 2013;267:858–68 CrossRef Medline
7. Lubicz B, Collignon L, Raphaeli G, et al. **Pipeline flow-diverter stent for endovascular treatment of intracranial aneurysms: preliminary experience in 20 patients with 27 aneurysms.** *World Neurosurg* 2011;76:114–19 CrossRef Medline
8. Lylyk P, Miranda C, Ceratto R, et al. **Curative endovascular reconstruction of cerebral aneurysms with the Pipeline embolization device: the Buenos Aires experience.** *Neurosurgery* 2009;64:632–42; discussion 642–43 CrossRef Medline
9. Nelson PK, Lylyk P, Szikora I, et al. **The Pipeline embolization device for the intracranial treatment of aneurysms trial.** *AJNR Am J Neuroradiol* 2011;32:34–40 CrossRef Medline
10. Szikora I, Berentei Z, Kulcsar Z, et al. **Treatment of intracranial aneurysms by functional reconstruction of the parent artery: the Budapest experience with the Pipeline embolization device.** *AJNR Am J Neuroradiol* 2010;31:1139–47 CrossRef Medline
11. Wakhloo AK, Lylyk P, de Vries J, et al. **Surpass flow diverter in the treatment of intracranial aneurysms: a prospective multicenter study.** *AJNR Am J Neuroradiol* 2015;36:98–107 CrossRef Medline
12. Moon K, Albuquerque FC, Ducruet AF, et al. **Treatment of ophthalmic segment carotid aneurysms using the Pipeline embolization device: clinical and angiographic follow-up.** *Neurol Res* 2014;36:344–50 CrossRef Medline
13. Zanaty M, Chalouhi N, Barros G, et al. **Flow-diversion for ophthalmic segment aneurysms.** *Neurosurgery* 2015;76:286–89 CrossRef Medline
14. Burrows AM, Cloft H, Kallmes DF, et al. **Periprocedural and midterm technical and clinical events after flow diversion for intracranial aneurysms.** *J Neurointerv Surg* 2015;7:646–51 CrossRef Medline
15. Sahlein DH, Fouladvand M, Becske T, et al. **Neuroophthalmological outcomes associated with use of the Pipeline embolization device: analysis of the PUFS trial results.** *J Neurosurg* 2015;123:897–905 CrossRef Medline
16. Kallmes DF, Hanel R, Lopes D, et al. **International retrospective study of the Pipeline embolization device: a multicenter aneurysm treatment study.** *AJNR Am J Neuroradiol* 2015;36:108–15 CrossRef Medline
17. Chalouhi N, Daou B, Kung D, et al. **Fate of the ophthalmic artery after treatment with the Pipeline embolization device.** *Neurosurgery* 2015;77:581–84; discussion 584 CrossRef Medline
18. Puffer RC, Kallmes DF, Cloft HJ, et al. **Patency of the ophthalmic artery after flow diversion treatment of paraclinoid aneurysms.** *J Neurosurg* 2012;116:892–96 CrossRef Medline
19. Mattingly T, Kole MK, Nicolle D, et al. **Visual outcomes for surgical treatment of large and giant carotid ophthalmic segment aneurysms: a case series utilizing retrograde suction decompression (the "Dallas technique").** *J Neurosurg* 2013;118:937–46 CrossRef Medline
20. Lai LT, Morgan MK. **Outcomes for unruptured ophthalmic segment aneurysm surgery.** *J Clin Neurosci* 2013;20:1127–33 CrossRef Medline
21. Yadla S, Campbell PG, Grobelny B, et al. **Open and endovascular treatment of unruptured carotid-ophthalmic aneurysms: clinical and radiographic outcomes.** *Neurosurgery* 2011;68:1434–43; discussion 1443 CrossRef Medline

# Ocular Signs Caused by Dural Arteriovenous Fistula without Involvement of the Cavernous Sinus: A Case Series with Review of the Literature

T. Robert, D. Botta, R. Blanc, R. Fahed, G. Ciccio, S. Smajda, H. Redjem, and M. Piotin

## ABSTRACT

**SUMMARY:** Carotid cavernous fistula is a well-known clinical and angiographic entity responsible for ocular signs and symptoms. On the contrary, ocular signs are unusual in the presentation of cranial dural arteriovenous fistulas at locations other than the cavernous sinus. We retrospectively analyzed data focusing on the pathophysiology of ophthalmologic signs and their angiographic explanations. Thirteen patients were included with a mean age of 50 years. The most common signs were chemosis (61.5%), loss of visual acuity (38.5%), exophthalmia (38.5%), and ocular hypertension (7.7%). Dural arteriovenous fistulas presenting with ocular signs could be classified into 4 types due to their pathologic mechanism (local venous reflux into the superior ophthalmic vein, massive venous engorgement of the cerebrum responsible for intracranial hypertension, compression of an oculomotor nerve by a venous dilation, or intraorbital fistula with drainage into the superior ophthalmic vein).

**ABBREVIATIONS:** dAVF = dural arteriovenous fistula; SOV = superior ophthalmic vein

Carotid-cavernous fistula is a well-known clinical and angiographic entity responsible for ocular signs and symptoms.[1,2] The venous engorgement transmitted from the cavernous sinus to the superior and/or, rarely, the inferior ophthalmic veins could explain these ocular signs. On the contrary, ocular signs are very unusual in the presentation of cranial dural arteriovenous fistulas (dAVFs) in locations other than the cavernous sinus.[3] In the literature, isolated cases of dAVFs without involvement of the cavernous sinus, revealed by ocular signs, could be found.[4,5] These particular and well-described cases were rarely accompanied by a pathophysiologic explanation of the clinical signs. The authors categorized the different dAVFs associated with ocular signs on the basis of a 15-year-experience in the endovascular treatment of cranial dAVFs.

## MATERIALS AND METHODS

### *Patient Selection*

We have maintained an ongoing prospective data base with demographic, clinical, and angiographic information regarding patients with cranial dAVFs. From 2000 to 2015, 305 patients with dAVFs have been evaluated in our institution. In this study, we retrospectively reviewed data of patients who met the following criteria: 1) the first clinical sign was ophthalmic, 2) a cranial dAVF was confirmed by digital subtraction angiography, and 3) the location of the fistulous point of the dAVF was not in the cavernous sinus. Demographic data were recorded for each patient, including age, sex, vascular risk factors, and clinical presentation.

### *Pretherapeutic Clinical Evaluation*

A clinical history and a neurologic examination were performed for each patient before the treatment of the fistula. We mainly looked for the presence of an etiology, the duration of symptoms, the type of clinical sign, and the evaluation with a modified Rankin Scale score. Each patient also benefited from an ophthalmologic examination, including a visual acuity examination, a Lancaster test, a funduscopy, and a Goldman test.

### *Analysis of the Dural Arteriovenous Anatomy*

Each patient underwent a 6-vessel pretherapeutic DSA under local anesthesia. We reviewed these examinations with attention paid to the location of the fistulous point and angiographic factors that could explain the ocular sign (venous reflux, compression of a cranial nerve, or venous congestion). The presence of a venous thrombosis, stenosis, or ectasia was also noted. Special attention was paid to the pathophysiology of ocular signs presented by each patient.

### *Endovascular Treatment*

All endovascular treatment was performed with the patient under general anesthesia. After cerebral MR imaging and DSA were per-

Received February 2, 2016; accepted after revision March 31.

From the Department of Interventional Neuroradiology, Rothschild Foundation Hospital, Paris, France.

T. Robert and D. Botta have participated equally in this work.

Please address correspondence to Thomas Robert, MD, Rothschild Foundation Hospital, 25 Rue Manin, 75019 Paris, France; e-mail: thomas.robert43@gmail.com

http://dx.doi.org/10.3174/ajnr.A4831

formed, the location and the anatomy of the dAVF were discussed, with the aim of choosing the more appropriate treatment.

### *Postoperative Follow-Up*

Follow-up started at the time of the last embolization session and finished with the last visit or angiography. Angiographic follow-up was performed 6 months after treatment to confirm the occlusion of the arteriovenous shunt. A neurologic examination with evaluation with the mRS was systematically performed for each visit. An ophthalmologic examination was performed in the posttreatment period (within 3 months after each embolization session).

**Table 1: Demographic and clinical data of the population**

| Variable | Patients (*n* = 13) |
|---|---|
| Age (yr) (median) (range) | 50.3 (15–72) |
| Men | 9 (69.2%) |
| Clinical signs | |
| Pulsatile tinnitus | 5 (38.5%) |
| Chemosis | 8 (61.5%) |
| Exophthalmia | 5 (38.5%) |
| Loss of visual acuity | 5 (38.5%) |
| Ocular hypertension | 1 (7.7.%) |
| Oculomotor palsy | 4 (30.8%) |
| Third CN palsy | 2 (15.4%) |
| Fourth CN palsy | 2 (15.4%) |
| Sixth CN palsy | 3 (23.1%) |
| Papillary edema | 9 (69.2%) |
| Time between first sign and diagnosis (mo) | 10 (1–36) |
| mRS score before treatment | |
| 1 | 9 (69.2%) |
| 2 | 4 (30.8%) |

**Note:**—CN indicates cranial nerve.

## RESULTS

### *Demographic Data and Clinical Presentation*

Between 2000 and 2015, 13 patients met the inclusion criteria of this study. Patient baseline data and clinical signs are described in Table 1. The mean age was 50.3 years (range, 15–72 years) with a male preponderance (M/F ratio = 2.25 and 2:25). The most common clinical sign was chemosis in 8 patients (61.5%), followed by loss of visual acuity (5 patients, 38.5%), exophthalmia (5 patients, 38.5%), and ocular hypertension in 1 patient (7.7%). Papillary edema was noted in 9 patients (69.2%) and was unilateral in 7 cases and bilateral in 2 others.

### *Local Venous Reflux into the Ophthalmic Veins*

Ocular signs could be explained by ophthalmic venous engorgement secondary to venous reflux from the fistulous point in most cases (7/13) in our series. All patients in this group presented with a chemosis, which was associated with proptosis in 5 patients, progressive loss of acuity in 1 patient, ocular hypertension in 1 patient, and oculomotor nerve paresis in 2 patients. The classifi-

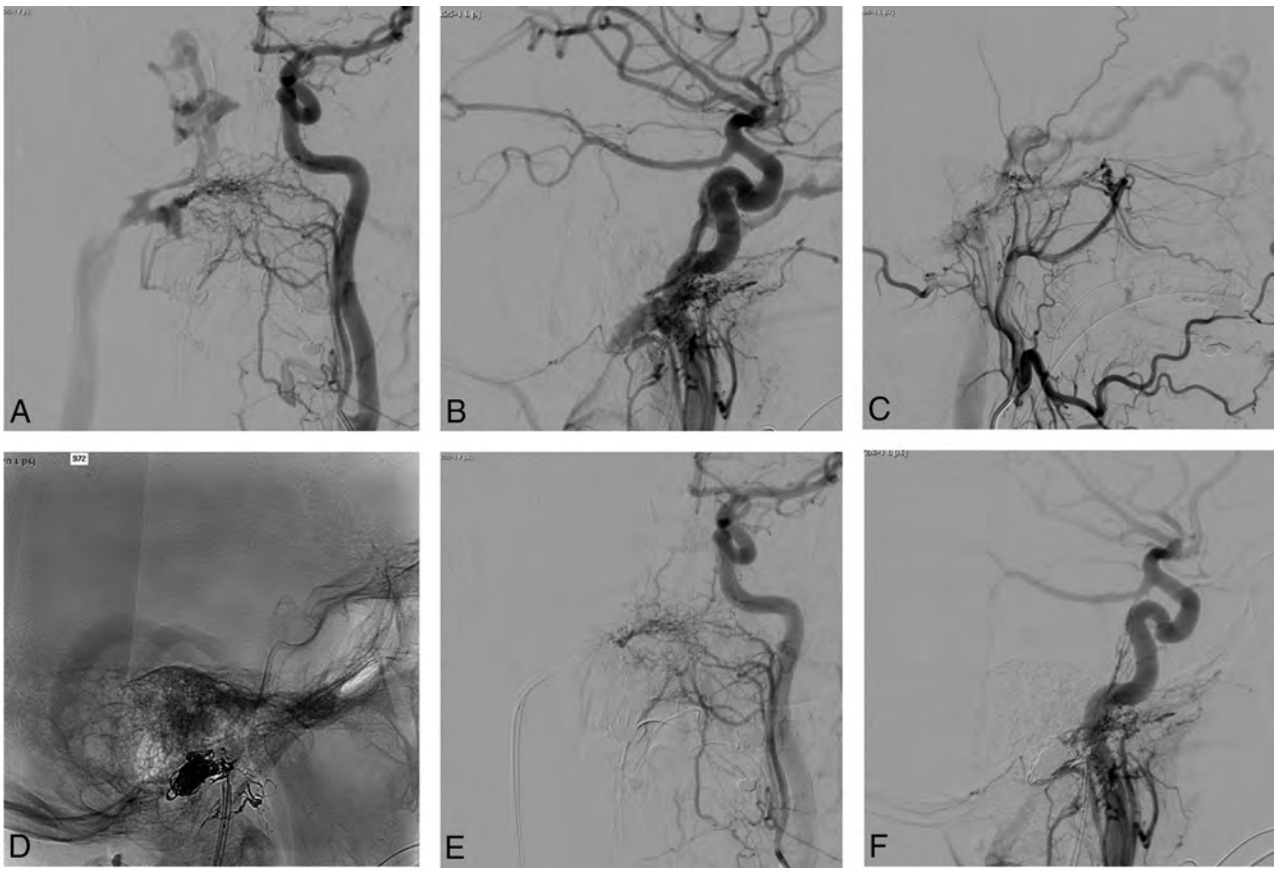


**FIG 1.** Pretherapeutic left common carotid artery DSA in anteroposterior (*A*) and lateral (*B*) projections and external carotid artery DSA in a lateral projection (*C*) highlighting a right jugular foramen dAVF with venous reflux into the right inferior petrosal sinus, the right cavernous sinus, and the right superior ophthalmic vein in a patient presenting with right chemosis and exophthalmia. *D*, Note the cast of Onyx (Covidien, Irvine, California) after an arterial embolization. Posttherapeutic left common carotid injections in anteroposterior (*E*) and lateral (*F*) projections.

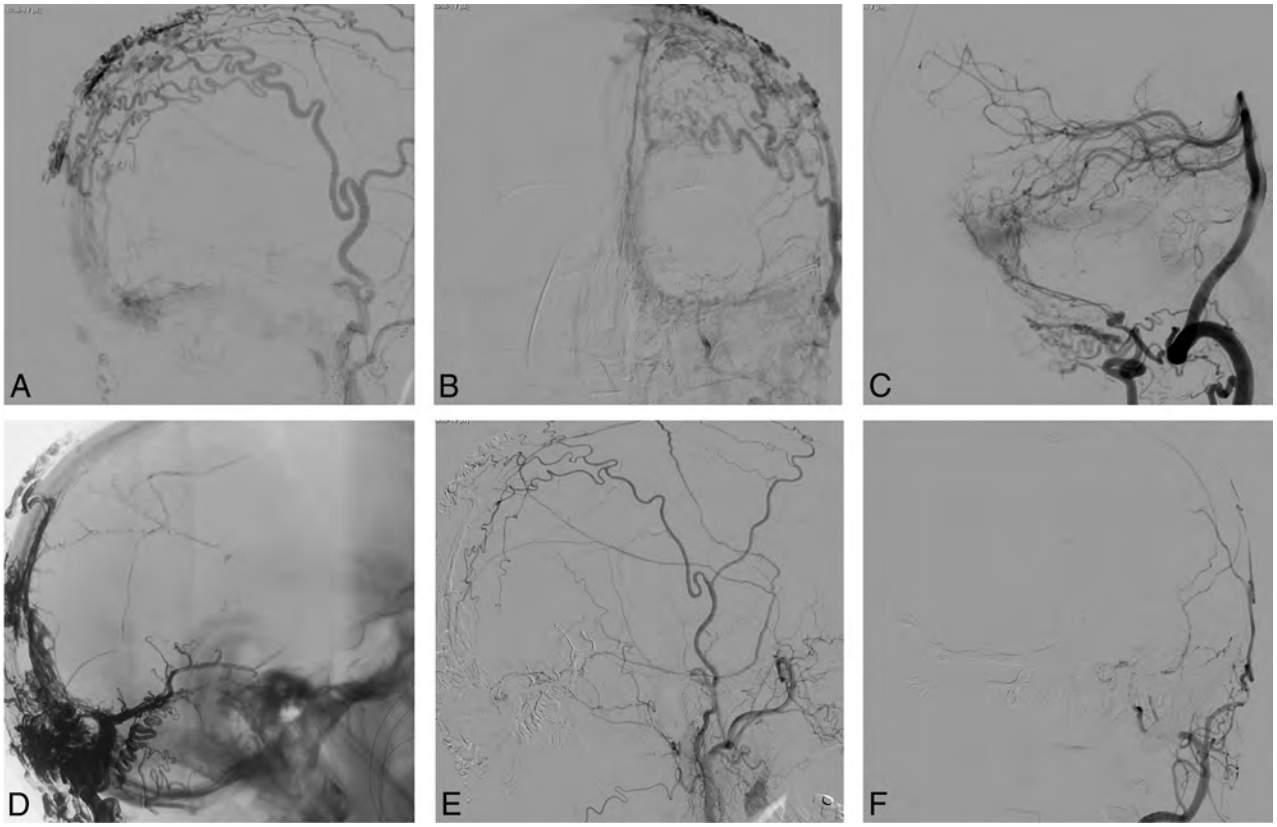


**FIG 2.** Lateral (*A*) and anteroposterior (*B*) projections of a pretherapeutic left external carotid artery DSA showing a complex fistula of the posterior third of the superior sagittal sinus in a patient with signs of intracranial hypertension. Lateral projection (*C*) of the left vertebral artery injection in the same patient shows multiple fistulous points on the transverse and sigmoid sinuses. *D*, A lateral skull x-ray with the important cast of Onyx used to treat the fistulas. Posttherapeutic lateral (*E*) and anteroposterior (*F*) projections of the left external carotid artery injection.

cation of Lariboisière was 2a+b in 4 cases and 3 in 3 cases. Three fistulas were located in the middle cranial fossa, with venous drainage involving the sphenoparietal sinus, the cavernous sinus, and the superior ophthalmic vein (SOV). The venous reflux also involved the uncal vein in 1 of these cases. Two other fistulas were located in the lateral sinus with a venous reflux important enough to involve the vein of Labbé, the superficial middle cerebral vein, the cavernous sinus, and the SOV. The last 2 fistulas were located at the jugular foramen, and the venous reflux involved the inferior petrosal sinus, the cavernous sinus, and, finally, the SOV (Fig 1).

### *Intracranial Hypertension due to Venous Reflux*

In this series, 4 patients had signs of intracranial hypertension syndrome, in particular a progressive decrease of visual acuity associated with headache (1 case) and sixth nerve palsy (1 case). In all cases, a bilateral papillary edema was found at funduscopy. All these patients had high-flow dAVFs with bilateral venous reflux and type 2a+b fistulas. The fistulous point was always located on a large venous sinus: the rectus sinus in 1 case, lateral sinuses in 2 cases, and the superior sagittal sinus in 1 case (Fig 2). Arterial feeders of these fistulas did not present particularity instead of their high number (4–12) and the recruitment of transosseous branches from occipital and superficial temporal arteries. In 3 of these 4 cases, multiple fistulous points were identified along the sinus wall. In 1 case, a sinus thrombosis, which increases venous reflux, was present. None of these cases had reversal flow of the SOV, and the ocular signs could not be explained by local orbital venous obstruction.

### *Cranial Nerve Compression by a Venous Ectasia*

In 2 patients in this series, the ocular signs could only be explained by cranial nerve compression. The first one was a dAVF located on the free border of the tentorium. Feeding arteries were the medial tentorial artery (meningohypophyseal trunk), the petrous branch of the middle meningeal artery, and the mastoid branch of the occipital artery. The venous drainage interested the basal vein of Rosenthal without venous reflux but with a venous ectasia of the posterior third of the basal vein of Rosenthal (Lariboisière fistula type 4). This patient was admitted for a progressive trochlear nerve palsy, which could easily be explained by the compression of the trochlear nerve by the dilated basal vein of Rosenthal in the ambient cistern (Fig 3).

The second case was a man who had a 1-month history of progressive unilateral oculoparesis. The ophthalmologic examinations revealed third, fourth, and sixth cranial nerve paresis. The DSA showed a dAVF located under the lesser sphenoid wing in the region of the superior orbital fissure. Arterial feeders were the recurrent meningeal artery, the middle meningeal artery, and the deep temporal artery. Venous drainage involved the SOV and the cavernous sinus, with a venous ectasia of the SOV in the superior orbital fissure (Lariboisière fistula type 4). This venous ectasia was the only explanation for the oculomotor paresis.

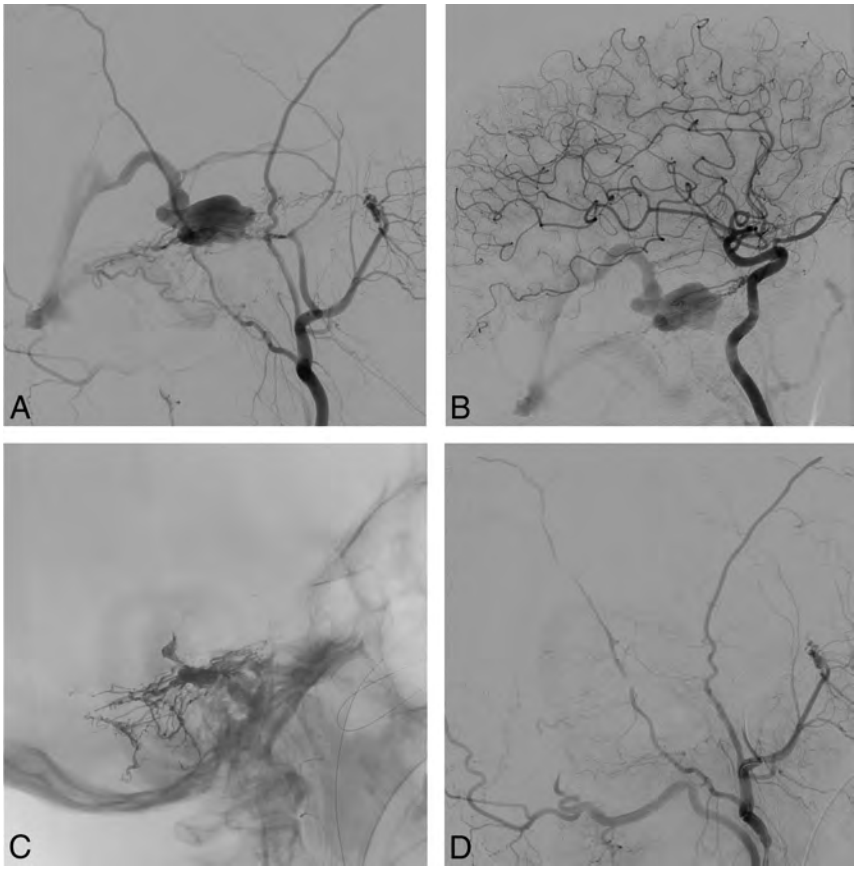


**FIG 3.** Pretherapeutic lateral projections of the right external (*A*) and internal (*B*) carotid artery DSA highlighting a tentorial dAVF with venous ectasia of the third portion of the basal vein in a patient with a trochlear nerve deficit. *C*, Note the cast of Onyx (Covidien, Irvine, California) after injection through the middle meningeal artery branches. *D*, Posttherapeutic right external carotid artery DSA in a lateral projection without a residual fistula.

### *Treatment of the Pathology*

Treatment details and outcome are summarized in Table 2. Every patient was treated by endovascular therapy. Twenty-three embolization sessions were necessary to treat the fistulas. Seven patients were successfully treated in 1 session, 4 patients had 2 sessions, and 2 fistulas needed 3 sessions to be completely obliterated. One patient was treated by microsurgical exclusion of a middle cranial fossa fistula after failed embolization.

An arterial approach was used in 8 sessions; a venous approach, in 14 patients; and a combined approach, in 1 patient. The overall success rate per embolization session was 52.2% (12 embolization sessions). In 4 patients (15.4%), the fistula persisted after the injection of the embolic agent, and in 2 patients (7.7%), the venous access to the fistula was impossible. Among these 4 patients, in 2, a partial embolization was planned to reduce the venous reflux and to decrease the intracranial pressure. In 2 patients (8.8%), the implantation of coils in an arterial feeder near the fistulous point was sufficient to obliterate the fistula.

### *Clinical and Angiographic Follow-Up*

The fistula was cured at the 6-month follow-up DSA in 11 cases (78.5%). A partial embolization was planned for 2 patients who had a complex dAVF and intracranial hypertension.

Neurologic complications were found after 2 embolization sessions. One patient with a tentorial fistula developed an extensive venous thrombosis a few hours after the embolization, responsible for a hemiplegia and multiple cranial nerve palsies. This patient was dependent and died 1 year after the treatment. The other patient with a complication had a middle cranial fossa dAVF treated by coils and Glubran Tiss (Aspide Medical, La Talaudiére, France). Twenty-four hours after the treatment, she developed a temporal lobe hematoma with a contralateral hemiparesis (mRS 3). The mean clinical follow-up was 10.1 months (range, 1–48 months). At the last follow-up visit, 3 patients had mRS 0; 6, mRS 1; 2, mRS 2; 1, mRS 3; and 1, mRS 6. The ophthalmologic examination findings 3 months after treatment were normal in 8 patients.

## DISCUSSION

Cranial dural arteriovenous fistulas are often symptomatic, with a pulsatile tinnitus with or without headache, focal neurologic deficit, or compressive signs.[1,3,6] The occurrence of an intracerebral hematoma is also a well-known entity, in particular in cases of venous reflux, cortical vein involvement, or venous ectasia.[1] In rare cases, a dAVF could be symptomatic by ocular signs such as chemosis, exophthalmia, loss of visual acuity, or oculomotor nerve palsy.[5] The literature of these dAVFs is exclusively represented by case reports and small case series.[3,16,19] These articles generally described the symptoms and angiographic anatomy of the fistula well but detailed analysis of the pathophysiology was always missed except for the series of Cognard et al.[4]

The first and most frequent type of fistula in our series occurred when the ocular signs could be explained by a direct venous reflux into the orbital veins. This was also the most frequent type in the literature.[7] These fistulas are generally located on the transverse sinus,[8] with a reflux through the vein of Labbé or at the foramen magnum. For a venous reflux to produce orbital venous hypertension, thrombosis or noncompetence of a large venous collector (jugular bulb or transverse sinus) is necessary. The middle cranial fossa is also described with reflux into the sphenoparietal sinus.[3] The anatomic variant of the paracavernous sinus could be an important factor in venous reflux into the superior orbital vein. Two case reports[9,10] of tentorial dAVFs with venous reflux into a basal vein, an uncal vein, and a superior ophthalmic vein are also described, but they seem to be rare. The importance of the venous reflux and the high frequency of venous ectasia in these fistulas are 2 reasons for aggressive management. These fistulas were treated by an arterial approach in all cases described. In the literature and in our series, ocular symptoms and signs were reversible after endovascular treatment of the fistula. With a sim-

**Table 2: Details of endovascular treatment and outcome**

| Variable | No. (%) |
|---|---|
| Total No. of embolization sessions | 23 |
| Embolization per patient (mean) (range) | 1.8 (1–3) |
| Venous approach | 14 (60.8%) |
| Arterial approach | 8 (34.8%) |
| Combined approach | 1 (4.3%) |
| Overall success rate | 12 (52.2%) |
| Incomplete closed fistula | 4 (15.4%) |
| Impossible to catheterize | 2 (7.7%) |
| Embolic agent used | |
| Onyx | 12 (52.2%) |
| Coils + Onyx | 5 (21.7) |
| Glubran Tiss | 4 (17.4%) |
| Coils | 2 (8.8%) |
| Success rate | |
| By patient | 11/14 (78.5%) |
| Associated microsurgery | 1/14 (7.2%) |
| Complications | |
| Permanent | 2 (8.7%) |
| Death | 1 (4.3%) |
| Follow-up | |
| Mean (range) (mo) | 10.1 (1–48) |
| Last mRS | |
| 0 | 3 (23.1%) |
| 1 | 6 (46.2%) |
| 2 | 2 (15.4%) |
| 3 | 1 (7.2%) |
| 6 | 1 (7.2%) |
| Ophthalmologic follow-up | |
| Normal findings | 8 (61.5%) |
| Central scotoma | 1 (7.2%) |
| Third and sixth nerve palsy | 1 (7.2%) |
| Ocular hypertonia | 1 (7.2%) |
| Persistent papillary edema | 1 (7.2%) |
| Lost to follow-up | 1 (7.2%) |

ilar pathologic mechanism, few cases of cerebral arteriovenous malformations[11] with ocular signs were reported.

Intracranial hypertension syndrome could also explain the ocular signs. Patients had a loss of visual acuity secondary to papillary edema or optic disc atrophy.[1,12,13] Generally, these dAVFs were multiple arteriovenous shunts located on large sinuses, important because they could influence the venous drainage of the encephalon.[4] The venous engorgement or reflux provoked by the high flow of the fistula causes hydrocephalus and possibly parenchymal edema. The first article describing an elevation of intracranial pressure in a posterior fossa dAVF was that of Lamas et al[14] in 1977. In 1998, Cognard et al[4] published a series including 13 patients with dAVFs with signs of intracranial hypertension. Among these 13 patients, 8 had a papilledema and 4 had optic disc atrophy. Other clinical signs described were seizures, tinnitus, headache, and diplopia.

As for patients in our series, the location of the fistula was always on a large dural sinus with multiple arteriovenous shunts. We found a sinus anomaly (thrombosis, agenesis) in 7 of 13 patients. The treatment of this type of fistula must be aggressive to avoid the progression of intracranial hypertension signs and irreversibility of optic disc atrophy. This treatment is always challenging because of the multiplicity of shunts. Partial embolization could be an alternative to decrease the flow of the pathology without risking occlusion of a large dural sinus. This partial treatment is often temporary. An aggressive arterial embolization of the fistulas could be performed with concomitant inflation of a large balloon into the dural sinus, but this treatment exposes the patient to a higher risk of complications.[15] The placement of a ventriculoperitoneal shunt is also a palliative solution. The choice of treatment depends on the anatomy of the arteriovenous shunts, their location, the severity of the clinical signs, and the patient's comorbidities.

The compression of a cranial nerve by venous dilation in case of arteriovenous shunt is well-known, especially for the trigeminal nerve. The occurrence of an oculomotor paresis secondary to the same diagnosis is rarely reported in the literature, perhaps due to lack of knowledge of anatomic details. Only 1 case report[16] of a trochlear nerve deficit caused by a tentorial dAVF and, in particular, a venous ectasia could be found in the literature. The anatomic details and the relationship between the trochlear nerve and the venous structures in the perimesencephalic cisterns were not well-developed in this article. In our series, a similar case is presented. This is a dAVF located in the posterior incisural space with its venous drainage involving the posterior part of the basal vein. As described by Ono et al[17] and by Joo and Rhoton,[18] the trochlear nerve has an intimal relationship with the third portion of the basal vein and with the superior cerebellar artery into the ambient cistern. A dilation of the basal vein in its ambient course could easily result in trochlear nerve compression and a dilation of the lateromesencephalic vein. The other case in our series with the same pathologic mechanism is a dAVF located in the region of the superior orbital fissure with drainage into the sphenoparietal sinus and the superior ophthalmic vein. This latter vein had an important dilation at its intracanalicular portion that caused a compression of nerves (third, fourth, and sixth nerves associated with an ophthalmic hypoesthesia, typical of superior orbital fissure syndrome).

Another type of fistula with ocular signs is an intraorbital fistula, with direct drainage into the superior ophthalmic vein. We did not have fistulas of this type in our series, but in 2 case reports,[7,19] they are well-documented. These fistulas were fed by ethmoidal branches and were directly drained by the superior ophthalmic vein; this scenario created intraorbital hypertension. One of these 2 cases was successfully treated by arterial embolization[7]; the other, by a venous approach after surgical exposure of the superior ophthalmic vein. Pan et al[5] also reported 3 other cases of intraorbital shunt treated by radiosurgery, but not enough details were reported to understand the pathophysiology of these fistulas.

## CONCLUSIONS

DAVFs with ocular signs could be classified into 4 types due to the pathologic mechanisms that explain these signs. The first type is a local venous reflux into the superior ophthalmic vein, the second is a massive venous engorgement of the cerebrum responsible for intracranial hypertension, the third is a direct compression of an oculomotor nerve by a venous dilation, and the last is an intraorbital fistula with direct drainage into the superior ophthalmic vein.

Disclosures: Michel Piotin—*UNRELATED*: *Consultancy*: Medtronic,* Stryker,* MicroVention,* Balt*; *Payment for Lectures (including service on Speakers Bureaus)*: Penumbra.* *Money paid to the institution.

## REFERENCES


1. Awad IA, Little JR, Akarawi WP, et al. **Intracranial dural arteriovenous malformations: factors predisposing to an aggressive neurological course.** *J Neurosurg* 1990;72:839–50 Medline
2. Cognard C, Gobin YP, Pierot L, et al. **Cerebral dural arteriovenous fistulas: clinical and angiographic correlation with a revised classification of venous drainage.** *Radiology* 1995;194:671–80 Medline
3. Hayreh SS. *Ocular Vascular Occlusion Disorders.* New York: Springer; 2015
4. Cognard C, Casasco A, Toevi M, et al. **Dural arteriovenous fistulas as a cause of intracranial hypertension due to impairment of cranial venous outflow.** *J Neurol Neurosurg Psychiatry* 1998;65:308–16 Medline
5. Pan HC, Sun MH, Chen WH, et al. **Minimally invasive approaches to treating chemosis of the eyes from unusual dural arteriovenous fistulae.** *Minim Invasive Neurosurg* 2009;52:222–28 CrossRef Medline
6. Gandhi D, Chen J, Pearl M, et al. **Intracranial dural arteriovenous fistulas: classification, imaging findings, and treatment.** *AJNR Am J Neuroradiol* 2012;33:1007–13 CrossRef Medline
7. Inoue A, Tagawa M, Kumon Y, et al. **Ethmoidal dural arteriovenous fistula with unusual drainage route treated by transarterial embolization.** *J Neurointerv Surg* 2015;7:e15 CrossRef Medline
8. Feyissa AM, Ponce LL, Patterson JT, et al. **Dural arteriovenous fistula presenting with exophthalmos and seizures.** *J Neurol Sci* 2014; 338:229–31 CrossRef Medline
9. Benndorf G, Schmidt S, Sollmann WP, et al. **Tentorial dural arteriovenous fistula presenting with various visual symptoms related to anterior and posterior visual pathway dysfunction: case report.** *Neurosurgery* 2003;53:222–26; discussion 226–27 Medline
10. Iizuka Y, Maehara T, Hishii M, et al. **Successful transarterial glue embolisation by wedged technique for a tentorial dural arteriovenous fistula presenting with a conjunctival injection.** *Neuroradiology* 2001;43:677–79 Medline
11. Gregory ME, Berry-Brincat A, Ghosh YK, et al. **An arteriovenous malformation masquerading as a carotid-cavernous sinus fistula.** *Am J Ophthalmol* 2005;140:548–50 Medline
12. Biousse V, Mendicino ME, Simon DJ, et al. **The ophthalmology of intracranial vascular abnormalities.** *Am J Ophthalmol* 1998;125: 527–44 Medline
13. Gelwan MJ, Choi IS, Berenstein A, et al. **Dural arteriovenous malformations and papilledema.** *Neurosurgery* 1988;22:1079–84 Medline
14. Lamas E, Lobato RD, Esperarza J, et al. **Dural posterior fossa AVM producing raised sagittal simus pressure: case report.** *J Neurosurg* 1977;46:804–10 Medline
15. Zako M, Murata K, Inukai T, et al. **Long-term progressive deterioration of visual function after papilledema improved by embolization of a dural arteriovenous fistula in the sigmoid sinus: a case report.** *J Med Case Rep* 2014;8:392 CrossRef Medline
16. Mariniello G, Briganti F, Vergara P, et al. **Dural tentorial arteriovenous fistula causing isolated trochlear nerve palsy: remission after endovascular embolization.** *J Neurointerv Surg* 2012;4:e5 CrossRef Medline
17. Ono M, Rhoton AL Jr, Peace D, et al. **Microsurgical anatomy of the deep venous system of the brain.** *Neurosurgery* 1984;15:621–57 Medline
18. Joo W, Rhoton AL Jr. **Microsurgical anatomy of the trochlear nerve.** *Clin Anat* 2015;28:857–64 CrossRef Medline
19. Daou B, Chalouhi N, Williams K, et al. **An unusual case of an ethmoidal arteriovenous fistula draining into the superior ophthalmic vein.** *Neurosurgery* 2015 Aug 6. [Epub ahead of print] Medline

# Computational Modeling of Venous Sinus Stenosis in Idiopathic Intracranial Hypertension

M.R. Levitt, P.M. McGah, K. Moon , F.C. Albuquerque, C.G. McDougall, M.Y.S. Kalani, L.J. Kim, and A. Aliseda

## ABSTRACT

**BACKGROUND AND PURPOSE:** Idiopathic intracranial hypertension has been associated with dural venous sinus stenosis in some patients, but the hemodynamic environment of the dural venous sinuses has not been quantitatively described. Here, we present the first such computational fluid dynamics model by using patient-specific blood pressure measurements.

**MATERIALS AND METHODS:** Six patients with idiopathic intracranial hypertension and at least 1 stenosis or atresia at the transverse/sigmoid sinus junction underwent MR venography followed by cerebral venography and manometry throughout the dural venous sinuses. Patient-specific computational fluid dynamics models were created by using MR venography anatomy, with venous pressure measurements as boundary conditions. Blood flow and wall shear stress were calculated for each patient.

**RESULTS:** Computational models of the dural venous sinuses were successfully reconstructed in all 6 patients with patient-specific boundary conditions. Three patients demonstrated a pathologic pressure gradient (≥8 mm Hg) across 4 dural venous sinus stenoses. Small sample size precludes statistical comparisons, but average overall flow throughout the dural venous sinuses of patients with pathologic pressure gradients was higher than in those without them (1041.00 ± 506.52 mL/min versus 358.00 ± 190.95 mL/min). Wall shear stress was also higher across stenoses in patients with pathologic pressure gradients (37.66 ± 48.39 Pa versus 7.02 ± 13.60 Pa).

**CONCLUSIONS:** The hemodynamic environment of the dural venous sinuses can be computationally modeled by using patient-specific anatomy and physiologic measurements in patients with idiopathic intracranial hypertension. There was substantially higher blood flow and wall shear stress in patients with pathologic pressure gradients.

**ABBREVIATIONS:** CFD = computational fluid dynamics; IIH = idiopathic intracranial hypertension; WSS = wall shear stress

Idiopathic intracranial hypertension (IIH), also known as pseudotumor cerebri or benign intracranial hypertension, has been associated with dural venous sinus stenosis.[1,2] While many patients with IIH have anatomic evidence of venous sinus stenosis,[3] cerebral venography and invasive manometry are often used to differentiate patients with a "pathologic" stenosis, which demonstrates a pressure gradient across the stenosis, from those without such a gradient, to determine which patients may benefit from endovascular stent placement.[4,5] That some patients with IIH present with this pressure gradient and others do not, despite similar anatomic narrowing of the dural venous sinuses, suggests that the mechanism by which IIH is related to venous sinus stenosis may depend on hemodynamic characteristics of dural venous sinus drainage.[6] However, venous manometry measures only blood pressure rather than blood flow through the complex 3D hemodynamic environment of the dural venous sinuses.

Patient-specific computational fluid dynamics (CFD) modeling of the hemodynamic environment of patients with IIH with and without a physiologic stenosis could improve the understanding of IIH pathophysiology and potentially aid in patient selection for endovascular stent placement. In this study, we constructed CFD models of patients' dural venous sinuses, with simulated blood flow informed by patient-specific pressure measurements obtained during invasive cerebral venography, to accurately model the hemodynamics of IIH in patients with dural venous sinus stenosis.

Received October 12, 2015; accepted after revision March 31, 2016.

From the Departments of Neurological Surgery (M.R.L., L.J.K.), Radiology (M.R.L., L.J.K.), and Mechanical Engineering (M.R.L., P.M.M., A.A.), University of Washington, Seattle, Washington; and Department of Neurosurgery (K.M., F.C.A., C.G.M., M.Y.S.K.), Barrow Neurological Institute, Phoenix, Arizona.

This work was supported in part by National Institutes of Health/National Institute of Neurological Disorders and Stroke grant 1R01NS088072 (M.R.L., P.M.M., L.J.K., A.A.).

Please address correspondence to Michael R. Levitt, MD, University of Washington, 325 9th Ave, Box 359924, Seattle, WA 98104; e-mail: mlevitt@uw.edu; @DrMichaelLevitt

Indicates open access to non-subscribers at www.ajnr.org

Indicates article with supplemental on-line appendix and table.

http://dx.doi.org/10.3174/ajnr.A4826

**Table 1: Venography and manometry measurements**

| Patient | Side | Blood Pressure (mm Hg) | | | Pressure Gradient (mm Hg) | % Stenosis[a] |
|---|---|---|---|---|---|---|
| | | Superior Sagittal Sinus | Transverse Sinus | Sigmoid Sinus | | |
| 1 | Left | 7 | 5 | 2 | 3 | 60.34 |
| | Right | | 7 | 8 | −1 | 2.41 |
| 2 | Right | 10 | 8 | 7 | 1 | 2.13 |
| 3 | Right | 23 | 24 | 19 | 5 | 14.81 |
| 4 | Left | 56 | 34 | 16 | 18 | 50 |
| | Right | | 16 | 15 | 1 | 33.33 |
| 5 | Left | 39 | 29 | 18 | 11 | 82.35 |
| | Right | | 34 | 17 | 17 | 26.47 |
| 6 | Right | 83 | 88 | 7 | 81 | 61.64 |

[a] Defined as the percentage change between the narrowest point of the transverse sinus and the midpoint of the ipsilateral sigmoid sinus.

## MATERIALS AND METHODS

### *Patient Population and Venogram Procedure*

Institutional review board approval (Barrow Neurological Institute, Phoenix, Arizona) was obtained for this retrospective study. Six patients with a previous diagnosis of untreated IIH (determined by intracranial pressure of ≥25 cm $H_2O$ without structural or CSF abnormality[7]) and MR venography demonstrating dural venous sinus atresia or stenosis of >50% in at least 1 location underwent cerebral venography with manometry. Cerebral venography was performed with the patient under local anesthesia by using a transfemoral access. A 5F guide catheter (Envoy; Codman & Shurtleff, Raynham, Massachusetts) was navigated into the right jugular bulb, and a microcatheter (Excelsior SL-10; Stryker, Kalamazoo, Michigan) was placed in the dural venous sinuses. Manometry was then performed in the bilateral transverse and sigmoid sinuses and the posterior third of the superior sagittal sinus by transducing the blood pressure through the microcatheter. In 2 patients in whom the transverse and sigmoid sinuses were atretic or absent on 1 side, measurements were obtained in all other locations. Stenoses were considered pathologic if a pressure gradient of ≥8 mm Hg was observed across the segment of narrowed lumen.[5] Patients were grouped into pathologic and nonpathologic groups based on the presence of such a gradient across ≥1 stenotic venous sinus.

### *Computational Modeling*

3D reconstructions of each patient's venous sinuses were created from the preprocedural MR venography by using the Vascular Modeling Toolkit (VMTK; www.vmtk.org), which uses a gradient-based level set method. The model inflows were truncated at the posterior third of the superior sagittal sinus and the midpoint of the straight sinus. The model outflows were truncated at the bilateral distal sigmoid sinuses, unless 1 side was atretic, in which case it was excluded.

Two models were created for each patient: one with a virtual microcatheter in the center of the lumen from the sigmoid sinus through the transverse sinus on the right side (as it was placed during the actual venogram procedure) and one without. We created both models for each patient to address a common concern with venographic manometry, which is that the placement of a microcatheter through a venous sinus stenosis could, in itself, alter the hemodynamics of the venous sinus stenosis and affect the results. The virtual microcatheter was modeled after the Excelsior SL-10 microcatheter used during venographic manometry, with an identical diameter of 0.57 mm.

A computational mesh was also created with VMTK. The spatial resolution of the mesh was a uniform 0.4 mm in all meshes without virtual microcatheter placement, while meshes with the virtual microcatheters decreased in resolution to 0.07 mm around the catheter surface. Meshes had 1–4 million finite volumes. Steady flow CFD simulations were conducted by using Fluent 14 (ANSYS, Canonsburg, Pennsylvania) with a spatially second-order upwind scheme. Blood pressure at the inflow (posterior third of the superior sagittal sinus) and outflow (sigmoid sinuses) as measured by venographic manometry was directly prescribed as the CFD boundary conditions. Gravity was also included in the simulations because pressure measurements in the venous system can be influenced by hydrostatic pressure gradients. The CFD simulations assumed rigid sinus walls and Newtonian blood rheology with a density of 1.05 g/cm$^3$ and a viscosity of 3.5 cP. Flow was determined to be laminar or turbulent on the basis of the results of the CFD calculations, which resolved velocity and pressure fluctuations if present. Laminar flow was not presupposed.

Each patient-specific CFD model was analyzed for blood pressure, flow rate, and wall shear stress (WSS) both with and without the virtual microcatheter. Values of each variable at key anatomic locations (superior sagittal, straight, and sigmoid sinuses) were calculated with and without virtual microcatheter placement, and contour maps of blood pressure and WSS throughout the venous sinuses were created for each patient.

Separate 2D blood flow velocity profiles across dural venous sinus stenoses were created by using the patient-specific flow data. The magnitude of the flow velocity across each stenosis was visualized by manually placing a 2D plane along a longitudinal section of the affected dural sinus.

## RESULTS

Sinus measurements and venographic pressures for each patient are shown in Table 1. Three patients had pathologic pressure gradients of ≥8 mm Hg across 4 stenoses (the pathologic group), while 3 other patients did not have a substantial pressure gradient (the nonpathologic group). One patient in the pathologic group and 2 patients in the nonpathologic group had atretic sinus systems on one side. The average severity of the stenosis was 50.76% ± 22.42% in the pathologic group and 24.34% ± 32.31% in the nonpathologic group as determined by the 3D imaging.

Results from CFD simulations are shown in Table 2 and Figs 1 and 2. Data in Table 2 and all figures are displayed on the basis of calculations with the virtual microcatheter in place, to better represent the hemodynamic environment during venous pressure measurements obtained with the microcatheter in vivo. The average outflow was 1041.00 ± 506.52 mL/min for the pathologic group and 358.00 ± 190.95 mL/min for the nonpathologic group.

**Table 2: CFD calculations of blood flow and WSS with virtual microcatheter placement**

| Patient | Side | Blood Flow (mL/min) | | | Wall Shear Stress (Pa) | | | | WSS Gradient across Stenosis |
|---|---|---|---|---|---|---|---|---|---|
| | | Superior Sagittal Sinus | Straight Sinus | Sigmoid Sinus | Superior Sagittal Sinus | Straight Sinus | Transverse Sinus | Sigmoid Sinus | |
| 1 | Left | 370 | 50 | 171 | 0.72 | 0.27 | 29 | 1.59 | 27.41 |
| | Right | | | 248 | | | 0.36 | 0.82 | −0.46 |
| 2 | Right | 433 | 78 | 511 | 2.59 | 0.89 | 1.88 | 1.16 | 0.72 |
| 3 | Right | 71 | 72 | 144 | 0.67 | 0.84 | 1.33 | 0.93 | 0.4 |
| 4 | Left[a] | 1582 | 0 | 196 | 14.74 | 0.09 | 8.24 | 1.21 | 7.03 |
| | Right | | | 1386 | | | 37.94 | 18.72 | 19.22 |
| 5 | Left[a] | 457 | 121 | 112 | 2.37 | 0.82 | 38.21 | 4.63 | 33.58 |
| | Right[a] | | | 466 | | | 16.36 | 9.82 | 6.54 |
| 6 | Right[a] | 816 | 147 | 963 | 5.23 | 1.79 | 163.01 | 41.07 | 121.94 |

[a] Pathologic pressure gradient (≥ 8 mm Hg) on venographic manometry.

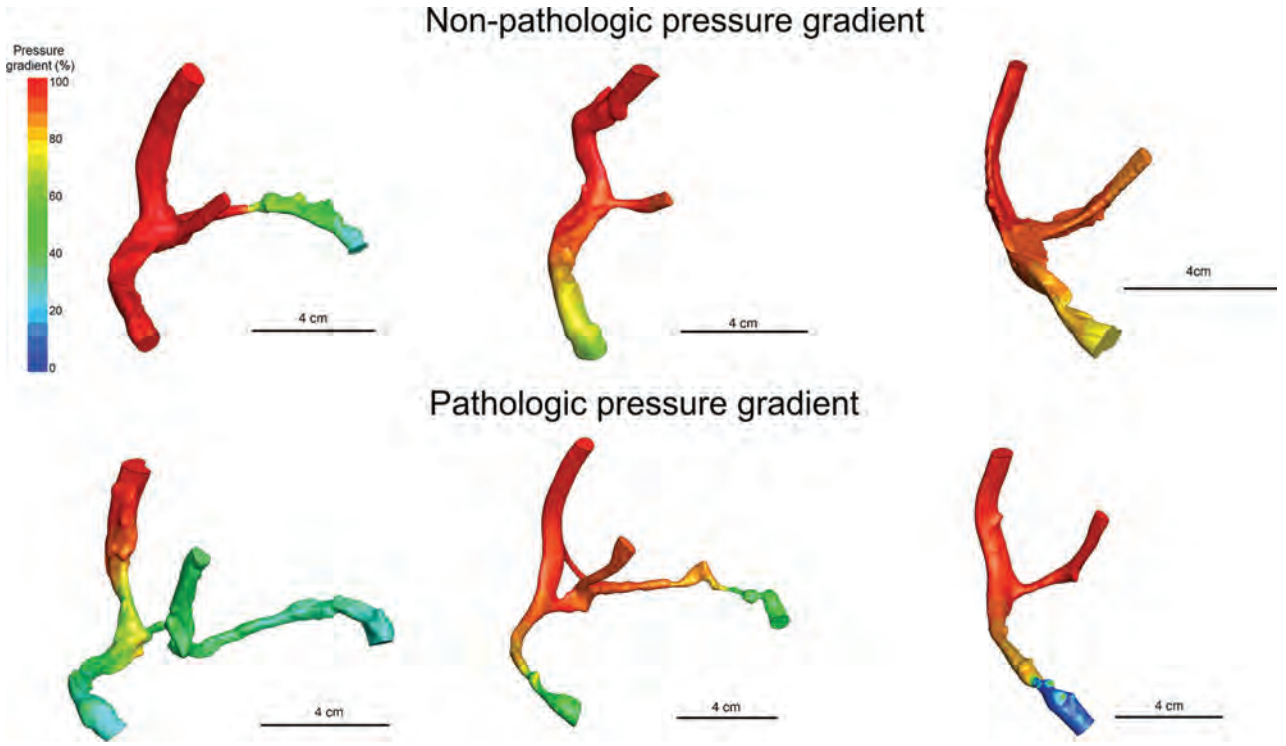


**FIG 1.** Computational fluid dynamics calculations of blood pressure gradients in the dural venous sinuses of patients with IIH. Pressure gradients are shown as a percentage of the blood pressure in the superior sagittal sinus (assigned as 100% in each patient). Patients without pathologic pressure gradients (*upper row*) show very little pressure drop across venous sinus stenoses compared with patients with pathologic pressure gradients (*lower row*). Sinuses are truncated at the posterior third of the superior sagittal sinus, midpoint of the straight sinus, and the end of each sigmoid sinus (see "Materials and Methods") and are shown in a right anterior oblique/Towne projection.

The average WSS gradient across stenotic segments (defined as the difference in WSS between the narrowest point of each stenosis and the midpoint of the ipsilateral sigmoid sinus) was 37.66 ± 48.39 Pa for the pathologic group and 7.02 ± 13.60 Pa for the nonpathologic group.

Figures 1 and 2 are visual depictions of blood pressure and WSS in the dural venous sinus models. Blood pressure is displayed as a percentage of the pressure in the superior sagittal sinus to normalize the results of pressure drops across the stenotic segments, while WSS is shown on a constant scale. This display permits comparison between patients with and without pathology. Visual inspection suggests minimal or low pressure drops across stenotic segments in the nonpathologic group (Fig 1, top row), compared with more substantial reduction in the pathologic group (Fig 1, lower row). Wall shear stress also appears minimally changed in the nonpathologic group (Fig 2, upper row) but elevated at and downstream of stenotic segments in the pathologic group (Fig 2, lower row).

Figure 3 shows 2D blood flow velocity profiles across dural venous sinus stenoses in patients in the nonpathologic (upper row) and pathologic groups (lower row). Projections are oriented through a cross-section of the maximal area of stenosis in each case. Visual inspection demonstrates substantially higher poststenotic velocities and disordered flow in the patients with pathology. The elevated velocities in Fig 3 correspond to the increased WSS and pressure drops in patients with pathology in Figs 1 and 2, while lower peak poststenotic velocities mirror the minimal WSS elevation and pressure drop seen in patients without pathology.

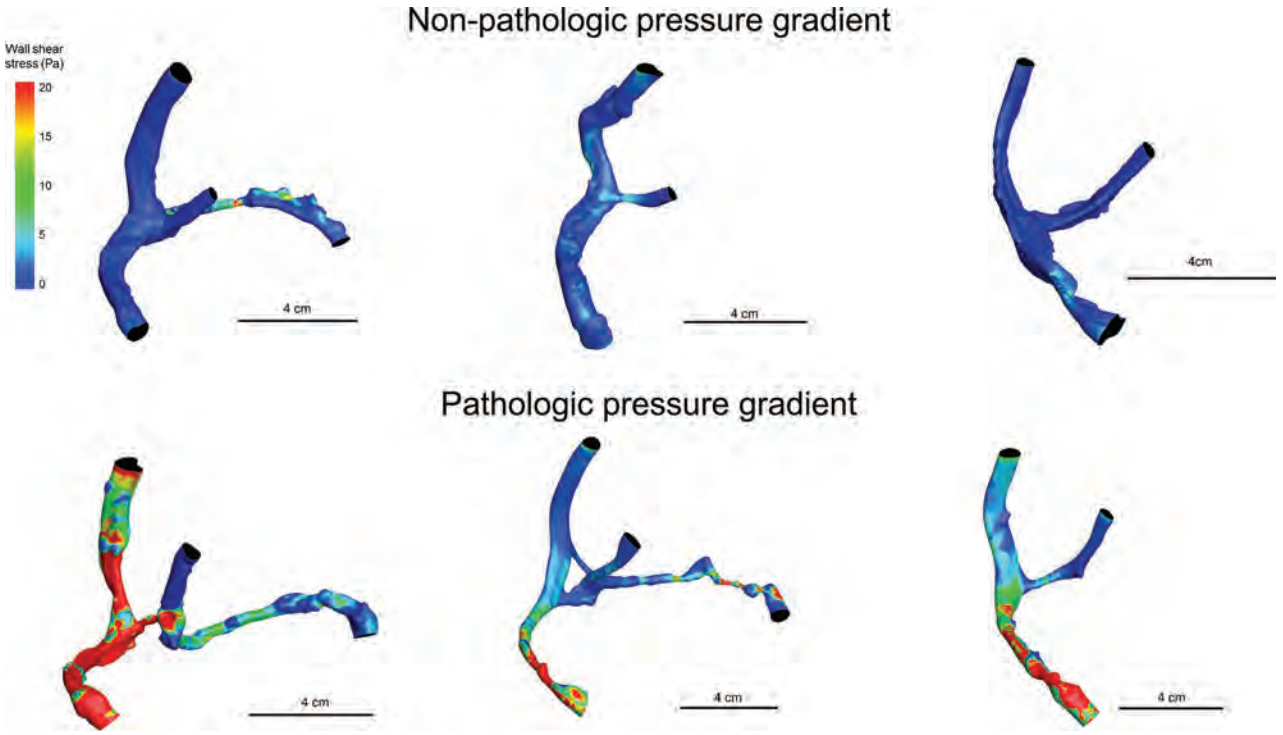


**FIG 2.** Computational fluid dynamics calculations of wall shear stress in the dural venous sinuses of patients with IIH. Patients without pathologic pressure gradients (*upper row*) show very little change in WSS at and beyond venous sinus stenoses compared with patients with pathologic pressure gradients (*lower row*), who have more severe elevations in WSS.

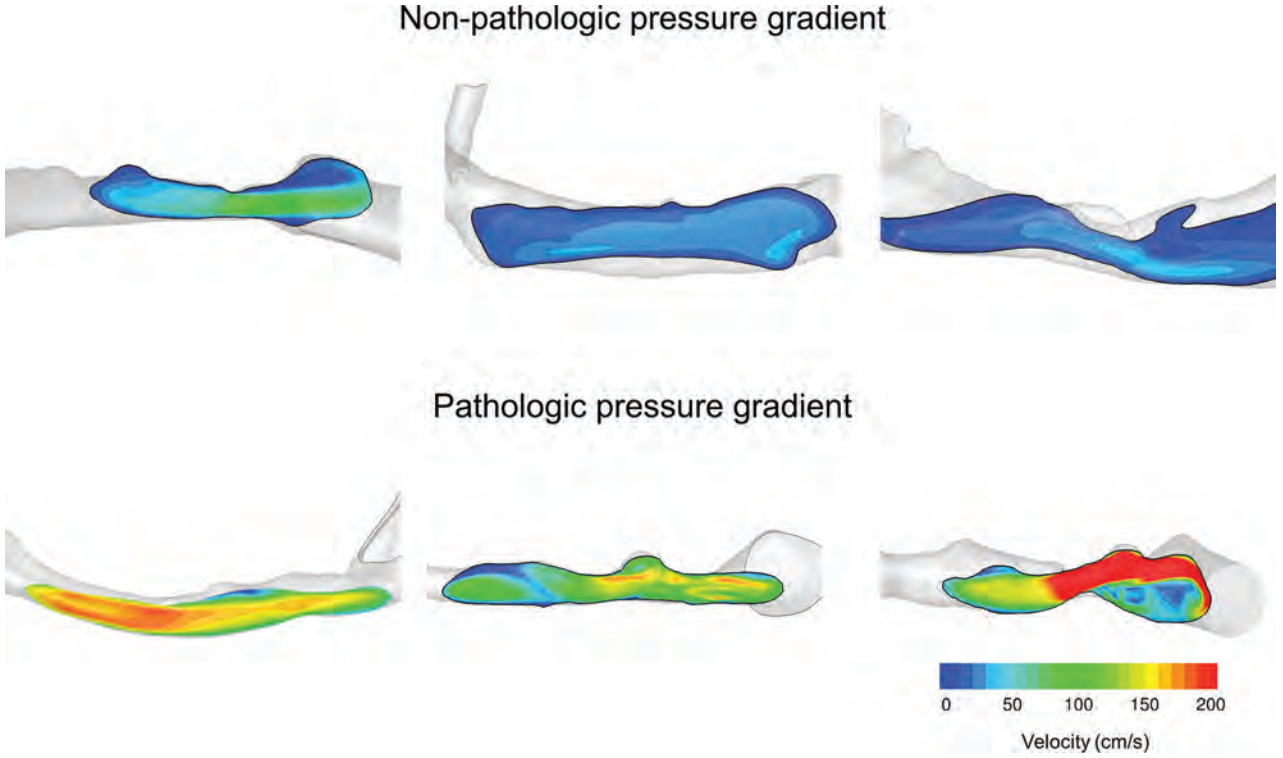


**FIG 3.** Computational fluid dynamics calculations of 2D velocity profiles oriented through the point of maximal venous sinus stenoses in patients in the nonpathologic (*upper row*) and pathologic (*lower row*) groups. Blood flow is from left to right. Substantially higher blood flow velocity is observed across stenoses in patients in the pathologic group.

The On-line Table shows CFD results without the virtual microcatheter. The effect of the virtual microcatheter on CFD was minimal on both total outflow (mean outflow reduction, 7.76% ± 3.98%) and WSS gradients across each transverse-sigmoid junction or stenosis (mean WSS reduction, 1.81% ± 24.19%).

## DISCUSSION

We have modeled the hemodynamic environment of patients with IIH with dural venous sinus stenosis. Our CFD models used patient-specific anatomic information from each patient's MR venography and incorporated patient-specific venographic manometry measurements for use as boundary conditions. Patient-specific inlet and outlet boundary conditions have been shown to be more accurate than stereotypic boundary conditions (derived from literature averages of individual cases or healthy volunteer cohorts) in the CFD modeling of other cerebrovascular diseases such as intracranial aneurysms.[8,9] These CFD models permit the comparison of the hemodynamics of patients with IIH with similar anatomic venous sinus stenoses to better understand why some patients' stenoses were pathologic and were responsive to treatment with dural venous sinus stent placement, while others were not.

Patients with pathologic pressure gradients did have higher overall venous outflow rates through the transverse and sigmoid sinuses than those with low or absent pressure gradients (1041 versus 358 mL/min). The high flow rate in patient 4, who had a pathologic pressure gradient, may be an overestimate due to errors inherent in CFD reconstructions from MR venography data with large voxel sizes but is near previously published values of overall cerebral blood flow.[10] Despite anatomic abnormalities in both groups, flow rates of patients without pathology were similar to previously reported values for jugular flow in healthy controls.[11] This finding supports the theory that the presence of a stenotic or atretic segment may be necessary but not sufficient to cause pathologic pressure gradients across venous stenosis, because the presence of an atretic transverse/sigmoid sinus system (with 100% of outflow through the remaining stenotic segment) was seen in patients with and without pathologic pressure gradients in the current study, and others have observed no correlation between stenosis severity and IIH symptoms.[12] The presence of unilateral sinus hypoplasia or atresia in up to 33% of asymptomatic patients also argues against a purely anatomic source of flow disturbance.[13,14]

Wall shear stress also differed between patient groups. In the nonpathologic group, minimal or no elevation in WSS was observed in stenotic segments, while large elevations in WSS were seen at and downstream from stenoses in the pathologic group. Since WSS has been related to downstream vascular resistance,[15] the difference in WSS profiles between groups further underscores the lack of adequate collateral pathways (and thus increased vascular resistance across the stenosis) in the pathologic group. Similarly, the 2D velocity profiles across the stenosis in patients with and without pathology demonstrate higher poststenotic velocity in the pathologic group, indicating more disordered flow and vascular resistance, which could also correspond to reduced collaterals.

While the underlying mechanism for venous sinus stenosis in patients with IIH remains unclear, these results suggest that patients with anatomic but not pathologic stenosis may have collateral venous drainage in addition to the transverse/sigmoid sinus system. These collateral venous pathways prevent the increased resistance of an anatomic stenosis from affecting the overall pressure gradient across it and thus limit the elevation of blood pressure upstream from the stenosis. In patients in whom collaterals are sparse or absent, the resistance created by the narrowing of 1 or both primary venous outflow channels (the sigmoid sinuses) increases the pressure upstream from the stenosis, creating a pathologic gradient and elevating the pressure in the entire venous sinus system. Cerebral venous hypertension further limits CSF reabsorption, increasing intracranial pressure and further exacerbating IIH by compressing the already stenosed segment acting as a Starling resistor.[16,17] On the other hand, in vitro and animal studies on the influence of extravascular pressure on cerebral venous outflow do not perfectly follow this model.[18]

Because the compliance and elasticity of the dural venous sinuses are not known, we are unable to incorporate intracranial pressure measurements into the model calculations. The near-instantaneous nature of the CFD calculations (by using a single time point of venous pressure) should limit the effects of intracranial pressure on our calculations, but the complex relationship between intracranial pressure and pathologic dural venous sinus stenosis remains incompletely explained.[18] In the pathologic group, all 3 patients had intracranial pressures of $>40$ cm $H_2O$, while in the nonpathologic group, intracranial pressures were lower ($<30$ cm $H_2O$). Future study of CFD before and after stent treatment would be improved with incorporation of intracranial pressure changes to ensure accurate modeling of the influence of external compression on the dural venous sinus stenosis.

The results of this study could have practical applications for the noninvasive screening of patients with IIH for a pathologic pressure gradient. A review of our large cohort of 158 patients with and without IIH who underwent diagnostic cerebral venography and manometry showed that noninvasive vascular imaging (such as MR venography and CT venography) was an imperfect predictor of the pathologic pressure gradient, even in the presence of anatomic dural venous sinus stenosis.[19] This finding is consistent with the findings of the current study of different flow and WSS profiles between patients with and without pathology, despite similar degrees of anatomic stenoses or atresia. Recent advances in noninvasive quantitative phase-contrast MR venography show promise in measuring blood flow through venous sinuses.[20] Applying such measurements as boundary conditions in the CFD simulation methodology of the current study may allow noninvasive, patient-specific, and accurate determination of pathologic and nonpathologic stenoses without the need for invasive venography. This method could be used for enhanced screening of patients with IIH at the time of diagnosis and is under investigation by our group. In addition, the hemodynamic changes before and after stent placement across pathologic segments could be virtually modeled before the procedure to help predict the restoration of normal blood pressure, blood flow, and WSS.

We observed a minimal effect on flow when the virtual microcatheter was placed across the venous sinus stenosis in our simulations. This is an important finding relative to the methods by which pressure gradients are obtained in venographic manometry because a catheter placed through an already narrow vessel (such as a venous sinus stenosis) could impart a "loading error," further reducing the cross-sectional area of the lumen and falsely elevating the pressure measurements.[21] This is a common critique of

the results of venographic manometry because there is concern that the procedure in which pressures are measured may skew the measured results and potentially affect patient treatment strategy. However, we observed a minimal loading error for both outflow and the WSS gradients, and the large SD observed for WSS gradients was the result of the effect of the microcatheter on very small (<1 Pa) absolute WSS values in 3 patients. This minimal loading error is unlikely to be clinically relevant because a substantially larger error would be required to create a falsely elevated flow leading to a pressure gradient of ≥8 mm Hg, which would change clinical decision-making toward stent placement.[5] Other CFD studies using patient-specific boundary conditions measured by intravascular devices may require integration of the presence of the device into determining the load error, though in our study, this did not have a substantial influence on calculations and should not be considered as a source of clinically relevant error on venographic manometry measurements in patients with IIH.

A simplified mathematic model was also created in an attempt to predict the degree of flow disturbance created by a microcatheter of a certain diameter (On-line Appendix). This model predicts that a microcatheter one-tenth of the diameter of the stenotic segment of the vessel causes approximately 40% reduction in flow, and that a microcatheter one-hundredth of the diameter of the stenosis causes approximately 22% reduction in flow assuming that the pressure gradient is fixed. The ability of the model to make quantitative predictions is limited by a number of important factors. In a stenosis, the spatial accelerations are likely important and the flow is not fully developed; thus, these features violate a key assumption of the model. More important, the excess resistance is highly dependent on the individual anatomy of each stenosis and not just the ratio of the diameters of the catheter and stenosis as the model predicts. Thus, CFD modeling with patient-specific anatomic and physiologic data as presented above is more likely to reflect accurate hemodynamic conditions on a case-by-case basis.

This work has several limitations. First, the sample size is small, precluding statistical comparison between patients with and without pathology. However, this study demonstrates the methodology for CFD modeling of the dural venous sinuses by using patient-specific physiologic measurements as boundary conditions, which has not been reported before, to our knowledge. Second, the voxel size of the MR venography used to reconstruct the dural venous sinuses, which ranged from 0.43 to 0.86 $mm^3$, could potentially miss fine webbing that could be better seen by using high-resolution techniques such as conebeam CT venography[22] or felt during microcatheterization during invasive venography. A 10% error in stenosis diameter estimation can change the flow rate by 40%, and it is unclear how equally the errors in the reconstructions affect patients with and without pathology. Third, prescribing only the pressures (without velocities) as the CFD boundary conditions may be more susceptible to random errors subject to the precision of the pressure transducer (±1 mm Hg), especially in cases in which the pressure gradients are small. The prescribed pressure gradients in CFD may have relative errors of up to 25%, and the calculated flow rates may subsequently have similar relative errors. However, the relative errors are likely much smaller in pathologic cases in which large pressure gradients were measured and are thus unlikely to be clinically significant. Fourth, there were differences in the severity of stenoses in patients with pathologic and nonpathologic stenoses. However, all patients had documented IIH and some degree of venous sinus abnormality (stenosis, atresia, or both), which could cause outflow abnormalities and influence hemodynamics across the entire dural sinus system, as has been proposed by others.[23]

## CONCLUSIONS

Dural venous sinus stenosis in patients with IIH can be computationally modeled by using patient-specific anatomic and physiologic data. Increased overall blood flow and WSS were found in patients with a pathologic pressure gradient.

Disclosures: Michael R. Levitt—*RELATED*: *Grant*: National Institutes of Health/National Institute of Neurological Disorders and Stroke (grant 1R01NS088072)*; *UNRELATED*: *Stock/Stock Options*: Sanofi Pasteur, *Comments*: equity stock <$5000. Patrick M. McGah—*RELATED*: *Grant*: National Institutes of Health/National Institute of Neurological Disorders and Stroke (grant 1R01NS088072).* Louis J. Kim—*RELATED*: *Grant*: National Institutes of Health/National Institute of Neurological Disorders and Stroke (grant 1R01NS088072)*; *UNRELATED*: *Consultancy*: MicroVention, *Comments*: Data and Safety Monitoring Board chair for an ongoing device trial. Alberto Aliseda—*RELATED*: *Grant*: National Institutes of Health/National Institute of Neurological Disorders and Stroke (grant 1R01NS088072).* *Money paid to the institution.

## REFERENCES

1. Higgins JN, Owler BK, Cousins C, et al. **Venous sinus stenting for refractory benign intracranial hypertension.** *Lancet* 2002;359:228–30 Medline
2. Puffer RC, Mustafa W, Lanzino G. **Venous sinus stenting for idiopathic intracranial hypertension: a review of the literature.** *J Neurointerv Surg* 2013;5:483–86 CrossRef Medline
3. Farb RI, Vanek I, Scott JN, et al. **Idiopathic intracranial hypertension: the prevalence and morphology of sinovenous stenosis.** *Neurology* 2003;60:1418–24 CrossRef Medline
4. Albuquerque FC, Dashti SR, Hu YC, et al. **Intracranial venous sinus stenting for benign intracranial hypertension: clinical indications, technique, and preliminary results.** *World Neurosurg* 2011;75:648–52; discussion 592–95 CrossRef Medline
5. Ahmed RM, Wilkinson M, Parker GD, et al. **Transverse sinus stenting for idiopathic intracranial hypertension: a review of 52 patients and of model predictions.** *AJNR Am J Neuroradiol* 2011;32:1408–14 CrossRef Medline
6. Bateman GA. **Arterial inflow and venous outflow in idiopathic intracranial hypertension associated with venous outflow stenoses.** *J Clin Neurosci* 2008;15:402–08 CrossRef Medline
7. Friedman DI, Jacobson DM. **Diagnostic criteria for idiopathic intracranial hypertension.** *Neurology* 2002;59:1492–95 CrossRef Medline
8. McGah PM, Levitt MR, Barbour MC, et al. **Accuracy of computational cerebral aneurysm hemodynamics using patient-specific endovascular measurements.** *Ann Biomed Eng* 2014;42:503–14 CrossRef Medline
9. Venugopal P, Valentino D, Schmitt H, et al. **Sensitivity of patient-specific numerical simulation of cerebral aneurysm hemodynamics to inflow boundary conditions.** *J Neurosurg* 2007;106:1051–60 CrossRef Medline
10. Ford MD, Alperin N, Lee SH, et al. **Characterization of volumetric flow rate waveforms in the normal internal carotid and vertebral arteries.** *Physiol Meas* 2005;26:477–88 CrossRef Medline
11. Kim J, Thacker NA, Bromiley PA, et al. **Prediction of the jugular venous waveform using a model of CSF dynamics.** *AJNR Am J Neuroradiol* 2007;28:983–89 Medline
12. Riggeal BD, Bruce BB, Saindane AM, et al. **Clinical course of idiopathic intracranial hypertension with transverse sinus stenosis.** *Neurology* 2013;80:289–95 CrossRef Medline
13. Ayanzen RH, Bird CR, Keller PJ, et al. **Cerebral MR venography:**

**normal anatomy and potential diagnostic pitfalls.** *AJNR Am J Neuroradiol* 2000;21:74–78 Medline
14. Durst CR, Ornan DA, Reardon MA, et al. **Prevalence of dural venous sinus stenosis and hypoplasia in a generalized population.** *J Neurointerv Surg* 2016 Jan 8. [Epub ahead of print] CrossRef Medline
15. Van Steenkiste C, Trachet B, Casteleyn C, et al. **Vascular corrosion casting: analyzing wall shear stress in the portal vein and vascular abnormalities in portal hypertensive and cirrhotic rodents.** *Lab Invest* 2010;90:1558–72 CrossRef Medline
16. De Simone R, Ranieri A, Bonavita V. **Advancement in idiopathic intracranial hypertension pathogenesis: focus on sinus venous stenosis.** *Neurol Sci* 2010;31(suppl 1):S33–39 CrossRef Medline
17. Stevens SA, Previte M, Lakin WD, et al. **Idiopathic intracranial hypertension and transverse sinus stenosis: a modelling study.** *Math Med Biol* 2007;24:85–109 Medline
18. Schaller B. **Physiology of cerebral venous blood flow: from experimental data in animals to normal function in humans.** *Brain Res Brain Res Rev* 2004;46:243–60 CrossRef Medline
19. Levitt MR, Hlubek RJ, Moon K, et al. **Incidence and predictors of dural venous sinus pressure gradient in idiopathic intracranial hypertension and non-idiopathic intracranial hypertension headache patients: results from 164 cerebral venograms.** *J Neurosurg* 2016 Mar 11. [Epub ahead of print] Medline
20. Esfahani DR, Stevenson M, Moss HE, et al. **Quantitative magnetic resonance venography is correlated with intravenous pressures before and after venous sinus stenting: implications for treatment and monitoring.** *Neurosurgery* 2015;77:254–60 CrossRef Medline
21. Torii R, Wood NB, Hughes AD, et al. **A computational study on the influence of catheter-delivered intravascular probes on blood flow in a coronary artery model.** *J Biomech* 2007;40:2501–09 CrossRef Medline
22. Hiu T, Kitagawa N, Morikawa M, et al. **Efficacy of DynaCT digital angiography in the detection of the fistulous point of dural arteriovenous fistulas.** *AJNR Am J Neuroradiol* 2009;30:487–91 CrossRef Medline
23. Rohr A, Bindeballe J, Riedel C, et al. **The entire dural sinus tree is compressed in patients with idiopathic intracranial hypertension: a longitudinal, volumetric magnetic resonance imaging study.** *Neuroradiology* 2012;54:25–33 CrossRef Medline

# Peritherapeutic Hemodynamic Changes of Carotid Stenting Evaluated with Quantitative DSA in Patients with Carotid Stenosis

M.M.H. Teng, F.-C. Chang, C.-J. Lin, L. Chiang, J.-S. Hong, and Y.-H. Kao

## ABSTRACT

**BACKGROUND AND PURPOSE:** Quantitative data from DSA have become important tools for understanding hemodynamic changes of intracranial lesions. In this study, we evaluated 8 hemodynamic parameters in patients before and after carotid artery angioplasty.

**MATERIALS AND METHODS:** DSA images of 34 patients with carotid stenosis who underwent angioplasty and stent placement were retrospectively analyzed. Eleven ROIs (M1, M2, A1, A2, the parietal vein, superior sagittal sinus, internal jugular vein, and 4 in the ICA) were selected on color-coded DSA. Eight hemodynamic parameters (bolus arrival time, TTP, relative TTP, full width at half maximum, wash-in slope, washout slope, maximum enhancement, and area under the curve) were measured from the time-concentration curves of these ROIs. The dependent *t* test for paired samples was applied to these parameters before and after stent placement.

**RESULTS:** We found that the treatment significantly reduced TTP, relative TTP, bolus arrival time, and washout slope at all arterial ROIs and full width at half maximum and area under the curve at some arterial ROIs. Bolus arrival time was significantly reduced after treatment for all arterial ROIs, the parietal vein, and the superior sagittal sinus. The maximum enhancement and wash-in slope did not show significant changes after treatment. After treatment, the relative TTP from the ICA to M1, M2, and the parietal vein returned to normal values.

**CONCLUSIONS:** In addition to TTP and relative TTP, other parameters can be used to evaluate peritherapeutic cerebral hemodynamic changes. Bolus arrival time has the potential to evaluate brain circulation at arterial and venous sites, especially when TTP cannot be measured because of an incomplete time-concentration curve.

**ABBREVIATIONS:** AUC = area under the curve; BAT = bolus arrival time; FWHM = full width at half maximum; ME = maximal enhancement; PA = posterior-anterior; PV = parietal vein; rTTP = relative TTP; SSS = superior sagittal sinus; WI = wash-in slope; WO = washout slope

Digital subtraction angiography has been the criterion standard for diagnosing cerebral vascular disease since 1970s. DSA imaging demonstrates the intravascular changes of concentration in the time domain and can be used as a surrogate marker for cerebral hemodynamics. Time-concentration curve analysis is the most commonly used approach because the results are easily accessible and intuitive for interventional purposes. Time-to-peak (also called time-to-maximum in some previous publications) is the most commonly used parameter. It is applied to detect intra-aneurysmal flow, and larger aneurysms demonstrate more prolonged TTP than smaller aneurysms.[1] The difference in TTP between the parietal vein and cavernous ICA has been used to monitor cerebral hemodynamic changes to improve patient safety.[2] Detecting shorter TTPs in carotid cavernous fistulas helps determine whether the venous outlets contain higher blood flow, which deserves treatment priority.[3] In control angiography, normalization of blood flow indicates spontaneous latent obliteration.[4] Other applications include monitoring angioplasty for vasospasm after subarachnoid hemorrhage[5] and quantitatively grading Moyamoya disease.[2]

The standard gray-scale images of DSA are first encoded into a single composite color image according to the contrast bolus arrival time (BAT) at each point in the circulatory system of the brain. This single composite color image improves the speed of manual delineation of AVMs and makes the angioarchitecture

Received December 16, 2015; accepted after revision March 20, 2016.

From the Department of Medical Imaging (M.M.H.T.), Cheng Hsin General Hospital, Taipei, Taiwan; Department of Radiology (F.-C.C., C.-J.L., L.C.), Taipei Veterans General Hospital, Taipei, Taiwan; and School of Medicine (F.-C.C., C.-J.L.) and Department of Biomedical Imaging and Radiological Sciences (J.-S.H., Y.-H.K.), National Yang-Ming University, Taipei, Taiwan.

This work was supported, in part, by the Cheng Hsin General Hospital and National Yang Ming University cooperative project (grant No. 103F003C10) and Taipei Veterans General Hospital (grant No. V104-C-012).

Please address correspondence to Chung-Jung Lin, PhD, Radiology Department, Taipei Veterans General Hospital, No. 201, Section 2, Shipai Rd, Beitou District, Taipei, Taiwan; e-mail: bcjlin@gmail.com; Yi-Hsuan Kao, MD, Department of Biomedical Imaging and Radiological Sciences, National Yang-Ming University, No. 155, Section 2, Li-Nong St, Beitou District, Taipei, Taiwan; e-mail: yhkao@ym.edu.tw

http://dx.doi.org/10.3174/ajnr.A4813

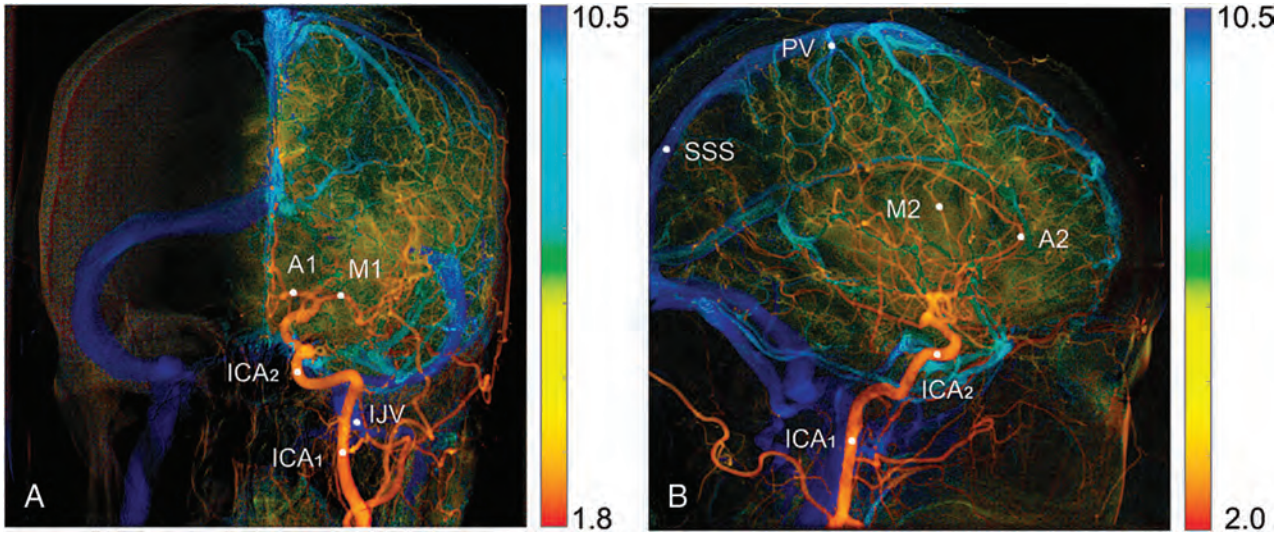


**FIG 1.** Color-coded DSA images in the PA (*A*) and lateral (*B*) views. Eleven ROIs are manually selected for quantification of perfusion parameters. $ICA_1$ on the PA view and $ICA_1$ on lateral view are planned to be at the same place.

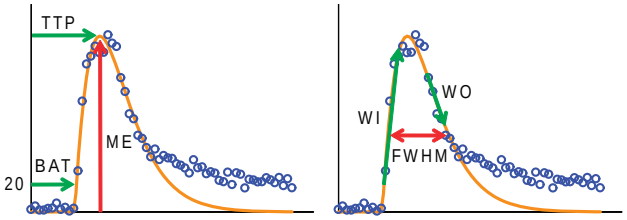


**FIG 2.** The measured (*blue open circle*) and fitted (*orange line*) time-concentration curves. Hemodynamic parameters such as maximum enhancement, time to peak, bolus arrival time, wash-in slope, wash-out slope, and full width at half maximum are all derived from the fitted curve.

and the flow characteristics of aneurysms, AVMs, fistulas, stenosis, occlusions, dissections, and tumors easier to understand.[6] The color-coding of DSA was also developed by calculation of the maximal enhancement (ME) and the TTP of the time-concentration curve of each pixel.[7] It improves the conspicuity of findings on DSA images of cerebral vascular lesions and helps with the visualization of fistula angioarchitecture and venous drainage patterns in patients with carotid cavernous fistulas.[7] In addition, it facilitates real-time hemodynamic monitoring, helps determine the end point of embolization, and increases patient safety in the treatment of carotid cavernous fistulas.[8,9]

For carotid stenosis, the TTP or relative TTP (rTTP) of color-coded quantitative DSA has been used to evaluate cerebral circulation time and peritherapeutic hemodynamic changes in the intracranial circulation.[3] rTTP was found to be a definitive alternative method of measuring cerebral circulation.[10] Maximal slope and full width at half maximum (FWHM) are found to complement rTTP in the evaluation of cerebral circulation.[10] Furthermore, the area under the curve (AUC) of the proximal common carotid arteries can be calculated from the time-concentration curves of color-coded DSA. A good correlation was found between the AUC and the relative CBV obtained from flat panel detector CT by injecting contrast medium into the ascending aorta.[11] In this study, we evaluated 8 parameters obtained from color-coded quantitative DSA to understand the hemodynamic changes before and after stent placement in patients with carotid stenosis.

## MATERIALS AND METHODS

DSA images of 34 patients (mean age, 72.3 years; 27 men and 7 women) who underwent carotid angioplasty and stent placement were collected for retrospective analysis. The patients had unilateral carotid stenosis of >70%, according to the NASCET criteria. The DSA images were acquired on a clinical scanner (Artis zee; Siemens, Erlangen, Germany) with a frame rate of 6 frames/s for 9~12 seconds. The image size was 1440 × 1440 pixels, the FOV was 22 cm, and the pixel size was 0.154 × 0.154 $mm^2$. A power injector (Liebel-Flarsheim Angiomat; Illumina, San Diego, California) was used to inject the contrast bolus in the common carotid artery at the C4 vertebral body level, by using a 4F angiocatheter. A bolus of 12 mL of 60% diluted contrast medium (340 mg I/mL) was administered in 1.5 seconds. The injection catheter was placed at the same place in the pre- and postintervention acquisitions. The injection was synchronized with the start of the image acquisition. The scanning protocol was the same in the 2 sets of images obtained before and after stent placement. This retrospective study was approved by the institutional review board.

Image postprocessing was performed on a personal computer by using software programs written in Matlab (MathWorks, Natick, Massachusetts). In our Matlab program, the TTP and ME values of the time-concentration curve for each pixel were used to generate color-coded DSA images (Fig 1). The first image obtained in each view of the angiograms was defined as time = 0 for the TTP calculation. The color spectrum was used to represent TTP values, with a hot color (red) assigned to small TTP values and a cold color (blue) assigned to large TTP values. The ME was used to assign the brightness of these colors.

Eleven ROIs were selected for comparing hemodynamic parameters. The ROI was composed of 3 × 3 pixels with an area of 0.462 × 0.462 $mm^2$. On the posterior-anterior (PA) view, we selected 5 ROIs: the internal carotid artery in 2 locations ($ICA_1$ and $ICA_2$) and the A1, M1, and internal jugular vein. On the

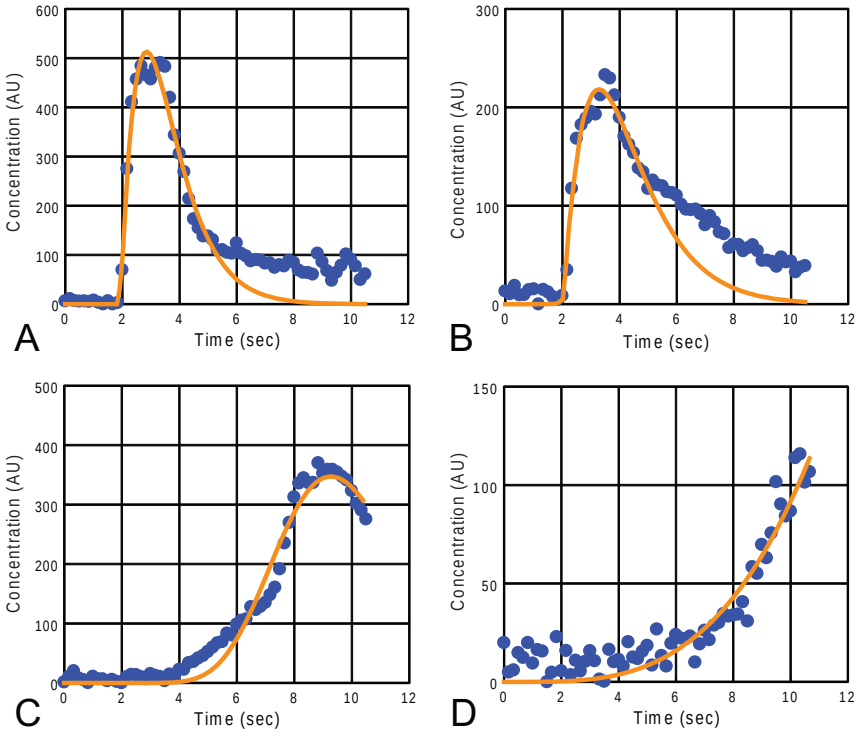


**FIG 3.** Measured (*blue circle*) and fitted (*orange line*) time-concentration curves of representative ROIs before the stent-placement treatment: $ICA_2$ (*A*), M2 (*B*), PV (*C*), SSS (*D*). Note that the time-concentration curve of the PV (*C*) lacks the middle and lower descending portion. The ME in the time-concentration curve of the SSS (*D*) is at the last temporal point. AU indicates arbitrary unit.

**Table 1: *P* values of all hemodynamic parameters before and after stenting at each ROI[a]**

| ROI Locations | PA View | | | | | Lateral View | | | | | |
|---|---|---|---|---|---|---|---|---|---|---|---|
| | $ICA_1$ | $ICA_2$ | M1 | A1 | IJV | $ICA_1$ | $ICA_2$ | M2 | A2 | PV | SSS |
| ME | .27 | .11 | .15 | .79 | NA | .68 | .99 | .20 | * | .55 | NA |
| TTP | * | * | * | * | NA | * | * | * | * | * | NA |
| rTTP | – | *[b] | *[b] | *[b] | NA | – | *[c] | *[d] | *[d] | *[d] | NA |
| BAT | * | * | * | * | .32 | * | * | * | * | * | * |
| FWHM | * | * | * | .08 | NA | * | * | * | * | NA | NA |
| WI | .97 | .88 | .09 | .64 | .15 | .37 | .20 | .12 | .06 | .20 | NA |
| WO | * | * | * | * | NA | * | * | * | * | NA | NA |
| AUC | * | * | .06 | .39 | NA | * | * | * | .83 | NA | NA |

**Note:**—NA indicates not available because of incomplete data; –, not calculated; *, significant difference before and after stenting ($P < .05$); IJV, internal jugular vein.

[a] Details for significant results are shown in Tables 2 and 3.

[b] TTP relative to $ICA_1$ in the PA view.

[c] TTP relative to $ICA_1$ in the lateral view.

[d] TTP relative to $ICA_2$ in the lateral view.

lateral view, we selected 6 ROIs: $ICA_1$, $ICA_2$ (at middle of cavernous segment of the ICA), the A2, M2, parietal vein (PV), and the superior sagittal sinus (SSS). The PA view of $ICA_1$ and the lateral view of $ICA_1$ were selected at the same place in the upper neck because they were easily and consistently identified in the respective views. The locations of these ROIs are shown in Fig 1.

The time-concentration curves of the selected ROIs were fitted to a gamma-variate function described by

$$1) \qquad C_\gamma(t) = K(t - t_0)^\alpha \cdot e^{-(t - t_0)/\beta},$$

where $K$ is a constant, $t_0$ is the contrast arrival time of the fitted curve, and $\alpha$ and $\beta$ are related to the wash-in and washout phases of the curve, respectively.[12] The trust-region-reflective algorithm was used in the Matlab curve-fitting subroutine.[13,14] An example is shown in Fig 2. The concentration is represented in arbitrary units.

According to the literature, the fitted $t_0$ does not reliably represent the BAT.[15] We calculated the BAT by using the first time point with a concentration higher than 20 arbitrary units. To evaluate the wash-in and washout of the contrast media, we fitted 4 consecutive temporal data points of $C_\gamma(t)$ to a straight line described by

$$2) \qquad C_\gamma(t) = mt + b,$$

by using a least squares technique.[16] The largest and smallest m-values were recorded to represent the wash-in slope (WI) and washout slope (WO), respectively. The ME, TTP, full width at half maximum, and the area under the curve of the fitted curve were measured to depict the curve.

The hemodynamic parameters, ME, TTP, BAT, FWHM, WI, WO, and AUC, measured on the ROIs before and after the stent placement treatment, were evaluated. The dependent $t$ test for paired samples described by

$$3) \qquad t = \frac{\overline{X_M} - \mu_0}{\overline{X_{SD}}/\sqrt{n}},$$

was applied to the measured hemodynamic parameters before and after treatment, where $\overline{X_M}$ and $\overline{X_{SD}}$ were the mean and SD of the difference in a hemodynamic parameter measured before and after stent placement treatment, $\mu_0 = 0$, and $n$ is the number of measurements.

## RESULTS

The anterior cerebral artery may not appear on the angiogram before stent placement because of insufficient blood flow. We measured the A1 in 18 cases and the A2 in 17 cases because their ROIs could be identified both before and after treatment on their color-coded images. All identified arterial ROIs, including the ICAs, M1, M2, A1, and A2, in these cases were successfully evaluated with all 8 parameters.

Figure 3 shows measured and fitted time-concentration curves of representative ROIs. Before stent placement, the MEs of the identified SSS in 16 patients and the internal jugular vein in 28 patients were found from the last image in their time-concentration curves (eg, Fig 3*D*). Assuming that the TTP occurred at the last time point was not correct. Therefore, TTP, rTTP, ME, FWHM, WO, and AUC of the SSS and internal jugular vein were listed as not measurable in Table 1. Furthermore, the FWHM, WO, or AUC was not measurable or not reliable for some ROIs in the PV and some other veins because of early termination in the washout phase (eg, Fig 3*C*). Only the BAT could be evaluated in all ROIs.

Figure 4 demonstrates the measured and fitted time-concen-

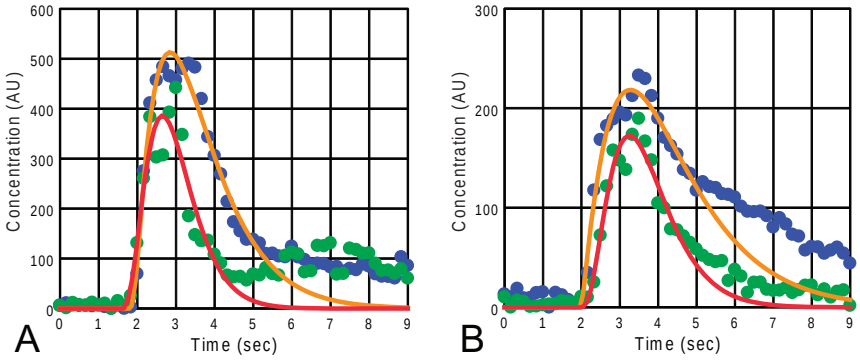


**FIG 4.** A comparison of the time-concentration curves before and after the stent placement treatment for the $ICA_2$ (*A*) and M2 (*B*) in the lateral view. The *blue solid circles* are measured data, and *orange lines* are the fitted curves before the treatment. The *green solid circles* and *red lines* are measured data and fitted curves, respectively, after treatment. AU indicates arbitrary unit.

**Table 2: Results for the hemodynamic parameters with significant changes ($P < .05$) after the stenting procedure in the PA view**

| ROI | Before Treatment (Mean ± SD) | After Treatment (Mean ± SD) | No. |
|---|---|---|---|
| TTP (sec) | | | |
| $ICA_1$ | 2.89 ± 0.62 | 2.46 ± 0.27 | 34 |
| $ICA_2$ | 3.16 ± 0.70 | 2.60 ± 0.25 | 34 |
| M1 | 3.70 ± 0.92 | 2.95 ± 0.31 | 34 |
| A1 | 3.42 ± 0.67 | 2.95 ± 0.37 | 18 |
| rTTP (sec) | | | |
| $ICA_1$–$ICA_2$ | 0.27 ± 0.22 | 0.14 ± 0.13 | 34 |
| $ICA_1$–M1 | 0.81 ± 0.43 | 0.49 ± 0.18 | 34 |
| $ICA_1$–A1 | 0.74 ± 0.25 | 0.54 ± 0.23 | 18 |
| BAT (sec) | | | |
| $ICA_1$ | 1.37 ± 0.29 | 1.15 ± 0.20 | 34 |
| $ICA_2$ | 1.63 ± 0.37 | 1.27 ± 0.29 | 34 |
| M1 | 1.91 ± 0.48 | 1.49 ± 0.31 | 34 |
| A1 | 1.85 ± 0.45 | 1.51 ± 0.31 | 18 |
| FWHM (sec) | | | |
| $ICA_1$ | 2.54 ± 0.81 | 1.95 ± 0.46 | 34 |
| $ICA_2$ | 2.53 ± 0.89 | 1.96 ± 0.50 | 34 |
| M1 | 3.27 ± 0.91 | 2.62 ± 0.63 | 34 |
| WO (AU/s) | | | |
| $ICA_1$ | −209 ± 79 | −264 ± 80 | 34 |
| $ICA_2$ | −202 ± 80 | −247 ± 91 | 34 |
| M1 | −86 ± 44 | −112 ± 44 | 34 |
| A1 | −73 ± 29 | −90 ± 30 | 18 |
| AUC (AU/sec) | | | |
| $ICA_1$ | 1268 ± 426 | 942 ± 324 | 34 |
| $ICA_2$ | 1188 ± 476 | 866 ± 269 | 34 |

**Note:**—No. indicates number of cases measured; AU, arbitrary unit.

tration curves for ROIs at the $ICA_2$ and M2 in the lateral view, obtained before and after the stent-placement procedure. In this case, the contrast media arrived at these arteries at similar times, but they flushed out faster after the stent placement was performed. As a result of the faster washout of the contrast media, the FWHM and WO for these arteries decreased significantly after stent placement.

Table 1 is a list of comparisons of the hemodynamic parameters before and after stent placement at different ROIs. According to Table 1, TTP and BAT showed significant differences before and after stent placement in 9 and 10 ROIs, respectively. The TTP, BAT, and WO showed significant changes before and after stent placement at all arterial ROIs and FWHM for most arterial ROIs. Among the venous ROIs measured, significant changes in TTP were found at the PV, and significant changes in the BAT were found at the PV and SSS. The ME and WI had no value in demonstrating the hemodynamic changes before and after stent placement. The *P* values of many of the venous ROIs were not available because their time-concentration curves did not reach a maximum or lacked a sufficient downward curve.

The statistical data for hemodynamic parameters with significant changes are shown in the PA (Table 2) and lateral (Table 3) views. For the TTP calculation, the first image was defined as time = 0. The rTTP value represents the time difference from an upstream vessel to a downstream one. After the stent-placement procedure, there was a generalized decrease in TTP, BAT, rTTP, FWHM, WO, and AUC compared with the measurements on the prestent angiograms. Figure 5 shows the means of the BAT and TTP before and after stent treatment. From the map, we can see that the treatment reduced both the BAT and TTP in the neck and intracranial vascular segments.

## DISCUSSION

Quantitative DSA facilitates real-time hemodynamic monitoring and helps determine the optimal angioplasty in carotid stenosis to avoid hyperperfusion[4] and the end point of embolization in carotid cavernous fistulas.[8,10] A previous study by Lin et al[8] in 2012 showed significant reduction in rTTP at the ICA (in both PA and lateral views), A1, M1, and M2 after stent placement compared with pretreatment data. Lin et al[10] reported a study of cerebral circulation time by calculating the rTTP relative to the cervical ICA on the PA view (same location as $ICA_1$ in our report) and relative to the cavernous segment of the ICA on the lateral view (same location as $ICA_2$ in our report). We found that the poststenting mean circulation times of M1, M2, and PV (corresponding to rTTP of the following segments: $ICA_1$–M1, $ICA_2$–M2, and $ICA_2$–PV) in our study (0.49, 0.50, and 4.14 seconds, respectively) were close to those of healthy controls (0.46, 0.58, and 4.38 seconds, respectively).[10] Therefore, the cerebral circulation time returned to normal for M1, M2, and the PV after treatment. If the posttreatment cerebral circulation time does not decrease to normal, we have to consider a hemodynamically significant residual stenosis, arterial spasm, hidden tandem stenotic lesion, and microemboli. Those above-mentioned phenomena will alert medical professionals to do further clinical management.

Lin et al[10] also evaluated the maximal slope of the wash-in phase (the same as WI in our study) in the time-concentration curve and found significant changes in the maximal slope before and after treatment for M2, SSS, and M1. Our study found that the WI had no significant peritherapeutic change for all ROIs evaluated (Table 1). Both previous studies and ours evaluated FWHM. The study of Lin et al showed significant change at M1 and M2 only.[10] Our study showed significant changes for all arterial ROIs except A2. The discrepancy in maximal slope (WI in our

**Table 3: Results for the hemodynamic parameters with significant changes ($P < .05$) after the stenting procedure in the lateral view**

| ROI | Before Treatment (Mean ± SD) | After Treatment (Mean ± SD) | No. |
|---|---|---|---|
| TTP (sec) | | | |
| $ICA_1$ | 2.96 ± 0.69 | 2.47 ± 0.25 | 34 |
| $ICA_2$ | 3.30 ± 0.81 | 2.66 ± 0.27 | 34 |
| M2 | 3.98 ± 0.98 | 3.15 ± 0.30 | 34 |
| A2 | 3.70 ± 0.88 | 2.97 ± 0.41 | 17 |
| PV | 8.01 ± 1.28 | 6.79 ± 0.68 | 30 |
| rTTP (sec) | | | |
| $ICA_1$–$ICA_2$ | 0.34 ± 0.24 | 0.19 ± 0.13 | 34 |
| $ICA_2$–M2 | 0.68 ± 0.25 | 0.50 ± 0.16 | 34 |
| $ICA_2$–A2 | 0.66 ± 0.38 | 0.34 ± 0.17 | 17 |
| $ICA_2$–PV | 4.73 ± 1.00 | 4.14 ± 0.69 | 30 |
| M2–PV | 4.06 ± 0.93 | 3.67 ± 0.65 | 30 |
| BAT (sec) | | | |
| $ICA_1$ | 1.39 ± 0.37 | 1.19 ± 0.26 | 34 |
| $ICA_2$ | 1.70 ± 0.37 | 1.33 ± 0.29 | 34 |
| M2 | 2.14 ± 0.54 | 1.65 ± 0.34 | 34 |
| A2 | 2.17 ± 0.69 | 1.74 ± 0.37 | 17 |
| PV | 4.88 ± 0.94 | 3.87 ± 0.69 | 30 |
| SSS | 5.35 ± 1.53 | 4.39 ± 1.09 | 34 |
| FWHM (sec) | | | |
| $ICA_1$ | 2.66 ± 1.01 | 1.93 ± 0.41 | 34 |
| $ICA_2$ | 2.66 ± 0.93 | 2.01 ± 0.50 | 34 |
| M2 | 3.22 ± 0.88 | 2.54 ± 0.65 | 34 |
| A2 | 2.90 ± 0.84 | 2.27 ± 0.83 | 17 |
| WO (AU/s) | | | |
| $ICA_1$ | −217 ± 110 | −281 ± 91 | 34 |
| $ICA_2$ | −229 ± 91 | −305 ± 107 | 34 |
| M2 | −90 ± 49 | −120 ± 46 | 34 |
| A2 | −79 ± 37 | −116 ± 34 | 17 |
| AUC (AU/sec) | | | |
| $ICA_1$ | 1413 ± 692 | 1002 ± 340 | 34 |
| $ICA_2$ | 1561 ± 753 | 1160 ± 385 | 34 |
| M2 | 879 ± 377 | 750 ± 299 | 34 |
| ME (AU) | | | |
| A2 | 203 ± 74 | 234 ± 72 | 17 |

**Note:**—No. indicates number of cases measured; AU, arbitrary unit.

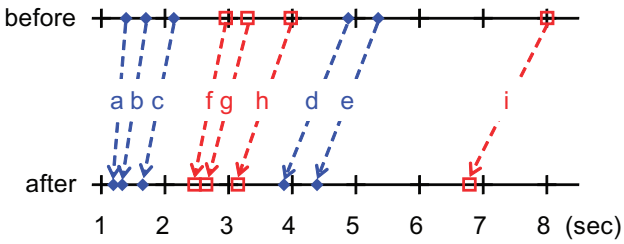


**FIG 5.** Comparison of the mean BAT (blue, a–e) and mean TTP (red, f–i) before (*upper line*) and after (*lower line*) treatment for different vascular ROIs in the lateral view: $ICA_1$ (a and f), $ICA_2$ (b and g), M2 (c and h), PV (d and i), and SSS (e). The TTP and rTTP are reduced after treatment in the extracranial (a and f) and intracranial segments, being more obvious in segments between the $ICA_1$ and the PV (a–d and f–i) and less obvious from PV to SSS (d and e).

study) and FWHM is most likely caused by the difference in calculation algorithm. Curve fitting in our study made the time-concentration curve smooth; thus, the measured slope may be less than the maxillary slope obtained without curve fitting in the previous study.[10]

We evaluated the BAT in intracranial vascular points. The BAT was first used to make a color-coded image from angiograms obtained by 1 contrast media injection.[6] The BAT has not been further evaluated for hemodynamic information of DSA, to our knowledge. Measurements of TTP, rTTP, ME, FWHM, WO, and AUC in venous structures were limited by the absence of late washout phase images. The calculation of BAT does not need the presence of a peak in the time-concentration curve and is not limited by late contrast media washout or early halting of the imaging process. Therefore, the BAT can be used in the evaluation of hemodynamic changes of veins with late washout, such as in conditions of dural sinus stenosis and dural sinus thrombosis.

During the DSA imaging, the contrast medium was injected at the common carotid artery proximal to the stenosis. The amount of contrast media injected for angiography before and after stent placement was the same, and it took longer for the contrast media to travel through the stenotic segment before stent placement. As a result, the TTP, which represents the contrast transit time, is significantly longer at the cervical ICA, M1, M2, A1, A2, and PV before stent placement (Tables 2 and 3). After the stenosis was relieved by stent placement, the transit time of contrast media through the previously stenotic segment recovered, and the washout process was quicker, reflected by a shorter TTP (Tables 2 and 3).

The carotid stenosis before stent placement not only caused a longer transit time in the stenotic segment that caused TTP prolongation at the $ICA_1$ but also caused prolongation of the transit time in the distal segments of this artery, as shown by the significantly longer rTTP (Tables 2 and 3 and Fig 5). Prolongation of the transit time in the distal segments of this artery indicates that the blood flow rate was slower distal to the stenosis before stent placement. This finding is compatible with previous transcranial Doppler sonography demonstrations of reduced peak systolic velocity in the middle cerebral artery on the side of significant internal carotid artery stenosis.[17]

In this experiment, the sampling rate for acquiring DSA images was 6 frames/s. As a result, the temporal resolution of time-concentration curves was $\Delta t = 0.17$ seconds. The theoretic SD[18] of this digitized data in measuring BAT is $\Delta t/\sqrt{12} = 0.05$ seconds, which is relatively small compared with the SD of the BAT in Tables 2 and 3. The effect of the sampling rate on TTP is more complicated because we applied curve fitting to the measured data. Computer simulation is needed to study this effect.[15]

## CONCLUSIONS

We compared the changes in 8 hemodynamic parameters before and after stent placement treatment of carotid stenosis. We found that the stent-placement procedure significantly reduced TTP, BAT, and WO at all arterial ROIs and FWHM and AUC at some arterial ROIs. The evaluation of venous structures by using TTP, rTTP, FWHM, WI, WO, ME, and AUC was limited if either the ME fell at the last image or a washout phase in the time-concentration curve was deficient. More images must be obtained for the late washout veins to evaluate venous ROIs with these 7 parameters.

The BAT showed significant changes not only at all arterial ROIs but also at the PV and SSS. Thus, the BAT can be used for the evaluation of cerebral circulation of venous structures when the TTP cannot be measured because of an incomplete time-concen-

tration curve. This study also found that carotid stenosis resulted in longer transit times not only in the stenotic segment but also in the distal intracranial segments.

## REFERENCES


1. Tenjin H, Asakura F, Nakahara Y, et al. **Evaluation of intraaneurysmal blood velocity by time-density curve analysis and digital subtraction angiography.** *AJNR Am J Neuroradiol* 1998;19:1303–07 Medline
2. Hung SC, Liang ML, Lin CF, et al. **New grading of moyamoya disease using color-coded parametric quantitative digital subtraction angiography.** *J Chin Med Assoc* 2014;77:437–42 CrossRef Medline
3. Gölitz P, Struffert T, Lücking H, et al. **Parametric color coding of digital subtraction angiography in the evaluation of carotid cavernous fistulas.** *Clin Neuroradiol* 2013;23:113–20 CrossRef Medline
4. Lin CJ, Chang FC, Tsai FY, et al. **Stenotic transverse sinus predisposes to poststenting hyperperfusion syndrome as evidenced by quantitative analysis of peritherapeutic cerebral circulation time.** *AJNR Am J Neuroradiol* 2014;35:1132–36 CrossRef Medline
5. Levitt MR, Morton RP, Haynor DR, et al. **Angiographic perfusion imaging: real-time assessment of endovascular treatment for cerebral vasospasm.** *J Neuroimaging* 2014;24:387–92 CrossRef Medline
6. Cover KS, Lagerwaard FJ, van den Berg R, et al. **Color intensity projection of digitally subtracted angiography for the visualization of brain arteriovenous malformations.** *Neurosurgery* 2007;60:511–14; discussion 514–15 Medline
7. Strother CM, Bender F, Deuerling-Zheng Y, et al. **Parametric color coding of digital subtraction angiography.** *AJNR Am J Neuroradiol* 2010;31:919–24 CrossRef Medline
8. Lin CJ, Hung SC, Guo WY, et al. **Monitoring peri-therapeutic cerebral circulation time: a feasibility study using color-coded quantitative DSA in patients with steno-occlusive arterial disease.** *AJNR Am J Neuroradiol* 2012;33:1685–90 CrossRef Medline
9. Lin CJ, Luo CB, Hung SC, et al. **Application of color-coded digital subtraction angiography in treatment of indirect carotid-cavernous fistulas: initial experience.** *J Chin Med Assoc* 2013;76:218–24 CrossRef Medline
10. Lin CJ, Chang FC, Guo WY, et al. **Changes of time-attenuation curve blood flow parameters in patients with and without carotid stenosis.** *AJNR Am J Neuroradiol* 2015;36:1176–81 CrossRef Medline
11. Zhang Q, Xu R, Sun Q, et al. **Exploring the value of using color-coded quantitative DSA evaluation on bilateral common carotid arteries in predicting the reliability of intra-ascending aorta flat detector CT–CBV maps.** *AJNR Am J Neuroradiol* 2015;36:960–66 CrossRef Medline
12. Thompson HK Jr, Starmer CF, Whalen RE, et al. **Indicator transit time considered as a gamma variate.** *Cir Res* 1964;14:502–15 CrossRef Medline
13. Coleman TF, Li Y. **On the convergence of interior-reflective Newton methods for nonlinear minimization subject to bounds.** *Math Prog* 1994;67:189–224 CrossRef
14. Coleman TF, Li Y. **An interior trust region approach for nonlinear minimization subject to bounds.** *SIAM J Optim* 1996;6:418–45 CrossRef
15. Bahn MM. **A single-step method for estimation of local cerebral blood volume from susceptibility contrast MRI images.** *Magn Reson Med* 1995;33:309–17 CrossRef Medline
16. Kenney JF, Keeping ES. *Mathematics of Statistics: Part 1*. 3rd ed. Princeton: Van Nostrand; 1962
17. Can U, Furie KL, Suwanwela N, et al. **Transcranial Doppler ultrasound criteria for hemodynamically significant internal carotid artery stenosis based on residual lumen diameter calculated from en bloc endarterectomy specimens.** *Stroke* 1997;28:1966–71 CrossRef Medline
18. Gray RM, Neuhoff DL. **Quantization.** *IEEE Trans Inf Theory* 1998;44:2325–83 CrossRef

# Intervention versus Aggressive Medical Therapy for Cognition in Severe Asymptomatic Carotid Stenosis

C.-J. Lin, F.-C. Chang, K.-H. Chou, P.-C. Tu, Y.-H. Lee, C.-P. Lin, P.-N. Wang, and I.-H. Lee

## ABSTRACT

**BACKGROUND AND PURPOSE:** Asymptomatic carotid stenosis of ≥70% increases the incidence of microembolism and/or chronic hypoperfusion, which may consequently impair neurocognition and brain connections. We sought controlled evidence for any cognitive benefit of aggressive medical therapy and combined carotid revascularization.

**MATERIALS AND METHODS:** Patients with asymptomatic, unilateral, ≧70% stenosis of the extracranial ICA chose either aggressive medical therapy alone or in combination with carotid artery stent placement in this nonrandomized controlled study. They were examined with a battery of neuropsychological tests, structural MR imaging, DTI, and resting-state fMRI before and 3 months after treatment.

**RESULTS:** Forty patients were included with 15 in the medical group and 25 in the stent-placement group. Among them, 13 and 21 in the respective groups completed neuroimaging follow-up. The baseline characteristics and the changes in cognitive performance during 3 months showed no differences between treatment groups. Nevertheless, compared with the medical group, the stent-placement group showed subjective dizziness alleviation ($P = .045$) and a small increase in fractional anisotropy at the splenium of the corpus callosum and the posterior periventricular white matter ipsilateral to carotid artery stent placement. Moreover, only the stent-placement group showed interval improvement in immediate memory and visuospatial performance, which was accompanied by an increase of functional connectivity at the insular cortex of the dorsal attention network and the medial prefrontal cortex of the default mode network.

**CONCLUSIONS:** Both aggressive medical therapy alone and combined carotid revascularization in ≧70% asymptomatic carotid stenosis similarly preserved cognition during 3-month follow-up, though the latter had the potential for dizziness alleviation and cognitive and connectivity enhancement.

**ABBREVIATIONS:** CAS = carotid artery stent placement; FA = fractional anisotropy; Fc = functional connectivity; MCI = mild cognitive impairment; VCIND = vascular cognitive impairment no dementia

Interventional revascularization for ≥60% asymptomatic ICA stenosis has long been debated, given the decreasing annual risk of ipsilateral ischemic stroke in these patients from 2.3% to 0.5% with the development of contemporary optimal medical treatment.[1-4] However, some of these patients carry a higher risk of stroke than others despite optimal medical treatment. Patients with detectable embolic signals by transcranial Doppler have a high annual risk (7%) of stroke.[5] Stenotic degree of ≥90%, poor collaterals, and echolucent plaque texture could also stratify patients into groups with varying high stroke risk to >4% annually.[6,7] Thus, interventional revascularization should be considered in such patients. Recently, long-term randomized trials, the Asymptomatic Carotid Trial[8] and the Carotid Revascularization Endarterectomy versus Stenting Trial (CREST)[9] demonstrated that there was no difference in the rate of late ipsilateral stroke after carotid endarterectomy or carotid artery stent placement (CAS) in asymptomatic and symptomatic patients. Of asymptomatic patients, the 5-year cumulative rate of stroke-free survival was 93.1% in the CAS group and 94.7% in the carotid endarterectomy group.[8]

Hence, asymptomatic carotid stenosis has been viewed from a changing perspective from stroke risk to cognitive susceptibility.[10,11] We previously demonstrated that patients with unilateral asymptomatic carotid stenosis of ≥70% had more dizziness/

Received October 16, 2015; accepted after revision March 10, 2016.

From the Departments of Neurology (C.-J.L., P.-N.W., I.-H.L.), Radiology (F.-C.C.), and Medical Education and Research (P.-C.T.), Taipei Veterans General Hospital, Taipei, Taiwan; and Institute of Brain Science (C.-J.L., P.-C.T., I.-H.L.), Institute of Neuroscience (K.-H.C., C.-P.L.), Department and Institute of Physiology (Y.-H.L.), and School of Medicine (P.-N.W.), National Yang-Ming University, Taipei, Taiwan.

This work was sponsored by Taiwan Ministry of Science and Technology (MOST 103-2320-B-075-002, MOST 103-2314-B-075-008, MOST 104-2320-B-075-001) and the Taipei Veterans General Hospital (V103C-171, V104C-059, V105B-029) in Taiwan.

Please address correspondence to I-Hui Lee, MD, PhD, Department of Neurology, Taipei Veterans General Hospital. 201, Section 2, Shipai Rd, Beitou District, Taipei, Taiwan; e-mail: ihlee@vghtpe.gov.tw

Indicates open access to non-subscribers at www.ajnr.org

http://dx.doi.org/10.3174/ajnr.A4798

unsteadiness and poorer verbal memory, executive function, and visuospatial perception than the healthy controls, accompanied by extensive widespread disruption of long-range structural and functional connectivity.[12,13] The mechanisms are likely attributed to microemboli from unstable carotid plaques[5] and/or chronic hypoperfusion.[14,15] Single-arm studies of carotid revascularization accomplished by either carotid endarterectomy or CAS reported the controversial results of cognitive enhancement in patients with asymptomatic carotid stenosis.[15-20] However, there is a lack of medical-controlled evidence reflecting contemporary medical improvement and risk-benefit balance of interventions for cognitive preservation. Here, we investigate the impact of aggressive medical treatment with or without combined carotid revascularization on neurocognitive and connectivity outcomes at 3 months after treatment in patients with ≧70% asymptomatic carotid stenosis.

## MATERIALS AND METHODS

### Subjects, Treatment, and Neuropsychological Tests

We enrolled patients with asymptomatic, unilateral severe stenosis of the extracranial ICA at our dizziness outpatient clinic of Taipei Veterans General Hospital between March 2010 and July 2015. The inclusion criteria were between 20 and 80 years of age and ICA stenotic degree of ≥70% identified by both duplex ultrasonography[21] and gadolinium-enhanced MR angiography (North American Symptomatic Carotid Endarterectomy trial criteria).[22] The exclusion criteria included transient ischemic attack or stroke, functional disability (modified Rankin Scale score of ≥3), carotid dissection, and the presence of contralateral ICA stenosis of ≥50% and comorbidities of dementia, major depression (based on the *Diagnostic and Statistical Manual of Mental Disorders-IV*), Parkinsonism, multiple sclerosis, brain tumor, congestive heart failure (left ventricular ejection fraction <40%), chronic obstructive pulmonary disease, cirrhosis, renal failure (estimated glomerular filtration rate <30 mL/min/1.73 $m^2$), and malignancy. The medications of all subjects were recorded. Written informed consent was obtained from each participant before enrollment. This study was approved by the ethics committee of the Taipei Veterans General Hospital (VGHIRB No. 2012–01-016AC).

All patients received aggressive medical treatment (dual antiplatelets if tolerated or at least 1 antiplatelet, statin therapy goal of low-density lipoprotein of <100 mg/dL, diabetes treatment goal of glycated hemoglobin level of <7%, hypertension treatment goal of systolic blood pressure of <140 mm Hg, smoking cessation) with or without carotid revascularization treatment in a nonrandomized fashion tailored for the individual procedure and preference. For CAS, conventional angiography of the supra-aortic arteries and branches was performed by using a transfemoral arterial approach. An embolic protection device (FilterWire EX or EZ; Boston Scientific, Natick, Massachusetts) was carefully navigated through the stenotic lesion and placed in the distal cervical ICA. Then a self-expandable stent (Wallstent, Boston Scientific; or Precise; Cordis, Fremont, California) was introduced and adjusted to the dimension of the stenotic artery, followed by postdilation with a balloon of 5–6 mm in diameter. Angiography was repeated for the ICA and its intracranial branches to ensure the residual stenosis of the target site was <50% and absence of endovascular complications.

All subjects were evaluated with a battery of neuropsychological tests before and 3 months after treatment by a blinded trained examiner, including the Dizziness Handicap Inventory,[23] the Mini-Mental State Examination, memory tests (verbal selective reminding test; an auditory verbal learning test, including total immediate recall and 15-minute delayed recall of 12 items),[24] executive tests (the Modified Trail-Making Test A and B[25]; the Stroop Color and Word Test[26]), an attention test (the Symbol Digit modalities Test),[27] and complex visuospatial perception tests (the Modified Complex Figure Test with Copy and Recall).

### MR Imaging Acquisition

Before and 3 months after the treatment, patients were subjected to MR imaging and instructed to hold still, keep their eyes open, and think of nothing in a 3.0 Discovery 750 (GE Healthcare, Milwaukee, Wisconsin) MR imaging scanner. All images were acquired along the anteroposterior commissural plane, according to multiplanar T1-weighted BRAVO anatomica images (http://www3.gehealthcare.com/en/Products/Categories/Magnetic_Resonance_Imaging/Neuro_Imaging/BRAVO) (TR = 12.2 ms; TE = 5.2 ms; flip angle = 12°; voxel size = 1 × 1 × 1 mm; FOV = 256 × 256 mm). A series of fluid-attenuated inversion recovery sequences was acquired to rate leukoaraiosis severity. The stent-placement group received additional diffusion-weighted imaging and apparent diffusion coefficient imaging within 3 days after the procedure to exclude any periprocedural insult. For DTI, a single-shot diffusion spin-echo echo-planar imaging sequence (TR/TE = 9500/85.6 ms; thickness = 2 mm; matrix = 128 × 128; FOV = 256 × 256 mm; 30 directions) was adopted. For resting-state fMRI, the blood oxygen level–dependent signals from a task-free run (124 time points/372 seconds) of a gradient-echo echo-planar imaging sequence (TR/TE = 3000/30 ms; flip angle = 90°; FOV = 222 × 222 mm; thickness = 3 mm) were recorded.

### MR Imaging Processing and Analysis

A blinded neurologist and a neuroradiologist reviewed all images. The severity of leukoaraiosis was assessed by the semiquantitative Scheltens rating scale.[28] The hemisphere ipsilateral to the ICA stenosis was flipped to the right side along the midsagittal plane. We analyzed T1-weighted anatomic images and manually outlined the bilateral hippocampi to calculate the hippocampal volumes of each patient[29,30] and brain volume by using the voxel-based morphometry approach.[31] Statistical Parametric Mapping software (SPM8; http://www.fil.ion.ucl.ac.uk/spm/software/spm12) was used to segment the gray and white matter intensities and normalize them to Montreal Neurological Institute space. The gray and white matter volumes were compared within each group by paired *t* tests with a threshold of $P < .05$. For DTI, voxelwise fractional anisotropy (FA) was analyzed after applying preprocessing with Tract-Based Spatial Statistics from the FMRIB Software Library (TBSS; http://fsl.fmrib.ox.ac.uk/fsl/fslwiki/TBSS), as previously described.[12] We performed a paired *t* test for within-group interval changes of the FA maps and then a 2-sample *t* test for between-group comparison of the interval changes with a significance set at $P < .05$ with family-wise error rate correction for multiple comparisons (random permutations, $n = 5000$).

The mean FA values of the whole brain or each hemisphere, as

**Table 1: Baseline characteristics**

| | Med | Med+CAS | *P* Value |
|---|---|---|---|
| Age (yr) | 68.8 ± 8.8 | 71.4 ± 7.8 | .348 |
| Male sex (%) | 11 (73) | 21 (84) | .687 |
| Education (yr) | 12 (7.5–12) | 10 (7–12) | .602 |
| Stenotic degree (%) | 81.3 ± 12.0 | 81.0 ± 9.8 | .928 |
| Total occlusion (No.) (%) | 3 (20) | 0 (0) | .543 |
| Hypertension (No.) (%) | 12 (80) | 20 (80) | .611 |
| Mean BP (mm Hg) | 95.1 ± 9.5 | 95.3 ± 10.2 | .887 |
| Diabetes mellitus (No.) (%) | 7 (47) | 9 (36) | .268 |
| HbA1c (%) | 6.6 ± 1.2 | 6.4 ± 0.4 | .254 |
| Hypercholesterolemia (No.) (%) | 9 (60) | 17 (68) | .444 |
| LDL (mg/dL) | 85.3 ± 20.1 | 89.1 ± 14.7 | .851 |
| Smoking (No.) (%) | 5 (33) | 9 (36) | .542 |
| Atrial fibrillation (No.) (%) | 1 (6.6) | 0 (0) | .118 |
| Double antiplatelets (No.) (%) | 8 (53) | 18 (72) | .345 |
| Statins (No.) (%) | 8 (53) | 15 (60) | .488 |
| Dizziness Handicap Inventory | 14.7 ± 19.5 | 18.3 ± 13.8 | .541 |
| Mini-Mental State Examination | 28.4 ± 1.2 | 28.2 ± 1.8 | .641 |
| Verbal memory tests | | | |
| Total immediate recall | 38.3 ± 10.5 | 46.1 ± 7.9 | .086 |
| Delayed recall | 7.3 ± 2.3 | 8.1 ± 2.3 | .571 |
| Attention tests | | | |
| Symbol Digit Modalities Test | 45.5 ± 16.3 | 41.9 ± 20.1 | .559 |
| Executive function tests | | | |
| Modified Trail-Making Test A | 16.4 ± 8.6 | 22.4 ± 15.1 | .214 |
| Modified Trail-Making Test B | 43.6 ± 28.9 | 53.1 ± 31.1 | .455 |
| Stroop Color and Word Test | 33. ± 13.4 | 32.9 ± 14.6 | .819 |
| Complex visuospatial perception | | | |
| Complex Figure Test (Copy) | 16.4 ± 1.2 | 15.5 ± 1.8 | .109 |
| Complex Figure Test (Recall) | 10.4 ± 4.5 | 9.7 ± 4.2 | .631 |
| MCI/VCIND (No.) (%) | 6 (40%) | 7 (28%) | .318 |
| Scheltens leukoaraiosis score | 5.2 ± 2.7 | 5.4 ± 3.1 | .889 |
| Hippocampal volume (mL) | 3.3 ± 0.3 | 3.2 ± 0.2 | .533 |
| Ipsilateral hemispheric FA | 0.50 ± 0.01 | 0.49 ± 0.01 | .471 |
| Contralateral hemispheric FA | 0.51 ± 0.01 | 0.50 ± 0.01 | .375 |

**Note:**—Med indicates medical therapy alone; Med+CAS, medical therapy combined with carotid artery stent placement; BP, blood pressure; LDL, low-density lipoprotein; HbA1c, hemoglobin A1c test.

well as of the focal clusters with significant interval changes, were extracted in each patient for statistical analysis. For resting-state-fMRI, preprocessing and analytic procedures were performed as previously described.[13] ROIs with 4-mm radii were defined in the hemisphere ipsilateral to ICA stenosis (flipped to the right), representing the seed regions for 6 resting-state networks, including the posterior cingulate cortex (0, −50, 22) and the medial prefrontal cortex (1, 48, −4) for the default mode network, right frontal eye field (26, 6, 48) for the dorsal attention network, the middle frontal gyrus (45, 29, 32) for the frontoparietal network, the primary motor cortex (41, −20, 62) for the sensorimotor network, the dorsal anterior cingulate cortex (1, 10, 46) for the salience network, and, last, the primary visual cortex (4, 81, −10) for the visual network as a control supplied by the vertebrobasilar circulation.[13]

The temporal correlations between the blood oxygen level–dependent signals from each ROI and brain-wise voxels were calculated and presented as Pearson correlation coefficients ($r$), followed by a Fisher r-$z$ transformation. $Z$ values from a single ROI in each network were defined as functional connectivity (Fc) and were computed with 1-sample $t$ tests by using SPM8 to generate the Fc map in both groups. For within-group analysis, the Fc interval changes in each group were obtained by a paired $t$ test, followed by false discovery rate correction with a significance defined as $q < .05$.

### *Statistical Analyses of Demographic/Neuropsychological Variables and Multivariate Regression Models*

SPSS software (Version 18.0; IBM, Armonk, New York) was used for the statistical analyses. Categoric variables between groups were compared by using $\chi^2$ or Fisher exact tests if the expected number was ≤5. The baseline dizziness, neuropsychological tests, leukoaraiosis scores, hippocampal volumes, and the mean FA values were compared by 2-sample $t$ tests between groups. The within-group interval changes of parameters were compared by paired $t$ tests. The between-group interval changes of each value were then compared by using 2-sample $t$ tests.

Significance was defined as $P < .05$. The significance of 9 neuropsychological measures was corrected by the Bonferroni method ($P < .0056$). The changes of the dizziness scale and neuropsychological scores were classified as improvement from the baseline (>0), no change (= 0), or decline (<0), and the percentages of each condition were compared between groups by using $\chi^2$ or Fisher exact tests. To investigate the relationship between the connectivity measures (ie, FA or Fc) and the neuropsychological changes after treatments, we used a multivariate regression model adjusted for age, sex, years of education, treatment group, the stenotic degree, the baseline presence of mild cognitive impairment (MCI), and vascular risk factors. We defined MCI or vascular cognitive impairment no dementia (MCI/VCIND) with a delayed verbal recall score of <8 (ie, 1.5 SDs below the mean of the healthy controls according to the previous literature).[13,32]

## RESULTS

### *Ischemic Events and the Neurocognitive Changes after Treatment*

Forty-seven subjects were consecutively enrolled, with 5 being excluded due to the presence of ≥50% stenosis in the bilateral ICA and 2 being lost to follow-up. Therefore, 40 subjects, 15 in the medical group and 25 in the stent-placement group, completed the neuropsychological follow-up; 34 of them also completed the neuroimaging follow-up (13 and 21 in respective groups). The baseline characteristics, scores on the Dizziness Handicap Inventory and neuropsychological tests, percentage of MCI/VCIND, Scheltens leukoaraiosis score, hippocampal volumes, and hemispheric mean FA values between groups were not different (Table 1). Six of 15 patients in the medical group (40%) and 7 of 25 in the stent-placement group (28%) were considered to have MCI/VCIND ($P = .318$). The stent-placement group had 100% suc-

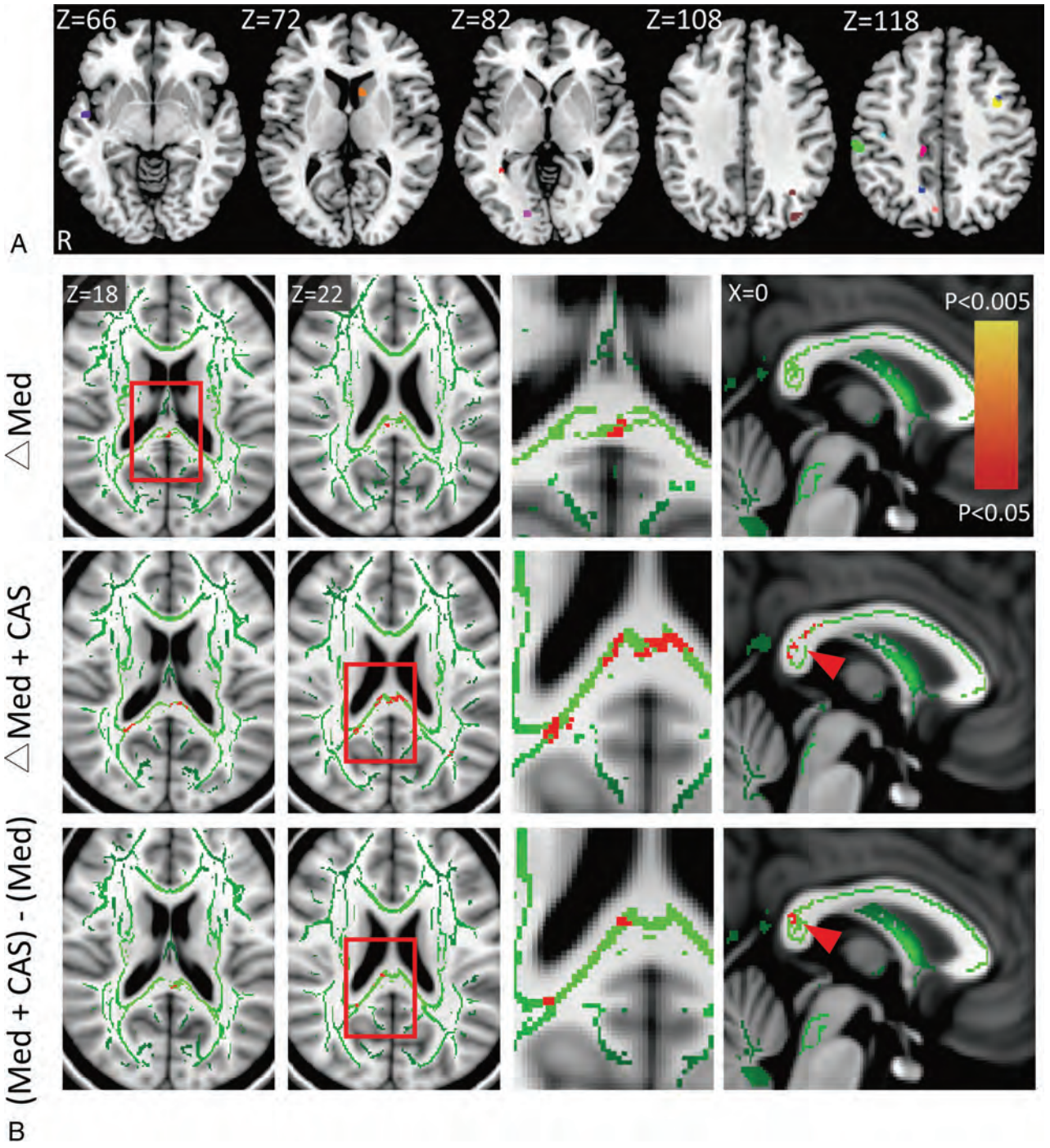


**FIG 1.** *A*, Procedure-related microemboli based on the diffusion-weighted images are overlaid on a standard Montreal Neurological Institute template from 12 of 25 patients in the stent-placement group, indicated by different colors. *B*, The increases (red-yellow) of fractional anisotropy (the white matter skeleton is shown in green) at 3 months after aggressive medical therapy alone (Med, upper row) or combined carotid artery stent placement (Med+CAS, middle row) and the between-group comparisons (lower row). The carotid stenotic side was set to the right in all subjects. The third column from the left represents the high-power views of the insets. Note significant FA increases at the posterior corpus callosum (*arrowheads*) and the posterior periventricular white matter ipsilateral to the CAS in the stent-placement group.

cessful carotid revascularization with residual stenosis of <50% and no periprocedural events, though 12 patients (48%) had asymptomatic tiny cerebral emboli after the procedure according to MR imaging (Fig 1*A*).

At 3 months after treatment, there were no vascular events among all subjects. There was no between-group difference in the changes of neurocognitive function, except that the stent-placement group showed subjectively better dizziness alleviation ($P = .045$) compared with the medical group. However, the stent-placement group, but not the medical group, had notable within-group improvement in the total immediate recall of verbal memory ($P = .001$, uncorrected; with $P < .0056$ as significant) and the visuospatial performance (Complex Figure Test [Copy], $P = .001$, uncorrected) (Table 2). In the total immediate recall test, 21

**Table 2: Interval changes within and between groups**

| ΔChanges | Med | Med+CAS | *P* Value |
|---|---|---|---|
| Dizziness Handicap Inventory | −2.7 ± 4.8 | −6.7 ± 7.1[a] | .045[a] |
| Neuropsychological tests | | | |
| Mini-Mental State Examination | −0.2 ± 1.7 | 0.1 ± 1.0 | .525 |
| Total immediate recall | 2.2 ± 5.6 | 4.2 ± 5.6[a] | .296 |
| Delayed recall | −0.3 ± 1.2 | 0.6 ± 1.7 | .050 |
| Symbol Digit Modalities Test | 1.7 ± 5.2 | 2.3 ± 4.4 | .710 |
| Modified Trail-Making Test A | −0.1 ± 8.1 | −2.6 ± 4.5 | .309 |
| Modified Trail-Making Test B | 1.7 ± 31.9 | −4.9 ± 13.1 | .405 |
| Stroop Color and Word Test | 1.7 ± 5.8 | 2.9 ± 6.4 | .545 |
| Complex Figure Test (Copy) | 0.2 ± 1.4 | 1.1 ± 1.4[a] | .064 |
| Complex Figure Test (Recall) | 0.1 ± 3.1 | 1.7 ± 3.7 | .157 |
| Scheltens leukoaraiosis score | 0.1 ± 0.3 | 0.2 ± 0.5 | .561 |
| Ipsilateral hemispheric FA | 0.002 ± 0.04 | 0.009 ± 0.004 | .447 |
| Contralateral hemispheric FA | 0.002 ± 0.05 | 0.004 ± 0.005 | .681 |

**Note:**—Med indicates medical therapy alone.

[a] For dizziness and imaging measures, $P < .05$ was defined as significant. For the 9 neuropsychological tests, $P < .0056$ was defined as significant with the Bonferroni correction.

of 25 in the stent-placement group (84%) and 9 of 15 in the medical group (60%) showed improvement after treatment ($P = .057$), while 3 in the stent-placement group (12%) and 3 in the medical group (20%) performed worse ($P = .199$).

### *Changes of Structural and Functional Connectivity by Treatment*

Most interesting, both groups showed localized FA increases at the posterior corpus callosum after treatment. The between-group comparison of the FA changes showed that the stent-placement group had small-but-significant FA increments at the posterior corpus callosum and the posterior periventricular white matter ipsilateral to the stenosis/CAS compared with the medical group (Fig 1*B*). Neither the leukoaraiosis score nor the hemispheric mean FA showed notable changes in both groups (Table 2). On the examined functional networks, we noted within-group, but no between-group, enhancement of Fc strength in the stent-placement group, but not in the medical group, between the posterior cingulate cortex and the medial prefrontal cortex contralateral to the stenosis/CAS in the default mode network as well as between the frontal eye field and the insular cortex contralateral to the stenosis/CAS in the dorsal attention network (Fig 2*A*, -*B*).

### *Correlation between Neurocognitive Changes and Connectivity Measures*

Using a multivariate regression model, we found that the baseline whole-brain mean FA ($P = .002$) and the treatment technique (stent-placement better, $P = .034$) correlated with the decreases in dizziness (Dizziness Handicap Inventory) ($R^2 = 0.411$) after adjusting for age, sex, years of education, stenotic degree, presence of MCI, and vascular risk factors. Figure 3*A* shows a reverse linear relationship between the whole-brain mean FA and decreases in the Dizziness Handicap Inventory in both groups, suggesting the lower mean connectivity of the patients at baseline and more dizziness alleviation felt after treatment. With regard to the variables affecting the total immediate recall scores, age ($P = .021$) and interval changes of focal FA at the posterior corpus callosum ($P = .040$) correlated with the changes of the total immediate recall performance ($R^2 = 0.331$) in the stent-placement group, but not in the medical group (Fig 3*B*). Neither the baseline status of MCI/VCIND (Fig 3*C*) nor the baseline stenotic degree predicted the changes of either total immediate recall scores or complex figure recall scores (Fig 3*D*).

## DISCUSSION

This was a nonrandomized controlled study of revascularization plus aggressive medical therapy for severe asymptomatic carotid stenosis with respect to the possibility of cognitive and connectivity enhancement. We found that combined revascularization and aggressive medical treatment significantly alleviated subjective dizziness but did not enhance cognitive performance after 3 months compared with the aggressive medical treatments alone. The above findings were accompanied by greater increases of microstructural connectivity at the splenium of the corpus callosum and the posterior periventricular white matter ipsilateral to the stenosis/CAS. The baseline whole-brain mean FA was inversely correlated with the dizziness alleviation. Moreover, only the stent-placement group showed interval improvement in the short-term verbal memory and visuospatial performance after 3 months. Most interesting, the higher the FA increase at the posterior corpus callosum after CAS, the greater was the improvement in short-term verbal memory, suggesting that augmented microstructural connectivity of the posterior white matter might mediate revascularization-related cognitive changes. The stent-placement group also had focal increases of Fc at the medial prefrontal cortex in the default mode network and at the insula in the dorsal attention network contralateral to the stenosis/CAS, which we previously disclosed as susceptible regions in unilateral severe asymptomatic carotid stenosis patients.[13] These Fc changes were not significantly different between groups but might implicate partial reversibility by a combined revascularization therapy. Thus, it is important to identify those asymptomatic patients at risk and offer timely treatment.

A previous uncontrolled case series of uncomplicated carotid endarterectomy in symptomatic ($n = 50$) and asymptomatic ($n = 30$) patients with >70% carotid stenosis showed an increase of the hemispheric mean FA ipsilateral to the surgery site after 1 month in association with posttreatment cognitive improvement.[33] In contrast, others reported postoperative memory decline in a portion of patients with symptomatic or asymptomatic carotid stenosis 1 month after undergoing carotid endarterectomy or CAS. The multivariate regression analysis showed that memory decline was associated with periprocedural microemboli (11/21 = 52%) and baseline neurologic deficits.[34] In our study, a similar proportion (48%) in the stent-placement group was found to have procedure-related silent microemboli. Nevertheless, we found a modest memory enhancement instead of decline in the stent-placement group and no correlation between the microemboli and cognitive changes at 3 months. The focal FA at the watershed posterior corpus callosum and the posterior periventricular region, rather than the hemispheric mean FA, increased, particu-

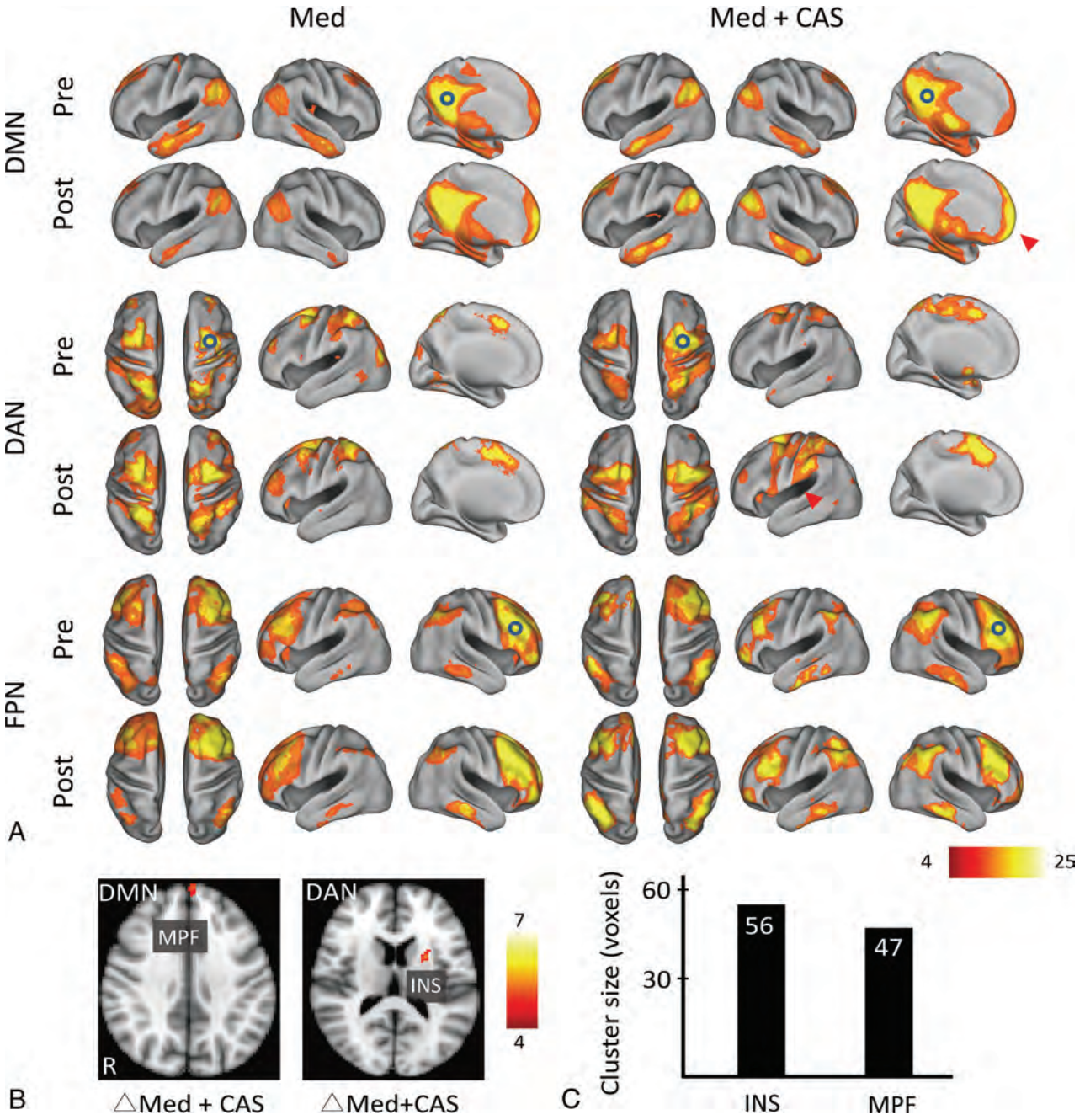


**FIG 2.** *A* and *B*, The functional connectivity correlation maps of both groups (Med indicates medical group; Med+CAS, stent placement group) before (pre) and 3 months after treatment (post). The carotid stenotic side was set to the right. *Hollow circles* indicate the predefined ROIs for individual networks at the right brain. Color bars represent T values. Q indicates the false discovery rate–corrected *P* value. The stent-placement group, not the medical group, showed within-group enhancement of Fc at the medial prefrontal cortex (MPF, T = 5.27, cluster size = 47, Q = .027) of the default mode network (DMN) and at the insular cortex (INS; T = 5.35, cluster size = 56, Q = .040) of the dorsal attention network (DAN) (*arrowheads*). *C*, The bar chart of the aforementioned cluster sizes with increased Fc is shown. FPN indicates frontoparietal network.

larly in the stent-placement group. The posterior corpus callosum (ie, the splenium) is supplied by both the anterior cerebral artery and the posterior cerebral artery,[35] perfusion of which can be augmented by revascularization therapy. The nearby retrosplenial cortex is structurally connected with the medial prefrontal cortex and medial temporal regions and involved in memory processing[36] with the precuneus, posterior cingulate cortex, and hippocampus.[37] Lesions in the splenium or the retrosplenial cortex have been reported to result in verbal and visual memory deficits.[38,39] The cellular components of the observed FA or Fc increases are still unknown. They can be attributed to increased vasodilation and blood flow, improved neurovascular reactivity,[40] neural plasticity,[41] and/or remyelination[42] as suggested by MR spectroscopic studies.

This study has limitations. The nonrandomized controlled design was due to the interventional limitations (eg, medical therapy alone suited patients with total ICA occlusion or those older than 70 years of age with tortuous vessels) and personal hesitation for intervention. Therefore, currently ongoing large-scale randomized controlled trials such as CREST-2 are warranted to determine

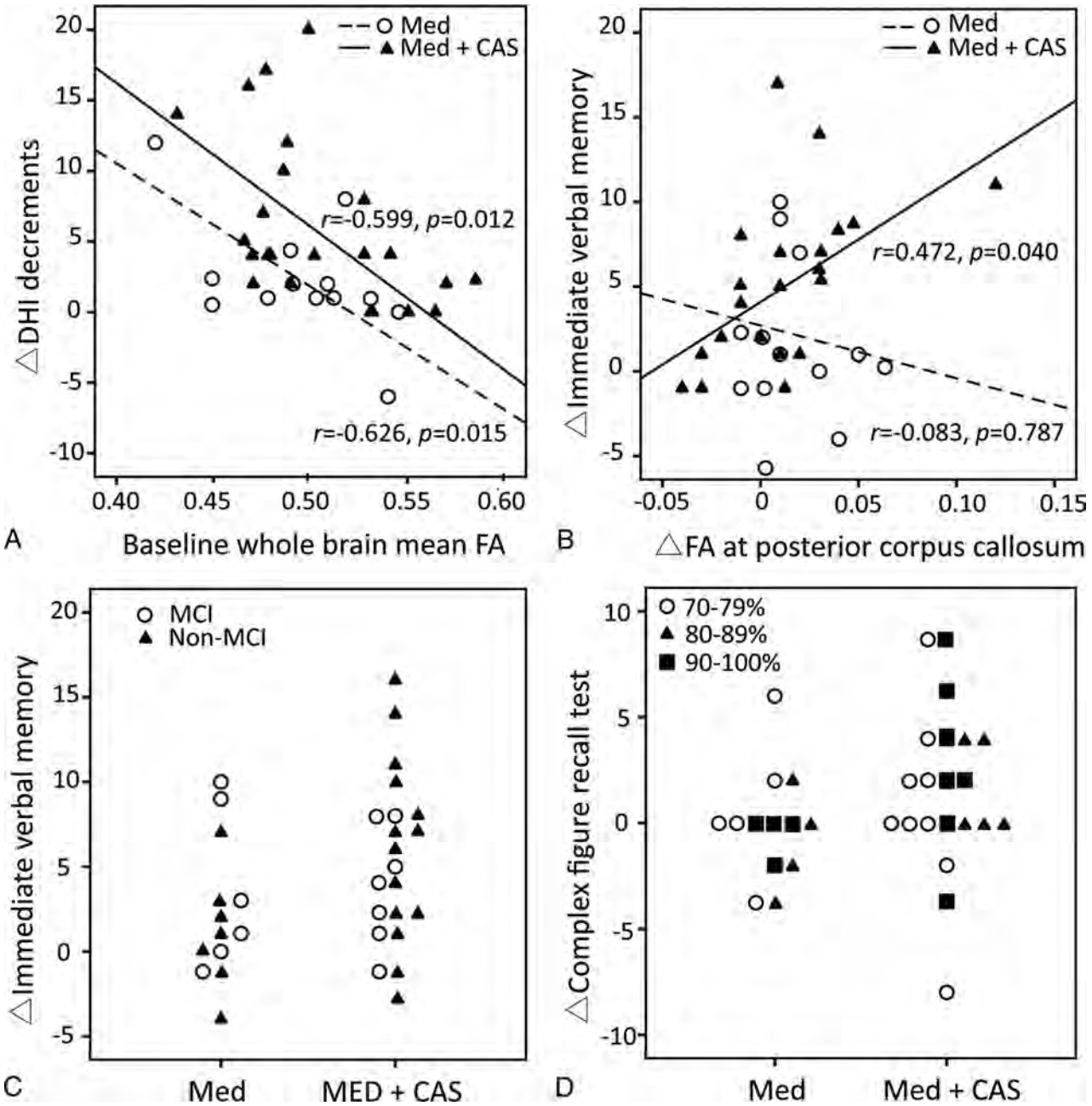


**FIG 3.** Scatterplots of the correlation analyses in the medical (Med) and the stent placement group (Med+CAS). *A*, The baseline whole-brain mean fractional anisotropy negatively correlates with dizziness alleviation (decreases in Dizziness Handicap Inventory [DHI]) in both groups. *B*, The focal FA increases in the posterior corpus callosum positively correlate with the improvement of immediate verbal memory only in the stent-placement group. *C*, The relationship is shown between the baseline presence of mild cognitive impairment/vascular cognitive impairment no dementia and the improvement of immediate verbal memory in the 2 groups. *D*, The baseline stenotic degree is not related to the changes of Complex Figure Test (Recall) scores.

long-term differences in efficacy between optimal medical therapy alone and combined revascularization therapy for stroke prevention (primary outcome) and cognitive preservation (secondary outcome) in patients with asymptomatic severe carotid stenosis. However, this small single-center trial provides new evidence of the benefit-risk balance for revascularization therapy and proposes a possible connectivity target for treating cognitive dysfunction in these patients. Furthermore, we did not assess the plaque-related microemboli and cerebrovascular reperfusion. Successful restoration of cerebral hypoperfusion was shown to correspond to the cognitive improvement after CAS.[17] Additional transcranial emboli detection and perfusion imaging may help to elucidate the therapeutic mechanisms underlying cognitive and/or connectivity changes. Last, we cannot exclude the short-term placebo effects of subjective dizziness alleviation in the stent-placement group or a superimposed vestibular component in these patients.

## CONCLUSIONS

Patients with severe asymptomatic carotid stenosis showed subjective dizziness alleviation in association with greater increases in

microstructural connectivity at the posterior corpus callosum and periventricular white matter by aggressive medical therapy plus successful revascularization compared with aggressive medical therapy alone. However, the cognitive benefit was insignificant between groups at 3 months after treatment in our study. Unlike neurodegenerative causes of cognitive impairment, vascular damage is preventable and treatable. Our results suggest the feasibility of combined medical and revascularization treatment in severe asymptomatic carotid stenosis for limiting cognitive decline, possibly through ancillary connectivity enhancement. Large long-term controlled studies are warranted to provide a risk-benefit assessment for prophylactic carotid revascularization.

## ACKNOWLEDGMENTS

We gratefully acknowledge Wen-Yung Sheng for providing statistical advice. We also thank the Clinical Research Core Laboratory of Taipei Veterans General Hospital for providing experimental space and facilities.

Disclosures: Chun-Jen Lin—*RELATED*: *Grant*: Taipei Veterans General Hospital, Taiwan (V103C-171, V104C-059, V105B-029).* I-Hui Lee—*RELATED*: *Grant*: Ministry of Science and Technology, Taiwan (MOST103–2320-B-075–002, MOST103–2314-B-075–008, MOST104–2320-B-075–001), Taipei Veterans General Hospital, Taiwan (V103C-171, V104C-059, V105B-029)*; *Support for Travel to Meetings for the Study or Other Purposes*: Ministry of Science and Technology, Taiwan.* *Money paid to the institution.

## REFERENCES

1. Executive Committee for the Asymptomatic Carotid Atherosclerosis Study. **Endarterectomy for asymptomatic carotid artery stenosis.** *JAMA* 1995;273:1421–28 CrossRef Medline
2. Halliday A, Mansfield A, Marro J, et al; MRC Asymptomatic Carotid Surgery Trial (ACST) Collaborative Group. **Prevention of disabling and fatal strokes by successful carotid endarterectomy in patients without recent neurological symptoms: randomised controlled trial.** *Lancet* 2004;363:1491–502 CrossRef Medline
3. Marquardt L, Geraghty OC, Mehta Z, et al. **Low risk of ipsilateral stroke in patients with asymptomatic carotid stenosis on best medical treatment: a prospective, population-based study.** *Stroke* 2010; 41:e11–17 CrossRef Medline
4. den Hartog AG, Achterberg S, Moll FL, et al; SMART Study Group. **Asymptomatic carotid artery stenosis and the risk of ischemic stroke according to subtype in patients with clinical manifest arterial disease.** *Stroke* 2013;44:1002–07 CrossRef Medline
5. Markus HS, King A, Shipley M, et al. **Asymptomatic embolisation for prediction of stroke in the Asymptomatic Carotid Emboli Study (ACES): a prospective observational study.** *Lancet Neurol* 2010;9: 663–71 CrossRef Medline
6. Nicolaides AN, Kakkos SK, Kyriacou E, et al. **Asymptomatic internal carotid artery stenosis and cerebrovascular risk stratification.** *J Vasc Surg* 2010;52: 1486–1496.e1–5 CrossRef Medline
7. Gupta A, Chazen JL, Hartman M, et al. **Cerebrovascular reserve and stroke risk in patients with carotid stenosis or occlusion: a systematic review and meta-analysis.** *Stroke* 2012;43:2884–91 CrossRef Medline
8. Rosenfield K, Matsumura JS, Chaturvedi S, et al. **Randomized trial of stent versus surgery for asymptomatic carotid stenosis.** *N Engl J Med* 2016;374:1011–20 CrossRef Medline
9. Brott TG, Howard G, Roubin GS, et al; CREST Investigators. **Long-term results of stenting versus endarterectomy for carotid-artery stenosis.** *N Engl J Med* 2016;374:1021–31 CrossRef Medline
10. Johnston SC, O'Meara ES, Manolio TA, et al. **Cognitive impairment and decline are associated with carotid artery disease in patients without clinically evident cerebrovascular disease.** *Ann Intern Med* 2004;140:237–47 CrossRef Medline
11. Popovic IM, Lovrencic-Huzjan A, Simundic AM, et al. **Cognitive performance in asymptomatic patients with advanced carotid disease.** *Cogn Behav Neurol* 2011;24:145–51 CrossRef Medline
12. Cheng HL, Lin CJ, Soong BW, et al. **Impairments in cognitive function and brain connectivity in severe asymptomatic carotid stenosis.** *Stroke* 2012;43:2567–73 CrossRef Medline
13. Lin CJ, Tu PC, Chern CM, et al. **Connectivity features for identifying cognitive impairment in presymptomatic carotid stenosis.** *PLoS One* 2014;9:e85441 CrossRef Medline
14. Silvestrini M, Paolino I, Vernieri F, et al. **Cerebral hemodynamics and cognitive performance in patients with asymptomatic carotid stenosis.** *Neurology* 2009;72:1062–68 CrossRef Medline
15. Ortega G, Alvarez B, Quintana M, et al. **Asymptomatic carotid stenosis and cognitive improvement using transcervical stenting with protective flow reversal technique.** *Eur J Vasc Endovas Surg* 2014;47: 585–92 CrossRef Medline
16. Grunwald IQ, Papanagiotou P, Reith W, et al. **Influence of carotid artery stenting on cognitive function.** *Neuroradiology* 2010;52: 61–66 CrossRef Medline
17. Chen YH, Lin MS, Lee JK, et al. **Carotid stenting improves cognitive function in asymptomatic cerebral ischemia.** *Int J Cardiol* 2012;157: 104–07 CrossRef Medline
18. Antonopoulos CN, Kakisis JD, Sfyroeras GS, et al. **The impact of carotid artery stenting on cognitive function in patients with extracranial carotid artery stenosis.** *Ann Vasc Surg* 2015;29:457–69 CrossRef Medline
19. Yoon BA, Sohn SW, Cheon SM, et al. **Effect of carotid artery stenting on cognitive function in patients with carotid artery stenosis: a prospective, 3-month-follow-up study.** *J Clin Neurol* 2015;11:149–56 CrossRef Medline
20. Mendiz OA, Sposato LA, Fabbro N, et al. **Improvement in executive function after unilateral carotid artery stenting for severe asymptomatic stenosis.** *J Neurosurg* 2012;116:179–84 CrossRef Medline
21. Grant EG, Benson CB, Moneta GL, et al. **Carotid artery stenosis: gray-scale and Doppler US diagnosis—Society of Radiologists in Ultrasound Consensus Conference.** *Radiology* 2003;229:340–46 CrossRef Medline
22. North American Symptomatic Carotid Endarterectomy Trial Collaborators. **Beneficial effect of carotid endarterectomy in symptomatic patients with high-grade carotid stenosis.** *N Engl J Med* 1991;325: 445–53 CrossRef Medline
23. Jacobson GP, Newman CW. **The development of the Dizziness Handicap Inventory.** *Arch Otolaryngol Head Neck Surg* 1990;116: 424–27 CrossRef Medline
24. Hannay HJ, Levin HS. **Selective reminding test: an examination of the equivalence of four forms.** *J Clin Exp Neuropsychol* 1985;7: 251–63 CrossRef Medline
25. Tombaugh TN. **Trail Making Test A and B: normative data stratified by age and education.** *Arch Clin Neuropsychol* 2004;19:203–14 CrossRef Medline
26. Jensen AR, Rohwer WD Jr. **The Stroop color-word test: a review.** *Acta Psychol (Amst)* 1966;25:36–93 CrossRef Medline
27. Erber JT, Botwinick J, Storandt M. **The impact of memory on age differences in digit symbol performance.** *J Gerontol* 1981;36:586–90 CrossRef Medline
28. Scheltens P, Barkhof F, Leys D, et al. **A semiquantative rating scale for the assessment of signal hyperintensities on magnetic resonance imaging.** *J Neurol Sci* 1993;114:7–12 CrossRef Medline
29. Lehéricy S, Baulac M, Chiras J, et al. **Amygdalohippocampal MR volume measurements in the early stages of Alzheimer disease.** *AJNR Am J Neuroradiol* 1994;15:929–37 Medline
30. Wang PN, Lirng JF, Lin KN, et al. **Prediction of Alzheimer's disease in mild cognitive impairment: a prospective study in Taiwan.** *Neurobiol Aging* 2006;27:1797–806 CrossRef Medline
31. Ashburner J, Friston KJ. **Voxel-based morphometry: the methods.** *Neuroimage* 2000;11:805–21 CrossRef Medline

32. Larrabee GJ, Trahan DE, Levin HS. **Normative data for a six-trial administration of the Verbal Selective Reminding Test.** *Clin Neuropsychol* 2000;14:110–18 CrossRef Medline
33. Sato Y, Ito K, Ogasawara K, et al. **Postoperative increase in cerebral white matter fractional anisotropy on diffusion tensor magnetic resonance imaging is associated with cognitive improvement after uncomplicated carotid endarterectomy: tract-based spatial statistics analysis.** *Neurosurgery* 2013;73:592–98; discussion 598–99 CrossRef Medline
34. Zhou W, Hitchner E, Gillis K, et al. **Prospective neurocognitive evaluation of patients undergoing carotid interventions.** *J Vasc Surg* 2012;56:1571–78 CrossRef Medline
35. Kahilogullari G, Comert A, Ozdemir M, et al. **Arterial vascularization patterns of the splenium: an anatomical study.** *Clin Anat* 2013; 26:675–81 CrossRef Medline
36. Vann SD, Aggleton JP, Maguire EA. **What does the retrosplenial cortex do?** *Nat Rev Neurosci* 2009;10:792–802 CrossRef Medline
37. Wang L, Laviolette P, O'Keefe K, et al. **Intrinsic connectivity between the hippocampus and posteromedial cortex predicts memory performance in cognitively intact older individuals.** *Neuroimage* 2010; 51:910–17 CrossRef Medline
38. Kim JH, Park KY, Seo SW, et al. **Reversible verbal and visual memory deficits after left retrosplenial infarction.** *J Clin Neurol* 2007;3:62–66 CrossRef Medline
39. Jeong SH, Lee JH, Lee AY. **Reversible visual memory in transient splenial lesion.** *Neurology* 2009;73:647 CrossRef Medline
40. Schaaf M, Mommertz G, Ludolph A, et al. **Functional MR imaging in patients with carotid artery stenosis before and after revascularization.** *AJNR Am J Neuroradiol* 2010;31:1791–98 CrossRef Medline
41. Saito H, Ogasawara K, Nishimoto H, et al. **Postoperative changes in cerebral metabolites associated with cognitive improvement and impairment after carotid endarterectomy: a 3T proton MR spectroscopy study.** *AJNR Am J Neuroradiol* 2013;34:976–82 CrossRef Medline
42. Kim GE, Lee JH, Cho YP. **Can carotid endarterectomy improve metabolic status in patients with asymptomatic internal carotid artery flow lesion? Studies with localized in vivo proton magnetic resonance spectroscopy.** *J Vasc Surg* 2002;36:559–64 CrossRef Medline

# Clinical Significance of the Champagne Bottle Neck Sign in the Extracranial Carotid Arteries of Patients with Moyamoya Disease

C. Yasuda, S. Arakawa, T. Shimogawa, Y. Kanazawa, T. Sayama, S. Haga, and T. Morioka

## ABSTRACT

**BACKGROUND AND PURPOSE:** The champagne bottle neck sign represents a rapid reduction in the extracranial ICA diameters and is a characteristic feature of Moyamoya disease. However, the clinical significance of the champagne bottle neck sign is unclear. We investigated the relationship between the champagne bottle neck sign and the clinical and hemodynamic stages of Moyamoya disease.

**MATERIALS AND METHODS:** We analyzed 14 patients with Moyamoya disease before revascularization (5 men, 9 women; age, 43.2 ± 19.3 years). The ratio of the extracranial ICA and common carotid artery diameters was determined using carotid ultrasonography or cerebral angiography; a ratio of < 0.5 was considered champagne bottle neck sign–positive. The clinical disease stage was determined using the Suzuki angiographic grading system. CBF and cerebral vasoreactivity also were measured.

**RESULTS:** The ICA/common carotid artery ratio (expressed as median [interquartile range]) decreased as the clinical stage advanced (stages I–II, 0.71 [0.60–0.77]; stages III–IV, 0.49 [0.45–0.57]; stages V–VI, 0.38 [0.34–0.47]; $P < .001$). Lower ICA/common carotid artery ratio tended to occur in symptomatic versus asymptomatic arteries (0.47 [0.40–0.53] versus 0.57 [0.40–0.66], respectively; $P = .06$). Although the ICA/common carotid artery ratio was not related to cerebral perfusion, it decreased as cerebral vasoreactivity decreased ($P < .01$). All champagne bottle neck sign–positive arteries were classified as Suzuki stage ≥III, 73% were symptomatic, and 89% exhibited reduced cerebral vasoreactivity. In contrast, all champagne bottle neck sign–negative arteries were Suzuki stage ≤III, 67% were asymptomatic, and all showed preserved cerebral vasoreactivity.

**CONCLUSIONS:** The champagne bottle neck sign was related to advanced clinical stage, clinical symptoms, and impaired cerebral vasoreactivity. Thus, detection of the champagne bottle neck sign might be useful in determining the clinical and hemodynamic stages of Moyamoya disease.

**ABBREVIATIONS:** CBNS = champagne bottle neck sign; CCA = common carotid artery; CVR = cerebral vasoreactivity; MMD = Moyamoya disease

Moyamoya disease (MMD) is a cerebrovascular disorder characterized by progressive bilateral stenosis or occlusion of the distal portion of the ICA and the proximal portion of the MCAs and anterior cerebral arteries. Affected patients also have an abnormal vascular network (Moyamoya vessels) at the base of the brain. The vascular stenosis extends to the extracranial ICA as the disease advances.[1] In 1997, Yang et al[2] used angiography to demonstrate stenotic lesions of the extracranial ICA in 60% of patients with MMD. In 2006, Yasaka et al[3] reported that carotid ultrasonography showed rapid reduction of the diameter at the proximal portion of the ICA, revealing the appearance of a champagne bottle neck in a patient with MMD. The champagne bottle neck sign (CBNS), which is easily detected noninvasively via carotid ultrasonography, is an important morphologic feature of the extracranial ICA of patients with MMD.[3–5] Although the CBNS is reportedly present in 74% of patients with MMD,[3] the time at which the CBNS begins to appear during the course of MMD is unclear. In addition, whether the CBNS is related to the clinical or hemodynamic stage of MMD is unknown. Therefore, we investigated the relationship between the appearance of the CBNS and the clinical stage, presence of clinical symptoms, and hemodynamic stage in patients with MMD.

Received December 16, 2015; accepted after revision March 18, 2016.

From the Departments of Cerebrovascular Disease (C.Y., S.A., Y.K.) and Neurosurgery (T.Shimogawa, T.Sayama, S.H., T.M.), Japan Labour Health and Welfare Organization, Kyushu Rosai Hospital, Kitakyushu, Japan.

Authors' contributions: Literature search, figures, study design, data collection, data analysis, data interpretation, writing (C.Y.); literature search, study design, data analysis, data interpretation, writing (S.A.); data interpretation (T.Shimogawa, T.Sayama, S.H.); literature search, data interpretation (Y.K.); study design, data interpretation, writing (T.M.).

Please address correspondence to Chiharu Yasuda, MD, Department of Neurology, University of Occupational and Environmental Health of Japan, Wakamatsu Hospital, 1-17-1 Hamamachi Wakamatsu-ku, Kitakyushu 808-0024, Japan; e-mail: akaike_komachi@yahoo.co.jp

http://dx.doi.org/10.3174/ajnr.A4815

## MATERIALS AND METHODS

### Patients

We retrospectively evaluated 24 patients newly diagnosed with MMD according to the guidelines proposed by the Ministry of Health, Labour and Welfare of Japan[6] at our hospital from April 2007 to October 2012. The inclusion criteria were evaluation of the patient before revascularization, evaluation of the extracranial ICA via carotid ultrasonography or DSA, and determination of the severity of MMD via DSA. These criteria excluded 10 patients because DSA was not performed ($n = 5$) or extracranial ICA data were not available ($n = 5$). Therefore, 14 patients with 27 affected arteries were enrolled (bilateral MMD: 13 patients; unilateral MMD: 1 patient). This study was approved by our institutional review committee.

### Evaluation of the Extracranial ICA

The ratio of the ICA diameter (below the mandibular bone) to the common carotid artery (CCA) diameter (proximal aspect to bulbus) was measured via carotid ultrasonography. Arteries with a ratio of $< 0.5$ were defined as CBNS-positive.[3] In 7 arteries, the extracranial ICA diameter could not be adequately estimated via carotid ultrasonography because of the high position of the carotid bifurcation. Therefore, the DSA findings were used to obtain the ICA/CCA ratio in these arteries. Evaluation of this sign was based on visual inspection by 2 experienced neuroradiologists in our hospital who were blinded to the clinical and imaging data. No differences in the radiologists' interpretations were noted on independent assessments.

### Clinical Stage

The clinical stage of MMD was determined according to the Suzuki angiographic grading system[1] as follows: In stage I, the carotid fork is narrowed with no other abnormalities. In stage II, the intracerebral main arteries are dilated because of stenosis at the terminal portion of the ICA. In stage III, the MCAs and anterior cerebral arteries are narrowed, and the basal Moyamoya is intensified. In stage IV, the occlusion of the ICA extends to the junction of the posterior communicating artery, resulting in enlargement of the intraorbital Moyamoya vessels and collateral vessels from the external carotid artery. In stage V, the basal Moyamoya vessels shrink, and the MCAs and anterior cerebral arteries disappear; occlusion of the ICA extends as far as C2 or above C3. In stage VI, the siphon of the ICA completely disappears.

### Clinical Symptoms

Clinical symptoms at diagnosis were investigated. The ICA that was responsible for symptoms was defined as symptomatic, and the contralateral side of the ICA was defined as asymptomatic. In incidentally diagnosed cases, the bilateral ICAs were defined as asymptomatic.

### SPECT

CBF and cerebral vasoreactivity (CVR) to acetazolamide in the MCA territory were measured by SPECT.[7-9] In this study, 6 patients (12 arteries) who underwent semiquantitative SPECT with iodine 123 *N*-isopropyl-p-iodoamphetamine were included to evaluate the relationship between the appearance of the CBNS and impairment of cerebral hemodynamics. CBF was semiquantitatively measured before and 15 minutes after intravenous injection of 10 mg/kg acetazolamide on separate days, with an interval of 2–3 days. ROIs were placed automatically on the bilateral MCA territories with commercially available software (GMS7700R, E.CAM Signature; Toshiba Medical Systems, Tokyo, Japan). The CBF in the MCA territory was obtained, excluding ischemic or hemorrhagic lesions. The CVR to acetazolamide was calculated as follows:

$$\mathrm{CVR} = 100 \times (\mathrm{CBF}_{\mathrm{ACZ}} - \mathrm{CBF}_{\mathrm{rest}})/\mathrm{CBF}_{\mathrm{rest}},$$

where CVR is expressed as a percentage and $\mathrm{CBF}_{\mathrm{rest}}$ and $\mathrm{CBF}_{\mathrm{ACZ}}$ represent CBF before and after intravenous injection of acetazolamide, respectively. CVR of <20% was defined as reduced CVR.[8,9]

**Patient characteristics**

| Characteristic | |
|---|---|
| Patients (no.) | 14 |
| Age (mean ± SD, range) (y) | 43.2 ± 19.3, 6–71 |
| Sex (no.) | |
| Male | 5 |
| Female | 9 |
| Clinical diagnoses at onset (no.) | |
| Hemorrhagic stroke | 4 |
| Ischemic stroke | 5 |
| Transient ischemic attack | 4 |
| Asymptomatic | 1 |
| Arteries (no.) | 27 |
| Suzuki grades (no. of arteries) | |
| Stage I | 3 |
| Stage II | 2 |
| Stage III | 12 |
| Stage IV | 4 |
| Stage V | 3 |
| Stage VI | 3 |
| Evaluation of ICA/CCA ratio (no. of arteries) | |
| Ultrasonography | 20 |
| DSA | 7 |
| CBNS (no. of arteries) | |
| Positive | 15 |
| Negative | 12 |

### Data Analysis

The relationships between the ICA/CCA ratio (ie, the CBNS) and Suzuki grade, the presence of clinical symptoms, and impairment of cerebral hemodynamics were investigated. Data are expressed as median (interquartile range). Differences in the ICA/CCA ratio among clinical stages and between symptomatic and asymptomatic arteries were examined by the Kruskal-Wallis test followed by the Bonferroni multiple comparison and the Mann-Whitney *U* test, respectively. Correlation of the ICA/CCA ratio and CVR were evaluated by using the Pearson correlation coefficient. The level of statistical significance was set at $P < .05$. All analyses were performed with JMP 10 software (SAS Institute, Cary, North Carolina).

## RESULTS

We analyzed 27 arteries of 14 patients (5 men, 9 women [mean age, 43.2 ± 19.3 years; age range, 6–71 years]). Their clinical

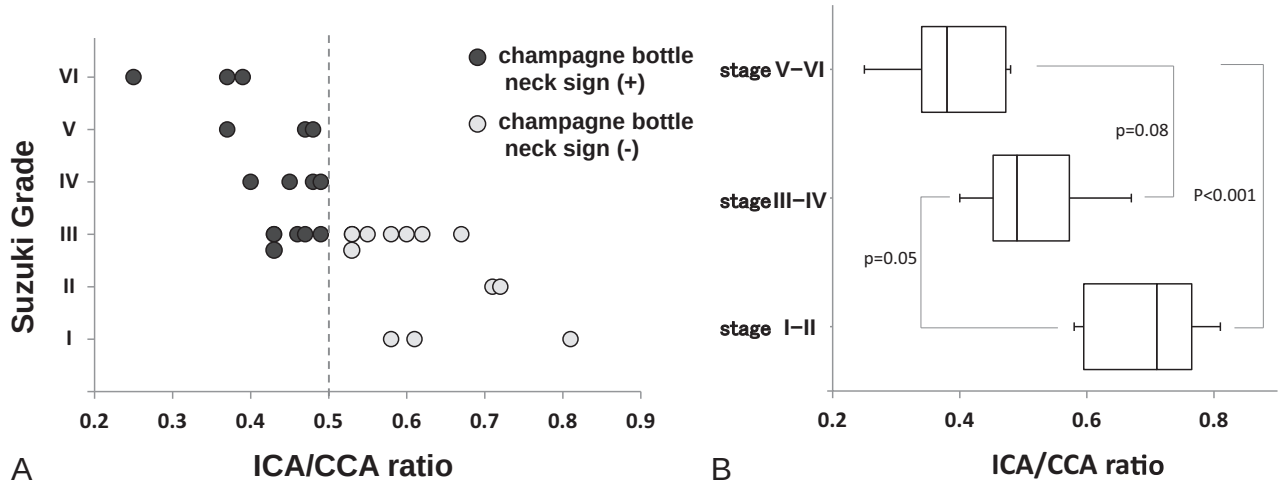


**FIG 1.** Relationship between the ICA/CCA ratio and the clinical stage (Suzuki stage, I–VI [early–advanced]). *A*, The ICA/CCA ratio decreased as the clinical stage advanced, and the CBNS was observed in stage III or higher. *B*, The median ICA/CCA ratio, expressed as median (interquartile range) was 0.71 (0.60–0.77) in stages I and II, 0.49 (0.45–0.57) in stages III and IV, and 0.38 (0.34–0.47) in stages V and VI ($P < .001$). The ICA/CCA ratio was significantly lower in stages V and VI than in stages I and II.

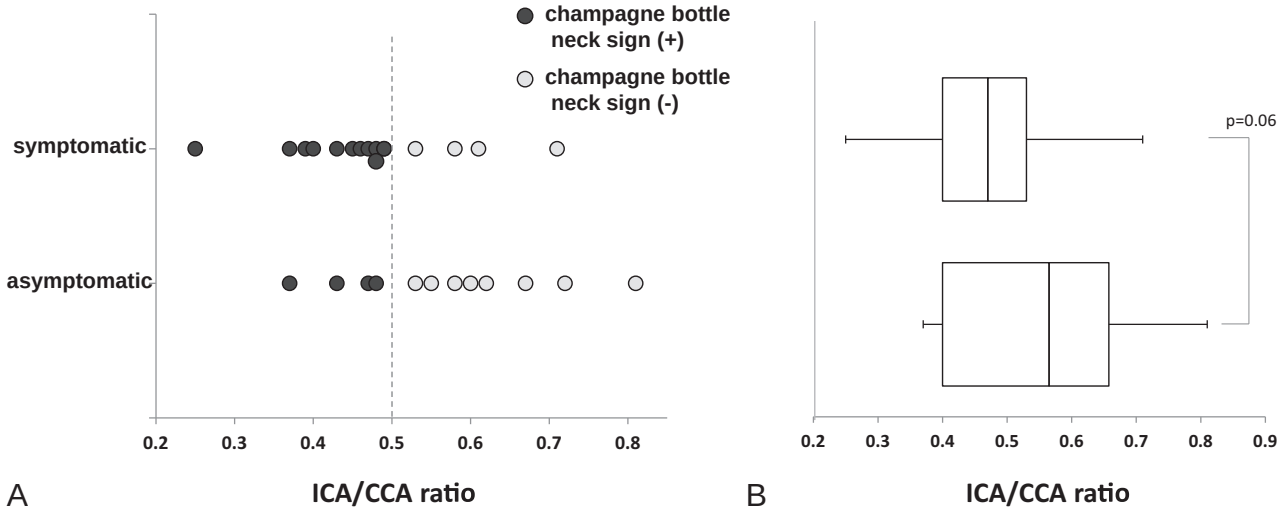


**FIG 2.** Relationships between the ICA/CCA ratio and clinical symptoms. *A*, Symptomatic arteries were more frequently observed in the CBNS-positive group than in the CBNS-negative group (73% versus 33%, respectively; Fisher exact test, $P = .06$). *B*, The median ICA/CCA ratio in symptomatic arteries tended to be lower than that in asymptomatic arteries (0.47 [interquartile range: 0.40–0.53] versus 0.57 [0.47–0.66], respectively; $P = .06$).

diagnoses at onset included hemorrhagic stroke ($n = 4$), ischemic stroke ($n = 5$), and transient ischemic attack ($n = 4$). The remaining patient was asymptomatic. Suzuki grades were stage I in 3 arteries, stage II in 2 arteries, stage III in 12 arteries, stage IV in 4 arteries, stage V in 3 arteries, and stage VI in 3 arteries. The ICA/CCA ratio was obtained by carotid ultrasonography in 20 of 27 arteries and DSA in the remaining 7 arteries. We found CBNS positivity in 15 of the 27 arteries (56%) (Table).

The ICA/CCA ratio decreased as the clinical stage advanced (Fig 1*A*). No CBNS was observed in stages I or II, although the CBNS was observed in 5 of 12 stage III arteries (42%) and in all stage IV–VI arteries. The median ICA/CCA ratio was 0.71 (0.60–0.77) in stages I and II, 0.49 (0.45–0.57) in stages III and IV, and 0.38 (0.34–0.47) in stages V and VI ($P < .001$) (Fig 1*B*). With respect to the relationships between the ICA/CCA ratio and clinical symptoms, symptomatic arteries were more frequently observed in the CBNS-positive group (Fig 2*A*). Of 15 CBNS-positive arteries, 11 (73%) were symptomatic (ischemic stroke [$n = 5$], transient ischemic attack [$n = 4$], intracerebral hemorrhage [$n = 1$], and subarachnoid hemorrhage [$n = 1$]) and 4 (27%) were asymptomatic. However, of 12 CBNS-negative arteries, 4 (33%) were symptomatic (ischemic stroke [$n = 1$], transient ischemic attack [$n = 1$], and intracerebral hemorrhage [$n = 2$]) and 8 (67%) were asymptomatic. The ICA/CCA ratio tended to be lower in symptomatic arteries than in asymptomatic arteries (0.47 [0.40–0.53] versus 0.57 [0.47–0.66], respectively; $P = .06$) (Fig 2*B*).

In the 6 patients (12 arteries) who underwent semiquantitative SPECT with iodine 123 *N*-isopropyl-p-iodoamphetamine, the ICA/CCA ratio was not related to cerebral perfusion at rest in the MCA territory. However, the CVR in the MCA territory decreased as the ICA/CCA ratio decreased ($R = 0.80$, $P < .01$) (Fig 3). Of 9

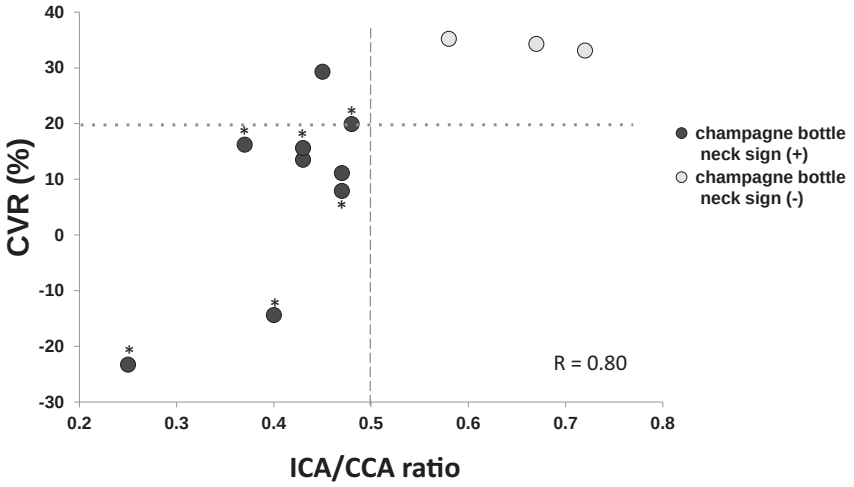


**FIG 3.** Relationship between the ICA/CCA ratio and CVR to acetazolamide in the MCA territory. The CVR decreased as the ICA/CCA ratio decreased ($R = 0.80$, $P < .01$). Of 9 arteries with a CBNS, 8 (89%) exhibited a reduced CVR. Symptomatic arteries exhibited both the CBNS and a reduced CVR. *Asterisk* indicates symptomatic arteries.

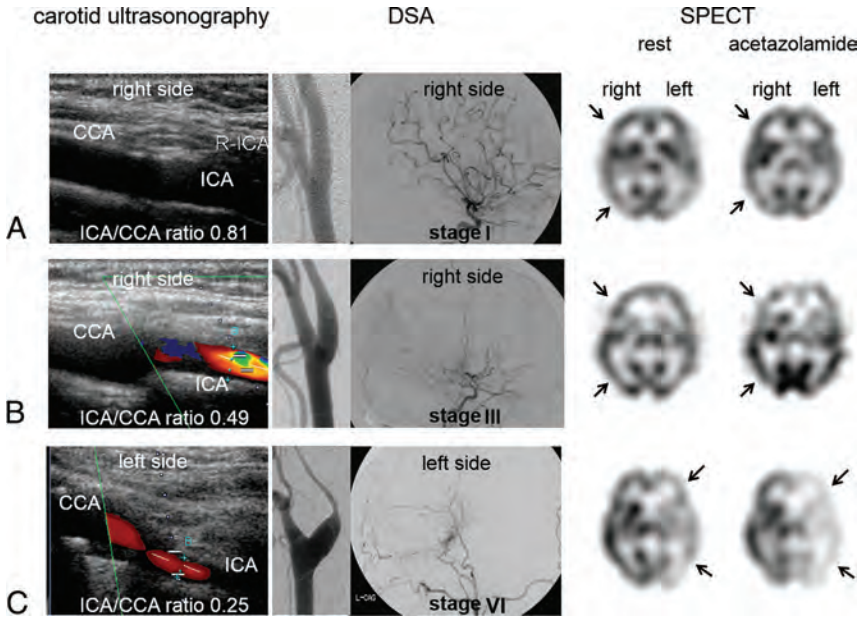


**FIG 4.** Representative cases. The left, middle, and right columns show the features of carotid ultrasonography, a lateral view of DSA of the carotid and intracranial arteries, and an axial SPECT image from 3 cases: *A*, A 15-year-old girl had a Suzuki stage I artery on the right (asymptomatic) and a stage II artery on the left (symptomatic). The CBNS was negative on the right by carotid ultrasonography and DSA, with preserved CVR (*arrows*). *B*, A 37-year-old woman had a stage III artery on the right (symptomatic) and a stage IV artery on the left (asymptomatic). The CBNS was positive on the right, with a mildly decreased CVR (*arrows*). *C*, A 58-year-old woman had a stage II artery on the right (asymptomatic) and a stage VI artery on the left (symptomatic). The CBNS was positive on the left, with a markedly decreased CVR (*arrows*).

arteries with a CBNS, 8 (89%) exhibited a reduced CVR. On the other hand, all 3 arteries without a CBNS exhibited a preserved CVR. We observed both the CBNS and a reduced CVR in 6 symptomatic arteries. Of the remaining 6 asymptomatic arteries, only 2 showed both the CBNS and a reduced CVR. Representative cases are shown in Fig 4.

## DISCUSSION

Histopathologic examination of tissue specimens from patients with MMD reveals eccentrically laminated thickening of the intracranial major cerebral arteries.[10] This fibrocellular intimal thickening extends to the extracranial ICA as the disease advances[1]; it is also observed in other arteries, such as the pulmonary, renal, and coronary arteries.[11-13] At the carotid bifurcation, there is a transitional zone between the elastic (>5 mm proximal to the bifurcation) and muscular (>15 mm distal to the bifurcation) portions of the carotid arteries, and the elastic arteries typically have thicker walls (1–2 mm) to tolerate the increased pressure.[14,15] Therefore, the muscular portion is thought to be more commonly affected, and the narrowing at the transitional zone results in formation of the CBNS.[5]

No systematic studies on the relationship between the presence of the CBNS and the angiographic Suzuki grade have been performed. However, Yasuda et al[4] reported that the CBNS might be observed in advanced cases. Our study clearly demonstrated that the CBNS was not observed in the early stage; it began to appear in Suzuki stage III, and all higher Suzuki stages showed the CBNS. The relationships between the CBNS and the presence of clinical symptoms or cerebral hemodynamics also have not been reported. In our study, CBNS-positive arteries were more likely to be symptomatic than CBNS-negative arteries. These findings support the concept that a cerebral hemodynamic state with a reduced CVR is responsible for the occurrence and recurrence of stroke.[16,17] Previous reports regarding the cerebral hemodynamics of patients with MMD have indicated that cerebral perfusion at rest is not significantly different among the various clinical stages. This is because the blood supply through collateral pathways can compensate for the reduced CBF, even with advancement of the disease.[1,18] However, CVR tends to diminish as MMD progresses.[18] We also found that the CBNS was related to impaired CVR, though not to cerebral perfusion. Our results indicate that the risk of stroke can be predicted by the presence of the CBNS.

Although MR imaging is a useful technique with which to evaluate MMD, the extracranial ICAs, unlike the intracranial ICAs, are not always investigated by MRA. An advantage of carotid ultrasonography is that it enables direct evaluation of the extracranial ICAs in real time. Furthermore, it can be noninvasively and repeatedly performed on an outpatient basis or at the

bedside. Because of the increasing number of elderly patients with MMD,[19] differential diagnosis between MMD and atherosclerotic occlusive cerebrovascular disease is becoming more important. Although advantages of high-resolution MR wall imaging for the differential diagnosis between MMD and atherosclerosis have been reported,[20] ultrasonography would be helpful to differentiate these 2 diseases with respect to the morphologically different features of their vessel walls. Especially in young children, sedation is sometimes necessary to perform MR imaging, but not carotid ultrasonography. Therefore, we believe that carotid ultrasonography is useful for screening of MMD and estimation of the clinical stages of MMD. Notably, however, the CBNS is not observed in the early stages of MMD and can also be seen in other diseases such as dissection, fibromuscular dysplasia, and intracranial ICA occlusion of other causes.

This study had some limitations. First, the number of patients was relatively small because we included patients with MMD who underwent DSA. The prevalence of MMD in the general population is low. Furthermore, MMD has recently tended to be more frequently diagnosed by MR imaging or MRA rather than DSA. Second, the arteries of patients with lower Suzuki grades were relatively small. This may suggest bias in the selection process, leading to over-representation of higher Suzuki grades and inflation of the significance of a positive CBNS. Third, a quarter of arteries were evaluated by DSA instead of carotid ultrasonography because of the high position of the carotid bifurcation. However, in the remaining arteries, the ICA/CCA ratio obtained by carotid ultrasonography and that obtained by DSA were not different; therefore, we do not believe that the results were affected.

## CONCLUSIONS

The CBNS is related to Suzuki stage III or higher and impaired CVR with clinical symptoms in patients with MMD. Detection of the CBNS via carotid ultrasonography is useful for not only screening of MMD, but also for determining the clinical and hemodynamic stages of MMD.


## ACKNOWLEDGMENTS

The authors thank the staff of the Departments of Cerebrovascular Disease and Neurosurgery, Japan Labour Health and Welfare Organization, Kyushu Rosai Hospital, Kitakyushu, Japan.

Disclosures: Shuji Arakawa—*UNRELATED: Payment for Lectures (including service on Speakers Bureaus)*: Kyushu Nutrition Welfare University, *Comments*: Gave lectures on stroke.


## REFERENCES


1. Suzuki J, Takaku A. **Cerebrovascular "Moyamoya" disease. Disease showing abnormal net-like vessels in base of brain.** *Arch Neurol* 1969;20:288–99 CrossRef Medline
2. Yang SH, Li B, Wang CC, et al. **Angiographic study of Moyamoya disease and histological study in the external carotid artery system.** *Clin Neurol Neurosurg* 1997;99:S61–63 CrossRef Medline
3. Yasaka M, Ogata T, Yasumori K, et al. **Bottle neck sign of the proximal portion of the internal carotid artery in Moyamoya disease.** *J Ultrasound Med* 2006;25:1547–52 Medline
4. Yasuda C, Yakusiji Y, Eriguchi M, et al. **Usefulness of carotid ultrasonography for the early detection of Moyamoya disease** [in Japanese]. *Rinsho Shinkeigaku* 2007;47:441–43 Medline
5. Shimogawa T, Morioka T, Sayama T, et al. **Champagne bottle neck sign in a patient with Moyamoya syndrome.** *World J Clin Cases* 2014; 2:474–77 CrossRef Medline
6. Fukui M. **Guidelines for the diagnosis and treatment of spontaneous occlusion of the circle of Willis ('Moyamoya' disease). Research Committee on Spontaneous Occlusion of the Circle of Willis (Moyamoya Disease) of the Ministry of Health and Welfare, Japan.** *Clin Neurol Neurosurg* 1997;99:S238–40 CrossRef Medline
7. Nakagawara J, Takeda R, Suematsu K, et al. **Quantification of regional cerebral blood flow and vascular reserve in childhood Moyamoya disease using [123I]IMP-ARG method.** *Clin Neurol Neurosurg* 1997;99:S96–99 CrossRef Medline
8. Saito N, Nakagawara J, Nakamura H, et al. **Assessment of cerebral hemodynamics in childhood Moyamoya disease using a quantitative and a semiquantitative IMP-SPECT study.** *Ann Nucl Med* 2004; 18:323–31 CrossRef Medline
9. Honda M, Ezaki Y, Kitagawa N, et al. **Quantification of the regional cerebral blood flow and vascular reserve in Moyamoya disease using split-dose iodoamphetamine I 123 single-photon emission computed tomography.** *Surg Neurol* 2006;66:155–59; discussion 159 CrossRef Medline
10. Fukui M, Kono S, Sueishi K, et al. **Moyamoya disease.** *Neuropathology* 2000;20:S61–64 Medline
11. Ikeda E. **Systemic vascular changes in spontaneous occlusion of the circle of Willis.** *Stroke* 1991;22:1358–62 CrossRef Medline
12. Kaczorowska M, Jozwiak S, Litwin M, et al. **Moyamoya disease associated with stenosis of extracranial arteries: a case report and review of the literature.** [in Polish] *Neurol Neurochir Pol* 2005;39:242–46 Medline
13. Lee JH, Youn TJ, Yoon YE, et al. **Coronary artery stenosis in Moyamoya disease: tissue characterization by 256-slice multi-detector CT and virtual histology.** *Circulation* 2013;127:2063–65 CrossRef Medline
14. Hori E, Hayashi N, Hamada H, et al. **A development of atheromatous plaque is restricted by characteristic arterial wall structure at the carotid bifurcation.** *Surg Neurol* 2008;69:586–90; discussion 590–91 CrossRef Medline
15. Janzen J, Lanzer P, Rothenberger-Janzen K, et al. **Variable extension of the transitional zone in the medial structure of carotid artery tripod.** *Vasa* 2001;30:101–06 CrossRef Medline
16. Grubb RL, Derdeyn CP, Fritsch SM, et al. **Importance of hemodynamic factors in the prognosis of symptomatic carotid occlusion.** *JAMA* 1998;280:1055–60 CrossRef Medline
17. Yamauchi H, Higashi T, Kagawa S, et al. **Is misery perfusion still a predictor of stroke in symptomatic major cerebral artery disease?** *Brain* 2012;135:2515–26 CrossRef Medline
18. Kang KH, Kim HS, Kim SY. **Quantitative cerebrovascular reserve measured by acetazolamide-challenged dynamic CT perfusion in ischemic adult Moyamoya disease: initial experience with angiographic correlation.** *AJNR Am J Neuroradiol* 2008;29:1487–93 CrossRef Medline
19. Kuriyama S, Kusaka Y, Fujimura M, et al. **Prevalence and clinicoepidemiological features of Moyamoya disease in Japan: findings from a nationwide epidemiological survey.** *Stroke* 2008;39:42–47 CrossRef Medline
20. Ryoo S, Cha J, Kim SJ, et al. **High-resolution magnetic resonance wall imaging findings of Moyamoya disease.** *Stroke* 2014;45: 2457–60 CrossRef Medline

# Blood-Labyrinth Barrier Permeability in Menière Disease and Idiopathic Sudden Sensorineural Hearing Loss: Findings on Delayed Postcontrast 3D-FLAIR MRI

M.N. Pakdaman, G. Ishiyama, A. Ishiyama, K.A. Peng, H.J. Kim, W.B. Pope, and A.R. Sepahdari

## ABSTRACT

**BACKGROUND AND PURPOSE:** Menière disease and idiopathic sudden sensorineural hearing loss can have overlapping clinical presentation and may have similar pathophysiology. Prior studies using postcontrast 3D-FLAIR MR imaging suggest abnormal blood-labyrinth barrier permeability in both conditions, but the 2 diseases have not been directly compared by using the same imaging techniques. We hypothesized that delayed postcontrast 3D-FLAIR MR imaging would show differences in blood-labyrinth barrier permeability between Menière disease and idiopathic sudden sensorineural hearing loss.

**MATERIALS AND METHODS:** Patients with unilateral Menière disease ($n = 32$) and unilateral idiopathic sudden sensorineural hearing loss ($n = 11$) imaged with delayed postcontrast 3D-FLAIR MR imaging were retrospectively studied. Signal intensities of the medulla and perilymph of the cochlear basal turns of both ears in each patient were measured in a blinded fashion. Cochlea/medulla ratios were calculated for each ear as a surrogate for blood-labyrinth barrier permeability. The ears were segregated by clinical diagnosis.

**RESULTS:** Cochlea/medulla ratio was higher in symptomatic ears of patients with Menière disease (12.6 ± 7.4) than in patients with idiopathic sudden sensorineural hearing loss (5.7 ± 2.0) and asymptomatic ears of patients with Menière disease (8.0 ± 3.1), indicating increased blood-labyrinth barrier permeability in Menière disease ears. The differences in cochlea/medulla ratio between symptomatic and asymptomatic ears were significantly higher in Menière disease than in idiopathic sudden sensorineural hearing loss. Asymptomatic ears in patients with Menière disease showed higher cochlea/medulla ratio than symptomatic and asymptomatic ears in patients with idiopathic sudden sensorineural hearing loss.

**CONCLUSIONS:** Increased cochlea/medulla ratio indicates increased blood-labyrinth barrier permeability in Menière disease compared with idiopathic sudden sensorineural hearing loss. Increased cochlea/medulla ratio in asymptomatic ears of patients with Menière disease also suggests an underlying systemic cause of Menière disease and may provide a pathophysiologic biomarker.

**ABBREVIATIONS:** BLB = blood-labyrinth barrier; CM = cochlea/medulla; ISSNHL = idiopathic sudden sensorineural hearing loss; MD = Menière disease

Four-hour delayed intravenous contrast-enhanced inner ear MR imaging is a recently described technique that has been used to image patients with known or suspected Menière disease (MD).[1-4] This technique distinguishes the endolymphatic and perilymphatic compartments of the inner ear by allowing dilute contrast to accumulate within the perilymphatic compartment, where the blood-labyrinth barrier (BLB) is permeable, outlining the impermeable endolymphatic compartment. This allows for demonstration of endolymphatic hydrops, the characteristic pathologic alteration in MD. Nevertheless, 10%–33% of patients with MD do not have MR-demonstrable changes of hydrops.[2,5,6] This clinical-radiologic discrepancy reflects an incomplete understanding of the disease process and limitations of imaging.

Additional imaging biomarkers of disease activity in MD may be helpful beyond visualization of hydrops. One previous study has explored a relationship between increased BLB permeability and MD,[7] finding increased BLB permeability in the symptomatic ears of patients with unilateral MD compared with their asymptomatic ears, which is in keeping with findings from animal studies of hydrops.[8,9] Although BLB permeability in MD is a promising target for further exploration, it is not clear that these findings

Received December 17, 2015; accepted after revision March 26, 2016.

From the Departments of Radiological Sciences (M.N.P., H.J.K., W.B.P., A.R.S.), Neurology (G.I.), and Head and Neck Surgery (A.I., K.A.P.), David Geffen School of Medicine, University of California, Los Angeles, Los Angeles, California.

M.N. Pakdaman and G. Ishiyama contributed equally to this work.

Paper previously presented at: Annual Meeting of the American Society of Head and Neck Radiology, September 10–14, 2014; Seattle, Washington.

Please address correspondence to Ali R Sepahdari, MD, Department of Radiological Sciences, David Geffen School of Medicine, University of California, Los Angeles, 757 Westwood Plaza, Suite 1621D, Los Angeles, CA 90095; e-mail: alisepahdari@gmail.com; @alisepahdari

http://dx.doi.org/10.3174/ajnr.A4822

**Table 1: Patient demographics**

| | ISSNHL | Menière Disease |
|---|---|---|
| Total, *n* | 11 | 32 |
| Female, *n* | 3 | 17 |
| Male, *n* | 8 | 15 |
| Affected ear–AS, *n* | 4 | 14 |
| Affected ear–AD, *n* | 7 | 18 |
| Age (years) | 50.1 | 55.4 |

**Note:**—AS indicates left ear; AD, right ear.

are specific for MD. Similar findings have been seen in patients with idiopathic sudden sensorineural hearing loss (ISSNHL),[10] which can present similarly, and in a series of nonspecific sudden hearing loss.[11]

The purpose of this study is to compare MD with ISSNHL with respect to BLB permeability. Our hypothesis is that increased BLB permeability is a feature more strongly associated with MD than ISSNHL.

## MATERIALS AND METHODS

### *Patients*

Institutional review board approval was obtained for creation of a prospective data base of patients imaged with delayed intravenous contrast-enhanced hydrops-protocol inner ear MR imaging, including a waiver of Health Insurance Portability and Accountability Act authorization and waiver of informed consent. Patients with ISSNHL or MD imaged between November 2012 and September 2013 were included in the study. Patients with bilateral disease and patients with unspecified laterality were excluded. All patients were followed clinically to establish a diagnosis based on the American Academy of Otolaryngology–Head and Neck Surgery criteria for ISSNHL and MD. A total of 84 patients were imaged, including 38 patients with definite MD and 12 with ISSNHL. The remaining patients ($n = 34$) did not have a clinical diagnosis of either condition and were excluded. Of the 50 patients with MD or ISSNHL, 5 patients with MD and 1 patient with ISSNHL were excluded because of bilateral disease or unspecified laterality of disease and 1 patient with MD was excluded because of history of endolymphatic shunt surgery. The final analysis group included 43 patients, 32 with MD (15 male, 17 female) and 11 with ISSNHL (8 male, 3 female), with an average age of 53.6 ± 13.4 years (range, 27–89 years). Demographic data are summarized in Table 1.

### *Imaging Protocol*

Imaging was performed on a 3T Magnetom Skyra unit (Siemens, Erlangen, Germany) by using a 16-channel head and neck coil 4 hours after an intravenous injection of 0.2 mmol/kg gadopentate dimeglumine (Magnevist; Bayer HealthCare Pharmaceuticals, Wayne, New Jersey). Scanning consisted of a "cisternographic" heavily T2-weighted 3D TSE sequence (sampling perfection with application-optimized contrasts by using different flip angle evolutions [T2 SPACE]; Siemens) and a heavily T2-weighted 3D FLAIR sequence. The T2 SPACE sequence was acquired with the following parameters: section thickness, 1 mm; TR/TE, 1430/265 ms; number of averages, 2; echo-train length, 98; flip angle, 140; matrix, 320 × 320; FOV, 200 × 200 mm. The heavily T2-weighted FLAIR sequence was acquired with the following parameters: section thickness, 0.8 mm; TR/TE, 9000/534 ms; inversion time, 2350 ms; number of averages, 2; echo-train length, 144; flip angle, 120; matrix, 320 × 260; FOV, 200 × 167 mm. All sequences were performed as high-resolution axial scans through the inner ear and internal auditory canals. The imaged volume included both inner ears.

The T2 SPACE sequence shows bright signal in both the endolymph and perilymph. The heavily T2-weighted FLAIR sequence shows bright signal only in the perilymphatic space because of diffusion of gadolinium into this compartment. The endolymphatic space remains low in signal on these sequences because of the impermeability of the tight junctions in the membranous labyrinth.

### *Measurement of Perilymph Signal as a Surrogate Marker of BLB Permeability*

Increasing perilymph signal intensity on the heavily T2-weighted FLAIR sequence is related to increased BLB permeability,[12,13] though the exact relationship has not been determined. In an animal model, the injection of lipopolysaccharide induced an increase in permeability as measured by iron oxide particle extravasation, which correlated with increased gadolinium enhancement in the perilymph.[14] Perilymph signal was evaluated quantitatively. A postdoctoral research fellow with 3 years of experience in temporal bone imaging research (M.N.P.) performed all measurements, which were reviewed by a subspecialty-certified diagnostic neuroradiologist (A.R.S.) with 10 years of experience in MR imaging interpretation who interprets all hydrops-protocol MRIs at our institution. A freehand polygonal ROI was set manually in the basal turn of the cochlea on the heavily T2-weighted FLAIR image to include as much of the perilymph as possible, with size of approximately 5 $mm^2$. A 50-$mm^2$ circular ROI in the same plane as the cochlear basal turn was drawn in the medulla. The mean signal intensity was recorded for each ROI. The cochlea/medulla (CM) ratio was defined as the signal intensity of the basal turn divided by that of the medulla. The mean CM ratio of all affected and unaffected ears was calculated for all patients. An example ROI is shown in Fig 1.

### *Evaluation of Hydrops*

Each ear was evaluated for the presence or absence of hydrops by using quantitative criteria. At the time of initial scan acquisition, the images were reconstructed as 3D maximum intensity projections. The neuroradiologist (A.R.S.), who was blind to the diagnosis and side of symptoms, outlined the endolymph and vestibule with freehand ROIs. The endolymph/vestibule ratio was calculated. Endolymph occupying >50% of the vestibule was graded as positive for hydrops, as per the criteria of Sepahdari et al.[2]

### *Statistical Analysis*

Ears were segregated into 4 groups: symptomatic MD ears, asymptomatic ears in patients with MD, symptomatic ISSNHL ears, and asymptomatic ears in patients with ISSNHL. Descriptive statistics of mean and standard deviation were obtained. A least-squares difference method was used to compare groups; ANOVA was performed initially, with subsequent Student *t* test between

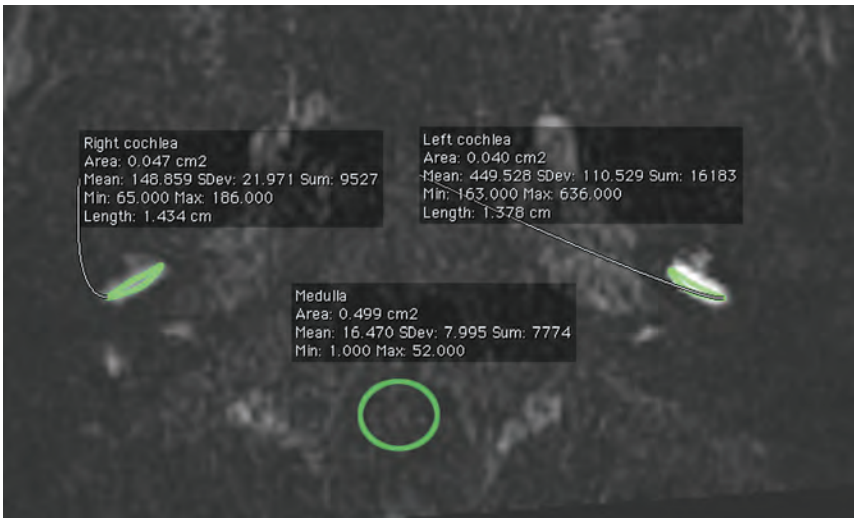


**FIG 1.** 3D-FLAIR MR imaging signal intensity measurements. Measurement of signal intensity was performed by drawing an elliptical ROI at the basal turn of each cochlea and a circular ROI at the medulla. The average intensity of each ROI was used to calculate the CM ratio.

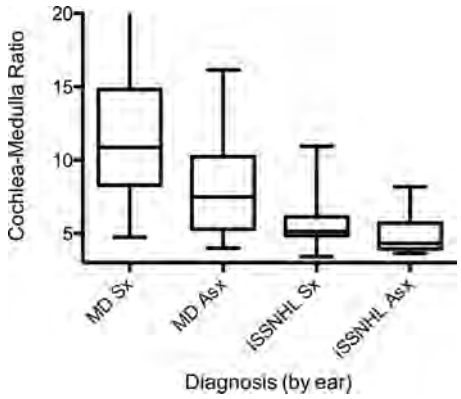


**FIG 2.** CM ratio for all groups. Box plots show median and interquartile ranges, with bars depicting range. Note the significant increase in CM ratio among symptomatic MD ears when compared with all other ears and increased CM ratio in asymptomatic ears of patients with MD.

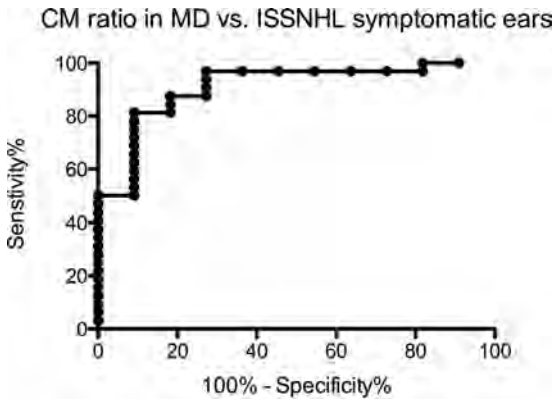


**FIG 3.** Receiver operating characteristic curve for CM ratio, comparing symptomatic MD ears to symptomatic ISSNHL ears. This curve demonstrates high discriminatory power of increased signal for MD. A CM ratio > 7.3 was 81% sensitive and 91% specific for MD.

groups. $P < .05$ was used as the threshold for statistical significance.

A mixed-effect model with a random intercept was used to test the differences in perilymph signal intensity between the affected and nonaffected ear and between the MD and ISSNHL groups after Box-Cox transformation for normality in the intensity. Patients were used as a random effect.

Receiver operating characteristic analysis was used to determine the performance of various CM ratios for identifying MD. For receiver operating characteristic analysis, the asymptomatic ear of patients with ISSNHL was set as a control value. This determination was based on the fact that there are no known or previously proposed MR imaging abnormalities in the asymptomatic ear of patients with ISSNHL.

The signal intensity ratios of symptomatic ears and asymptomatic ears in the same patients were also compared. Finally, the relationship between CM ratio and endolymphatic space dilation was assessed in a descriptive categoric fashion and quantitatively by using Spearman rank order correlation.

## RESULTS

### *CM Ratio in All Ears*

ANOVA showed significant differences across the 4 groups ($F = 10.1$, $P < .0001$). The results are shown graphically in Fig 2. Symptomatic MD ears showed the highest CM ratio (mean and standard deviation of 12.6 ± 7.4), indicative of the highest permeability. This was significantly higher than all other ears, with statistically significant differences compared with asymptomatic ears in patients with MD (8.0 ± 3.1, $P = .0002$), symptomatic ISSNHL ears (5.7 ± 2.0, $P < .0001$), and asymptomatic ears in patients with ISSNHL (5.0 ± 1.5, $P < .0001$). Among the 11 patients with ISSNHL, a paired $t$ test revealed no significant difference between affected and unaffected sides. Receiver operating characteristic analysis for CM ratio demonstrated 0.91 area under the curve in differentiating MD from ISSNHL in the symptomatic ear (Fig 3). A CM ratio > 7.3 was 81% sensitive and 91% specific for MD. Other CM ratios and their associated sensitivities and specificities for MD are provided in Table 2.

Mean intensity of perilymph signal was significantly different between the symptomatic and nonsymptomatic ear ($P < .001$) and between the MD and ISSNHL group ($P < .001$) with 4.99 and 3.57 perilymph signal ratios, respectively. After adding an interaction between MD versus ISSNHL group and symptomatic versus nonsymptomatic in the model, the mean intensity was still significant between the clinical groups (MD versus ISSNHL, $P < .001$) and the interaction ($P = .041$). The mean intensity was 3.9 times higher for the symptomatic ear in the MD group compared with the intensity from all other ears.

### *CM Ratio Asymmetry in MD versus ISSNHL*

Patients with MD showed a greater degree of asymmetry of the affected ear to the unaffected ear compared with patients with

**Table 2: CM ratios and associated performance for diagnosing MD compared with a control group of asymptomatic ears of patients with ISSNHL**

| CM Ratio | Sensitivity | Specificity |
|---|---|---|
| >4.5 | 100% | 55% |
| >5.5 | 91% | 73% |
| >6.5 | 84% | 82% |
| >7.5 | 81% | 91% |
| >8.5 | 75% | 100% |

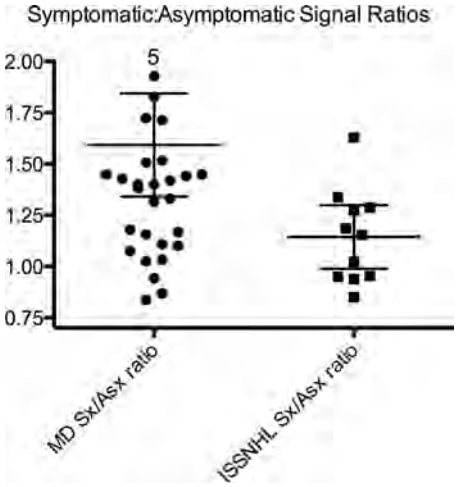


**FIG 4.** Comparison of symptomatic and asymptomatic perilymph signal ratios between MD and ISSNHL. Patients with MD had a significantly greater asymmetry ($P = .03$), though 11 of 32 patients with MD showed virtually no asymmetry. Five patients had greater than double the perilymph signal intensity in the symptomatic ear.

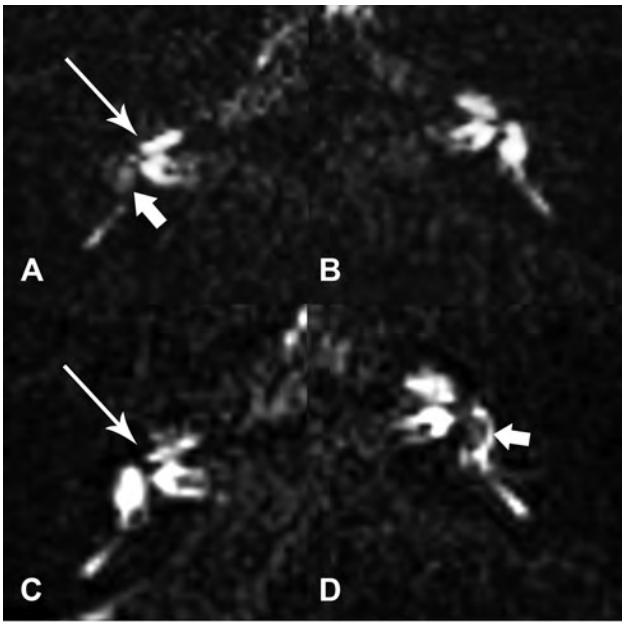


**FIG 5.** Initial and follow-up studies in a patient with unilateral right MD that progressed to bilateral disease. *A* and *B*, Initial MR imaging shows hydrops involving the right vestibule (*short arrow*) and cochlea (*long arrow*). There is increased perilymph signal intensity in both ears, but the left ear (*B*) is asymptomatic and shows no hydrops. The patient underwent right vestibular neurectomy, with improvement in symptoms. *C* and *D*, Follow-up study 18 months after *A* and *B*, performed because of new symptoms of aural fullness in the left ear, shows new hydrops involving the left vestibule (*short arrow*). Hydrops in the right vestibule has improved, though there is persistent hydrops in the right cochlea (*long arrow*).

ISSNHL. The symptomatic/asymptomatic CM ratio was 1.6 ± 0.7 in patients with MD, compared with 1.2 ± 0.2 in patients with ISSNHL ($P = .04$) (Fig 4). Although there was greater asymmetry between symptomatic and asymptomatic ears in MD compared with ISSNHL with respect to CM ratio, the effect was blunted by the often bilateral nature of CM ratio elevation in the setting of MD. As a result, the area under the receiver operating characteristic curve was only 0.75 when comparing MD to ISSNHL based on the degree of symptomatic/asymptomatic CM ratio asymmetry. A symptomatic/asymptomatic ratio of >1.4 was 50% sensitive and 90% specific in differentiating MD from ISSNHL.

### *CM Ratio in Asymptomatic Ears: Comparison of MD and ISSNHL*

For asymptomatic ears, the mean CM ratio was higher in patients with MD than in patients with ISSNHL (8.0 ± 3.1 in patients with MD versus 5.0 ± 1.5 in patients with ISSNHL; $P = .003$) (Fig 2). Elevated CM ratio in both ears was seen in 1 patient with right-sided MD who subsequently developed symptoms in the left ear with confirmatory imaging evidence of hydrops (Fig 5). CM ratio also was higher in asymptomatic MD ears than in symptomatic ISSNHL ears ($P = .02$).

### *Relationship between Hydrops, CM Ratio, and Diagnosis*

Endolymph/vestibule ratio of >50% was present in 22 of 32 patients with MD for a sensitivity of 69%. This finding was 100% specific for symptomatic hydrops (ie, none of the asymptomatic ears in patients with MD and none of the 11 symptomatic or 11 asymptomatic ears in patients with a clinical diagnosis of ISSNHL showed hydrops). Of the 10 patients with a clinical diagnosis of MD but no MR evidence of hydrops, 5 had CM ratio > 10.8 in the symptomatic ear, which was greater than the maximum CM ratio of the ISSNHL group. There was no relationship between the CM ratio and the degree of hydrops as measured quantitatively from 3D maximum intensity projections (Spearman $r = 0.08$, $P = .71$).

## DISCUSSION

Increased postcontrast signal intensity in the cochlear basal turn has been shown to reflect BLB breakdown with associated increased contrast permeability.[15,16] This permeability increase has been identified in patients with MD and in patients with ISSNHL,[7,17] but these conditions have not previously been compared with each other in a quantitative manner with respect to this finding. Our results show that increased BLB permeability is a feature that is more clearly associated with MD than with ISSNHL. We also observed increased average permeability of asymptomatic ears of patients with MD compared with asymptomatic ears of patients with ISSNHL. Furthermore, in the subset of patients with MD without MR evidence of hydrops, 50% (5/10) showed markedly increased BLB permeability.

There are several implications of our results. First, these results could improve the ability to confirm a clinical suspicion of MD by using delayed intravenous contrast-enhanced 3D-FLAIR MR imaging. The actual diagnostic performance of this test and its interpretation are incompletely understood. Although some previous studies have reported 90% sensitivity of delayed intravenous con-

trast-enhanced 3D-FLAIR MR imaging for identifying ballooning of the endolymphatic system in the setting of MD,[3,6] those results must be interpreted with caution. These studies did not include a sufficient control group of patients without MD, and they report hydrops in asymptomatic contralateral ears of patients with MD at a frequency of 22%–75%.[3,6] Although it is certainly possible that hydrops may be present in asymptomatic ears of patients with MD, such findings could also reflect a systematic overcalling of hydrops. Our 69% sensitivity for hydrops in clinically involved MD ears is lower than other studies, but we did not observe hydrops in ears that were not clinically involved by MD. This may reflect more stringent criteria for calling hydrops and a lower rate of false-positives. Specifically, we do not identify hydrops if there is not involvement of the vestibule, as we find that evaluation of cochlear hydrops is inconsistent. It is clear that radiologic assessments of hydrops are sometimes discordant from the clinical diagnosis of MD, which itself can be controversial. The addition of imaging information related to increased BLB permeability in these patients could reduce this discrepancy.

A second implication of these results is that increased BLB permeability may be a biomarker of disease status in MD. This does not replace clinical evaluation, but could be complementary to clinical evaluation, particularly when assessing the effectiveness of various treatments. Clinical symptoms in MD are known to fluctuate or even burn out completely, and the clinical course does not always indicate whether an apparent response to treatment truly reflects modification of the disease process versus the natural course of the disease.[18] Further follow-up of patients imaged with hydrops-protocol MR imaging is essential for answering these questions.

The finding of increased BLB permeability in asymptomatic ears of patients with MD also suggests that MD may be a systemic process that involves both ears to some degree. This is supported by clinical data showing that many patients with MD suffer bilateral disease, with onset of symptoms in each ear often occurring at different times.[19] Although the true rate of bilateral involvement by MD is difficult to determine, it is undoubtedly sufficiently high as to eliminate the possibility that MD reflects an entirely random event localized to the inner ear. Anecdotally, we have clinically observed patients with bilateral disease who only have apparent hydrops in 1 ear. The current study was limited to patients with unilateral clinical disease, but future systematic analysis of patients with clinically bilateral disease may further clarify these issues.

Our data show a wide distribution of signal intensities in the asymptomatic ears of patients with MD. In contrast, we observed a tight distribution of signal intensities in asymptomatic ears of patients with ISSNHL. One patient with MD in our cohort showed increased permeability in both the symptomatic ear and asymptomatic contralateral ear and subsequently developed MD symptoms in the contralateral ear with imaging evidence of hydrops on a follow-up study (Fig 5). Although this was just a single case, it suggests that increased signal in the asymptomatic ear could predict progression to bilateral disease. Further follow-up of this cohort would help elucidate the relationship between changes in signal intensity and clinical course. In addition, studies on larger groups of patients would help increase the specificity of the CM ratio in differentiating MD from ISSNHL.

### *Limitations*

The major limitation of this study is that it lacked a control group of asymptomatic healthy patients. The asymptomatic ear was used as an internal control in all cases, but systemic processes may affect BLB permeability in both ears and, therefore, may mask abnormalities in the symptomatic ears. A second limitation was the relatively small number of patients and relatively short follow-up period. We cannot exclude the possibility that some patients with apparent ISSNHL had incipient MD with monosymptomatic onset. This could produce factitious overlap between the MD and ISSNHL groups. Analysis of larger groups of patients, imaging of normal controls, and further clinical follow-up are necessary to confirm our findings and establish their significance. A third limitation is that imaging was obtained at only a single time point without obtaining precontrast 3D-FLAIR sequences or postcontrast sequences at multiple time points. In theory, increased signal on the 4-hour delay postcontrast 3D-FLAIR sequence could reflect a process other than increased permeability. For example, intrinsic precontrast hyperintensity can relate to proteinaceous signal contents, a phenomenon that has been noted in vestibular schwannoma[20,21] and in ISSNHL.[22] However, precontrast FLAIR hyperintensity has not been described in MD. Therefore, we think it is unlikely that the apparent BLB permeability increase in patients with MD in our study was influenced by precontrast asymmetries. Alternatively, increased basal turn perilymph signal could reflect impaired reabsorption of contrast from the inner ear or more inhomogeneous contrast distribution throughout the inner ear rather than excessive permeability. A final limitation is that the precise relationship between perilymph signal intensity and gadolinium concentration by using the heavily T2-weighted FLAIR pulse sequence is not known. It would be helpful to establish the mathematical relationship between perilymph signal and gadolinium concentration for this particular sequence and contrast agent so that the results could be applied to other centers.

## CONCLUSIONS

We found that apparent BLB permeability was higher in MD than ISSNHL. This apparent permeability increase was seen in the absence of hydrops in some patients with clinical diagnoses of definite MD and in the asymptomatic ears of some patients with unilateral MD, suggesting a systemic abnormality in MD. BLB permeability may prove to be a biomarker of MD.

Disclosures: Whitney B. Pope—*UNRELATED*: *Consultancy*: Celldex Therapeutics, Tocagen; *Payment for Lectures (including service on Speakers Bureaus)*: Blue Earth Diagnostics.

## REFERENCES

1. Naganawa S, Nakashima T. **Visualization of endolymphatic hydrops with MR imaging in patients with Ménière's disease and related pathologies: current status of its methods and clinical significance.** *Jpn J Radiol* 2014;32:191–204 CrossRef Medline
2. Sepahdari AR, Ishiyama G, Vorasubin N, et al. **Delayed intravenous contrast-enhanced 3D FLAIR MRI in Meniere's disease: correlation**

**of quantitative measures of endolymphatic hydrops with hearing.** *Clin Imaging* 2015;39:26–31 CrossRef Medline
3. Baráth K, Schuknecht B, Naldi AM, et al. **Detection and grading of endolymphatic hydrops in Menière disease using MR imaging.** *AJNR Am J Neuroradiol* 2014;35:1387–92 CrossRef Medline
4. Sepahdari AR, Vorasubin N, Ishiyama G, et al. **Endolymphatic hydrops reversal following acetazolamide therapy: demonstration with delayed intravenous contrast-enhanced 3D-FLAIR MRI.** *AJNR Am J Neuroradiol* 2016;37:151–54 CrossRef Medline
5. Seo YJ, Kim J, Choi JY, et al. **Visualization of endolymphatic hydrops and correlation with audio-vestibular functional testing in patients with definite Meniere's disease.** *Auris Nasus Larynx* 2013; 40:167–72 CrossRef
6. Pyykkö I, Nakashima T, Yoshida T, et al. **Meniere's disease: a reappraisal supported by a variable latency of symptoms and the MRI visualisation of endolymphatic hydrops.** *BMJ Open* 2013;3:pii: e001555 CrossRef Medline
7. Yamazaki M, Naganawa S, Tagaya M, et al. **Comparison of contrast effect on the cochlear perilymph after intratympanic and intravenous gadolinium injection.** *AJNR Am J Neuroradiol* 2012;33:773–78 CrossRef Medline
8. Marshall AF, Jewells VL, Kranz P, et al. **Magnetic resonance imaging of guinea pig cochlea after vasopressin-induced or surgically induced endolymphatic hydrops.** *Otolaryngol Head Neck Surg* 2010; 142:260–65 CrossRef Medline
9. Ishiyama G, Lopez IA, Sepahdari AR, et al. **Meniere's disease: histopathology, cytochemistry, and imaging.** *Ann N Y Acad Sci* 2015; 1343:49–57 CrossRef Medline
10. Zou J, Poe D, Bjelke B, et al. **Visualization of inner ear disorders with MRI in vivo: from animal models to human application.** *Acta Otolaryngol Suppl* 2009;(560):22–31 CrossRef Medline
11. Tagaya M, Teranishi M, Naganawa S, et al. **3 Tesla magnetic resonance imaging obtained 4 hours after intravenous gadolinium injection in patients with sudden deafness.** *Acta Otolaryngol* 2010;130: 665–69 CrossRef Medline
12. Tagaya M, Yamazaki M, Teranishi M, et al. **Endolymphatic hydrops and blood-labyrinth barrier in Ménière's disease.** *Acta Otolaryngol* 2011;131:474–79 CrossRef Medline
13. Naganawa S, Kawai H, Sone M, et al. **Increased sensitivity to low concentration gadolinium contrast by optimized heavily T2-weighted 3D-FLAIR to visualize endolymphatic space.** *Magn Reson Med Sci* 2010;9:73–80 CrossRef Medline
14. Floc'h JL, Tan W, Telang RS, et al. **Markers of cochlear inflammation using MRI.** *J Magn Reson Imaging* 2014;39:150–61 CrossRef Medline
15. Sugiura M, Naganawa S, Teranishi M, et al. **Three-dimensional fluid-attenuated inversion recovery magnetic resonance imaging findings in patients with sudden sensorineural hearing loss.** *Laryngoscope* 2006;116:1451–54 CrossRef Medline
16. Berrettini S, Seccia V, Fortunato S, et al. **Analysis of the 3-dimensional fluid-attenuated inversion-recovery (3D-FLAIR) sequence in idiopathic sudden sensorineural hearing loss.** *JAMA Otolaryngol Head Neck Surg* 2013;139:456–64 CrossRef Medline
17. Lee HY, Jung SY, Park MS, et al. **Feasibility of three-dimensional fluid-attenuated inversion recovery magnetic resonance imaging as a prognostic factor in patients with sudden hearing loss.** *Eur Arch Otorhinolaryngol* 2012;269:1885–91 CrossRef Medline
18. Hamill TA. **Evaluating treatments for Ménière's disease: controversies surrounding placebo control.** *J Am Acad Audiol* 2006;17:27–37 CrossRef Medline
19. Balkany TJ, Sires B, Arenberg IK. **Bilateral aspects of Meniere's disease: an underestimated clinical entity.** *Otolaryngol Clin North Am* 1980;13:603–09 Medline
20. Miller ME, Mafee MF, Bykowski J, et al. **Hearing preservation and vestibular schwannoma: intracochlear FLAIR signal relates to hearing level.** *Otol Neurotol* 2014;35:348–52 CrossRef Medline
21. Yamazaki M, Naganawa S, Kawai H, et al. **Increased signal intensity of the cochlea on pre- and post-contrast enhanced 3D-FLAIR in patients with vestibular schwannoma.** *Neuroradiology* 2009;51: 855–63 CrossRef Medline
22. Yoshida T, Sugiura M, Naganawa S, et al. **Three-dimensional fluid-attenuated inversion recovery magnetic resonance imaging findings and prognosis in sudden sensorineural hearing loss.** *Laryngoscope* 2008;118:1433–37 CrossRef Medline

# Evaluating Instantaneous Perfusion Responses of Parotid Glands to Gustatory Stimulation Using High-Temporal-Resolution Echo-Planar Diffusion-Weighted Imaging

T.-W. Chiu, Y.-J. Liu, H.-C. Chang, Y.-H. Lee, J.-C. Lee, K. Hsu, C.-W. Wang, J.-M. Yang, H.-H. Hsu, and C.-J. Juan

## ABSTRACT

**BACKGROUND AND PURPOSE:** Parotid glands secrete and empty saliva into the oral cavity rapidly after gustatory stimulation. However, the role of the temporal resolution of DWI in investigating parotid gland function remains uncertain. Our aim was to design a high-temporal-resolution echo-planar DWI pulse sequence and to evaluate the instantaneous MR perfusion responses of the parotid glands to gustatory stimulation.

**MATERIALS AND METHODS:** This prospective study enrolled 21 healthy volunteers (M/F = 2:1; mean age, 45.2 ± 12.9 years). All participants underwent echo-planar DWI (total scan time, 304 seconds; temporal resolution, 4 s/scan) on a 1.5T MR imaging scanner. T2WI ($b$ = 0 s/mm$^2$) and DWI ($b$ = 200 s/mm$^2$) were qualitatively assessed. Signal intensity of the parotid glands on T2WI, DWI, and ADC was quantitatively analyzed. One-way ANOVA with post hoc group comparisons with Bonferroni correction was used for statistical analysis. $P < .05$ was statistically significant.

**RESULTS:** Almost perfect interobserver agreement was achieved ($\kappa \geq 0.656$). The parotid glands had magnetic susceptibility artifacts in 14.3% (3 of 21) of volunteers during swallowing on DWI but were free from perceptible artifacts at the baseline and at the end of scans on all images. Increased ADC and reduced signal intensity of the parotid glands on T2WI and DWI occurred immediately after oral administration of lemon juice. Maximal signal change of ADC (24.8% ± 10.8%) was significantly higher than that of T2WI (−10.1% ± 5.2%, $P < .001$). The recovery ratio of ADC (100.71% ± 42.34%) was also significantly higher than that of T2WI (22.36% ± 15.54%, $P < .001$).

**CONCLUSIONS:** Instantaneous parotid perfusion responses to gustatory stimulation can be quantified by ADC by using high-temporal-resolution echo-planar DWI.

**ABBREVIATIONS:** MSC = maximal signal change; RR = recovery ratio

Quantification of normal salivary gland function is of paramount clinical importance because it is the foundation of accurately evaluating disease-related salivary gland functional impairment. Salivary gland function can be estimated by several methods such as saliva collection,[1] laboratory measurement of the chemical and biochemical components,[2] scintigraphy,[3] single-photon emission CT,[4] and positron-emission tomography.[5] MR imaging is superior to saliva collection and laboratory and biologic studies by providing morphologic and functional information of the parotid glands simultaneously and specifically for individual salivary glands. On the other hand, MR imaging is also superior to scintigraphy, SPECT, and PET because of its high spatial resolution and radiation-free nature.

In recent decades, DWI has been increasingly applied to probe salivary gland function in addition to evaluating tumors,[6-11] connective tissue disorders,[12] Sjögren syndrome,[13,14] and postradiotherapy change[15-19] of the parotid glands. However, 2 mutually opposed trends of parotid apparent diffusion coefficient changes after gustatory stimulation have been observed in different study groups, even in healthy volunteers. While some researchers demonstrated an increase of parotid ADC after gustatory stimulation,[14,16,20-23] others showed a decrease of parotid ADC after this

Received November 16, 2015; accepted after revision April 3, 2016.

From the Departments of Radiology (T.-W.C., C.-W.W., H.-H.H., C.-J.J.) and Dentistry (K.H.), National Defense Medical Center, Taipei, Taiwan; Department of Medicine (T.-W.C.), Taipei Medical University, Taipei, Taiwan; Department of Automatic Control Engineering (Y.-J.L., Y.-H.L.), Feng Chia University, Taichung, Taiwan; Department of Diagnostic Radiology (H.-C.C.), The University of Hong Kong, Hong Kong; Department of Otolaryngology-Head and Neck Surgery (J.-C.L.), Tri-Service General Hospital, National Defense Medical Center, Taipei, Taiwan; Department of Biological Science and Technology (J.-C.L., J.-M.Y.), Institute of Bioinformatics and Systems Biology, National Chiao Tung University, Hsinchu, Taiwan; and Department of Radiology (C.-W.W., H.-H.H., C.-J.J.), Tri-Service General Hospital, Taipei, Taiwan.

Please address correspondence to Chun-Jung Juan, MD, PhD, Section of Radiology, School of Medicine, National Defense Medical Center, Section of Neuroradiology, Department of Radiology, Tri-Service General Hospital, 325, Section 2, Cheng-Kong Rd, Neihu, Taipei, Taiwan, Republic of China; e-mail: peterjuancj@yahoo.com.tw

http://dx.doi.org/10.3174/ajnr.A4852

stimulation.[15,24] Such discrepancy has been partially attributed to the different types and dosages of the stimulators.[16] Nevertheless, the discrepancy of diffusional responses to gustatory stimulation in the aforementioned DWI studies has raised concern for whether the normal salivary gland function has been evaluated appropriately with DWI.

The role of the temporal resolution of DWI, which might potentially influence researchers in interpreting parotid gland function, has not been documented to date, to our knowledge. Via parasympathetic innervation, salivary glands secrete and empty saliva into the oral cavity rapidly after gustatory stimulation. Current DWI studies might have limitations in catching the instantaneous responses of the parotid glands due to insufficient temporal resolution. We hypothesized that the parotid glands respond to the oral administration of lemon juice on the order of seconds. The aim of our study was to design a high-temporal-resolution echo-planar pulse sequence for DWI and to quantify the instantaneous MR perfusion responses of the parotid glands to gustatory stimulation.

## MATERIALS AND METHODS

This prospective study was approved by the institutional review board at Tri-Service General Hospital. Written informed consent was obtained.

### Subjects

This study initially enrolled 22 healthy volunteers who were free from tumor, inflammation, autoimmune disease, operations, and radiation therapy involving any parotid gland. One subject was excluded due to severe imaging distortion related to a fixed metallic dental brace. Finally, 21 healthy volunteers were enrolled, including 14 men and 7 women (mean age, 45.2 ± 12.9 years). Saliva production of each volunteer was quantified 1 hour before DWI by using the Saxon test.[1]

### MR Imaging Protocol

All MR images were performed on a 1.5T whole-body scanner (Signa HDx; GE Healthcare, Milwaukee, Wisconsin) by using an 8NV head and neck array coil. Three-plane orthogonal gradient-echo images were acquired for anatomic localization. Single-shot echo-planar DWI (TR/TE/NEX, 2000/53.3 ms/1) with fat saturation was performed on axial planes with diffusion-probing gradients ($b$=0 and 200 s/mm$^2$) applied on each of 3 orthogonal directions alternatively. We intentionally chose a b-value of 200 s/mm$^2$ for 3 reasons: First, a b-value higher than 200 s/mm$^2$ has been shown to be perfusion-insensitive in ADC measurements.[25,26] Accordingly, choosing a b-value of 200 s/mm$^2$ allows better evaluation of perfusion-sensitive changes of the parotid glands than by using a b-value of 300 s/mm$^2$ or higher. Second, apparent bulk motion artifacts have been demonstrated in dynamic scans on DWI with a high b-value of 1000 s/mm$^2$ in the parotid glands.[27] On the contrary, DWI with a low b-value of 200 s/mm$^2$ has a higher signal-to-noise ratio[28] and is theoretically less susceptible to bulk motion artifacts than with higher b-values. Third, although it has been documented that b-values lower than 200 s/mm$^2$ are critical to obtain perfusion-sensitive information from DWI, there is no consensus on the magnitude of b-values that should be applied.[29] We chose a b-value of 200 s/mm$^2$ rather than 100 s/mm$^2$ to reduce potential contamination of signal loss from the faster flow of small arteries or veins. Other MR imaging parameters included an FOV of 240 × 240 mm, matrix size of 256 × 256, echo-train length of 76, bandwidth of 1953 Hz/pixel, and section thickness of 5 mm. Each DWI examination contained 152 excitations. Each excitation obtained 14 sections covering from the cerebellum to the submandibular glands. The total scan time was 5 minutes 4 seconds.

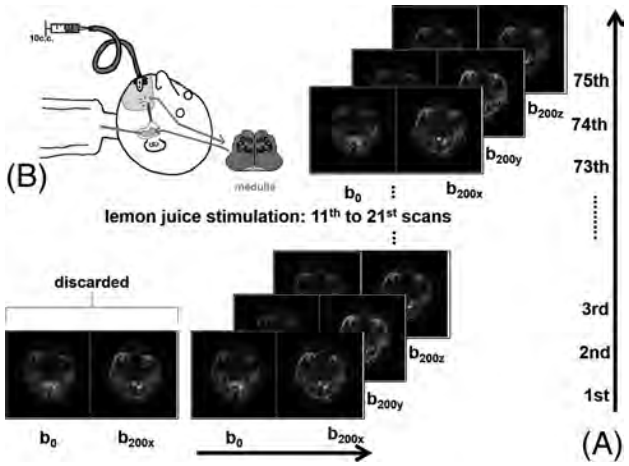


**FIG 1.** Demonstration of data acquisition and arrangement of DWI. *A*, The first 2 images were discarded. T2-weighted images ($b_0$) and diffusion-weighted images ($b_{200}$) were arranged alternatively for 75 dynamic scans. For DWI, diffusion gradients were applied along the x, y, and z axes periodically. *B*, Lemon juice was introduced into the oral cavity via a connecting tube at the 11th scan and swallowed at 21st scan. Figure 1*B* is courtesy of Cheng-Hsuan Juan.

### MR Imaging Acquisition

T2WI ($b$ = 0 s/mm$^2$) and DWI ($b$ = 200 s/mm$^2$) were acquired alternatively. The first 2 excitations were discarded. The direction of the diffusion gradients was changed periodically in the order of the x, y, and z axes, allowing acquisition of a series of T2WI-$DWI_x$-T2WI-$DWI_y$-T2WI-$DWI_z$ scans for the rest of the 150 excitations as illustrated in Fig 1*A*. Accordingly, 75 dynamic scans were used for analysis with each dynamic scan containing a T2WI and a DWI. The temporal resolution was 4 seconds per scan.

### Gustatory Stimulation by Lemon Juice

As shown in Fig 1*B*, 10 mL of commercial lemon juice was administrated via a connecting tube into the oral cavity at the 11th dynamic scan. Each subject was instructed to swallow the lemon juice at the 21st scan. The duration of lemon juice stasis in the oral cavity was 40 seconds.

### Qualitative Assessment of Imaging Quality

All MR imaging data were processed by software developed in-house (T.-W.C., Y.-H.L., and C.-J.J.) by using Matlab (MathWorks, Natick, Massachusetts). Magnetic susceptibility artifacts on T2WI and DWI were qualitatively and independently evaluated by 2 neuroradiologists (C.-J.J. and C.-W.W. with >10 and 3 years' experience in head and neck MR imaging interpretation, respectively) by using a 4-point grading score system (0, severe magnetic susceptibility artifacts: distortion and signal loss that

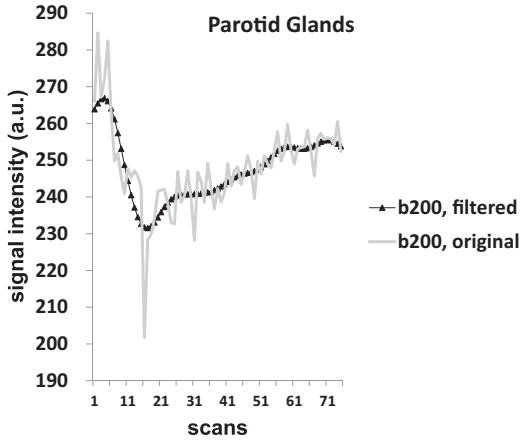


**FIG 2.** Signal intensity–time curves before and after fifth-order Butterworth low-pass filtering on DWI (b200). High-frequency noises (*gray peaks*) are apparently reduced, while the trend of time-series data in response to gustatory stimulation is preserved. a.u. indicates arbitrary unit.

involved the entire image; 1, moderate magnetic susceptibility artifacts: distortion and signal loss involving the parotid glands; 2, mild magnetic susceptibility artifacts: distortion and signal loss involving the oral cavity, nasal cavity, oropharynx, maxillary sinuses, or masticator spaces but sparing the parotid glands; and 3, no magnetic susceptibility artifacts). Qualitative analysis was performed on T2WI and DWI at baseline, during swallowing, and at the end of dynamic scans, respectively.

### *Imaging Processing and Quantitative Data Analysis*

Quantitative analysis was performed on 3 contiguous sections covering the largest areas of the parotid glands, respectively. Polygonal ROIs were drawn within the bilateral parotid glands on the T2WIs, respectively, avoiding the partial volume effects from visible vessels and adjacent tissues. These ROIs were then automatically copied to the DWI for concurrent measurement of signal intensity. Time signal data of T2WI and DWI were treated by a fifth-order Butterworth low-pass filter with a cutoff frequency of 0.025Hz (Fig 2) to eliminate high-frequency noise that occurred during the dynamic scans.

ADC was calculated on the basis of the following equation:

$$1) \qquad ADC = \ln\frac{(S_{200} - S_0)}{-b},$$

where $S_{200}$ and $S_0$ were signal intensities of images with b-values of 200 s/mm$^2$ and 0 s/mm$^2$, respectively. Signal intensity–time curves for T2WI, DWI, and ADC maps were plotted. In addition, signal intensity–time curves were further normalized according to equation 2:

$$2) \qquad SC_n = \frac{(SI_i - SI_0)}{SI_0},$$

where $SC_n$ was the normalized signal change, $SI_i$ was the signal intensity at the ith scan, and $SI_0$ was the baseline signal intensity averaged from the first 9 (first to ninth) scans. Salivary parameters, including maximal signal change (MSC), time to peak, and recovery ratio (RR), were further derived from the normalized signal change–time curves, respectively, to characterize the individual parotid responses to gustatory stimulation. MSC was defined as the maximal normalized signal change, TTP referred to the time interval from the start of dynamic scans to the time of MSC, and RR was calculated according to equation 3:

$$3) \qquad RR = \frac{(MSC - SC_{end})}{MSC},$$

where $SC_{end}$ refers to the normalized signal change averaged from the last 9 (67th to 75th) scans.

**Magnetic susceptibility artifact scores of T2WI and DWI**

| | At the Baseline | | During Swallowing | | At the End | |
|---|---|---|---|---|---|---|
| MSA Score | Rater 1 | Rater 2 | Rater 1 | Rater 2 | Rater 1 | Rater 2 |
| T2WI ($b_0$) | | | | | | |
| 0 | 0 | 0 | 0 | 0 | 0 | 0 |
| 1 | 0 | 1 | 0 | 1 | 0 | 1 |
| 2 | 20 | 19 | 20 | 19 | 20 | 19 |
| 3 | 1 | 1 | 1 | 1 | 1 | 1 |
| DWI ($b_{200}$) | | | | | | |
| 0 | 0 | 0 | 0 | 0 | 0 | 0 |
| 1 | 0 | 0 | 3 | 2 | 0 | 0 |
| 2 | 20 | 20 | 17 | 18 | 20 | 20 |
| 3 | 1 | 1 | 1 | 1 | 1 | 1 |

**Note:**—MSA indicates magnetic susceptibility artifacts.

### *Statistical Analysis*

Statistical analysis was performed by using SPSS software (SPSS 20.0; IBM, Armonk, New York) and MedCalc for Windows (MedCalc Software, Mariakerke, Belgium). Interobserver reliability for imaging distortion was evaluated by linear-weighted $\kappa$ statistics. The normality of baseline signal intensity and salivary parameters was analyzed by Kolmogorov-Smirnov tests. A paired Student *t* test was used for comparisons between the left and right parotid glands. Salivary parameters were analyzed by 1-way ANOVA; and post hoc group comparisons, with a Bonferroni correction. A $P$ value $< .05$ was statistically significant.

## RESULTS

The saliva collected within 2 minutes was 5.78 ± 2.61 g (mean ± standard deviation). Results of qualitative analysis of T2WI and DWI were summarized in the Table. Linear-weighted $\kappa$ analysis revealed substantial agreement between the 2 raters with a $\kappa$ value of 0.656 on all T2WIs and almost perfect agreement, with a $\kappa$ value ranging from 0.842 (during swallowing) to 1 (at baseline and at the end of dynamic scans) on DWI. The parotid glands were free from perceptible artifacts at the baseline or at the end of scans on both T2WI and DWI (Fig 3). However, the parotid glands had magnetic susceptibility artifacts on DWI during swallowing in 14.3% (3 of 21) of volunteers who had metallic dental implants (Fig 4).

The left parotid glands did not differ from the right parotid glands in baseline signal intensity on either T2WI ($P = .148$) or DWI ($P = .227$). Therefore, data of both parotid glands of each subject were averaged to represent each individual in further analysis. Averaged signal intensity–time curves of the parotid glands on T2WI, DWI, and ADC were plotted in Fig 5. On both T2WI and DWI, the signal intensity decreased immediately after oral administration of lemon juice and kept declining during the gustatory stimulation. After swallowing, the signal intensity began to

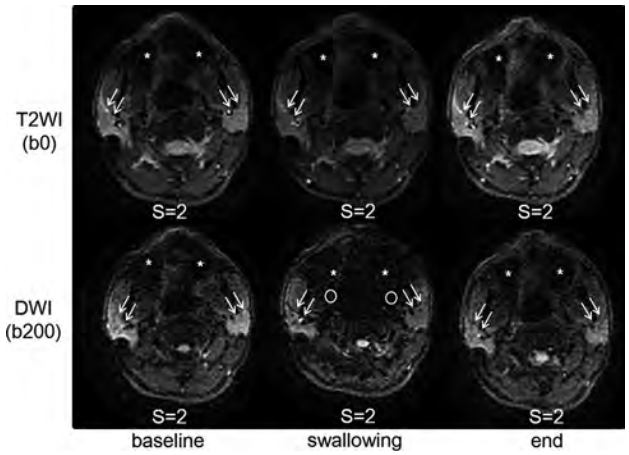


**FIG 3.** Magnetic susceptibility artifacts on T2WI and DWI. Mild distortion and signal loss involving the bilateral maxillary sinuses (*stars*) occur on all T2WI and DWI scans. During swallowing, the parotid glands are still free from artifacts, though more extensive artifacts involve the nasal cavity, oropharynx, and bilateral masticator spaces (*circles*). The anterior margins of the parotid glands are indicated by *arrows*. S indicates magnetic susceptibility artifact score.

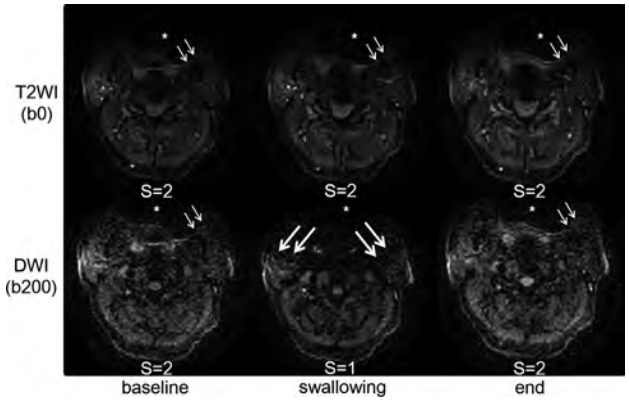


**FIG 4.** Magnetic susceptibility artifacts involving the bilateral masticator spaces and parotid glands (*long arrows*) are observed during swallowing on DWI in a volunteer with metallic dental implants. Artifacts involving the oral cavity (*stars*) and left masticator space (*short arrows*) are evident on all T2WI and DWI. S indicates magnetic susceptibility artifact score.

increase slowly on DWI but further dropped without perceptible recovery on T2WI (Fig 5*A*). On the contrary, the ADC increased abruptly during the lemon juice stimulation, reached the peak at swallowing, and then declined to the baseline level at the end of scans (Fig 5*B*).

Figure 6 demonstrates the normalized signal change–time curves of the parotid glands. The normalized signal change–time curves of the parotid glands on T2WI (Fig 6*A*), DWI (Fig 6*B*), and ADC (Fig 6*C*) revealed trends similar to signal intensity–time curves, respectively. One-way ANOVA showed significant differences in all salivary parameters, including MSC, TTP, and RR among T2WI, DWI, and ADC, respectively (all, $P \leq .001$). The results of post hoc analysis with Bonferroni correction of salivary parameters are described below. The MSC of ADC (24.8% ± 10.8%) was significantly higher than that of T2WI (−10.1% ± 5.2%; $P < .001$) and DWI (−14.2% ± 5.5%; $P < .001$). The MSC of T2WI did not differ from that of DWI ($P = .437$). TTP was significantly higher in T2WI (47.0 ± 17.3 scans) than in DWI (31.0 ± 16.4 scans; $P < .001$) and ADC (21.6 ± 11.1 scans; $P = .004$). There was no difference in TTP between DWI and ADC ($P = .132$). The RR of ADC (100.71% ± 42.34%) was significantly higher than in T2WI (22.36% ± 15.54%; $P < .001$) and DWI (42.3% ±21.7%; $P < .001$). There was no difference in RR between the T2WI and DWI ($P = .143$).

## DISCUSSION

Temporal resolution is an important factor in analyzing immediate responses of the parotid glands to gustatory stimulation. Such immediate responses have not been emphasized in prior research,[14-16,20-24] in which DWI was performed without concurrent gustatory stimulation and the temporal resolution of DWI was rather low, ranging from 74 seconds per scan[21] to 162 seconds per scan.[16] Discrepant observations of parotid responses to the gustatory stimulation in prior research (ie, decreased ADC after gustatory stimulation in some studies[15,24] but increased ADC in others[14,16,20-23]) might be partly affected by the time gap between the gustatory stimulation and the poststimulation DWI and the low temporal resolution of DWI. Both factors limit DWI in detecting the maximal change of parotid ADC after gustatory stimulation.

In this prospective study, we successfully demonstrated the instantaneous responses of the parotid glands to gustatory stimulation by using echo-planar DWI at a high temporal resolution of 4 seconds. The overall signal intensity of the parotid glands on T2WI and DWI was altered at the start of stimulation, as was the parotid ADC. Our results support the hypothesis that the response of the parotid glands to gustatory stimulation occurs in seconds after oral intake of lemon juice.

On T2WI, the rapid reduction of signal intensity of the parotid glands might indirectly reflect an immediate reduction of saliva in the parotid glands after gustatory stimulation. Our result is consistent with the observations of quantitative salivary gland scintigraphic studies with a temporal resolution of 15 seconds per scan.[30] The immediate reduction of parotid radioactivity and accumulation of oral radioactivity following stimulation[30,31] supports saliva being emptied from the parotid glands immediately after the stimulation. After swallowing, the parotid glands showed persistent low signal intensity without recovery in averaged signal intensity–time curves and showed an RR of 22.36%, derived from individual signal intensity–time curves. Our results suggest that the refill of the water component of the parotid gland is a process longer than 3 minutes after removing the stimulator.

Because the signal intensity of vascular flow is attenuated rapidly under low b-values,[32] ADC calculated from low b-values (0 s/mm$^2$ and 200 s/mm$^2$) can be considered perfusion-sensitive in our study. Our study showed a maximal increase of 24.8% in the parotid ADC at 44.6 seconds (TTP = 21.6 scans) after the start of lemon juice stimulation. Such a rapid increase of parotid ADC implies an instantaneous increase of parotid perfusion after gustatory stimulation. The parotid response to gustatory stimulation has been recently investigated by arterial spin-labeling perfusion-weighted MR imaging,[33] showing a mean increase of 62% of parotid blood flow. However, arterial

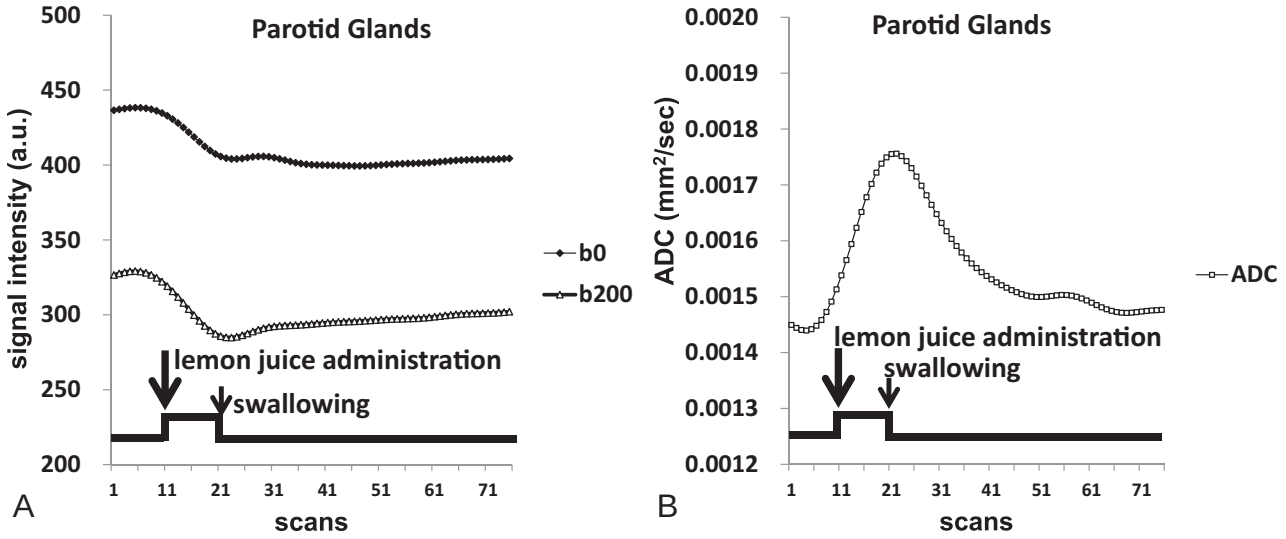


**FIG 5.** Averaged signal intensity–time curves of T2WI (b0) and DWI (b200) (*A*) and ADC time curves of the parotid glands (*B*). Lemon juice is administrated (*long arrow*) at the 11th scan and is swallowed (*short arrow*) at the 21st scan. a.u. indicates arbitrary unit.

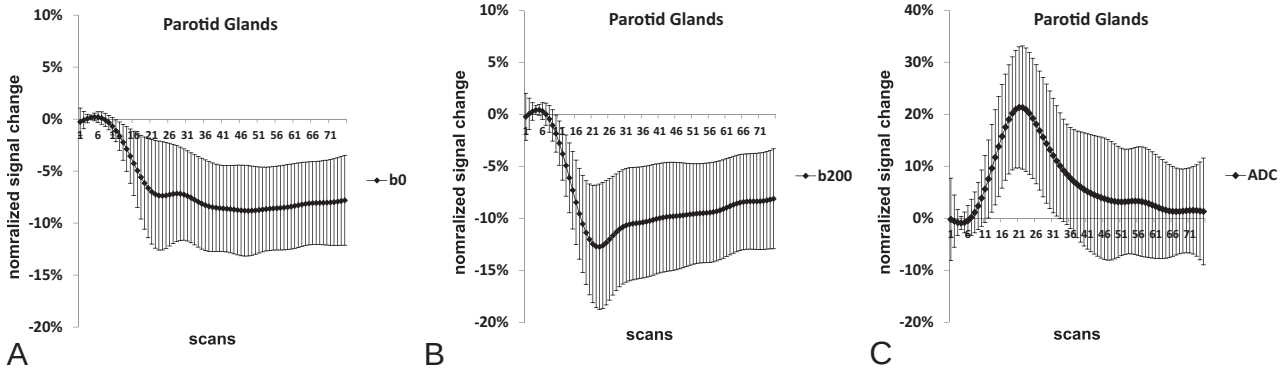


**FIG 6.** Normalized signal change–time curves (mean ± SD) of the parotid glands. During gustatory stimulation, the normalized signal change decreases rapidly on T2WI (*A*) and DWI (*B*), while it increases rapidly on ADC (*C*). After swallowing, the normalized signal change remains stagnant on T2WI, increases slowly on DWI, and reduces rapidly on ADC.

spin-labeling MR imaging is also limited in depicting the instantaneous response of the parotid glands due to its low temporal resolution of 160 seconds per scan.[33] Evaluation of parotid gland function by using blood oxygen level–dependent MR imaging showed an initial drop of signal intensity after gustatory stimulation by using ascorbic acid.[34] In addition to the aforementioned MR imaging techniques, dynamic contrast-enhanced MR imaging has also been applied to evaluate the perfusion change caused by salivary stimulation recently.[35] After swallowing, the parotid glands showed rapid reduction of ADC toward the baseline with an RR of 100% in our study. Our results reflect rapid reduction of parotid perfusion after swallowing lemon juice. The parotid ADC showed significantly higher RR than T2WI ($P < .001$). Our results suggest that the parotid perfusion has returned to the baseline level at the end of the dynamic scans, while the water refill of the parotid glands has not.

Our results also show apparent intersubject variations regarding all salivary parameters, especially after swallowing lemon juice. The intersubject variations might reflect the biologic diversity. If one takes TTP for example, possible reasons for the variations of TTP include residual lemon juice in the oral cavity, repeated swallowing, and other involuntary motions or background noises during dynamic scanning.

Our study has several potential limitations. First, there is a trade-off between temporal resolution and signal-to-noise ratio in our study. Therefore, we performed an analysis of imaging quality to examine the severity of magnetic susceptibility artifacts. Our results showed that the parotid glands were free from magnetic susceptibility artifacts at baseline and at the end of dynamic scans with substantial-to-almost perfect interobserver agreement. Second, the signal intensity of DWI might be influenced by bulk motion in our study. Therefore, we applied a low-pass filter to reduce the high-frequency signal fluctuations. Our results are consistent with the aforementioned quantitative salivary gland scintigraphic studies[30,31] regarding rapid emptying of saliva and arterial spin-labeling MR imaging studies[33] regarding increased blood flow after gustatory stimulation. Third, signal intensity on T2WI and DWI might be not only attributed to water molecules but also affected by fat molecules.[36,37] To verify the change of the water component in response to gustatory stimulation, another high-temporal-resolution echo-planar dual-echo MR imaging pulse sequence has been designed for direct measurement of the proton density of the parotid glands.

## CONCLUSIONS

Instantaneous parotid perfusion responses to gustatory stimulation can be quantified by ADC by using high-temporal-resolution echo-planar DWI.


## ACKNOWLEDGMENTS

The authors are grateful to Cheng-Hsuan Juan for contributing the comprehensive cartoon illustration of gustatory stimulation.

Disclosures: Y.-J. Liu—*UNRELATED: Grants/Grants Pending:* Received support in part from the Ministry of Science and Technology under Grant No. NSC 102-2221-E-035–003–MY.


## REFERENCES


1. Kohler PF, Winter ME. **A quantitative test for xerostomia: the Saxon test, an oral equivalent of the Schirmer test.** *Arthritis Rheum* 1985; 28:1128–32 CrossRef Medline
2. Chiappin S, Antonelli G, Gatti R, et al. **Saliva specimen: a new laboratory tool for diagnostic and basic investigation.** *Clin Chim Acta* 2007;383:30–40 Medline
3. Arrago JP, Rain JD, Brocheriou C, et al. **Scintigraphy of the salivary glands in Sjögen's syndrome.** *J Clin Pathol* 1987;40:1463–67 CrossRef Medline
4. van Acker F, Flamen P, Lambin P, et al. **The utility of SPECT in determining the relationship between radiation dose and salivary gland dysfunction after radiotherapy.** *Nucl Med Commun* 2001;22: 225–31 CrossRef Medline
5. Buus S, Grau C, Munk OL, et al. **11C-methionine PET, a novel method for measuring regional salivary gland function after radiotherapy of head and neck cancer.** *Radiother Oncol* 2004;73:289–96 CrossRef Medline
6. Ikeda M, Motoori K, Hanazawa T, et al. **Warthin tumor of the parotid gland: diagnostic value of MR imaging with histopathologic correlation.** *AJNR Am J Neuroradiol* 2004;25:1256–62 Medline
7. Eida S, Sumi M, Sakihama N, et al. **Apparent diffusion coefficient mapping of salivary gland tumors: prediction of the benignancy and malignancy.** *AJNR Am J Neuroradiol* 2007;28:116–21 Medline
8. Yerli H, Agildere AM, Aydin E, et al. **Value of apparent diffusion coefficient calculation in the differential diagnosis of parotid gland tumors.** *Acta Radiol* 2007;48:980–87 CrossRef Medline
9. Yabuuchi H, Matsuo Y, Kamitani T, et al. **Parotid gland tumors: can addition of diffusion-weighted MR imaging to dynamic contrast-enhanced MR imaging improve diagnostic accuracy in characterization?** *Radiology* 2008;249:909–16 CrossRef Medline
10. Habermann CR, Arndt C, Graessner J, et al. **Diffusion-weighted echo-planar MR imaging of primary parotid gland tumors: is a prediction of different histologic subtypes possible?** *AJNR Am J Neuroradiol* 2009;30:591–96 CrossRef Medline
11. Celebi I, Mahmutoglu AS, Ucgul A, et al. **Quantitative diffusion-weighted magnetic resonance imaging in the evaluation of parotid gland masses: a study with histopathological correlation.** *Clin Imaging* 2013;37:232–38 CrossRef Medline
12. Patel RR, Carlos RC, Midia M, et al. **Apparent diffusion coefficient mapping of the normal parotid gland and parotid involvement in patients with systemic connective tissue disorders.** *AJNR Am J Neuroradiol* 2004;25:16–20 Medline
13. Sumi M, Takagi Y, Uetani M, et al. **Diffusion-weighted echoplanar MR imaging of the salivary glands.** *AJR Am J Roentgenol* 2002;178: 959–65 CrossRef Medline
14. Regier M, Ries T, Arndt C, et al. **Sjögren's syndrome of the parotid gland: value of diffusion-weighted echo-planar MRI for diagnosis at an early stage based on MR sialography grading in comparison with healthy volunteers.** *Rofo* 2009;181:242–48 CrossRef Medline
15. Dirix P, De Keyzer F, Vandecaveye V, et al. **Diffusion-weighted magnetic resonance imaging to evaluate major salivary gland function before and after radiotherapy.** *Int J Radiat Oncol Biol Phys* 2008;71: 1365–71 CrossRef Medline
16. Zhang Y, Ou D, Gu Y, et al. **Diffusion-weighted MR imaging of salivary glands with gustatory stimulation: comparison before and after radiotherapy.** *Acta Radiol* 2013;54:928–33 CrossRef Medline
17. Marzi S, Forina C, Marucci L, et al. **Early radiation-induced changes evaluated by intravoxel incoherent motion in the major salivary glands.** *J Magn Reson Imaging* 2015;41:974–82 CrossRef Medline
18. Juan CJ, Cheng CC, Chiu SC, et al. **Temporal evolution of parotid volume and parotid apparent diffusion coefficient in nasopharyngeal carcinoma patients treated by intensity-modulated radiotherapy investigated by magnetic resonance imaging: a pilot study.** *PLoS One* 2015;10:e0137073 CrossRef Medline
19. Studer G, Kirilova A, Jaffray D, et al. **Major salivary gland function: diffusion-weighted MRI (DWI) assessment before, during and after radiation therapy.** *International Journal of Radiation Oncology* 2005;63:S361 CrossRef
20. Habermann CR, Cramer MC, Graessner J, et al. **Functional imaging of parotid glands: diffusion-weighted echo-planar MRI before and after stimulation.** *Rofo* 2004;176:1385–89 CrossRef Medline
21. Habermann CR, Gossrau P, Kooijman H, et al. **Monitoring of gustatory stimulation of salivary glands by diffusion-weighted MR imaging: comparison of 1.5T and 3T.** *AJNR Am J Neuroradiol* 2007; 28:1547–51 CrossRef Medline
22. Ries T, Arndt C, Regier M, et al. **Value of apparent diffusion coefficient calculation before and after gustatory stimulation in the diagnosis of acute or chronic parotitis.** *Eur Radiol* 2008;18:2251–57 CrossRef Medline
23. Kato H, Kanematsu M, Toida M, et al. **Salivary gland function evaluated by diffusion-weighted MR imaging with gustatory stimulation: preliminary results.** *J Magn Reson Imaging* 2011;34: 904–09 CrossRef Medline
24. Thoeny HC, De Keyzer F, Claus FG, et al. **Gustatory stimulation changes the apparent diffusion coefficient of salivary glands: initial experience.** *Radiology* 2005;235:629–34 CrossRef Medline
25. Freiman M, Voss SD, Mulkern RV, et al. **In vivo assessment of optimal b-value range for perfusion-insensitive apparent diffusion coefficient imaging.** *Med Phys* 2012;39:4832–39 CrossRef Medline
26. Dikaios N, Punwani S, Hamy V, et al. **Noise estimation from averaged diffusion weighted images: can unbiased quantitative decay parameters assist cancer evaluation?** *Magn Reson Med* 2014;71: 2105–17 CrossRef Medline
27. Liu YJ, Lee YH, Chang HC, et al. **A potential risk of overestimating apparent diffusion coefficient in parotid glands.** *PLoS One* 2015;10: e0124118 CrossRef Medline
28. Lemke A, Stieltjes B, Schad LR, et al. **Toward an optimal distribution of b values for intravoxel incoherent motion imaging.** *Magn Reson Imaging* 2011;29:766–76 CrossRef Medline
29. Koh DM, Collins DJ, Orton MR. **Intravoxel incoherent motion in body diffusion-weighted MRI: reality and challenges.** *AJR Am J Roentgenol* 2011;196:1351–61 CrossRef Medline
30. Hermann GA, Vivino FB, Shnier D, et al. **Variability of quantitative scintigraphic salivary indices in normal subjects.** *J Nucl Med* 1998; 39:1260–63 Medline
31. Aung W, Murata Y, Ishida R, et al. **Study of quantitative oral radioactivity in salivary gland scintigraphy and determination of the clinical stage of Sjögren's syndrome.** *J Nucl Med* 2001;42:38–43 Medline
32. Koh DM. **Qualitative and quantitative analyses: image evaluation and interpretation.** In: Koh DM, Theony HC. *Diffusion-Weighted MR Imaging: Applications in the Body.* Berlin: Springer-Verlag; 2010:33–47
33. Schwenzer NF, Schraml C, Martirosian P, et al. **MR measurement of blood flow in the parotid gland without contrast medium: a functional study before and after gustatory stimulation.** *NMR Biomed* 2008;21:598–605 CrossRef Medline
34. Simon-Zoula SC, Boesch C, De Keyzer F, et al. **Functional imaging of the parotid glands using blood oxygenation level dependent**

**(BOLD)-MRI at 1.5T and 3T.** *J Magn Reson Imaging* 2008;27:43–48 CrossRef Medline

35. Clark HD, Moiseenko VV, Rackley TP, et al. **Development of a method for functional aspect identification in parotid using dynamic contrast-enhanced magnetic resonance imaging and concurrent stimulation.** *Acta Oncol* 2015;54:1686–90 CrossRef Medline
36. Juan CJ, Chang HC, Hsueh CJ, et al. **Salivary glands: echo-planar versus PROPELLER diffusion-weighted MR imaging for assessment of ADCs.** *Radiology* 2009;253:144–52 CrossRef Medline
37. Chang HC, Juan CJ, Chiu HC, et al. **Effects of gender, age, and body mass index on fat contents and apparent diffusion coefficients in healthy parotid glands: an MRI evaluation.** *Eur Radiol* 2014;24:2069–76 CrossRef Medline

# The CT Prevalence of Arrested Pneumatization of the Sphenoid Sinus in Patients with Sickle Cell Disease

A.V. Prabhu and B.F. Branstetter IV

## ABSTRACT

**BACKGROUND AND PURPOSE:** Arrested sphenoid pneumatization is an incidental radiologic finding on CT and MR imaging that may be confused with more aggressive pathologic conditions. No definite etiology for arrested sphenoid pneumatization has been established, though changes in regional blood flow during childhood, as is seen with sickle cell disease, have been proposed. The purpose of our study was to compare the prevalence of arrested pneumatization of the sphenoid sinus in patients with and without sickle cell disease.

**MATERIALS AND METHODS:** We retrospectively identified 146 patients with sickle cell disease who had undergone CT scans of the skull base between January 1990 and May 2015. We identified 292 control patients without sickle cell disease matched for age and sex in a 1:2 ratio. We tabulated the prevalence of arrested pneumatization as well as the location and size of the lesions. We used the Fisher exact test to correlate sickle cell disease with arrested pneumatization of the sphenoid sinus and the *t* test to correlate sickle cell disease with lesion size.

**RESULTS:** Of the 146 patients with sickle cell disease, 14 (9.6%) had arrested pneumatization of the sphenoid sinus. In the 292 control patients, 6 (2.1%) had arrested pneumatization. Patients with sickle cell disease had a statistically significant higher rate of arrested pneumatization compared with patients without sickle cell disease ($P < .001$). There was no statistically significant correlation between lesion size and diagnosis of sickle cell disease.

**CONCLUSIONS:** Patients with sickle cell disease have a greater prevalence of arrested pneumatization of the sphenoid sinus than patients without sickle cell disease. This supports the theory that either regional blood flow anomalies or increased serum erythropoietin causes arrested sinus pneumatization.

**ABBREVIATION:** SCD = sickle cell disease

The normal development of the sphenoid sinus is preceded by a phase of fatty transformation and fat involution in the bone marrow, followed by aeration of the marrow that then results in full pneumatization.[1,2] This process begins at 4 months of age and usually ends at 10–14 years of age.[3,4] This process may be interrupted, leaving atypical fatty marrow that persists into adulthood.

Change in regional blood flow has been suggested as a potential stimulus for fatty marrow conversion.[5] If this theory is correct, then diseases that produce aberrant regional blood flow might predispose a person to arrested sinus pneumatization. Sickle cell disease (SCD) is an example of a disorder that produces regional blood flow changes in childhood, but no study has investigated the correlation between arrested sphenoid pneumatization and SCD.

We hypothesized that there is an increased prevalence of arrested pneumatization of the sphenoid sinus in patients with SCD compared with those without SCD.

## MATERIALS AND METHODS

### *Study Participants*

The institutional review board at the University of Pittsburgh Medical Center approved this retrospective study of existing imaging data, and written consent was waived. We retrospectively searched our electronic medical records to identify CT scans of the face, orbit, sinuses, and temporal bones obtained between January 1990 and May 2015, each performed on a different patient at least 1 year of age.

We identified 146 patients with SCD (cohort group) and then identified 292 patients from the same date range without SCD (control group) matched for age and sex at a 1:2 ratio. The diagnosis of SCD was confirmed with genetic testing for every patient in the cohort group. Patients were excluded if they had undergone

Received December 20, 2015; accepted after revision March 4, 2016.

From the Departments of Radiology (A.V.P., B.F.B.) and Otolaryngology (B.F.B.), University of Pittsburgh School of Medicine, Pittsburgh, Pennsylvania.

Please address correspondence to Arpan V. Prabhu, B.S., Department of Radiology, University of Pittsburgh School of Medicine, 200 Lothrop St, Pittsburgh, PA 15213; e-mail: prabhuav2@upmc.edu

http://dx.doi.org/10.3174/ajnr.A4801

**FIGURE.** Axial (*A*) and sagittal (*B*) contrast-enhanced CT images show a nonexpansile lesion (*arrows*) located at a normal left sphenoid sinus pneumatization site with a thin cortical margin, internal fatty content, and curvilinear internal calcifications. This is the characteristic appearance and location for arrested pneumatization of the sphenoid sinus.

**Table 1: Frequency and size of sphenoid fibro-osseous lesions visualized on head CT**

| Group | Frequency (%) | Size[a] ± SD (mm) |
|---|---|---|
| SCD ($n = 146$) | 14 (9.6%) | 14.3 ± 10.2 |
| Control ($n = 292$) | 6 (2.1%) | 8.85 ± 5.6 |

[a] Size is the maximal axial dimension. There was a statistically significant relationship ($P < .001$) between presence of SCD and frequency of sphenoid fibro-osseous lesions. There was no statistically significant relationship between lesion size and SCD status ($P = .24$).

**Table 2: Location of sphenoid fibro-osseous lesions in patients with and without SCD**

| Location | Frequency | | |
|---|---|---|---|
| | Patients with SCD[a] | Patients without SCD[a] | Total Frequency[a] |
| Left greater sphenoid wing | 7 (50) | 4 (67) | 11 (55) |
| Right greater sphenoid wing | 3 (21) | 2 (33) | 5 (25) |
| Bilateral sphenoid wings | 4 (29) | 0 (0) | 4 (20) |
| Total | 14 (70) | 6 (30) | 20 (100) |

[a] Data presented as number of patients (%).

surgery or radiation to the skull base, if the scans demonstrated skull base pathology, if there was inadequate scan coverage of the skull base, or if streak artifact prevented clear evaluation of the region of the sphenoid sinuses.

### *Imaging*

CT was performed on a 64-channel scanner (VCT, HD, and Optima LightSpeed systems; GE Healthcare, Milwaukee, Wisconsin) with variable mA, kVP of 120, section thickness reconstructed at 1.25 mm, and section spacing of either 1.25 mm or 0.625 mm. Display field of view varied with patient size but was approximately 25 mm. Coronal and sagittal reformatted images were routinely obtained but were not used in this evaluation.

Each examination was evaluated in random order by a medical student trained to identify sphenoid lesions. The medical student intentionally interpreted the examinations with very high sensitivity so that no true lesions would be overlooked. Each case with a possible lesion was then re-evaluated by a fellowship-trained neuroradiologist with Certificate of Added Qualification in neuroradiology and 13 years of dedicated experience in head and neck imaging. The location of the lesion and greatest axial length were recorded. Both observers were blinded to the clinical history of the patient and the SCD status.

Using guidelines from Welker et al,[6] arrested pneumatization was defined on CT as a nonexpansile lesion located at a normal sphenoid sinus pneumatization site with a thin cortical margin, internal fatty content, and curvilinear internal calcifications (Figure). The lesion must respect the margins of adjacent neural foramina and lack a normal trabecular pattern.

### *Statistical Tests*

The percentage of patients with arrested sphenoid pneumatization in each group was tabulated. The Fisher exact test was used to determine correlation between a diagnosis of SCD and arrested pneumatization of the sphenoid sinus. The test was 2-sided, and a *P* value of .05 was chosen as the threshold for statistical significance. A *t* test was used to determine any relationship between a diagnosis of SCD and maximum axial dimension of the sphenoid lesions, again by using a *P*-value threshold of .05.

## RESULTS

The 146 patients in the cohort group included 58 male (39.7%) and 88 female patients (60.3%), with a median age of 30 years (mean, 35.0 years; range, 1–100 years). Of the 146 patients, 5 (3%) were 1–4 years old, and 15 (10%) were 5–14 years old. The same demographic percentages applied to the matched control group.

Of the 146 patients with SCD, 14 (9.6%) had arrested pneumatization of the sphenoid sinus. In the 292 control patients, 6 (2.1%) had arrested pneumatization ($P < .001$). The size of the lesions (mean ± SD) was 14.3 ± 10.2 mm in patients with SCD and 8.85 ± 5.6 mm in patients without SCD (Table 1). The most frequent location of the lesions was the left greater wing of the sphenoid bone (11 of 20 patients, 55%) (Table 2).

A Fisher exact test demonstrated that patients with SCD had a statistically significant higher rate of arrested pneumatization compared with patients without SCD ($P < .001$). A *t* test showed no significant relationship between a diagnosis of SCD and the size of the lesions ($P = .24$).

## DISCUSSION

The normal pneumatization process of the sphenoid sinus begins after birth and usually ends at 10–14 years of age with the formation of a fully pneumatized sinus lined by respiratory epithelium.[3,4] This process can be interrupted for unclear reasons, especially in the sphenoid sinus. The most familiar etiology is chronic inflammation, as seen in patients with cystic fibrosis,[7-9] but other factors can produce a similar result. It is also unclear why arrested pneumatization has been shown to occur most often in the sphenoid sinuses, though it may be because of greater variation in the extent of aeration in the sphenoid sinus compared

with other paranasal sinuses.[6] Regarding arrested pneumatization, there is a theory that aeration triggers the fatty marrow conversion in the sphenoid sinus,[1] whereas another theory suggests that the ratio of trabecular to cortical bone is the driving mechanism.[10] Yonestu et al[5] suggested a subsequent theory of regional blood flow changes as the reason for atypical fatty marrow that persists into adulthood.

It is important to note that the theory of regional blood flow has not been proved. Using MR signal intensity changes on T1WI, Yonetsu et al [5] showed sphenoid marrow conversion before 1 year of age, when aeration of the sphenoid bone does not occur.[4,11] This suggested that factors other than air supply, such as blood supply, play an important role in conversion of the marrow.[5] Humoral factors also may play a role in arrested pneumatization of the sphenoid sinus, considering that serum erythropoietin levels have been shown to be elevated in patients with SCD.[12] The elevated erythropoietin may interrupt the conversion of hematopoietic to fatty marrow.

The phrase "arrested pneumatization" makes an assumption about the etiology of the sphenoid lesions that has not been proved. In fact, radiologists may be uncomfortable using the phrase because it is only one of several theories for the etiology of these fibro-osseous lesions. Our study supports this terminology and the theory of regional blood flow anomalies or increased serum erythropoietin as a potential cause of arrested sinus pneumatization.

The differential diagnosis for a mass in a normal sphenoid sinus pneumatization site includes fibrous dysplasia, clival chordoma, chondrosarcoma, intraosseous lipoma, intraosseous hemangioma, hamartoma, ossifying fibroma, enchondroma, and fibrous osteoma.[6,13-16] Arrested pneumatization may be distinguished from these entities as a nonexpansile lesion with a thin cortical margin, internal fatty content, and curvilinear internal calcifications (Figure).[6] These calcifications differ from the "ring and arc" calcifications seen with chondroid tumors.[13] Intraosseous lipomas share some imaging characteristics with arrested sinus pneumatization,[14] leading to the theory that these entities are of similar etiology. However, our findings do not support this theory. In particular, arrested pneumatization should not be confused with ossifying fibroma. Whereas the internal matrix of arrested pneumatization is characterized by curvilinear calcification and fatty contents, ossifying fibromas exhibit ground-glass marrow on CT, often with an overlying radial pattern of calcification.[17] Ossifying fibromas are also expansile and may be exophytic into the sinus itself.[18]

Our study has some important limitations. The study was retrospective, and all the patients in the study were imaged for various clinical reasons. The number of patients was too small to break down our results by age to determine when these lesions formed and determine whether age is predictive of prevalence. Although the control patients were matched for age and sex, patient race was not reliably available to us, so we could not account for this potential confounder. Serial CT scans could provide more information about the usual development of arrested sphenoid pneumatization, but in our series, no patients with lesions had serial scans. Although the total number of patients in our series who had arrested pneumatization was small, the statistical results comparing the 2 groups were robust, with a *P* value less than .001.

Our study included some patients younger than 14 years of age, when the development of the sphenoid sinuses is still ongoing. Although these patients may be less likely to have fibro-osseous lesions, we felt justified to include these patients because 2 patients with SCD (ages 8 and 14 years) had evidence of arrested sphenoid pneumatization. Additionally, the case-control format of our study would prevent this from biasing our overall results.

## CONCLUSIONS

Patients with SCD exhibit a higher prevalence of arrested pneumatization of the sphenoid sinus than patients without SCD. This supports the theories that either regional blood flow anomalies or increased serum erythropoietin cause arrested sinus pneumatization and supports the continued use of this terminology.


## ACKNOWLEDGMENTS

The authors thank Rose Jarosz for her role as research coordinator for this study.

Disclosures: Arpan V. Prabhu—*RELATED*: *Grant*: University of Pittsburgh School of Medicine through the Dean's Summer Research Program.


## REFERENCES


1. Aoki S, Dillon WP, Barkovich AJ, et al. **Marrow conversion before pneumatization of the sphenoid sinus: assessment with MR imaging.** *Radiology* 1989;172:373–75 CrossRef Medline
2. Scuderi AJ, Harnsberger HR, Boyer RS. **Pneumatization of the paranasal sinuses: normal features of importance to the accurate interpretation of CT scans and MR images.** *AJR Am J Roentgenol* 1993; 160:1101–04 CrossRef Medline
3. Jang YJ, Kim SC. **Pneumatization of the sphenoid sinus in children evaluated by magnetic resonance imaging.** *Am J Rhinol* 2000;14: 181–85 CrossRef Medline
4. Szolar D, Preidler K, Ranner G, et al. **Magnetic resonance assessment of age-related development of the sphenoid sinus.** *Br J Radiol* 1994; 67:431–35 CrossRef Medline
5. Yonetsu K, Watanabe M, Nakamura T. **Age-related expansion and reduction in aeration of the sphenoid sinus: volume assessment by helical CT scanning.** *AJNR Am J Neuroradiol* 2000;21:179–82 Medline
6. Welker KM, DeLone DR, Lane JI, et al. **Arrested pneumatization of the skull base: imaging characteristics.** *AJR Am J Roentgenol* 2008; 190:1691–96 CrossRef Medline
7. Bonfield TL, Konstan MW, Berger M. **Altered respiratory epithelial cell cytokine production in cystic fibrosis.** *J Allergy Clin Immunol* 1999;104:72–78 CrossRef Medline
8. Chmiel JF, Berger M, Konstan MW. **The role of inflammation in the pathophysiology of CF lung disease.** *Clin Rev Allergy Immunol* 2002; 23:5–27 CrossRef Medline
9. Nichols D, Chmiel J, Berger M. **Chronic inflammation in the cystic fibrosis lung: alterations in inter- and intracellular signaling.** *Clin Rev Allergy Immunol* 2008;34:146–62 CrossRef Medline
10. Gurevitch O, Slavin S, Feldman AG. **Conversion of red bone marrow into yellow - cause and mechanisms.** *Med Hypotheses* 2007;69: 531–36 CrossRef Medline
11. Madeline LA, Elster AD. **Suture closure in the human chondrocranium: CT assessment.** *Radiology* 1995;196:747–56 CrossRef Medline
12. Ballas SK, Marcolina MJ. **Determinants of red cell survival and erythropoietic activity in patients with sickle cell anemia in the steady state.** *Hemoglobin* 2000;24:277–86 CrossRef Medline

13. Weerakkody Y. **Arrested pneumatisation of the skull base (sphenoid sinus).** *EuroRad* 2013;Case 10648 CrossRef
14. Jalali E, Tadinada A. **Arrested pneumatization of the sphenoid sinus mimicking intraosseous lesions of the skull base.** *Imaging Sci Dent* 2015;45:67–72 CrossRef Medline
15. Politi M, Romeike BF, Papanagiotou P, et al. **Intraosseous hemangioma of the skull with dural tail sign: radiologic features with pathologic correlation.** *AJNR Am J Neuroradiol* 2005;26:2049–52 Medline
16. Srubiski A, Csillag A, Timperley D, et al. **Radiological features of the intraosseous lipoma of the sphenoid.** *Otolaryngol Head Neck Surg* 2011;144:617–22 CrossRef Medline
17. Baumann I, Zimmermann R, Dammann F, et al. **Ossifying fibroma of the ethmoid involving the orbit and the skull base.** *Otolaryngol Head Neck Surg* 2005;133:158–59 CrossRef Medline
18. Eversole R, Su L, ElMofty S. **Benign fibro-osseous lesions of the craniofacial complex. A review.** *Head Neck Pathol* 2008;2:177–202 CrossRef Medline

# High-Resolution MRI Findings following Trigeminal Rhizotomy

B.G. Northcutt, D.P. Seeburg, J. Shin, N. Aygun, D.A. Herzka, D. Theodros, C.R. Goodwin, C. Bettegowda, M. Lim, and A.M. Blitz

## ABSTRACT

**BACKGROUND AND PURPOSE:** Patients with trigeminal neuralgia often undergo trigeminal rhizotomy via radiofrequency thermocoagulation or glycerol injection for treatment of symptoms. To date, radiologic changes in patients with trigeminal neuralgia post-rhizotomy have not been described, to our knowledge. The aim of this study was to evaluate patients after trigeminal rhizotomy to characterize post-rhizotomy changes on 3D high-resolution MR imaging.

**MATERIALS AND METHODS:** A retrospective review of trigeminal neuralgia protocol studies was performed in 26 patients after rhizotomy compared with 54 treatment-naïve subjects with trigeminal neuralgia. Examinations were reviewed independently by 2 neuroradiologists blinded to the side of symptoms and treatment history. The symmetry of Meckel's cave on constructive interference in steady-state and the presence of contrast enhancement within the trigeminal nerves on volumetric interpolated breath-hold examination images were assessed subjectively. The signal intensity of Meckel's cave was measured on coronal noncontrast constructive interference in steady-state imaging on each side.

**RESULTS:** Post-rhizotomy changes included subjective clumping of nerve roots and/or decreased constructive interference in steady-state signal intensity within Meckel's cave, which was identified in 17/26 (65%) patients after rhizotomy and 3/54 (6%) treatment-naïve patients ($P < .001$). Constructive interference in steady-state signal intensity within Meckel's cave was, on average, 13% lower on the side of the rhizotomy in patients posttreatment compared with a 1% difference in controls ($P < .001$). Small regions of temporal encephalomalacia were noted in 8/26 (31%) patients after rhizotomy and 0/54 (0%) treatment-naïve patients ($P < .001$).

**CONCLUSIONS:** Post-trigeminal rhizotomy findings frequently include nerve clumping and decreased constructive interference in steady-state signal intensity in Meckel's cave. Small areas of temporal lobe encephalomalacia are encountered less frequently.

**ABBREVIATIONS:** CISS = constructive interference in steady-state; SI = signal intensity; VIBE = volumetric interpolated breath-hold examination; SPACE = sampling perfection with application-optimized contrasts by using different flip angle evolution

Trigeminal neuralgia is a debilitating condition characterized by sharp pain in the distribution of the trigeminal nerve. First described in 1773 by John Fothergill, trigeminal neuralgia is now a widely recognized and frequently encountered condition with a prevalence as high as 200/100,000 individuals and an overall incidence of 2.7/100,000/year.[1-5] First-line treatment commonly consists of medical management with carbamazepine, followed by additional second- and third-line medical treatments.[1,6] If medical management fails, imaging of the trigeminal nerves is often performed to assess causes such as compression of the cisternal segment of the trigeminal nerve from vascular structures or, less commonly, mass lesions along the course of this nerve.

Trigeminal rhizotomy, which is performed by percutaneous insertion of a needle through the foramen ovale into Meckel's cave to damage the nerve by balloon compression, glycerol injection, or radiofrequency thermocoagulation, is often performed as a first-line procedure and may be the only procedure available to patients unable to undergo the more invasive surgical intervention of microvascular decompression. Microvascular decompression is an invasive method of treatment with reported higher patient satisfaction and an overall lower symptom recurrence rate compared with rhizotomy, but it requires an open neurosurgical approach.[7,8]

High-resolution MR imaging of the trigeminal nerves has allowed radiologists to see the cisternal and Meckel's cave segments of the trigeminal nerve with exquisite detail. In particular, con-

Received January 21, 2016; accepted after revision April 16.

From the Departments of Radiology and Radiologic Sciences, Division of Neuroradiology (B.G.N., D.P.S., J.S., N.A., A.M.B.), Biomedical Engineering (D.A.H.), and Neurosurgery (D.T., C.R.G., C.B., M.L.), Johns Hopkins Hospital, Baltimore, Maryland.

Please address correspondence to Ari M. Blitz, MD, Johns Hopkins Medical Institutions, Diagnostic Radiology, Division of Neuroradiology, 600 North Wolfe St, Baltimore, MD 21287; e-mail: ablitz1@jhmi.edu

http://dx.doi.org/10.3174/ajnr.A4868

structive interference in steady-state (CISS) imaging, a free precession technique with intrinsic flow suppression and high signal-to-noise ratio, allows visualization of fine structures, including individual rootlets of the trigeminal nerve in Meckel's cave. We have also observed that CISS is sensitive to small perturbations in the content of fluid and can demonstrate reduced signal compared with CSF, even when differences are not visualized on spin-echo-based imaging. Because patients can have high-resolution imaging after trigeminal rhizotomy for a number of indications, including recurrence of symptoms, the goal of this study was to determine the findings expected on postprocedural imaging following percutaneous rhizotomy.

Given the postulated mechanism of action of rhizotomy—that is, changes in osmolarity and resulting demyelination and neurolysis with glycerol or direct heat neurolysis with radiofrequency thermocoagulation—we hypothesized the following: the rootlets of the trigeminal nerve in the region of the injection would demonstrate visible changes in their course due to clumping and adhesion; and the signal on CISS imaging would be reduced within Meckel's cave due to injectate and/or inflammatory debris.[9] In addition, we sought to evaluate whether enhancement of the trigeminal nerve or Meckel's cave should be expected following rhizotomy. The rates of other changes to surrounding structures and the muscles of mastication that are innervated by the mandibular division of the trigeminal nerve (cranial nerve V.3) were recorded.

**Table 1: Subject age and sex**

| | Post-Rhizotomy | Treatment-Naïve | *P* Value |
|---|---|---|---|
| No. of Subjects | 26 | 54 | |
| Age (mean) (range) (yr) | 60 (27–85) | 55 (29–74) | .09 |
| Sex | 6 Men, 20 women | 20 Men, 34 women | .31 |

**Table 2: Frequency of findings within Meckel's cave in treatment-naïve versus post-rhizotomy patients[a]**

| | Post-Rhizotomy | Treatment-Naïve | *P* Value |
|---|---|---|---|
| Subjective clumping | 16/26 (62%) | 3/54 (6%) | <.001 |
| Decreased CISS | 13/26 (50%) | 3/54 (6%) | <.001 |
| Subjective clumping without decreased CISS SI | 4/26 (15%) | 0/54 (0%) | .01 |
| ↓ CISS SI without clumping | 1/26 (4%) | 0/54 (0%) | .33 |
| Subjective nerve clumping and ↓ CISS SI | 12/26 (46%) | 3/54 (6%) | <.001 |
| Subjective nerve clumping and/or ↓ CISS SI | 17/26 (65%) | 3/54 (6%) | <.001 |

**Note:**— ↓ indicates decrease.
[a] Interobserver agreement = 90%, $\kappa = 0.69$.

## MATERIALS AND METHODS

### *Patient Sample*

A retrospective review of dedicated high-resolution 3D trigeminal neuralgia protocol MR imaging studies was performed from 2011 to 2014. The study was approved by the institutional review board and was Health Insurance Portability and Accountability Act–compliant. Three hundred ten examinations were performed on 261 patients during the study period. Subjects were stratified into preprocedural trigeminal neuralgia and post-rhizotomy groups. Subjects were included in the post-rhizotomy group if they had a documented history of either glycerol and/or radiofrequency thermocoagulation rhizotomy before imaging. All rhizotomies were performed with fluoroscopic image guidance. Subjects were excluded from both groups if they had symptoms atypical for trigeminal neuralgia ($n = 51$), mass lesions in Meckel's cave ($n = 11$), and a history of microvascular decompression ($n = 65$) or gamma knife treatment ($n = 4$) before imaging. Twenty-six studies qualified for the post-rhizotomy group. One hundred fifty-three examinations qualified for the preprocedural trigeminal neuralgia control group, of which 54 were selected at random at approximately 2 controls per case with no statistically significant difference between age and sex compared with the post-rhizotomy group.

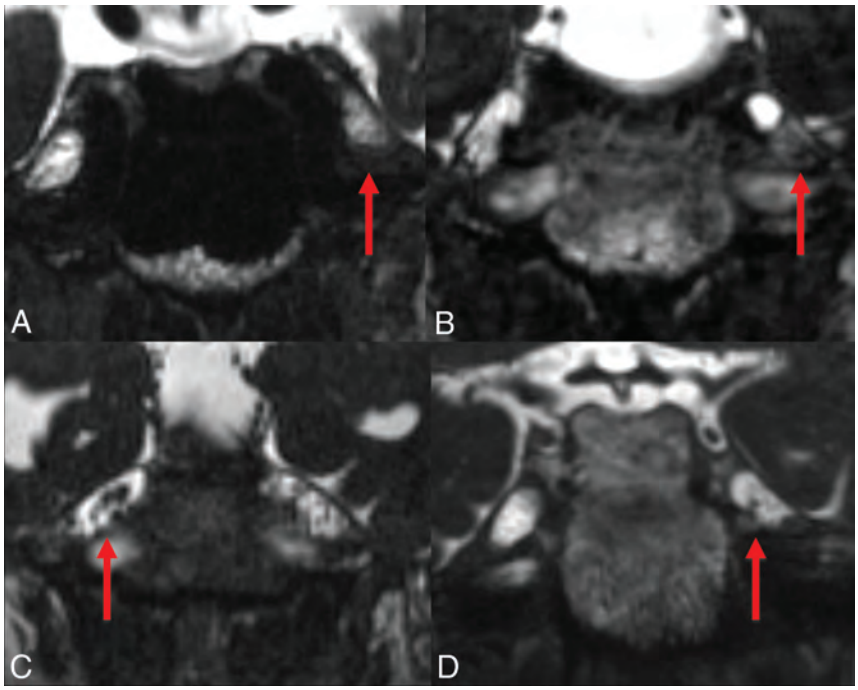


**FIG 1.** Coronal CISS precontrast images at the level of Meckel's cave. *A*, Decreased T2 signal intensity and poorly delineated nerve rootlets in the left Meckel's cave after rhizotomy. Note a normal-appearing right Meckel's cave. *B*, A different patient with clumping of the nerve rootlets inferiorly within the left Meckel's cave post-rhizotomy. *C*, Central clumping of nerve rootlets in the right Meckel's cave post-rhizotomy. *D*, A different patient with more subtle clumping of the nerve rootlets in the left Meckel's cave and subtle decreased CISS SI post-rhizotomy.

### *Imaging Technique*

All studies were conducted at our institution on Verio or Trio 3T scanners (75 examinations) or Magnetom Espree or Avanto 1.5T scanners (3 examinations) (Siemens, Erlangen, Germany) by using a high-resolution trigeminal neuralgia protocol. The protocol consisted of a sagittal T1, isovolumetric T2 sampling perfection with application-optimized contrasts by using different flip angle

evolution sequence (SPACE; Siemens), FLAIR, and axial diffusion-weighted images of the brain. High-resolution sequences were acquired, including CISS pre- and postcontrast (section thickness, 0.6 mm; matrix, 256/256; FOV, 16.9 × 24.6) and volumetric interpolated breath-hold examination (VIBE) pre- and postcontrast (section thickness, 0.8 mm; matrix, 256/256; FOV, 16.9 × 24.6), with fat saturation applied on the postcontrast VIBE imaging. Postcontrast images were acquired after administration of 0.1 mL/kg of gadobutrol (Gadavist; Bayer Schering Pharma, Berlin, German) if the glomerular filtration rate was above 60, and half-dose of gadobenate dimeglumine (MultiHance; Bracco Diagnostics, Princeton, New Jersey) was used if the glomerular filtration rate was below 60, per institutional protocol. 3D-time-of-flight MRA of the circle of Willis was also performed as part of the high-resolution trigeminal neuralgia protocol.

### *Image and Data Analysis*

The selected treatment-naïve and post-rhizotomy studies were intermixed and reviewed independently by 2 neuroradiologists (with >5 years experience) blinded to a history of prior treatment. All study sequences were reviewed on a PACS. Meckel's caves were evaluated subjectively for asymmetry, including clumping of the nerve roots and altered signal intensity on both non-contrast-enhanced and contrast-enhanced CISS sequences. Trigeminal nerves were assessed for enhancement on postcontrast VIBE images. The signal intensity of Meckel's cave was objectively measured by a central freehand ROI within the largest area of Meckel's cave on coronal non-contrast-enhanced CISS imaging for each case, avoiding Meckel's cave borders. Postprocedural changes in the adjacent structures were evaluated on pre- and postcontrast CISS and VIBE sequences. These adjacent structures included cranial nerves III and VI as they are readily visualized; however, cranial nerve IV was not assessed as it is not well-visualized routinely. Additionally, the medial temporal lobes were assessed as they closely approximate and often abut the lateral dural margin of the Meckel's cave and can be penetrated by piercing the lateral dura of Meckel's cave.[10,11] The adjacent petrous and cavernous segments of the internal carotid arteries and cavernous sinuses were also assessed on 3D TOF MRA.

**Table 3: Ratio of CISS SI in treatment-naïve versus post-rhizotomy patients**

| | Control Right MC/Left MC (mean ratio ± SD) | Rhizotomy MC/Contralateral MC (mean ratio ± SD) | *P* Value |
|---|---|---|---|
| Ratio of CISS SI | 0.99 (±0.09) | 0.87 (±0.15) | <.001 |

**Note:**—MC indicates Meckel cave.

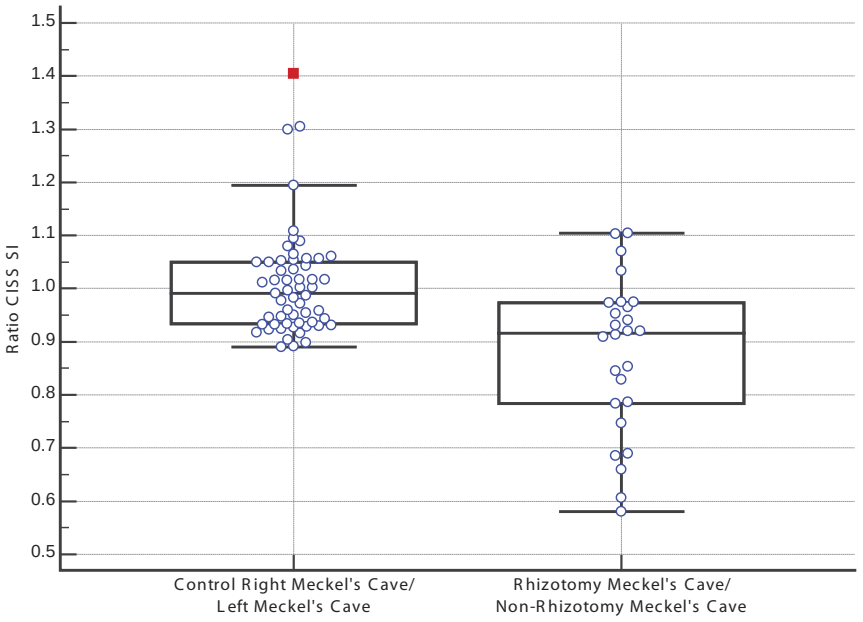


**FIG 2.** Graph showing the ratio of CISS SI of the right and left Meckel's caves in control patients and rhizotomy/nonrhizotomy in Meckel's caves in post-rhizotomy patients. The control group ratio was 0.99 compared with 0.87 for patients who underwent rhizotomy ($P < .001$).

### *Statistical Analysis*

Patients in the control and post-rhizotomy groups were compared for age by using a *t* test of independent samples, assuming unequal variances, and compared for sex with the Fisher exact test with MedCalc for Windows, Version 15.8 (MedCalc Software; Mariakerke, Belgium). A *P* value <.05 was considered significant.

The sensitivity, specificity, and positive and negative predictive values of subjective nerve clumping or decreased CISS signal intensity (SI) for post-rhizotomy were calculated. Statistical significance was calculated via the Fisher exact test. Interobserver agreement and κ were calculated between observers.

A *t* test of independent samples assuming unequal variance was performed to compare measurements of CISS SI between groups on the basis of the ROI SI values. The Fisher exact test and interobserver agreement were calculated for changes of the structures adjacent to Meckel's cave, including hematoma, encephalomalacia, atrophy of muscles of mastication, cranial nerve III, V, and VI enhancement, and vascular injury of the adjacent petrous and cavernous internal carotid artery, or cavernous-carotid fistula. A *P* value <.05 was considered significant.

## RESULTS

Twenty-six unique subjects were included in the post-rhizotomy group, 12 with glycerol treatment and 14 receiving both glycerol rhizotomy and radiofrequency thermocoagulation rhizotomy before imaging. Fifty-four subjects were included in the trigeminal neuralgia procedure-naïve group. There were no statistically significant differences in age or sex between groups (Table 1).

Subjective nerve clumping or decreased CISS SI was present in 17/26 (65%) patients after rhizotomy, compared with only 3/54 (6%) treatment-naïve patients ($P < .001$) (Table 2 and Fig 1). Of the 17 patients with changes in Meckel's cave after rhizotomy, 12/17 (71%) had a

combination of clumping and decreased overall subjective CISS signal intensity, 4/17 (24%) demonstrated only subjective clumping of nerve rootlets, and 1/17 (5%) demonstrated only decreased subjective CISS signal intensity. All 3 treatment-naïve patients with subjective changes in Meckel's cave demonstrated both clumping and decreased CISS signal. No nerve clumping or altered signal was noted in Meckel's cave on VIBE precontrast and postcontrast sequences or FLAIR sequences, though clumping was identified in 2 patients after rhizotomy on T2 SPACE sequences by both reviewers.

In the patients having undergone rhizotomy, objective measurements of CISS SI by ROI in Meckel's cave demonstrated a statistically significant decrease in CISS SI on the side of the rhizotomy compared with the contralateral side and with control groups, with an average 13% decreased CISS SI on the side of the rhizotomy (Table 3 and Fig 2). Encephalomalacia of the adjacent temporal lobe was present in 8/26 (31%) patients post-rhizotomy compared with 0/54 (0%) patients in the treatment-naïve group ($P < .001$) (Fig 3). One small hematoma was present in the post-rhizotomy group (4%), with no hematoma present in the treatment-naïve group ($P = .33$). All cases of noted encephalomalacia and hematoma on CISS were also identified on FLAIR, VIBE, and T2 SPACE sequences by both reviewers. Atrophy of the muscles of mastication was present in both groups, 3/26 (12%) in the rhizotomy group and 3/54 (6%) in the treatment-naïve group ($P = .38$). Cranial nerve enhancement (of CN III, V, and VI) was not present in either group, nor was there damage to the adjacent petrous or cavernous internal carotid arteries or evidence of cavernous carotid fistula ($P = 1$) (Table 4).

The average time of imaging after the most recent rhizotomy was 17.2 months, with a range of 1–63 months. The average time of follow-up of patients with nerve clumping or decreased CISS signal was 16.5 months, compared with 18.4 months in those patients without clumping or CISS signal change ($P = .56$). The average number of rhizotomy treatments in patients with subjective clumping or decreased CISS SI was 2.9, compared with 1.3 treatments for those who did not have clumping or decreased CISS SI ($P < .01$). Seven of 12 (58%) patients who had undergone rhizotomy with only glycerol treatment had subjective changes in Meckel's cave, while 10/14 (63%) patients who had glycerol and radiofrequency treatment had subjective changes ($P = .68$). All subjects in our sample treated with radiofrequency rhizotomy had also undergone glycerol rhizotomy. The average number of rhizotomies in those with encephalomalacia was 3.8, compared with 1.5 for those without encephalomalacia ($P = .03$). Three of 12 (25%) patients who had only glycerol treatment had encephalomalacia compared with 6/14 (42%) patients who had a combination of glycerol and radiofrequency treatment ($P = .43$).

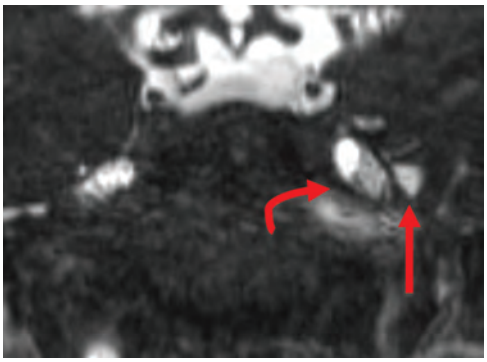

**FIG 3.** Coronal CISS precontrast at the level of Meckel's caves. Encephalomalacia of the medial left temporal lobe (*straight arrow*) adjacent to Meckel's cave. Also note clumping of the nerve rootlets in the left Meckel's cave (*curved arrow*) status post rhizotomy.

**Table 4: Frequency of findings in the adjacent structures in treatment-naïve versus post-rhizotomy patients**

| | Post-Rhizotomy | Treatment-Naïve | *P* Value | Interobserver Agreement | κ |
|---|---|---|---|---|---|
| Encephalomalacia | 8/26 (31%) | 0/54 (0%) | <.001 | 98.8% | 0.93 |
| Hematoma | 1/26 (4%) | 0/54 (0%) | .33 | 100% | 1 |
| Atrophy of muscles of mastication | 3/26 (10%) | 3/54 (4%) | .38 | 96.3% | 0.64 |
| CN V enhancement | 0/26 (0%) | 0/54 (0%) | 1.00 | 100% | 1 |
| Vascular injury | 0/26 (0%) | 0/54 (0%) | 1.00 | 100% | 1 |

**Note:**—CN indicates cranial nerve.

## DISCUSSION

Studies to date on patients post-rhizotomy have primarily focused on clinical outcomes, notably comparison of different forms of rhizotomy with each other and with microvascular decompression. While these articles offer occasional images of complications associated with rhizotomy, no studies to date, to the authors' knowledge, have evaluated patients after rhizotomy in an effort to describe postprocedural findings on MR imaging. This study was performed to determine what findings can be encountered on postprocedural MR imaging.

Subjective changes, such as decreased CISS SI and clumping of nerve roots, are commonly encountered (65%) after rhizotomy; however, these changes are rarely seen in treatment-naïve patients (6%). These results suggest that the radiologic findings are associated with the rhizotomy procedure rather than the underlying pathophysiology of trigeminal neuralgia. Objective measurements of signal intensity in Meckel's cave support our subjective findings by showing a statistically significant decrease in CISS SI in Meckel's cave after rhizotomy. The mechanism underlying these changes is presumed to be the result of chemical- or heat-induced neurolysis of the nerve rootlets in Meckel's cave. Notably, the patients with changes in Meckel's cave had undergone, on average, more rhizotomy treatments ($n = 2.9$) compared with those who did not have such changes ($n = 1.3$). Although the cause is unknown, similar changes demonstrated in procedure-naïve patients could reflect a prior inflammatory event predating the development of trigeminal neuralgia. Conversely, there could be recall bias in our study, with the possibility that some subjects failed to report their rhizotomy at another institution to the clinician.

Small foci of encephalomalacia of the temporal lobe adjacent to Meckel's cave were encountered in 31% of patients post-rhizotomy and not in the control group. One such focus demonstrated minimal blood products. These findings could be due to the adjacent temporal lobe being within the thermal zone of the radiofrequency probe and/or direct surgical ma-

nipulation.[10,11] No adverse clinical signs or symptoms related to the temporal lobe encephalomalacia were reported in these patients.

Weakness of muscles of mastication frequently occurs after trigeminal rhizotomy, with a recent review noting weakness in 16% of patients, which is often transient lasting 6–12 months.[12] In our review, atrophy of the muscles of mastication was present in patients with and without rhizotomy, with no statistically significant difference between groups. No enhancement of trigeminal nerve roots was encountered after treatment, though it is unclear whether more immediate postprocedural imaging would perhaps reveal enhancement in the acute injury phase after treatment. Additional complications such as vascular injury (cavernous carotid fistula, internal carotid artery pseudoaneurysms), abscess, meningitis, and cranial nerve III and VI injury, noted in previous publications, were not encountered clinically or on imaging in our series.[10-18]

There were several limitations in this study, including the inherent biases associated with the retrospective study design. Subjects were grouped according to a review of the medical record, depending on whether the patient was documented as having previously undergone rhizotomy. The patients were seen by experienced clinicians in a dedicated trigeminal neuralgia clinic, and documentation of prior procedures is standard, but we cannot exclude the possibility that subjects had undergone rhizotomy at another institution and failed to report this to the clinician. All patients in our study who had rhizotomy underwent glycerol rhizotomy or glycerol in combination with radiofrequency thermocoagulation rhizotomy. No patients had balloon compression rhizotomy, a method not used at our institution due to the preference of the surgeons. Another limitation of this retrospective study was lack of pre-rhizotomy imaging in those patients who underwent rhizotomy, with the exception of 1 patient. In the case of the 1 patient who underwent high-resolution imaging both before and after treatment, no difference was noted within Meckel's cave or the adjacent structures between studies. Additionally, no correlation between the degree of clumping or decreased CISS SI in Meckel's cave and the degree of symptoms could be made due to the retrospective nature of the study and in the absence of clinically reported grading of symptoms.

The timing of imaging after rhizotomy greatly varied, which could potentially influence the degree of changes seen in Meckel's cave, though the average time of imaging in those with and without nerve clumping was similar. Additionally, more acute changes within Meckel's cave after rhizotomy (<1 month) could not be accurately assessed. Last, the pain of trigeminal neuralgia is known to recur frequently following rhizotomy. Many of the subjects imaged after rhizotomy experienced recurrence of symptoms. Because patients who responded positively to trigeminal rhizotomy are unlikely to have undergone follow-up imaging, whether or to what extent these findings might correlate with degree or duration of therapeutic response remains a subject for further investigation.

## CONCLUSIONS

Post-trigeminal rhizotomy changes in patients with trigeminal neuralgia frequently include nerve clumping and decreased CISS SI within Meckel's cave, findings that are not commonly encountered in patients before treatment. Tiny foci of encephalomalacia can also be seen in the adjacent temporal lobe. Further investigation is necessary to determine whether and how such findings are related to the extent and durability of pain relief following rhizotomy.

Disclosures: C. Rory Goodwin—*UNRELATED*: *Grants/Grants Pending*: UNCF Merck Postdoctoral Fellow,* Burroughs Wellcome Fund (award).* Ari M. Blitz—*UNRELATED*: *Payment for Lectures (including service on Speakers Bureaus)*: Siemens, *Comments*: honorarium for an educational talk on imaging of the cranial nerves in 2014. Michael Lim—*UNRELATED*: *Consultancy*: Bristol-Myers Squibb, Stryker, *Comments*: research related to my laboratory research in immunotherapy (BMS); *Grants/Grants Pending*: Stryker,* Bristol-Myers Squibb,* Aegenus,* Celldex,* Arbor,* ImmunoCellular Therapeutics,* *Comments*: grant for studying CSF leak rates in patients after MVD (Stryker), research pertaining to immunotherapy outside the scope of this article (others); *Patents (planned, pending or issued)*: related to immunotherapy*; *Travel/Accommodations/Meeting Expenses Unrelated to Activities Listed*: for travel to consultant activities. *Money paid to the institution.

## REFERENCES

1. Prasad S, Galetta S. **Trigeminal neuralgia: historical notes and current concepts.** *Neurologist* 2009;15:87–94 CrossRef Medline
2. Penman J, **Trigeminal neuralgia.** In: Vinken PJ; Bruyn GW, eds. *Handbook of Clinical Neurology*. Vol 5. Amsterdam: North Holland; 1968:296–322
3. Katusic S, Beard CM, Bergstralh E, et al. **Incidence and clinical features of trigeminal neuralgia, Rochester, Minnesota, 1945–1984.** *Ann Neurol* 1990;27:89–95 CrossRef Medline
4. Rozen TD. **Trigeminal neuralgia and glossopharyngeal neuralgia.** *Neurol Clin* 2004;22:185–206 CrossRef Medline
5. Manzoni GC, Torelli P. **Epidemiology of typical and atypical craniofacial neuralgias.** *Neurol Sci* 2005;26(suppl 2):s65–s67 CrossRef Medline
6. Campbell FG, Graham JG, Zilkha KJ. **Clinical trial of carbazepine (tegretol) in trigeminal neuralgia.** *J Neurol Neurosurg Psychiatry* 1966;29:265–67 CrossRef Medline
7. Tatli M, Satici O, Kanpolat Y, et al. **Various surgical modalities for trigeminal neuralgia: literature study of respective long-term outcomes.** *Acta Neurochir (Wien)* 2008;150:243–55 CrossRef Medline
8. Barker FG 2nd, Jannetta PJ, Bissonette DJ, et al. **The long-term outcome of microvascular decompression for trigeminal neuralgia.** *N Engl J Med* 1996;334:1077–83 CrossRef Medline
9. Missios S, Mohammadi A, Barnett GH. **Percutaneous treatments for trigeminal neuralgia.** *Neurosurg Clin N Am* 2014;25:751–62 CrossRef Medline
10. Arrese I, Lobato R, Alén JF, et al. **Acute subdural and intratemporal hematoma as a complication of percutaneous compression of the gasserian ganglion for trigeminal neuralgia.** *Neurocirugia (Astur)* 2005;16:177–82 Medline
11. Rath GP, Dash HH, Bithal PK, et al. **Intracranial hemorrhage after percutaneous radiofrequency trigeminal rhizotomy.** *Pain Pract* 2009;9:82–84 CrossRef Medline
12. Tew JM, Morgan CJ, Grande AW. **Percutaneous stereotactic rhizotomy in treatment of intractable facial pain.** In: Quinones-Hinojosa A, ed. *Schmidek and Sweet's Operative Neurosurgical Techniques: Indications, Methods, and Results*. 6th ed. Philadelphia: Elsevier Saunders; 2012
13. Taha JM, Tew JM Jr. **Comparison of surgical treatments for trigeminal neuralgia: reevaluation of radiofrequency rhizotomy.** *Neurosurgery* 1996;38:865–71 CrossRef Medline
14. Sweet WH, Poletti CE, Roberts JT. **Dangerous rises in blood pressure upon heating of trigeminal rootlets: increasing bleeding times in patients with trigeminal neuralgia.** *Neurosurgery* 1985;17:843–44 Medline
15. Sekhar LN, Heros RC, Kerber CW. **Carotid-cavernous fistula following percutaneous retrogasserian procedures: report of two cases.** *J Neurosurg* 1979;51:700–06 CrossRef Medline
16. Gökalp HZ, Kanpolat Y, Tümer B. **Carotid-cavernous fistula following percutaneous trigeminal ganglion approach.** *Clin Neurol Neurosurg* 1980;82:269–72 CrossRef Medline
17. Harrigan MR, Chandler WF. **Abducens nerve palsy after radiofrequency rhizolysis for trigeminal neuralgia: case report.** *Neurosurgery* 1998;43:623–25 Medline
18. Acqui M, Familiari P, Pesce A, et al. **Brain abscess after percutaneous therapy for trigeminal neuralgia.** *Case Rep Infect Dis* 2015;2015:162793 CrossRef Medline

# Imaging Appearance of *SMARCB1* (INI1)-Deficient Sinonasal Carcinoma: A Newly Described Sinonasal Malignancy

D.R. Shatzkes, L.E. Ginsberg, M. Wong, A.H. Aiken, B.F. Branstetter IV, M.A. Michel, and N. Aygun

## ABSTRACT

**SUMMARY:** *SMARCB1* (INI1)-deficient sinonasal carcinomas were first described in 2014, and this series of 17 cases represents the first imaging description. This tumor is part of a larger group of *SMARCB1*-deficient neoplasms, characterized by aggressive behavior and a rhabdoid cytopathologic appearance, that affect multiple anatomic sites. Clinical and imaging features overlap considerably with other aggressive sinonasal malignancies such as sinonasal undifferentiated carcinoma, which represents a common initial pathologic diagnosis in this entity. *SMARCB1* (INI1)-deficient sinonasal tumors occurred most frequently in the nasoethmoidal region with invasion of the adjacent orbit and anterior cranial fossa. Avid contrast enhancement, intermediate to low T2 signal, and FDG avidity were frequent imaging features. Approximately half of the lesions demonstrated calcification, some with an unusual "hair on end" appearance, suggesting aggressive periosteal reaction.

Malignancy of the sinonasal cavity is characterized by considerably greater heterogeneity than malignancy of the upper aerodigestive tract, where squamous cell carcinoma predominates. Though squamous cell carcinoma remains the most common sinonasal malignancy (approximately 60% of cases), there is a diverse and growing array of additional histologies, including tumors of epithelial, neuroectodermal, lymphoproliferatve, and mesenchymal origins.[1-4] Though imaging features of the various histologies overlap considerably, some tumors demonstrate characteristic findings that support a particular diagnosis, such as T1 shortening in melanoma or chondroid calcification in chondrosarcoma. Other tumors might demonstrate findings that, though not specific to a single diagnosis, suggest their aggressive nature. Ultimately, tissue sampling is necessary to confirm pathologic diagnosis before treatment planning. Nevertheless, most sinonasal masses present with very nonspecific clinical findings indistinguishable from rhinosinusitis, and the ability of the radiologist to suggest an underlying malignancy is useful in directing short-term management, including the need for further imaging and tissue sampling.[3-8]

*SMARCB1* (INI1) is a tumor-suppressor gene that has been implicated in a growing number of malignancies involving multiple anatomic sites, including the kidneys, soft tissues, and CNS.[1,2,9-11] The first reports of *SMARCB1* (INI1)-deficient tumors of the sinonasal cavity appeared in the pathology literature in 2014,[1,9] followed by an additional small case series in 2015.[2] To our knowledge, there have been 16 cases reported in the world literature. However, the imaging appearance of *SMARCB1* (INI1)-deficient sinonasal tumors has not yet been described. By analyzing a case series of 17 patients collected from 6 different centers, some of whom were included in the pathologic reports listed above, we aimed to provide a comprehensive description of the appearance of these tumors on CT, MR imaging, and PET/CT studies. We also hoped to increase awareness of this relatively new entity among both radiologists and clinicians to facilitate its diagnosis when encountered in clinical practice.

## MATERIALS AND METHODS

This retrospective case series was performed with institutional review board approval and exemption from informed consent following the guidelines of the Health Insurance Portability and Accountability Act. Records of cases presented at our multidisciplinary tumor board since 2014 were reviewed for the pathologic diagnosis of *SMARCB1* (INI1)-deficient sinonasal tumors. In addition, cases were solicited from head and neck radiologists at other medical centers. In all, 17 cases were collected from 6 cen-

Received March 31, 2016; accepted after revision April 22.

From the Department of Radiology (D.R.S., M.W.), Lenox Hill Hospital, Northwell Health, New York, New York; Department of Radiology (L.E.G.), The University of Texas MD Anderson Cancer Center, Houston, Texas; Department of Radiology (A.H.A.), Neuroradiology Division, Emory University Hospital, Atlanta, Georgia; Department of Radiology (B.F.B.), Presbyterian Hospital, Pittsburgh, Pennsylvania; Department of Radiology (M.A.M.), Medical College of Wisconsin, Milwaukee, Wisconsin; and Department of Radiology (N.A.), Johns Hopkins Medicine, Baltimore, Maryland.

Please address correspondence to Deborah R. Shatzkes, MD, Department of Radiology, Lenox Hill Hospital, Northwell Health, 100 E 77th St, New York, NY 10075; e-mail: DShatzkes@northwell.edu

Indicates article with supplemental on-line table.

http://dx.doi.org/10.3174/ajnr.A4841

**Patient demographics**

| Patient | Age (y) | Sex | Original Pathology Diagnosis | Stage Reference[a] | Clinical Status | Published? |
|---|---|---|---|---|---|---|
| 1 | 35 | Female | Poorly differentiated carcinoma with squamoid features | T4bN0M0 | NED at 10 months | N |
| 2 | 51 | Male | Poorly differentiated carcinoma with glandular differentiation | T4aN0M0 | NED at 1 month | N |
| 3 | 45 | Male | Poorly differentiated adenocarcinoma | T4b | NED at 48 months | N |
| 4 | 50 | Female | Poorly differentiated SCC with papillary features | T4aN0M0 | NED at 9 months | N |
| 5 | 72 | Male | *SMARCB1* (INI 1)-deficient sinonasal carcinoma | T4aN0M0 | NED at 12 months | N |
| 6 | 43 | Male | Poorly differentiated SCC | T1 | NED at 9 months | N |
| 7 | 59 | Male | NA | NA | NED at 12 months | Bishop et al[9] |
| 8 | 54 | Female | SNUC | T4b | AWD at 6 months | Bishop et al[9] |
| 9 | 44 | Male | Poorly differentiated basaloid SCC | T4bN0 | NED at 18 months | Bishop et al[9] |
| 10 | 78 | Female | Myoepithelial carcinoma | N0M0 | NED at 24 months | Bishop et al[9] |
| 11 | 77 | Male | Myoepithelial carcinoma | T4bN0M0 | DOD at 12 months | Bishop et al[9] |
| 12 | 32 | Male | SNUC | T4b | AWD at 24 months | Bishop et al[9] |
| 13 | 64 | Female | SNUC | T4bN0M0 | AWD at 13 months | Bell et al[2] |
| 14 | 75 | Male | Basaloid SCC | T4bN0M0 | NA | Bell et al[2] |
| 15 | 33 | Female | High-grade mixed germ cell tumor | T4bN0M0 | DOD at 12 months | Bell et al[2] |
| 16 | 51 | Female | SNUC | T4N0M0 | DOD at 24 months | Bell et al[2] |
| 17 | 62 | Male | SNUC | T4bN0M1 | NED at 3 months | N |

**Note:**—AWD indicates alive with disease; DOD, dead of disease; N, not previously published; NA, not available; NED, no evidence of disease; SCC, squamous cell carcinoma; SNUC, sinonasal undifferentiated carcinoma.

[a] Based on American Joint Commission on Cancer, 7th Edition.

ters, 10 of which were included in prior case series.[2,9] In most cases, the diagnosis of *SMARCB1* (INI1)-deficient carcinoma represented an amendment of an initial alternate diagnosis. Patient demographics, original pathologic diagnoses, cancer stage, current clinical status, and publication history (where applicable) are summarized in the Table.

All available pretreatment CT, MR imaging, and/or PET/CT studies were reviewed on a PACS or DICOM viewer by a single radiologist with over 20 years of experience in head and neck imaging. MR and PET/CT imaging were available in 14 and 11 patients, respectively. CT images, either as a stand-alone examination or as part of a PET/CT examination, were available in 13 patients. Tumor characteristics compiled were specific location within the sinonasal cavity; the presence of any intracranial, orbital, or perineural extension; and the presence of regional nodal or distant metastases. Imaging parameters included CT attenuation, enhancement, and calcification patterns; MR signal characteristics and enhancement pattern; and the predominant pattern of osseous change. Osseous change was characterized as expansion, erosion, or a combination of both by review of both CT and MR images. PET/CT studies were reviewed for tumor FDG avidity and for the presence of regional nodal or distant metastases. Standard uptake values were unavailable for most of the imaging studies and were not recorded. Similarly, CT and MR imaging technical parameters were not recorded because most imaging was performed at facilities outside of the tertiary centers where the patients were referred for treatment.

## RESULTS

### *Patient Characteristics*

Patient characteristics are summarized in the Table. There were 10 men and 7 women, with an average age of 54 years (range, 33–78 years; median 51 years). The initial pathologic diagnoses were sinonasal undifferentiated carcinoma in 5 patients, poorly differentiated carcinoma (squamous, basaloid, adeno, or not otherwise specified) in 6, myoepithelial carcinoma in 2, high-grade mixed germ cell tumor in 1, and *SMARCB1* (INI1) sinonasal carcinoma in 1. All but 1 patient presented with T4 disease ($n = 15$, T-stage was not available for 2 patients). There were no regional nodal metastases detected in the 12 patients for whom preoperative PET/CT was available. A contralateral mandibular lesion in patient 17 represented the only distant metastasis identified in this subgroup of 12 patients. All patients underwent surgery and variable chemoradiation regimens, and 10 patients were alive without evidence of disease at last available follow-up (average follow-up interval, 14.6 months; range, 1–48 months; median, 11 months). In patient 3, with a follow-up interval of 48 months, the initial pathology was reviewed at the time of suspected recurrence and the diagnosis amended from poorly differentiated adenocarcinoma to *SMARCB1* (INI1)-deficient carcinoma. To date, 4 patients with recurrence are alive and 3 have died.

### *Tumor Characteristics*

Tumor characteristics are summarized in the On-line Table, and representative images are provided in Figs 1 and 2. The most common tumor location was nasoethmoidal ($n = 8$), followed by nasal ($n = 5$) and sphenoethmoidal ($n = 2$), and 1 tumor was centered in the frontoethmoidal region with a large supraorbital component. Another very extensive tumor had components in the nasal cavity and ethmoid, sphenoid, and maxillary sinuses. There was epidural intracranial extension in 8 tumors and intradural extension in 3. Orbital invasion, present in 9 patients, was characterized as extraconal and/or conal in all. In patient 16, a tumor was identified in the cavernous sinus and foramen ovale; this tumor originated in the sphenoethmoidal region, and direct cavernous sinus invasion was suspected. In patient 10, only PET/CT was available and deemed insufficient to accurately assess potential intracranial, intraorbital, or perineural extension. In 2 other patients, imaging was deemed to be of insufficient quality to assess for perineural spread.

Precontrast CT images were available in 8 patients, and the tumor was isoattenuated to skeletal muscle in 6. Contrast en-

**FIG 1.** Patient 1. *A*, Coronal enhanced CT image shows moderately enhancing tumor in the nasoethmoidal region eroding the cribriform plate and ethmoid roof, with intracranial extension more conspicuous on the left (*dashed arrow*). There is also erosion through the right lamina papyracea with contact to the right superior oblique muscle (*solid arrow*). Bone changes in this case were deemed primarily erosive rather than expansile. *B*, Coronal enhanced and fat-suppressed T1WI shows avid heterogeneous enhancement in the transcranial mass. *C*, Coronal T2WI shows mild T2 hyperintensity of the transcranial mass compared with the cerebral cortex. Though there is signal abnormality in the left frontal lobe, no intradural disease was identified during surgical resection.

**FIG 2.** Patient 2. *A*, Coronal enhanced and fat-suppressed T1WI shows avid heterogeneous enhancement in right nasal cavity mass. There is no intracranial or orbital extension, and this mass was characterized as expansile. *B*, On this coronal STIR image, the mass is approximately isointense to cerebral cortex and can be distinguished from obstructive secretions in the adjacent ethmoid and maxillary sinuses. *C*, Coronal fused image from PET/CT examination demonstrates avid uptake in the right nasal cavity mass.

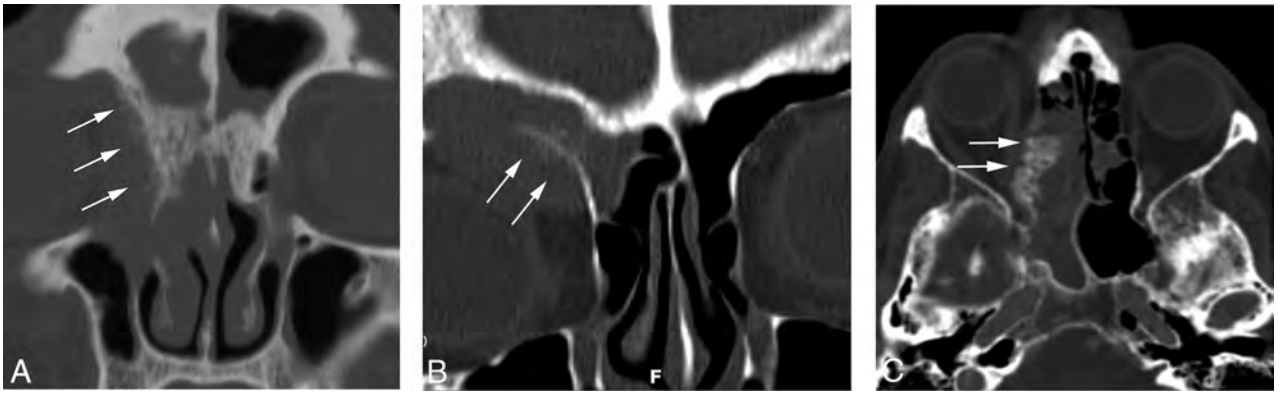


**FIG 3.** Calcification. *A*, Patient 9. Coronal CT bone image demonstrates spiculated, "hair on end" calcification along right medial orbital wall, with permeative lytic change in the adjacent bone (*arrows*). *B*, Patient 13. There is a similar pattern of "hair on end" calcification involving the floor of the right frontal sinus on this coronal CT image (*arrows*). In both patients, the involved bone is demineralized but not destroyed. *C*, Patient 11. There is a more solid, floccular pattern of calcification along the right medial orbital wall on this axial CT image (*arrows*).

hancement of the tumor was identified in all 7 patients for whom both pre- and postcontrast CT images were available. This was graded as moderate in 6 patients and avid in 1 and further characterized as heterogeneous in 6. Calcification was present in 6 of the 13 patients for whom CT imaging was available. In 3 patients, there was a spiculated "hair on end" pattern of calcification along the interface, with adjacent bone suggesting aggressive periosteal reaction (Fig 3). In patient 11, floccular calcification present along the margin of the tumor with the medial orbital wall was deemed to potentially represent a more solid pattern of periosteal

reaction. In 2 patients, stippled and curvilinear calcifications were present within the tumor, thought to likely represent retained bone fragments within a background of bone destruction. The impact on adjacent bony structures was assessed on both CT and MR imaging. Bone changes were classified as predominantly erosive in 9 patients, expansile in 5, and a combination of expansile and erosive in 3.

The tumor was isointense to cortex in 11 of the 14 patients for whom precontrast T1WI was available. In the remaining 3 patients, the tumor was graded as mildly hypointense. The tumor was variably mildly hypointense ($n = 4$), isointense ($n = 4$), moderately hyperintense ($n = 3$), and mildly hyperintense ($n = 3$) to cortex on T2WI. Enhancement was graded as avid in 11 of the 14 patients for whom postcontrast MR imaging was available, with the remaining tumors demonstrating moderate enhancement. Enhancement was additionally characterized as heterogeneous ($n = 7$) and homogeneous ($n = 7$). DWI was available for 9 patients. Most lesions ($n = 7$) showed moderate diffusion restriction.

FDG uptake was demonstrated in all 12 patients who underwent PET/CT scanning. Radiotracer uptake was graded as avid in 9 patients and moderate in 3.

## DISCUSSION

*SMARCB1* is a tumor-suppressor gene located on chromosome 22q11.2.[1,2,9,10] Deficiency of *SMARCB1* (INI1) was first implicated in malignant rhabdoid tumors of infancy, followed by rhabdoid tumor of the CNS, kidney, and soft tissue.[1,2,9,10] This list has since grown to include a diverse group of neoplasms in multiple anatomic sites, all of which are characterized by a rhabdoid appearance on cytopathologic examination and generally aggressive behavior.[1,2,9,10] The first descriptions of *SMARCB1* (INI1)-deficient neoplasms of the sinonasal tract were published simultaneously in the pathology literature by 2 separate groups in September 2014.[1,9] A third case series, completing a total of 16 reported cases, was published in September 2015.[2] Our series, with an additional 7 cases, represents the fourth report and the first detailed imaging description of this entity.

It is difficult to estimate the prevalence of this disease because most cases were initially diagnosed as other high-grade malignant tumors, most commonly sinonasal undifferentiated carcinoma and other poorly differentiated carcinomas often qualified as having rhabdoid or basaloid features. In their review of their own cases and those previously reported, Bell et al[2] found that *SMARCB1* (INI1)-deficient sinonasal carcinomas represented 3.3% of a combined series of 484 sinonasal primary tumors. However, Bishop et al[9] noted that *SMARCB1* (INI1)-deficient sinonasal carcinomas represented 14% of previously diagnosed sinonasal undifferentiated carcinomas.[9] More accurate estimates will likely be available once the diagnosis is more widely known in the head and neck oncologic community.

There are few sinonasal tumors with highly characteristic or pathognomonic imaging or clinical features, and this tumor is no exception. With regard to patient demographics, the wide age range and median age of 51 years overlap with virtually all sinonasal malignancies except those found in pediatric age groups, such as juvenile nasopharyngeal angiofibroma and rhabdomyosarcoma. A clear predilection for late-stage presentation was identified in our series, with only 1 patient staged below T4. However, this is the case in most aggressive sinonasal malignancies.[6,8,12,13] We found a predilection for central structures, with 13 of 17 tumors described as nasal or nasoethmoidal in origin, with frequent invasion into the adjacent orbital and intracranial compartments. Other sinonasal malignancies such as sinonasal undifferentiated carcinoma, esthesioneuroblastoma, lymphoma, and melanoma arise most frequently in the superior nasal cavity with similar patterns of invasion. The tendency toward avid enhancement, intermediate T2 signal intensity, moderate diffusion restriction, and FDG avidity demonstrated in our series is characteristic for sinonasal undifferentiated carcinoma and squamous cell carcinoma, which, though occurring most commonly in the paranasal sinuses (75%), must still be considered when nasal cavity masses are identified because of the high relative prevalence of this diagnosis.[1-4,7,12] CT imaging demonstrated associated calcification in close to half of the tumors (6 of 13), though no tumor calcification was reported on histopathologic analysis. In considering this discrepancy, we felt that calcification might reflect retained bone fragments in 2 patients and an aggressive periosteal reaction in 4. Nevertheless, our observed frequency of calcification on CT exceeds that reported in the literature, and the perpendicular "hair on end" appearance suggesting aggressive periosteal reaction is a particularly unusual feature.[5,7,12,14] A more accurate estimation of the incidence of this and other imaging features, and of their potential utility as indicators of this disease, will require a larger sample size.

### *Limitations*

In addition to the small sample size, other substantial limitations are related to the pooling of data from multiple centers. Much of the imaging reviewed was performed outside of these tertiary referral centers, and both imaging protocols and quality varied widely. Technical specifications of scanners and specifics of pulse sequence parameters were generally unavailable and were not compiled. There were similar limitations on the availability of clinical information, and length of follow-up was necessarily limited because of the short interval after initial description of the entity. There are few prospectively acquired data regarding imaging appearance of sinonasal malignancies, and available information is largely limited to relatively small case series such as ours. Therefore, comparisons with other sinonasal malignancies are fraught with similar limitations of small sample size and heterogeneous data.

## CONCLUSIONS

The recently described entity of *SMARCB1* (INI1)-deficient sinonasal carcinoma should be included in the differential diagnosis of a central sinonasal mass demonstrating aggressive imaging features, particularly when there is associated calcification. Overlap in clinical and imaging features of *SMARCB1* (INI1)-deficient carcinoma with other sinonasal malignancies, such as sinonasal undifferentiated carcinoma, underscores the challenges currently faced in diagnosis of these entities. The presence of rhabdoid features on cytopathologic examination will help alert pathologists and clinicians to the possibility of this diagnosis so confirmation

can be achieved using appropriate testing. As the diagnosis becomes more widely known, we anticipate the opportunity for larger series and more accurate assessment of clinical and imaging features of this disease.

## ACKNOWLEDGMENTS

The authors gratefully acknowledge contribution of case material from Drs. Justin A. Bishop and John M. DelGaudio.

Disclosures: Michelle A. Michel—*UNRELATED*: *Payment for Lectures (including service on speakers bureaus)*: iiCME, *Comments*: lectured at a continuing medical education course in January 2016 and received honoraria; *Royalties*: Elsevier, *Comments*: received a royalty check for prior contributions to *Diagnostic Imaging* textbooks; *Stock/Stock Options:* Fidelity, Transamerica, *Comments*: personal investments only.

## REFERENCES

1. Agaimy A, Koch M, Lell M, et al. **SMARCB1(INI1)-deficient sinonasal basaloid carcinoma: a novel member of the expanding family of SMARCB1-deficient neoplasms.** *Am J Surg Pathol* 2014;38:1274–81 CrossRef Medline
2. Bell D, Hanna EY, Agaimy, et al. **Reappraisal of sinonasal undifferentiated carcinoma: SMARCB1 (INI1)-deficient sinonasal carcinoma: a single-institution experience.** *Virchows Arch* 2015; 467:649–56 CrossRef Medline
3. Eggesbø HB. **Imaging of sinonasal tumours.** *Cancer Imaging* 2012; 12:136–52 CrossRef
4. Sen S, Chandra A, Mukhopadhyay S, et al. **Sinonasal tumors: computed tomography and MR imaging features.** *Neuroimaging Clin N Am* 2015;25:595–618 CrossRef Medline
5. Loevner LA, Sonners AI. **Imaging of neoplasms of the paranasal sinuses.** *Neuroimaging Clin N Am* 2004;14:625–46 CrossRef Medline
6. Lund VJ, Stammberger H, Nicolai P, et al. **European position paper on endoscopic management of tumours of the nose, paranasal sinuses and skull base.** *Rhinol Suppl* 2010;22:1–143 Medline
7. Phillips CD, Futterer SF, Lipper MH, et al. **Sinonasal undifferentiated carcinoma: CT and MR imaging of an uncommon neoplasm of the nasal cavity.** *Radiology* 1997;202:477–80 CrossRef Medline
8. Sen S, Chandra A, Mukhopadhyay S, et al. **Imaging approach to sinonasal neoplasms.** *Neuroimaging Clin N Am* 2015;25:577–93 CrossRef Medline
9. Bishop JA, Antonescu CR, Westra WH. **SMARCB1 (INI-1)-deficient carcinomas of the sinonasal tract.** *Am J Surg Pathol* 2014;38:1282–89 CrossRef Medline
10. Bishop JA. **Newly described tumor entities in sinonasal tract pathology.** *Head Neck Pathol* 2016;10:23–31 CrossRef Medline
11. Kalimuthu SN, Chetty R. **Gene of the month: SMARCB1.** *J Clin Pathol* 2016;69:484–89 CrossRef Medline
12. Sivalingam J, Sarawagi R, Raghuwanshi S, et al. **Sinonasal neoplasia: clinicopathological profile and importance of computed tomography.** *J Clin Diagn Res* 2015;9:TC01–4 CrossRef Medline
13. Xu CC, Dziegielewski PT, McGaw WT, et al. **Sinonasal undifferentiated carcinoma (SNUC): the Alberta experience and literature review.** *J Otolaryngol Head Neck Surg* 2013;42:2 CrossRef Medline
14. Rana RS, Wu JS, Eisenberg RL. **Periosteal reaction.** *AJR Am J Roentgenol* 2009;193:W259–72 CrossRef Medline

# MRI Evaluation of Non-Necrotic T2-Hyperintense Foci in Pediatric Diffuse Intrinsic Pontine Glioma

O. Clerk-Lamalice, W.E. Reddick, X. Li, Y. Li, A. Edwards, J.O. Glass, and Z. Patay

## ABSTRACT

**BACKGROUND AND PURPOSE:** The conventional MR imaging appearance of diffuse intrinsic pontine glioma suggests intralesional histopathologic heterogeneity, and various distinct lesion components, including T2-hypointense foci, have been described. Here we report the prevalence, conventional MR imaging semiology, and advanced MR imaging features of non-necrotic T2-hyperintense foci in diffuse intrinsic pontine glioma.

**MATERIALS AND METHODS:** Twenty-five patients with diffuse intrinsic pontine gliomas were included in this study. MR imaging was performed at 3T by using conventional and advanced MR imaging sequences. Perfusion (CBV), vascular permeability ($v_e$, $K^{trans}$), and diffusion (ADC) metrics were calculated and used to characterize non-necrotic T2-hyperintense foci in comparison with other lesion components, namely necrotic T2-hyperintense foci, T2-hypointense foci, peritumoral edema, and normal brain stem. Statistical analysis was performed by using Kruskal-Wallis and Wilcoxon rank sum tests.

**RESULTS:** Sixteen non-necrotic T2-hyperintense foci were found in 12 tumors. In these foci, ADC values were significantly higher than those in either T2-hypointense foci ($P = .002$) or normal parenchyma ($P = .0002$), and relative CBV values were significantly lower than those in either T2-hypointense ($P = .0002$) or necrotic T2-hyperintense ($P = .006$) foci. Volume transfer coefficient values in T2-hyperintense foci were lower than those in T2-hypointense ($P = .0005$) or necrotic T2-hyperintense ($P = .0348$) foci.

**CONCLUSIONS:** Non-necrotic T2-hyperintense foci are common, distinct lesion components within diffuse intrinsic pontine gliomas. Advanced MR imaging data suggest low cellularity and an early stage of angioneogenesis with leaky vessels resulting in expansion of the extracellular space. Because of the lack of biopsy validation, the underlying histoarchitectural and pathophysiologic changes remain unclear; therefore, these foci may correspond to a poorly understood biologic event in tumor evolution.

**ABBREVIATIONS:** DCE = dynamic contrast-enhanced; DIPG = diffuse intrinsic pontine glioma; $K^{trans}$ = volume transfer coefficient; rCBV = relative cerebral blood volume; $T2_{HoF}$ = T2-hypointense foci; $T2^{HrF}$ = T2-hyperintense foci; $v_e$ = fractional volume of the extravascular extracellular space

Most pediatric brain stem tumors are of glial origin.[1] The largest subgroup of brain stem gliomas is diffusely infiltrative; those originating from the pons are referred to as diffuse intrinsic pontine glioma (DIPG), and their outcomes are among the worst in pediatric neuro-oncology, with a median survival of <1 year from diagnosis.[2-4]

The diagnosis of DIPG relies heavily on conventional MR imaging, which has remarkably high accuracy for this purpose (approximately 95%–97%). The typical DIPG appears as a poorly marginated, intra-axial mass lesion that is centered on the ventral pons, involves >70% of the cross-sectional area of the brain stem, and exhibits ventral exophytism with more or less engulfment of the basilar artery.

The MR imaging appearance of DIPG suggests intralesional heterogeneity, and it is conceivable that all apparent lesion components and areas in heterogeneous tumors may not have the same pathologic relevance and diagnostic imaging significance. The prognostic value of conventional MR imaging features is controversial. Recently, investigators found that ring enhancement and small tumor size at diagnosis are associated with poor outcome.[5,6] Other MR imaging features, such as necrosis, intratumoral hemorrhage, and tumor extensions beyond the pons, while important at diagnosis, were not found to have predictive value for outcomes, likely because they are nonspecific for neoplastic processes and difficult to interpret, representing crude, indirect approximations of actual changes in tumor biology and burden.[7]

Received January 14, 2016; accepted after revision March 21.

From the Departments of Diagnostic Imaging (O.C.-L., W.E.R., A.E., J.O.G., Z.P.) and Biostatistics (X.L., Y.L.), St. Jude Children's Research Hospital, Memphis, Tennessee.

This work was supported, in part, by grant no. CA021765 from the National Cancer Institute and by the American Lebanese Syrian Associated Charities.

Please address correspondence to Zoltan Patay, MD, PhD, Department of Diagnostic Imaging, St. Jude Children's Research Hospital, MS220, 262 Danny Thomas Place, Memphis, TN 38105; e-mail: zoltan.patay@stjude.org

Indicates open access to non-subscribers at www.ajnr.org

http://dx.doi.org/10.3174/ajnr.A4814

Alternatively, advanced imaging characterization of distinct lesion components ("building blocks") with potentially distinct histopathologic and/or pathophysiologic interpretation may be more valuable, allowing a more direct and selective modular approach to the imaging evaluation of DIPG.

Several distinct lesion components or MR imaging features reflecting different forms or types of lesion heterogeneity in DIPG and other tumors, such as cysts, necrosis, and edema, have been described.[7] Furthermore, intratumoral T2-hypointense foci ($T2_{HoF}$) characterized by low ADC and high CBV values have been reported in 11.6% of patients and have been putatively attributed to foci of anaplasia.[8] Also, a peculiar form of postcontrast T1 signal enhancement ("occult enhancement") has been described in subtraction postcontrast T1-weighted images and was found to be associated with increased CBV[9]; hence, this type of enhancement is thought to correspond to the MR imaging substrate of intratumoral angioneogenesis.

A systematic review of a cohort of pediatric patients enrolled in a clinical trial for the treatment of DIPG led us to recognize a previously unreported lesion component in DIPG: solitary or multiple, relatively well-defined, intratumoral, non-necrotic T2-hyperintense foci ($T2^{HrF}$) that are typically associated with local mass effect. We, therefore, set out to evaluate and describe the prevalence, conventional MR imaging semiology, and advanced MR imaging features of non-necrotic $T2^{HrF}$ in DIPG in comparison with those of $T2_{HoF}$, necrotic $T2^{HrF}$, peritumoral edema, and normal brain stem.

## MATERIALS AND METHODS

### Patients

We reviewed and analyzed the baseline conventional and advanced MR imaging data of patients with newly diagnosed DIPG who were enrolled in an institutional review board–approved prospective phase I clinical trial (PDGFR [platelet-derived growth factor receptor] Inhibitor Crenolanib in Children/Young Adults With Diffuse Intrinsic Pontine Glioma or Recurrent High-Grade Glioma [SJPDGF]) in our institution between July 2011 and December 2013. The primary objective of that clinical trial was to evaluate the toxicity of crenolanib, an inhibitor of platelet-derived growth factor receptor–kinase, in children and young adults with newly diagnosed DIPG (or recurrent, progressive, or refractory high-grade gliomas, including DIPG). Consent was obtained from patients or legal representatives before enrollment. The full description of the SJPDGF trial protocol is available on-line (http://clinicaltrials.gov/ct2/show/NCT01393912).

Twenty-eight patients with newly diagnosed DIPG were initially enrolled in the SJPDGF study; however, after reviewing the available images, advanced MR imaging datasets, and the participants' medical records, we excluded 3 patients from the current study. Two patients were excluded because the MR imaging features and clinical evolution were uncharacteristic of DIPG and, in retrospect, more suggestive of a lower grade astrocytoma (ie, the patient was still alive 3 years after the initial diagnosis; tumor regressed and was stable after treatment). One other patient was excluded because of a very hemorrhagic tumor, which led to suboptimal DSC perfusion MR imaging datasets. Thus, 25 patients were included in the current study (14 females and 11 males; mean age, 6.94 years; age range, 2.08–17 years). No biopsies were performed; therefore, no histopathologic data were available for any of these patients at enrollment.

### Normative MR Imaging Data of the Pons

To establish normative diffusion and DSC perfusion values for the pons in children, we used advanced MR imaging data from an age-matched (mean age, 5.23 years; age range, 2–12 years) cohort of patients ($n = 17$) who had MR imaging studies for supratentorial CNS malignancies (5 pineoblastomas, 1 ependymoma, 1 astrocytoma, 1 anaplastic ganglioma, 1 choroid plexus carcinoma, 1 high-grade glioma, 3 primitive neuroectodermal tumors, and 4 atypical teratoid/rhabdoid tumors) at the time of initial diagnosis and who had no visible structural abnormalities in the posterior fossa. Conventional MR images were screened for any visible abnormality before analysis of advanced MR imaging data, and findings were unremarkable. The small SD of the ADC and CBV values in this cohort suggests homogeneity of the normative dataset.

### Conventional MR Imaging and IV Contrast Injection

While patients were under sedation or general anesthesia, all MR imaging studies were performed on 3T scanners (Magnetom Trio or Skyra; Siemens, Erlangen, Germany) by using 32-channel (Trio) or 20-channel (Skyra) phased array head coils. The standard conventional MR imaging protocol included axial T2-weighted turbo spin-echo (TR/TE = 3800/83 ms), pre- and postcontrast axial T1-weighted gradient-echo (TR/TE = 236/2.31 ms), and postcontrast FLAIR (TR/TE = 10,000/108 ms; TI = 2600 ms) sequences with a section thickness of 4 mm. Axial susceptibility-weighted images (TR/TE = 56/25 ms) had a section thickness of 2 mm. A total of 0.2 mL/kg (0.1 mmol/kg) of gadopentetate dimeglumine (Magnevist; Bayer HealthCare Pharmaceuticals, Wayne, New Jersey) was administered in all patients in 2 equally divided doses for the dynamic contrast-enhanced (DCE) and DSC perfusion MR imaging studies (see below) before performing the postcontrast T1-weighted imaging sequences. In all cases and for all contrast-enhanced sequences, Gd-DTPA was injected intravenously at a rate of 2 mL/s through a 22-ga IV catheter by using an infusion pump synchronized with the MR imaging scanner. A saline flush of 20 mL, also administered at a rate of 2 mL/s, followed each Gd-DTPA injection.

### Advanced MR Imaging

DCE-MR Imaging. First, 3 series of 3D gradient-echo images were collected to calculate T1 maps in the brain parenchyma (TR/TE = 5.3/3.2 ms; flip angle = 2°, 10°, and 20°). Subsequently, a total of 50 dynamic series of 16 images covering the brain stem and posterior fossa were acquired by using a 3D gradient-echo sequence with parallel imaging (TR/TE = 5/3.2 ms, generalized autocalibrating partially parallel acquisition accelerating factor R = 2, 24 reference lines, average = 1, flip angle = 15°, 16 sections, section thickness = 4 mm [no gap], matrix size = 128 × 128, in-plane resolution = 1.8 × 1.8 mm, temporal sampling = 6.84 seconds). The IV injection of Gd-DTPA (0.1 mL/kg) started 20 seconds after the initiation of the DCE sequence.

DSC-MR Imaging. The first dose of Gd-DTPA used for the DCE-MR imaging study served as preloading to allow leakage correction.[10-12] DSC–MR imaging data were obtained after a sec-

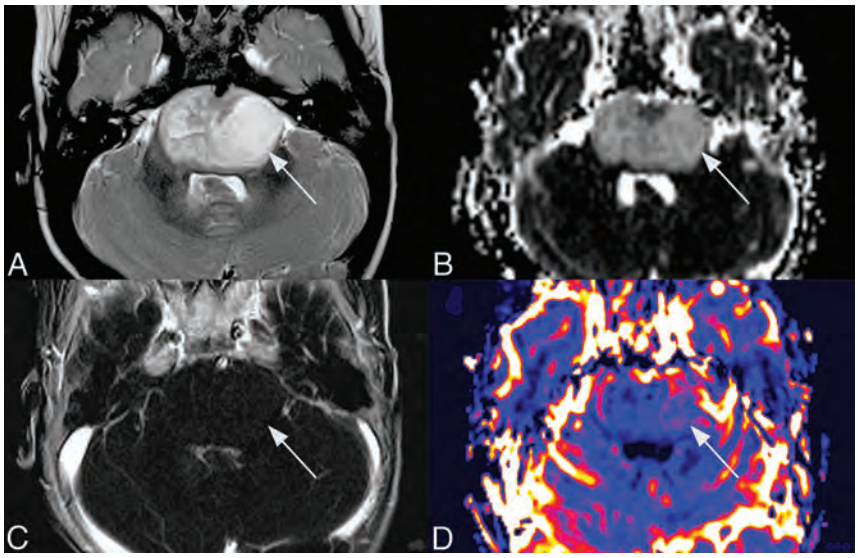


**FIG 1.** Axial MR images centered on the pons and showing non-necrotic $T2^{HrF}$ (*long arrow*). T2-weighted image (*A*), ADC map (*B*), TI-weighted postcontrast subtraction image (*C*), and CBV map (*D*). These images show a well-defined, fairly voluminous $T2^{HrF}$ within the left hemipons (a smaller similar lesion may be present on the right side, too), which is associated with mass effect, slightly increased signal in ADC (*B*), lack of contrast enhancement after IV gadolinium injection (*C*), and moderately increased CBV (*D*).

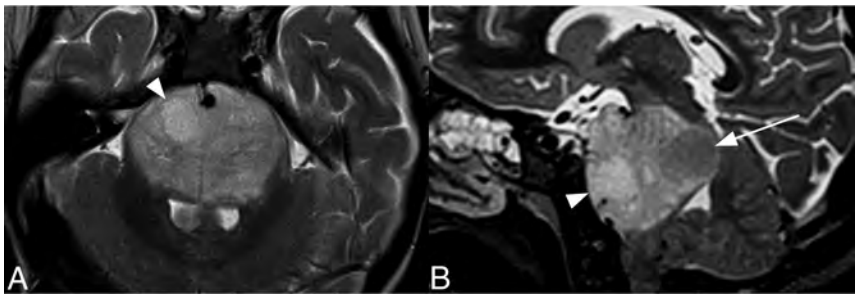


**FIG 2.** Axial (*A*) and sagittal (*B*) T2-weighted MR images of a DIPG with both non-necrotic $T2^{HrF}$ (*arrowhead*) and $T2_{HoF}$ (*long arrow*).

ond dose of Gd-DTPA (0.1 mL/kg) was injected 10 seconds after the beginning of the DSC sequence (single-shot free induction decay EPI, TR/TE = 1980/50 ms [Trio] and 2030/52 ms [Skyra], average = 1, flip angle = 90°, 16 contiguous sections, section thickness = 4 mm, matrix size = 256 × 256, in-plane resolution = 0.82 × 0.82 mm, 50 image sets, temporal sampling = 2.06 seconds).

Diffusion Imaging. Diffusion data were acquired by using a single-shot spin-echo EPI sequence (TR/TE = 6500/120 [Trio] and 7500/120 ms [Skyra], $b$=700 ms, section thickness = 3 mm, no gap, matrix size = 128 × 128, in-plane resolution = 1.5 × 1.5 mm). Twelve noncoplanar, noncollinear diffusion gradient directions and 4 acquisitions were used to calculate the diffusion tensor for each voxel within the images. ADC values were derived from the DTI dataset.

### *Image Analysis: Conventional MR Images*

Conventional MR images were jointly evaluated on a PACS workstation by a board-certified neuroradiologist (25 years of experience interpreting pediatric MR imaging studies) and a radiology resident (3 years of experience interpreting pediatric brain MR imaging studies). Before the extraction of advanced MR imaging data and statistical analysis, all MR imaging studies were reviewed twice, with a 1-week interval between reviews, to ensure consistency of results and minimize interobservation variance. Because of satisfactory correspondence, the latter was not further evaluated statistically.

Bidimensional tumor measurements were made at the level of the largest pontine cross-sectional lesion area by using a PACS workstation. Volumetric evaluations of the tumor lesions were made by using an in-house–developed C++ program to segment the tumor area on axial T2-weighted images from the pontomesencephalic-through-the-pontomedullary junction.

$T2^{HrF}$ was defined as a well-marginated, relative T2-hyperintense area (compared with the surrounding dominant "mean" T2-hyperintense signal) within the pontine lesion area. A distinction was made between necrotic and non-necrotic $T2^{HrF}$. A $T2^{HrF}$ was considered necrotic if its geometry and margins were irregular; the lesion typically had a thin, somewhat T2-hypointense rim with signal enhancement on postcontrast T1-weighted images. The presence of multiple prominent hypointensities (blood-degradation products) in the $T2^{HrF}$ on susceptibility-weighted images was also considered suggestive of necrosis. Conversely, a $T2^{HrF}$ was considered non-necrotic if the relative T2-hyperintense area was rounded or slightly oval, well-marginated without a T2-hypointense rim, free of hemorrhagic stigmata in susceptibility-weighted images, and without perceptible signal enhancement on postcontrast T1-weighted images. Non-necrotic $T2^{HrF}$ appear to be somewhat expansile; this appearance is best shown by the splaying of transverse pontine fibers or vertical transpontine fiber bundles in their proximity (Fig 1). Necrotic and non-necrotic $T2^{HrF}$ and $T2_{HoF}$ are not mutually exclusive: They may be seen in the same patient (Fig 2), and multiple foci of each type can be seen in the same tumor.

### *Postprocessing of Advanced MR Imaging Data*

Quantitative T1 maps, calculated from the variable flip angle images acquired before IV contrast administration, were used with a 2-compartment pharmacokinetic model[13] and an experimentally derived population-based arterial input function,[14] to analyze the DCE dataset and generate parametric maps of volume transfer coefficient ($K^{trans}$) and fractional volume of the extravascular extracellular space ($v_e$).

For the DSC perfusion datasets, an iterative automated process by using a Kohonen self-organizing map was used to identify

the arterial input function from a constrained set of images at the level of the basilar artery.[15] Additional DSC perfusion MR imaging data-processing was performed by a truncated, single-value deconvolution combined with a standard Tikhonov regularization and generalized cross-validation to yield parametric maps of CBV.

Voxelwise calculations of the diffusion datasets were performed by using the DTI toolkit in SPM8 (http://www.fil.ion.ucl.ac.uk/spm/). Parametric maps of ADC values were generated from these datasets.

Segmentation of the entire tumor lesion area in the pons was performed on axial T2-weighted images by using an in-house–developed C++ program.

To allow us to work in a common space and retrieve advanced imaging data, we coregistered raw images obtained from the DCE, DSC, and diffusion acquisitions to respective T2-weighted images by using FSL (http://www.fmrib.ox.ac.uk/fsl). To accommodate misregistration between T2 and echo-planar images, we used a kernel of 5 × 5 to erode the pons ROI to ensure alignment with the spatially normalized parametric maps.

### Image Analysis: Advanced MR Imaging

The mean and SD of each advanced MR imaging parametric value were calculated for 4 types of ROIs within the pontine tumor lesion: non-necrotic $T2^{HrF}$, $T2_{HoF}$, necrotic $T2^{HrF}$, and "none of the previous" (believed to correspond to edema). Also, mean normative ADC and CBV values for the entire pons of control patients were calculated.

All ROIs were manually drawn on T2 images by using in-house software coded in C++. Visual inspection of postcontrast T1 images was performed, when useful, to help more confidently classify and delimit the different foci. If a T2-hypointense or -hyperintense focus was appreciated on multiple axial T2 images, then the image passing by the center of the lesion was used to draw the representative ROI. We also calculated the mean sizes of all ROIs.

The ROIs drawn were then superimposed on the coregistered ADC, CBV, $K^{trans}$, and $v_e$ maps to calculate the mean values of each corresponding focus. To reduce CBV value variations related to technical and physiologic variations among patients, we created relative CBV (rCBV) values by normalizing CBV values within the ROIs to those of ROIs placed within normal-appearing cerebellar white matter. This normalization was performed by using an ROI drawn at the level of one of the middle cerebellar peduncles on axial T2 images and subsequently coregistered with CBV perfusion maps.

### Statistical Analysis

Perfusion (rCBV), tissue permeability ($v_e$, $K^{trans}$), and diffusion (ADC) metrics of the 4 ROI types were calculated and used in conjunction with normative brain stem values to characterize each of the 4 types of ROIs. The Kruskal-Wallis test was used to evaluate whether ADC, rCBV, $K^{trans}$, and $v_e$ values were significantly different among the different ROI types. Pair-wise comparisons through a Wilcoxon rank sum test adjusted by Bonferroni multiple testing correction were also performed. A $P$ value $< .05$ was considered significant. Bidimensional and volumetric tumor measurements and ROI areas are reported as mean values ± SD (range). Poisson regression models were used to determine whether there was any association between the patient's' age or tumor size and the number of non-necrotic $T2^{HrF}$. All statistical analyses were performed by using SAS 9.3 software (SAS Institute, Cary, North Carolina).

## RESULTS

### Conventional MR Imaging Results

Data from 25 tumors were used in this study. In all, 16 non-necrotic $T2^{HrF}$ were found in 12 patients (48% of patients); of these 12 patients, 2 patients had 2 $T2^{HrF}$ and 1 had 3 $T2^{HrF}$. Furthermore, 13 $T2_{HoF}$ were found in 8 patients (32%), and 9 necrotic $T2^{HrF}$ were found in 8 patients (32%) at initial diagnosis. The mean of non-necrotic $T2^{HrF}$, $T2_{HoF}$, and necrotic $T2^{HrF}$ were 299.19 ± 358.40 $mm^2$ (range, 24.22–1086.08 $mm^2$), 367.10 ± 450.74 $mm^2$ (range, 40.37–1249.60 $mm^2$), and 1216.18 ± 1215.06 $mm^2$ (range, 102.28–2788.49 $mm^2$), respectively.

The mean bidimensional measurements of the tumors were 4.48 ± 0.67 cm (range, 2.78–5.97 cm) × 3.62 ± 0.65 cm (range, 2.72–5.22 cm). The mean pontine tumor volume in our cohort was 29.65 ± 9.21 $cm^3$ (range, 9.56–49.56 $cm^3$). In addition to conventional features of DIPG (poorly marginated intra-axial mass lesion, involving >70% of the cross-sectional area of the pons, exhibiting ventral exophytism with, in some cases, engulfment of the basilar artery), we found that 12 patients (48%) had noticeable signal enhancement on conventional postcontrast T1-weighted images. In addition, no association was seen between the number of non-necrotic T2 foci and age ($P = .1297$) or tumor size ($P = .5727$).

### Advanced MR Imaging Results

The Table shows the quantitative values (mean ± SD) for each of the 4 advanced MR imaging–based surrogate biomarkers (ADC, rCBV, $K^{trans}$, $v_e$) in all 4 ROI categories: peritumoral edema, non-necrotic $T2^{HrF}$, $T2_{HoF}$, and necrotic $T2^{HrF}$. For normal brain stem parenchyma, only ADC and rCBV data were available.

ADC values in non-necrotic $T2^{HrF}$ were significantly higher than those in $T2_{HoF}$ ($P = .002$) or even normal brain parenchyma ($P = .0002$) and quite similar to values in peritumoral edema. Relative CBV values in non-necrotic $T2^{HrF}$ were significantly lower than those in $T2_{HoF}$ ($P = .0002$) or necrotic $T2^{HrF}$ ($P = .006$), similar to those in normal brain stem parenchyma and somewhat higher than those in perilesional edema. $K^{trans}$ values in $T2^{HrF}$ were significantly lower than those in $T2_{HoF}$ ($P = .0005$) or necrotic $T2^{HrF}$ ($P = .0348$) but only moderately higher than those in perilesional edema. For $v_e$, no significant differences were seen between non-necrotic $T2^{HrF}$ and other evaluated lesion components (Table and Fig 3).

## DISCUSSION

To allow more consistency in therapeutic trials (especially multicenter ones), standardization of reproducible and quantifiable imaging criteria is indispensable.[16] Simultaneously, there is a growing need for using more robust, quantitative advanced MR imaging–based biomarkers, which have more or

**Measurement of advanced MRI-based surrogate biomarkers in 5 regions[a]**

| Region | ADC ($\times 10^{-3}$ mm$^2$/s) | rCBV | $K^{trans}$ (min$^{-1}$) | $v_e$ |
|---|---|---|---|---|
| Normal brain stem ($n = 17$) | 0.75 ± 0.04 | 1.36 ± 0.21 | NA | NA |
| Peritumoral edema ($n = 22$) | 1.42 ± 0.27[b] | 1.04 ± 0.31[b] | 0.0028 ± 0.0020 | 0.0035 ± 0.0030 |
| Non-necrotic $T2^{HrF}$ ($n = 16$) | 1.48 ± 0.41[b,c] | 1.38 ± 0.68[c,d] | 0.0034 ± 0.0025[c,d] | 0.0057 ± 0.0042 |
| $T2_{HoF}$ ($n = 13$) | 0.82 ± 0.16[d,e] | 3.82 ± 1.32[b,e] | 0.0112 ± 0.0071[e] | 0.0163 ± 0.0184[e] |
| Necrotic $T2^{HrF}$ ($n = 9$) | 1.47 ± 0.23[b] | 3.61 ± 1.63[b,e] | 0.0108 ± 0.0072[e] | 0.0171 ± 0.0132[e] |

**Note:**—NA indicates not applicable.

[a] Mean values ± SD are shown. Statistical differences between groups ($P < .05$) are signified as follows:

[b] Normal brain stem.

[c] $T2_{HoF}$.

[d] Necrotic $T2^{HrF}$.

[e] Edema.

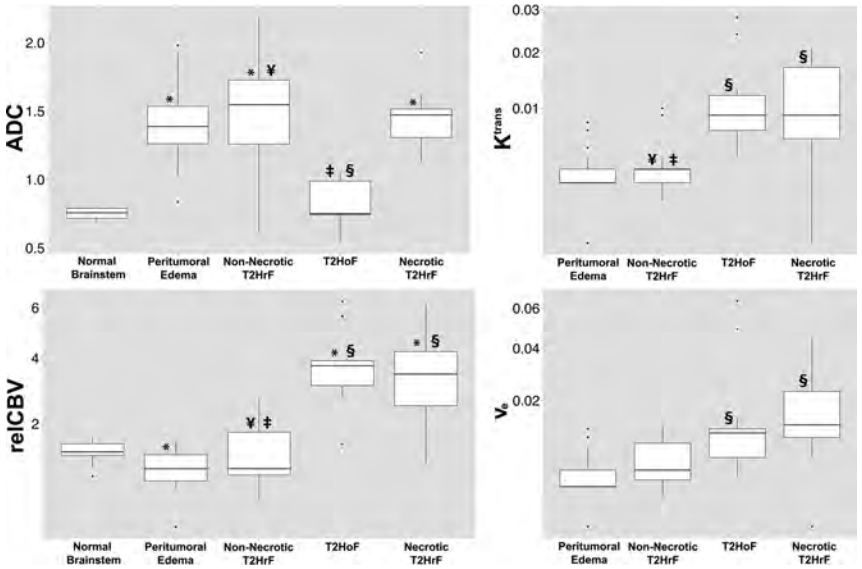


**FIG 3.** Boxplots of ADC, rCBV, $K^{trans}$, and $v_e$ for the different ROI types analyzed in DIPG. The y-axis of boxplots was rescaled for rCBV, $K^{trans}$, and $v_e$. Error bars represent SDs. Statistical differences between groups ($P < .05$) are signified as follows: The asterisk indicates normal brain stem, ¥, $T2_{HoF}$; ‡, necrotic $T2^{HrF}$; §, edema.

less validated histopathologic and/or pathophysiologic interpretation and which take into account microenvironmental factors such as blood supply, oxygenation, and metabolic activity, which are also known to influence drug delivery and therapeutic outcome.[17]

Recently, quantitative MR imaging–based biomarkers, which have more or less validated histopathologic and/or pathophysiologic interpretation, have become robust enough to be feasible in clinical settings. For example, DSC perfusion MR imaging–based biomarkers, rCBV in particular, are surrogate markers to quantitatively assess the vascular support system (ie, angioneogenesis) in tumors. ADC is a well-established surrogate for cell density in neoplastic processes. In addition, permeability metrics, such as $K^{trans}$ and $v_e$, characterize vessel wall integrity and the flux of bulk water from intravascular space into the extracellular compartment, allowing quantitation of vessel wall leakiness and resultant vasogenic edema.

The necessary next step is recognizing that tumors are not histopathologically or pathophysiologically homogeneous; therefore, evaluating a lesion as an all-inclusive whole may "dilute" critical information. To avoid this issue, one needs to define selective, targeted ROIs and draw them on specific parts of the tumor lesion. To define relevant, meaningful ROIs, we need to improve our ability to recognize distinct building blocks of tumors (eg, clones of densely packed tumor cells, areas of angioneogenesis, hemorrhage, and edema) on the basis of their conventional MR imaging appearance and to use advanced MR imaging techniques to characterize them. Previous investigators have already advocated this "modular approach" and described such "building blocks" that represent key histopathologic or pathophysiologic processes in DIPG, including $T2_{HoF}$ (focal anaplasia), "occult" enhancement (angioneogenesis), and petechial hemorrhages.[9,18]

Recently, histogram analysis has been used with success to quantify intratumoral heterogeneity. Histogram-derived parameters such as skewness, kurtosis, and percentiles have been found to be useful in differentiating types of gliomas.[19] Other investigators found that rCBV histograms correspond with glioma grades,[20] and ADC histograms can stratify progression-free survival in glioblastomas.[21,22] A similar technique has been used in DIPG to demonstrate significant intratumoral and interpatient mean diffusivity heterogeneity,[23] and shorter overall survival was found to be associated with increased ADC histogram skewness.[24] Although these studies have undeniable merits, in this research, we took a different approach. We believe that it is important to identify distinct "building blocks" in tumors on the basis of their conventional features, characterize those by using advanced MR imaging techniques, and provide putative histopathologic and pathophysiologic interpretations.

Our advanced MR imaging data allow some speculation about the underlying histoarchitectural and pathophysiologic mechanisms occurring intrinsically within these foci. Our data suggest that non-necrotic $T2^{HrF}$ are potentially evaluable distinct lesion components in DIPG (and possibly in other tumors of the CNS). Non-necrotic $T2^{HrF}$ appear to be more common than are $T2_{HoF}$ or necrotic $T2^{HrF}$. Non-necrotic and necrotic $T2^{HrF}$ may exhibit similarities other than T2 hypersignal on conventional MR imaging, such as mass effect splaying transverse pontine fibers. However, non-necrotic $T2^{HrF}$ typically do not show peripheral enhancement or punctate microhemorrhagic foci, which are common in necrotic foci.

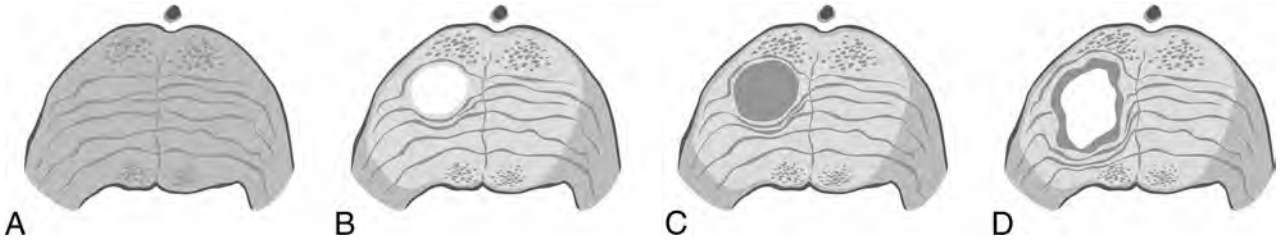


**FIG 4.** Feature comparison of the 4 ROIs. *A*, Normal brain stem. *B*, A non-necrotic $T2^{HrF}$ is a well-circumscribed intratumoral area exhibiting high T2 signal and is often associated with local mass effect on surrounding structures, shown by splaying transverse pontocerebellar fibers. *C*, $T2_{HoF}$ are characterized by low T2 signal and are locally expansile. *D*, Necrotic $T2^{HrF}$ exhibit irregular margins, central T2 hypersignal, peripheral T2 hyposignal, and postcontrast signal enhancement. On the basis of their advanced MR imaging features, we speculate that non-necrotic $T2^{HrF}$, $T2_{HoF}$, and necrotic $T2^{HrF}$, while possibly coexisting, may indicate sequential steps in the evolution of tumor cell populations (clones).

Previous work in adult supratentorial glioma[25] and in DIPG[26] suggested that higher ADC values correlate with lower tumor cellularity and grade. Furthermore, patients with DIPG having higher ADC values seem to have longer survival times.[27] Because of the high frequency of such foci in DIPG, it is reasonable to speculate that non-necrotic $T2^{HrF}$ might contribute to higher ADC values within DIPG and represent a relatively "good" prognostic biomarker. Conversely, $T2^{HoF}$ may indicate the presence of more aggressive tumor cell populations (focal anaplasia).[8] Elevated ADC may indicate low relative cellular density within $T2^{HrF}$ and/or considerable vasogenic edema, which could indicate the presence of a small-but-aggressive population of tumor cells, possibly undergoing malignant transformation.

A positive correlation between histologic grade and rCBV in adult supratentorial gliomas has been established by other investigators.[28-30] In our study, perfusion metrics (rCBV) showed a relatively broad range within non-necrotic $T2^{HrF}$. Overall, they were higher than those in edema and, in some individual cases (4 patients), than in normal brain stem parenchyma (Fig 1). Relative CBV values in non-necrotic $T2^{HrF}$ are not elevated as much as in $T2_{HoF}$. This could be interpreted as an early stage of angioneogenesis in non-necrotic $T2^{HrF}$, despite the lack of apparent "occult" enhancement.

Elevated $K^{trans}$ values in $T2_{HoF}$ and necrotic $T2^{HrF}$ indicate higher tumor grade.[31,32] Volume transfer constants between the intravascular plasma and extravascular, interstitial compartments in non-necrotic $T2^{HrF}$ are somewhat higher than those in edema but not as high as those in $T2_{HoF}$ or necrotic $T2^{HrF}$. Quite remarkably, extravascular extracellular space volume fraction ($v_e$) values increase almost linearly from edema to non-necrotic $T2^{HrF}$ to $T2_{HoF}$ to necrotic $T2^{HrF}$ tissues; this increase suggests a trend in global vessel wall permeability, in other words, an increasing proportion of leaky vessels, characteristic of angioneogenesis.

On the basis of this information, one cannot help speculating that non-necrotic $T2^{HrF}$, $T2_{HoF}$, and necrotic $T2^{HrF}$, though possibly coexisting, may indicate sequential steps in the evolution of tumor cell populations (clones). When a biopsy is performed, initial diagnostic specimens in DIPG often indicate fibrillary astrocytoma,[33] but postmortem specimens almost invariably correspond to high-grade glioma.[34] We, therefore, hypothesize that non-necrotic $T2^{HrF}$ may be a precursor of $T2_{HoF}$, which may thereafter evolve to necrotic $T2^{HrF}$. Non-necrotic $T2^{HrF}$ would correspond to an emerging clone of cells undergoing malignant transformation, with yet relatively low density of aggressive, highly edematigenous cells, inducing early angioneogenesis. In non-necrotic $T2^{HrF}$, edema may be the dominant pathophysiologic phenomenon associated with expansion of the extracellular space and the resultant local mass effect. As cellular density increases, a $T2_{HoF}$ develops and angioneogenesis leads to a dense microvascular network, which is seen as occult enhancement in postcontrast subtraction T1-weighted images. As the vascular support system becomes insufficient, $T2_{HoF}$ ultimately undergo necrosis; hence, necrotic $T2^{HrF}$ develop (Fig 4).

### *Limitations*

Besides its obvious virtues (prospective design, relatively large patient cohort), this study has several limitations, most important, the lack of histopathologic correlations and longitudinal follow-up data. In our center, diagnostic biopsies are rarely performed at the initial diagnosis of DIPG. We evaluated non-necrotic $T2^{HrF}$ (and other distinct lesion foci) only at baseline because all patients were enrolled in a clinical trial using a new investigational drug (crenolanib) in addition to conformal radiation therapy. These therapies are expected to alter tumor biology and hence represent confounders rendering the assessment of the natural evolution of various lesion components impossible. Therefore, our proposal of the sequential nature of the various distinct lesion foci remains speculative, though supported by advanced MR imaging data obtained by us and other investigators.

## CONCLUSIONS

Our data and previous reports by other investigators advocate the value of the "modular" approach to the MR imaging evaluation of DIPG, by using multiparametric quantitative analysis of distinct lesion components for staging and, possibly, monitoring during treatment. We postulate that non-necrotic $T2^{HrF}$ are common, distinct, lesion components within DIPG. Advanced MR imaging data suggest that they are characterized by relatively low cellularity, and somewhat increased vascular permeability without substantial increase in the blood volume fraction, the latter suggesting an early stage of angioneogenesis with leaky vessels. We speculate that these foci may correspond to poorly understood biologic events in tumor evolution, pos-

sibly representing clones of transforming cell populations evolving toward foci of anaplasia. Future work is needed to acquire histopathologic validation of our findings and the derived hypotheses and to determine the value of various distinct tumor components (eg, $T2^{HrF}$, $T2_{HoF}$) in the prognostication of key outcome metrics, such as progression-free survival and overall survival.


## ACKNOWLEDGMENTS

The authors thank Cherise M. Guess, PhD, ELS, for reviewing and editing the manuscript and Edwina Anderson for data management.

Disclosures: Olivier Clerk-Lamalice—*RELATED*: National Cancer Institute,* American Lebanese Syrian Associated Charities. Zoltan Patay—*RELATED*: *Grant*: National Cancer Institute (P30 CA021765)*; *UNRELATED*: *Travel/Accommodations/Meeting Expenses Unrelated to Activities Listed*: Sao Paulo Radiological Society, European Society of Neuroradiology, Erasmus Course in MRI, European Course in Pediatric Neuroradiology, Hamad Medical Corporation, China International Forum of Pediatric Development, Indian Society of Neuroradiology, *Comments*: Sao Paulo Radiological Society (2013), travel and accommodations for lecturing; European Society of Neuroradiology (2015), travel and accommodations for invited lecture; Erasmus Course in MRI (2013, 2014, 2015), travel and accommodations for lecturing; European Course On Pediatric Neuroradiology (2014), travel and accommodations for lecturing; Hamad Medical Corporation (2014, 2015), travel and accommodations for lecturing at a symposium in Doha, Qatar; China International Forum (2015), travel and accommodations for lecturing; International Symposium on Neural Regeneration (2013), travel and accommodations for lecturing. *Money paid to the institution.


## REFERENCES


1. Ostrom QT, Gittleman H, Liao P, et al. **CBTRUS statistical report: primary brain and central nervous system tumors diagnosed in the United States in 2007–2011.** *Neuro Oncol* 2014;16(suppl 4):iv1–iv63 CrossRef Medline
2. Warren KE. **Diffuse intrinsic pontine glioma: poised for progress.** *Front Oncol* 2012;2:205 CrossRef Medline
3. Broniscer A, Baker JN, Tagen M, et al. **Phase I study of vandetanib during and after radiotherapy in children with diffuse intrinsic pontine glioma.** *J Clin Oncol* 2010;28:4762–68 CrossRef Medline
4. Broniscer A, Baker SD, Wetmore C, et al. **Phase I trial, pharmacokinetics, and pharmacodynamics of vandetanib and dasatinib in children with newly diagnosed diffuse intrinsic pontine glioma.** *Clin Cancer Res* 2013;19:3050–58 CrossRef Medline
5. Poussaint TY, Kocak M, Vajapeyam S, et al. **MRI as a central component of clinical trials analysis in brainstem glioma: a report from the Pediatric Brain Tumor Consortium (PBTC).** *Neuro Oncol* 2011; 13:417–27 CrossRef Medline
6. Jansen MH, Veldhuijzen van Zanten SE, Sanchez Aliaga E, et al. **Survival prediction model of children with diffuse intrinsic pontine glioma based on clinical and radiological criteria.** *Neuro Oncol* 2015; 17:160–66 CrossRef Medline
7. Hargrave D, Chuang N, Bouffet E. **Conventional MRI cannot predict survival in childhood diffuse intrinsic pontine glioma.** *J Neurooncol* 2008;86:313–19 Medline
8. Löbel U, Sedlacik J, Reddick WE, et al. **Quantitative diffusion-weighted and dynamic susceptibility-weighted contrast-enhanced perfusion MR imaging analysis of T2 hypointense lesion components in pediatric diffuse intrinsic pontine glioma.** *AJNR Am J Neuroradiol* 2011;32:315–22 CrossRef Medline
9. Conway AE, Reddick WE, Li Y, et al. **"Occult" post-contrast signal enhancement in pediatric diffuse intrinsic pontine glioma is the MRI marker of angiogenesis?** *Neuroradiology* 2014;56:405–12 CrossRef Medline
10. Paulson ES, Schmainda KM. **Comparison of dynamic susceptibility-weighted contrast-enhanced MR methods: recommendations for measuring relative cerebral blood volume in brain tumors.** *Radiology* 2008;249:601–13 CrossRef Medline
11. Hu LS, Baxter LC, Pinnaduwage DS, et al. **Optimized preload leakage-correction methods to improve the diagnostic accuracy of dynamic susceptibility-weighted contrast-enhanced perfusion MR imaging in posttreatment gliomas.** *AJNR Am J Neuroradiol* 2010;31: 40–48 CrossRef Medline
12. Boxerman JL, Prah DE, Paulson ES, et al. **The role of preload and leakage correction in gadolinium-based cerebral blood volume estimation determined by comparison with MION as a criterion standard.** *AJNR Am J Neuroradiol* 2012;33:1081–87 CrossRef Medline
13. Tofts PS, Brix G, Buckley DL, et al. **Estimating kinetic parameters from dynamic contrast-enhanced T(1)-weighted MRI of a diffusable tracer: standardized quantities and symbols.** *J Magn Reson Imaging* 1999;10:223–32 Medline
14. Parker GJM, Roberts C, Macdonald A, et al. **Experimentally-derived functional form for a population-averaged high-temporal-resolution arterial input function for dynamic contrast-enhanced MRI.** *Magn Reson Med* 2006;56:993–1000 CrossRef Medline
15. Harreld JH, Helton KJ, Kaddoum RN, et al. **The effects of propofol on cerebral perfusion MRI in children.** *Neuroradiology* 2013;55: 1049–56 CrossRef Medline
16. Ellingson BM, Bendszus M, Boxerman J, et al; Jumpstarting Brain Tumor Drug Development Coalition Imaging Standardization Steering Committee. **Consensus recommendations for a standardized Brain Tumor Imaging Protocol in clinical trials.** *Neuro Oncol* 2015; 17:1188–98 CrossRef Medline
17. Just N. **Improving tumour heterogeneity MRI assessment with histograms.** *Br J Cancer* 2014;111:2205–13 CrossRef Medline
18. Löbel U, Sedlacik J, Sabin ND, et al. **Three-dimensional susceptibility-weighted imaging and two-dimensional T2*-weighted gradient-echo imaging of intratumoral hemorrhages in pediatric diffuse intrinsic pontine glioma.** *Neuroradiology* 2010;52:1167–77 CrossRef Medline
19. Just N. **Histogram analysis of the microvasculature of intracerebral human and murine glioma xenografts.** *Magn Reson Med* 2011;65: 778–89 CrossRef Medline
20. Law M, Young R, Babb J, et al. **Histogram analysis versus region of interest analysis of dynamic susceptibility contrast perfusion MR imaging data in the grading of cerebral gliomas.** *AJNR Am J Neuroradiol* 2007;28:761–66 Medline
21. Pope WB, Kim HJ, Huo J, et al. **Recurrent glioblastoma multiforme: ADC histogram analysis predicts response to bevacizumab treatment.** *Radiology* 2009;252:182–89 CrossRef Medline
22. Pope WB, Qiao XJ, Kim HJ, et al. **Apparent diffusion coefficient histogram analysis stratifies progression-free and overall survival in patients with recurrent GBM treated with bevacizumab: a multicenter study.** *J Neurooncol* 2012;108:491–98 CrossRef Medline
23. Steffen-Smith EA, Sarlls JE, Pierpaoli C, et al. **Diffusion tensor histogram analysis of pediatric diffuse intrinsic pontine glioma.** *Biomed Res Int* 2014;2014:647356 CrossRef Medline
24. Poussaint TY, Vajapeyam S, Ricci KI, et al. **Apparent diffusion coefficient histogram metrics correlate with survival in diffuse intrinsic pontine glioma: a report from the Pediatric Brain Tumor Consortium.** *Neuro Oncol* 2015 Oct 20. [Epub ahead of print] Medline
25. Sugahara T, Korogi Y, Kochi M, et al. **Usefulness of diffusion-weighted MRI with echo-planar technique in the evaluation of cellularity in gliomas.** *J Magn Reson Imaging* 1999;9:53–60 Medline
26. Lober RM, Cho YJ, Tang Y, et al. **Diffusion-weighted MRI derived apparent diffusion coefficient identifies prognostically distinct subgroups of pediatric diffuse intrinsic pontine glioma.** *J Neurooncol* 2014;117:175–82 CrossRef Medline
27. Chen HJ, Panigrahy A, Dhall G, et al. **Apparent diffusion and fractional anisotropy of diffuse intrinsic brain stem gliomas.** *AJNR Am J Neuroradiol* 2010;31:1879–85 CrossRef Medline
28. Al-Okaili RN, Krejza J, Woo JH, et al. **Intraaxial brain masses: MR imaging–based diagnostic strategy—initial experience.** *Radiology* 2007;243:539–50 CrossRef Medline
29. Law M, Yang S, Wang H, et al. **Glioma grading: sensitivity, specificity, and predictive values of perfusion MR imaging and proton MR**

**spectroscopic imaging compared with conventional MR imaging.** *AJNR Am J Neuroradiol* 2003;24:1989–98 Medline
30. Law M, Young RJ, Babb JS, et al. **Gliomas: predicting time to progression or survival with cerebral blood volume measurements at dynamic susceptibility-weighted contrast-enhanced perfusion MR imaging.** *Radiology* 2008;247:490–98 CrossRef Medline
31. Cha S. **Dynamic susceptibility-weighted contrast-enhanced perfusion MR imaging in pediatric patients.** *Neuroimaging Clin N Am* 2006;16:137–47, ix CrossRef Medline
32. Roberts HC, Roberts TP, Brasch RC, et al. **Quantitative measurement of microvascular permeability in human brain tumors achieved using dynamic contrast-enhanced MR imaging: correlation with histologic grade.** *AJNR Am J Neuroradiol* 2000;21:891–99 Medline
33. Schumacher M, Schulte-Mönting J, Stoeter P, et al. **Magnetic resonance imaging compared with biopsy in the diagnosis of brainstem diseases of childhood: a multicenter review.** *J Neurosurg* 2007;106(2 suppl):111–19 CrossRef Medline
34. Yoshimura J, Onda K, Tanaka R, et al. **Clinicopathological study of diffuse type brainstem gliomas: analysis of 40 autopsy cases.** *Neurol Med Chir (Tokyo)* 2003;43:375–82; discussion 382 Medline

# Volumetric Description of Brain Atrophy in Neuronal Ceroid Lipofuscinosis 2: Supratentorial Gray Matter Shows Uniform Disease Progression

U. Löbel, J. Sedlacik, M. Nickel, S. Lezius, J. Fiehler, I. Nestrasil, A. Kohlschütter, and A. Schulz

## ABSTRACT

**BACKGROUND AND PURPOSE:** Experimental therapies for ceroid lipofuscinosis, neuronal, 2 (CLN2), a genetic disorder of childhood associated with progressive brain atrophy, are currently being developed. Because quantitative descriptions of the natural course of brain volume loss are needed to evaluate novel therapies, we performed MR imaging volumetry of patients with CLN2 to identify a suitable MR imaging marker of disease progression.

**MATERIALS AND METHODS:** Thirteen patients (8 females, 5 males) were recruited from a prospective natural disease cohort of patients with neuronal ceroid lipofuscinosis. Repeated MR imaging volumetric analysis (29 datasets) was performed by using the FreeSurfer Software Suite. Follow-up time ranged from 8 months to 5.3 years. MR imaging–segmented brain volumes were correlated to patient age and clinical scores.

**RESULTS:** Segmented brain volumes correlated significantly with patient age (lateral ventricles, $r = 0.606$, $P = .001$; supratentorial cortical GM, $r = -0.913$, $P < .001$; supratentorial WM, $r = -0.865$, $P < .001$; basal ganglia/thalamus, $r = -0.832$, $P < .001$; cerebellar GM, $r = -0.659$, $P < .001$; cerebellar WM, $r = -0.830$, $P < .001$) and clinical scores (lateral ventricles, $r = -0.692$, $P < .001$; supratentorial cortical GM, $r = 0.862$, $P < .001$; supratentorial WM, $r = 0.735$, $P < .001$; basal ganglia/thalamus, $r = 0.758$, $P < .001$; cerebellar GM, $r = 0.609$, $P = .001$; cerebellar WM, $r = 0.638$, $P < .001$). Notably, supratentorial cortical GM showed a uniform decline across the patient cohort. During late stages of the disease when the clinical score was zero, segmented brain volumes still correlated with patient age; this finding suggests that MR imaging volumetry allows quantitative assessment of disease progression at stages when it cannot be detected by clinical assessment alone.

**CONCLUSIONS:** Automated MR imaging volumetry, as a nonsubjective and highly sensitive tool, is feasible in CLN2 disease and provides a quantitative basis to evaluate novel experimental therapies.

**ABBREVIATIONS:** CLN = ceroid lipofuscinosis, neuronal; NCL = neuronal ceroid lipofuscinoses; TPP1 = tripeptidyl-peptidase-1

Neuronal ceroid lipofuscinoses (NCL) are a group of neurodegenerative disorders with onset in childhood and are typically inherited in an autosomal recessive fashion. Their incidence in European countries ranges from 1:14,000 to 1:100,000.[1] To date, at least 13 different genetic defects, ceroid lipofuscinosis neuronal (CLN) 1–14, are known.[2] They form the basis of a novel classification system that includes the genetic defect and the time of disease onset (eg, CLN2, late-infantile).[3]

CLN2 is one of the most common forms of NCL (MIM No. 204500). It is caused by mutations in the *CLN2* gene, which codes for the lysosomal enzyme tripeptidyl-peptidase-1 (TPP1). TPP1 is a serine protease responsible for the breakdown of certain neuropeptides. A deficiency of TPP1 leads to an accumulation of lysosomal storage material in different cell types, including neurons, astrocytes, vascular endothelial and smooth-muscle cells, fibroblasts, adipocytes, and skeletal muscle.[2] CLN2 disease subsequently leads to neuronal degeneration and brain atrophy. Patients with CLN2 have epilepsy and a decline in cognition,

Received December 22, 2015; accepted after revision March 21, 2016.

From the Departments of Diagnostic and Interventional Neuroradiology (U.L., J.S., J.F.), Pediatrics (M.N., A.K., A.S.), and Medical Biometry and Epidemiology (S.L.), University Medical Center Hamburg-Eppendorf, Hamburg, Germany; and Department of Pediatrics (I.N.), University of Minnesota, Minneapolis, Minnesota.

The research leading to this publication received funding from the European Union Seventh Framework Program as part of the project "DEM-CHILD" (Grant agreement number 281234 to Angela Schulz) and from the German Federal Ministry of Education and Research (Grant NCL2Treat to Angela Schulz).

Paper previously presented at: European Society of Magnetic Resonance in Neuropediatrics, May 14–16, 2015; Porto, Portugal.

Please address correspondence to Ulrike Löbel, MD, Department of Diagnostic and Interventional Neuroradiology, O-22, Martinistr 52, 20246 Hamburg, Germany; e-mail: u.loebel@uke.de

Indicates open access to non-subscribers at www.ajnr.org

Indicates article with supplemental on-line table.

http://dx.doi.org/10.3174/ajnr.A4816

language, and gross motor function starting at 2–4 years of age. The disease rapidly progresses, with loss of vision due to optic atrophy and macular and retinal changes occurring in later disease stages.[4] Nonclassic presentations (ie, juvenile, adult, or infantile onset) exist as well.[3,5-8]

On conventional MR imaging, a marked supratentorial and infratentorial atrophy with ventriculomegaly is the typical finding. In addition, a progressive-but-mild increase of WM signal intensity on T2WI and increased ADC values are observed.[9,10] These findings have been largely related to myelin loss and gliosis[11] and contrast with the decreasing ADC values observed during normal brain maturation and myelination.[12] Longitudinal MR imaging is rarely performed in patients with NCL because therapeutic options do not exist. Longitudinal MR brain volumetric studies have only been reported for CLN3 disease,[13] and only 1 cross-sectional study in patients with CLN2, focusing on the size of CSF spaces, is available.[14]

The purpose of our study was to test our hypothesis that MR imaging brain volumetry provides a quantitative tool to assess the natural course of disease progression in CLN2 disease. More specifically, we hypothesized that GM volumes would be more strongly linked to the clinical disease course compared with WM regions and CSF spaces because CLN2 primarily involves the degeneration of neurons in the cerebral and cerebellar cortices. We aimed to establish reference values for current and future clinical studies (intraventricular enzyme replacement [NCT01907087], gene therapy [NCT01414985]; www.clinicaltrials.gov).

## MATERIALS AND METHODS

### Patients

Thirteen patients with confirmed defects of the *CLN2* gene underwent MR imaging between 2008 and 2015 (On-line Table). Two patients are identical twins (457–1 and 457–2). Approval from the local ethics committee and written informed consent from the parents were obtained before inclusion of the patients into the study.

### Clinical Scoring

The clinical course was assessed by using an established clinical rating scale for CLN2 disease.[15] The scale represents a 12-point inventory of disease-based clinical assessments. The original scale consists of 4 functional domains: motor, language, vision, and tonic-clonic seizures. Within each domain, scores ranging from 0 to 3 are given, with 0 representing the absence of function and 3, the age-appropriate normal function. The clinical score for tonic-clonic seizures may be strongly influenced by the individual pharmacologic management of each patient and may show high variability. Therefore, it was not used in this study. To address the period before the diagnosis of CLN2 disease, we performed ratings retrospectively on the basis of patient charts and parent interviews. Once the diagnosis of CLN2 was established, ratings were obtained prospectively at 6-month intervals at the NCL specialty clinic in Hamburg. Three independent raters performed the clinical scoring, and the average score of all 3 raters was used for the final result. Patient characteristics and clinical scores are summarized in the On-line Table.

### Imaging

MR imaging was performed on a 1.5T scanner (Avanto; Siemens, Erlangen, Germany). Most children required either sedation or general anesthesia to obtain adequate images. The imaging protocol included conventional MR imaging sequences (ie, FLAIR, T2WI, DWI) and a 3D-T1-weighted MPRAGE sequence (TR/TE/TI/flip angle, 1900/2.97/1100 ms/15°; matrix, 256 × 176; voxel size, 1 × 1 × 1 $mm^3$; whole-brain coverage), which was used for the volumetric analysis. Initially, the 3D-T1-weighted MPRAGE sequence was acquired in the axial plane. Due to relatively long observation periods and updates to the software of the scanner, scans were later acquired in the sagittal plane (TR/TE/TI/flip angle, 2280/3.64/1000 ms/8°; matrix, 256 × 256; voxel size, 1 × 1 × 1 $mm^3$).

### Data Evaluation

We performed brain segmentation by using the FreeSurfer Software Suite (stable Version 5.3.0, May 15, 2013; http://surfer.nmr.mgh.harvard.edu), while disabling the skull-stripping option of FreeSurfer.[16]

Before the segmentation in FreeSurfer, soft tissue and skull were removed by using the Brain Extraction Tool in FSL (BET, Version 2.1, FSL release 5.0, September 2012; http://fsl.fmrib.ox.ac.uk/fsl/fslwiki/BET).[17] Several options for brain extraction were tested for each dataset, including robust brain center estimation, bias field and neck cleanup, and different fractional intensity threshold "f" values for the "standard_space_roi" command. We found that an optimal brain extraction, defined as removal of as much extracranial tissue as possible without removing brain tissue, could be achieved by using either robust brain estimation or the standard_space_roi command at f = 0.15. For patients with >1 study, the longitudinal processing pipeline was used with an intraindividual consistent skull-stripping mask. After segmentation, all datasets were checked visually for major segmentation errors (ie, obvious errors of GM and WM segmentation, inclusion of large amounts of dural venous sinuses or soft tissue). Such studies would have resulted in exclusion from the final analysis. No manual corrections for small segmentation errors were performed to ensure standardized processing.

Of the large number of brain structures segmented by FreeSurfer, the following regions were used for further evaluation based on our hypothesis: supratentorial cortical GM (ie, total cortical GM volume), supratentorial WM (ie, total cortical WM volume), deep GM structures (sum of segmented regions of caudate nucleus, putamen, pallidum, and thalamus), cerebellar GM, cerebellar WM, and lateral ventricles (sum of the lateral ventricles and choroid plexus).

### Statistical Analysis

For the assessment of correlation between different variables, the Pearson correlation coefficient ($r$) was calculated. A linear correlation was assumed. The first step included the calculation of a correlation of volumetric data and clinical scoring with the age of the patients. Then, a correlation analysis of volumetric data to the overall clinical scoring was performed. Because the clinical score was zero for 15 of 29 data points, the analysis was also performed for clinical scores of <1 to demonstrate the ability of the volumetric data to deliver reliable measurements of disease progression,

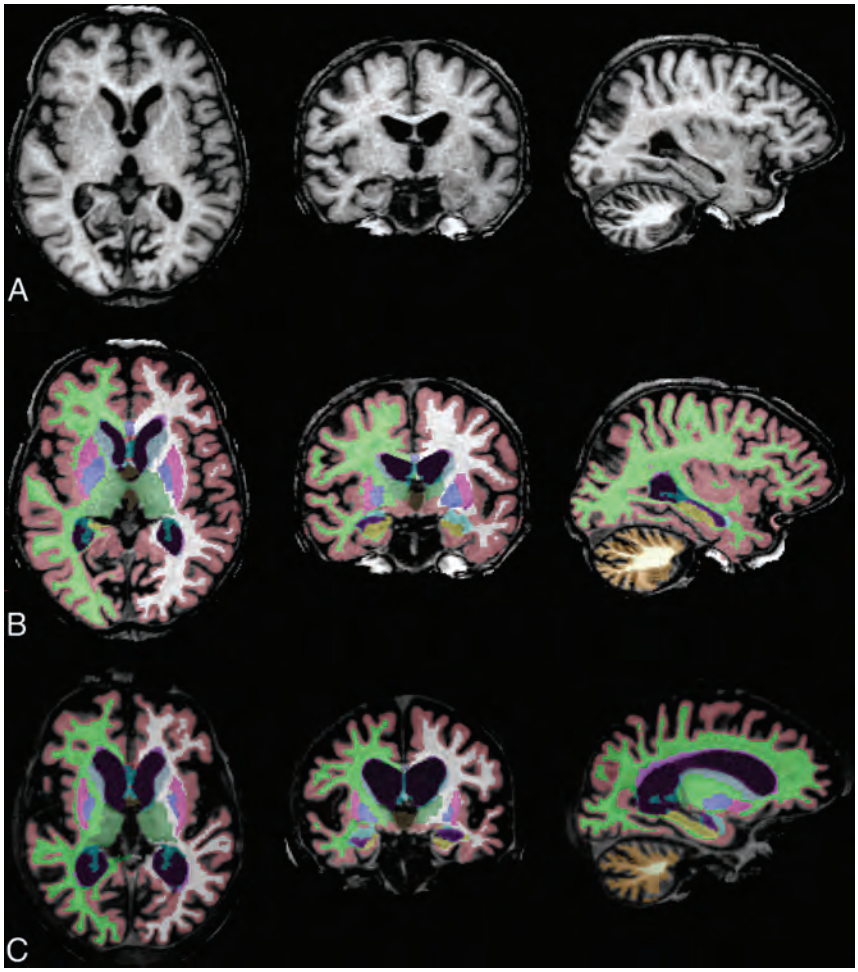


**FIG 1.** Progressive brain atrophy in CLN2 disease. Baseline 3D-T1-weighted MPRAGE images in axial, coronal, and sagittal planes (left to right) of patient 457–1 (*A*), segmented brain volumes (*B*), and segmented brain volumes 4 years later (*C*).

even at the late stages of the disease. All comparisons were performed at $\alpha = .05$, without adjustment for multiplicity. Patient 467–1 was not included in the statistical analysis due to his unusual clinical presentation (see "Results"). For graphic depiction of the data, we used logarithmic fit functions and confidence intervals and calculated $r^2$, again assuming a logarithmic relationship.

## RESULTS

### Clinical Data

Individual clinical disease scores of each patient at the time of baseline and follow-up MR imaging are given in the On-line Table. Most patients had a highly predictable disease course with symptom onset between 2 and 4 years of age and disease progression with complete loss of motor, language, and visual functions by 4–7.5 years of age. Patient 467–1 showed a very different disease course with late-onset and slower disease progression.

### MR Imaging

Thirty-one 3D-T1-weighted MPRAGE datasets were available for the 13 patients included in this study. Two datasets could not be processed in FreeSurfer because Talairach transform did not run; this scenario resulted in 29 datasets available for the final data analysis.

Volumes of supratentorial cortical GM, basal ganglia/thalamus, cerebellar GM, and cerebellar WM decreased with age, while the size of the lateral ventricles increased (Figs 1 and 2).

We found that supratentorial cortical GM showed a very uniform decline across the patient cohort. Also, the regions of basal ganglia/thalamus and infratentorial WM showed a strong decline, while the decline was less uniform for cerebellar GM. Supratentorial WM remained relatively stable with time (Fig 2). Patient 467–1, who presented with a juvenile disease onset and first seizures at 8.8 years of age, showed larger brain volumes at 14 years of age compared with all other patients and was, therefore, not included in the statistical analysis.

### Correlation of MR Imaging Volumetry with Patient Age and Clinical Scores

The correlation of volumetric data with patient age was statistically significant for all regions studied but was strongest for supratentorial cortical GM ($r = -0.913$, $P < .001$) (Table 1). Strong correlations were also observed for the basal ganglia/thalamus ($r = -0.832$, $P < .001$) and cerebellar WM ($r = -0.830$, $P < .001$). Correlations of segmented volumes with patient age were significant but less marked for the lateral ventricles ($r = 0.606$, $P = .001$) and cerebellar GM ($r = -0.659$, $P < .001$).

The correlation of volumetric data with clinical scores resulted in high $r$ values for the supratentorial cortical GM ($r = 0.862$, $P < .001$) and the basal ganglia/thalamus ($r = 0.758$, $P < .001$), but the correlation was significant for all regions studied. In addition, clinical scores also correlated significantly with patient age ($r = -0.781$, $P < .001$).

### Correlation of MR Volumetry with Patient Age and Clinical Scores for Scores of Less Than 1

Generally, clinical motor-language-visual scores of <1 were observed in the late disease stages and in older patients (6–7 years and older). Looking at MR imaging scans of patients with clinical scores of zero, we found that patient age was significantly correlated with volumes of supratentorial cortical GM, basal ganglia/thalamus, cerebellar GM, and cerebellar WM, but not with the lateral ventricles and supratentorial WM (Table 2).

## DISCUSSION

MR imaging brain volumes of patients with genetically confirmed CLN2 disease showed a marked decline with age for all brain regions studied, while ventricular volumes increased. Segmented

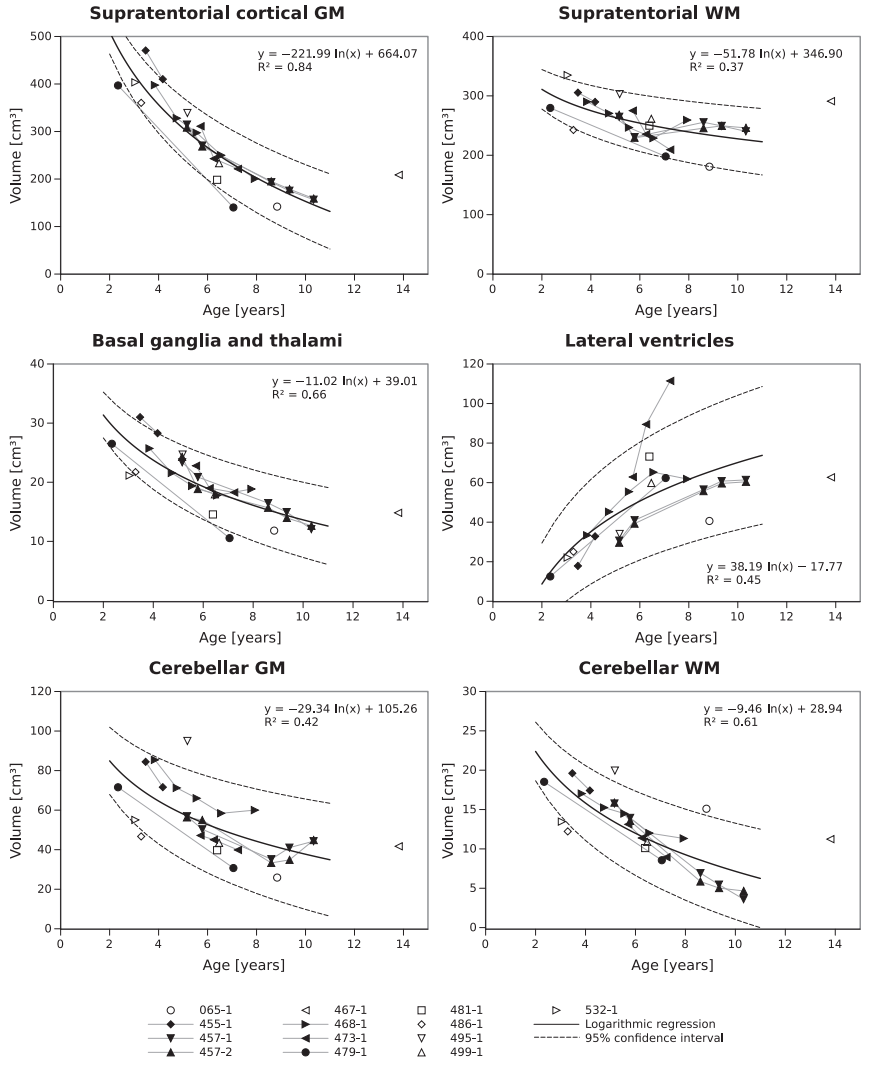


**FIG 2.** Age dependence of segmented brain volumes, logarithmic fit functions, and confidence intervals.

brain volumes were strongly correlated to patient age and, though to a lesser extent, to a disease-specific clinical score. In line with our hypothesis, we observed the strongest correlation with age and clinical scores for GM regions, more specifically, supratentorial cortical GM and basal ganglia/thalamus. In addition, we correlated brain volumes with the age of the patient during the late stages of the disease when the clinical scoring cannot assess disease progression because the combined motor, language, and visual scores were zero. We found that in those patients, brain volumes were still significantly correlated with age for supratentorial cortical GM, basal ganglia/thalamus, cerebellar GM, and cerebellar WM. A single patient, who presented with a juvenile disease onset, showed much higher brain volumes compared with patients with late-infantile presentation.

The strong correlation of GM volumes to patient age and clinical scores implies that GM regions are more suitable to assess disease progression in CLN2 disease compared with the size of lateral ventricles or supratentorial WM used previously.[13,14,18] Of GM regions studied, the supratentorial cortical GM showed the highest correlation to age and clinical scoring but also a relatively uniform decline across the patient cohort. Therefore, supratentorial cortical GM appears to be the region most suited for an assessment of disease progression in CLN2 disease. The finding that GM regions showed a more uniform decline compared with WM regions is also in keeping with histopathologic findings of the underlying neuronal degeneration in CLN2 disease.[4,19] In addition to cortical regions, neuronal depletion of deep GM regions (ie, the basal ganglia and thalamus) is not well-studied but is reported to be less extensive compared with the cerebral and cerebellar cortices.[19]

In contrast, we observed stronger correlations of brain volumes of the basal ganglia/thalamus with patient age and clinical scores compared with cerebellar GM. This may be related to difficulties in segmenting the cerebellum in patients with very significant brain atrophy. Figure 2 shows that cerebellar GM volumes slightly increased for patients 457–1, 457–2, and 468–1 at the latest follow-up scan. This finding is unexpected with respect to the clinical disease course with progressive loss of motor, language, and visual functions. Therefore, these findings must represent segmentation artifacts, which are most likely due to small cerebellar volumes and tight folding compared with the cerebrum (see Fig 1*B*, *-C*, column far right). The finding that MR imaging brain volumes correlated with age, even at disease stages when clinical scores were zero, suggests that MR imaging volumetry provides a quantitative tool to assess disease progression even at late stages of the disease when progression cannot be detected by clinical scoring.

Patient 467–1 was an outlier with a juvenile disease onset at 8 years of age. Patients with CLN2 usually present between 2 and 4 years of age. The different phenotype may be explained by the patient's genetic background (compound heterozygous mutation with c.509–1G>C/c.1439T>G). The c.509–1G>C mutation usually occurs in patients with the classic late-infantile phenotypes, while the c.1439T>G mutation has been reported in patients with early juvenile disease.[3,6]

The most suitable study for a comparison of our data with that of healthy volunteers was published in 2012.[20] A comparison of brain volumes of our patients for whole-brain GM and WM, whole cerebellum, and ventricles starting at 4.8 years of age revealed distinctively smaller volumes for whole-brain GM, whole-brain WM, and the cerebellum compared with healthy controls. In contrast, the size of the lateral ventricles was increased. These differences were much more pronounced for older patients.

Previously, longitudinal brain atrophy in CLN2 has only been assessed indirectly by using the size of CSF spaces.[14] CSF space was

**Table 1: Correlation of brain volumes with patient age and clinical motor-language-visual scores**

| | Patient Age | | Clinical Score | |
|---|---|---|---|---|
| | Correlation Coefficient *r* | *P* Value[a] | Correlation Coefficient *r* | *P* Value[a] |
| ROI | | | | |
| Lateral ventricles | 0.606 | .001 | −0.692 | <.001 |
| Supratentorial cortical GM | −0.913 | <.001 | 0.862 | <.001 |
| Supratentorial WM | −0.865 | <.001 | 0.735 | <.001 |
| Basal ganglia/thalamus | −0.832 | <.001 | 0.758 | <.001 |
| Cerebellar GM | −0.659 | <.001 | 0.609 | .001 |
| Cerebellar WM | −0.830 | <.001 | 0.638 | <.001 |
| Clinical score | −0.781 | <.001 | NA | |

**Note:**—NA indicates not applicable.
[a] All *P* values are statistically significant.

**Table 2: Correlation of brain volumes with patient age and clinical motor-language-visual scores for patients with very low clinical scores (<1)**

| | Patient Age | | Clinical Scores <1 | |
|---|---|---|---|---|
| | Correlation Coefficient *r* | *P* Value | Correlation Coefficient *r* | *P* Value |
| ROI | | | | |
| Lateral ventricles | −0.068 | .810 | NA | NA |
| Supratentorial cortical GM | −0.903 | <.001[a] | NA | NA |
| Supratentorial WM | 0.111 | .695 | NA | NA |
| Basal ganglia/thalamus | −0.822 | <.001[a] | NA | NA |
| Cerebellar GM | −0.548 | .035[a] | NA | NA |
| Cerebellar WM | −0.795 | <.001[a] | NA | NA |
| Clinical score | NA | NA | NA | NA |

**Note:**—NA indicates not applicable.
[a] Statistically significant.

inversely correlated with the clinical scoring. However, the correlations of brain volume changes of GM and WM regions in our cohort were stronger; this finding suggests that whole-brain segmentation is more suitable to assess disease progression.

Some limitations of our study need to be addressed. The recruitment of patients and collection of clinical and MR imaging data were initiated in a prospective fashion. However, 3D-T1WI parameters (ie, primary imaging plane, TR, TE, water excitation) of the datasets used in this report varied due to the long observation period and adjustments due to scanner software updates. This may have resulted in a higher variability of segmentation results, especially during the late stages of the disease. Here, optimization of sequence parameters, including the use of multiecho MPRAGE, may improve the segmentation process in patients with severe atrophy. However, the decline of GM volumes was very homogeneous, especially for supratentorial cortical GM. It can, therefore, be concluded that slight changes to the sequence parameters may not strongly affect volumetric outcomes in our patients with CLN2. Possibly, the use of a more standardized dataset may have provided significant correlations to the clinical scores for supratentorial WM regions as well.

## CONCLUSIONS

The MR imaging assessment of brain volumes in patients with genetically confirmed CLN2 disease revealed a very uniform progression of brain atrophy, strongly related to patient age. Brain volumes also correlated with the clinical score, but to a slightly lesser extent. MR imaging volumetry allows the assessment of progressive brain volume loss even during late stages of the disease when the clinical disease score cannot depict any clinical changes. Our data suggest that MR imaging volumetry is an objective and highly sensitive tool to quantitatively describe disease progression and to assess the efficacy of experimental therapies in all stages of CLN2 disease.


## ACKNOWLEDGMENTS

We would like to extend our gratitude to Waltraud Hubert (children's nurse/study nurse) for her outstanding patient care. We thank all patients and families as well as referring physicians for giving us the opportunity to collect these data.

Disclosures: Miriam Nickel—*RELATED*: *Grant*: DEM-CHILD* (A Treatment-Oriented Research Project of NCL Disorders as a Major Cause of Dementia in Childhood); *UNRELATED*: *Consultancy*: BioMarin, Spark Therapeutics. Jens Fiehler—*UNRELATED*: *Consultancy*: Acandis, Medina Medical/Medtronic, Sequent Medical, Stryker; *Grants/Grants Pending*: MicroVention*; *Payment for Lectures (including service on Speakers Bureaus)*: Boehringer Ingelheim, Covidien/Medtronic, Penumbra; *Travel/Accommodations/Meeting Expenses Unrelated to Activities Listed*: Medtronic. Igor Nestrasil—*UNRELATED*: *Consultancy*: BioMarin, ArmaGen; *Grants/Grants Pending*: BioMarin,* Shire,* Genzyme.* Alfried Kohlschütter—*UNELATED*: *Consultancy*: BioMarin, *Comments*: consulting on the natural clinical course of the disease in question and on a clinical trial with an experimental drug; *Travel/Accommodations/Meeting Expenses Unrelated to Activities Listed*: BioMarin Pharmaceuticals. Angela Schulz—*RELATED*: *Grant*: European Commission (FP7 Project DEM-CHILD)*; *UNRELATED*: *Consultancy*: BioMarin,* Spark Therapeutics*; *Grants/Grants Pending*: BioMarin,* *Comments*: grant to support development of an international DEM-CHILD patient registry. *Money paid to the institution.


## REFERENCES


1. Haltia M, Goebel HH. **The neuronal ceroid-lipofuscinoses: a historical introduction.** *Biochim Biophys Acta* 2013;1832:1795–800 CrossRef Medline
2. Warrier V, Vieira M, Mole SE. **Genetic basis and phenotypic correlations of the neuronal ceroid lipofusinoses.** *Biochim Biophys Acta* 2013;1832:1827–30 CrossRef Medline
3. Kousi M, Lehesjoki AE, Mole SE. **Update of the mutation spectrum and clinical correlations of over 360 mutations in eight genes that underlie the neuronal ceroid lipofuscinoses.** *Hum Mutat* 2012;33:42–63 CrossRef Medline
4. Jadav RH, Sinha S, Yasha TC, et al. **Clinical, electrophysiological, imaging, and ultrastructural description in 68 patients with neuronal ceroid lipofuscinoses and its subtypes.** *Pediatr Neurol* 2014;50:85–95 CrossRef Medline
5. Bessa C, Teixeira CA, Dias A, et al. **CLN2/TPP1 deficiency: the novel mutation IVS7–10A>G causes intron retention and is associated with a mild disease phenotype.** *Mol Genet Metab* 2008;93:66–73 CrossRef Medline
6. Elleder M, Dvoráková L, Stolnaja L, et al. **Atypical CLN2 with later onset and prolonged course: a neuropathologic study showing different sensitivity of neuronal subpopulations to TPP1 deficiency.** *Acta Neuropathol (Berl)* 2008;116:119–24 CrossRef Medline
7. Kohan R, Carabelos MN, Xin W, et al. **Neuronal ceroid lipofuscinosis type CLN2: a new rationale for the construction of phenotypic subgroups based on a survey of 25 cases in South America.** *Gene* 2013;516:114–21 CrossRef Medline

8. Schulz A, Kohlschütter A, Mink J, et al. **NCL diseases: clinical perspectives.** *Biochim Biophys Acta* 2013;1832:1801–06 CrossRef Medline
9. Paniagua Bravo A, Forkert ND, Schulz A, et al. **Quantitative T2 measurements in juvenile and late infantile neuronal ceroid lipofuscinosis.** *Clin Neuroradiol* 2013;23:189–96 CrossRef Medline
10. Dyke JP, Voss HU, Sondhi D, et al. **Assessing disease severity in late infantile neuronal ceroid lipofuscinosis using quantitative MR diffusion-weighted imaging.** *AJNR Am J Neuroradiol* 2007;28:1232–36 CrossRef Medline
11. Autti T, Raininko R, Santavuori P, et al. **MRI of neuronal ceroid lipofuscinosis, II: postmortem MRI and histopathological study of the brain in 16 cases of neuronal ceroid lipofuscinosis of juvenile or late infantile type.** *Neuroradiology* 1997;39:371–77 CrossRef Medline
12. Löbel U, Sedlacik J, Güllmar D, et al. **Diffusion tensor imaging: the normal evolution of ADC, RA, FA, and eigenvalues studied in multiple anatomical regions of the brain.** *Neuroradiology* 2009;51:253–63 CrossRef Medline
13. Autti TH, Hämäläinen J, Mannerkoski M, et al. **JNCL patients show marked brain volume alterations on longitudinal MRI in adolescence.** *J Neurol* 2008;255:1226–30 CrossRef Medline
14. Dyke JP, Sondhi D, Voss HU, et al. **Assessment of disease severity in late infantile neuronal ceroid lipofuscinosis using multiparametric MR imaging.** *AJNR Am J Neuroradiol* 2013;34:884–89 CrossRef Medline
15. Steinfeld R, Heim P, von Gregory H, et al. **Late infantile neuronal ceroid lipofuscinosis: quantitative description of the clinical course in patients with CLN2 mutations.** *Am J Med Genet* 2002;112:347–54 CrossRef Medline
16. Fischl B. **FreeSurfer.** *Neuroimage* 2012;62:774–81 CrossRef Medline
17. Smith SM. **Fast robust automated brain extraction.** *Hum Brain Mapp* 2002;17:143–55 CrossRef Medline
18. Worgall S, Kekatpure MV, Heier L, et al. **Neurological deterioration in late infantile neuronal ceroid lipofuscinosis.** *Neurology* 2007;69:521–35 CrossRef Medline
19. Anderson GW, Goebel HH, Simonati A. **Human pathology in NCL.** *Biochim Biophys Acta* 2013;1832:1807–26 CrossRef Medline
20. Brain Development Cooperative Group. **Total and regional brain volumes in a population-based normative sample from 4 to 18 years: the NIH MRI Study of Normal Brain Development.** *Cereb Cortex* 2012;22:1–12 CrossRef Medline

# MR Imaging of the Cervical Spine in Nonaccidental Trauma: A Tertiary Institution Experience

R. Jacob, M. Cox, K. Koral, C. Greenwell, Y. Xi, L. Vinson, K. Reeder, B. Weprin, R. Huang, and T.N. Booth

## ABSTRACT

**BACKGROUND AND PURPOSE:** Cervical MR imaging has demonstrated a utility for detecting soft tissue injury in nonaccidental trauma. The purpose of this study was to identify the incidence and types of cervical spine injury on MR imaging in nonaccidental trauma and to correlate cervical spine injury with parenchymal injury on brain MR imaging and findings on head CT.

**MATERIALS AND METHODS:** A retrospective review of children diagnosed with nonaccidental trauma in a tertiary referral pediatric hospital over 8 years was performed. Inclusion criteria were children younger than 5 years of age, a confirmed diagnosis of nonaccidental trauma, and cervical spine MR imaging within 1 week of presentation. Brain and cervical spine MR imaging, head CT, cervical radiographs, and skeletal surveys were reviewed.

**RESULTS:** There were 89 patients included in this study (48 males; mean age, 9.1 months [range, 1–59 months]). Cervical spine injury on MR imaging was found in 61 patients (69%). Ligamentous injury was seen in 60 patients (67%), with interspinous ligaments being most commonly involved. Abnormal capsular fluid (atlanto-occipital and atlantoaxial) was present in 28 patients (32%). Cervical spine injury on MR imaging was significantly associated with parenchymal restricted diffusion on brain MR imaging and parenchymal injury on head CT ($P = .0004$ and $P = .0104$, respectively). Children with restricted diffusion on brain MR imaging were 6.22 (point estimate) times more likely to have cervical spine injury on MR imaging.

**CONCLUSIONS:** There is a high incidence of cervical spine injury in pediatric nonaccidental trauma. Positive findings may affect management and suggest a traumatic etiology.

**ABBREVIATIONS:** AHT = abusive head trauma; CSI = cervical spine injury; NAT = nonaccidental trauma

Cervical spine injury (CSI) is uncommon in children, accounting for only 1–2% of pediatric trauma.[1] There is a higher prevalence of upper cervical injury in infants and toddlers, secondary to mechanism of injury and physiologic immaturity. Younger children are also more likely to have a ligamentous injury than fractures.[2] A high clinical suspicion and the appropriate use of imaging are the key factors in identifying CSI. Ligamentous injury to the cervical spine is a well-recognized but likely underdocumented condition in pediatric cervical spine trauma, especially when accompanied by complex coexistent injuries or a delay in clinical symptoms.[3]

Received January 20, 2016; accepted after revision March 21.

From the Departments of Radiology (R.J., K.K., Y.X., T.N.B.), Pediatrics (M.C., K.R., B.W., R.H.), Pediatric Surgery (C.G., L.V.), and Neurological Surgery (B.W.), Children's Health, Children's Medical Center of Dallas, University of Texas Southwestern Medical Center, Dallas, Texas.

Please address correspondence to Timothy N. Booth, MD, Department of Radiology, Children's Medical Center of Dallas, 1935 Medical District Dr, Dallas, TX 75235; e-mail: tim.booth@childrens.com

http://dx.doi.org/10.3174/ajnr.A4817

Recent literature suggests ligamentous injury documented on cervical MR imaging is commonly found in children with abusive head trauma (AHT).[4,5] Spinal injuries in AHT described in various studies include compression fractures, ligamentous injury, cord injury, and subdural hematoma.[6-9] The ligamentous injury is believed to be secondary to a hyperflexion/hyperextension mechanism of injury, and the younger the child, the more likely the upper cervical spine is at risk for injury. The infant or young child's physical features increase the risk of ligamentous CSI because of the presence of a relatively large head size, ligamentous laxity, and poorly developed paraspinal musculature.[1,2] The incidence of CSI is likely underestimated because cervical MR imaging is not generally part of the routine evaluation of nonaccidental trauma (NAT) with or without evidence of AHT. This is frequently secondary to the absence of abnormalities on radiographs that are part of the routine NAT evaluation. The lack of clinical suspicion of CSI, along with coexistent head injuries, increases the risk of masking the clinical detection of CSI.

The purpose of our study was to identify the incidence and

types of CSI on MR imaging in a cohort of pediatric patients diagnosed with NAT with or without AHT and to correlate CSI with parenchymal injury on brain MR imaging and findings on head CT.

## MATERIALS AND METHODS

### Patients

This was a Health Insurance Portability and Accountability Act–compliant descriptive retrospective study performed after approval from the institutional review board at a pediatric tertiary referral center. Using the center's trauma registry, a query was generated to provide a study data base including all children younger than 5 years of age who presented with NAT from July 2004 through September 2012. The trauma registry is a disease-specific data collection composed of a file of uniform data elements designed to capture data. From the generated query results, charts were evaluated thoroughly to determine study eligibility. Children with spinal injuries resulting from mechanisms other than NAT were not included. Only the patients in whom NAT had been documented by the child abuse team were included in the study data base. The presence of AHT was not a requirement for inclusion, but the diagnosis of NAT was. The discharge status was evaluated to identify mortality related to NAT in this cohort.

The inclusion criteria were children younger than 5 years of age presenting during the study period with a diagnosis of NAT and sagittal STIR cervical spine MR imaging performed within 1 week of presentation. Patients with nondiagnostic sagittal STIR images were excluded. Children with NAT admitted to the inpatient service or intensive care unit typically had cervical MR imaging performed along with brain MR imaging. All records from the study data base labeled as NAT were reevaluated by the medical providers with training and experience in child abuse pediatrics. All patients were evaluated based on the criteria adapted from Feldman et al[10] in 2001 for classifying children with head trauma as either abusive or accidental. Based on this classification schema, which takes into account other injuries, the developmental level of the child, the history of trauma provided, and whether a witness was present, cases found to be highly likely abusive and definitely abusive were included in our final study data base. Highly likely abusive was defined as injuries of different ages and not appropriate for given history, absent history, or developmentally unlikely history. Definitely abusive was defined as a corroborated, witnessed, or confessed event. Definitely abusive was also defined as multiple injuries that are incompatible with normal, unintentional childhood injury. Children classified as likely abused or indeterminate were not included because the diagnosis was less than certain.

MR imaging of the cervical spine and brain was reviewed by consensus of 2 experienced pediatric neuroradiologists with 13 and 17 years of experience. Cervical radiographs, skeletal surveys, and available brain imaging were also reviewed.

### Imaging Analysis

Cervical spine MR imaging was performed at 1.5T or 3T. Imaging sequences obtained for a routine trauma cervical spine MR imaging include sagittal STIR images, sagittal T1WIs, axial T2WIs, and axial T2 gradient-echo images. Image quality was assessed with attention to SNR, extent of fat suppression on STIR images, and motion artifacts. The studies were subjectively categorized as nondiagnostic, diagnostic, and superior; nondiagnostic studies were excluded from evaluation.

MR imaging evaluation of the cervical spine included the presence or absence of cord edema or hemorrhage, ligamentous injury, joint capsule fluid (atlanto-occipital and atlanto-axial) with or without distension, marrow edema, and subdural and epidural hemorrhage or fluid. Craniocervical ligamentous structures evaluated included tectorial and atlanto-occipital (anterior and posterior) membranes. Lower cervical ligamentous structures included anterior and posterior longitudinal ligament and ligamentum flavum. Interspinous ligaments were deemed abnormal when abnormal increased T2 signal was present in the interspinous location and classified as cervical or upper thoracic. Injury to the nuchal ligament was identified when fluid signal intensity was seen both anterior and posterior to the structure. CSI by MR imaging was defined when one of the following was present: bone marrow edema, ligamentous injury, joint capsular fluid, regional soft tissue edema including epidural fluid, or spinal cord edema/hemorrhage. Subdural hemorrhage was not included because this most likely resulted from redistribution of intracranial subdural hemorrhage.

Cervical spine radiographs were classified as diagnostic or nondiagnostic. The quality of the study was evaluated based on proper positioning of the patient, visibility of 7 cervical vertebrae, and image quality. Cervical spine radiographs were evaluated for alignment, prevertebral swelling, and fractures.

The brain MR imaging was evaluated for the presence of parenchymal restricted diffusion. The restricted diffusion was classified as focal, multifocal, or diffuse. A focal injury was defined as an injury in 1 or 2 lobes. A multifocal injury was defined as an injury in more than 2 lobes. A diffuse pattern injury was defined as diffuse bilateral distribution, suggesting a hypoxic-ischemic insult. There were 4 patients who had a cervical MR imaging, but no brain MR imaging.

Baseline head CT was available for all patients and assessed for presence of parenchymal injury, SAH, subdural hemorrhage or fluid, and fractures. If present, subdural hemorrhage was evaluated and classified based on its attenuation into hypoattenuated (hygroma), mixed (hypo- and hyperattenuated components), and hyperattenuated subdural hemorrhage. When available, follow-up head CT was evaluated for presence of redistribution of subdural hemorrhage. Redistribution was defined as an increase in the dependent located subdural hemorrhage with a corresponding decrease in the volume of subdural hemorrhage located anterior and superior.

Skeletal surveys were evaluated for the presence of fractures, which were classified as acute, healing, and mixed age.

### Statistical Analysis

Univariate tests (Wilcoxon rank-sum test and Fisher exact test) were performed to characterize the age of the patient on measured parameters including the presence of spinal injury diagnosed by MR imaging, bone marrow edema, ligamentous injury, restricted diffusion in brain, and subdural hematoma on head CT. In addi-

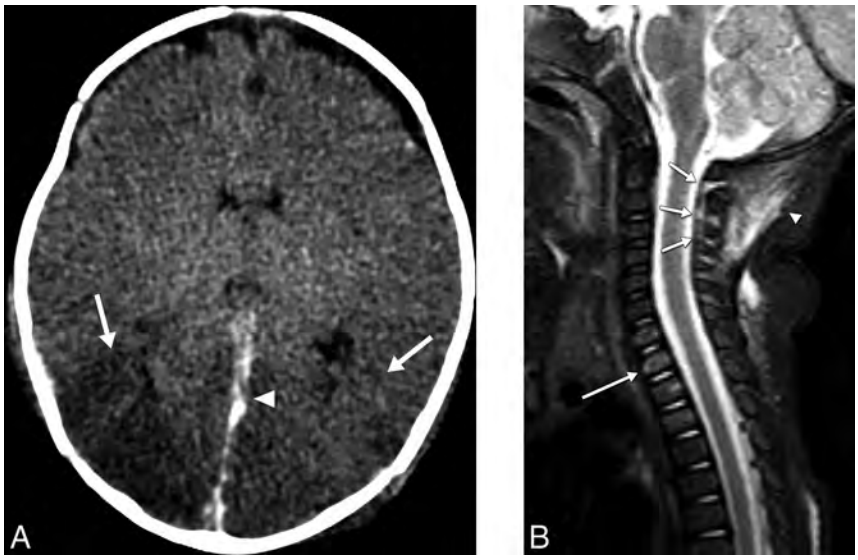


**FIG 1.** Three-month-old patient. *A*, Axial CT demonstrates interhemispheric subdural hemorrhage (*arrowhead*) and symmetric edema of the bilateral occipital lobes (*arrows*). There is abnormal low attenuation in the basal ganglia. Superior frontal parietal edema is present as well (not shown). *B*, Sagittal midline STIR image shows interspinous ligamentous injury at all cervical levels (*arrows*), paraspinous muscular injury, nuchal ligament injury (*arrowhead*), and marrow edema involving the lower cervical and upper thoracic vertebral bodies, most prominent at T1 (*long arrow*).

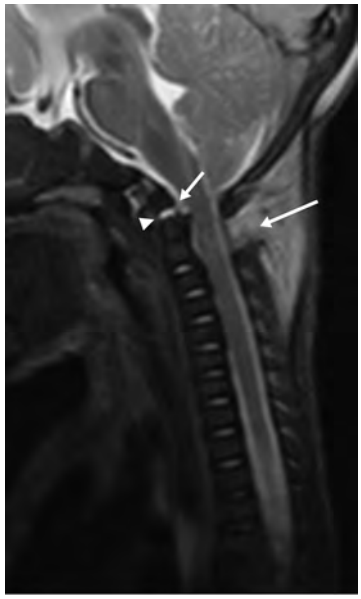

**FIG 2.** Five-month-old patient. Sagittal midline STIR image shows a dens fracture (*arrowhead*) and disruption of the inferior tectorial ligament anterior longitudinal ligament junction (*short arrow*). Extensive injury to the C1–2 interspinous ligamentous structures (*long arrow*) and edema in the posterior paraspinal musculature are present. Diffuse parenchymal injury was present on CT and MR imaging (not shown).

tion, CSI diagnosed by MR imaging was correlated with age, parenchymal injury on CT and MR imaging, subdural collections, and skull fracture. A stepwise logistic regression model was performed, accounting for the significant univariate parameters. All analyses were performed with the SAS 9.3 system (SAS Institute, Cary, North Carolina). All $P$ values $< .05$ were considered statistically significant.

## RESULTS

### Clinical

The retrospective review of medical records of children with MR imaging of the cervical spine performed within 1 week of admission identified 94 patients, of which 5 were excluded either because of absence of a sagittal STIR sequence ($n = 3$) or nondiagnostic quality of the study ($n = 2$). The established criteria were met by 89 patients (48 males). The median and mean ages were 5 and 9.1 months, respectively (range, 1–59 months). There was 5% mortality during the hospital stay ($n = 5$). Abusive head trauma was present in 92% ($n = 82$) of patients. In the remainder of cases ($n = 7$), the diagnosis of NAT was made based on evidence of other non-neurologic injuries.

### Imaging Findings

In this study, 85 children (96%) with NAT admitted to the inpatient service or intensive care unit had cervical MR imaging performed; brain MR imaging was used to further evaluate NAT. Of the 4 patients without a brain MR imaging, head CT was normal in 1 and showed subdural hemorrhage in 3. All patients were imaged with a head CT, which was interpreted as normal in 9% of patients ($n = 8$). Of these patients with a normal CT, brain MR imaging was obtained in 7; 6 patients demonstrated normal brain MR findings and restricted diffusion was seen in 1 patient.

Cervical MR imaging was performed on a 1.5T magnet in 82% of the cases. The quality of the MR imaging was superior in 43% and diagnostic in 57% of the cases. CSI diagnosed by MR imaging was present in 69% ($n = 61$). The mean age of children with CSI by imaging was 9.4 months, and the mean age of children without CSI by imaging was 8.54 months ($P = .46$). Bone marrow edema was more commonly seen in older children (mean age, 14.9 months; $P = .028$), and capsular injury was seen in younger children (mean age, 5.5 months; $P = .0064$). Of the patients who displayed CSI by MR imaging, 64% had diagnostic-quality cervical radiographs. Only 10% of patients in this group had abnormal findings on the cervical radiograph, most commonly nonspecific prevertebral soft tissue prominence greater than one-half of adjacent vertebral body at C2–3. Only 2 patients had an abnormal basion-dens interval measuring greater than 12 mm. No cervical fractures were present.

Ligamentous injury was seen in 67% of patients ($n = 60$). The most common types of ligamentous injury were cervical interspinous ligaments (65%), upper thoracic interspinous ligaments (46%), and nuchal ligament (39%) (Fig 1). There were 3 patients with tectorial membrane injury (Fig 2), 2 with ligamentum flavum injury, and 1 with posterior atlanto-occipital membrane injury. There were no cases of transverse ligament, anterior longitudinal ligament, or posterior longitudinal liga-

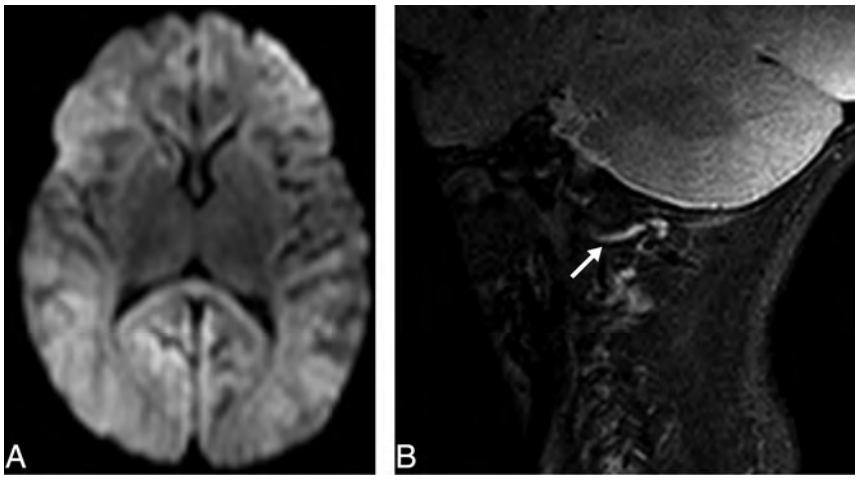


**FIG 3.** Two-month-old patient. *A*, Axial trace DWI shows diffuse restricted diffusion involving the bilateral cerebral hemispheres. *B*, Sagittal paramidline STIR image shows abnormal fluid within the atlanto-occipital joint space with mild distension (*arrow*), consistent with capsular injury.

**FIG 4.** Four-month-old patient. Sagittal midline T2WI shows abnormal posterior extradural fluid within the cervical and thoracic region (*arrows*). The fluid was isointense to CSF on T1-weighted images. Interspinous ligamentous injury is present (not shown).

ment injury. Joint capsule fluid at the craniocervical junction was present in 32% ($n = 28$), which was associated with capsular distention in 13% out of the 28 patients with joint fluid. Patients with restricted diffusion on brain MR imaging were associated with joint capsule fluid at the craniocervical junction (43% versus 11%, $P = .0032$) (Fig 3). Bone marrow edema was present in 9% of the patients ($n = 8$). Cord hemorrhage was seen in 5% ($n = 4$) of the cases. Epidural fluid/epidural edema was present in 10% ($n = 9$) (Fig 4). Interspinous ligamentous injury was present in 89% of patients with abnormal epidural fluid. Subdural hemorrhage in the cervical and upper thoracic spinal canal was present in 18% of the patients ($n = 16$) and was always associated with intracranial subdural hemorrhage (Fig 5).

Parenchymal restricted diffusion on the brain MR imaging was identified in 65% of the patients ($n = 58$). Patients with restricted diffusion on brain MR imaging were associated with CSI by imaging (81% versus 41%, $P = .0004$) (Fig 3). However, for patients with restricted diffusion in the brain, we did not find statistical evidence that different types of restricted diffusion distribution were associated with CSI by imaging ($P = 1$) (Fig 6). Of the patients with restricted diffusion, diffuse distribution of the restricted diffusion was present in 70%, multifocal pattern in 15%, and focal pattern in 15%.

All patients had head CT performed at admission. Parenchymal injury was seen in 56% of the patients ($n = 50$), of whom global parenchymal injury was seen in 76%. Normal head CT with no evidence of intracranial injury was noted for 8 patients, and 3 of these patients had evidence of CSI. Of these 3 patients, 1 had parenchymal restricted diffusion on brain MR imaging and 2 showed no intracranial injury on MR imaging. Documentation of additional non-neurologic injuries allowed a diagnosis of NAT in the patients without evidence of AHT on either CT or MR imaging. Patients with parenchymal injury on CT were associated with spine injury by imaging (82% versus 51%, $P = .0027$) (Fig 1). Patients with global parenchymal injury on head CT were associated with CSI by imaging (84% versus 57%, $P = .0104$). Patients with global parenchymal injury on head CT were also associated with joint capsule fluid at the craniocervical junction (45% versus 22%, $P = .0233$). Intracranial subdural hematomas were present in 85% of the patients ($n = 76$). The most common pattern of subdural hematomas was hyperattenuated (44%). Mixed-attenuation subdural hematomas were present in 36% of the patients, and hypoattenuated subdural collections were present in 5%. There was no statistically significant association between subdural hemorrhage on head CT and spine injury on imaging. However, there was a statistically significant association between the types of subdural hematoma and spine injury by imaging, with mixed-attenuation and hyperattenuated subdural hemorrhage being more common in children with spine injury by imaging ($P = .0253$). A follow-up CT was performed in 56 patients (63%), of which 21 (38%) showed redistribution of the subdural hemorrhage.

The skeletal survey was positive for fractures other than skull in 36% of the patients ($n = 32$). Of the fractures found on skeletal survey, healing fractures were most common (47%). Skull fractures were present in 29% of the patients ($n = 29$). Of the patients with skull fractures, linear skull fractures (18%) were more common than comminuted fractures (11%). There was no statistically significant association between presence of skull fracture on head CT and presence of spine injury on imaging.

Logistic regression with stepwise variable selection method was used to select the most predictive variables for each outcome of interest, including spine injury by imaging, joint capsule fluid at craniocervical junction, and presence of any ligamentous injury. Restricted diffusion on brain MR imaging was the most pre-

dictive variable of CSI on MR imaging ($P = .0004$) and ligamentous injury ($P = .0001$). Children with restricted diffusion on brain MR imaging were 6.22 (point estimate) times more likely to have CSI by imaging and 7.26 times more likely to have ligamentous injury as the finding on MR imaging (Fig 7). No other variables, including parenchymal injury on CT, presence of subdural hemorrhage on CT, and skull fracture, had a significant addition in prediction power. Restricted diffusion ($P = .0057$) and age ($P = .0390$) were the 2 most predictive variables of joint capsule fluid at the craniocervical junction.

## DISCUSSION

To date, this study includes the largest number of patients ($n = 89$) with verified NAT, originating from a trauma registry, with CSI evaluated on MR imaging. Each of the patients' records were reevaluated independently, based on the criteria adapted from a classification schema developed by Feldman et al[10] in 2001, by medical providers trained and certified in child abuse pediatrics. The only patients included in this study were those who had a verified clinical diagnosis of NAT. Typically, children with clinically suspected CSI are evaluated initially with cervical radiographs. In our series, we found that only 64% of the patients who had CSI by MR imaging had diagnostic-quality cervical radiographs, with few demonstrating abnormal findings.

**FIG 5.** Three-month-old patient. Sagittal midline T1WI shows intracranial and intraspinal T1 hyperintense subdural hemorrhage (*arrows*).

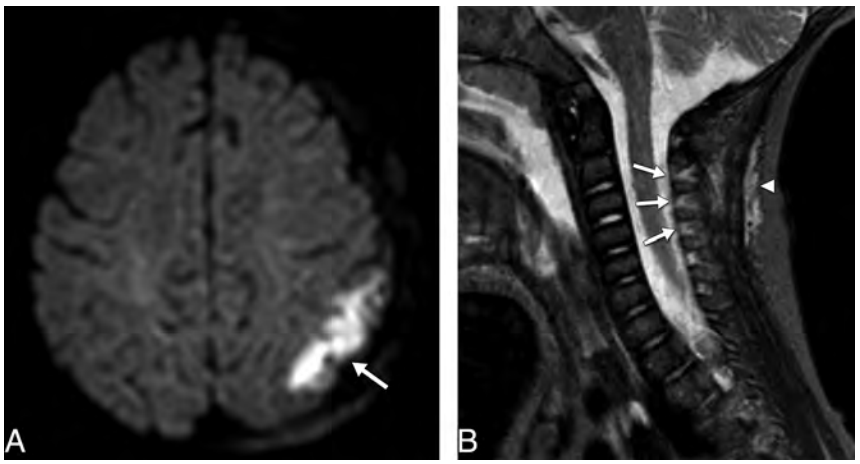


**FIG 6.** Seven-month-old patient. *A*, Axial DWI shows focal restricted diffusion in the left parietal lobe (*arrow*). *B*, Sagittal midline STIR image demonstrates interspinous ligamentous injury (*arrows*) and injury to the nuchal ligament (*arrowhead*).

Cervical radiographs were performed at a tertiary pediatric hospital by technologists with experience in pediatric emergency radiography. This emphasizes both the difficulty in obtaining quality cervical radiographs in patients with NAT and the inherent low sensitivity of the technique in diagnosing ligamentous and soft tissue injury. It has been reported that cervical radiographs have a borderline sensitivity of 78% in the general pediatric trauma population, but this is compared with cervical CT, which is insensitive for soft tissue injury.[11] A relatively low incidence of skull fractures was also present in our patient group. This may be because of the lack of an impact injury, which has been reported to occur in NAT and the subset of children with AHT.[12]

Most patients in our study were infants and toddlers. Only 2 (2%) children were older than 3 years, and 73% were younger than 1 year of age. Only 43% of patients had MR imaging studies of superior quality. This highlights the challenge of performing MR imaging in this particular population, where many of the children are critically sick and/or unstable. The small size of the patients, presence of a cervical collar, and multiple life support devices complicate the image acquisition. Sagittal STIR sequences were found to be most useful for assessing the presence of CSI in this cohort, similar to previous reports.[2,13] Axial T2WIs were used to confirm cord edema and evaluate the integrity of the transverse ligament. Sagittal T1WIs and axial gradient-echo T2WIs were optimal for the evaluation of extra- and intramedullary hemorrhage, respectively.[2,13]

In our cohort, we found CSI by MR imaging in 69% of patients. Katz et al[14] examined the prevalence of cervical injury associated with head trauma from all causes in infants and found only 2 of the 905 infants (0.2%) in their cohort had spine injury; both of the infants had head injury secondary to NAT. The study by Katz et al[14] study was limited by the small number of patients evaluated by MR imaging (1%). A study of children with AHT by Kadom et al[4] found 36% of 38 children had CSI by MR imaging. Choudhary et al[6] found a higher incidence (78%) in children evaluated with AHT and a higher frequency of CSI compared with an accidental cohort. The study also reviewed cervical MR imaging examinations in a nontraumatic cohort and found only 5 of 70 patients had abnormal imaging examinations, with 4 explained by other mechanisms. Only 1 patient had imaging findings not readily explained, and the authors postulated tonic-clonic seizures as a potential etiology. This study offers evidence that the findings demonstrated on cervical MR imaging are not normal variants and, in fact, relate to pathology. The latter 2 studies found an association between brain injury and CSI. Injury of the tectorial membrane was uncommon in our group (3%) and has not been previously reported in the

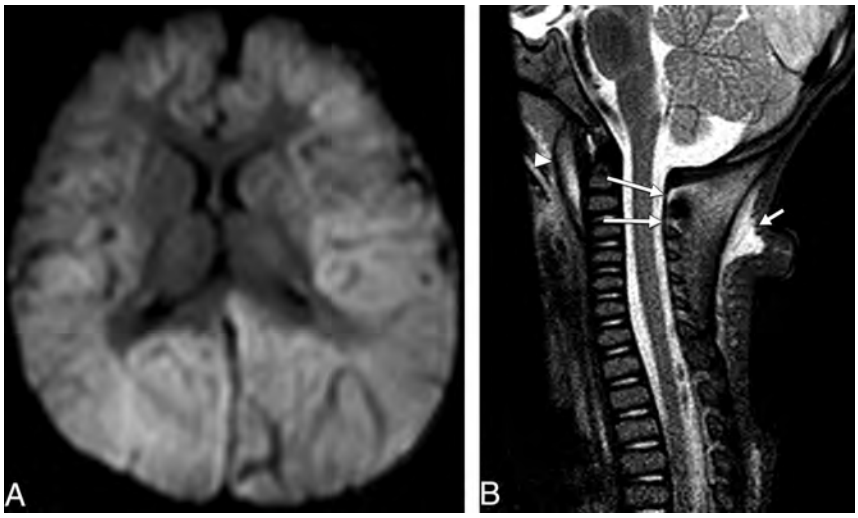


**FIG 7.** Seven-month-old patient. *A*, Axial DWI shows diffuse cerebral restricted diffusion, worse on the left. There is mild midline shift, left to right, caused by a left hemispheric convexity subdural hemorrhage (not shown). *B*, Sagittal midline STIR image demonstrates interspinous (*long arrows*) and nuchal ligament injury (*short arrow*). There is also prevertebral edema (*arrowhead*).

setting of NAT.[4,6] Although not evaluated with MR imaging, injury to the tectorial membrane may be inferred in the study by Silvera et al,[15] where 14% of their abusive head trauma cohort had retroclival epidural hemorrhage. Most of the ligamentous injuries in our cohort, as well as previously reported studies,[4,6] were cervical interspinous and nuchal ligament injuries.

Abnormal capsular fluid was seen in 32% of patients, with distention seen in 13% of these patients. This finding was reported by Choudhary et al,[6] but was more commonly seen in our patient group (22% versus 32%). Most of our patients with abnormal capsular fluid were infants (mean age, 5.6 months), highlighting that the fluid at the craniocervical junction may be related to a flexion/hyperextension mechanism of injury. Interestingly, marrow edema was significantly associated with an older age group (mean age, 14.9 months). There also was a significant relationship between restricted diffusion on brain MR imaging and capsular fluid at the craniocervical junction. The presence of CSI as diagnosed with MR imaging may suggest a traumatic cause to findings demonstrated on head imaging and, thus, is potentially important in the investigation of these cases. It is important to note that 3 cases of CSI were found in 8 patients with a normal head CT.

Spinal subdural hemorrhage was seen in 18% ($n = 16$) of patients in our study, all of whom also had subdural hemorrhage on brain CT. This finding has been noted by other authors and may be related to redistribution of intracranial blood products into the spinal canal.[5,16] Redistribution of intracranial subdural blood was commonly found in our group of patients. Imaging the entire spine may provide an advantage over imaging the cervical spine alone because hemorrhage has been shown to layer within the subdural space of the thoracolumbar spine in cases of abusive head trauma. None of our patients had subdural hemorrhage confined to the spine; however, the presence of spinal subdural hemorrhage is uncommon in the accidental trauma population and may suggest NAT.[5]

Mixed-attenuation and hyperattenuated intracranial subdural hemorrhage were statistically associated with CSI by MR imaging. Hypoattenuated collections may be caused by a more remote traumatic event and were not associated with CSI, possibly because of normal resolution of the MR imaging findings. Spinal epidural fluid was seen in 10% ($n = 9$) of the patients and was commonly associated with interspinous ligamentous injury. This finding has been described previously as a possible postmortem artifact.[7,17] We suggest that abnormal epidural fluid collections are likely the result of trauma; however, a history of a recent lumbar puncture should be excluded before attributing epidural fluid collections to trauma.[18]

Restricted diffusion in brain MR imaging had a very strong association with spine injury and any ligamentous injury. This finding highlights the importance of obtaining cervical spine MR imaging in patients with abnormal restricted diffusion on brain MR imaging. Future studies would help evaluate any association between the pattern of restricted diffusion in the brain and presence of spine injury. We did not find an association between the type of parenchymal injury and CSI; however, this may be because of the predominance of diffuse parenchymal injury and the relatively small number of cases with focal or multifocal parenchymal injury. Global parenchymal injury on CT was statistically associated with spine injury by MR imaging. These results support the hypothesis that injury to the cervical spine can result in occult injury to the brain stem or upper cord, resulting in a hypoxic-ischemic insult.

Limitations of our study include a retrospective design and a case selection bias, in that patients with lower severity of injuries or normal head CT may not have had brain or cervical MR imaging performed. The patients included in our study were more likely to have experienced severe trauma, with most admitted to the intensive care unit. Another challenge was the lack of a uniform protocol for spine imaging, along with the fact that the presence of comorbidity made early MR imaging difficult to perform. Finally, to date, there is no published certified tool to use when determining NAT. Our study employed the expertise of the medical providers trained and certified in child abuse pediatrics, who based their diagnosis on a classification schema from a paper published by Feldman et al[10] in 2001.

## CONCLUSIONS

The children we evaluated with cervical MR imaging for NAT had a high incidence of CSI. Children with head CT or MR imaging evidence of parenchymal injury or restricted diffusion on brain MR imaging have an increased incidence of CSI diagnosed by MR imaging. Although the presence of parenchymal injury is associated with CSI in NAT, a large number of patients without parenchymal injury had evidence of CSI on MR imaging. Especially important is the small group of children who had normal head imaging and evidence of CSI. Our evidence suggests that including cervical spine MR imaging should be included as part of the armamentarium of tests performed

while working up a child with NAT. The presence of CSI may be additional evidence of a traumatic etiology. In addition, performing cervical MR imaging would further enhance the understanding and characterization of spinal injuries in children with NAT.

## REFERENCES


1. Hofbauer M, Jaindl M, Höchtl LL, et al. **Spine injuries in polytraumatized pediatric patients: characteristics and experience from a level I trauma center over two decades.** *J Trauma Acute Care Surg* 2012;73:156–61 CrossRef Medline
2. Booth TN. **Cervical spine evaluation in pediatric trauma.** *AJR Am J Roentgenol* 2012;198:W417–25 CrossRef Medline
3. Feldman KW, Avellino AM, Sugar NF, et al. **Cervical spinal cord injury in abused children.** *Pediatr Emerg Care* 2008;24:222–27 CrossRef Medline
4. Kadom N, Khademian Z, Vezina G, et al. **Usefulness of MRI detection of cervical spine and brain injuries in the evaluation of abusive head trauma.** *Pediatr Radiol* 2014;44:839–48 CrossRef Medline
5. Choudhary AK, Bradford RK, Dias MS, et al. **Spinal subdural hemorrhage in abusive head trauma: a retrospective study.** *Radiology* 2012;262:216–23 CrossRef Medline
6. Choudhary AK, Ishak R, Zacharia TT, et al. **Imaging of spinal injury in abusive head trauma: a retrospective study.** *Pediatr Radiol* 2014; 44:1130–40 CrossRef Medline
7. Kemp AM, Joshi AH, Mann M, et al. **What are the clinical and radiological characteristics of spinal injuries from physical abuse: a systematic review.** *Arch Dis Child* 2010;95:355–60 CrossRef Medline
8. Koumellis P, McConachie NS, Jaspan T. **Spinal subdural haematomas in children with non-accidental head injury.** *Arch Dis Child* 2009;94:216–19 CrossRef Medline
9. Rooks VJ, Sisler C, Burton B. **Cervical spine injury in child abuse: report of two cases.** *Pediatr Radiol* 1998;28:193–95 CrossRef Medline
10. Feldman KW, Bethel R, Shugerman RP, et al. **The cause of infant and toddler subdural hemorrhage: a prospective study.** *Pediatrics* 2001; 108:636–46 CrossRef Medline
11. Silva CT, Doria AS, Traubici J, et al. **Do additional views improve the diagnostic performance of cervical spine radiography in pediatric trauma?** *AJR Am J Roentgenol* 2010;194:500–08 CrossRef Medline
12. Adamsbaum C, Grabar S, Mejean N, et al. **Abusive head trauma: judicial admissions highlight violent and repetitive shaking.** *Pediatrics* 2010;126:546–55 CrossRef Medline
13. Benedetti PF, Fahr LM, Kuhns LR, et al. **MR imaging findings in spinal ligamentous injury.** *AJR Am J Roentgenol* 2000;175:661–65 CrossRef Medline
14. Katz JS, Oluigbo CO, Wilkinson CC, et al. **Prevalence of cervical spine injury in infants with head trauma.** *J Neurosurg Pediatr* 2010; 5:470–73 CrossRef Medline
15. Silvera VM, Danehy AR, Newton AW, et al. **Retroclival collections associated with abusive head trauma in children.** *Pediatr Radiol* 2014;44(Suppl 4):S621–31 CrossRef Medline
16. Kemp A, Cowley L, Maguire S. **Spinal injuries in abusive head trauma: patterns and recommendations.** *Pediatr Radiol* 2014; 44(Suppl 4):S604–12 CrossRef Medline
17. Rutty GN, Squier WM, Padfield CJ. **Epidural haemorrhage of the cervical spinal cord: a post-mortem artifact?** *Neuropathol Appl Neurobiol* 2005;31:247–57 CrossRef Medline
18. Koch BL, Moosbrugger EA, Egelhoff JC. **Symptomatic spinal epidural collections after lumbar puncture in children.** *AJNR Am J Neuroradiol* 2007;28:1811–16 CrossRef Medline

# CT Fluoroscopy–Guided Blood Patching of Ventral CSF Leaks by Direct Needle Placement in the Ventral Epidural Space Using a Transforaminal Approach

T.J. Amrhein, N.T. Befera, L. Gray, and P.G. Kranz

## ABSTRACT

**BACKGROUND AND PURPOSE:** Epidural blood patch treatment of spontaneous intracranial hypotension arising from ventral CSF leaks can be difficult secondary to challenges in achieving ventral spread of patching material. The purpose of this study was to determine the technical success rates and safety profile of direct needle placement into the ventral epidural space via a posterior transforaminal approach.

**MATERIALS AND METHODS:** We retrospectively reviewed consecutive CT fluoroscopy–guided epidural blood patches from June 2013 through July 2015. Cases were included if a posterior transforaminal approach was taken to place the needle directly in the ventral epidural space. Rates of technical success (defined as contrast in the spinal canal ventral epidural space) and optimal epidurogram (defined as contrast spreading into or beyond the middle third of the spinal canal ventral epidural space) were determined. Factors influencing these rates were assessed. All complications, inadvertent intravascular injections, and intrathecal punctures were recorded.

**RESULTS:** A total of 72 ventral epidural blood patches were identified; immediate technical success was achieved in 95.8% and an optimal epidurogram in 47.2%. Needle position within the spinal canal ventral epidural space was associated with obtaining an optimal epidurogram ($P = .005$). Inadvertent intravascular injection was identified in 29.3% of cases, but all were venous. There were no inadvertent intrathecal punctures or complications.

**CONCLUSIONS:** Direct needle placement in the ventral epidural space via a transforaminal approach for treatment of ventral CSF leaks has an excellent technical success rate and safety profile. This technique can be considered as a treatment option in selected patients with ventral CSF leaks for whom traditional techniques are unsuccessful.

**ABBREVIATIONS:** EBP = epidural blood patch; VES = ventral epidural space

Spontaneous intracranial hypotension is thought to be the result of CSF hypovolemia, most commonly secondary to spinal CSF leaks arising from dural defects. These defects can occur in a variety of locations, including along the nerve root sleeves and the ventral dural surface (Fig 1).[1-3] CSF leaks arising from the ventral dural surface are difficult to treat given the considerable challenges in gaining access to this location during both surgery and imaging-guided epidural blood patching.[4] Conventional imaging-guided epidural blood patch (EBP) approaches do not always result in ventral epidural spread of patching material. Improved ventral epidural spread can be achieved with alternative approaches, which could potentially result in improved efficacy for treatment of ventral CSF leaks.

Previously described imaging-guided EBP approaches include posterior interlaminar needle placement in the dorsal epidural space of the spinal canal and transforaminal placement of the needle posterior to the spinal nerve root. Both of these methods can fail to result in ventral epidural spread of injectate.[5-7] Improved ventral spread can be achieved by placing the needle tip directly within the ventral epidural space (VES). A group of investigators has recognized the potential utility of this needle positioning, publishing single-case reports describing transforaminal and anterior transintervertebral disc techniques.[8,9] However, no larger case series have been published evaluating the technical efficacy and safety of direct ventral EBP techniques.

The purpose of this study was to determine the technical success rates and safety profile of direct needle placement into the VES via a posterior transforaminal approach.

Received February 25, 2016; accepted after revision April 22.

From the Department of Radiology, Duke University Medical Center, Durham, North Carolina.

Please address correspondence to Timothy J. Amrhein, MD, Department of Radiology, Duke University Medical Center, DUMC Box 3808, Durham, NC 27710; e-mail: timothy.amrhein@duke.edu; @TimAmrheinMD

http://dx.doi.org/10.3174/ajnr.A4842

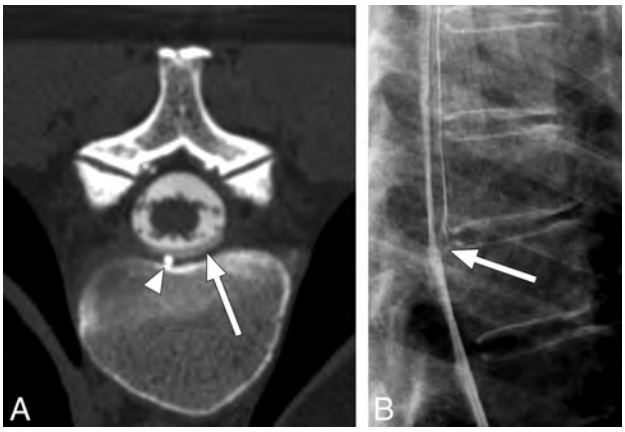


**FIG 1.** A 55-year-old woman with spontaneous intracranial hypotension secondary to a CSF leak. *A*, Postmyelogram CT at the level of the T7–8 disc interspace demonstrates a ventral CSF leak (*white arrow*) containing contrast with an attenuation slightly less than that of intrathecal contrast. A small spiculated osteophyte (*white arrowhead*) is the presumed cause for the leak. *B*, Lateral projection dynamic myelogram of the midthoracic spine confirms the origin of the CSF leak at T7–8. Note the split of the contrast column at this level consistent with a ventral CSF leak (*white arrow*).

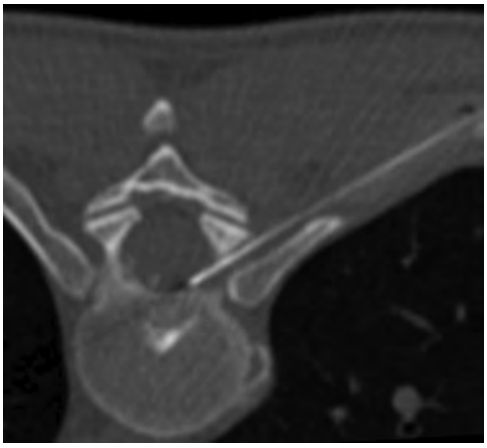

**FIG 2.** Needle-tip placement in the ipsilateral third of the spinal canal ventral epidural space via right T8–9 posterior transforaminal approach for epidural blood patch treatment of a ventral CSF leak confirmed via dynamic thoracic myelogram (*not shown*). All of the patient's symptoms resolved after the procedure.

## MATERIALS AND METHODS

### Study Cohort

We retrospectively reviewed consecutive CT fluoroscopy–guided targeted EBPs performed on patients diagnosed with spontaneous intracranial hypotension (based on the criteria outlined by Schievink et al[10]) from June 2013 through July 2015. The electronic medical records and departmental procedure schedules were reviewed to identify cases. Cases were included if a posterior transforaminal approach was taken to place the needle tip directly in the VES of the neuroforamen or the spinal canal (Fig 2). All patients had imaging findings concerning for a ventral CSF leak. Data analysis was performed on a single needle placement basis (ie, if a patient underwent 2 posterior transforaminal approach VES needle placements at different locations during the same procedure, each individual needle placement would be considered a separate case).

Our local institutional review board approved this Health Insurance Portability and Accountability Act–compliant study and granted a waiver of informed consent.

### Ventral Epidural Blood Patch Technique

All procedures were performed on the same CT fluoroscopy–equipped scanner (LightSpeed 16; GE Healthcare, Milwaukee, Wisconsin) by 1 of 3 neuroradiologists with 5, 8, or 10 years of experience performing CT-guided EBPs, respectively. The standard CT fluoroscopy–guided posterior transforaminal epidural approach was taken as previously described, but with a slight modification: for these procedures, a 22-gauge Quincke point needle (BD Medical, Franklin Lakes, New Jersey) was advanced through the neuroforamen such that the tip terminated within the VES.[11,12] Once in the VES, approximately 0.2 mL of contrast material (iopamidol, Isovue-M 200; Bracco, Princeton, New Jersey) was injected to assess needle-tip position and potential spread of patching material and to exclude intravascular injection (Fig 3). Intravascular injection was excluded by using the previously described "double-tap" technique.[13] After confirmation of both satisfactory needle positioning and absence of inadvertent intravascular injection, patching material (typically a total volume of 1–5 mL of autologous blood with fibrin glue [Tisseel; Baxter, Deerfield, Illinois]) was injected.

### Image Analysis

Procedural images from the study cohort were reviewed by a board-certified radiologist with a Certificate of Added Qualification in neuroradiology and 5 years of experience performing CT fluoroscopy–guided targeted patching for spontaneous intracranial hypotension. The following information was recorded: neuroforamen level and laterality, the angle of the needle approach as measured from the long axis of the vertebral body spinous process, z-axis position of the needle within the neuroforamen (inferior third, middle third, or superior third), needle-tip location, the extent of the resultant contrast epidurogram, the presence of inadvertent intrathecal puncture or intravascular injection, and any procedural complications or adverse events.

We categorized the extent of the resultant contrast epidurogram by presence of the leading edge of contrast within 1 of 5 anatomic zones: 1) extraforaminal space; 2) foraminal VES; 3) ipsilateral third of the spinal canal VES; 4) middle third of the spinal canal VES; or 5) contralateral third of the spinal canal VES (Fig 4). Immediate technical success was defined as the presence of contrast within the spinal canal VES. Technically successful procedures were further characterized as exhibiting an optimal epidurogram if contrast extended into or beyond the middle third of the spinal canal VES (Fig 3). Needle-tip position was categorized by using the same anatomic zones as for the contrast epidurogram.

Inadvertent intravascular injection was classified as definitely venous, probably venous, indeterminate, probably arterial, or definitely arterial by using previously described criteria.[13] An inadvertent intrathecal puncture was deemed present if contrast was identified within the thecal sac on the procedural images or if such an event was documented in the procedural report (eg, CSF return during needle placement).

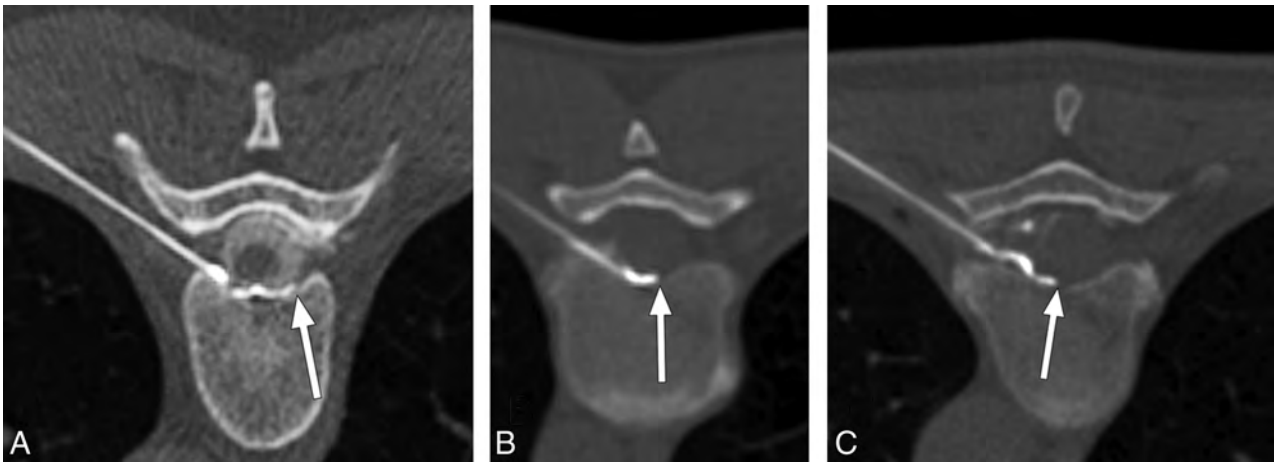


**FIG 3.** Examples of successful ventral epidural spread of contrast (optimal epidurograms). *A*, A 48-year-old woman with a ventral CSF leak treated via left T7–8 transforaminal approach ventral patch. Contrast spreads to the contralateral third of the ventral epidural space (*white arrow*). *B*, A 41-year-old man with a ventral CSF leak treated via left T8–9 transforaminal approach ventral patch. Contrast spreads past the midline in the ventral epidural space (*white arrow*). *C*, A 54-year-old woman with a ventral CSF leak treated via left T7–8 transforaminal approach ventral patch. Contrast spreads into the middle third of the ventral epidural space (*white arrow*).

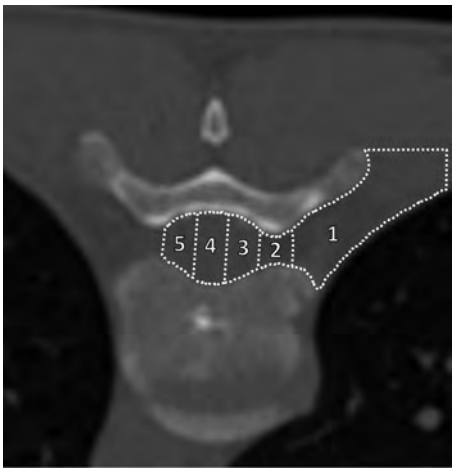


**FIG 4.** Classification scheme for both final needle-tip position and determining the extent of the contrast epidurogram. Example is for a right-sided transforaminal approach to the VES at T8–9. The final needle-tip position or the leading edge of the contrast epidurogram was classified as terminating within 1 of 5 zones: 1) extraforaminal space; 2) foraminal VES (defined as between the medial and lateral margins of the pedicle); 3) ipsilateral third of the spinal canal VES; 4) middle third of the spinal canal VES; or 5) contralateral third of the spinal canal VES.

### *Patient Outcomes*

Patient outcomes were determined by a retrospective review of the patient's electronic medical record. A successful ventral epidural patch was defined as absence of the patient's presenting symptoms at 2 months after the procedure. Patients who received a subsequent patch within 2 months were automatically deemed treatment failures.

### *Statistics*

A Mann-Whitney test was used to compare needle angles between patients with an optimal epidurogram and those without an optimal epidurogram. Two-tailed Fisher exact tests were used to assess for factors predictive of an optimal epidurogram, including needle-tip position, neuroforaminal level, and needle laterality. Two-tailed Fisher exact tests also were used to assess for factors predictive of inadvertent intravascular injection, including needle-tip position, neuroforaminal level, needle laterality, and the presence of an optimal epidurogram. A $\chi^2$ test was used to compare the incidence of inadvertent intravascular injection between different needle z-axis locations within the neuroforamen.

All statistical analyses were conducted by using GraphPad Prism software (Version 6.0b; GraphPad Software, San Diego, California). Statistical significance was considered at a threshold of $P < .05$.

## RESULTS

### *Study Cohort*

A total of 1116 procedures were reviewed during the study period, and 72 ventral EBPs were identified (occurring during 39 separate procedure encounters). These ventral EBPs were performed in 35 patients, all with imaging findings concerning for a ventral CSF leak. This patient group included 25 women (71.4%) and 10 men (28.6%) with a mean age of 47.3 years (range, 15–81 years). Most cases (89%) were performed after failure of at least 1 prior conventional EBP. There were no major complications or adverse events in any patient.

### *Image Analysis*

Most needle placements were performed in the thoracic spine (71 of 72 [98.6%]; 1 at L3–4), and there were nearly equal numbers of right- and left-sided approaches (38 and 34, respectively).

Immediate technical success was achieved in 95.8% (69 of 72) of needle placements. An optimal epidurogram, defined as contrast reaching or extending beyond the middle third of the spinal canal VES, was achieved in 47.2% (34 of 72) of needle placements. Contrast reached the contralateral third of the spinal canal VES in 13.9% (10 of 72) of needle placements.

An optimal epidurogram was achieved more commonly when the needle tip was placed into the spinal canal VES compared with the foraminal VES ($P = .005$) (Table). There was a trend toward increased needle angle (indicating a shallower approach) result-

**Factors associated with achieving an optimal epidurogram[a]**

| Factor | Optimal Epidurogram Achieved? | | *P* Value |
|---|---|---|---|
| | Yes (*n* = 34) | No (*n* = 38) | |
| Needle angle (mean [SD]) | 48.2 (7.3) | 45.2 (6.8) | .08 |
| Foraminal level (% [*n*]) | | | .80 |
| Upper thoracic (T3–4 to T6–7) | 37 (13 of 35) | 63 (22 of 35) | |
| Lower thoracic (T7–8 to T12–L1) | 56 (20 of 36) | 44 (16 of 36) | |
| Laterality (% [*n*]) | | | .16 |
| Right | 55 (21 of 38) | 45 (17 of 38) | |
| Left | 38 (13 of 34) | 62 (21 of 34) | |
| Needle-tip position (% [*n*]) | | | .005 |
| Foraminal VES | 29 (10 of 34) | 63 (24 of 38) | |
| Spinal canal VES | 71 (24 of 34) | 37 (14 of 38) | |

[a] Optimal epidurogram is defined as reaching the middle third of the spinal canal VES.

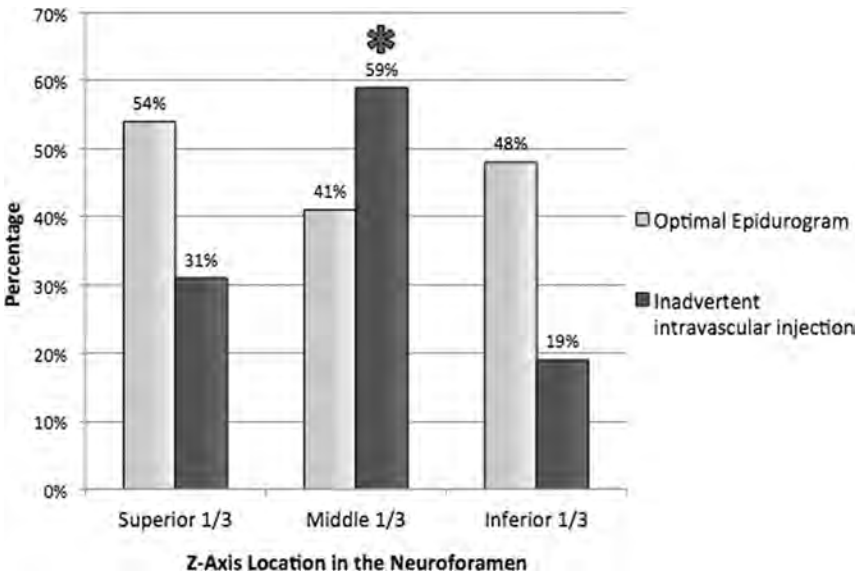


**FIG 5.** Incidence of optimal epidurogram and inadvertent intravascular injection per needle z-axis location in the neuroforamen. *Asterisk* indicates significant increase in inadvertent intravascular injection ($P = .01$).

ing in optimal epidurograms, though this did not reach statistical significance ($P = .08$). Neither the side of injection nor the foraminal level was a significant predictor for achieving an optimal epidurogram ($P = .16$ and $P = .80$, respectively).

Inadvertent intravascular injection during the epidurogram was identified in 29.3% (22 of 75) of needle placements, necessitating needle repositioning before injection of patching material. All cases were considered venous (13 probably venous, 9 definitely venous). None were indeterminate or considered arterial. There was no significant association between inadvertent intravascular injection and side of injection ($P = 1$), achieving an optimal epidurogram ($P = 1$), foraminal level ($P = .43$), or needle-tip position ($P = .80$). There was a significantly increased likelihood of inadvertent intravascular injection when the needle traversed the middle third of the neuroforamen in the z-axis ($P = .01$) (Fig 5). There were no cases of inadvertent intrathecal puncture.

### *Patient Outcomes*

Forty-one percent (16 of 39) of ventral epidural patches resulted in successful resolution of patient symptoms for at least 2 months after the procedure. In 8 cases (21%), there was a subsequent repeat patch within 2 months of the ventral patch attempt. Thirteen patients (37%) underwent surgical repair of their CSF leak. No patients were lost to follow-up.

## DISCUSSION

CT fluoroscopy–guided EBP via direct needle placement in the VES by using a transforaminal approach has an excellent technical success rate. In 72 needle placements, 95.8% were technically successful, and nearly half (47.2%) resulted in an optimal epidurogram. Given these findings, we conclude that this technique can result in substantial spread of patching material throughout the ventral epidural space.

This technique should be considered when treating patients with a CSF leak arising from the ventral dural surface, particularly in cases refractory to conventional blood patch methods. In these patients, surgery is often the only remaining possibility for treatment. Though potentially curative, such surgical interventions carry with them the risk of significant morbidity as well as higher costs and longer recovery times, all of which could be avoided with a successful ventral EBP.[14,15]

Previously described methods for imaging-guided EBPs typically involve either a posterior interlaminar epidural approach or a posterior transforaminal approach, analogous to those used with corticosteroid injections.[16,17] These techniques result in needle-tip placement within the dorsal epidural space of the spinal canal or the dorsal epidural space of the neuroforamen, respectively. In either case, the needle tip remains far removed from the dural defect responsible for a ventral CSF leak. Prior studies investigating the spread of epidurographic contrast by using a posterior interlaminar approach during corticosteroid injections have consistently demonstrated relatively poor spread to the VES.[5,7] For example, Botwin et al[5] found that only 36% of interlaminar injections resulted in ventral epidural spread despite using 5 mL of contrast (significantly more than used in this study). Prior studies of transforaminal approaches have demonstrated slightly better rates of success, ranging from 61.4%–88%.[6,18,19] However, it is important to note that in all of these studies, "ventral" was defined as the anterior aspect of the neuroforamen. This was because the investigators were interested in the efficacy of corticosteroid injections for nerve origin pain. Furthermore, these investigations all involved procedures guided by conventional fluoroscopy, which limited their ability to assess for contrast spread into the spinal canal VES rather than simply the neuroforaminal VES. Therefore, it is impossible to know what percentage of these cases

would be considered as either technically successful or optimal epidurograms according to the metrics defined in our study; presumably, it would be considerably less than the percentages previously reported. Achieving contrast spread into the spinal canal VES is important when treating a ventral CSF leak because an inability to deliver patching material to the site of the dural tear will preclude successful treatment.

Importantly, there were no complications in any of our cases. A potential risk of this procedure might include injection into a radiculomedullary artery, given the transforaminal approach used. Transforaminal epidural needle placement, performed during corticosteroid injections for pain, has been associated with rare but serious reported complications, including paralysis, stroke, and death.[20-24] These events are thought to be the result of either embolic injection into, or direct vascular injury to, a radiculomedullary artery supplying the spinal cord. Embolic injection is the more likely mechanism, considering that no catastrophic events have been reported with nonparticulate corticosteroids.[25] We performed 72 needle placements without a complication. Furthermore, we found no cases of intra-arterial contrast injection. We did identify an inadvertent intravascular injection rate of 29.3%, which is slightly higher than the reported rates in the literature for posterior interlaminar and transforaminal needle placements.[13,26-28] The rich epidural venous plexus within the spinal canal is presumably responsible for the relatively increased incidence of vascular cannulation in our study. The fact that all of these incidents were classified as either "definitely venous" or "probably venous" supports this supposition. We recommend an approach through the inferior third of the neuroforamen, where possible, for 2 reasons. First, there was a relatively increased incidence of inadvertent venous injection when the needle traversed the middle third of the foramen. Second, a radiculomedullary artery will usually be located anterior to the nerve root within the superior third of the neuroforamen within the thoracic spine.[29,30] Therefore, an inferior approach will help to avoid it. Of course, any potential risk associated with placement of a needle in the ventral epidural space via a posterior transforaminal approach should be considered in the context of the available alternative treatment options. For patients with ventral CSF leaks that have failed conventional treatments, it is often the case that the sole remaining option is a complex and challenging surgical intervention with significant morbidity and potential mortality.

In limited case reports, prior investigators have recognized the potential benefit of direct, targeted placement of patching material within the ventral epidural space. Park and Villablanca[8] published a single-case report of an anterior approach through the C5–6 intervertebral disc under conventional fluoroscopic guidance. This anterior needle approach courses between the pretracheal fascia and the carotid sheath and is commonly used during cervical discography and disc biopsy.[31] Given the presence of the mediastinal structures and the lungs, this technique would not be feasible in the thoracic spine, which is where most ventral CSF leaks occur. Furthermore, the technique is not without significant risk because of the need to displace the carotid artery as well as avoid the vertebral artery. In fact, multiple complications have been previously reported, including hemorrhage, vertebral artery injury, damage to the spinal cord, and injury to the trachea and carotid artery.[32] Zaw et al[9] reported a single case of successful epidural blood patch achieved by placement of the needle tip in a ventral epidural collection at T6 via a posterior transforaminal approach. This procedure was performed after several failed conventional blood patch attempts. Similarly, most of our cases also were performed after failure to achieve a durable treatment with more conventional methods. Our study is the first to investigate this transforaminal approach to the ventral epidural space in a large series of patients. Furthermore, it includes new information about the extent of ventral epidural spread of patching material and provides insight into the safety profile of this approach.

There are several limitations to our investigation. First, this was a retrospective study of a relatively limited number of procedures performed by highly experienced interventionalists. We recommend caution for proceduralists with limited experience. In addition, rare complications could have been missed given the number of patients. However, 72 consecutive needle placements without a complication suggests that the incidence of such adverse events is likely very low. Second, we did not perform a direct comparison of the contrast epidurograms achieved by using conventional CT fluoroscopy–guided patching methods (ie, interlaminar and traditional transforaminal approaches) with the experimental technique outlined in this manuscript. There might be a different and more efficacious mechanism for achieving an optimal epidurogram in the VES. However, prior studies suggested that conventional interlaminar and transforaminal approaches under fluoroscopic guidance do not result in adequate spread to the ventral epidural space of the spinal canal.[5-7,18,33] Finally, though we noted that 41% of patches resulted in successful resolution of patient symptoms for at least 2 months, prospective patient outcomes were not assessed in this investigation. A more structured evaluation with validated headache outcome measures could be included in a future prospective investigation. Furthermore, a study comparing patient outcomes for interlaminar epidural, transforaminal epidural, and ventral epidural approaches is needed to justify more widespread adoption of this technique in patients with ventral CSF leaks.

## CONCLUSIONS

This study confirms that direct needle placement in the VES via a transforaminal approach for treatment of ventral CSF leaks has an excellent technical success rate. Furthermore, it demonstrates an acceptable risk profile given the absence of complications in 72 consecutive needle placements. This technique can be considered as a treatment option in selected patients with ventral CSF leaks for whom traditional techniques are unsuccessful. Further prospective studies comparing patient outcomes when using this technique with those for alternative treatments of ventral CSF leaks are warranted.

## REFERENCES


1. Schievink WI. **Spontaneous spinal cerebrospinal fluid leaks and intracranial hypotension.** *JAMA* 2006;295:2286–96 CrossRef Medline
2. Yoshida H, Takai K, Taniguchi M. **Leakage detection on CT myelography for targeted epidural blood patch in spontaneous cerebrospinal fluid leaks: calcified or ossified spinal lesions ventral to the thecal sac.** *J Neurosurg Spine* 2014;21:432–41 CrossRef Medline
3. Brus-Ramer M, Dillon WP. **Idiopathic thoracic spinal cord**

**herniation: retrospective analysis supporting a mechanism of diskogenic dural injury and subsequent tamponade.** *AJNR Am J Neuroradiol* 2012;33:52–56 CrossRef Medline

4. Schievink WI, Maya MM, Nuño M. **Chronic cerebellar hemorrhage in spontaneous intracranial hypotension: association with ventral spinal cerebrospinal fluid leaks: clinical article.** *J Neurosurg Spine* 2011;15:433–40 CrossRef Medline
5. Botwin KP, Natalicchio J, Hanna A. **Fluoroscopic guided lumbar interlaminar epidural injections: a prospective evaluation of epidurography contrast patterns and anatomical review of the epidural space.** *Pain Physician* 2004;7:77–80 Medline
6. Candido KD, Raghavendra MS, Chinthagada M, et al. **A prospective evaluation of iodinated contrast flow patterns with fluoroscopically guided lumbar epidural steroid injections: the lateral parasagittal interlaminar epidural approach versus the transforaminal epidural approach.** *Anesth Analg* 2008;106:638–44 CrossRef Medline
7. Gupta R, Singh S, Kaur S, et al. **Correlation between epidurographic contrast flow patterns and clinical effectiveness in chronic lumbar discogenic radicular pain treated with epidural steroid injections via different approaches.** *Korean J Pain* 2014;27:353–59 CrossRef Medline
8. Park JK, Villablanca JP. **Feasibility of placement of an anterior cervical epidural blood patch for spontaneous intracranial hypotension.** *AJNR Am J Neuroradiol* 2013;34:E84–86 CrossRef Medline
9. Zaw TM, Park JK, Al-Tariq Q, et al. **Feasibility of ventral epidural blood patch placement via CT-guided transforaminal approach for the treatment of intracranial hypotension.** *Neurographics* 2014;4:101–05 CrossRef
10. Schievink WI, Dodick DW, Mokri B, et al. **Diagnostic criteria for headache due to spontaneous intracranial hypotension: a perspective.** *Headache* 2011;51:1442–44 CrossRef Medline
11. Wagner AL. **Selective lumbar nerve root blocks with CT fluoroscopic guidance: technique, results, procedure time, and radiation dose.** *AJNR Am J Neuroradiol* 2004;25:1592–94 Medline
12. Wagner AL, Murtagh FR. **Selective nerve root blocks.** *Tech Vasc Interv Radiol* 2002;5:194–200 CrossRef Medline
13. Kranz PG, Amrhein TJ, Gray L. **Incidence of inadvertent intravascular injection during CT fluoroscopy–guided epidural steroid injections.** *AJNR Am J Neuroradiol* 2015;36:1000–07 CrossRef Medline
14. Pricola Fehnel K, Borges LF. **Posterior thoracic laminoplasty with dorsal, intradural identification of ventral defect and transdural discectomy for a spontaneous cerebrospinal fluid leak: case report.** *J Neurosurg Spine* 2015;22:478–82 CrossRef Medline
15. Schievink WI, Morreale VM, Atkinson JL, et al. **Surgical treatment of spontaneous spinal cerebrospinal fluid leaks.** *J Neurosurg* 1998;88:243–46 CrossRef Medline
16. Agarwal V, Sreedher G, Rothfus WE. **Targeted CT-guided epidural blood patch for treatment of spontaneous intracranial hypotension due to calcified intradural thoracic disc herniation.** *Interv Neuroradiol* 2013;19:121–26 Medline
17. Bowden K, Wuollet A, Patwardhan A, et al. **Transforaminal blood patch for the treatment of chronic headache from intracranial hypotension: a case report and review.** *Anesthesiol Res Pract* 2012;2012:923904 CrossRef Medline
18. Desai MJ, Shah B, Sayal PK. **Epidural contrast flow patterns of transforaminal epidural steroid injections stratified by commonly used final needle-tip position.** *Pain Med* 2011;12:864–70 CrossRef Medline
19. Manchikanti L, Cash KA, Pampati V, et al. **Evaluation of lumbar transforaminal epidural injections with needle placement and contrast flow patterns: a prospective, descriptive report.** *Pain Physician* 2004;7:217–23 Medline
20. Brouwers PJ, Kottink EJ, Simon MA, et al. **A cervical anterior spinal artery syndrome after diagnostic blockade of the right C6-nerve root.** *Pain* 2001;91:397–99 CrossRef Medline
21. Huston CW, Slipman CW, Garvin C. **Complications and side effects of cervical and lumbosacral selective nerve root injections.** *Arch Phys Med Rehabil* 2005;86:277–83 CrossRef Medline
22. Ludwig MA, Burns SP. **Spinal cord infarction following cervical transforaminal epidural injection: a case report.** *Spine (Phila Pa 1976)* 2005;30:E266–68 CrossRef Medline
23. Ma DJ, Gilula LA, Riew KD. **Complications of fluoroscopically guided extraforaminal cervical nerve blocks. An analysis of 1036 injections.** *J Bone Joint Surg Am* 2005;87:1025–30 CrossRef Medline
24. Tiso RL, Cutler T, Catania JA, et al. **Adverse central nervous system sequelae after selective transforaminal block: the role of corticosteroids.** *Spine J* 2004;4:468–74 CrossRef Medline
25. Emanuel EJ. **Reform of clinical research regulations, finally.** *N Engl J Med* 2015;373:2296–99 CrossRef Medline
26. El Abd OH, Amadera JE, Pimentel DC, et al. **Intravascular flow detection during transforaminal epidural injections: a prospective assessment.** *Pain Physician* 2014;17:21–27 Medline
27. Furman MB, Giovanniello MT, O'Brien EM. **Incidence of intravascular penetration in transforaminal cervical epidural steroid injections.** *Spine (Phila Pa 1976)* 2003;28:21–25 CrossRef Medline
28. McLean JP, Sigler JD, Plastaras CT, et al. **The rate of detection of intravascular injection in cervical transforaminal epidural steroid injections with and without digital subtraction angiography.** *PM R* 2009;1:636–42 CrossRef Medline
29. Demondion X, Lefebvre G, Fisch O, et al. **Radiographic anatomy of the intervertebral cervical and lumbar foramina (vessels and variants).** *Diagn Interv Imaging* 2012;93:690–97 CrossRef Medline
30. Murthy NS, Maus TP, Behrns CL. **Intraforaminal location of the great anterior radiculomedullary artery (artery of Adamkiewicz): a retrospective review.** *Pain Med* 2010;11:1756–64 CrossRef Medline
31. Smith GW, Nichols P Jr. **The technic of cervical discography.** *Radiology* 1957;68:718–20 CrossRef Medline
32. Lee SH, Kim KT, Jeong BO, et al. **The safety zone of percutaneous cervical approach: a dynamic computed tomographic study.** *Spine (Phila Pa 1976)* 2007;32:E569–74 CrossRef Medline
33. Botwin K, Natalicchio J, Brown LA. **Epidurography contrast patterns with fluoroscopic guided lumbar transforaminal epidural injections: a prospective evaluation.** *Pain Physician* 2004;7:211–15 Medline

# Automated Quantitation of Spinal CSF Volume and Measurement of Craniospinal CSF Redistribution following Lumbar Withdrawal in Idiopathic Intracranial Hypertension

N. Alperin, A.M. Bagci, S.H. Lee, and B.L. Lam

## ABSTRACT

**BACKGROUND AND PURPOSE:** Automated methods for quantitation of tissue and CSF volumes by MR imaging are available for the cranial but not the spinal compartment. We developed an iterative method for delineation of the spinal CSF spaces for automated measurements of CSF and cord volumes and applied it to study craniospinal CSF redistribution following lumbar withdrawal in patients with idiopathic intracranial hypertension.

**MATERIALS AND METHODS:** MR imaging data were obtained from 2 healthy subjects and 8 patients with idiopathic intracranial hypertension who were scanned before, immediately after, and 2 weeks after diagnostic lumbar puncture. Imaging included T1-weighted and T2-weighted sequences of the brain and T2-weighted scans of the spine. Repeat scans in 4 subjects were used to assess measurement reproducibility. Whole CNS CSF volumes measured prior to and following lumbar puncture were compared with the withdrawn amounts of CSF.

**RESULTS:** CSF and cord volume measurements were highly reproducible with mean variabilities of $-0.7\% \pm 1.4\%$ and $-0.7\% \pm 1.0\%$, respectively. Mean spinal CSF volume was $77.5 \pm 8.4$ mL. The imaging-based pre- to post-CSF volume differences were consistently smaller and strongly correlated with the amounts removed ($R = 0.86$, $P = .006$), primarily from the lumbosacral region. These differences are explained by net CSF formation of $0.41 \pm 0.18$ mL/min between withdrawal and imaging.

**CONCLUSIONS:** Automated measurements of the craniospinal CSF redistribution following lumbar withdrawal in idiopathic intracranial hypertension reveal that the drop in intracranial pressure following lumbar puncture is primarily related to the increase in spinal compliance and not cranial compliance due to the reduced spinal CSF volume and the nearly unchanged cranial CSF volume.

**ABBREVIATIONS:** IIH = idiopathic intracranial hypertension; LP = lumbar puncture

The total amount of CSF and its craniospinal distribution are important for understanding of CSF-related brain and spinal cord disorders and CSF physiology in general. Changes in CSF circulation or distribution between the cranium and spinal canal or both have been observed in several neurologic disorders, including Alzheimer disease,[1] idiopathic normal pressure hydrocephalus,[2] idiopathic intracranial hypertension (IIH),[3] and even during pregnancy.[4] A change in body posture also affects the craniospinal CSF distribution, with a shift from the cranium to the spinal canal contributing to the lower intracranial pressure observed in the upright-versus-supine postures.[5] CSF volume in the spinal canal is also influenced by abdominal compression and hyperventilation.[6] In addition, the amount of CSF in the thecal sac has been shown to influence the effectiveness of spinal anesthesia.[7] Not only the spinal CSF volume but also the spinal cord volume is of clinical relevance, especially for cord atrophy progression such as in multiple sclerosis.[8]

MR imaging–based automated methods of quantitation of brain tissues and intracranial CSF volumes[9,10] have considerably advanced the quantitative-based diagnostic capability of many neurologic problems, yet comparable methods for the spinal cord and the spinal CSF volumes are not widely available. Measurement of the spinal CSF volume in MR imaging is challenging because of the overall smaller volumes compared with the brain and cranial volumes and due to the length of the spinal canal, which necessitates the use of multiple overlapping acquisitions with potentially varying image nonuniformity.

Received November 25, 2015; accepted after revision April 19, 2016.

From the Department of Radiology (N.A., A.M.B., S.H.L.), University of Miami, Miami, Florida; and Bascom Palmer Eye Institute (B.L.L.), University of Miami, Miami, Florida.

This study was funded by a seed grant from the North American Neuro-Ophthalmology Society.

Paper previously presented in part at: Annual Meeting of the American Society of Neuroradiology and the Foundation of the ASNR Symposium, May 21–26, 2016; Washington DC.

Please address correspondence to Noam Alperin, PhD, Department of Radiology, University of Miami, Professional Arts Center, Suite 713, 1150 NW 14th St, Miami, FL 33136; e-mail: NAlperin@med.miami.edu

http://dx.doi.org/10.3174/ajnr.A4837

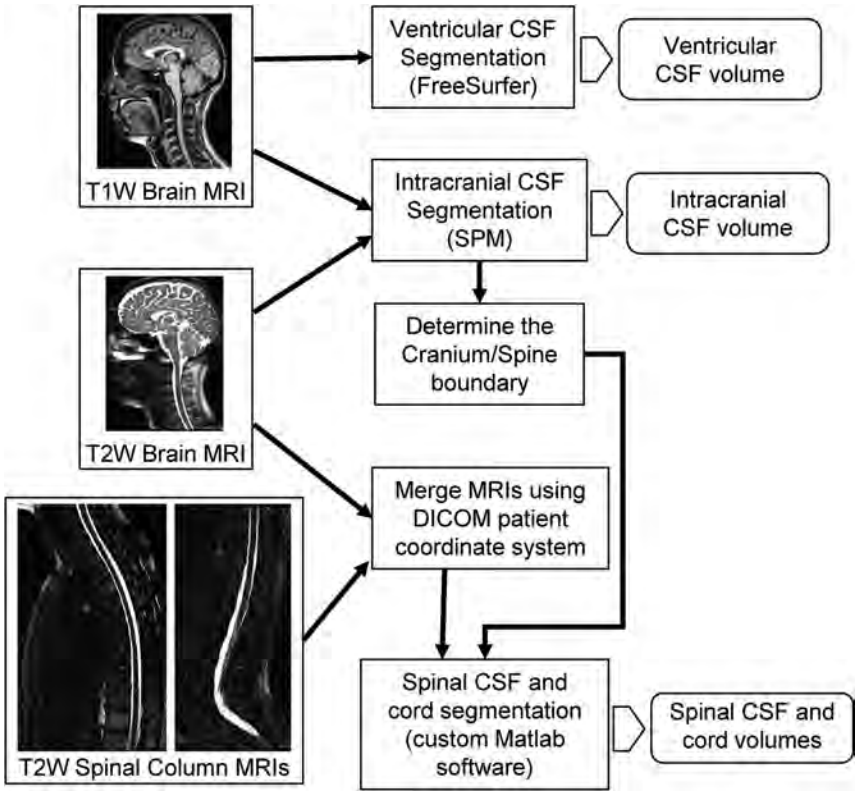


**FIG 1.** Flow chart of the CSF segmentation method. T1- and T2-weighted brain images are used to obtain the ventricular and intracranial CSF volumes by using publicly available software packages. Spinal CSF and cord volumes are obtained using the 3 T2-weighted scans with a custom-developed software.

Previous studies on dose response in epidural anesthesia focused on measurements of the CSF volumes in the low thoracic and lumbosacral regions.[4,6,11] The CSF volume in the whole spinal canal was reported only in a small number of studies that were constrained by limited image resolution and manual delineation of the CSF space.[11,12] A recent advancement toward automated spinal CSF volume measurements is the development of a method that uses thresholding and voxel connectivity.[13] Recent effort in the assessment of spinal cord atrophy in multiple sclerosis includes semiautomated approaches for the measurement of the cord cross-sectional areas in both cervical and thoracic regions.[14]

This article describes an iterative method of delineating the CSF spaces and the spinal cord throughout the spinal canal. Measurement reproducibility was assessed from repeat measurements in the same subjects. The method efficacy is demonstrated by its application to studying the impact of CSF withdrawal by lumbar puncture (LP) on the craniospinal CSF redistribution in IIH. Only limited information on CSF redistribution following withdrawal is available, even though this is a commonly used diagnostic procedure in CSF-related disorders.

## MATERIALS AND METHODS

### Study Participants

Data from a cohort of 8 overweight women (age 29 ± 6 years; range, 19–37 years; mean body mass index: 34 ± 7 kg/m$^2$; range, 26–43 kg/m$^2$) who underwent lumbar puncture for the suspected diagnosis of IIH and from 2 healthy female subjects (ages, 27 and 31 years; body mass index, 20 and 27 kg/m$^2$) were used in the evaluation of the method. Written informed consent was obtained on enrollment, and the study was approved by the institutional review board. Each of the 8 patients underwent 3 MR imaging scans, immediately before and after (22 ± 7 minutes) diagnostic lumbar puncture and a follow-up scan 15 ± 5 days (range, 8–23 days) after lumbar puncture. In 4 subjects, MR imaging was repeated to assess measurement reproducibility and as a control for the subjects who underwent CSF withdrawal between scans.

Lumbar punctures were performed as a routine clinical procedure by a neurologist by using a 20-ga needle. The procedure was performed in a room adjacent to the MR imaging suite, with the patient in a lateral recumbent position. The CSF drainage was continued until 15–20 mL of fluid was collected or until the flow stopped. Following LP, all patients reported improvement of symptoms with no relapse at the follow-up MR imaging, and none reported post-LP headache.

### MR Imaging Acquisition

MR imaging studies were performed by with a 1.5T scanner (Symphony; Siemens, Erlangen, Germany) and the scanner-integrated Tim head, neck, and spine coils. Volumetric assessment of the cranial compartments was obtained from 3D T1-weighted and T2-weighted MPRAGE and sampling perfection with application-optimized contrasts by using different flip angle evolution (SPACE; Siemens) sequences, respectively. Imaging parameters of the T1-weighted scans included TR/TE/TI of 2200/2.37/1000 ms, flip angle of 8°, FOV of 25.6 × 22.4 cm, 1-mm isotropic resolution, and scan duration of 4 minutes and 15 seconds. Imaging parameters for the T2-weighted scan included the following: TR/TE of 1800/193 ms, flip angle of 150°, FOV of 25.0 × 23.8 cm, 1-mm isotropic resolution with scan duration of 3 minutes and 15 seconds. The spinal column was imaged by using 2 separate 3D T2-weighted scans with approximately 10% overlap in coverage with TR/TE of 1500/245 ms; flip angle of 120°; FOV of 30 × 30 cm; acquisition matrix of 330 × 330 with no zero-filling, yielding 0.9-mm isotropic voxels; and scan duration of 5 minutes each. Images were acquired in the sagittal orientation.

### Segmentation of the Craniospinal CSF Volume

The flowchart of the procedure for segmentation of the entire spinal canal CSF and spinal cord is shown in Fig 1. The ventricular and intracranial CSF volumes were quantified by using the publicly available FreeSurfer (http://surfer.nmr.mgh.harvard.edu) and SPM8 software (http://www.fil.ion.ucl.ac.uk/spm/) packages,[9,10] respectively. The method for the segmenta-

tion of the spinal CSF and cord volumes was implemented in Matlab, Version 2015a (MathWorks, Natick, Massachusetts).

### Segmentation of Intracranial CSF Volume

Delineation of the ventricles was obtained from T1-weighted sequences with the FreeSurfer software,[9] which uses an atlas-based method as prior information in a Bayesian parameter estimation framework to identify several brain regions, including the ventricular system.

Intracranial CSF was obtained with the New Segment tool in SPM8 software, which allows multitechnique segmentation by using both T1-weighted and T2-weighted images and incorporates a priori spatial information by using tissue probability maps.[10] Regions outside the cranium with image intensity like CSF (eg, vitreous humor) were removed from the final segmentation by using a skull mask generated by the FSL Brain Extraction Tool (http://fsl.fmrib.ox.ac.uk/fsl/fslwiki/BET).[15] The coordinates of the most inferior axial section containing CSF segmentation are automatically determined and used to initialize the automated segmentation of the spinal CSF.

### Segmentation of Spinal CSF and Spinal Cord

Before spinal canal CSF segmentation, T2-weighted scans of the cranium and cervical-thoracic and thoracic-lumbar regions were merged on the basis of the patient coordinates. The CSF and cord segmentation was initialized at the coordinates of the most inferior voxels of CSF from intracranial segmentation. The segmentation was performed automatically on axial reformatted sections, superior-to-inferior. A Laplacian of Gaussian filter ($\sigma = 1.2$ mm, filter size $= 9 \times 9$ mm) was then applied to enhance the CSF/cord edge pixels. The resulting edge-enhanced image is then convolved with 2D-matched filters to detect the size and the position of the cord. The filter kernels, optimized to detect elliptic structures, varied from 5- to 15-mm diameter and were elliptic with varying aspect ratios from 1:1 to 1:2. The shape, location, and size of the cord are determined on the basis of the filter kernel with the highest frequency response. This initial boundary is further refined by moving the boundary pixels to the zero-crossings on the edge-enhanced image within a 1-mm range. The spinal CSF is segmented by using an active contour algorithm[16] on the edge-enhanced image. Segmentation of the consecutive sections is separated into 2 different regions: the cervical and thoracic regions that include a cord and a lumbar region that does not include a cord. The location of the center voxel of the CSF segmentation serves as the initialization point for segmentation on the next axial slide. The volume of the CSF in the spinal canal is then obtained by summation of the voxels identified as spinal canal CSF. Additionally, the cross-sectional area of the CSF spaces along the spinal column was determined to assess the redistribution of CSF along the spinal canal following CSF withdrawal.

### Assessment of CSF Volumes before and after Lumbar Puncture

The cranial and spinal CSF volumes measured by MR imaging before the lumbar puncture scan were compared with values measured after lumbar puncture and follow-up scans. The locations along the space where there was a change in the CSF volume were identified by plotting the mean difference between pre- and post-lumbar puncture cross-sectional areas with respect to the distance from the foramen magnum. The amount of CSF collected during lumbar puncture was compared with differences in the CSF volume measured by MR imaging pre- to post and pre- to follow-up scans. The effective CSF formation rate was estimated to account for CSF formed between the lumbar puncture and the MR imaging acquisition.

### Measurement Reproducibility and Accuracy

Measurement reproducibility of spinal canal CSF and cord volume was assessed by calculating the mean and SD of the relative and absolute differences between the 2 repeat scans. Calibration of the volume measurement was assessed by using a CSF canal-like water phantom built by using a 42-cm rod with a diameter of 1.2 cm inserted into a 56-cm-long hollow tube with an inner diameter of 2.6 cm. The phantom was filled with 252.5 mL of water, as measured with a graduated cylinder. The phantom was scanned by using the same imaging parameters as those used for subjects.

### Statistical Analysis

The within-subject differences in CSF and cord volumes were tested for statistical significance by using paired *t* tests following testing for normality by using the Shapiro-Wilk test. Associations between pre- to post-lumbar puncture differences in CSF volume and the amounts withdrawn were tested by calculating the Pearson correlation coefficient. A $P$ value $< .05$ was considered significant. The intersubject variability for CSF volume of each compartment was calculated as the ratio of its mean to SD. The repeatability coefficient (ie, the maximum difference that is expected to occur between repeat measurements) was calculated as 1.96 times the SD of the differences between the repeat measurements. All results are expressed as mean ± SD. All statistical analyses were performed by using MedCalc for Windows, Version 15.8 (MedCalc Software, Mariakerke, Belgium).

## RESULTS

The mean and SD of the relative and absolute differences in CSF volume measurements between repeat scans were $-0.5 \pm 1.0$ and $0.8 \pm 0.7$ mL, respectively, which correspond to a percentage difference of $-0.7 \pm 1.4\%$ and $1.1 \pm 0.9\%$, respectively, and a repeatability coefficient of 1.9 mL. The mean and SD and percentage differences in cord volume were $0.1 \pm 0.2$ mL and $-0.7 \pm 1.0\%$, respectively, with a repeatability coefficient of 0.4 mL. Absolute volume measurements obtained with the spine phantom demonstrated good accuracy with a small error of only 0.4%.

An example of whole craniospinal CSF segmentation is shown in Fig 2. Sample segmented spinal CSF spaces and cord segmentations in regions with and without cord are shown in Fig 3. Prelumbar puncture cranial CSF (intra- and extraventricular), spinal CSF, and cord volumes measured in each of the 8 patients are listed in Table 1. The mean total craniospinal CSF volume measured in the patient cohort was $258 \pm 35.6$ mL, with $164 \pm 32$ mL in the extraventricular (sulcal) cranial CSF spaces, $16.2 \pm 6.0$ mL in the ventricles, and $77.5 \pm 8.4$ mL in the spinal canal. CSF volumes in the different compartments varied among individuals,

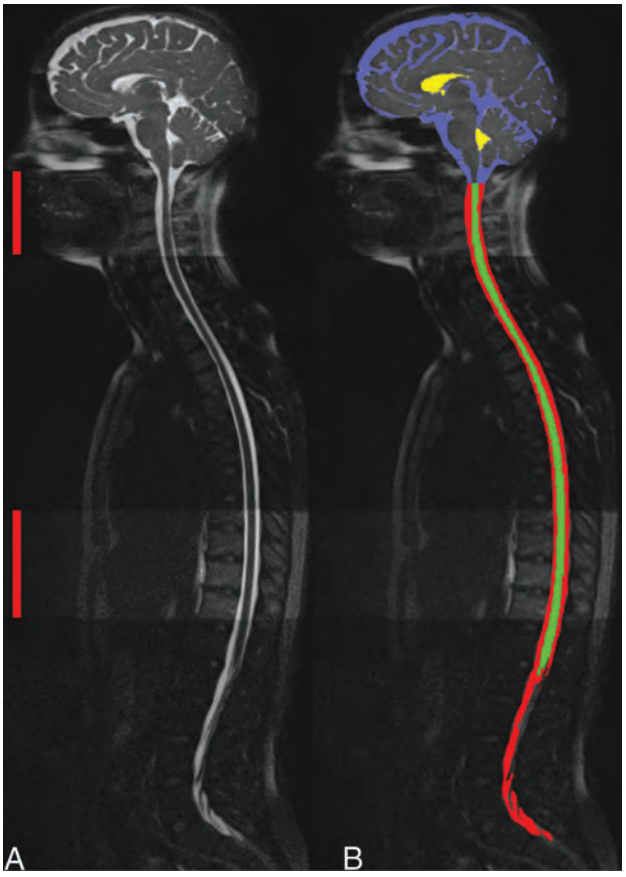


**FIG 2.** A mid-sagittal image demonstrating complete coverage of the CNS generated by merging 3 separate acquisitions (*A*) with overlapping coverage indicated by *red bars* on the left. *B*, Segmentation of cranial (blue), ventricular (yellow), and spinal (red) CSF and cord (green).

with the largest variability found in the ventricular CSF volume (37%) and smallest variability in the spinal CSF volume (11%). The mean cord volume was 21.0 ± 2.0 mL, with a relatively small interindividual variability of 10%.

The differences between the pre- and post-LP measurements of intracranial pressure and CSF volumes at the various craniospinal compartments for each of the 8 patients are listed in Table 2. Following lumbar puncture, closing pressure was significantly lower with a mean pressure change of −17 ± 8.6 cm $H_2O$ ($P$ = .002), and the measured total CSF volume was significantly reduced, as expected, by an average of −7.5 ± 2.9 mL ($P$ = .0002). Most of the change in CSF volume occurred in the spinal canal, with a mean value of −6.7 ± 3.2 mL ($P$ = .0007). A plot of the mean CSF cross-sectional area as a function of the distance from the foramen magnum obtained before and after lumbar puncture is shown in Fig 4*A*. The difference between these 2 plots is shown in Fig 4*B*, demonstrating that the reduction is primarily localized at the lumbosacral region. The spinal CSF volume measured at the 2-week post-LP-scan follow-up was still significantly lower than that of the pre-lumbar puncture by an average of 1.9 ± 1.7 mL ($P$ = .016). No significant differences were observed in the other compartments. As expected, no significant differences were measured in the cord volume between scans. Mean differences between the pre- and post-LP and the pre- and 2-week follow-up scans were −0.3 ± 0.5 and +0.1 ± 0.5 mL, respectively.

The difference in measured CSF volume in the spinal canal between the pre- and post-LP scans and the 2-week follow-up scan were linearly correlated with the withdrawn amount of CSF with strong correlation coefficients of $R$ = 0.86, $P$ = .006, and $R$ = 0.75, $P$ = .03, respectively. The scatterplots for these relationships are shown in Fig 5. The measured pre- to post-LP difference of 7.5 ± 2.9 mL was lower than the withdrawn amount of 15.8 ± 3.9 mL. Assuming that this difference is, in part, due to net CSF

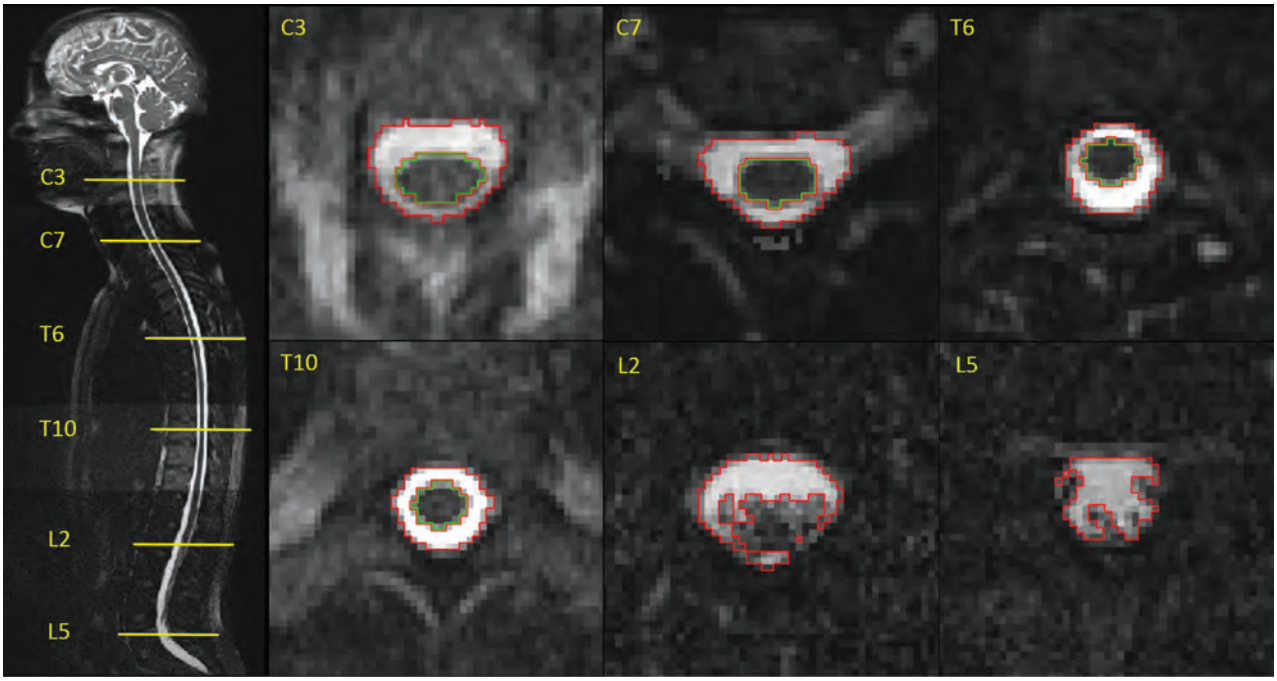


**FIG 3.** Sample CSF (red outline) and cord (green) segmentations along the spinal column at the level of C3, C7, T6, T10, L2, and L5 vertebrae.

**Table 1: Compartmental CSF volumes measured before lumbar puncture in patients**

| | Age (yr) | BMI | Opening Pressure (cm $H_2O$) | EVC CSF Vol (mL) | Ventricular CSF Vol (mL) | SC CSF Vol (mL) | Total CSF Vol (mL) | Cord Vol (mL) |
|---|---|---|---|---|---|---|---|---|
| Subject No. | | | | | | | | |
| 1 | 28 | 34 | 39 | 164 | 18.9 | 86.7 | 269 | 20.8 |
| 2 | 37 | 33 | 45 | 169 | 15.6 | 83.1 | 268 | 23.5 |
| 3 | 19 | 26 | 17 | 157 | 16.4 | 76.8 | 250 | 21.9 |
| 4 | 33 | 27 | 29 | 171 | 11.6 | 77.3 | 260 | 20.7 |
| 5 | 28 | 43 | 34 | 213 | 12.8 | 67.6 | 293 | 19.9 |
| 6 | 32 | 40 | 34 | 166 | 28.9 | 89.8 | 285 | 23.9 |
| 7 | 30 | 41 | 25 | 176 | 15.8 | 68.9 | 261 | 18.8 |
| 8 | 22 | 30 | 40 | 98 | 9.2 | 69.9 | 177 | 18.6 |
| Mean | 29 ± 6 | 34 ± 6.7 | 33 ± 9.1 | 164 ± 31.8 | 16.2 ± 6.0 | 77.5 ± 8.4 | 258 ± 35.6 | 21.0 ± 2.0 |
| Variability (SD/Mean) | | | | 19% | 37% | 11% | 14% | 10% |

**Note:**—BMI indicates body mass index; EVC, extraventricular cranial; SC, spinal canal; Vol, volume.

**Table 2: Pre- to post-lumbar puncture changes in ICP and CSF volume differences in the various compartments, amounts of CSF withdrawn, and the calculated effective CSF production rates**

| | Closing-Opening Pressure (cm $H_2O$) | EVC CSF Vol Change (mL) | Ventricular CSF Vol Change (mL) | SC CSF Vol Change (mL) | Total CSF Vol Change (mL) | Amount of CSF Collected (mL) | Effective CSF Production Rate (mL/min) |
|---|---|---|---|---|---|---|---|
| Subject No. | | | | | | | |
| 1 | NA | −1.6 | 0.0 | −5.3 | −6.9 | −16.0 | 0.25 |
| 2 | −26 | −2.0 | −0.1 | −6.2 | −8.2 | −16.0 | 0.24 |
| 3 | −3 | −3.6 | −0.1 | −6.0 | −9.6 | −14.0 | NA[a] |
| 4 | −15 | 0.7 | 0.2 | −3.3 | −2.5 | −14.0 | 0.65 |
| 5 | −16 | 2.0 | 0.1 | −12.7 | −10.5 | −21.0 | 0.43 |
| 6 | −20 | −1.6 | −0.6 | −8.1 | −10.3 | −20.0 | 0.63 |
| 7 | −12 | −1.0 | −0.2 | −2.7 | −3.9 | −8.5 | 0.24 |
| 8 | −28 | 0.8 | 0.1 | −9.1 | −8.2 | −17.0 | 0.40 |
| Mean | −17 ± 8.6 | −0.8 ± 1.8 | −0.1 ± 0.2 | −6.7 ± 3.2 | −7.5 ± 2.9 | −15.8 ± 3.9 | 0.41 ± 0.18 |
| *P* value | .002[b] | .24 | .45 | .0007[b] | .0002[b] | | |

**Note:**—ICP indicates intracranial pressure; NA, not available; EVC, extraventricular cranial; SC, spinal canal; Vol, volume.
[a] Effective CSF production rate for subject 3 was not calculated because the lumbar puncture time was not available.
[b] Significant.

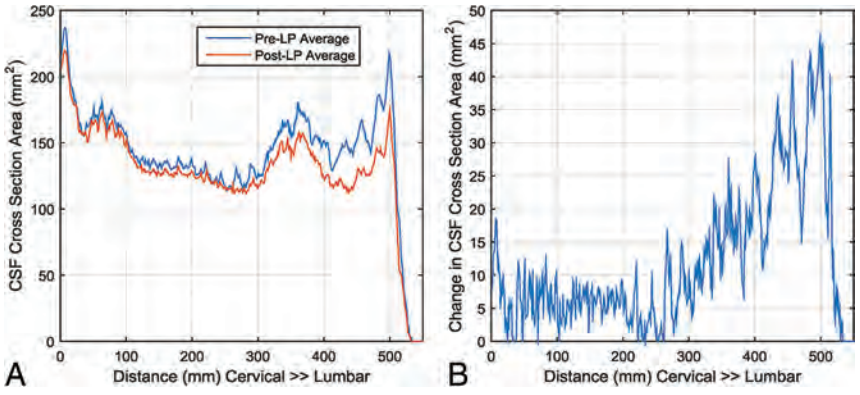


**FIG 4.** Average CSF cross-sectional area before and after lumbar puncture (*A*) and average change in CSF cross-sectional area following CSF withdrawal with respect to the distance from the foramen magnum to the caudal end of the thecal sac (*B*).

formed between the LP and MR imaging, we calculated a mean effective net CSF formation rate of 0.41 ± 0.18 mL/min. The calculated net CSF production rates for each subject are listed in Table 2.

## DISCUSSION

The method for segmentation of the spinal CSF spaces and spinal cord demonstrated highly reproducible measurements with a measurement variability of around 1% for both the spinal CSF and cord volumes. This method, in combination with existing methods for segmentation of the cranial CSF and brain tissue volumes, provides means for determining normative and altered spinal CSF volumes in the healthy and disease states, respectively. The improved performance of the method is attributed to the iterative approach to overcome biases due to image nonuniformities associated with large anatomic coverage.

The mean spinal CSF volume measured in a cohort of patients with IIH of 77.5 ± 8.4 mL is comparable with a previously reported value of 76 ± 23 mL measured in a healthy cohort of mixed sex (5 men/7 women) and a wide age range (25–84 years).[13] The much wider SD measured in that study is likely due to the mixed sex and wider age range. A slightly larger spinal CSF volume of 81 ± 13 mL was reported in 22 healthy elderly subjects (11 men/11 women) (70 ± 4 years), but most interesting, the cord volume of 20 ± 3 mL measured manually in that study[12] is similar to the value of 21.0 ± 2.0 mL measured in the current cohort.

The automated measurement of the spinal CSF volumes was applied to investigate interindividual variability in different compartments and the redistribution of the CSF volume in the craniospinal system following removal via lumbar puncture. Inter-

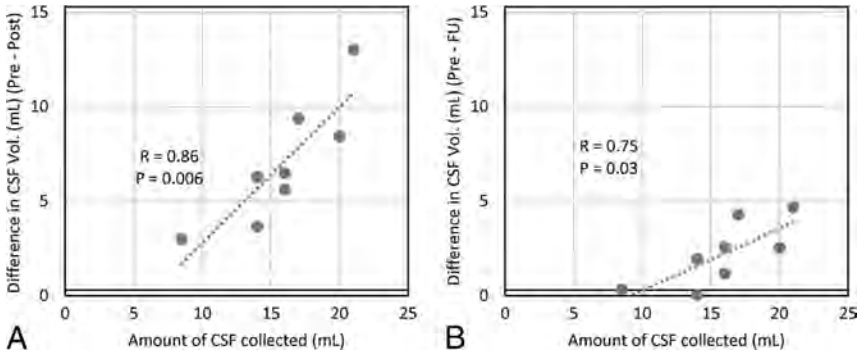


**FIG 5.** The relationship between the CSF volume withdrawn during lumbar puncture and CSF volume change in the spinal canal between the pre- and post-lumbar puncture scan (*A*) and the pre- and the 2-week follow-up scan (*B*) as measured by the proposed method.

estingly, the interindividual variability in CSF volumes in the IIH cohort was largest in the ventricles and smallest in the spinal canal. Automated whole CNS segmentation provides the means to determine the role of the spinal CSF volume in various diseases.

Craniospinal redistribution of the CSF volumes following withdrawal of CSF has not been reported previously. A small reduction of 1.4% in ventricular volume was reported following high-volume CSF withdrawal in elderly patients with normal pressure hydrocephalus.[2] In contrast, in our study of younger patients with IIH, the ventricular volume was unchanged following CSF withdrawal. This finding can be partly attributed to the much smaller ventricular volume (16.2 versus 160 mL) and the smaller amount of CSF removed (15.8 versus 35 mL) in the current study.

This study provides important insight into the pathophysiology of IIH. The reduction in CSF volume following lumbar puncture was predominantly from the spinal compartment, with nearly unchanged CSF volume in the cranial compartment. This finding implies that the drop in opening pressure following LP in IIH while the patients are in the supine posture is primarily due to an increase in the spinal canal compliance and less due to changes in the cranial compartment. The increased spinal canal compliance measured in the supine posture has implications for the upright posture because it allows larger amounts of CSF to shift from the cranium into the spinal canal following a change from a supine to an upright posture. This result, in turn, leads to a larger decrease in intracranial pressure in the upright posture. This observation that CSF volume reduction following LP is primarily from the spinal canal is consistent with a previous report that obesity-related IIH is associated with reduced spinal canal compliance.[17] It seems that the therapeutic effect of CSF withdrawal by LP in IIH is achieved by improving the impaired spinal canal compliance.

The reduction in the spinal CSF volume was found to be localized primarily to the lumbar region. This finding is consistent with previous findings that regional compliance varies along the spinal canal, with the lumbar region providing the largest contribution to the overall spinal compliance.[18] This is also consistent with radionuclide cisternography studies in which tracer injected into the lumbar region demonstrated slow dispersion along the spinal canal and the tracer distribution after 30 minutes was still localized to the lower lumbar region,[19] similar to the pattern of volume difference shown in Fig 4*B* in our study. The possibility of changing the spinal canal compliance locally by CSF withdrawal demonstrated in this study has important implications for the delivery of spinal anesthesia because the magnitude of the compliance at the lumbar region strongly influences the rate of dispersion of injected material in the CSF spaces.

Measurements of the entire CSF volume before and after CSF withdrawal in conjunction with other approaches for measurement of CSF formation rates[20] are potentially useful for understanding the impact of treatment on CSF homeostasis in IIH. The imaging-based measurements of reduction in the craniospinal CSF volumes were consistently smaller than the withdrawn amounts. This outcome is not likely due to a measurement error, which would have resulted in both positive and negative changes. The most likely explanation for the smaller measured differences is a net CSF formation that occurred during nearly half an hour between the LP and the post-LP MR imaging. The effective increase in the net rate of CSF formation is well-explained by a lower CSF absorption rate caused by the lower intracranial pressure.[21] An effective net formation rate was derived on the basis of the differences between the withdrawn and measured CSF volumes. The estimated mean effective formation rate of 0.41 $\pm$ 0.18 mL/min is larger than the normative value of 0.30 $\pm$ 0.14 mL/min reported in healthy subjects[20] but similar to the CSF formation rate of 0.44 $\pm$ 0.28 mL/min previously reported in 11 female patients with IIH and obesity.[22] Another interesting finding is that the measured pre- to post-lumbar puncture differences in the CSF volumes were strongly correlated with the amount withdrawn, even at the 2-week follow-up MR imaging; this finding is consistent with reports in the literature of improved symptoms for 2 weeks following lumbar puncture.[23]

Limitations of this study are the relatively small number of patients, with one patient not meeting the modified Dandy criteria for IIH due to normal opening pressure. Another possible limitation is the lack of comparison with manually segmented CSF spaces. On the other hand, manual segmentations are not only time-consuming but also highly variable; thus, they may not be a reliable criterion standard. The use of a phantom, repeat measurements in the same subjects, and measurement before and after lumbar withdrawals provided an alternative approach for assessment of the reliability of the method. Finally, performing the CSF volume measurements in only the supine posture is another limitation of the study.

## CONCLUSIONS

An automated method for delineation of the spinal CSF spaces has been developed and applied to study the effect of lumbar CSF withdrawal on the craniospinal CSF redistribution in IIH. The study reveals that the drop in the opening pressure following CSF withdrawal is related to an increase in the spinal canal compliance caused by reduction in spinal CSF volume localized to the lumbar region. The study demonstrates the importance of the spinal com-

partment in intracranial pressure regulation and the benefit of automated craniospinal CSF volumetry to further elucidate the pathophysiology of CSF-related diseases.

Disclosures: Noam Alperin—*UNRELATED*: *Board Membership*: Alperin Noninvasive Diagnostics. Byron L. Lam—*RELATED*: *Grant*: North American Neuro-Ophthalmology Society pilot grant.* *Money paid to the institution.

## REFERENCES


1. Silverberg GD, Heit G, Huhn S, et al. **The cerebrospinal fluid production rate is reduced in dementia of the Alzheimer's type.** *Neurology* 2001;57:1763–66 CrossRef Medline
2. Singer OC, Melber J, Hattingen E, et al. **MR volumetric changes after diagnostic CSF removal in normal pressure hydrocephalus.** *J Neurology* 2012;259:2440–46 CrossRef Medline
3. Alperin N, Ranganathan S, Bagci AM, et al. **MRI evidence of impaired CSF homeostasis in obesity-associated idiopathic intracranial hypertension.** *AJNR Am J Neuroradiol* 2013;34:29–34 CrossRef Medline
4. Onuki E, Higuchi H, Takagi S, et al. **Gestation-related reduction in lumbar cerebrospinal fluid volume and dural sac surface area.** *Anesth Analg* 2010;110:148–53 CrossRef Medline
5. Alperin N, Lee SH, Sivaramakrishnan A, et al. **Quantifying the effect of posture on intracranial physiology in humans by MRI flow studies.** *J Magn Reson Imaging* 2005;22:591–96 CrossRef Medline
6. Lee RR, Abraham RA, Quinn CB. **Dynamic physiologic changes in lumbar CSF volume quantitatively measured by three-dimensional fast spin-echo MRI.** *Spine (Phila Pa 1976)* 2001;26:1172–78 CrossRef Medline
7. Higuchi H, Adachi Y, Kazama T. **The influence of lumbosacral cerebrospinal fluid volume on extent and duration of hyperbaric bupivacaine spinal anesthesia: a comparison between seated and lateral decubitus injection positions.** *Anesth Analg* 2005;101:555–60 CrossRef Medline
8. Rashid W, Davies GR, Chard DT, et al. **Increasing cord atrophy in early relapsing-remitting multiple sclerosis: a 3 year study.** *J Neurol Neurosurg Psychiatry* 2006;77:51–55 CrossRef Medline
9. Fischl B, Salat DH, Busa E, et al. **Whole brain segmentation: automated labeling of neuroanatomical structures in the human brain.** *Neuron* 2002;33:341–55 CrossRef Medline
10. Ashburner J, Friston KJ. **Unified segmentation.** *Neuroimage* 2005;26:839–51 CrossRef Medline
11. Hogan QH, Prost R, Kulier A, et al. **Magnetic resonance imaging of cerebrospinal fluid volume and the influence of body habitus and abdominal pressure.** *Anesthesiology* 1996;84:1341–49 CrossRef Medline
12. Edsbagge M, Starck G, Zetterberg H, et al. **Spinal cerebrospinal fluid volume in healthy elderly individuals.** *Clin Anat* 2011;24:733–40 CrossRef Medline
13. Lebret A, Hodel J, Rahmouni A, et al. **Cerebrospinal fluid volume analysis for hydrocephalus diagnosis and clinical research.** *Comput Med Imaging Graph* 2013;37:224–33 CrossRef Medline
14. Horsfield MA, Sala S, Neema M, et al. **Rapid semi-automatic segmentation of the spinal cord from magnetic resonance images: application in multiple sclerosis.** *Neuroimage* 2010;50:446–55 CrossRef Medline
15. Smith SM. **Fast robust automated brain extraction.** *Hum Brain Mapp* 2002;17:143–55 CrossRef Medline
16. Chan TF, Vese LA. **Active contours without edges.** *IEEE Trans Image Process* 2001;10:266–77 CrossRef Medline
17. Tain RW, Bagci AM, Lam BL, et al. **Determination of cranio-spinal canal compliance distribution by MRI: methodology and early application in idiopathic intracranial hypertension.** *J Magn Reson Imaging* 2011;34:1397–404 CrossRef Medline
18. Yallapragada N, Alperin N. **Characterization of spinal canal hydrodynamics and compliance using bond graph technique and CSF flow measurements by MRI.** In: *Proceedings of the Scientific Meeting and Exhibition of the International Society for Magnetic Resonance in Medicine,* Kyoto, Japan. May 15–21, 2004:2658
19. Greitz D, Hannerz J **A proposed model of cerebrospinal fluid circulation: observations with radionuclide cisternography.** *AJNR Am J Neuroradiol* 1996;17:431–38 Medline
20. Huang TY, Chung HW, Chen MY, et al. **Supratentorial cerebrospinal fluid production rate in healthy adults: quantification with two-dimensional cine phase-contrast MR imaging with high temporal and spatial resolution.** *Radiology* 2004;233:603–08 CrossRef Medline
21. Cutler RW, Page L, Galicich J, et al. **Formation and absorption of cerebrospinal fluid in man.** *Brain* 1968;91:707–20 CrossRef Medline
22. Alperin N, Lam BL, Tain RW, et al. **Evidence for altered spinal canal compliance and cerebral venous drainage in untreated idiopathic intracranial hypertension.** *Acta Neurochir Suppl* 2012;114:201–05 CrossRef Medline
23. Scoffings DJ, Pickard JD, Higgins JN. **Resolution of transverse sinus stenoses immediately after CSF withdrawal in idiopathic intracranial hypertension.** *J Neurol Neurosurg Psychiatry* 2007;78:911–12 CrossRef Medline

# Dual-Energy CT and Spot Sign

We read with great interest the article published by Morotti et al, "Effect of CTA Tube Current on Spot Sign Detection and Accuracy for Prediction of Intracerebral Hemorrhage Expansion."[1] We agree with the authors that the spot sign and also the newly described "leakage sign"[2] represent very useful signs to predict expansion of intracranial hemorrhage of different origins. However, the optimal CT protocol to detect the spot sign is still unknown, and it is not known if new techniques such as dual energy will improve its detection. This is of great importance because the spot sign has changed the way patients with intracranial hemorrhage are managed acutely. It is well known that dual-energy CT increases the sensitivity for the detection of ischemia in patients after mechanical thrombectomy,[3] and it is also very useful to differentiate between hemorrhage and contrast media.[4] The question is, what about the spot sign and dual energy?

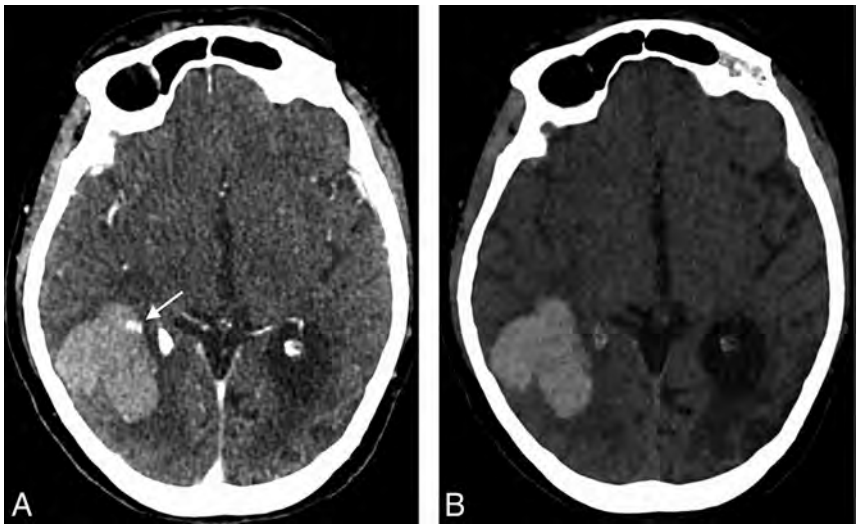


**FIG 1.** CT (80 Kv) performed with a Siemens machine after contrast agent shows the spot sign in a patient with intracerebral hemorrhage (*A*, *arrow*). The spot sign disappears on the virtual unenhanced image (*B*).

We have to pay attention to the use of new technologies such as dual-energy CT and these signs because the spot or leakage sign corresponds to leakage of contrast medium, and these might disappear with dual energy in a patient with hemorrhage (Fig 1). Further, the nonvisualization of the spot sign or low sensitivity on CTA (53%) as described by Orito et al[2] might be due to the CTA being done in dual energy.

## REFERENCES

1. Morotti A, Romero JM, Jessel MJ, et al. **Effect of CTA tube current on spot sign detection and accuracy for prediction of intracerebral hemorrhage expansion.** *AJNR Am J Neuroradiol* 2016 May 19. [Epub ahead of print] CrossRef Medline
2. Orito K, Hirohata M, Nakamura Y, et al. **Leakage sign for primary intracerebral hemorrhage: a novel predictor of hematoma growth.** *Stroke* 2016;47:958–63 CrossRef Medline
3. Gariani J, Cuvinciuc V, Courvoisier D, et al. **Diagnosis of acute ischemia using dual energy CT after mechanical thrombectomy.** *J Neurointerv Surg* 2015 Nov 3. [Epub ahead of print] CrossRef Medline
4. Tijssen MP, Hofman PA, Stadler AA, et al. **The role of dual energy CT in differentiating between brain haemorrhage and contrast medium after mechanical revascularisation in acute ischaemic stroke.** *Eur Radiol* 2014;24:834–40 CrossRef Medline

**M.I. Vargas**
**K. Lovblad**
Division of Neuroradiology
Department of Medical Imaging
Geneva University Hospital
Geneva, Switzerland

http://dx.doi.org/10.3174/ajnr.A4894

***REPLY:***

We thank Drs Vargas and Lovblad for their interest and comments on our article investigating the influence of CTA tube current on spot sign detection and prediction of intracerebral hemorrhage expansion. The role of dual-energy CT (DECT) in spot sign identification has not been extensively and systematically investigated, to our knowledge, and we agree that more research on the use of this technique is needed. DECT can distinguish different types of materials with high sensitivity and specificity.[1,2] As shown in the figure provided by Drs Vargas and Lovblad, DECT can remove spots of iodine extraction from the virtual noncontrast images and map them to the iodine-overlay images. The degree to which this separation is effective and the minimum concentration of extravasated iodine separable from hematoma, in situ, are currently unknown. Therefore, how the single-energy CT spot sign should be translated in the context of dual-energy remains a topic of research. For example, it is not clear whether one should be counting the number of spots on the iodine-overlay images or computing the total amount of extravasated iodine in the iodine-overlay images. We would like to highlight the following additional points:

1) There is great heterogeneity in the CTA acquisition protocol,[3] and several factors such as the time from stroke onset to CTA and acquisition of delayed images[4,5] can influence the rate of spot sign identification and its ability to identify patients at high risk of hematoma expansion. Therefore, the relatively low sensitivity (53%) reported by Du et al[6] in a recent meta-analysis cannot be directly attributed to the use of DECT.

2) It is difficult to compare the frequency and diagnostic performance of the spot sign across different studies because several definitions of spot sign and hematoma expansion have been reported and used in clinical practice.[4]

3) DECT has the ability to reduce artifacts and to remodel the signal-to-noise ratio[7] and may therefore provide an additional diagnostic value in case of poor-quality scans.

4) Vascular and nonvascular cerebral lesions like aneurysms or calcifications can mimic the spot sign,[8] and DECT appears superior to conventional CTA in the identification of these mimics.[7]

5) There are multiple implementations of DECT, and not all of them are dose-neutral compared with a single-energy CT scan. In general, the advantages of DECT use need to be balanced against the risk of increased radiation delivery.[9]

In conclusion, DECT is a promising technique, but its role in spot sign identification is still unclear.

http://dx.doi.org/10.3174/ajnr.A4887

## REFERENCES


1. Gupta R, Phan CM, Leidecker C, et al. **Evaluation of dual-energy CT for differentiating intracerebral hemorrhage from iodinated contrast material staining.** *Radiology* 2010;257:205–11 CrossRef Medline
2. Phan CM, Yoo AJ, Hirsch JA, et al. **Differentiation of hemorrhage from iodinated contrast in different intracranial compartments using dual-energy head CT.** *AJNR Am J Neuroradiol* 2012;33:1088–94 CrossRef Medline
3. Huynh TJ, Demchuk AM, Dowlatshahi D, et al; PREDICT/Sunnybrook ICH CTA Study Group. **Spot sign number is the most important spot sign characteristic for predicting hematoma expansion using first-pass computed tomography angiography: analysis from the PREDICT study.** *Stroke* 2013;44:972–77 CrossRef Medline
4. Brouwers HB, Goldstein JN, Romero JM, et al. **Clinical applications of the computed tomography angiography spot sign in acute intracerebral hemorrhage: a review.** *Stroke* 2012;43:3427–32 CrossRef Medline
5. Ciura VA, Brouwers HB, Pizzolato R, et al. **Spot sign on 90-second delayed computed tomography angiography improves sensitivity for hematoma expansion and mortality: prospective study.** *Stroke* 2014;45:3293–97 CrossRef Medline
6. Du F, Jiang R, Gu M, et al. **The accuracy of spot sign in predicting hematoma expansion after intracerebral hemorrhage: a systematic review and meta-analysis.** *PLoS One* 2014;9:e115777 CrossRef Medline
7. Postma AA, Das M, Stadler AA, et al. **Dual-energy CT: what the neuroradiologist should know.** *Curr Radiol Rep* 2015;3:16 CrossRef Medline
8. Gazzola S, Aviv RI, Gladstone DJ, et al. **Vascular and nonvascular mimics of the CT angiography "spot sign" in patients with secondary intracerebral hemorrhage.** *Stroke* 2008;39:1177–83 CrossRef Medline
9. Smith AB, Dillon WP, Gould R, et al. **Radiation dose-reduction strategies for neuroradiology CT protocols.** *AJNR Am J Neuroradiol* 2007;28:1628–32 CrossRef Medline



**A. Morotti**
Department of Clinical and Experimental Sciences, Neurology Clinic
University of Brescia, Brescia, Italy
J. P. Kistler Stroke Research Center
Massachusetts General Hospital, Harvard Medical School
Boston, Massachusetts
**J.M. Romero**
**R. Gupta**
Neuroradiology Service, Department of Radiology
Massachusetts General Hospital, Harvard Medical School
Boston, Massachusetts
**J.N. Goldstein**
J. P. Kistler Stroke Research Center
Department of Emergency Medicine
Massachusetts General Hospital, Harvard Medical School
Boston, Massachusetts

# Comment on "SAPHO Syndrome: Imaging Findings of Vertebral Involvement"

I have read with great interest the article by McGauvran et al[1] regarding an MR imaging study in patients with synovitis, acne, pustulosis, hyperostosis, and osteitis (SAPHO) syndrome. I fully agree with the authors both that the differentiation of SAPHO syndrome from spondyloarthropathies (SpA), especially psoriatic arthritis (PsA), is mandatory and that MR imaging could improve the understanding of the course of the disease and lead to an earlier diagnosis.

SAPHO syndrome is actually considered a rare disease, but growing awareness among dermatologists, radiologists, and rheumatologists is going to increase its diagnosis.

The peculiar bone involvement, represented by osteitis, is the common denominator of SAPHO syndrome, either by its radiologic appearance or its pathologic features (Table). In a case series described in *Arthritis and Rheumatism*, my colleagues and I indicated that sternocostoclavicular hyperostosis (SCCH) represented the first symptom in 70% of patients and was involved in about 80% of the cases.[2] In addition, many patients had a history of several admissions to the emergency department for a suspected acute cardiac event. It is of basic importance to distinguish patients with psoriatic arthritis from those with SAPHO syndrome with psoriasis. The paravertebral ossification seen in SAPHO syndrome is completely different from syndesmophytes; in fact, close observation of the published pictures may enable them to be properly defined as enthesophytes. Moreover, spine lesions are segmental in SAPHO syndrome. Besides, in SAPHO syndrome, the most typical symptom is a precocious anterior chest wall involvement, while inflammatory low back pain represents the most relevant clinical symptom in only a minority of patients. SCCH is the typical manifestation of SAPHO syndrome, representing the mainstay for diagnosis, but it is not pathognomonic for the disease. A similar involvement may also be seen in PsA. In PsA, however, SCCH is more frequently a late complication of the disease and does not usually involve the medial end of the clavicular. Thus, osteitis/hyperostosis of this difficult anatomic site (anterior chest wall) should be regarded as a distinguishing feature of SAPHO syndrome. In up to 20% of cases, cutaneous lesions may be lacking; thus, this form represents a purely rheumatologic variant of the disease.

**Proposed classification criteria of SAPHO syndrome (from Kahn MF,[4] 2003 ACR 67th Annual Scientific Meeting)**

| Classification Criteria |
|---|
| Inclusion |
| Bone ± joint involvement associated with PPP and PV |
| Bone ± joint involvement associated with severe acne |
| Isolated sterile hyperostosis/osteitis (adults)[a] |
| Chronic recurrent multifocal osteomyelitis (children) |
| Bone ± joint involvement associated with chronic bowel diseases |
| Exclusion |
| Infectious osteitis |
| Tumoral conditions of bone |
| Noninflammatory condensing lesions of bone |

[a] With the exception of *P acnes*.

I also agree with McGauvran et al[1] that misinterpretation of MR imaging usually leads to unnecessary biopsies. Nevertheless, the diagnosis of SAPHO syndrome could be challenging, and it is very important to be cautious in cases with involvement of soft tissues because it is necessary to exclude a malignancy.[3] Besides, in these cases, the biopsy may also be useful for directing the treatment in case of isolation of pathogens.

Although it has repeatedly been related to the SpA family, the emerging evidence suggests that SAPHO syndrome may be a primitive inflammatory osteitis. Different stimuli have been implicated as inciting factors, in particular the low-virulence pathogen *Propionibacterium acnes*, either alive or as dead antigens, but autoimmune or autoinflammatory mechanisms have not been ruled out. However, the etiopathogenesis of SAPHO syndrome and its nosology still remain largely enigmatic. If one combines bacteriologic, immunologic, and genetic data, an appealing hypothesis involves a pathogenetic sequence in which an opportunistic germ such as *P acnes*, a skin saprophyte, takes advantage of genetically determined deficiencies in antibacterial mechanisms and subsequently induces an autoamplification of the inflammatory response, supporting the concept of SAPHO syndrome as a reactive osteitis.

## REFERENCES

1. McGauvran AM, Kotsenas AL, Diehn FE, et al. **SAPHO syndrome: imaging findings of vertebral involvement.** *AJNR Am J Neuroradiol* 2016;37:1567–72 CrossRef Medline

http://dx.doi.org/10.3174/ajnr.A4912

2. Colina, Govoni M, Orzincolo C, et al. **Clinical and radiological evolution of synovitis, acne, pustulosis, hyperostosis, and osteitis syndrome: a single center study of a cohort of 71 subjects.** *Arthritis Rheum* 2009;61:813 CrossRef Medline
3. Colina M. **Diagnostic challenges of SAPHO syndrome.** *J Rheumatol* 2015;42:2514 CrossRef Medline
4. Kahn MF. **Proposed classification criteria of SAPHO syndrome.** In: *Proceedings of the Annual Meeting of the American College of Radiology*, Orlando, Florida. October 23–28, 2003

**M. Colina**
Rheumatology Service
Department of Internal Medicine and Oncology
Ospedale Santa Maria della Scaletta
Imola, Bologna, Italy

***REPLY:***

We thank Dr Colina for his comments regarding our recent article "SAPHO Syndrome: Imaging Findings of Vertebral Involvement."[1] We agree that growing awareness of SAPHO syndrome and its clinical and imaging findings will lead to earlier diagnosis.

In response to the comment that sternocostoclavicular hyperostosis represented the first symptom in 70% of the patients reported in the study by Colina et al,[2] 39% of the patients in our series had concurrent sternoclavicular involvement and 22% involvement of the first costovertebral joint, supporting this being a common symptom. We believe knowledge of the typical vertebral findings is critical in making an appropriate diagnosis in the substantial minority of patients who do not present with sternocostoclavicular hyperostosis.

Because our article focused on the unique spinal manifestations of SAPHO syndrome, we did not investigate the frequency with which patients in our series presented to the emergency department with chest pain or a coronary work-up. This would be an interesting area for further investigation.

Finally, we agree that the diagnosis of SAPHO syndrome is challenging and requires a multidisciplinary approach. In patients presenting with the unique curvilinear or semicircular pattern of contiguous vertebral involvement that we described along with sclerosis along ligamentous attachment sites and the absence of abnormal T2 hyperintensity and enhancement of the intervertebral disc, SAPHO syndrome should be included in the differential diagnosis. A search for the concurrent sternoclavicular involvement and consultation with dermatology and/or rheumatology colleagues to identify the typical skin manifestations may prevent misinterpretation of the imaging findings as discitis/osteomyelitis or metastases, with subsequent potential reduction in the number of unnecessary biopsies and delayed diagnoses.

http://dx.doi.org/10.3174/ajnr.A4913

## REFERENCES

1. McGauvran AM, Kotsenas AL, Diehn FE, et al. **SAPHO syndrome: imaging findings of vertebral involvement.** *AJNR Am J Neuroradiol* 2016;37:1567–72 CrossRef Medline
2. Colina, Govoni M, Orzincolo C, et al. **Clinical and radiological evolution of synovitis, acne, pustulosis, hyperostosis, and osteitis syndrome: a single center study of a cohort of 71 subjects.** *Arthritis Rheum* 2009;61:813 CrossRef Medline

**A.M. McGauvran**
**A.L. Kotsenas**
Department of Radiology
Mayo Clinic
Rochester, Minnesota

# Synthetic MR Imaging Sequence in Daily Clinical Practice

We read with great interest the article published in June by Granberg et al, "Clinical Feasibility of Synthetic MRI in Multiple Sclerosis: A Diagnostic and Volumetric Validation Study."[1] At the moment, another technique called MR fingerprinting allows quantitative T1, T2, and proton density measurements (and potentially other parameters such as diffusion) and has been presented at most MR imaging international meetings as very promising. Indeed, MR imaging quantification (through the MR fingerprinting method) was clearly expected to be "more accurate and reproducible than traditional MR imaging" by the European Society of Radiology.[2] However, its use in clinical daily practice is, at the moment, not consistently evaluated. Synthetic MR imaging is yielding identical outcomes for radiologists, which is, in our opinion, an enormous advantage. This is a more readily available technique which already gives us access to these quantified parameters on a daily basis thus allowing us to evaluate this future evolution of MR in today's clinical practice. In addition, synthetic MR imaging has the ability to produce morphologic conventional sequences, particularly in diseases such as multiple sclerosis, with considerable time-savings. Other clinical applications of this sequence, in our opinion, will be in oncologic patients and the assessment of hydrocephaly and the syndrome of the trephined,[3] due to its ability to efficiently and reliably quantify lesions in the brain parenchyma and also to detect increased or decreased volume of CSF.

Further developments are necessary, nevertheless, until its use in clinical routine and replacement of conventional sequences can be a reality. For instance, technical developments are needed, as mentioned in the article, to solve problems related to artifacts such as partial volume effects in FLAIR sequences, which may mimic a subarachnoid hemorrhage (this effect was also reported with MR fingerprinting methodology) (Fig 1).[4]

Finally, with the technical improvements likely to take place, we think this sequence could be applied to other organ systems for selected pathologies and that the related findings will be essential for the evolution to systematic quantitative MR imaging.

http://dx.doi.org/10.3174/ajnr.A4895

## REFERENCES

1. Granberg T, Uppman M, Hashim F, et al. **Clinical feasibility of synthetic MRI in multiple sclerosis: a diagnostic and volumetric validation study.** *AJNR Am J Neuroradiol* 2016;37:1023–29 CrossRef Medline
2. European Society of Radiology (ESR). **Magnetic resonance fingerprinting: a promising new approach to obtain standardized imaging biomarkers from MRI.** *Insights Imaging* 2015;6:163–65 CrossRef Medline
3. Vasung L, Hamard M, Soto MC, et al. **Radiological signs of the syndrome of the trephined.** *Neuroradiology* 2016;58:557–68 CrossRef Medline
4. Deshmane A, McGivney D, Badve C, et al. **Accurate synthetic FLAIR images using partial volume corrected MR fingerprinting.** In: *Proceedings of the Annual Meeting and Exhibition of International Society for Magnetic Resonance in Medicine*; Singapore. May 7–13, 2016; Poster No. 1909

**M.I. Vargas**
**J. Boto**
Division of Neuroradiology
**B.M. Delatre**
Division of Radiology
Department of Medical Imaging
Geneva University Hospital
Geneva, Switzerland

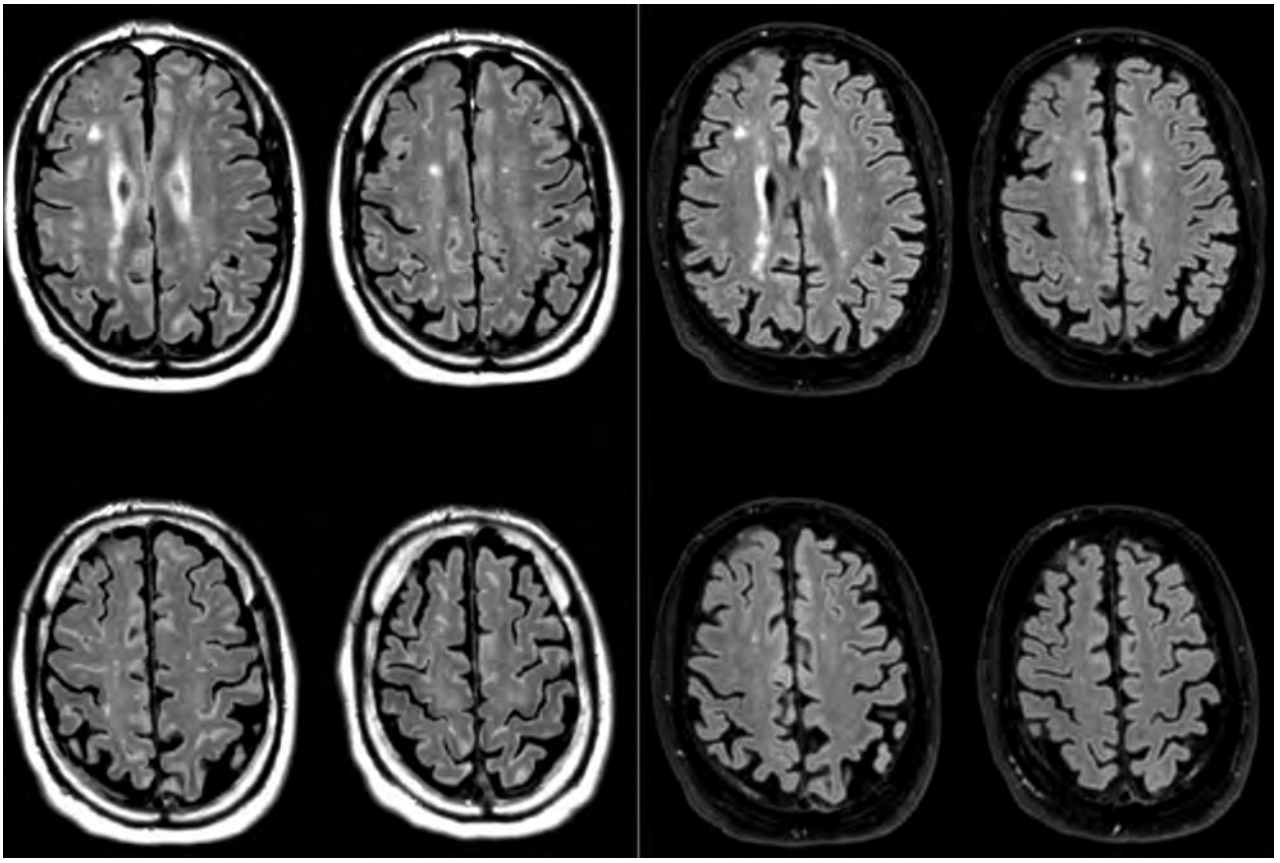

**FIG 1.** Four consecutive sections acquired with a synthetic MR imaging T2 FLAIR sequence (left) and a conventional FLAIR sequence (right) in the same patient at the same time. Note hyperintensities within and adjacent to the cerebral cortex on the synthetic sequence mimicking a subarachnoid hemorrhage. These abnormalities disappear on the conventional FLAIR sequence.

***REPLY:***

We thank Vargas et al for their interest in our work and agree that synthetic MR imaging indeed is a promising technique with many potential applications for both clinical practice and research. As the authors mention, there are similarities between synthetic MR imaging and MR fingerprinting in their potential to reduce scanning time and provide quantitative MR imaging measurements to more objectively characterize tissue properties.[1]

In terms of clinical applications, SyMRI (SyntheticMR, Linköping, Sweden) has come far in making the sequence available on clinical scanners and integrating the analysis software in the clinical PACS system, making it feasible for clinical practice.[2] Further validations of the technique are expected, and recently its quantification of proton-density, T1, and T2 have been shown to be accurate and reproducible, even with different coils.[3] These results are promising for multicenter and longitudinal use. A precision study of synthetic MR imaging across scanners and field strengths would, therefore, be especially valuable for future studies and is planned. There are also areas for future developments of the technique, in which FLAIR artifacts are currently being addressed. 3D and further accelerated acquisitions remain on the wish list. In our group, we are currently evaluating nonconventional synthetic contrast weightings, such as phase-sensitive inversion recovery for detecting cortical involvement in multiple sclerosis, and more advanced tissue modeling based on the relaxometry. Other likely future applications include spinal imaging and body imaging, such as musculoskeletal imaging.

Meanwhile, MR fingerprinting is still in the early phases of development with many promising applications. How and where these techniques can be applied and provide clinically important and possibly complementing information remains to be explored. As often found in MR imaging, the main bottleneck in terms of possibilities for both techniques is our imagination.[4]

http://dx.doi.org/10.3174/ajnr.A4896

## REFERENCES

1. European Society of Radiology (ESR). **Magnetic resonance fingerprinting: a promising new approach to obtain standardized imaging biomarkers from MRI.** *Insights Imaging* 2015;6:163–65 CrossRef Medline
2. Granberg T, Uppman M, Hashim F, et al. **Clinical feasibility of synthetic MRI in multiple sclerosis: a diagnostic and volumetric validation study.** *AJNR Am J Neuroradiol* 2016;37:1023–29 CrossRef Medline
3. Krauss W, Gunnarsson M, Andersson T, et al. **Accuracy and reproducibility of a quantitative magnetic resonance imaging method for concurrent measurements of tissue relaxation times and proton density.** *Magn Reson Imaging* 2015;33:584–91 CrossRef Medline
4. Ma D, Pierre EY, Jiang Y, et al. **Music-based magnetic resonance fingerprinting to improve patient comfort during MRI examinations.** *Magn Reson Med* 2016;75:2303–14 CrossRef Medline

**T. Granberg**
Department of Clinical Science, Intervention, and Technology
Karolinska Institutet
Stockholm, Sweden
Department of Radiology
Karolinska University Hospital
Stockholm, Sweden